Sheffield Hallam University

A Sheffield Hallam University thesis

A Mathematical and Experimental Analysis of Friction Stir Welding of Steel

Montadhar Al-Moussawi

A thesis submitted in partial fulfilment of the requirements of Sheffield Hallam University for the degree of Doctor of Philosophy

2018

Collaborating Organisation

TWI Yorkshire

Abstract

In the last decade there has been significant research into joining steel alloys using the Friction Stir Welding technique due to its ability to carry out welding below the melting point of the parent material and without using fillers such as in fusion welding techniques. This coincided with the increased use of DH36 and EH46 steel grades for ship building. The main reason for joining these steel grades by the friction stir welding technique is to reduce the weight of the vessel, as well as, the high welded joint quality especially mechanical properties such as fatigue and impact resistance. Other improved physical characteristics include increased tensile strength, microhardness and surface finish.

This research project has attempted to model friction stir welding using Computational Fluid Dynamics (CFD). Three different approaches have been used when considering the interface between the tool and the workpiece; these are torque, sticking/slipping and fully sticking. The project also investigates the mechanical properties of the welded joints including tensile, fatigue and microhardness. The microstructural evolution of welded joints carried out using different welding parameters is also investigated. The phenomenon of elemental precipitation/segregation during the friction stir welding process has been investigated and the limit of tool rotational speed at which the segregation occurs has been determined by modelling and also by heat treatment to simulate FSW. The purpose of the heat treatment trials was to attempt to replicate the temperature and time that the parent materials experiences during the FSW process. Defects in the weld joints associated with unsuitable friction stir welding parameters were also investigated and two new types of defect have been identified for the first time. Finally, tool wear has been investigated in the different weld joints in order to understand the suitable welding parameters that can prolong tool life.

The results from the mathematical modelling of FSW using CFD showed that the fully sticking assumption is the most effective approach for modelling friction stir welding of steel. The model also revealed that local melting at the advancing-trailing side of the tool is likely to occur at high tool rotational speeds. The experimental findings were in agreement with the results from the CFD model as the high tool rotational speed welded joints showed elemental segregation of Mn, Si, Al and O which only occurs when the peak temperature during welding approaches the melting point of steel.

Experimental work has also shown significant improvement in the mechanical properties of the welded joints in terms of fatigue and tensile strength after friction stir welding compared to the parent metal. However, the joints welded at high tool rotational/traverse speeds have shown lower mechanical properties as a result of defects such as weld root defect and microcrackes which have been introduced. Tool wear was found to increase with the increasing tool rotational speed as a result of the tools W-Re binder softening. Tool wear was also found to increase with increasing plunge depth as a result of the high shear stress originating from the high thermo-mechanical action at the FSW tool surface. The current project has contributed to knowledge in the friction stir welding of steel by revealing the limits of tool speed that causes elemental segregation. The new technique for estimating the peak temperature and cooling rate using TiN precipitates can also be an alternative to thermocouple measurements which can significantly underestimate the tool-workpiece interface temperature.

Project's Contribution to Knowledge for FSW of Steel.

The project has introduced new ideas and new techniques which can be a step forward to commercialize the FSW process of steel. The novel contributions are as follows:

- It was found that a non-metallic layer along the weld line has been formed between the SZ and HAZ in the high tool speeds welded joints (550 RPM, 400mm/min). This layer can affect the thermocouple's readings and increase the experimental error for the measurement of the peak temperature, so alternative methods of reading peak temperature were considered and introduced.

- Two new FSW defects have been identified,(1) a microcrack in the plunge-steady state region when using an unsuitable traverse speed. (2) Microcracks associated with precipitation of certain alloying elements such as TiN.

- The FSW process has been found to be very sensitive to plunge depth, parts of a millimetre can affect the heat generation, axial force values and defect formation.

- The introduction of an optimised stationary shoulder tool can address the issue of local melting, especially for high melting alloys with low thermal conductivity.

- The estimation of peak temperatures of FSW from the metallurgical examination and characterisation of TiN precipitates has been shown to be an alternative technique to using thermocouples.

- When CFD modelling the FSW process it has been shown that the fully sticking assumption, validated by elemental segregation, was the most effective way of assessing the tool-workpiece interface. Segregation of Mn, Al, Si and O was found to occur only when peak temperature reaches $1450^{\circ}C$.

Acknowledgements

Project Outcomes and Cooperation

The following journal and conference papers have been published as part of the project outcomes.

Conference Presentations.

- *AL-MOUSSAWI, M., SMITH, Alan , YOUNG, Andrew E, FARAJI, M. and CATER, S. (2016). An advanced numerical model of friction stir welding of DH36 steel. In: 11th International Symposium on Friction Stir Welding, TWI, Cambridge, 17-19 May 2016.*
- *Smith, Alan, Al-Moussawi, M., Young, Andrew E, Cater, S. and Faraji, M. (2016). Modelling of friction stir welding of 304 stainless steel. In: European Simulation and Modelling Conference, Univ. of Las Palmas, 26-28th October 2016.*
- *M. Al-Moussawi A J Smith, The Mechanism of Mn, Si, Al and O segregation in FSW of DH36 Steel, 8th International Conference and Exhibition on Materials Science and Engineering, May 29-31, 2017 Osaka, Japan.*

Journal Publications

- *M. Al-Moussawi, A. J. Smith, A. Young, S. Cater & M. Faraji, 2017, Modelling of friction stir welding of DH36 steel, Int J Adv Manuf Technol, Published online 24 Feb 2017 on 10.1007/s00170-017-0147-y.*
- *M. Al-Moussawi A J Smith, Thermo-Mechanical effect on Poly Crystalline Boron Nitride Tool life During Friction Stir Welding (Dwell Period), Accepted paper, Metals and Material international Journal.*
- *M. Al-Moussawi A J Smith, Friction Stir Welding of EH46 steel grade at Dwell Stage: Microstructure Evolution, Accepted paper, Journal of Metallurgy, Microstructure and Analysis.*
- *M. Al-Moussawi A J Smith, M. Faraji, Segregation of Mn, Si, Al, and Oxygen During the Friction Stir Welding of DH36 Steel, Accepted paper, Journal of Metallurgy, Microstructure and Analysis.*
- *M. Al-Moussawi A J Smith, Assumptions of Heat Generation in Modelling the Friction Stir Welding of Steel, Accepted paper, International Journal of Modelling and simulation.*

- *Journal Publications Under Review.*

- *M. Al-Moussawi A J Smith, M. Faraji, Estimation of Peak Temperature and Cooling Rate of Friction Stir Welding of EH46 Steel From TiN Precipitates, Under review, Journal of Material Science and Engineering A.*
- *M. Al-Moussawi A J Smith, Poly Crystalline Boron Nitride Tool Wear During the Friction Stir Welding of Steel, Under Review, Journal of Metallurgy, Microstructure and Analysis.*

> *As well as the publications above, there is also a cooperation with the university West in Sweden to simulate the FSW process for grade AA 6082-T6,aluminium (8mm thick) with a PhD student Ana-Catarina.*

Nomenclature

Greek Symbol	Definition	Units
α	CFD material constant	-------
α_p	Probe slope angle	degree
α_s	Shoulder slope angle	degree
σ	Stress	$N.\,m^{-2}$
σ_y	The yield stress	$N.\,m^{-2}$
σ_{xx}	Stress in X-direction	$N.\,m^{-2}$
σ_{zz}	Stress in Z-direction	$N.\,m^{-2}$
η	represent the amount of the mechanical energy converted to heat energy (machine efficiency)	----------
δ_o	the initial partition of heat generated from plastic deformation to heat generated from friction	----------
δ	The partition of heat generated from plastic deformation to heat generated from friction (0 sticking, 1 sliding)	----------
β	Stefan-Boltzmann constant. $5.670373(21) \times 10^{-8}$	$W\,m^{-2}\,K^{-4}$
ϵ	Emissivity of the plate surface.	---------
ε	strain	------------
ε_{ij}	strain tensor	-----------
$\dot{\varepsilon_p}$	equivalent plastic strain rate	s^{-1}
$\dot{\varepsilon_o}$	reference strain rate	s^{-1}
$\dot{\varepsilon}$	strain rate	s^{-1}
λ	wave length of XR used (Braggs law)	nm
φ	used to scale down heat generation (0-1)	---------
μ	Friction coefficient	-------
μ_u	Non-Newtonian viscosity	Pa.s
ρ	Material density	(Kg/m^3)
$\tau_{contact}$	Contact shear stress	$N.\,m^{-2}$
τ_y	The yield shear stress	$N.\,m^{-2}$
ϕ	The angle between a fixed direction in the plane of the specimen and the projection in that plane of the normal to the diffracting lattice planes	degree
θ	The Bragg angle	degree
θ	The rotation angle of the tool.	degree
υ	poisons ratio	--------
ω_o	The Maximum rotational speed,	RPM
ω	tool rotational speed.	RPM
Ω	The angle between the incident X-ray beam and the specimen surface	degree
ψ	The angle between the normal of the specimen and the normal of the diffracting lattice planes	degree
χ	The pitch of the pin	---------

Symbol	Definition	Units
A	Area	m^2
A$_{probend}$	Probe end area	m^2
A$_{probeside}$	Probe side area	m^2
A$_{shoulder}$	Shoulder area	m^2
Ai	material constant	-------
C$_p$	Specific heat	J/Kg.K
d$_o$	Free lattice space	nm
d$_{\phi\psi}$	The inter-planer distance (d spacing) of strained material in the direction of measurement defined by the angles $\emptyset$ and ψ	nm
E	Elastic modulus	GPa
F	Force	N
h	Heat convection coefficient	W m^{-2}. K^{-1}
h_j	The probe height	mm
HV	Vickers Hardness number	Kg/mm^2
k	thermal conductivity coefficient	W/m.K
M	The torque	
m^o	The flow rate of liquid or gas	KJ/Kg. K for liquids KJ/m^3. K for gas
m	The thermal softening slope constant	-----------
n	Strain rate slope	-----------
q	heat flux	W/m^2
Q$_e$	Activation energy	kJ mol^{-1}
Q_i	heat generated due to tool/workpiece interface.	W
Q_b	heat generated due to plastic deformation away from the interface.	W
Q_{total}	Total heat generated from the tool	W
$Q_{shoulder}$	Heat generated from the shoulder	W
$Q_{probeside}$	Heat generated from the probe-side	W
$Q_{probend}$	Heat generated from the probe end	W
r$_i$, r$_o$	Tool inner and out radii respectively	m
R$_{is}$, R$_{os}$	Maximum tool shoulder inner and outer respectively	m
R$_{ip}$, R$_{op}$	Maximum tool probe inner and outer respectively	m
T	Temperature	K
T^*	Homologous temperature	K
T$_o$	The initial temperature.	K
T$_m$	The solidus temperature.	K
T$_{NRX}$	temperature of no recrystallization	K
t	time	s
u	flow velocity	m/s
U	The velocity of the tool in the welding direction	m/s
V$_x$	Velocity in the x-direction	m/s
u, v, w	velocity vectors in X,Y and Z direction respectively	m/s
X	X-coordinate	m
Y	Y-coordinate	m
Z	Z-coordinate	m
Z$_n$	The Zener-Hollomon parameter	-----

Abbreviations

ALE: Arbitrary Lagrangian Eulerian

AS: Advancing Side

α_a: Acicular ferrite

α_{all}: Allotriomorphic ferrite

BCC: Body Centred Cubic

BN: Boron Nitride

B: Bainite

CFD: Computational Fluid Dynamics

EDS: Energy Dispersive Spectroscopy

FSW: Fiction Stir Welding

FCA: Ferrite Cementite aggregate.

FEM: Finite Element Method

HAZ: Heat Affected Zone

HSLA: High Strength Low Alloy

PCBN: Poly Crystalline Boron Nitride

RS: Retreating Side

RX: Recrystallization

SAW: Submerged Arc Welding

SEM: Scanning Electron Microscopy

SZ: Stirred Zone

TC: Thermo-Couple

TEM: Transmission Electron Microscopy

TMAZ: Thermo-Mechanical Affected Zone

List of Contents

List of Figures

List of Tables

1. Introduction

Welding, brazing and soldering can be defined as processes for joining materials together which includes a heat source. The Sumerians, during the Bronze age (3000BC) in Ur (Iraq), made swords which were joined by hard soldering [1].

The first recorded welding or solid-phase welding was carried out by Egyptian people when iron ore had converted to sponge iron by heating in a charcoal fire; the particles were then forge welded together by hammering, figure 1.1 is an example for Egyptian ancient soldering. The first US patent granted was to Coffin in 1892 for arc welding using a metal electrode [1]. Welding processes have evolved over time with much innovation occurring during the Second World War due to the need for weapons production. Friction welding has been classified as a solid state welding process because the workpiece to be joined is heated to about 0.8 of the melting point [2]. Heat generated in Friction welding comes from the mechanical action between one moving surface and another stationary thus producing heat mainly by friction. The main advantages of friction welding is that no filler material is added and also the welded joint is produced with lower heat input; thus reduced metallurgical degradation, distortion and residual stresses are expected [3].

Figure 1.1: Golden Mask of Tut-Ench-Amun as example of Egyptian soldering in 1330 B.C.[1]

Friction Stir Welding (FSW) can be classified as a modified version of traditional friction welding. It is a solid state welding process invented in the UK/TWI in 1991. The process was

originally employed primarily for welding aluminium grades which had been classified as un-weldable alloys by using existing fusion techniques. [4]

The high demands on obtaining sound welds especially in the marine industry has encouraged companies like TWI to extend the FSW technique to include the joining of steel alloys. However, the process to date is still under development and has not yet been commercialise due to the high cost of the FSW tool and the issues of tool wear/breakage associated with the welding process. Furthermore, the higher forces applied during FSW of steel require a very stiff and therefore expensive FSW machine. Figure 1.2 -a- and -b- shows the distribution of production cost per meter of FSW of steel compared to fusion Submerged Arc Welding (SAW) [5]. The machine direct cost in FSW is double that of SAW. Additionally, the tool costs in FSW represents 99% of the machine direct costs, as shown in Figure 1 -c-.
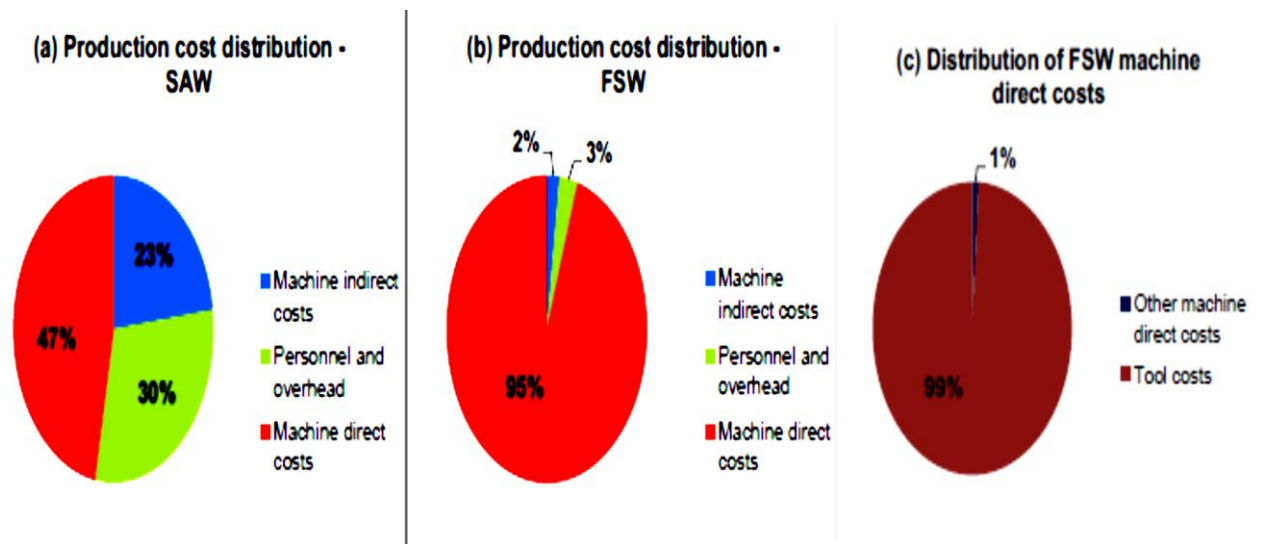
Figure 1.2: Distribution of production costs for (a) SAW; (b) FSW; (c) FSW machine direct cost.[5 p10]

In addition to the tool and machine cost challenge, the FSW process includes many complex parameters such as tool rotational speed, tool traverse speed, plunge depth, forces and clamping which must be carefully controlled in order to obtain a defect-free- joint. Measuring peak temperature at the tool/workpiece interface is also a challenge due to the difficulty of inserting thermocouples in the zone under stir zone of the FSW tool. Even the use of a thermal imaging camera does not provide an accurate measurement of the peak temperature because there is no direct view of the tool/workpiece interface.

Defects associated with unsuitable welding parameters especially tool rotational/traverse speeds and plunge depths also increase the cost of welding. The advance in technology of producing hard FSW tools including refractory tools based on tungsten such as W-Re and super-abrasive ceramic tools such as Poly Crystalline Boron Nitrides PCBN has reduced the weld joints production cost [6]. Also, following extensive research there is a greater understanding of how to control process parameters, thus reducing weld defects and bringing commercialisation a step closer.

Mathematical Modelling the FSW has been developed in recent years in order to cultivate a deeper understanding of the effect of process parameters on weld quality and efficiency and reduce the cost of trial and error experimental work [7]. However, the complexity of the process which includes heat transfer, material flow and heat generation by different techniques resulted in a variety of numerical assumptions and techniques being made which are not universally agreed. There is also a great debate about the frictional and plastic deformation as a heat source associated with the process, material flow is also complex and needs to be addressed for a better understanding to the process. [3] [4]

In the marine industry, steel alloys such as DH36 and EH46 grades have been used widely due to the appropriateness of their mechanical properties including tensile strength, impact and fatigue resistance. Thus, producing high quality welded joints from these alloys is important and can be obtained by welding techniques including the lower heat input FSW process. FSW offers significant improvements in mechanical properties, especially fatigue resistance, when compared with fusion welding techniques. [8]

The overall aim of this research is to investigate which assumptions for heat generation when modelling the FSW process of DH36 and EH46 steel grades provides the most accurate estimate of peak temperature and defects associated with unsuitable welding parameters. New types of defects that may occur during the FSW were also identified and a method for estimating the peak temperature that a FSW undergoes has been proposed which is based on a microstructural analysis and has been validated by a series of simulated laboratory based heat treatments looking at the effect of both time and temperature.

The research is also correlating the welding parameters to the microstructure evolution and the resulting mechanical properties.

1.1 Objectives

To obtain the main aim of the research the following objectives were identified:

- To produce a CFD model of FSW which most accurately predicts the temperature contour, torque and Stir Zone (SZ) size and refine and ultimately validate this model with the results from practical experimental work based on friction stir welded steel samples produced by TWI coupled with laboratory based heat treatment trials.
- To identify the correlation between welding parameters such as tool rotational/traverse speeds and the resulting welded joints mechanical properties such as tensile, fatigue and micro-hardness.
- To find the tool rotational/transvers speeds limits which can cause peak temperatures close to (or exceeding) the melting point of the workpiece and the consequences of possible non-metallic elemental segregation/precipitation.
- To seek to identify an alternative method of estimating the peak temperature achieved during the FSW process.
- To investigate possible new defects associated with using unsuitable FSW process parameters.

2. Literature Review

In this section the previous work related to the current study has been investigated extensively. The Friction Stir Welding (FSW) process and its parameters will be introduced and compared with other known welding techniques such as Submerged Arc Welding (SAW) and Manual metal Arc welding (MMA). The review will explore the advantages and limitations of the process and examine the feasibility of welding steel alloys. The review will also examine the two grades of steel (DH36 and EH46) which have been used in the project in terms of their physical metallurgy.

2.1 Friction Stir Welding (FSW)

Friction Stir Welding (FSW) was invented in 1991 at TWI/Cambridge, it is a solid state welding technique used initially to join aluminium alloys such as the 2XXX and 7XXX series which, at the time were regarded as unweldable alloys because of the issues of porosity and solidification cracking associated with fusion welding [4]. The success in joining light alloys by the FSW technique has encouraged TWI to extend the process to higher melting alloys such as steel grades. The development in technology regarding FSW tool manufacturing including the development of refractory tools such as tungsten based tools and ceramic tools such as Poly Crystalline Boron Nitrides PCBN has advanced the potential commercial opportunity of FSW of steel alloys.

2.2 FSW Process Technique

The FSW technique involves inserting a non-consumable rotating tool, consisting of a shoulder and probe, between two workpieces. The tool continues to rotate inside the workpiece (plunge and dwell steps) until the material gains enough thermal energy to reduce its yield strength; at which time the tool starts to move along the welding line at a steady state (constant rotational/traverse speeds). The process ends when the tool stops traversing along the weld line, the tool rotational speed reduces and the tool is lifted leaving a keyhole in the workpiece. Figure 2.1 shows the process steps of the FSW [3 p469]. The nature of the FSW process including the tool rotational and traverse speeds along the line of the two welded workpiece parts produces an asymmetrical stirred zone in the final weld joint. These two asymmetrical sides have been recognized and named as the Advancing side (AS) and the Retreating side (RS) as shown in Figure 2.1. In the AS the material is pushed toward the welding direction by the rotating tool while in the retreating side the rotating tool pushes the

material backwards away from the welding direction [5]. Other tool sides are located in front and behind of the moving tool which are the leading side and trailing side respectively as shown in Figure 2.1.
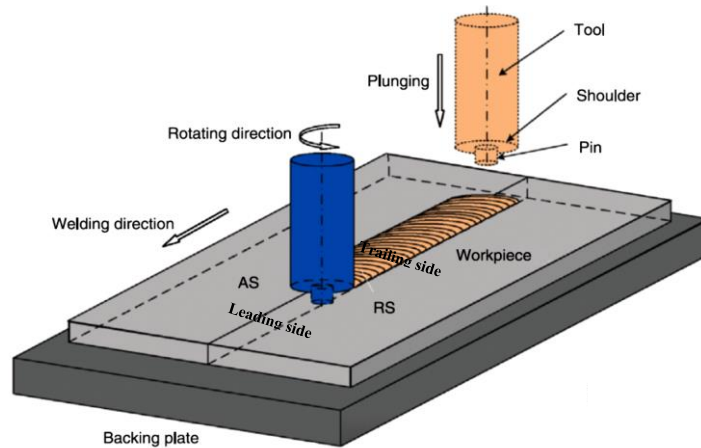
Figure 2.1: The steps of the FSW process [3 p469].

2.3 Friction Stir Welding Requirements:

The following equipment is required before carrying out the FSW process:

1. **A Stiff Machine:** FSW Machine should be able to stand with high loads applied during welding especially when welding high melting temperature alloys such as steel using refractory or ceramic FSW tools. The biggest issue faced by a FSW machine is the deflection under load which can cause fatigue failure. Machine stiffness has been determined in terms of deflection which should not exceed 0.75mm with a plunge force of 45KN. [6 P113]

2. **Precision Spindle:** Spindle wear is the most important factor which affects the FSW tool longevity especially those tools used for FSW of high melting alloys [6]. Maximum Spindle runout for ceramic tools such as Poly Crystalline Boron Nitride PCBN must not exceed 0.01 mm in order to avoid failure by fracture.[7]

3. **Tool cooling:** Tools for FSW of high melting alloys require a cooling system on the tool shank due to the high temperatures generated during welding and also the high thermal conductivity of the tool in use; such as refractory tools based on tungsten and ceramic tools like PCBN. The increase in tool temperature to a specific limit can cause damage to the spindle bearing and also can increase the tool wear. [6]

6

2.4 Advantages and limitations of FSW

4.2.1Advantages:

Despite the fact that steel can be joined faster and cheaper by other welding techniques such as SAW and MMA, using the FSW technique has many advantages over the other traditional welding methods. These advantages are:

- The process can be assumed environmentally friendly as it does not include metal fusion and thus it represents a healthy welding technique as very limited toxic fumes are generated.
- The welded joint consist of a finer microstructure and thus improved mechanical properties . The process keeps the same original material as it does not include a filler. There are also no elements lost during the process, the mechanical properties such as tensile strength [8] and especially fatigue resistance [9] are increased after welding.
- FSW offers the ability to join high strength unweldable alloys such as aluminium alloys, and also the ability to join dissimilar materials [10].
- It can be represented as a non-consumable process especially for aluminium alloys, FSW tool such as H13 can weld about 1000m of 6000 series aluminium plates. For welding steel alloys the process is still limited, the current PCBN tool can weld up to 40m of 6mm DH36 grade [5] and 80m of 1080 steel grade [6].
- Very little plate weld preparation requirements before the welding process.
- Low porosity and distortion after welding, also the problems of solidifications and liquation cracking are avoided.
- Because of there is no weld pool, the process is suitable to use in all directions including horizontal, vertical, circular and inclined.
- Less residual stresses are expected because of the lower heat input compare to fusion welding. [11]

4.2.2 The limitation of FSW process can be listed as follows

The process of FSW does not always produce defect free joints and it has also limitations in terms of tool wear and equipment cost as following:

- Tool life and cost are still the main obstacles to commercialise the FSW of high melting alloys such as steel.[5]
- The process is slow compared to other welding techniques such as SAW.
- The process ends with a key hole in the workpiece.
- The presence of defects such as wormholes [12], kissing bond [13] and weld root flaw [14] occur at specific welding conditions.
- The possibility of local melting and elemental segregation/precipitation when tool rotational speed exceeds a specific limit.
- The process requires high axial forces to keep the tool at the required plunge depth and also the need for clamping of the parent material.
- The process is limited to a constant workpiece thickness because of the fixed tool probe length. However, recent developments in tool manufacturing have produced a through-spindle retractable probe tool (RTP) which has the ability to extend or retract the probe end according to the workpiece thickness [3 P686].

2.5 Friction Stir Welding Applications

The FSW technique has been commercialised for some industry applications which mainly include using light alloys such as different types of aluminium series. Some of the most common important applications to date are considered below:

1. Automotive production: The automotive industry is aiming to reduce the weight and increase the strength of its vehicles; this has been fulfilled by using different aluminium series alloys and by using the FSW technique. Examples of parts welded by FSW in car manufacturing are crash boxes, drive shafts, suspension system, cylinder head, dash board, tailor welded blanks……etc.[3]. An entire body of a car has been made out of aluminium and fully welded by the FSW technique. This was displayed at booth of SAPA in 2002 Aluminium Fair in Germany as shown in Figure 2.2 [3].
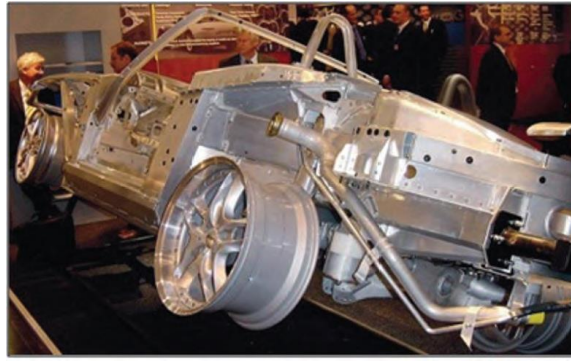
Figure 2.2: An entire body of a car made of aluminium and fully welded by FSW technique [3].

2. Aerospace: The aircraft industry has shown great interest in joining parts using the FSW techniques. Such parts used in the aircraft are wings, fuel tanks, ribs, spars, skin and stringer..etc. Using the FSW process instead of joining by rivets has been shown to increase strength, saving time by carrying out the joining in one step instead of drilling rivets holes, this in turn reduced the weight of final product. Other advantages of replacing rivets by welding include eliminating crack formation due to the homogeneous fully penetrated joint. It is worth noting that the first aircraft (Eclipse 500) has been assembled without using rivets where the entire body is only joined by FSW technique as shown in Figure 3 [15]. The FSW technique has also had a significant impact on welded joints when it replaced other traditional techniques such as fusion welding. Examples of the successful use of FSW is welding a newly developed Aluminium Lithium alloy Al-Li-2195 as a replacement for the previous alloy aluminium Al-2219 used in the Space Shuttle external tank as shown in Figure 2.4 [3]. The new aluminium alloy welded with the FSW process has higher strength than welding by fusion arc welding. The use of the FSW technique also reduced the weight of the external tanks by 3402Kg [3].

Figure 2.3: Eclips 500, the first aircraft to use FSW technique to replace traditional rivets [15]

9

Figure 2.4: The Space Shuttle with two gigantic external fuel tanks [3 P685].

3. Railway Application to FSW

FSW in railways applications include high speed trains, trams and underground train bodies which are mainly made of aluminium alloys [3 P690]. Examples from the train manufacturing industry which use the FSW technique for joining can be found in Hitachi Japan [3 P690], the final aluminium extrusion panels joined with the FSW technique have higher strength, smoother surface finish and reduced distortion compared to similar produced made using rivets or a fusion welding technique.

4. Ship Building and Marine Industry

Panels used for decks, floors, helicopter landing platforms ….etc (Figure 2.5) are some applications of the FSW techniques used in the marine industry.
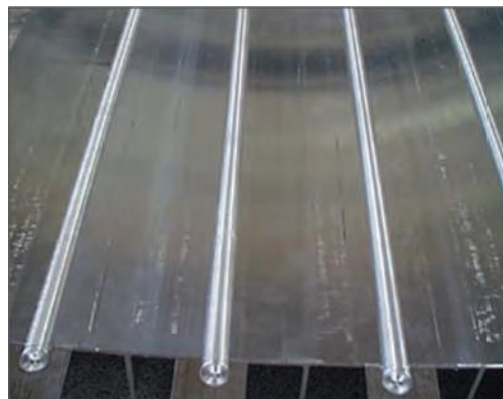
Figure 2.5: Panel joined by the FSW technique for marine applications [3].

Other applications include hollow aluminium stiff panels which serve as insulators on fishing boats to freeze fish. Honeycomb and sea water resistance panels are also examples of FSW applications in Japan used in ship cabin walls due to the weld root flatness. There is also a massive production of shipbuilding panels in Norway in the last ten years with a 70Km defect free FSW length. Another example of large ship manufactured by the FSW technique is from Friction Stir Link Inc. which is the Littoral Combat ship with 12 miles (19.3 Km) of FSW panels [3 P 695].

More industry applications of the FSW technique can be found in [3 P671]. The reduction in thermal residual stresses and distortion, as well as, higher strength of the joint and improved fatigue life are the most desired features which attract companies to swap to FSW in aerospace, railway, marine and other industries as a superior alternative to fusion welding.

2.6 FSW Tools

The FSW tool is the main driver for the process and its success. In an economic study [5] it was found that the Poly Crystalline Boron Nitride PCBN tool represents 99% of the machine direct cost. The average cost of the tool is 3000 Euro with a service life of 40m when welding 6mm DH36 steel plate grade. The FSW tool usually consists of a shoulder and probe (pin). The main role of the tool parts is to heat and stir the material in contact during the process. The first step of the FSW tool process is for the tool to plunge into the workpiece causing heat generation due to frictional/plastic deformation [16]. The temperature of the weld increases significantly to reach a maximum limit when the tool shoulder touches the top surface of the workpiece. The tool shoulder also acts as a forging surface thus preventing material under the welding process to escape outside the Stirred Zone SZ. The tool probe's main task is stirring and heating the material through the workpiece thickness.

2.6.1 FSW Tool Geometry

The tool geometry usually includes a concave shoulder with a conical/cylindrical probe [17]. For welding lightweight materials such as aluminium and magnesium alloys, tools are normally made of steel such as H13 grade and the geometry of the probe can be designed with different complex shapes in order to improve the material flow, plunge depth, heat generation and also reducing the plunge force. Complex shapes developed at TWI for welding aluminium and magnesium alloys include Whorl[TM] and MxTriflute[TM] [4] as shown in Figure

2.6 [18] These tools are mainly designed as an alternative to the tapered or cylindrical probe shape in order to improve the material flow and thus reduce defects such as wormholes [17]. The shape and size of the FSW tool is mainly dependant of the thickness of the workpiece. A cylindrical probe shape can be adequate for 12mm plate thickness, while a tapered Triflute probe is suitable for plate thickness exceeding 12mm [17]. For welding high melting point alloys such as steel, the tool geometry is usually simple as complex shapes are not applicable for ceramic tools such as PCBN. The main obstacles in manufacturing suitable tool sizes are the high pressure requirement, brazing difficulty and wear issues associated with complex shapes [6]. More information about tool geometry and design can be found in Mishara and Ma 2005 [4]
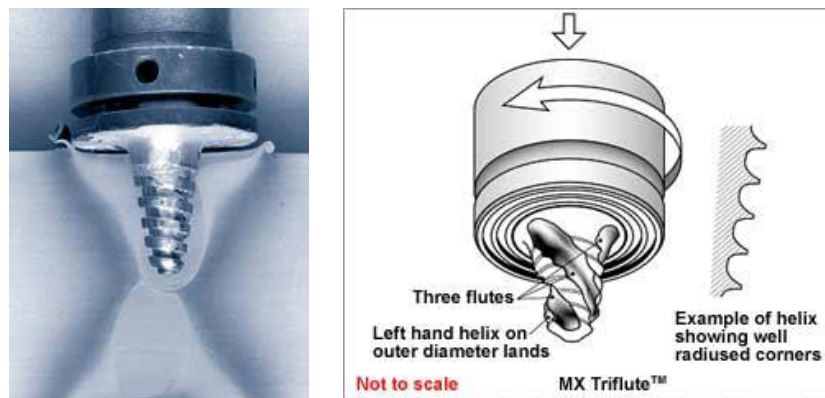
Figure 2.6: FSW tools developed at TWI company. -a- Whorl[TM] and -b- MxTriflute[TM] . [18]

2.6.2 FSW tool requirements: The material used to make a FSW tool must satisfy certain physical requirements such as high melting temperature, high wear resistance, high toughness and good dimensional stability. Other requirements include high strength at high temperature as the welding process is performed at 80-90% of workpiece melting point [19]. The material of the tool should be also inert to the workpiece so no detrimental reaction occurs during the welding process. A low coefficient of thermal expansion is also crucial in order to reduce thermal stresses on the tool surface. To meet these requirements, two types of materials have been chosen for FSW of high melting alloys: Ceramic super-abrasive tools and refractory metal tools [20].

2.6.3 FSW Tool Materials

For welding low melting alloys such as aluminium, tools are usually made of steel grades such as alloy H13 which can be used to make complex designs at low cost. However, for welding high melting alloys such as steel grades, FSW tool materials should have higher thermal and mechanical properties compared to other tools used for low melting point materials. PCBN is the most popular super-abrasive ceramic FSW tool used for that purpose, Table 2.1 [21] shows the mechanical and thermal properties of this tool compared to tungsten carbide WC and H13 FSW tools. The micro hardness of this tool HV(2600-3500) shows that the PCBN tool is the second hardest tool after diamond. It also has a low coefficient of friction which in turn helps in producing smooth surfaces after completing the FSW process [19]. However, a low coefficient of friction in a FSW tool necessitates an increase in tool rotational speed to produce the required heat for welding [22]. The PCBN tool represents an alternative to refractory tools such as tungsten based materials which showed sever wear especially during FSW of steel [23]. The PCBN tool usually contains Cubic Boron Nitride CBN particles in a binder of AlN [20], this combination between the CBN and the binder is designed to increase the strength of the tool. Despite the high strength and thermal properties, the PCBN tool has low fracture toughness and is also susceptible to wear problems especially during the plunge period due to the higher generated temperature which can cause a softening of the binder [19]. The plunge period is also associated with high plunge force which can encourage BN particles to detach from the tool and stick into the workpiece. The development in metal composite material has encouraged manufacturers such as MegaStir to produce new grades of PCBN tools with a longer service life. This development was a step forward in order to commercialise the FSW of high melting alloys. For example a FSW tool made from Q70 (70%PCBN, 30%WRe) has a higher toughness compared to the previous one which included an AlN binder [20]. The melting point of a Q70 tool was determined to exceed $3000^{\circ}C$, the microstructure and tool image are shown in Figure 2.7 -a- and -b- respectively [20]. The Q70 tool has been used extensively at TWI to join many steel grades including 316L stainless steel, 304 stainless steel, DH36 and EH46 steel grades which are under consideration in this work. PCBN-WRe Q70 tool as shown in Figure 2.7-b- consists of a shoulder and probe surrounded by a collar of Ni-Cr which works as an insulator for the tool from the environment, so the heat generated during the FSW is almost distributes between the PCBN tool and workpiece. The PCBN tool is also attached to a shank made of WC which acts as a holder and attaches the tool to the PowerStir FSW machine. Both parts of the tool including the PCBN

material and WC shank are fastened together by the collar. The different parts of the PCBN tool geometry are listed in Table 2.2 which are according to the workpiece thickness. Welding 6mm thickness is usually achieved using a PCBN tool with 5.5mm probe length while for 14mm thick workpieces a probe length of 12mm is usually used. The TWI PowerStir FSW machine includes a cooling system applied on the tool shank in order to reduce the temperature resulting from the high thermal conductivity of the PCBN tool and the temperature generated during welding of high melting point alloys. Argon shielding is usually applied during the FSW process mainly to extend the tool life and also to prevent oxidation of the welded joint. A thermocouple is usually attached to the tool shank and is located behind the PCBN tool (known as the telemetry system to monitor tool temperature) in order to measure the temperature during the FSW process as shown in figure 2.8. The temperature of the tool measured by the telemetry thermocouple system should be kept in the range of 800-900°C inorder to protect the tool from wear/breakage issues as recommended by the manufacturer [23].

Other tool materials and their properties which have been used for high melting alloys are usually made of refractory materials based on tungsten such as WC, W-Re, W-Co and can be found in the literature [19] [6]. This project is focused only on the PCBN tool as this is the tool which has been used to produce the samples under study.
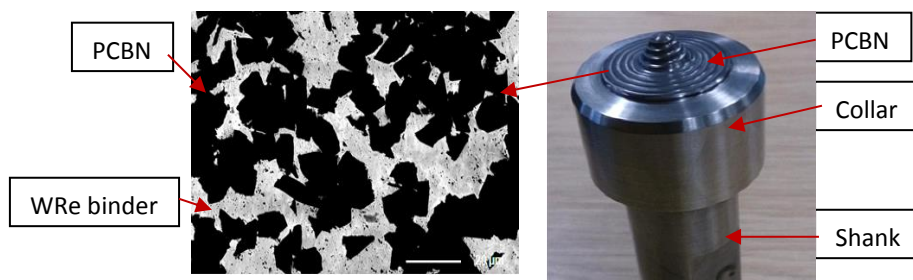
Figure 2.7: -a- SEM image of PCBN Q70 (70% cBN, 30%WRe) [20], -b-PCBN tool image.
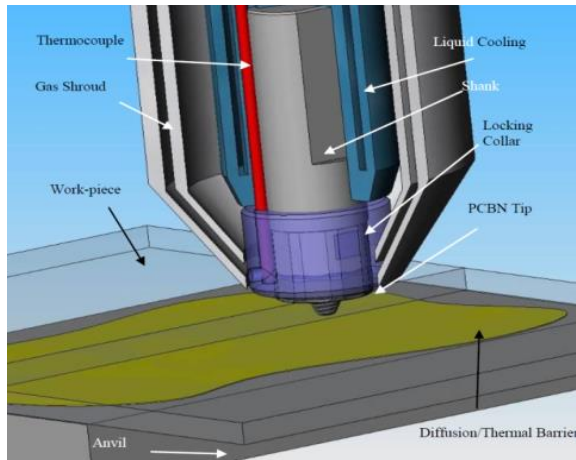
Figure 2.8: The Cooling system for a PCBN tool for FS welding ferrous alloys [21].

Table 2.1: The physical properties of PCBN compared with Tungsten carbide and 4340 steel [21].

Property	Units	PCBN	Tungsten Carbide	4340 Steel
Coefficient of Friction	-	0.10-0.15	0.2	0.78
Coefficient of Thermal Expansion	$10^{-6}/^{\circ}C$	4.6-4.9	4.9-5.1	11.2-14.3
Thermal Conductivity	W/mK	100-250	95	48
Compressive Strength	N/mm^2	2700-3500	6200	690
	10^3 psi	391-507	899	100
Fracture Toughness	MPa√m	3.5-6.7	11	100
Hardness	Knoop kg/mm^2	2700-3200	-	278
	Vickers kg/mm^2	2600-3500	1300-1600	280
Tensile Strength	N/mm^2	-	1,100	620
	10^3 psi	-	160	89.9
Transverse Rupture Strength	N/mm^2	500-800	2,200	-
	10^3 psi	72-115	319	-

Table 2.2: PCBN tool geometry provided by TWI

Tool	PCBN shoulder	PCBN probe	Collar	Shank
PCBN for welding 6-8mm thickness	23.7 mm diameter with spiral convex shape	5.5mm length, 10mm base diameter spiral tapered with 20 thread per inch (TPI)	23.9mm inner diameter 37mm outer diameter 24mm length	23.9mm Diameter 80.35mm length
PCBN for welding 10-15 mm thickness	38mm mm diameter with spiral convex shape	12mm length, 20mm base diameter spiral tapered with 20 thread per inch (TPI)	38.1mm inner diameter 52mm outer diameter 30mm length	38.1mm Diameter 100mm length

Table 2.3: shows the various coolant types for shank and collar parts of the tool with associated characteristics [21].

Coolant	Flow Rate	Specific Heat	Inlet Coolant Temperature ºC	Outlet Coolant Temperature ºC	Tool Surface Area exposed mm^2	Average Heat Flux W/mm^2
50% Ethanol glygol+50%distill water	5.3-13.3 L/min	3.41 KJ/Kg. ºC	15	17	4241.15	0.187
Air	5.7 m^3/hr	1.2 KJ/m^3. ºC	15-20	100-125	2760.67	0.0688

2.6.4 PCBN FSW Tool Limitations and Wear/Breakage Issues:

Wear resistance in hybrid PCBN FSW tool is considered better than other refractory materials such as tungsten based tools. W-25%Re FSW tool life of 4m was reported in welding steel grades and titanium [6]. However, wear issue still exist with PCBN tool when welding high melting alloys especially the high strength alloys such as EH46 steel grade. An experimental study of a PCBN tool has been carried out by [19] and showed that the main factors which can cause wear are abrasion and diffusion. Softening and recrystallization of the binder after reaching a welding temperature of $1000^{o}C$ is also found to be one reason for reducing tool resistance to wear [19 P45]. Ramalingam and Jacobson [24] reported a decrease in Knoop hardness (HK) of W-25Re from HK 675 (HV 638) to HK 500 (478) when carrying out heating from room temperature to $1225^{o}C$. The hardness was found to decrease dramatically to HK 300 (HV 290) when the temperature increases to $1450\,^{o}C$ [24].

Hooper et al. [25] suggested that the higher thermal conductivity of CBN (100-250 W/m.K) [26] can result in defects in the microstructure when the temperature exceeds 1200K, while with a comparison with CBN-TiC they found that a protective layer is formed on the latter and is associated with the higher temperature as a result of lower thermal conductivity of CBN-TiC. PCBN tool wear can also change the properties of the material being welded. For example, tool wear can negatively effect a stainless steel welded joint as boron particles can react with Cr to form borides which in turn can result in a reduction in corrosion resistance [19]. When welding titanium plates, boron can improve the mechanical properties of the joint because of the ability to react with Ti forming TiB_2 which in turn can cause grain refinement and a hardness increase [27]. PCBN tool breakage is highly likely to occur during the FSW process due to the lower fracture toughness as mentioned in Table 2.1 compared to WC tool. Unsuitable welding parameters such as improper plunging or extracting and low welding temperatures were determined as the main factors for tool breakage [23].

From the above discussion it can be concluded that the PCBN tool is sensitive to welding temperatures and plunging depth, low welding temperatures can lead to tool breakage while excessive welding temperature will increase PCBN wear due to binder softening. Higher temperatures may also result in PCBN separation from the locking collar [23]. Other limitations include limited depth of welding; the maximum probe length achieved to date by the manufacturer MegaStir is 13mm.

2.7 Material welded by a PCBN FSW tool

There are varieties of high melting point materials which have been welded by the hybrid PCBN tool as shown in Table 2.4 [6]. The table includes the tensile strength of some weld joints and associated welding parameters (tool rotational/traverse speeds). From Table 2.4 it can be noticed that the maximum rotational speed achieved does not exceed 600 RPM for A-36 and 301L grades with maximum travelling speed of 150 mm/min and 300mm/min respectively. Compared to welding light alloys such aluminium, FSW using PCBN is slower due to the higher temperature generated during the process and tool wear/breakage. PCBN tool life of 40m and 80m has been reported in FSW of DH36 [5] and 1018 steel grades [6] respectively. Further work on evaluating the feasibility of FSW of high melting alloys such as steel should be carried out in order to commercialise the process.

Table 2.4: Materials welded by PCBN tool [6 P116]

| Material | Yield strength (weld/base metal) | | Ultimate strength (weld/base metal) | | rpm/travel | |
	MPa	ksi	MPa	ksi	mm/min	in./min
A-36	N/A		N/A		600/150	24/6
Quenched and tempered C-Mn steel	1040/1400	151/203	1230/1710	178/248	545/130	21/5
DH-36	N/A		N/A		500/200	20/8
HSLA-65	597/605	87/88	788/673	114/98	500/200	20/8
L-80	N/A		N/A		550/100	22/4
X-80	N/A		N/A		550/100	22/4
X-120	N/A		N/A		550/100	22/4
Dual Ten 590 dual phase	496/340	72/49	710/590	103/86	450/240	18/9.5
304L	51/55	7.4/8.0	95/98	13.8/14	400/75	16/3.0
316L	434/338	63/49	641/674	93/98	550/80	22/3.2
AL-6XN	N/A		N/A		350/25	14/1.0
301L	N/A		N/A		600/300	24/12
430	N/A		N/A		550/80	22/3.2
2507 super duplex	762/705	110/102	845/886	123/128	450/60	18/2.4
201	193/103	28/15	448/406	65/59	1000/100	39/4.0
600	374/263	54/38	719/631	104/91	450/56	18/2.2
718	668/1172	97/170	986/1392	143/202	500/50	20/2.0
Narloy-Z	N/A		N/A		450/100	18/4.0
Invar	N/A		N/A		600/150	24/6.0
Ni-Al bronze	420/193	61/28	703/421	102/61	1000/102	39/4.0

2.8 FSW Process Parameters

In general, FSW process parameters include the tool, the workpiece and process parameters. This section is focused on the process parameters and their effects on the weld joint quality and also tool life. The FSW process parameters can be classified as independent such as tool rotational/traverse speeds and plunge depth. Other parameters such as welding forces and torque which are affected by the independent parameters are classified as dependent parameters. FSW machines such as PowerStir which has been used for joining high melting alloy has the ability to record welding parameters including plunge depth, time of welding, travelled distance, rotational and traverse speeds, forces and torque.

Independent parameters such as tool rotational and traverse speed play the most significant role in the FSW process. The rotational speed (ω) is mainly responsible of generating the heat and stirring the material at the tool/workpiece interface, so it is expected that higher heat generation and material flow will occur with increasing tool rotational speed. The traverse speed (V) completes the welding process by pushing the stirred material from the leading to the trailing edges of the tool. Traverse speed also controls the cooling rate of the process; faster traverse speed results in a higher cooling rate. The unsuitable combination between rotational/traverse speeds (ω/V) can cause a lack in material flow around the tool and in turn defects such as voids can be created in the SZ [28]. To produce a good quality welded joint, a suitable combination between (ω/V) is crucial.

Other important welding independent parameter is the plunge depth which is the insertion distance of the probe into the workpiece. A lack of plunge depth means that the shoulder is not totally touching the top surface of the workpiece, this in turn can cause less heat generation and also reduce stirring of the workpiece material. The resulting welds in this case may include a surface groove or inner channel [4]. An excessive plunge depth can also cause issues of flash formation and weld thinning. An example of the relationship between ω , V and plunge depth for FSW of AA6061-T651 is shown in Figure 2.9 [3 p479]. It can be shown that to produce a defect free welded joint; sufficient plunge depth and rotational speed are required; however, excessive rotational speeds can also cause surface deformation.
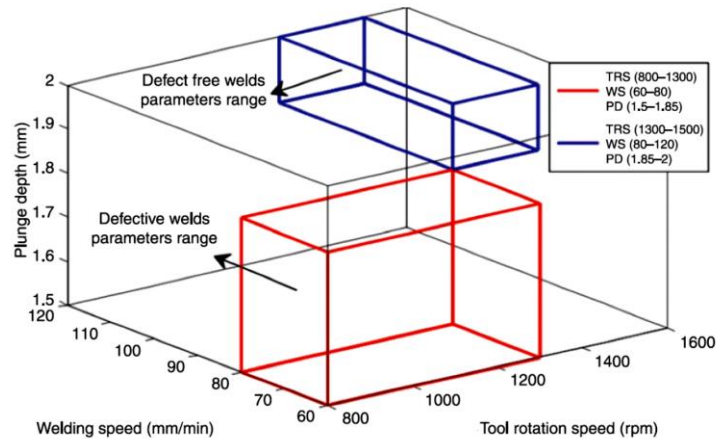
Figure 2.9: The relationship between ω , V and plunge depth as studied for FSW of AA6061-T651 [3 p479]

FSW dependent parameters include forces and torque, forces are mainly created around the tool due to rotational and linear movement which include (Figure 2.10)

- Axial or down force (known also as plunge force) which is parallel to the normal tool direction.
- Longitudinal (transverse) force along the welding line and
- Lateral force normal to the welding direction.

Torque and forces are measured mainly to control tool wear and deformation of the workpiece. High values of welding forces and torque are not desirable during the FSW process as they can cause tool wear/breakage and also workpiece distortion. Heat generated can also be predicted by monitoring welding parameters especially torque.
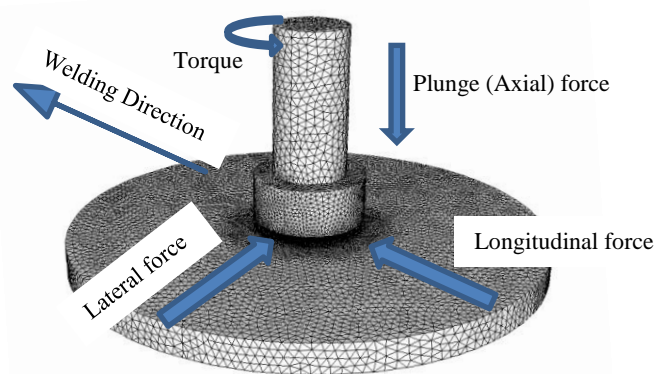
Figure 2.10: Forces and torque generated during the FSW process.

The relationship between independent parameters and welding forces has been investigated [29] and showed that plunge force is sensitive to tool rotational/traverse speeds and also tool shoulder diameter while the longitudinal force is sensitive to traverse speed and probe radius. [29]

Controlling axial forces during the FSW process is important; an excessive increase in force can result in tool breakage/wear increase [17]. Excessive axial force during the FSW also increases the pressure under the tool shoulder which in turn can result in removing material during welding as flash causing a reduction in the joint thickness [17]. Flaws in FSW joints may also be created when welding forces decrease suddenly during the steady state period [30] A torque, instead of force control, study has been carried out by Longhurst et al. 2010 [30] in order to reduce flaws in FSW of aluminium 6061. Their study found that by using a torque control method, the plunge depth and energy per unit length were more stable than where using a force control method. Torque was reported to increase with an increase in tool shoulder diameter and the decrease with increasing tool rotational speed [3 p493]. Also different methods have been used to monitor these dependent parameters, Mehta et al. 2013 [31] monitored torque and forces during FSW of AA7075-T6 and AA2524-T351 using an inexpensive procedure depending on the current and power of the electric motor which controls the tool rotational/traverse speeds. Results of torque and forces with different welding parameters including variation of tool rotational speed and tool shoulder were validated against 3 dimensional numerical modelling. [31].

Tool torque has been employed for a long time to calculate the heat generated during the FSW process. Extensive information about the effects of welding on FSW forces and torque can be found in [3 p470].

2.9 Material Flow around the FSW Tool

Material flow in the FSW process is significantly related to the heat generated from the tool rotation speed, tool design, tool material type, workpiece material and heat transfer. The optimum control of the flow during the process can help in producing defect free weld joints.

Many approaches have been used to investigate the material flow during the FSW process and can be classified as [4]:

- Using tracer markers.
- Using numerical modelling.
- Welding dissimilar alloys.

This section will discuss the techniques of using tracer markers and numerical simulation:

2.9.1 Revealing Flow by Tracer Markers: By using markers materials which are different from the workpiece under FSW process, the material flow can be observed. Tracer marker materials include tungsten tracers [33, 34 and 35], stainless steel wires [36], copper foils [37] [38], steel shot [39], Al-SiC, Al-W and aluminium etched differently from the workpiece [4]. Techniques associated with using tracers markers include X-ray radiography [33-35] [37], metallography and Computer Tomography (CT) [34 Schmidt et al. 2006]. Much effort to reveal the material flow pattern in FSW of aluminium and steel has been carried out in previous work.

Morisada et al. 2011 [35] used tungsten tracers with the aid of two pairs of X-ray radiography transmission real time system to visualise the material flow of aluminium during lab-based FSW. They found that the velocity of the material flow with the same position from the weld centre is proportional to the tool radius. Also the velocity on the retreating side (RS) is slightly higher than on the advancing side (AS). The authors extended their work on the same technique to compare the material flow of aluminium with low carbon steel [33] and they found that material flow pattern in steel is different and slower than in aluminium. In the case of steel the uniform material flow around the FSW tool is only obtained when the rotational and traverse speeds of FSW tool are slow. This nature of flow in steel was interpreted as a result of high deformation resistance. A stagnant zone on the advancing side was reported at high traverse speed and interpreted as a lack in material flow, the stagnant zone was believed to be the main cause of void formation.

Schmidt et al. 2006 [37] investigated the material flow of AA2024-T3 by the aid of X-ray, Computer Tomography (CT) and metallography using copper strip as markers to reveal the material flow. By tracing markers relative to the welding materials, the average velocities of the shear layer were estimated in the longitudinal and traverse direction. According to the findings, the flow of material under FSW has been classified to different zones including rotational, flow, transition, deflection zone and welding flow.

Reynold et al. 2000, 1999 [40],[41] studied the material flow of FSW of 2195Al-T8 by inserting markers of 5454Al-H32 along the welding line in the horizontal and vertical directions. By metallographic examination of 0.25mm thickness etched slices taken from the top surface of the FSW plate using a milling technique, the final position of markers has been revealed. Their study reported asymmetrical flow around the centreline of the weld between AS and RS. Markers in the RS moved behind its original location while on the AS they moved to the front of its original location. They also found that there is a stagnant zone between AS and RS in which the material under welding did not show stirring. The material during the FSW also showed a vertical downward flow on the AS and then upward flow towards the top of RS. The study indicates that a high percentage of material stirring is occurring on the top surface of the workpiece. The material is deflected by the shoulder and moves around the probe at the RS towards the AS. Tracer markers were also found to move less in the workpiece depth when the weld pitch (ω/V tool advance per revolution) is increased. The study showed that increasing the probe radius has caused an increase in the material movement around the centreline of the weld.

Colligan 1999 [39] investigated the material flow of aluminium alloys during FSW by using two techniques including steel shot markers and stop action. Steel balls of 1mm radius are inserted along the welding line and their distribution was revealed by X-ray radiography. The stop action technique was carried out by the sudden stop of the FSW tool and moving the tool back at the same time at a speed that cause unscrew to the tool probe into the workpiece without causing damage to the attached material. The material flow in the keyhole which is left by the sudden stop is revealed by carrying out a sectioning process. The experimental findings of the study by tracer markers of steel shot have revealed two pattern of distribution: chaotic on the top surface of the weld with a down movement from its original position. The other type of pattern was continuous line distribution behind the probe and its vertical movement into the workpiece depth was less than those in the chaotic distribution. The

authors also reported that some of the material during FSW did not experience stirring but extruded around the RS of the probe and deposited behind.

Guerra et al. 2001 [38] used 0.1 copper foils along the faying surface of 6061Al with the stop action technique to study the material flow during FSW. By preparing metallographic etched sections, the microstructure has examined and it is found that the material close to the top surface of the weld is highly affected by the tool shoulder rather than the probe. More investigation reported on material flow during the FSW process can be found in [40] [41] [42].

Generally speaking, uncertainty in flow markers can be increased when the marker material has different density from the original welded material.

2.9.2 Estimating Material Flow from Numerical Simulation

Material flow during FSW can be also estimated numerically using codes such as Computational Fluid Dynamic (CFD) which have the ability to solve momentum equation and calculating the strain rate. Smith et al. 1999 [43] used a fluid mechanics model with a viscos heating assumption to estimate the material flow during FSW. From their model it can be estimated that there are three types of flow pattern under the tool shoulder and around the probe which include: (a) rotational zone in contact with the tool shoulder and the flow is in the direction of tool rotation. (b) extrusion flow at the bottom of probe and (c) transition zone between zone (a) and (b) with chaotic flow.

Stewart et al. 1998 [44] carried out two mathematical models to monitor the material flow during the FSW process. The first model was called "mixed zone" in which the material flows in a vortex like system and has angular velocity equal to the FSW tool at the contact region between tool/workpiece (Sticking conditions). The flow velocity decreases away from the tool/workpiece until reaches zero at the end of the plastic zone (the end of the shear layer). The second model depends on a slipping approach (single slip surface model) at the tool/workpiece interface. The angular velocity of material during welding was assumed to be less than the tool rotational speed because of the slipping effect.

Arbegast 2003 [45] assumed that the FSW process can be treated as an extrusion process so that a metal working process model has been suggested which includes five zones as shown in

Figure 2.11 -a- and -b-. Zones include (a) Preheat zone, (b) initial formation zone, (c) Extrusion zone (d) forging zone and (e) post heat/cool down zone. The pre-heat zone is gaining temperature due to frictional/plastic heating coming mainly from the rotation of the FSW tool. The heating rate is controlled by material properties and tool traverse speed. The initial deformation zone is formed when the tool starts to move forward. Material in this zone is starting to flow as the temperature and flow stress rise to critical values. These conditions encourage the material when the tool advances to move upwards into the shoulder zone and downwards into the extrusion zone as shown in figure 2.11 -a-. After this zone the material start to flow from the leading side to the trailing side around the tool probe thus the extrusion zone is starting to form. After that, the forging zone is starting including filling the cavity left by the traverse motion of the tool probe by the material coming from the front of the tool under the effect of hydrostatic pressure. The material in the cavity is kept constraint under the effects of tool shoulder surface and axial force. During the period of extrusion, the material from the shoulder zone is forced to move around the retreating side towards the AS. This model has built a relationship between welding parameters, tool geometry and workpiece material flow stress. The model also showed good agreement with experimental finding in term of temperature, SZ size and strain rate.
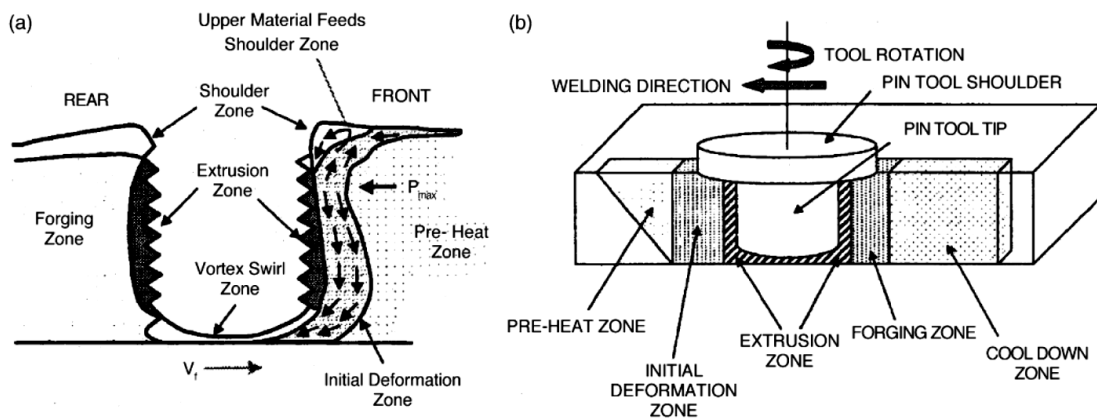
Figure 2.11: Metal working process model suggested by Arbegast , (a) Material flow map. (b) Suggested zones formed during FSW process [45].

Goetz and Jata 2001 [46] applied 2-dimensional FEM and DEFORM software to estimate the material flow of 1100Al and Ti-6Al-4V alloys and showed that the welding is occurring when the material starts to flow from RS to the AS and from the leading to trailing sides. They also showed that material flow is highly localised during the FSW process.

The variety of numerical and mathematical models used to estimate the material flow during FSW is associated with the debate in assumption of sticking, sliding, sticking/sliding and also assumption of heat generation during FSW process [44].

From the previous work it can be concluded that there are many parameters that can significantly effect the material flow during the FSW process. These parameters are related to FSW tool including material type (ceramic, refractory and metal), design and dimension [38] [18]. Welding parameters including tool rotational/traverse speeds [35], plunge depth and tilt angle also play an important role in controlling the material flow. All the mentioned parameters are adding more complexity in estimation of material flow especially when carrying out numerical modelling.

2.10. Modelling the FSW Process

The demand for modelling the FSW process in order to predict peak temperature, residual stresses and material flow patterns is still crucial for many companies. The main reason for employing modelling is to reduce time and cost arising from the requirements for numerous trial and error welding experiments in order to produce defect free joints. Such requirements include variation in process parameters such as tool rotational/traverse speeds, plunge depth and the associated dependant parameters including forces and torque. Add to that the variation in tool and workpiece parameters such as the tool material, design and geometry, workpiece thickness and material type and it becomes clear why modelling represent an attractive in addition to the experimental work.

Modelling of friction stir welding, particularly for high temperature alloys is a challenge due to the cost and complexity of the analysis. It is a process that includes thermo-mechanical coupling, high deformation and strain rate, complex material flow, phase change, sticking/slipping and complex heat exchange between the tool/workpiece and workpiece/backing plate. Nandan et al. 2008 [47] used 3D computational fluid dynamic CFD and reported that uncertainty in modelling FSW can be affected by five parameters including -a- the tool radius dependent coefficient of friction, -b- the tool radius dependent sticking/slipping parameter, -c- the extent of viscous dissipation -d- machine mechanical efficiency and -e- the exact heat fraction between the workpiece and the anvil. Models dependent upon input torque taken directly from the FSW machine [48] are usually simple but can give uncertainty coming mainly from fluctuations of data during the steady state welding process. TWI attributed the reason for torque fluctuation to two sources: -a-Process effects- as the material warms up and is plasticised, it will generate less torque on the rotating tool than cooler material. -b- Measurement variation: the FSW machine such as (PowerStir) is large and the torque sensors are relatively insensitive because they need to cover a wide torque range. Some fluctuation will be present in the form of signal noise, and overlaying these variations may be due to the size and inertia of the spindle as the control system seeks to keep it running at a constant pre-set speed as the workpiece material softens [TWI report]. Thus taking an average torque value can create error when carrying out a FSW model. Literatures reviews of different types of numerical analysis of FSW are available in He et. al [49] including simple thermal models, material flow models and fully coupled models for estimating both temperature field and residual stresses. The following models will be useful to outline in the literature review.

2.10.1 Thermo-pseudo mechanical model

This type of modelling is mainly based on pure thermal analysis including some mechanical effects without analysing the mechanical field. Schmidt and Hattel 2004, 2005 [50] [51] have used the thermo-pseudo mechanical model to study the effect of tool probe and the material flow characteristics on the heat generated during FSW. The contact conditions at the tool/workpiece interface were also studied extensively. They found that the convective heat transfer due to material flow greatly affects the temperature fields. Six cases of contact conditions have been introduced based on fully sticking, fully slipping and partial sticking/slipping conditions which were carried out in a model based on Thermo-Pseudo Mechanical simulation. Three heat sources including -a- shoulder only heat source, -b-shoulder/probe heat source in which the tool probe is represented as a volume flux and -c-shoulder probe heat source with no volume flux in the tool/workpiece interface. The non-symmetrical temperature distribution is produced by enforcing the heat flow around the probe volume by specifying a velocity field in shear layers at the tool/workpiece interface, this in turn showed that the temperature field did not only depend on the total heat generation but also on the contact conditions, tool rotational speed and shear layer thickness. For sliding condition a surface flux and for sticking conditions a volume flux in the shear layer were applied respectively. Modelling of FSW is also extended to predict defects such as cavity formation during the process. Schmidt and Hattel 2005 [28] used an Arbitrary Lagrangian Eulerian model (ALE) to study the conditions under which the cavity forms during FSW of aluminium. The main source of heat generated in their model was from plastic dissipation due to the assumption of sticking conditions. The Johnson-Cook (J-C) material law was used to represent the workpiece material viscoelastic behaviour during the process. A heat transfer coefficient with a value of $1000W/m^2.K$ has been used at the workpiece base in order to compensate for the heat transfer from the workpiece into the anvil. The shear layer which is formed during the FSW process has been designed as well in the model in order to represent the heat transfer by convection through the stirred material. Their research found that if the weld did not performed under suitable thermo-mechanical conditions, defects such as voids can exist in the welded joints. Such unsuitable welding conditions are caused by the lack of material flow when traverse speed exceed a specific limit. Their model has overestimated the exact temperature at the tool/workpiece interface and that has been interpreted as the result of neglecting the heat transfer through the tool. Schmidt and Hattel 2008 [52] discussed the heat generation from previous models based on solid (CSM) and fluid (CFD) assumptions and

established a model based on a Thermo-Pseudo Mechanical model. They reported that pure thermal models cannot predict the welding temperature without prior calculation of heat generation coming from expensive experimental work. An example of that is the difficulty of measuring the friction coefficient and yield stress in the laboratory because of the limits of slip rate and strain rate respectively. In their model the plastic behaviour of the material under welding (aluminium 7075-T6) was included and they found that at elevated temperatures, the yield stress which is the driver of the heat generated during the FSW process, decreases sharply when reaching the solidus temperature. A Spatial distribution for the surface heat flux was adopted and solved analytically.

The thermal pseudo-mechanical model was developed later by Hattel et. al. 2015 [53] to include calculating the residual stresses in the joint structure. The suggested model is dependent upon a Lagrangian global framework on a semi-coupled transient solution. The collected data of temperatures as a function of time and location were employed to estimate the transient strain rate and thermal stresses. Their thermo-mechanical model was improved by coupling it with a metallurgical model and taking into account the material flow to study the effect on the distribution and values of the calculated longitudinal residual stresses.

2.10.2 Models Based on Material Flow and Heat Transfer (CFD) Techniques

Many previous models have used CFD techniques to simulate the material flow, temperature and strain rate. FLUENT ,for example, was employed for a long time by many researchers due to its ability to cope with the high strain rate around the FSW tool and also its ability to capture the material flow.

Nandan et. al. 2008 [47], applied a CFD model on a Ti-alloy to calculate the heat and plastic flow during FSW. They showed that five parameters can affect the accuracy of the model in term of both the temperature field and the computed tool torque which are, the spatially variable friction coefficient, the spatially variable slip at the tool/workpiece interface, the extent of viscous dissipation, the mechanical efficiency and the spatially variable heat transfer rate from the bottom surface of the workpiece. So in order to alleviate the inaccuracy they have introduced an optimization factor which depends on the ratio of the calculated results and experiments. The same CFD approach was applied by Nandan et. al 2006 [54] on aluminium AA6061 and on mild steel [55] using a sticking slipping assumptions with a non-Newtonian viscosity depending on strain rate and temperature calculated from a flow stress equation proposed previously by Sheppered and Wright. They found that the asymmetry of

heat and mass flow was increased with increasing tool travers and rotational speeds. They also found that the forced convection in the stirred zone (SZ) plays a significant role in the heat transfer inside the SZ despite the higher thermal conductivity of workpiece in case of welding aluminium alloys. Their model results also showed that material flow mainly occurs on the retreating side. They determined a cut-off viscosity value beyond which no material flow occurs which is equal to 5,000,000 Pa.s for 6061 aluminium alloy and 9,900,000 Pa.s for mild steed.

Colegrove and Shercliff 2005 [56] applied a 3D CFD FLUENT model to simulate the material flow during the FSW process of aluminium alloys 5083 and 7075 including the rake angle of a threaded tool. Their model assumed fully sticking conditions by assuming that the velocity of workpiece material in contact with the FSW tool is equal to the tool rotational speed. Heat generation is calculated from the equation of viscous dissipation (viscosity over the second deviation of velocity field around the tool). The backing plate was represented with a contact resistance of $1000m^2$.K/W to represent a lack of contact with the workpiece. The model results have been compared with a threaded tool without a raked angle and also with a tool without a thread. The material flow of the three models was found to increase toward the tool shoulder. Their model did not predict the actual size of the SZ and also did not estimate welding forces. The model also predicted higher peak temperatures in the SZ compared to experimental measurements. The over predicted temperature in the model was interpreted as a result of using the viscosity equation without softening close to the material melting point. They suggested incorporating slipping conditions in order to overcome these limitations. The temperature was found to increase significantly with tool rotational speed while the traverse speed was found to has a small effect on weld power 1%.

Colegrove et. al. 2007 [57] applied a 2 dimensional axisymmetric numerical model on "aerospace" grade aluminium alloys without employing a complex CFD technique. The model depends on data of hot deformation and thermal properties of the material. The predicted temperatures in the tool/workpiece interface which were in good agreement with the experiments have been used to build an empirical equation of flow stress as a function of strain rate and temperature. The model data has been employed for optimising the FSW process in term of tool rotational speed, tool shoulder diameter and the best assumption of sticking/slipping conditions. They suggested extending hot experimental tests to a high strain rate and a temperature near the solidus to cover the material behaviour during FSW process.

Hasan et al. 2015 [58] applied a CFD isothermal model using FLUENT code with a sticking/slipping heat generation assumption to simulate the FSW of aluminium. They reported the effect of tool wear on the pattern of material flow and found that it can cause a lack of material flow as a result of low strain rate values leading to defect formation especially at the bottom of the SZ. The CFD FLUENT technique was also employed by Cox et al. 2010 [59] to simulate the effect of FSW parameters on aluminium using the viscoplastic material assumption in a fully sticking condition with a workpiece designed as a disc. The CFD model was run with another software package called DAKOTA in order to reduce the running time for optimising welding parameters and to find the optimal tool temperature.

Fairchild et al. 2009 [60] applied the CFD FLUENT model to simulate the FSW of pipe line steel. The heat generated was dependent up on the sticking/slipping assumption using two types of FSW tools including PCBN and W-Re. Peak temperatures resulting from CFD model have been compared with microstructure phase transformation in the welded material. The experimental test results showed that the tool type has a slight effect on mechanical properties of the welded joints. The lack of validation of the model in terms of the temperature field was attributed to the difficulty of measuring the thermal cycles in the SZ using thermocouples. They argued that extrapolation of the thermal cycles of the SZ coming from thermocouple readings far away from the SZ can give errors. The difference in the heat transfer mechanism between the SZ which is mainly by convection and the material just away from this zone where the heat transfer by conduction can increase the extrapolation error of the thermal cycle. A combination between CFD and the Lagrangian framework to track the material flow during the FSW process has been suggested. Material flow is found to be a function of the distance from the FSW tool, as well as, the asymmetry in material flow was suggested to be the reason for the asymmetry in the heat generated around the weld centreline. Defects were also postulated on the (AS) as a result of a stagnant zone formation. Increasing the welding (traverse) speed has caused an increase in the difference in relative velocity between AS and RS, the strain rate value was higher in the AS than the RS as a result of asymmetry. The authors suggested that in FSW of steel, the temperature in the SZ is higher than the one predicted in the CFD model.

Micallef et. al. [61] carried out 3D CFD modelling of FSW 6mm DH36 steel. The heat was generated mainly by plastic deformation and the tool was represented in the model with fully sticking conditions at the tool shoulder/workpiece interface. Viscosity was represented from flow stress which was calculated by carrying out a hot compression test at different ranges of

temperatures up to 1100°C and strain rates up to $100s^{-1}$. The effects of different welding conditions including slow, intermediate and fast rotational and traverse FSW tool speeds on Stir Zone (SZ) size and heat generated were investigated. The heat convection coefficient was represented as a function of distance at the workpiece bottom and the tool/workpiece contact region in order to increase the accuracy. The temperature field calculated from the CFD model was validated against data measured by a series of thermocouples. They found that the total heat generation for various welding conditions has a non-linear relationship with tool angular and radial position. The model also suggested that the shape and size of the SZ is highly affected by plunge depth.

Cho et al 2013 [62] carried out a 3D CFD model on ferritic stainless steel and validated the result by microstructure examination looking at post weld changes and also with thermal histories during the FSW process. They found that the maximum peak temperatures are generated in the tool/workpiece contact region and the non-Newtonian viscosity is changed significantly around the SZ and TMAZ (shear layer). Maximum material flow was found on the retreating side of the tool and the asymmetry between AS and RS was found to increase with increasing welding speed. Strain rate is found to increase around the tool/workpiece interface as a result of sever material stirring.

2.10.3 High Integrity Low Distortion Assembly (HILDA) project simulation work on DH36 steel

The HILDA project was carried out on grade DH36 steel in order to investigate the feasibility of using the FSW process to weld steel. The project included experimental work and numerical modelling.

Toumpis et. al. 2014 [16] established a 3D thermo-fluid model to simulate the material flow, strain-rate and temperature distribution in FSW of 6mm DH36 steel. The viscoplastic thermo-mechanical behaviour was characterised experimentally by a hot compression test on a Gleeble 3800 simulator with a range of temperatures from 700-1100°C and strain rate 10^{-3}-10^{2} s^{-1} and the flow stress equation was based on the Norton Hoff law. Heat generation was based on both plastic deformation and frictional heating. The workpiece and backing plate were designed as a disk; the PCBN tool was designed without thread and included in the geometry. The flow stress was found to increase at a test temperature 800 ^{o}C and attributed to the formation of a dual phase microstructure of ferrite and austenite at this temperature. The temperature distribution and geometry of TMAZ and HAZ were in a good agreement with

experimental results. The limits of temperature contours at 700 $^{\circ}$C was used to determine the extent of the heat affected zone (HAZ) which showed a good agreement with experimental macrograph measurements. A maximum temperature for cold conditions (200RPM /100mm/min) was 1050 $^{\circ}$C and for hot conditions (500RPM, 400mm/min) was 1250 $^{\circ}$C. The HAZ for hot conditions was found to be smaller than the one in cold conditions due to lower diffusion of heat resulting from high traverse speed. TMAZ was found to be asymmetrical; it is wider on the RS compared to the AS.

2.10.4 Advantages and Limitations of modelling using the CFD Technique: The following advantages and limitations can be concluded from the previous CFD modelling on FSW process:

Advantages:

- CFD modelling is a robust technique for simulating the FSW process as it is able to cope with the high deformation, material flow and strain rate.
- CFD technique is based on material flow and heat transfer, the analysis includes solving equations of momentum, mass and energy. Usually the analysis is under steady state conditions in a Eulerian framework, thus time of solving the required equation will be shorter when compared to the transient analysis.
- Viscosity in CFD models is usually represented as non-Newtonian and computed from the flow stress equation based on experimental hot working tests.
- The temperature field, relative velocity, viscosity cut-off limits and the SZ size can be estimated successfully. Torque around the tool can also be monitored during the analysis.
- CFD model results can be validated by different procedures including thermocouples measurements, microstructure evolution, the size of SZ, the change in viscosity values at the TMAZ and finally can be validated by tool torque.

Limitations:

- It is more a complex and potentially more expensive procedure compared to other techniques such as FEM as it requires data of viscosity taken from expensive hot working tests over a wide range of temperatures and strain rate such as hot compression test.

- It is unable to detect defects such as voids which required a robust transient analysis such as the ALE technique. However, defects related to the lack in material flow can be detected from the stagnant zone formation which was reported in the previous case study when traverse speed increases to a specific limit [60][58].
- It is unable to calculate the residual stresses associated with FSW as the analysis is based on the Eulerian local steady state model.

2.10.5 Models based on Torque

Such models usually calculate the heat generated from torque and tool rotational speed as follows [48]

Power Q (in watt) = torque M (N.m) × rotational speed ω (rad/sec)   (1)

The power is then converted into heat flux or volume flux by dividing its value on the surface contact area or contact volume of the tool/workpiece respectively.

Finite Element Method (FEM) analytical models which have used torque as the main source of heat during the FSW can be found in [48][63][64][65]. In these models the relationships between torque and welding parameters such as tool rotational/traverse speeds and plunge force have been correlated. [63] Khandkar 2003 experimentally correlated torque with heat input. Cui et al. 2010 [64] established an exponential expression of torque and related it to tool rotational and traverse speeds. They found that tool rotational speed significantly controls the torque value rather than the tool traverse speed. Roth et al. 2014 [66] applied a semi-analytical torque model based on sticking/sliding contact conditions. The relationship between torque, rotational speed and axial forces was addressed. The measured axial force and temperature were employed to calculate the coefficient of friction. They found that the friction coefficient has a value ranging from 0.3 to 0.4 when carrying out FSW of AA5083-H111 with a H13 steel tool. Its value was reported to decrease with increasing plunge depth and tool rotational speed. Long et al 2007 [67] extended the correlation of welding parameters such as axial force and rotational speed with torque to include the SZ size. They reported a decrease in torque with increasing tool rotational speed as a result of the increase in welding temperature close to the melting point and the consequences of the drop in material flow stress. Jefferson 2006 [48] used a variable spindle speed test over a wide range of welding parameters in order to build a relationship with the input torque. They found that at low feed rates, the heat input is significantly decreased with decreasing tool rotational speed or increasing welding speeds,

however, the effects on heat input was only slight at high feed rates. It is worth mentioning that using the variable spindle speed test has reduced the FSW process cost by reducing the number of weld joints required over a wide range of welding parameters to build a correlation with torque.

From previous work on the torque model it can conclude that there are the following advantages and limitations:

A. Advantages

- The torque model is simple and cheap as the heat generated during welding is calculated from the experimental input torque and tool rotational speed.
- There is availability to correlate torque with the welding parameters such as tool rotational speed, plunge (axial) force, SZ size and the coefficient of friction.
- The torque model ignored the convective heat transfer coming mainly from viscoplastic flow of metals.

B. Limitations

- Experimental input torque values measured from the FSW machine can be inaccurate due to the fluctuation of data during the steady state process.

2.10.6 Summary of Previous work on Modelling of the FSW

From previous work it is evident that the complexity of the FSW process including the debate about tool/workpiece contact conditions, sticking/slipping conditions, the heat source generated during the FSW process (frictional (coefficient of friction)/ plastic (shear yield stress)/ viscous heating (non-Newtonian viscosity and velocity gradient, torque ($M \times \omega$)) have resulted in many different models and assumptions. Most of the previous models also excluded the tool in modelling the FSW due to the complexity of tool meshing and surface contact. Only a few models have included the tool in simulating the FSW process [61] [16]. The current work has been introduced and compared the different contact conditions and heat source assumptions. The best assumption has been chosen according to a new method of validation depending on elemental segregation/precipitation as will be shown in the results and discussion section.

2.11 Materials

Two grades of steels used mainly in shipbuilding have been chosen for this study which includes ASTM A131 steel DH36 and EH46 mild steel grades. to the two grades will now be introduced in terms of chemical composition, physical properties and phase transformation.

DH36 high strength steel and EH46 extra high strength steel are grades used in ship building constructions, such as ship's hull due to their physical properties and corrosion resistance, high fatigue resistance, impact toughness and also good weldability [68]. The chemical composition of these grades of steel is given in Table 2.5 and Table 2.6 whereas Table 2.7 shows the physical properties. The average grain size of DH36 given by the supplier is D = 9±2µm, with a homogeneous microstructure and the same physical properties in the vertical and horizontal rolling direction. [69]. DH36 grade was reported to show linear strain aging increase when the temperature increased from 600 ^{o}C to 800°C as shown in Figure 2.12 [69]. This increase in strain aging can lead to an increase in the flow stress in that range of temperatures which in turn can affect the FSW parameters. The same phenomena of flow stress increasing when reaching to the 800°C limit was recorded by Toumpis et al. [16] while performing hot compression test on DH36 steel in a range of temperature 700-1100 ^{o}C. The flow stress was increased from 144 MPa at 750 ^{o}C to 156 MPa at 800 ^{o}C and was attributed to presence of dual phase of ferrite and austenite at that temperature.

EH46 is an improved steel grade for shipbuilding which works at lower temperatures; it has higher mechanical properties including toughness and fatigue due to the higher percentage of alloying elements such as V, Ti and Nb. The following sections will give more details about materials phase transformation, weldability, the effects of interstitial elements and nitrides/carbides precipitation.
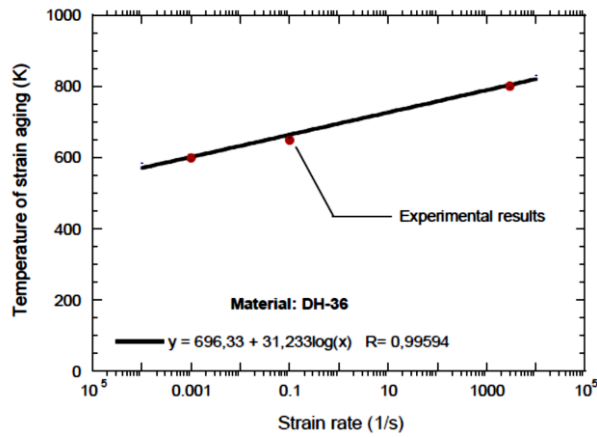
Figure 2.12: Strain aging temperature vs. strain rate for DH36 steel. Experimental results adapted from [69]

Table 2.5: Chemical Composition of as-Received DH36 Steel (wt%)

C	Si	Mn	P	S	Al	N	Nb	V	Ti	Cu	Cr	Ni	Mo
0.16	0.15	1.2	0.01	0.005	0.043	0.02	0.02	0.002	0.001	0.029	0.015	0.014	0.002

Table 2.6: Chemical composition of EH46 Steel Grade (wt%)

C	Si	Mn	P	S	Al	N	Nb	V	Ti
0.20	0.55	1.7	0.03	0.03	0.015	0.02	0.03	0.1	0.02

Table 2.7: Materials properties of DH36 and EH46 steel grades at room temperature.

Steel	Thermal conductivity W/m.K	Heat capacity J/kg.K	Density kg/m^3	elastic modulus GPa	Yield strength MPa	Ultimate tensile strength MPa	Poisons ratio	Melting point ^{o}C
DH36	48	455	7850	208	355	490-620	0.3	1450-1500
EH46	50	500	7870	208	460	570-720	0.3	1480-1520

2.11.1 Carbon Equivalency

Carbon equivalency (Ceq) is a guideline established by the International Institute of Welding (IIW) to help determine weldability of a steel product [70], [71]. Weldability is affected by multiple alloying elements, most   notably C, but is also influenced by Si, Mn, Cu, Ni, Cr, Mo, V   and Ti. Depending on the carbon content, the other elements affect weld ability and Ceq   differently. The carbon equivalent can be calculated as [72 P1015]:

Ceq = [C+(Mn+Si)/6+(Cr+Mo+V)/5+(Ni+Cu)/15]   (2.1)

So

   Carbon Equivalent EH46: Ceq = [C+(Mn+Si)/6+(Cr+Mo+V)/5+(Ni+Cu)/15]% = 0.58

   Carbon Equivalent DH36: Ceq = [C+(Mn+Si)/6+(Cr+Mo+V)/5+(Ni+Cu)/15]% = 0.39

Based on carbon equivalency values, the weldability of DH36 is expected to be better than EH46 grade due to lower value of carbon content and also other elements.

2.11.2 Phase Transformation Temperatures

Because the bainite (B) phase is usually expected in the SZ of the welded joints of these types of steel, it is beneficial to know the start and finish temperatures of bainite. The Bainitic start temperature of steel B_s can be calculated from the following empirical equation [73]

   Bainite starting temperature (B_s)=830-[270C+90Mn+37Ni+70Cr+83Mo]   (2.2)

   So: DH36 B_s= 677°C

      EH46 B_s= 623°C

The temperature at which austenite begins to transform to ferrite during cooling can be calculated by using the following formula [74]:

A_{r3}= 910- [310 C +80 Mn +20 Cu +15 Cr+80 Mo+ 55 Ni]   (2.3)

Where the concentrations are all in wt-%.

so for DH36 A_{r3}= 775 ^{o}C

And   EH46 A_{r3}= 712 ^{o}C

The temperature at which austenite begins to form during heating can also be calculated [74]:

$$Ac_1 \ [°C] = 739-22C+2Si-7Mn+14Cr+13Mo-13Ni \qquad (2.4)$$

DH36= 727.43 ^{o}C   ,   EH46= 723.8 ^{o}C

And the temperature at which transformation of ferrite to austenite is completed during heating can be as follows [74]

$$Ac_3 \ [°C] = 902- 255C+19Si-11Mn-5Cr+13Mo -20Ni+55V \qquad (2.5)$$

DH36 Ac_3= 850.6 ^{o}C   ,   EH46 Ac_3= 847.15 ^{o}C

The above calculated data is for equilibrium cases and the transformation temperatures in FSW may be affected by strain and strain rate. Previous work done on rolling [75] showed that the temperature of non-recrystallization (the temperature at which complete static recrystallization no longer occur for a specific hold time) can be affected by strain and strain rate, a decrease of 64°C was reported with increasing the strain rate from 0.5 s^{-1} to 2 s^{-1}. The same effect of strain on ferrite and bainite transformation temperature was reported by Failla 2009 [76] as a result of reduction in austenite grain size. Figure 2.13 shows the effect of deformation on the phase transformation of ferrite and bainite of HSLA-65, faster phase transformation occurs when deformation increases resulted from the reduction of the austenite grain size during FSW process [76].

CCT
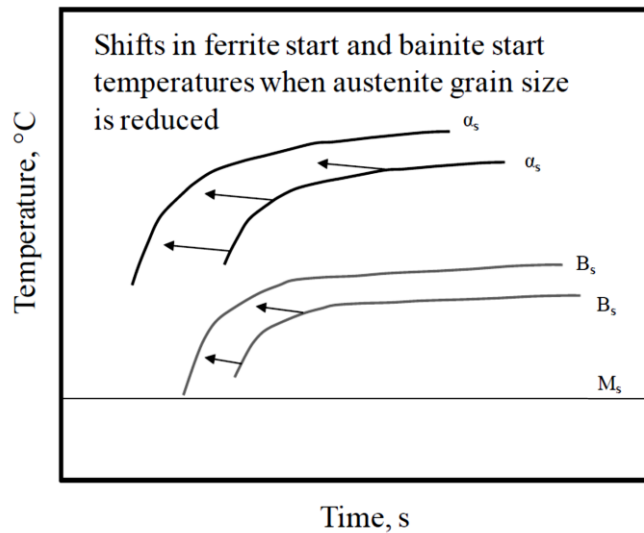
Figure 2.13: CCT diagram shows the effects of deformation on ferrite and bainite start temperatures of HSLA-65 steel grade [76].

Some previous work carried out on the phase transformation of a steel similar to DH36 with 0.17%C and 1.46%Mn is shown in Figure 2.14 [77]. The sample is heated to 1100 $^{\circ}$C and continuously cooled with many different cooling rates. It is reported that a higher Mn content can lead to an increase in the probability of bainite and martensite transformation [77], so for EH46 steel grade the same cooling rate can result in more bainite phase in weld joints. In their work the formation of an additional phase between the bainite and Widmanstatten ferrite called Ferrite/Cementite Aggregate (FCA) was noted which might be found in the weld joints of DH36 and EH46 steel grades. Table 2.8 gives the details of the heat treatment and the percentage of phase's present with respect to the cooling rate [77].
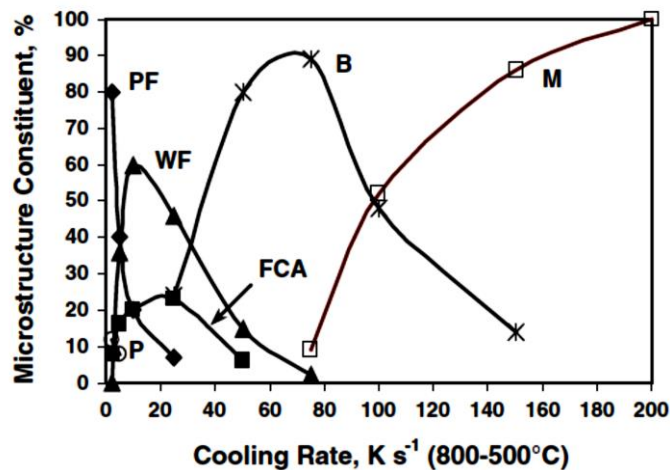
Figure 2.14: Volume percent microstructure constituents vs cooling rate in thermally cycled, 0.17 wt % C 1.46 wt % Mn steels Austenitized at 1100°C. [77 P587], B-bainite, M-martensite, PF-primary ferrite, WF-Widmanstatten Ferrite, FCA- ferrite cementite aggregate.

Table 2.8: Heat Treatment and Transformation Data for Continuously Cooled 0.17 wt %C 1.46 wt %Mn steels table adopted from [77 P586].

Steel Code	Peak Temp. [K (°C)]	Cooling Rate °C s⁻¹ [1073 K to 773 K (800 °C to 500 °C)]	Transformation Temp. (°C)				Phase Amount (Pct)							
			T_S	T_{50pct}	T_{PRTT}	T_F	PF	P	WF	MP	FCA	UB	LB	M
C (1.46 Wt Pct Mn)	1373 (1100)	2	747	630	620	491	80	12	—	—	8	—	—	—
		5	727	600	625	471	40	8	29	7	16	—	—	—
		10	713	600	600	446	20	—	44	16	20	—	—	—
		25	657	515	520	335	7	—	34	12	23	24	—	—
		50	612	405	410	284	—	—	11	4	6	52	28	—
		75	575	395	400	232	—	—	2	—	—	23	66	9
		100	514	390	395	222	—	—	—	—	—	—	48	52
		150	489	360	365	215	—	—	—	—	—	—	14	86
		200	484	380	380	196	—	—	—	—	—	—	—	100

PF: primary ferrite; P: pearlite; WF: Widmanstätten ferrite; MP: microphase; FCA: ferrite/carbide aggregate; UB: upper bainite; LB: lower bainite; M: martensite.

2.11.3 The mechanism of formation of acicular ferrite and bainite

Acicular ferrite (α_a) and bainite are the phases which are predominant in FSW of DH36 and EH46 steel joints [78] [79]. This section gives an introduction to these phases and summarise the mechanism by which these phases are formed during the heating and cooling cycles. A review on acicular ferrite α_a formation can be found in [80] in which four factors have been reported to affect the α_a formation mechanism which include:

- Austenite grain size
- Cooling rate
- Steel composition
- Non-Metallic inclusions

Acicular ferrite microstructure is usually described as chaotic, its plates are nucleating heterogeneously on non-metallic inclusions and grow in different directions [81]. The morphology of acicular ferrite microstructure has been reported to increase the weld joints toughness by resisting cleavage propagation as these types of cracks deflect when they start to propagate into the multi orientation acicular ferrite microstructure [81]. Bainite morphology is like sheaves which start to organise as parallel plates in series. It was found that bainite sheaves start at the austenite grain boundaries [82], so it is expected that the fine grains of austenite with a medium cooling rate make bainite the most dominant phase, whereas larger austenite grains leads to a microstructure consisting of other phases such as acicular ferrite as shown in Figure 2.15 [82]. Table 2.9 summarizes the difference between α_a and bainite in terms of nucleation/ growth direction and mechanism [80].
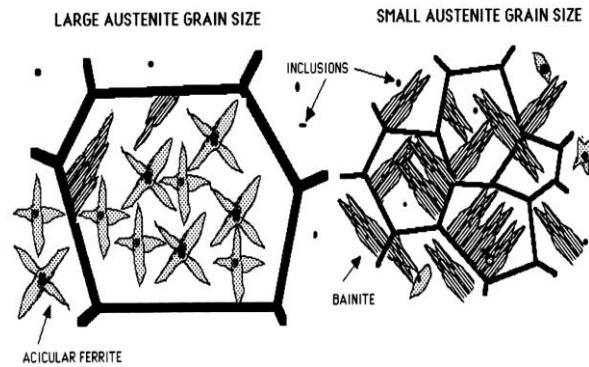
Figure 2.15: The effect of austenite grain size on the development of microstructure in steel containing inclusions. (Larger grains tends to transform to acicular ferrite whereas small grains tend to transform to B)[82 P242].

Table 2.9: The difference between acicular ferrite and bainite formation [80]

	Acicular ferrite	Bainite
Nucleation	intragranular	inter- or intragranular
Nucleation site	point sites (surface of NMI)	mostly austenite grain surface
Transition Temp.	similar	
Grain form	needle-shaped/lenticular plates	fine laths which form sheaves
Growth direction	various directions (star-like)	parallel laths
Parallelism	cannot form parallel laths	laths are parallel within package
Growth mechanism	diffusionless	
Growth stop reason	C-enrichment of austenite or impingement	

NMI-Non-Metallic Inclusion

The effective elements which act as nucleation sites for α_a usually include C, O, S, V, Ca, Ti, Nb, Mn and Al [81]. The most effective desirable element for α_a formation is Ti as shown in Figure 2.16, about 50ppm of Ti in a weld is enough for 70% of α_a phase transformation [81].
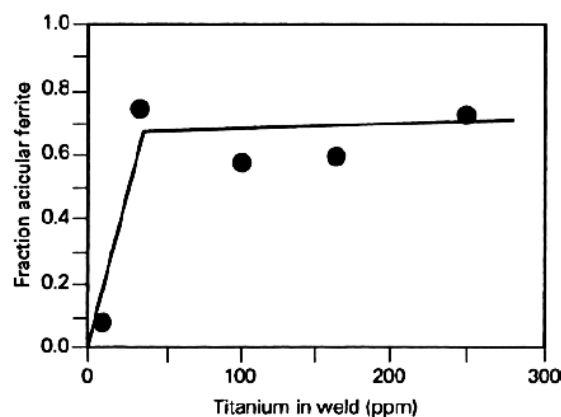
Figure 2.16: The effect of Ti element on the formation of acicular ferrite, more acicular ferrite with increasing Ti content [81]

42

2.11.4 The effects of chemical composition on austenite grain growth and precipitate formation

Nb, Ti and V are the most effective elements that control the Recrystallization (RX) temperature and each of these elements can form solid solutions with iron [83]. The ability of V, Nb, and Ti to form carbides and nitrides can cause pinning and precipitation strengthening to the austenite grains and grains boundaries during heating which in turn can result in grain refinement. Figure 2.17 shows the effect of these elements on austenite grain size with temperature [84], whereas figure 2.18 [85] shows the solubility of these elements as carbonitrides in austenite during heating of HSLA steel grade. Ti showed the lowest solubility compared to the other elements.
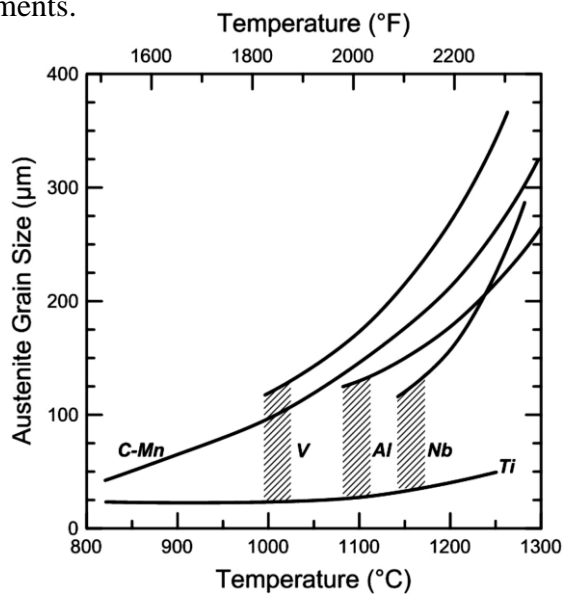
Figure 2.17: The effects of V,Ti,Nb and Al on the austenite grain size, titanium is the most effective element in preventing austenite grain growth when heating to high temperatures [84].
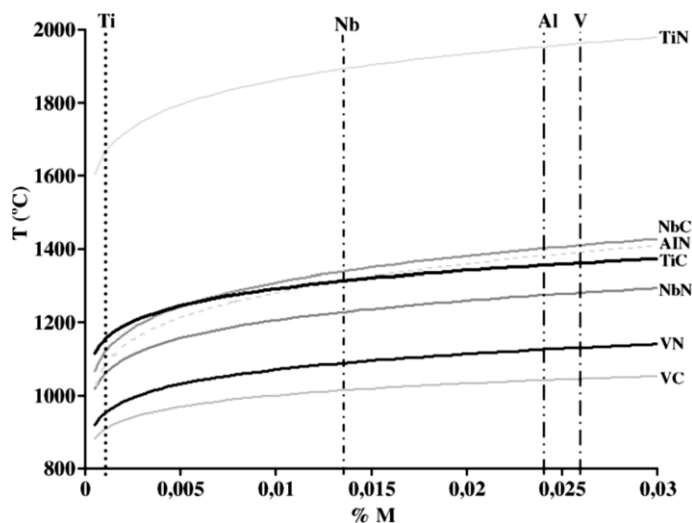
Figure 2.18: Equilibrium solubility products of carbides and nitrides in austenite [85].

Figure 2.19 shows the effect of the common elements on the non-RX temperature (T_{NRX}) as a function of initial solute content in steel with 0.07% C, 1.4% Mn, and 0.25% Si wt [85 Cuddy 1982]. Niobium shows a much greater effect in increasing the T_{NRX} than Ti, Al, and V. From the graph, it takes approximately 0.25 atomic pct of V to increase the TNR to roughly 875 °C, whereas it only requires approximately 0.05 atomic pct Ti for the same increase in temperature. The same increase in T_{NRX} can be achieved with only 0.005 atomic pct Nb, an order 10 times of magnitude less than Ti. The atomic radius of Fe is very close to the atomic radius of V, which may explain part of the reason V is not as effective at increasing T_{NRX} as Nb and Ti [86].
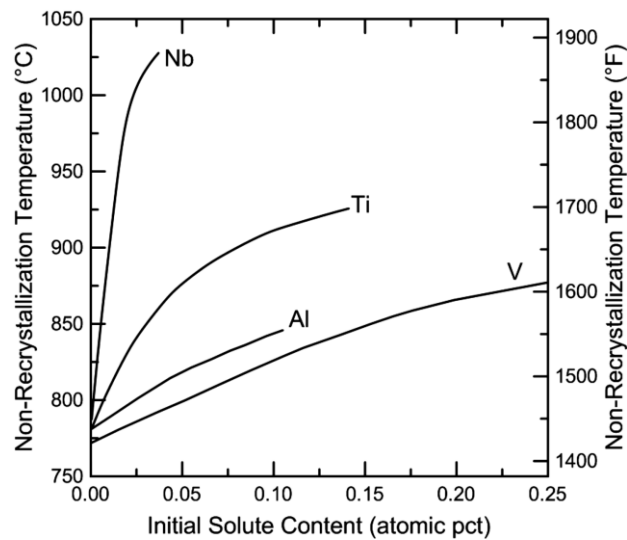
Figure 2.19: The effects of micro-alloying content on the recrystallization stop temperature of austenite in a 0.07 C, 1.4 Mn, 0.25 Si steel (in wt pct). Adapted from [86 pp129-140.]

2.11.5 The difference between DH36 and EH46 in term of interstitial elemental percentage

The previous information about phase transformation, interstitial elements percentage and the weld-ability of the two steel grades are paving the way for understanding the microstructural evolution and the expected precipitation after the FSW process. More wt% of interstitial elements such as Ti, Nb and V found in the microstructure of EH46 rather than DH36 grade mean that in EH46 grade, the austenite grains growth during the FSW process will be expected to be less and thus increasing the availability for bainite formation. EH46 is also expected to be harder to weld due to higher percentage of carbon and other interstitial elements (see Ceq number eq. 2.1), so PCBN tool wear is expected to be more than in DH36 especially at higher tool travelling speed.

2.11.6 TiN Precipitates in Steel

Titanium where present in steel can precipitate during the FSW process at specific conditions including a range of peak temperatures and cooling rates to form compounds such as TiN or Ti (N,C) depending on the chemical weight of elements present in the steel especially carbon [87] [88] [90] [91].

Much previous work has investigated the TiN precipitates in low carbon steel grades during heating and cooling cycles. Stockes et al. 2014 [87] has investigated the cooling rate effects on TiN precipitates in low carbon micro alloyed steel and found that TiN particles can precipitate at very high temperatures near the melting point of steel. They also found that TiN particles size increases with decreasing cooling rate and the size can reach to 1-2.5 µm at low cooling rate, whereas, the particles tend to cluster for higher cooling rates. Nagata et al. 2002 [88] studied the TiN particles distribution in HSLA steel grade by using TEM examination of carbon extraction replicas of eight thin slab samples. They found that TiN precipitates size decrease with increasing cooling rate. El-Fawakhry et al. 1991 [89] studied the formation of TiN precipitates in a Ti steel and found that the particle size can reach between 5-10µm during the rolling process at a temperature of 1250°C. The study findings also showed that TiN particles are mainly precipitated on CuS particles. Wang et al. 2010 [90] also investigated the size and distribution of Ti precipitates in low carbon steel and its relation with cooling rate, they found that the particle distribution increases and the size decreases with increasing the cooling rate. Their study also found that for the steel grade under study, the TiN particles is precipitate nucleate and mainly on Ti_2O_3 and Al_2O_3 particles. Hong et al. 2003 [91] investigated the precipitates of Ti and Nb in HSLA steel in a temperature range of 1373K-1673K (1100°C -1400°C) with the aid of TEM. Their study found that (Ti,Nb)(C,N) dendritic carbonitrides disappear after reheating to a temperature higher than 1273K (1000°C) and a new cubic shape precipitated in the microstructure appears with a size depending on the peak temperature and cooling rate.

2.12 Microstructure evolution and mechanical properties in FSW of Steel

There has been a great deal of work on FSW of steel in order to understand and commercialise the process and the HILDA project [5] which cost 2.1m Euro is an example of FSW research on DH36 steel grade. During FSW; the steel microstructure experiences phase transformation as the temperature is expected to reach the austenite field. It is beneficial to define different regions which appear in the weld joint after the FSW process as shown in Figure 2.20 which include [5]:

- SZ-The Stirred Zone, the region highly affected by the tool rotation and heating.
- Shear Layer: The Thermo-Mechanical Affected Zone (TMAZ) adjacent to the stirred zone in which the material has experienced both heating and stirring by the FSW tool.
- Weld root: The region around and below the end of FSW tool probe, this region is part of TMAZ.
- HAZ: Heat Affected Zone, the region adjacent to the TMAZ and only affected by the heat dissipated from the TMAZ.
- PM: Parent Material, which is the material not affected by the FSW process.
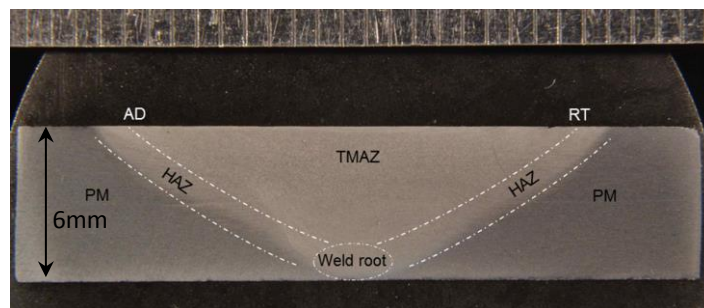
Figure 2.20: Macrograph of polished and etched FSW region of 6mm DH36 steel grade [5]

Mechanical properties can also show changes related to the phase transformation after the FSW process. Such mechanical properties are micro hardness, tensile strength, fatigue and impact strength. An example of phase transformation and mechanical properties correlation is found in work done on C-Mn steel [77]. Figure 2.21 relates the microhardness to the different phases obtained by heating the sample to $1100^{o}C$ and cooling at different rates [77]. It was found that the formation of a bainite phase increases the HV microhardness of the base metal by about 50-100 HV compared to the PM as shown in figure 2.21.
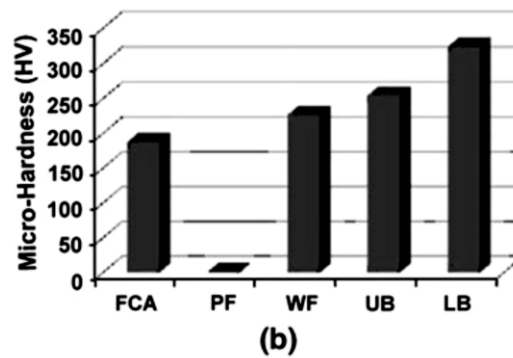
PF = Primary Ferrite; P = Pearlite; FCA = Ferrite/Carbide Aggregate;
WF = Widmanstatten Ferrite; UB = Upper Bainite; LB = Lower Bainite

Figure 2.21: Micro-hardness data for microstructure constituents in steel. [77 P586]

In order to understand the feasibility of the FSW process for welding steel alloys especially those under this study such as DH36 and EH46, the following literatures review are considered.

McPherson et al. 2013 [92] carried out a series of FSW on different thickness of 4, 6 and 8 mm DH36 steel plates and compared the mechanical properties with welds produced by the submerged arc welding (SAW) technique. It was found that distortion and fatigue at high stress range (0.6-0.8 of the yield stress) for all FSW samples thickness as shown in figure 2.22 is particularly improved in FSW compare to SAW. Other mechanical properties are also found to increase especially toughness when applying double sided FSW instead of single sided. The microstructure after the FSW process showed a significant improvement compare to SAW as shown in Figure 2.23 [92]. The coarse longitudinal visible grains in SAW are not found in FSW, also the HAZ is smaller in FSW than in SAW.
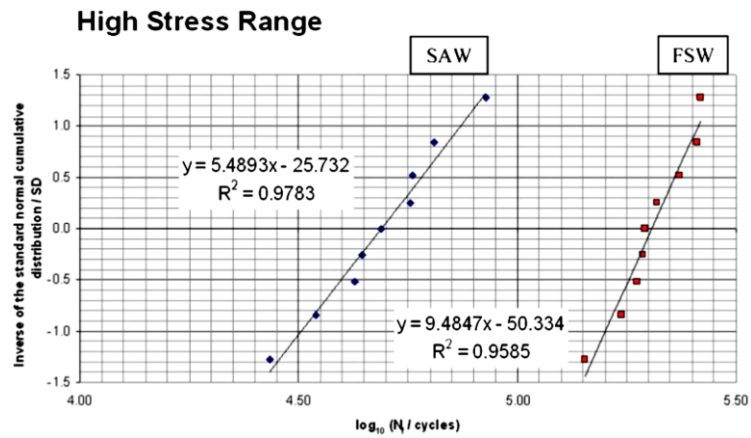
Figure 2.22: Fatigue testing of FSW samples compared to SAW samples [92].
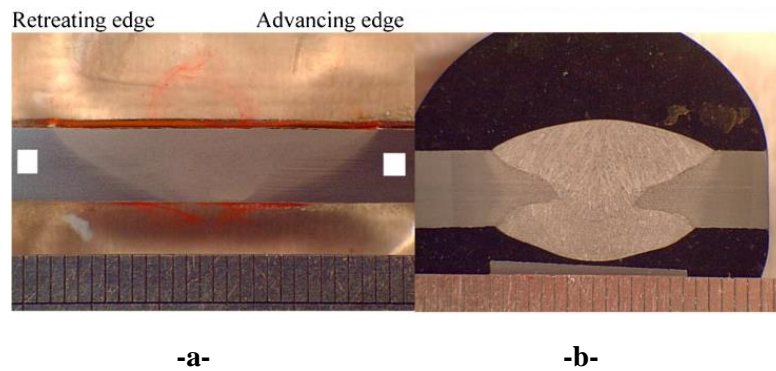
Figure 2.23:DH36 8mm thickness a-FSW single side, b-SAW double side [92].

Toumpis et al. 2014 [78] investigated the microstructure and mechanical properties of 19 FSW samples of DH36 at different ranges of tool rotational and traverse speeds in order to produce commercially viable welded joints. The welds were classified as slow (V<200 mm/min and ω=200rpm), intermediate (V=400-450 mm/min and ω=250-400RPM) and high (V=500 mm/min and ω=575-700RPM) speeds. Microstructure examination, tensile testing and Charpy impact testing were applied to evaluate the weld . They found that slow traverse speeds resulted in a microstructure that consisted of fine ferrite. At intermediate traverse speeds it was a uniformly distributed mixture of acicular ferrite and bainite with evidence of prior austenite associated with the bainite and finally at high traverse speeds a heterogeneous microstructure including specific regions of acicular ferrite and bainite

The two microstructure regions in both welds include bainite morphology with clear prior austenite grains and coarse ferrite/cementite identified as acicular ferrite were interpreted as a result of different cooling rates that the material under FSW had experienced. The low traverse speed welds produced welds with high tensile properties but at these low speeds productions rates were considered to be too slow. The intermediate range (ω/V(Rev/mm) = 450RPM/350mm/min) samples produced welds with the highest tensile properties. At higher welding speeds the samples of tensile test have failed in the welded region. The process of obtaining a reproducible relationship between traverse and rotational speed and weld mechanical properties were successful but, at the same time, expensive. Although non-metallic inclusions were found on the advancing side of the high welding speeds group (600RPM, 500mm/min) and (650RPM, 500mm/min) and were counted as flaws in the weld, it was considered that the welds were still acceptable and comparable to other traditional fusion welding processes.

Reynold et al. 2003 [79] studied the relationship between the mechanical properties and parameters of FSW of 6.4mm thickness DH36 steel at speeds of 3.4 mm s^{-1} (8 in min^{-1}), 5.1 mm s^{-1} (12 in min^{-1}), and 7.6 mm s^{-1} (18 in min^{-1}). Single pass defect free welds were produced for each welding condition. It was shown that the ferrite and pearlite bands of the parent metal have experienced phase transformation to bainite and martensite in the SZ during the FSW process. This crucial improvement, in the microstructure and resulting mechanical properties of the welded nugget compared to the base metal, has been achieved after the FSW process. Maximum hardness was found in the SZ with a gradual decrease toward the HAZ and the base metal. Increasing tool traverse speed has been found to achieve higher hardness and higher longitudinal tensile strengths.

Lienert 2004 [93] investigated the feasibility of welding 0.18 inch (4.5mm) DH36 steel by the FSW technique with a W-25% Re tool and a range of tool rotational speeds from 400-500RPM and traverse speeds of 200mm/min to 250mm/min. The microstructure of the as-received material experienced phase transformation from 15-20µm ferrite grains with continuous bands of pearlite to mainly acicular ferrite in the SZ whereas, a partially spheroidal pearlite was found in the HAZ. Both microhardness in the SZ and tensile strength have increased compared to the base metal. Defects have been found in the weld root of two samples, which were attributed to incomplete bonding, resulted in failures during tensile testing.

Fowler et al. 2016 [94] investigated the effect of defects such as weld root flaws on fatigue and bending strength of FSW DH36 steel with welding speed of 300mm/min and tool rotational speed of 400RPM. They found a slight reduction in the three point bend test results but this was small because the cracks associated with the weld flaw did not propagate. However, fatigue test results were significantly affected by this type of defect but were still found to be acceptable compared to fusion welding. They suggested optimization of the tool material and welding parameters in order to remove/ reduce FSW defects. The microstructure in the SZ was heterogeneous and mainly consists of acicular ferrite, fine ferrite grains and bainite. The weld root microstructure consisted of fine grains of ferrite which were attributed to the lower temperature experienced and the slower cooling rate compared to the top surface of the SZ. The grain size of ferrite in the weld root was finer than those in the PM due to the effects of dynamic recrystallization which resulted from high strain rate associated with material stirring. Toumpis et al. 2015 [9] examined the evolution of mechanical properties of FSW DH36 steel and investigated how changes in process parameters resulted in changes in the microstructure which in turn influenced fatigue performance. Three welding conditions were investigated including slow (200RPM, 100mm/min), intermediate (300RPM, 250mm/min) and fast (700RPM, 500mm/min). The effect of defects found in the SZ on the fatigue resistance was also discussed. It was found that defects resulted from the tool marks on the top surface of weld joint have a significant influence on reducing fatigue resistance. The slow (200RPM, 100mm/min) weld showed the best fatigue resistance as it was a defect free joint with homogeneous microstructure. It was suggested that an increase in the plunge depth would reduce defect formation in the FSW process especially weld root flaws, which would in turn improve fatigue performance.

Konkol and Mruczek 2007 [23] studied the feasibility of FSW HSLA-65 steel 6mm plate thickness and compared the produced weld joints with SAW in term of distortion and microstructure evolution. FSW samples showed no transverse distortion, higher toughness and tensile strength than SAW samples. The FSW microstructure showed fine grains of ferrite, whereas in SAW the grains were large columnar shaped, which gave an indication that higher temperatures are experienced by the workpiece in SAW than in FSW process. The microstructural evolution and micro-hardness of the same grade of steel HSLA-65 was also investigated after carrying out the FSW process including changing the traverse speeds and tool material.[95] The traverse speed and tool material were found to affect the micro hardness and microstructure evolution. In general it was found that after the FSW process a finer

microstructure (mix of bainite, acicular ferrite and martensite) and higher hardness has been obtained compared to the base metal. The width of the HAZ was less in the case of welding using a PCBN tool rather than a W-Re tool, this was attributed to the fact that the PCBN tool absorb more heat due to its higher thermal conductivity.

Lienert et. al. 2003 [96], studied the feasibility of welding mild steel AISI 1018 by relating peak temperature with the resulting microstructure. The temperature was measured experimentally using thermocouples and an infrared camera which recorded a peak temperature of 1000°C at the top surface of SZ. However, the authors suggested that the maximum temperature reach was 1200°C based on microstructural evidence and also by extrapolation of temperatures measured in a region away from the SZ.

The FSW process was also applied on the same grade of mild steel AISI 1018 in order to evaluate the microstructure and mechanical properties especially the tensile strength and impact toughness [97]. It was found that the fine microstructure which was achieved after the FSW process had caused in 8% increase in the weld joint tensile strength compared to the PM. However, it was found that when using a tungsten based FSW tool, the impact toughness and ductility decreased in the welded joint due to the formation of brittle tungsten inclusions [97]

FSW of three types of carbon steel (API grade X80 and L80) were also studied by Ozekcin et. al. 2004 [98]. It was found that, compared with the PM, the finer microstructure in the SZ resulted in an improvement in the mechanical properties especially the hardness of the alloy. They also found that rotational speed, travel speed and Z-load were the main effective parameters influencing the hardness of the welded regions.

Cho. et. al. 2012 [99], showed that microhardness has been increased in FSW of high-strength pipe line steel joints due to the formation of fine grains and acicular-shaped bainitic ferrites in the SZ. High strain rate and lower temperatures were attributed to the finer ferritic grains at the weld root compared to the PM as a result of continuous dynamic recrystallization.

Cui et. al. 2007 [100] studied the effect of FSW parameters on five grades of steels including (IF steel, S12C, S20C, S35C, S50C) and found that both the mechanical properties and microstructures of the FSW weld joints increased. They attributed the increase in mechanical properties to the phase transformation of ferrite-pearlite microstructures in the PM to a refined microstructure in the weld joints with carbon percentage less than or equal to 0.12 wt% and to a refined microstructure with harder phases like bainite and martensite in the case where carbon contents exceeded 0.2 wt%.

There are also some attempts to carry out the FSW process on steel alloys in temperature ranges below the A_1 and A_3 of the Fe-C phase diagrams. H. Fujii et.al. 2006 [101], used FSW to join three types of steel (IF steel, S12C, S35C) with different welding conditions. They found that the strength of the S12C steel joints increased with an increase in tool traverse speed and the maximum tensile strength of S35C steel was achieved at 200 mm/min. Their work also showed that a refined microstructure and a high strength could be obtained when carrying out the FSW in the ferrite-austenite two-phase region for all three grades. Chung Y.D et. al. 2010 [102], used FSW for hyper-eutectoid steel (0.85% wt. C, AISI, 1080) and by controlling the welding parameters and choosing a suitable tool material it was possible to produce a weld that did not show evidence of a martensite transformation. Although it was time-consuming, they succeeded to make FSW joints under the A_1 (723) ^{0}C transformation temperature with high toughness by controlling the tool pressure and using a tungsten-carbide (WC) tool with a rotational speed=100 RPM and welding velocity= 100mm/min. Y.D. Chung et. al. 2009 [103] used the same welding condition for FSW SK5 steel grade (0.85%C) to acquire a defect free weld under the A_1 line and a ferritic morphology with a globular cementite, this was to increase the toughness. It was found that increasing tool rotational speed above 100 RPM resulted in a martensitic microstructure with a very high hardness up to 1000 HV and a failure in the SZ, when a tensile test was performing.

The feasibility of FSW of high carbon steel grades was also studied by Sato et.al. 2007 [104] who successfully applied the FSW to ultrahigh carbon steel parent material consisting of a (ferrite cementite) duplex structure by using a PCBN tool with a rotational speed 400 RPM and welding velocity of 76 mm/min. They pre-heated samples before carrying out welding by heating them to 770°C for 1800 s and quenching in oil followed by tempering for 650°C and holding for 1800s in order to get the optimal structure (ferrite+ spheroidal cementite) with ferrite grain size less than 1 micro. The results showed that there was 11% retained austenite after welding and the remaining microstructure was a mixture of duplex (ferrite+ spheroidal cementite) and martensite. Other workers also tried to control the cooling rate during the FSW of steel by increasing workpiece temperature using another external heat source. Choi et al. 2011 [105] carried out a hybrid FSW technique for SK5 (0.84 wt. % C) steel with the aid of an oxy-fuel gas torch in order to control the cooling rate during welding. It was found that the volume fraction of martensite structure and associated hardness decreased because of the higher net heat input which resulted in a slower cooling rate.

In general, from the previous work described above on the evolution of the microstructure and mechanical properties of FSW of steel the following can be concluded:

- A finer microstructure can be produced in steel weld joints compare to the fusion welding technique such as SAW due to lower heat input as the process is a solid state and can be performed without melting. The severe deformation in the SZ is another reason of grain refining due to dynamic recrystallization.
- Mechanical properties such as tensile strength and micro hardness, in the weld SZ and HAZ compared to the PM, are significantly increased after the FSW process.
- Mechanical properties such as tensile, impact and fatigue strength also showed significant improvement compared to fusion welding, especially fatigue strength.
- Low and intermediate tool rotational/traverse speeds are almost producing a homogeneous microstructure; however, high tool traverse speeds can result in a heterogeneous microstructure and also a reduction in the mechanical properties of the resulting weld.
- Defects such as weld root flaws and wormholes which exist in FSW samples due to unsuitable welding conditions can reduce mechanical strength especially fatigue resistance of the weld joints.
- It is possible to join high carbon steel alloys by the FSW technique but the process is slow and expensive.

2.13 FSW Defects

Despite many advantages associated with the FSW process, the technique does not always produce defect free joints. Controlling the FSW process in order to produce high quality welded joints is a challenge due to the wide variety of welding process parameters. Such parameters include independent and dependent welding process parameters, tool material, tool design, workpiece material and thickness. The following types of defects were reported previously in FSW of aluminium and steel joints:

- Wormholes, voids and tunnels in the bottom of the weld joints: probably due to insufficient heat input and the lack of material flow. [17][106][107]

- Kissing bonds: cracks but in close contact usually located at the weld root which are caused by a lack of chemical and mechanical bonding [108]

- Hot kissing or root sticking is caused by excessive heat and contact time resulting in the workpiece sticking to the backing plate. [107]

- Incomplete fusion laps: As a result of impurities present at the top surface and edges of the workpiece as there is no cleaning of these surfaces before the FSW process. [14]

- Flash formation and material thinning: caused mainly by excessive heat as a result of excessive axial forces [109].

- Weld root flaw: cracks starting from the bottom of the workpiece at uneven surfaces toward the welded zone. [14]

- Oxidation: resulting from higher temperatures with no gas shield during the FSW process.

- Lack-of-fill defect: Resulting mainly from losing material support at the trailing side of the tool due to excessive heat input [22].

The defects mentioned can be caused by unsuitable welding parameters and/or tool profile [17]. Table 2.10 shows some of the unsuitable welding parameters conditions which created different types of defects during welding ferritic stainless steel [107]

Table 2.10: Defects in FSW ferritic stainless steel caused by unsuitable rotational/traverse tool speeds or shoulder diameter. [107]

Parameter	Range	Macrostructure	Observation
Rotational speed	< 800 rpm		Tunnel defect - Insufficient material transportation due to lesser frictional heat
	>1200 rpm		Tunnel defect and flash formation - excessive release of stirred materials to the upper surface, which resultantly left voids in the stir zone and formation of flash due to higher rotational speed.
Welding speed	< 30 mm/min		Root Sticking due to excessive contact time between the hot weld metal and the steel backing plate. Also caused thermal damage to the tool.
	>110 mm/min		Groove defect - Insufficient frictional heat hinders the viscoplastic material flow. Also high flow stresses in the material can cause the tool to fail.
Shoulder Diameter	<16 mm		Surface defect - The area between the shoulder diameter and pin diameter is reduced which in turn reduced the material flow from the leading to trailing edge
	> 24 mm		Tunnel Defect - Excessive Heat Generation and inadequate material flow and mixing.
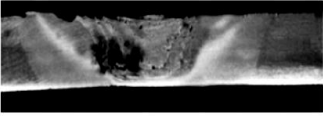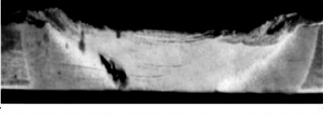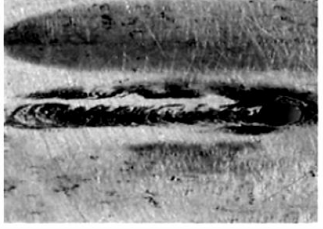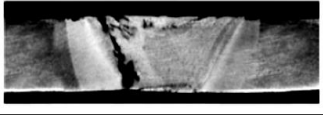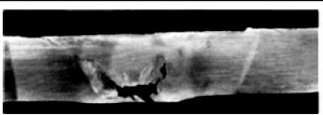
There has been a great deal of work investigating the types and sources of defects in FSW including numerical and experimental techniques. However, much of this has focused on low melting point alloys with far less information available about defect formation in FSW steels. Schmidt and Hattel 2005 [28] included the formation of the void in modelling FSW by establishing the dwell and weld periods as shown in Figure 2.24, they interpreted the formation of the void at the lower advancing trailing side of the probe/workpiece interface as a lack of contact between the tool and workpiece material because of the high traverse tool speed, whereas, Toumpis et. al. 2015 [9] demonstrated the formation of voids experimentally. They showed that the interruption in the surrounding phase has led to a minor cavity caused by non-metallic inclusions. Failla 2009 [76] related the void defect formation to the FSW tool travel speed. It was found that the increase in travel speed had reduced the heat input which had resulted in faster cooling of the material before this region becomes filled with stirred material which in turn had led to the void formation. Tingey et al. 2015 [110] investigated the

defects in DH36 steel during FSW due to tool deviation from its centreline. It was found that ductile fracture can be created when the tool is made to deviate by up to 2.5mm and the critical tolerance to the tool centreline deviation should not exceed 4mm. The material tensile strength has significantly reduced when the tool centreline deviation exceeds 4mm. Stevenson et al. 2015 [14] studied the defects and its effects on materials properties including fatigue and microstructure evolution of FSW 6mm thickness DH36 steel. Defects were divided into several types as shown in Figure 25 [14] including -a- incomplete fusion paths coming mainly from impurities on the top surface of the workpiece as there is no preparation of plate edges prior the FSW process, -b- weld root flaws at the plate bottom interpreted as a result of insufficient tool plunge depth and deviation of the tool from the normal centreline, -c- lower embedded flaw (Type 1) as a result of the lack in material stirring due to lower heat input, -d- lower embedded flaw (Type 2) as a result of the lack in axial force and material mixing -e- upper embedded flaw (swirl zone) at the AS with a vortex-like shape as a result of combination of two flows coming from the shoulder and probe and -f- connectivity flaws between TMAZ and HAZ boundary. It was found that fatigue resistance decreased significantly with the existence of flaws especially wormholes at the weld root. The longitudinal residual stresses measured by the hole drilling technique were also found to reduce the fatigue life. As the embedded flaws have sharp edges, they can act as stress concentration points leading to crack initiation and propagation inside the weld toward the top and bottom surfaces of the workpiece. Toumpis et al. 2014 [78] stated that flaws in FSW of DH36 steel can be created when the heat input from the tool is insufficient and thus a lack in material flow may occur. The authors also found in another experiment, including hot compression tests with a wide range of temperatures and strain rates, that the flow stress increases with the decrease in temperature and the increase in strain rate which is the case when tool traverse speed increases; leading to a lack in material flow and thus the possibility of defect formation in the stirred zone [14]. Han et al. 2014 [111] also reported that the lack of heat input and material flow which occurs at high traverse tool speed can create flaws in 18Cr-2Mo ferritic stainless steel samples during the FSW process. Morisada et al. 2015 [33] showed experimentally by the aid of an X-Ray transmission real time imaging system and monitoring the three-dimensional material flow during FSW of steel that defects formation on the advancing side are the result of material stagnation. Gibson et al. 2014 [112] showed that flaws in FSW is the result of unsuitable welding parameters and the source of surface breaking flaws comes from surface oxides penetrating into the stirred zone.
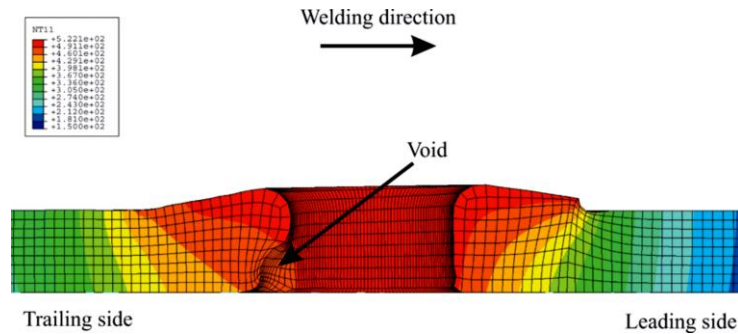
Figure 2.24: Void formation estimated from ALE model [28]
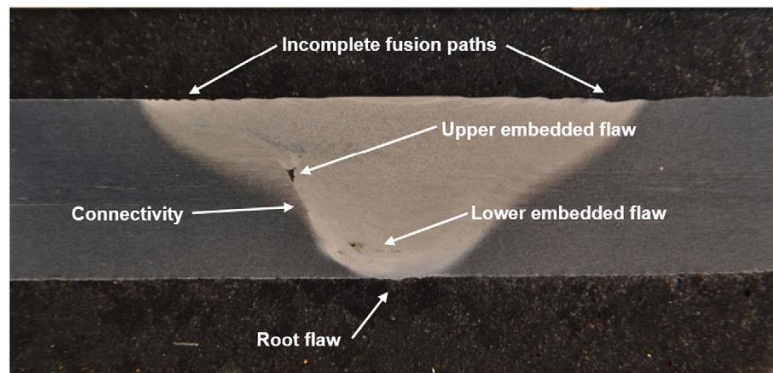
Figure 2.25: Defects found in FSW of 6mm DH36 steel [14]

Workpiece geometry can also be a challenge especially high material thickness, Seaman and Thompson 2011 [22] investigated challenges in FSW of thick steel and found that the possibility of defect formation in the weld joints increases with increasing workpiece thickness due to the increase in thermal diffusion distance. As the time to diffuse heat by the tool into the depth of workpiece is insufficient to create a uniform distribution of temperature throughout the thickness of the weld, isotherms will developed inside FSW region. In this case the top of the workpiece around the tool shoulder is expected to experience better stirring conditions than the bottom of the weld, thus the possibility of defects formation such as wormholes will increase. The authors attributed defects to a lack of forging forces or the heat imbalance. Defects such as lack-of-fill were also found in thick steel joints when the tool rotational speed and axial force increased; causing a loss in material support behind the tool. Reducing heat input by increasing weld heat extraction or increasing the shoulder radius has been suggested in order to constrain the stirred material.

The effect of dependent welding parameters such as welding forces on defect formation has also been investigated. Kim et al. 2006 [113] studied the effects of plunge forces on FSW of aluminium die casting and found that increasing plunge downforce results in improved weld quality . They found that excessive heat input increases the possibility of flash forming while insufficient heat input or abnormal stirring can cause a cavity defect.

Despite the existence of defects in FSW joints, the process is still competitive to fusion welding techniques such as SAW. An example of that is found in a study carried out on FSW of DH36 steel in which fatigue resistance of FSW joints was reported to be acceptable and in the range of standard welded joints despite the existence of defects [9]. Threadgill 2007 [114] investigated flaws associated with FSW and did not consider them defects as the FSW samples were still meeting the mechanical test standards. Information about quality and acceptability of flaws in the metallic structures can be found in the British Standard Institution 7910 [115].

From previous work it can be concluded that insufficient heat input during the FSW process was the main reason for defects. High welding speed can cause a lack of material flow and thus a stagnant zone can form at the probe advancing-trailing side.. Excessive heat input can cause defects such as lack-of-fill coming mainly from losing material support on the trailing side of the tool. Excessive contact time with high rotational speed can cause hot kissing, flash formation and tunnel defects. Controlling material thickness, welding parameters and choosing the suitable tool shape and size can all contribute to the production of an optimal defect-free joint.

2.14 Residual stresses

Residual stresses are one of the problems associated with welding, they are locked-in or self-equilibrium stresses found in manufactured products even with the absence of external thermal or mechanical loads [11]. Local volumetric changes in the product are detected as the main cause of residual stresses and welding is an example of a process which can result in these volumetric changes. It is worth noting that the maximum value of residual stresses is always located just below the yield stress of the product. When residual stresses exceeds the yield point then plastic deformation occurs in the form of distortion. The thermal cycle during the welding process including heating, reaching to a peak temperature and then cooling down to the room temperature can develop longitudinal and transverse residual stresses concentrated in the welded region. The high degree of longitudinal tensile stresses in the weld joint are usually balanced by an adjacent region to the welded in the form of a compressive stress as shown in Figure 2.26 [116]. Longitudinal residual stresses in the welded joint can cause a reduction in the component performance or even an early failure. Other detrimental implications of longitudinal residual stresses are failure by brittle fracture as a result of dimensional instability or crazing (crazing is a brittle mechanisms leading to the low ductility) due to distortion. The existence of compressive surface residual stresses in a component can also be beneficial as they can delay the damage caused by fatigue or creep. [117]. Compressive residual stresses are less harmful than the longitudinal residual stresses; however, excessive values can result in a reduction in buckling load [117].
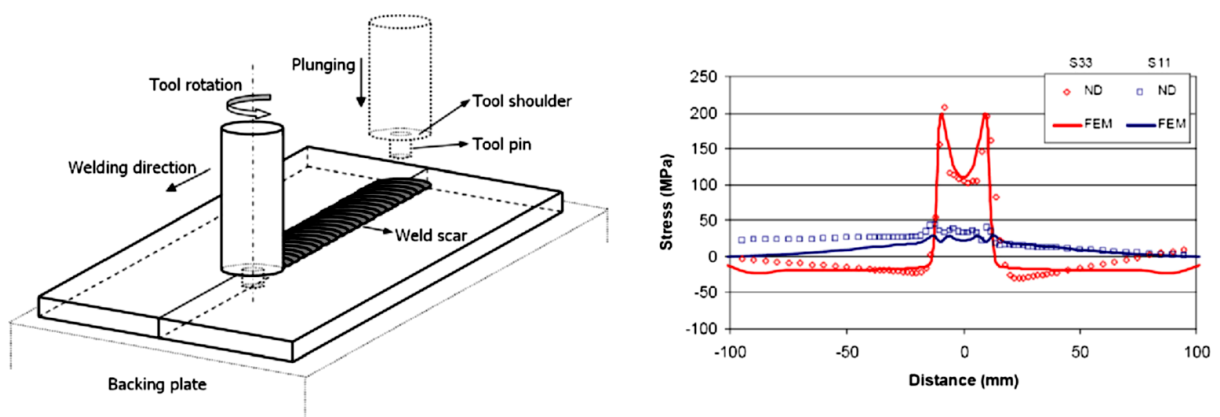
Figure 2.26: Residual stresses associated with FSW process, Longitudinal (red colour), transversal (blue colour)[116]

2.14.1 Method of measuring residual stresses

There are many methods of estimating the residual stresses in welded joints some of them are destructive such as hole drilling [14] and the Cut-compliance technique [118], others are non-destructive (ND) such as XRD-$\sin^2\Psi$ [128], Neutron diffraction [119] Synchrotron diffraction [120] and the Ultrasonic wave technique [121] Other techniques include numerical analysis such as the Finite Element Method FEM based on a transient Lagrangian framework with complex non-linear analysis.

2.14.1.1 Numerical methods validated by experimental results

Camilleri et al. 2015 [122] carried out experimental measurements for the transient strains and temperatures associated with FSW of 6mm DH36 steel to validate a numerical analysis employed to estimate the residual stresses. Several welding parameters were applied and compared regarding the developed residual stresses, these parameters including a slow weld (200 RPM, 100mm/min) with plunge force of 40KN and a faster weld (400RPM, 300mm/min) with plunge force of 55.4KN. Transient temperatures were measured by inserting thermocouples 10mm away from the SZ. Strain gauge rosettes fixed next to thermocouple positions were employed to measure the transient strain produced during the FSW process. Heat generated during welding was calculated from frictional/plastic deformation and applied as a heat flux at the tool shoulder/workpiece interface and as a volumetric heat input at the tool probe parts. As the FSW tool was not included in modelling, 50% of the heat generated was applied on the workpiece as the other half of the heat was assumed to be absorbed by the tool. It was found that tensile longitudinal residual stresses are slightly higher than steel yield stress at room temperature and this was interpreted as a result of phase changes and material hardening. They also found that in the case of the faster welding (traverse) speed the longitudinal residual stresses are decreased due to less heat input while the transverse residual stresses are increased as a result of higher plunge forces and the thermal gradient through the workpiece thickness. It was suggested that an optimal FSW joint can be produced by controlling welding parameters including tool rotational speed, welding speed and plunge force.

Colgrove et al. 2009 [123] carried out aa series of different welds on 4mm DH36 including SAW, SAW with DC Gas Metal Arc Welding (GMAW), autogenesis laser, and laser hybrid welding. Residual stresses were estimated using FEM numerical analysis and compared with

neutron diffraction technique results. Laser welding showed the lowest amount of distortion which was attributed to the lower amount of heat input. [123]

Chen and Kovacevic 2006 [124] calculated the residual stresses during FSW of aluminium alloy 6061-T6 by using a 3D FEM. The heat generated was based on the frictional contact between the tool and the welded plate. The work also included the effect of welding parameters on the residual stress variation. The total strain tensor in the mechanical model was estimated to take into account the elastic, plastic and thermal effects. It was reported that the maximum temperature gradients in both longitudinal and transverse directions were positioned just below the FSW tool shoulder periphery. Residual stresses were also increased in the weld and clamp zones when the rotational speed decreased. Releasing the clamping was found to also decrease the size and affect of the distribution of residual stresses.

Feng et. al. 2007 [125], modelled the FSW of Al6061-T6 using a thermo-mechanical model including metallurgical phase changes induced during welding. This work related the yield stress to the hardness change during the cooling cycle in the SZ and HAZ to estimate the plastic flow stress. The heat generated in the model was based on the phenomena of frictional heating. It was found that welding parameters and material softening during welding is the main factors which control the residual stresses distribution in the weld joint.

Some advanced work on estimating residual stresses in FSW joints incorporated the mechanical effects of the FSW tool in addition to the thermal effect. Buffa et al. 2009 [126], calculated residual stresses in FSW of AA7075-T6 using an experimental procedure based on the cut-compliance methodology and numerical analysis based on continuous rigid-viscoplastic FEM on a Lagrangian framework including the mechanical effects of the tool on the workpiece. It was reported that the source of residual stresses in FSW is not only from the thermal load but also from the mechanical effect. A good agreement was found between numerical and experimental results. [126]

Modelling by only FEM usually requires an explicit input for heat which is normally calculated from the frictional/plastic equation as a heat flux or volume flux. However, the complexity of FSW needs a robust method such as the CFD technique to estimate heat generation during the FSW process. Additionally there are the issues associated with Lagrangian analysis including mesh deformation and also the error in estimating the residual stresses arising from the fact that dynamic recrystallization is taking place in the SZ as a result of high temperatures and strains rate can result in partial strain relaxation [127]. Some work

has been reported which has calculated the temperature using a CFD technique and then transferred the data into an FEM model to calculate the strain and residual stresses [127]. The numerical analysis applied to aluminium alloy 6061 used a coupled system of the CFD module with steady state Eulerian multi-physics FEM with a sticking/slipping assumption between the tool and workpiece. Thermal history calculated from CFD was transferred to the elasto-viscoplastic model to calculate strain and stress resulting from thermal expansion. They found that the tensile longitudinal stress value was less than the 50% of room temperature yield stress at room temperature and also its profile is converted to compressive stress just after the HAZ and shear layer.

2.14.1.2 Non-destructive experimental methods based on X-ray diffraction

X-Ray Diffraction (XRD) - $Sin^2\Psi$

XRD measurements have been used widely in the last decades to calculate the residual stresses in the weld joints [120] [128]. The $Sin^2\Psi$-XRD technique is one such method which measures stresses in a two dimensional direction (i.e. only on the top surface of the sample under test) without the need for measuring the strain-free lattice spacing [129]. More information about methods of obtaining the strain-free lattice spacing and factors affecting the accuracy of there measurements can be found in [129]. Figure 2.27 shows a schematic drawing for the location of in-plane stresses and ψ angle [128]. The lattice space of the (hkl) can be accurately determined when the X-Ray beam hits the clean flattered surface of the FSW sample at an incident angle Ω, the angle between the normal surface of the sample and the normal of the diffracting lattice planes ψ can be easily determined. The free lattice space can be calculated according to Braggs law. $Sin^2\Psi$ is one of a multitude of X-ray measuring techniques used previously to measure the in-plane residual stresses in the thin films and also close to the surface of polycrystalline materials [130][131].
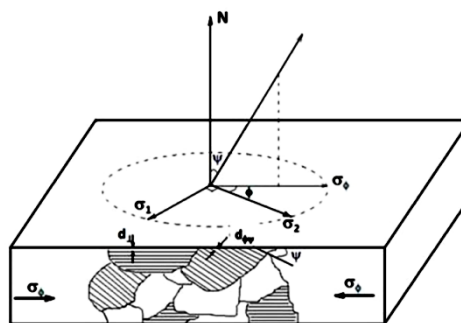
Figure 2.27: The location of ψ angle and the in-plane stresses .[128 P1404]

The principle formula for XRD-$Sin^2\psi$ stress measurement can be written as [128]:

$$\varepsilon_{\phi,\psi} = \frac{d_{\phi,\psi} - d_o}{d_o} = \frac{1+v}{E}\sigma_\phi.Sin^2\psi - \frac{v}{E}(\sigma_{xx} + \sigma_{zz}) \qquad (2)$$

Where E and v are the elastic modulus and poisons ratio of the base metal normal to the (hkl) orientation respectively. d_o is the lattice spacing in the stress free condition. dØψ is the inter-planer distance (d spacing) of a strained material in the direction of measurement defined by the angles Ø and ψ . σ_{xx} is Stress in the X-direction and σ_{zz} is Stress in the Z-direction . "ϕ - The angle between a fixed direction in the plane of the specimen and the projection in that plane of the normal to the diffracting lattice planes"," ψ - The angle between the normal of the specimen and the normal of the detracting lattice planes" [132]

The $Sin^2\Psi$ technique has been used successfully in [130] to estimate the residual stresses in SiC samples in 2 -dimension. They found that a simple surface treatment has created a complex residual stresses in the near-surface region [130]. Residual stresses of FSW HSLA-65 steel grade have been measured also in 3 dimensions by synchrotron X-ray diffraction SXRD [133].

It is found that residual stresses in a friction stir weld are sensitive to the traverse speed and also to FSW tool material. Welding with a W-Re tool with increasing traverse speed caused a decrease in the width of tensile residual stresses whereas in FSW using the PCBN tool the effect of traverse speed increase was only slight with regards to the width of tensile residual stresses. In all FSW cases the maximum measured tensile residual stresses were found just outside the HAZ and its value is below the room temperature yield stress. The phase transformation occurring during the FSW of steel was found not to affect the residual stress profile. Welding with a PCBN tool has resulted in lower values of residual stress compared to welding by W-Re tool; this was attributed to the higher thermal conductivity and lower coefficient of friction of the PCBN tool which has resulted in lower temperatures at the tool/workpiece interface. The same effects of decreasing heat input (traverse speed increase) on reducing the width of the tensile residual stresses was reported by Lombard et al. 2009 [134] in work carried out on measuring the residual stresses of FSW AA5083-H321 using SXRD technique [134].

From the previous demonstration of work carried out on measuring the residual stresses in FSW joints it can be can concluded that:

- Non-Destructive techniques such as using X-ray are effective for measuring residual stresses in welded joints without the need for expensive numerical analysis.

- Increasing tool traverse speed causes a decrease in the width of tensile residual stresses due to lower heat input. Also using tools with high thermal conductivity and low coefficient of friction such as PCBN tool results in lower temperatures at the tool/workpiece interface and thus lower residual stresses are expected in the weld joints.

2.14.2 Sin$^2\psi$ Method Limitations

Despite the accuracy and simplicity of X-Ray sin$^2\psi$ Method, it has the following limitations:

- The method is sensitive to surface conditions and nonlinearities in sin$^2\psi$ [128], but it can give an accurate result if the conditions of the test and sample preparation are standardised.

- It takes a significant amount of time to calculate residual stresses in a specific location on the welded joint surface.

- This XRD technique cannot measure the stresses in the depth of the sample (sub-surface) so a reduction in the sample thickness has to be done in order to estimate residual stresses in the sub-surface depth.

- Another source of errors could come from XRD instrument set-up and diffraction peak measurement. Furthermore, errors can come from the inaccuracy of the nonlinear relation between d-space and $Sin^2\psi$ due to in-depth stress profile and grains interaction [128].

- XRD-$Sin^2\psi$ can give errors from using improper elastic modulus E and poisons ratio υ due to the anisotropic elastic property of crystalline materials [135].

- Sample size can also be limited as the lab XRD equipment can only accommodate relatively small samples Cutting welded sample so that they can be accommodated into the XRD equipment may lead to relaxation of residual stresses as demonstrated by previous work [136], [137] [138].

2.14.3 Effect of Sectioning on Residual Stresses

Altenkirch et. al. 2008 has studied the effect of sectioning on residual stress relaxation in 7449Al alloy. The outcome of their study is shown in Figure 2.28, the relaxation of longitudinal residual stresses as a function of fractional length across the width of the welded plate is clearly evident from this figure.

Figure 2.29 shows variation of longitudinal residual stresses measured at the weld centreline as a function of fractional length of the plate. When fractional length of the welded plate is 0.4, very little relaxation can be observed in longitudinal residual stresses. At 0.1 fractional lengths, the residual stresses are 40% of the original longitudinal residual stresses. Altenkirch et al. [137] described the relaxation behaviour of residual stress by the following expression:

$$\sigma_{relax} = \sigma_o[1 - \exp\left(-\frac{l_r - l_{relax}}{l_{char}}\right)] \qquad (2.7)$$

where σ_{relax}, σ_0, are stresses before and after sectioning l_r and l_{relax}, are the , remaining length and length of zero residual stresses respectively. l_{char} is characteristic length; after no change occurs in the residual stresses distribution in the weld joint.
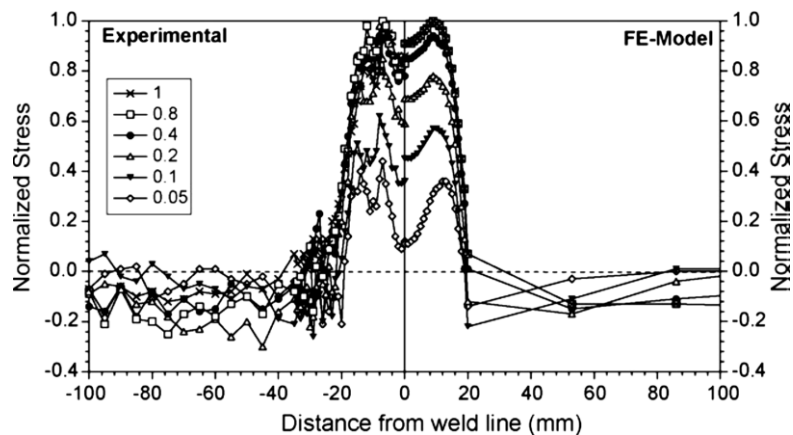
Figure 2.28: The effect of sectioning on RS relaxation in 7449Al alloy [137 P21]
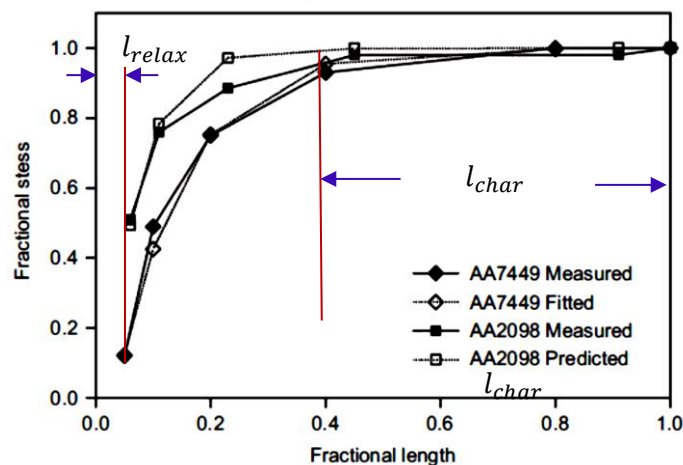
Figure 2.29: Variation of longitudinal residual stress at weld centreline as a function of fractional length of the 7449Al-welded plate [137 P22].

2.15 Measuring the FSW Temperature Experimentally

One of the most important factors in the FSW process is to monitor the exact temperature in order to control the tool wear/breakage and obtain high quality defect free welded joints. Experimental determination of this temperature in the workpiece/tool contact region during the friction stir welding process is usually difficult due to the process conditions. Thermocouples (TC) which are usually used for that purpose cannot be placed in the stir zone region because they will be damaged or displaced by the deforming material in the SZ before recording peak temperatures, leading to uncertain measurements. Thermocouples (TC) attached to the top surface of the parent plate adjacent to the edge of the stir zone are often severed by extrusion of the flash from under the tool shoulder before reaching peak temperature. Using a thermal imaging camera for measuring the temperature of the work-piece during FSW is also difficult and cannot produce useful information. This is because the field of view of the camera can be restricted by the presence of a gas shield to supply, for example, argon to the weld area, and the presence of clamps to hold down the workpiece. Also, the camera has no direct view of the tool itself, and measuring the temperatures on the surface of the plate adjacent to the weld area gives data that are unrepresentative of the internal weld temperatures. Finally, the emissivity of the tool can change significantly during the welding process and thus calibrating the camera accurately is also a significant problem.

Attaching TC's to the FSW tool shoulder and probe through holes seems an effective method to monitor the temperature of tool/workpiece interface. Fehrenbacher et al. 2014 [139] carried out this experimental method to record the temperature of FSW of aluminium by inserting TC through holes made inside the tool shoulder/probe end and with a direct contact with the workpiece. It was found that during a single rotation of the tool there are different readings of temperatures on the tool shoulder and probe. A higher temperature was recorded on the advancing trailing side of the tool compared with the retreating leading side. They also found that temperatures recoded on the tool shoulder can exceed the melting point of aluminium at specific welding conditions. The temperature distribution was found sensitive to tool transverse speed and plunge depth. However, for welding steel alloys which use a brittle ceramic refractory tool, this technique is not appropriate. The welding machine (PowerStir) for high melting point alloys using hybrid PCBN is provided with a telemetry system for monitoring tool temperature during the FSW process as shown in Figure 2.8. However, TC attached just behind the PCBN tool part cannot represent the actual temperatures in the

tool/workpiece interface and is mainly designed to protect the tool from the temperatures change which can cause excessive tool wear or breakage [23].

Locating a TC away from the SZ can give errors due to the difference in heat transfer mechanism between the SZ (convection) and the adjacent region (conduction) [60]. So it is beneficial to find alternative methods for estimating FSW temperatures at the tool/workpiece interface.

This project is suggesting new methods for estimating peaks temperatures of high tool speeds during FSW depending on elemental precipitation/segregation which will be described later. Despite the fact that the suggested procedure considers heating without considering the strain rate effect, it can give a reasonable approximation as the strain rate is likely to affect mainly the incubation time of phase transformation and elemental precipitation/segregation as shown by previous work [76] [140] [141] [142] [143] and [144].

2.16 Summary of Literature Review

As highlighted in the literature review there has been a great deal of work carried out on FSW of light alloys such as aluminium but only limited research has been carried out on FSW of steel. Much of the previous work has been focused on feasibility of FSW in term of mechanical properties, microstructure and defects in the welded joints. Welding parameters were correlated with tool type and geometry and also with workpiece material and thickness. Defects have been investigated and correlated to independent welding parameters such as tool rotational/traverse speeds and plunge depth. Temperatures during the FSW have been measured mainly by TC and also have been estimated from different types of numerical analysis.

The research carried out for this thesis has focused on CFD mathematical modelling the FSW process of two grades of steel used in shipbuilding which are DH36 and EH46. The research has then sought to validate the methodical models by experimental measurements of HAZ and SZ sizes which were then compared to numerical CFD results. The work has also attempted to determine the peak temperature, achieved during FSW by microstructural examination of welds SZ looking at the onset of precipitation of second phase particles and for evidence of segregation of certain elements. The tool's cut-off speeds at which no elemental segregation have been introduced in this work. The mechanical properties such as micro-hardness, tensile and fatigue and also microstructural evolution of the weld joints have been investigated extensively. New possible defects have also been introduced with suggestions to avoid them.

3   Numerical and Experimental Procedures

3.1 Introduction

This section describes the experimental and numerical methods which have been applied to the weld joints under study.

Experiments have been carried out in order to assess the welded joints in term of microstructure characterisation, evolution and elemental precipitation/segregation tests using Scanning Electron Microscope (SEM) and Energy Dispersive X-ray spectroscopy based SEM (EDS-SEM). Infinite Focus Microscopy (IFM) has also been employed to measure the size of the SZ and HAZ. Tensile and fatigue tests have been carried out to examine the mechanical properties and performance of the welded joints. Heat treatments in the temperature range of $1000^{o}C$-$1500^{o}C$ have been applied in order to understand the phase transformation and elemental segregation/precipitation. Finally X-ray diffraction has been used to measure the bi-axial residual stresses of the welded joints by using the $\sin^{2}\Psi$ technique.

Thermocouples have been embedded in different locations inside the plate including the top and bottom of the plate surfaces to measure the temperatures during the FSW process.

A numerical analysis based on the steady state Eulerian framework has been employed to simulate the FSW of 6mm DH36 and 14.8mm EH46 plates. ANSYS code FLUENT software has been employed due to its ability to solve equations of momentum, mass and energy. FLUENT software is also useful when analysing a high deformation, high material flow and high strain rate process such as FSW.

Three different models have been used to calculate the heat generated at the tool/workpiece interface:

- Input torque model
- Sticking/slipping model and
- Fully sticking model.

3.2 The Friction Stir Welding Machine and Samples Sizes

TWI's Powerstir™ FSW machine as shown in Figure 3.1 has been used to produce all the samples used in this study. The machine was specifically designed at TWI/Rotherham for welding thick section and high melting point materials. The machine is a moving gantry design and has been built to withstand the high forces with minimal structural deflection. The unique features of this machine are its large working envelope, a removable worktable for the accommodation of very large components, a very high torque capability and a secondary welding head mounted diametrically opposed to the primary welding head for simultaneous double sided welding.

Figure 3.1: TWI's PowerStir™ FSW machine.(Courtesy of TWI, Image No. SYF001357)

The machine is instrumented to measure all primary process parameters (forces in three perpendicular directions, spindle torque, rotation speed, travel speed etc.) and can operate under force, position or height control. Additional sensors, e.g. thermocouples and strain gauges can be added if required. The machine has full CNC capability with all axes fully programmable, specifications are shown in Table 3.1.

Table 3.1: TWI's PowerStir™ FSW machine Specifications.

Working envelope	6000 x 3000 x 500mm
Upper head	
No. of axes	8
Spindle power	132kW
Spindle Speed continuous	0-1000RPM
Axes traverse speed	0-3000mm/min
Max. Spindle torque	2480Nm @ 500RPM
Z force	0-150kN
Force on X and Y axes	0-100kN
A and B Axis tilt	± 15 °
Lower Head	
No. of axes	4
Spindle power	60kW
Spindle Speed continuous	0-1000RPM
Axes traverse speed	0-3000mm/min
Max. Spindle torque	1130Nm @ 500RPM
Z force	0-100kN
Force on X and Y axes	0-100kN
A and B Axis tilt	± 10 °

When carrying out welding on steel the machine is generally operated in position control to ensure full penetration and to eliminate the possibility of a root defect. Argon gas shielding has been used during the FSW process, primarily to protect the tool from oxidation but this has the benefit of also improving the weld surface finish. Weld temperature also can be monitored but TWI tends not to use this parameter as a control mechanism because of the slow response times and system hysteresis.

The current project is mainly dealing with FSW of 6mm thick plates of a DH36 grade of steel. The feasibility of FSW of 14.8mm thick plate EH46 grade was also studied. A PCBN FSW tool with probe length of 5.5mm has been used for welding 6mm plates while the PCBN tool

with 12mm probe length has been used for welding EH46 14.8mm plates (dimensions of both tools were given in Table 2.2). A variety of tool rotational and traverse speeds were applied to study their effects on heat generation and defects formation. Plunge only FSWing has been carried out on the EH46 plate with varying plunge depth and rotational speeds in order to study the effect of these parameters on heat generation and microstructure evolution.

All plates under study have been firmly fixed by clamps, mild steel and O_1 grades were used as backing plates.

Tool torque was calculated by multiplying the spindle motor torque (recorded by PowerStir FSW machine) by the transfer ratio of conveyor as in the following equation [3 p467]:

$$M_{tool} = TRC.M_{spindle} \qquad (3.1)$$

Where $M_{spindle}$ is the motor spindle torque N.m, TRC is the transfer ratio of conveyor which is equal to 0.38.

The relationship between torque and shear flow stress is as following [67]:

$$\tau = \frac{M_{tool}}{Vol_{contact}} \qquad (3.2)$$

Where τ is the flow shear stress Pa., M_{tool} is the tool torque (N.m), $Vol_{contact}$ is the tool/workpiece contact volume (m^3).

3.3 Experimental Procedures

3.3.1 Metallographic Examination

Microstructural evolution and grain size analysis of the PM, SZ and HAZ can be determined effectively by metallographic techniques. For SEM and micro-hardness tests, all samples were mounted in conductive Bakelite followed by grinding and polishing to a 1μm finish. Emersion etching by 2%Nital (a mix of Methanol and nitric acid) has been used to reveal the microstructure and grain boundaries.

The average grain size number of the PM, SZ and HAZ has been determined according to ASTM E112 standard test and depending on the Mean Linear Intercept Method (MLI) [145]. The technique of MLI consists of drawing a random line across the metallographic sample and counting the number of grain boundaries which intercept this line. At least three lines of intercept must be applied to obtain an accurate result. The equation of MLI can be represented as following [145]

$$\bar{d} = \frac{L}{N} \qquad (3.3)$$

Where, $\bar{d}$ is the grain size number in mm which is converted to the actual grain size by using tables provided in BS EN ISO 643:2003.

L- line length in (mm)

N- number of grain boundaries intercepted by the drawn line.

3.3.2 Scanning Electron Microscopy (SEM) and Energy Dispersive Spectroscopy (EDS)

SEM and EDS-SEM was carried out on the polished and etched (2% Nital) FSW samples using the FEI Nova Nano SEM. The examination includes the surface of the SZ, the HAZ and the PM. The SEM produced high quality and high resolution images of micro constituents by employing the Secondary Electron (SE) imaging mode with an accelerated voltages (10kV-20 kV) which gives relatively high penetration. The working distance (WD) used was 5 mm but in some cases altered (decreased or increased) to enhance the contrast at high magnification. The main aim of the microstructural examination is to generate clear information about phases which can be found in the welded joint and use that information to understand and predict the welded joints mechanical properties. Another aim is to gather data to identify unsuitable welding parameters which can create defects and may affect the process integrity. EDS-SEM examination is mainly used to analyse the chemical composition of elemental precipitation/segregation. Spot analysis (Point and ID) has been employed to reveal material elements on a small location in the scanned SEM image whereas, mapping technique has been used to analyse the whole scanned SEM image.

3.3.3 Calculation the percentage of Boronitride (BN) and Titanium nitride (TiN) in EH46 welded joints

The fraction volume of BN, which comes from the PCBN FSW tool, and TiN precipitates found in the microstructure of TMAZ of EH46 welds joints were calculated by the aid of SEM scanning. $1mm^2$ area between shoulder and probe side (W1-W7) and $1mm^2$ from the middle top of SZ of W8 and W10 has been scanned with maximum magnification of X10000. The fraction volume of BN particles and TiN precipitates has been measured manually using a square grid. The number of intersections of the grid falling on the BN particles are counted and compared with the total number of points laid down. Figure 3.2 shows an example of applying grid on SEM image.
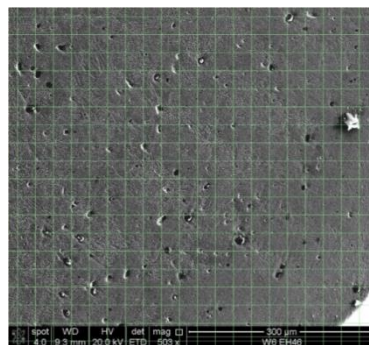
Figure 3.2: Applying grid on SEM image for calculating the fraction volume of BN particles in EH46 steel joints.

3.3.4 Infinite Focus Microscopy (IFM)

The Infinite Focus Microscopy IFM (Alicona) has been employed to create accurate optical light microscopy images of the welded joint and FSW tool. The IFM is a device based on optical 3-dimensional measurements which has the ability to varying the focus in order to obtain a 3D vertical scanned image of the surface. The scanned area of interest can be transferred into a 3-D image by the aid of Lyceum software, thus the surface area can be calculated accurately.

The 3D images obtained for the PCBN tool were employed in designing an accurate shape and size for the mathematical CFD model, whereas, the 2D images of welded joints were used to compare the SZ and HAZ sizes with the CFD results of viscosity and temperature cantors respectively.

3.3.5 Micro-Hardness Measurement

Measuring the hardness can give a reasonable estimation of the phase transformation that has occurred following FSW without examining the morphology. Hardness was measured using a Vickers micro-hardness testing device (HV) by applying 300gf load with a diamond indenter. The measurements were carried out along the horizontal and vertical surfaces of the FSW samples across the transverse direction with increments of 0.5 mm as shown in Figure 3.3. The measurements were carried out on the PM, SZ and HAZ and repeated twice for consistency and accuracy.
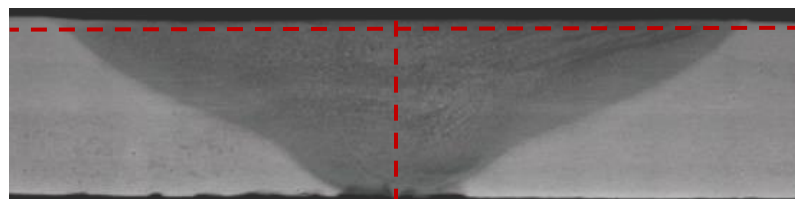
Figure 3.3: Micro-hardness profiles (horizontal and vertical in red) across the transverse direction of the FSW weld joint.

3.3.6 Specimen Preparation (FSW DH36 Steel) for Tensile and Fatigue Tests

The mechanical test specimens from the DH36 FWS steel joints were taken from the steady state region of FSW. AutoCAD drawings as shown in Figure 3.4 and Figure 3.5 were produced in order to determine the steady state region of the FSW so that material from this region could be examined. The sample dimension for fatigue and tensile testing according to EN-BS 895:1995 and BS 7270 [9] are shown in Figure 3.6. The mechanical test specimens were water jet cut from the as-welded plate to minimise mechanical damage. The diameter of water jet was 1mm with ±0.2mm tolerance. Photographs of the sample plates after water-jet cutting are shown in figure 3.7 and figure 3.8. The tensile and fatigue testing apparatus are shown in figure 3.9.

The tensile test samples were taken from the steady state region according to the British Standard EN-BS 895:1995 [182]. Six samples were tested, (2 parent metal samples taken in the direction of rolling for the best estimation of tensile parameters and 4 samples from the steady state welded zone in a normal direction to the welding). These tensile samples were tested at the test facility at Zwick/Roell company in Germany. The tensile test speed was 0.0067 s^{-1} and speed yield point was 30 MPa/s. The test was performed using hydraulic grips 250KN. (Machine Schindler Z250, test speed B, speed yield point 30 MPa/s, Pre-load 2 MPa, test speed 0.0067 1/s). The ultimate tensile strength, 0.2% yield stress, Young's modulus and the reduction in area were the main factors determined in the tensile test. Load against Extension was recorded to failure for each sample, thus the ultimate and yield stresses were determined by dividing the load by the original cross sectional area of the sample.

Four samples taken from each plate were prepared for the Fatigue test based on BS 7270 standard. The sides of samples were polished in the longitudinal direction to reduce the effects of any sharp edges that act as a stress concentration. The load set of 0.8 of the yield stress maximum of 305.6MPa and minimum of 30.56 MPa, mean stress=168.1MPa and amplitude=137.5MPa were used [9]. Stress frequency was kept constant at 10Hz during the testing program. Results of tensile and fatigue tests will be employed to estimate the success of the welds joints.
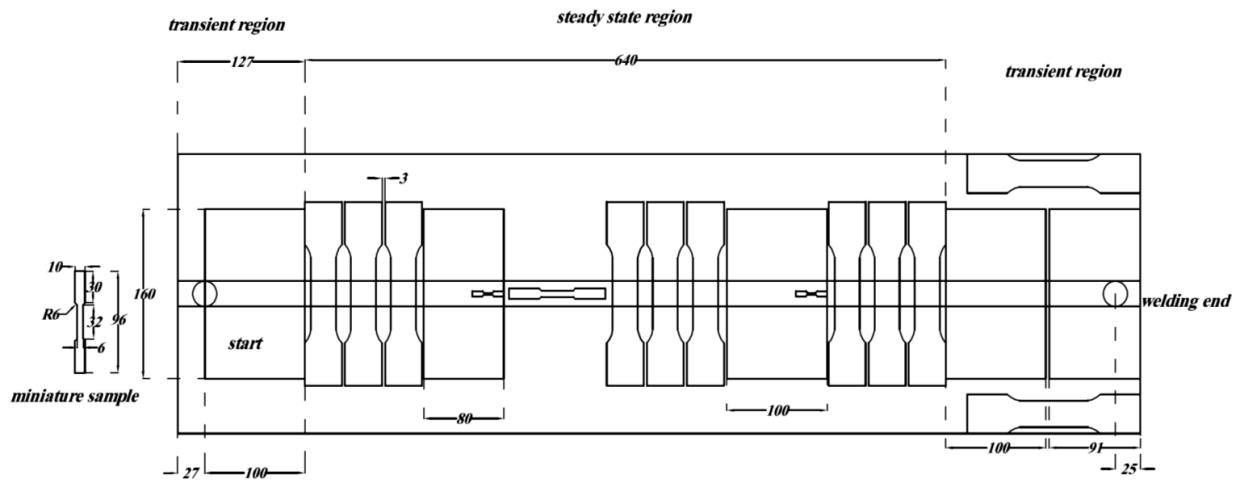
Figure 3.4: An AutoCAD design for the samples of the 1000mm plate before the water jet cutting process, all dimensions are in mm.
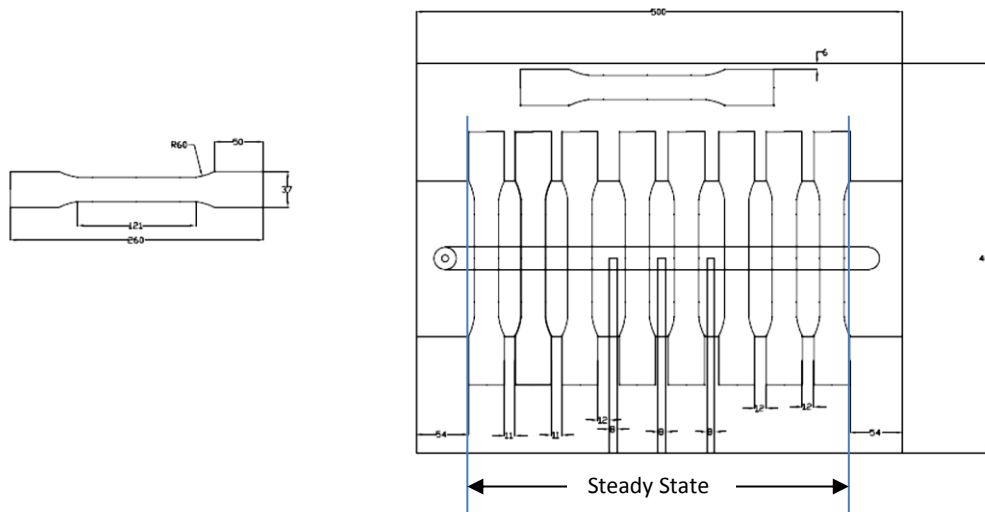
Figure 3.5: An AutoCAD design for the samples of the 500mm plate before the water jet cutting process, all dimensions are in mm.
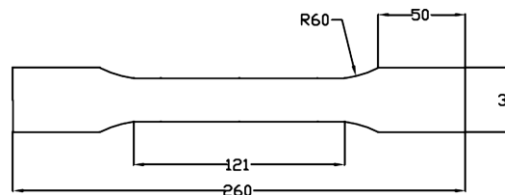
Figure 3.6: The dimensions of Tensile and Fatigue sample (in mm) conducted based on EN-BS 895:1995 and BS 7270 standards

77
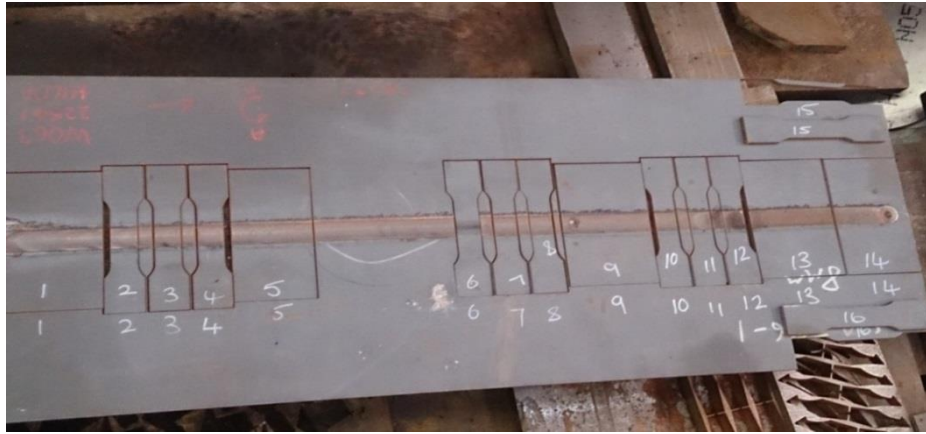
Figure 3.7: A photograph of the 1000mm plate after water-jet cutting.
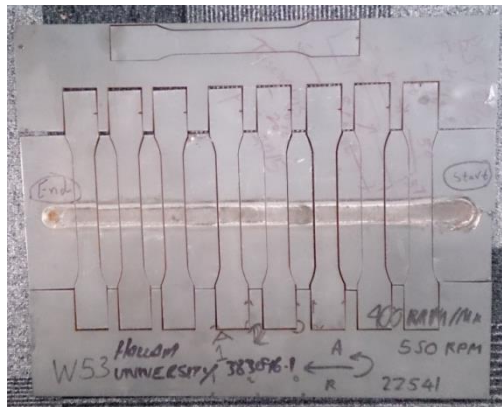
Figure 3.8: A photograph of the 500mm plate after water-jet cutting.
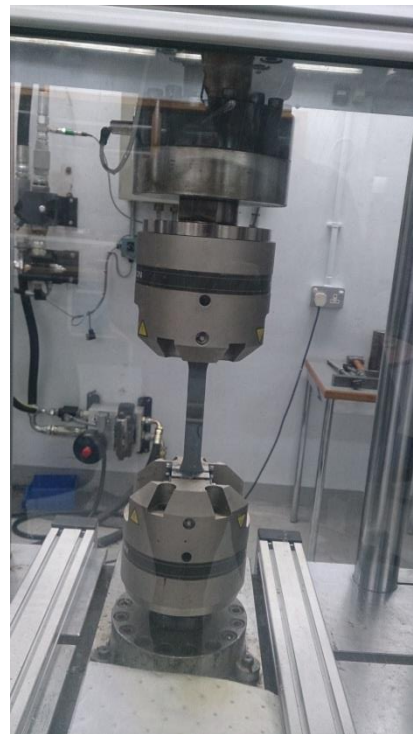
Figure 3.9: Tensile and fatigue testing machine.

3.3.7 Thermocouples Set-up

Thermocouples (TCs) K-type (1mm diameter) Omega manufacturer were inserted in blind holes (1mm depth) inside the plates and fixed firmly by using high thermal conductivity cement (OB-700). Three TC's were attached to the bottom of the 6mm thick DH36 plate in the steady state period at locations as shown in Figure 3.10. In the EH46 plate, TC's were attached to the top surface of the plate at 29mm away from the tool center for Plunge and steady state cases as shown in figure 3.11 and figure 3.12 respectively. Image of the EH46 plate including plunge/dwell and traverse steady state FSW is shown in figure 3.13.
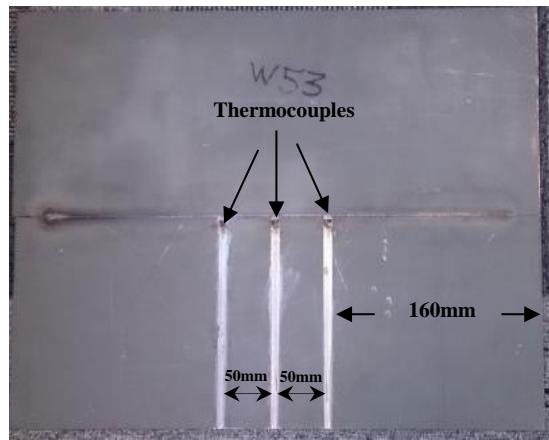
Figure 3.10: Thermocouples locations at the bottom of 6mm DH36 plate.
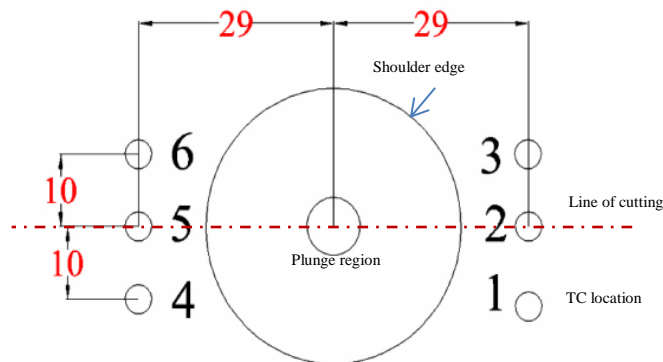
Figure 3.11: EH46 thermocouples location W1 to W7 (plunge/dwell period) at the top of the plate surface, all dimensions in mm.
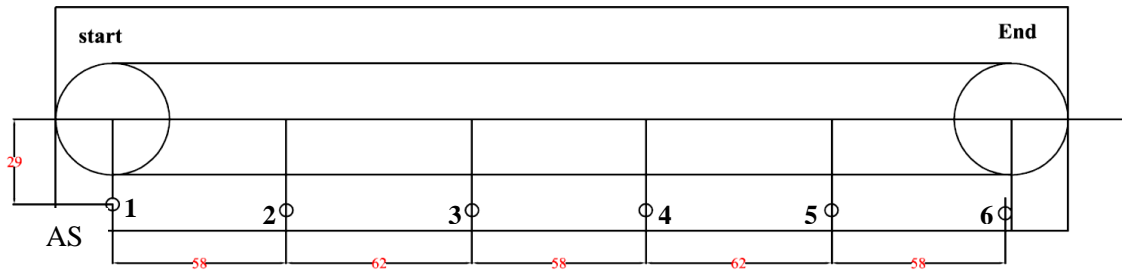
Figure 3.12: EH46 W8 to W10 showing the thermocouples location at the top of the plate surface, all dimensions in mm.
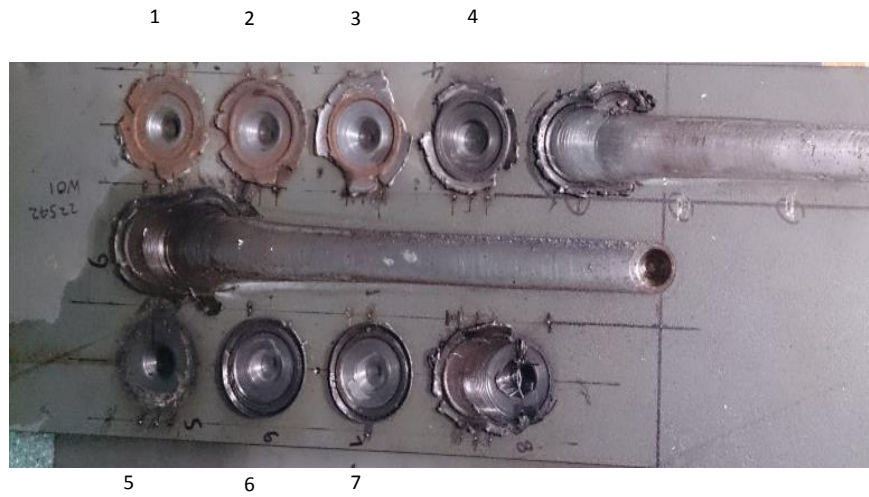
Figure 3.13: EH46 steel, 14.8mm plate thick with different plunge and weld conditions. six Thermocouples are set up around each weld, as shown in figure 3.11.

3.3.8 Heat Treatment of DH36 and EH46 grade steel as received

Heat treatments in the temperature range of 1000 ^{o}C to 1500 ^{o}C with different holding times from 0.5-15 min and cooling rate of 30°C/s (hot oil at 150 ^{o}C quenching) as shown in Table 3.2 have been carried out on as received DH36 and EH46 steel grades in order to examine the grain growth of austenite grains and elemental segregation/precipitation that occur in the steel. A relationship between the elemental segregation and temperature has been studied and related to the segregation which occurs in FSW at high tool speeds. A Strain rate effect was not included in the heat treatments as the maximum temperature on a Gleeble simulator hot compression test does not exceed 1100°C and the current heat treatments are mainly in the temperature ranges of between 1400 ^{o}C-1500 ^{o}C. However, it is expected that strain rate will affect mainly the time of phase transformation and elemental precipitation/segregation as demonstrated by previous work [76] [142] and will be discussed later.

The precipitation of TiN has been studied by carrying out heat treatments on EH46 steel grade at 1250 ^{o}C and 1400 ^{o}C with holding times of 30sec and 1min followed by different cooling rates including quenching in water (350°C/sec), oil quenching (90°C/sec), hot oil quenching (oil temperature is 150 ^{o}C) (30°C/sec), air cooling (5°C/sec) and cooling inside the furnace (0.35^{o}C/sec).

6 mm cubic samples have been prepared from as received DH36 and EH46 steel grades followed by grinding and polishing, each heat treatment at a specific peak temperature and cooling rate was applied for three samples for consistency and accuracy.

An electric furnace with a maximum temperature of 1550 ^{o}C and heating speed of (5 ^{o}C/s) was used for the heat treatments. For checking the furnace accuracy, TCs K-type have been attached to samples surfaces in one end and to a 4-channel thermometer data-logger (Omega HH1384) in another end. W-Re TC K-type has been used to check the higher temperatures in a range from 1200 ^{o}C to 1500 ^{o}C.

Table 3.2: Heat treatments of DH36 and EH46 in the temperature range 1000 ^{o}C to 1500 ^{o}C. Note: Maximum holding time for DH36 at 1450 ^{o}C is 10min.

No. of samples	Temperature ^{o}C	Holding time min
3	1000	0.5
3	1000	1
3	1000	2
3	1000	3
3	1000	4
3	1000	10
3	1000	15
3	1130	0.5
3	1130	1
3	1130	2
3	1130	3
3	1130	4
3	1130	10
3	1130	15
3	1250	0.5
3	1250	1
3	1250	2
3	1250	3
3	1250	4
3	1250	10
3	1250	15
3	1300	0.5
3	1300	1
3	1300	2
3	1300	3
3	1300	4
3	1300	10
3	1300	15
3	1400	0.5
3	1400	1
3	1400	2
3	1400	3
3	1400	4
3	1400	10
3	1400	15
3	1450	0.5
3	1450	1
3	1450	2
3	1450	3
3	1450	4
3	1450	10
[*]3	1450	15
3	1500	1

[*] **Only EH46 samples**

3.3.9 Residual Stresses Measurement using the X-ray Diffraction $Sin^2\psi$ Method

The residual stresses developed as a result of FSW process have been measured using the Empyrean Philips XRD device, assuming elastic isotropy in the individual crystallite and that the stress is independent of the orientation, the biaxial stress equation can be written as [128]:

$$\sigma_\phi = \sigma_{xx} \cos^2 \phi + \sigma_{xz} \sin(2\phi) + \sigma_{zz} \sin^2 \phi \qquad (3.4)$$

Biaxial surface stresses can be calculated from the above equations and determined directly from the slope of $d_{\phi\psi}$ and $Sin^2\psi$.

The method can be summarised as follows [128]:

1- Carry out normal scan to reveal the material peaks.

2- Choose a high peak angle 2θ (such as $82.3\,^\circ$ if it is ferritic microstructure) to increase the accuracy as X-Ray follows a sin relation represented by Bragg-Brentano equation.

$$\lambda = 2d\,sin\theta \qquad (3.5)$$

Where θ is the Bragg angle and λ wave length of XR used (Braggs law) [183]. The peak should also be well shaped and have a high intensity single diffraction peak (not overlapping with diffractions of the substrate material).

3- Choose a range of Ω angles (the angle between sample surface and the incident X-Ray) for the same 2θ angle by using a computer controlled Omega-goniometer for the ψ tilt.

4- For the selected diffraction peak range and for each Ω value, carry out a scan of $(\Omega - 2\theta)$ with a small step size and step period. Where Ω is the angle between the incident X-ray beam and the specimen surface.

5- Determine the peak background, strip out $K\alpha2$ to smooth the peak curve to improve the accuracy.

6- To determine the peak angle (2θ) location using the full width at half maximum (FWHM), this is done by finding the maximum intensity value and determining the peak limits $(2\theta_1 and\ 2\theta_2)$ from the curve referring to the half maximum intensity and finally getting the peak angle from the following equation:

$$2\theta = 0.5(2\theta_1 +\ 2\theta_2) \qquad (3.6)$$

7- Conduct the above for all curves and convert them into an Excel data sheet.

8- Calculate the angle ψ ($\psi = \theta - \Omega$) and d-space using Braggs law.

9- Assuming plain stress (biaxial surface stress) by treating the following equation as a linear function [128]:

$$[\varepsilon_{\phi,\psi} = \frac{d_{\phi,\psi} - d_o}{d_o} = \frac{1+v}{E}\sigma_\phi.Sin^2\psi - \frac{v}{E}(\sigma_{xx} + \sigma_{zz})]$$ (3.7)

The residual stresses can be calculated by the linear regression where the slope will be the residual stress value and the intercept will represent the free-lattice space.

10- Repeat the test for different points on the sample to get the residual stress distribution along the weld.

3.3.10 X-Ray Diffraction -Scanning

X-ray diffraction using the Empyrean Philips XRD has been carried out on the FSW samples for the following purposes:

- To reveal the as received sample phases to allow for the detection of any phase changes in the steel following FSWing.

- Detecting other additional phases, elements or/and oxides which may appear in the welded joints.

3.4 CFD Modelling of FSW

There has been much interest in modelling of the FSW process in recent years in an effort to quantitatively describe and predict the effect of changes in process parameters in order to cost effectively produce high quality welds with satisfactory mechanical properties.

Many numerical models of FSW have been generated for modelling aluminium alloys [50] [54] [146] but there has been comparatively few produced for FSW of steel [61] [16] [55].

The difficulty in modelling the FSW process comes from the fact that friction stir welding has many variables and challenging process parameters which make the model results based on potentially inaccurate estimations. The main challenges in modelling the FSW process are the thermo-mechanical coupling, high deformation and strain rate, complex material flow, phase change, sticking/slipping and complex heat exchange between the tool/workpiece and workpiece/backing plate. In order to alleviate these limitations, many experimental tests have to be carried out to build reliable equations; which in turn makes accurate modelling very expensive.

However, companies like TWI dealing with FSW of steel, would like to be able to accurately mathematically model the process in order to reduce the cost arising from the requirement for numerous welding trials which include variation of process parameters such as the tool geometry, and the rotational and traverse speeds in order to get a reliable product.

There are two types of mathematical modelling which can be employed to represent FSW [52].

1- Computational Solid Mechanics (CSM) which deals with simulating of solid parts using basically the Finite Element Method (FEM). The material matrix is usually represented as solid and can be assumed as viscoelastic or viscoplastic. The model is usually represented by a global Lagrangian framework with transient analysis. Residual stresses can be calculated effectively by using this type of modelling due to the ability to calculate the temperatures as a function of location and time.

2- Computational Fluid Dynamic (CFD) which deal with fluids and material flow. The model is usually represented by a local Eulerian framework in a steady state analysis. The material matrix is represented as liquid and the viscosity is represented in the model by a suitable equation in a non-Newtonian form.

A combination between the Lagrangian and Eulerian approach is also applicable, an example of this is found in an improved Arbitrary Lagrangian Eulerian approach (ALE) including material flow to estimate the residual stresses [53]

3.4.1 A Heat Equation for a Moving Heat Source

There are two frameworks in which heat equation can be represented

- **Eulerian:** In which the FSW tool is represented as a solid and stationary whereas the workpiece material is represented as a fluid that flows through the mesh usually in a steady state solution [51]

$$\rho C_p \nabla(uT) = \nabla(k\nabla T) - \rho C_p v_x \frac{\partial T}{\partial x} + Q_i + Q_b \qquad (3.8)$$

$\boldsymbol{\rho}$-Material density Kg/m^3, C_p- Specific heat J/Kg.K, v_x-Velocity m/s in the X-direction which is equal to zero in the plunge case, T- temperature K and k is the thermal conductivity W/m.K. Q_i- Heat generated at the tool/workpiece interface (W). Q_b- Heat generated due to plastic deformation away from the interface (W).

Lagrangian: The material of the workpiece follows the mesh (heat moves with the tool along the weld line, the tool is solid and the workpiece is stationary with viscoelastic behaviour) usually a transient solution [51]

$$\rho C_p \nabla(uT) = \nabla(k\nabla T) + \dot{Q_i} + Q_b \qquad (3.9)$$

3.4.2 Heat generated during the FSW Process

There are two main sources of the heat generated during the FSW process, the heat generated in the tool/workpiece interface and the heat generated from plastic deformation.

3.4.2.1 Heat generated due to plastic deformation away from the interface (Q_b)

The plastic deformation experienced by the material away from the tool/workpiece interface (the effect of tool rotation on the adjacent material) can produce some heat under the effects of viscous dissipation and can be calculated as [146]:

$$Q_b = \varphi \mu_u \aleph \qquad (3.10)$$

$$\aleph = 2 \sum_{i=1}^{3} \left(\frac{\partial u_i}{\partial x_i}\right)^2 + \left(\frac{\partial u_1}{\partial x_2} + \frac{\partial u_2}{\partial x_1}\right)^2 + \left(\frac{\partial u_1}{\partial x_3} + \frac{\partial u_3}{\partial x_1}\right)^2 + \left(\frac{\partial u_3}{\partial x_2} + \frac{\partial u_2}{\partial x_3}\right)^2 \qquad (3.11)$$

$\mu_u \aleph$:the heat generation in fluids which have much lower viscosity (W).

μ_u:non-Newtonian viscosity (Pa.s).

φ- a constant has a value (0 to 1 and equal 1 for a well-mixed system) and usually used to reduce the heat generation and make it suitable with the context of high-viscosity plasticized materials. It is also a method to show that a small amount of heat is generated due to plastic deformation. It is considered that the heat generated from this effect can be ignored as it only represents about 4% from the total heat in FSW [55].

3.4.2.2 Heat generated at Tool/Workpiece Interface (Q_i)

Depending on the available experimental data recorded by the FSW machine and the contact condition between the tool and workpiece, heat generated at the interface will be according to the following assumption:

- Input Torque taken directly from the machine.
- Sticking/slipping conditions in which the heat is generated due to plastic deformation and frictional heating.
- Fully sticking conditions, where the heat is generated mainly from viscous heating.

Thus for each assumption, a model has been established and the results of peak temperatures have been compared.

3.4.3 FSW Model Assumption

3.4.3.1 Torque Model

The heat generated due to Torque can be represented as [52]:

Heat generated (Q) = machine efficiency $\times$ tool rotational speed $\times$ measured torque

$$Q = \eta \times \omega \times M \tag{3.12}$$

Where M is the torque (N.m), η machine efficiency, ω tool rotational speed (rad/sec).

$$M = F \times r, \tag{3.13}$$

F is the force (N) which can be represented by:

$$dF = \tau_{cont}\, dA \tag{3.14}$$

Where A is the contact area (m^2).

So from eqs (3.12 to 3.14), the heat generation due to torque can be written as:

$$Q = \omega\, r\, \tau_{cont} \int_{r_i}^{r_o} dA \tag{3.15}$$

Where r_o and r_i are the outer and inner radius of the tool part in m.

So for a PCBN tool with a conical shape of shoulder and probe side, the heat in watts (W) can be calculated as:

$$Q_{shoulder} = \frac{2\pi}{3}\omega\tau_{contact}(1+\tan\alpha)[R_{o\,s}^3 - R_{i\,s}^3] \tag{3.16}$$

$$Q_{probside} = \frac{2\pi}{3}\omega\tau_{contact}(1+\tan\alpha)[R_{o\,p}^3 - R_{i\,p}^3] \tag{3.17}$$

$$Q_{probend} = \frac{2\pi}{3}\omega\tau_{contact}R_{i\,prob}^3 \tag{3.18}$$

R_{is}, R_{os} Tool shoulder maximum inner and outer radius respectively and R_{ip}, R_{op} Tool probe maximum inner and outer radius respectively.

The heat generation ratio ($f_{tool\ part}$) can be calculated by dividing the particular heat of the tool part by the total heat as:

$$Q_{total}= Q_{shoulder}+ Q_{probeside} +Q_{probend} \tag{3.19}$$

$$f_{shoulder} = \frac{Q_{shoulder}}{Q_{total}}, \tag{3.20}$$

$$f_{probeside} = \frac{Q_{probside}}{Q_{total}}, \tag{3.21}$$

$$f_{probend} = \frac{Q_{probend}}{Q_{total}} \tag{3.22}$$

For a PCBN geometry: R_{os}=24 mm, R_{is}=10mm, R_{op}=10mm, R_{ip}=4mm , the fractional heat for each part will be as follow:

$$f_{shoulder} = 0.836$$
$$f_{probside} = 0.16$$
$$f_{probend} = 0.003$$

The Spatial Heat Flux Equations:

Due to the weld type and its dependence on tool geometry, it is beneficial to represent the heat flux as a function of tool radius.

The total heat generated for each part can be represented as follow:

$$Q_{total} = Q_{shoulder} + Q_{probeside} + Q_{probend} \tag{3.23}$$

$$Q_{total} = \frac{2\pi}{3}\omega\tau_{contact}(1+\tan\alpha_s)[R_{os}^3 - R_{is}^3] + \frac{2\pi}{3}\omega\tau_{contact}(1+\tan\alpha_p)[R_{op}^3 - R_{ip}^3] + \frac{2\pi}{3}\omega\tau_{contact}R_{i\,prob}^3$$

--------------------------------------- (3.24)

Then:

$$Q_{total} = \frac{2\pi}{3}\omega\tau_{contact}[(1+\tan\alpha_s)[R_{os}^3 - R_{is}^3] + (1+\tan\alpha_p)[R_{op}^3 - R_{ip}^3] + R_{i\,prob}^3] \tag{3.25}$$

So : $\tau_{contact} = \dfrac{3Q_{total}}{2\pi\omega[(1+\tan\alpha_s)[R_{os}^3 - R_{is}^3] + (1+\tan\alpha_p)[R_{op}^3 - R_{ip}^3] + R_{i\,prob}^3]}$ (3.26)

But from equation 3.15 heat flux can be represented as:

$$q = \omega r \tau_{contact}$$

So $\quad q_{total} = \dfrac{3Q_{total}\,r}{2\pi[(1+\tan\alpha_s)[R_{os}^3 - R_{is}^3] + (1+\tan\alpha_p)[R_{op}^3 - R_{ip}^3] + R_{i\,prob}^3]}$ (3.27)

So for each part of the tool the spatial heat flux can be represented as:

$$q(r)_{shoulder} = \dfrac{3Q_{shoulder}\,r}{2\pi(1+\tan\alpha)[R_o^3 - R_i^3]}$$ (3.28)

$$q(r)_{probside} = \dfrac{3Q_{probside}\,r}{2\pi(1+\tan\alpha)[R_o^3 - R_i^3]}$$ (3.29)

$$q(r)_{probend} = \dfrac{3Q_{probend}\,r}{2\pi R}$$ (3.30)

By representing the heat generated from torque for each tool part and applying the values of tool geometry, the spatial heat flux can be implemented into ANSYS using User Defined Function (UDF).

3.4.3.2 Sticking/Slipping Mathematical Solution Model

Heat flux (q) between the tool/workpiece interfaces is derived from Q_i as in equation 3.15 ($q = \omega r \tau_{contact}$)

For the sticking and slipping conditions the contact shear stress between the tool and workpiece can be represented as following [51]:

$$\tau_{contact} = \tau_y \qquad \text{Sticking (represent the plastic deformation)} \qquad (3.31)$$

$$\tau_{contact} = P\mu \qquad \text{Sliding (represent the frictional force per unit area)} \qquad (3.32)$$

μ: Friction coefficient, P: Tool pressure (Pa). $\tau_{contact}$: contact shear stress (Pa). ω: Tool rotational speed (rad/s) and r is the tool radius (m).

τ_y : is the yield shear stress (Pa) and is a function of temperature and can be taken from previous work done on the same materials type or can be estimated from experimental work such as a hot compression test. The yield shear stress represents the heat generated from plastic deformation when multiplied by ωr and generally is calculated from the relationship with yield stress as follow [55]:

$$\tau_y = \frac{\sigma_y}{\sqrt{3}} \qquad (3.33)$$

σ_y is the yield stress, figure 3.14 shows the variation of yield stress with temperature for mild steel [55].
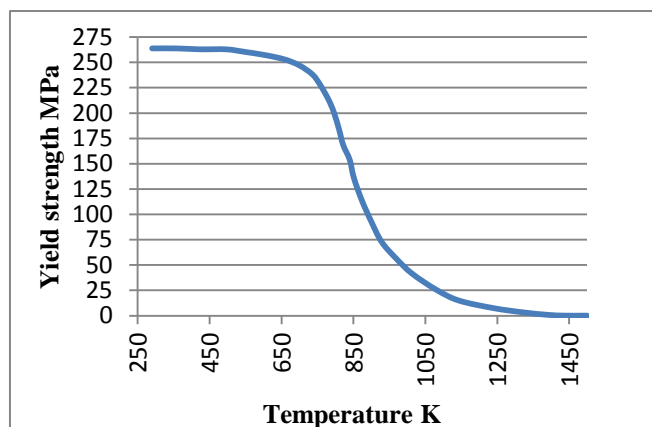
Figure 3.14: The variation of yield stress with temperature for mild steel [55 P885].

$P\mu$ -is the frictional force per unit area that when multiplied by ωr represents the rate of frictional heat per unite area. The sticking/slipping parameter, values of friction coefficient and sticking/slipping heat flux equation can be estimated as a function of tool radius and tool rotational speed as will be mentioned in the following sections.

A. The Sticking Slipping Parameter δ between the tool and workpiece

Sticking slipping parameter is a dimensionless parameter which controls the contact type between the FSW tool and the workpiece (0 sticking, 1 sliding and sticking/sliding if its value is between 0 and 1).

Previous work has represented the sticking slipping parameter as a spatial function dependant up on tool radius as [47]:

$$\delta(r) = \left\{1 - \exp\left(-\frac{\omega r}{\omega_o \delta_o R_o}\right)\right\} \qquad (3.34)$$

ω_o -The maximum rotational speed of the tool (RPM), δ_o is the initial partition of heat generated from plastic deformation to heat generated from friction and R_o is the tool outer radius, ω is the local rotational speed in the contact region.

This equation has been improved by fitting the measured values at various relative velocities [47]:

$$\delta(r) = 0.2 + 0.8 * \left\{1 - \exp\left(-\frac{\omega r}{\omega_o \delta_o R_o}\right)\right\} \qquad (3.35)$$

Relative velocity values vary from ωR_s at the tool shoulder periphery to zero at the axis of rotation.

ω can be expressed as:

$$\omega = \frac{\omega_o r}{R_o} \qquad (3.36)$$

According to equation (3.35) the sticking/slipping parameter variation with the PCBN tool radius (12mm) is as shown in Figure 3.15.
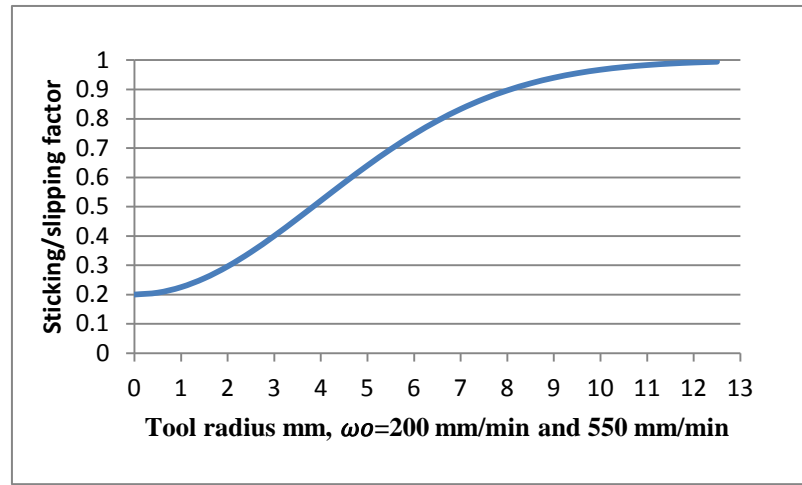
Figure 3.15: Variation of sticking/slipping parameter with the tool radius. The values calculated from eq. 3.35.

B. Estimation of Coefficient of friction μ during the FSW process

The value of friction coefficient (μ) can be estimated by considering the relative velocity between the tool and workpiece guided by previous work in the field of friction welding of steel bar [55]. Relative velocity values vary from ωR_s at the outer edge of tool shoulder to zero at the axis of rotation. The previous experimental work conducted during rolling of steel suggested that μ can be represented as [55]:

$$\mu = \mu_o \exp(-\delta \omega r) \tag{3.37}$$

δ - The sticking/slipping parameter (0 sticking, 1 sliding), r- Tool radius (m). μ_o - is the initial friction coefficient and can be estimated experimentally from the welding charts, here the initial value was taken as $\mu_o = 0.3$ [55]. However there has been much work done for mild steel and 304L steel [55] [62] and it appears that every type of steel has a different value, so for accuracy it is advisable to conduct experiments for the target grade of steel.

According to the sticking slipping parameter and tool rotational speed the value of friction coefficient μ can be estimated as shown in Figure 3.16. Variation of friction coefficient with the tool radius in which a significant drop is observed in its value at the tool periphery when the rotational speed increases.

93
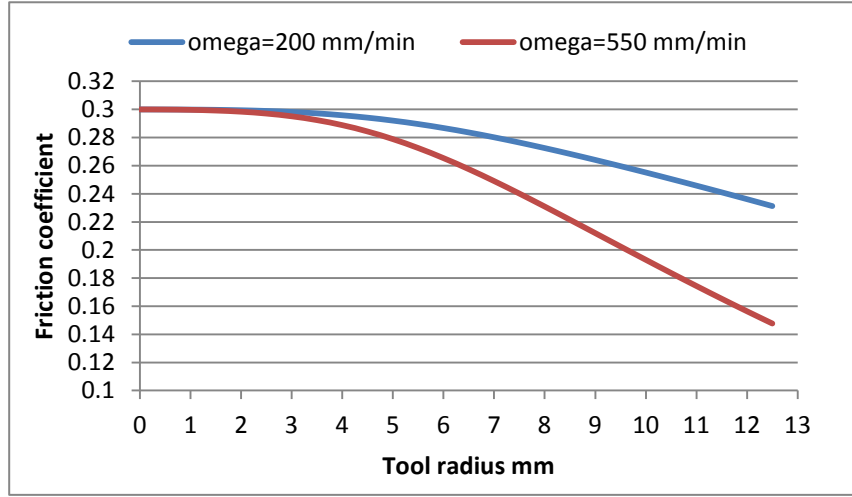
Figure 3.16: Variation of coefficient of friction with the tool radius. The value of friction coefficient decrease significantly at the tool periphery when the tool rotational speed increases.

C. Sticking-Slipping Heat Flux Equation

For sticking-slipping conditions the heat flux will be represented as follows [28]:

$$q = [(1-\delta)\eta\tau_y + \delta\mu P](\omega r - U\sin\theta)$$

(3.38)

U- the velocity of the tool in the welding direction (m/s) and η - the amount of mechanical energy converted to heat energy (machine efficiency). θ- The rotation angle of the tool.

The term $U\sin\theta$ represents a small amount in heat generation contribution so it can be neglected.

3.4.3.3 Fully Sticking Conditions

The heat generated in this model is based on viscosity dissipation and the material flow due to the tool rotation forming shear layers. The viscous heating ($\mu_u(\nabla^2 u)$) was assumed to be the main source of heat generation in this work. Previous work by Schmidt et. al. [50] and Atharifar et. al. [147] showed experimentally that sticking conditions are closer to the real contact situation between the tool and workpiece. Cox et. al. [59] carried out a CFD model on FSW and assumed pure sticking conditions at the tool/workpiece contact area.

3.4.4 CFD numerical analysis equations

The model created in this study uses CFD analysis and includes solving equations of momentum, mass and energy. Viscosity is also included in the model as a function of temperature and strain rate.

The continuity equation for incompressible material can be represented as [55]

$$\frac{\partial u_i}{\partial x_i} = 0 \tag{3.39}$$

u_i-is the velocity of plastic flow in index notation for i=1, 2 and 3 which representing the Cartesian coordinate of x,y and z respectively.

The temperature and velocity fields were solved assuming steady state behaviour. The plastic flow in a three dimensional Cartesian coordinates system can be represented by the momentum conservation equation in index notation with i and j = 1, 2 and 3, representing x, y and z respectively [55]

$$\rho \frac{\partial u_i u_j}{\partial x_i} = -\frac{\partial p}{\partial x_j} + \frac{\partial}{\partial x_i}\left(\mu_u \frac{\partial u_j}{\partial x_i} + \mu_u \frac{\partial u_i}{\partial x_j}\right) - \rho U \frac{\partial u_j}{\partial x_1} \tag{3.40}$$

Where ρ, p, U and μ_u are density, pressure, welding velocity, and non-Newtonian viscosity, respectively. Viscosity is determined using the flow stress (σ_f) and the effective strain rate ($\dot{\varepsilon}$) as follows [55] :

$$\mu_u = \frac{\sigma_f}{3\dot{\varepsilon}} \tag{3.41}$$

The flow stress in a perfectly plastic model, proposed by Sheppard and Wright [55] is:

$$\sigma_f = \frac{1}{\alpha}\sinh^{-1}[(\frac{Z_n}{Ai})^{\frac{1}{n}}] \tag{3.42}$$

n, *Ai*, α, are material constants. Previous work on C-Mn steel showed that the parameter *Ai* can be written as a function of carbon percentage (%C) as follow [55]:

$A_i=1.8\ x10^6 +1.74\ x10^8\ (\%C)- 6.5\ x\ 10^8\ (\%C)^2$ (3.43)

α and n are temperature dependents and can be represented as:

$\alpha=1.07+1.7\ x10^{-4}\ T-2.81\ x10^{-7}\ T^2$ (3.44)

$$n = 0.2 + 3.966 \times 10^{-4} T \tag{3.45}$$

Z_n is the Zener-Hollomon parameter which represents the temperature compensated effective strain rate as [55]:

$$Z_n = \varepsilon^{\cdot} \exp\left(\frac{Qe}{RT}\right) = Ai[\sinh \alpha \, \sigma_f \,)]^n \tag{3.46}$$

Qe-is the activation energy, R is the gas constant.

The effective strain rate can be represented as [55]:

$$\varepsilon^{\cdot} = \sqrt{\frac{2}{3}\varepsilon_{ij}\varepsilon_{ij}} \tag{3.47}$$

ε_{ij}- is the strain tensor and can be represented as [55]:

$$\varepsilon_{ij} = \frac{1}{2}\left(\frac{\partial u_j}{\partial x_i} + \frac{\partial u_i}{\partial x_j}\right) \tag{3.48}$$

3.4.5 Geometry and Mesh of the FSW Tool and Workpiece

Due to the difficulty of modelling and meshing the conical thread of the FSW tool, it was decided to model a smooth conical tool probe surface without threads (since meshing the threads with the current mesher would have been very laborious). The effects of probe threads have been represented by a vertical velocity using User Defined Function (UDF) in FLUENT software.

3.5.4.1 Geometry

The designed area for the tool without threads has to be equal to the actual area with threads; this has been achieved by calculating the exact surface area of the tool using the Infinite Focus Microscope (IFM) technique to model the dimension of the tool by the aid of CAD software. Figure 3.17 shows the three dimensional IFM image for the Poly Crystalline Boron Nitride (PCBN) tool used to weld the 6mm plate thick. The calculated surface area of the tool using the Infinite Focus Microscopy (IFM) technique, were as follows: $A_{shoulder} = 1499.2$ mm^2, $A_{probe\_side} = 373.2$ mm^2 , $A_{probe\_end} = 50.3$ mm^2.
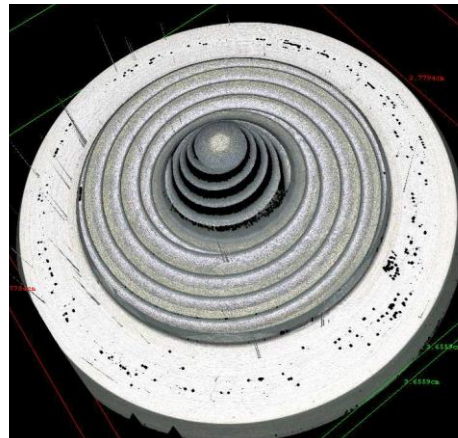
Figure 3.17: The three dimensional image for the PCBN tool using IFM shows the shoulder, probe side and probe end.
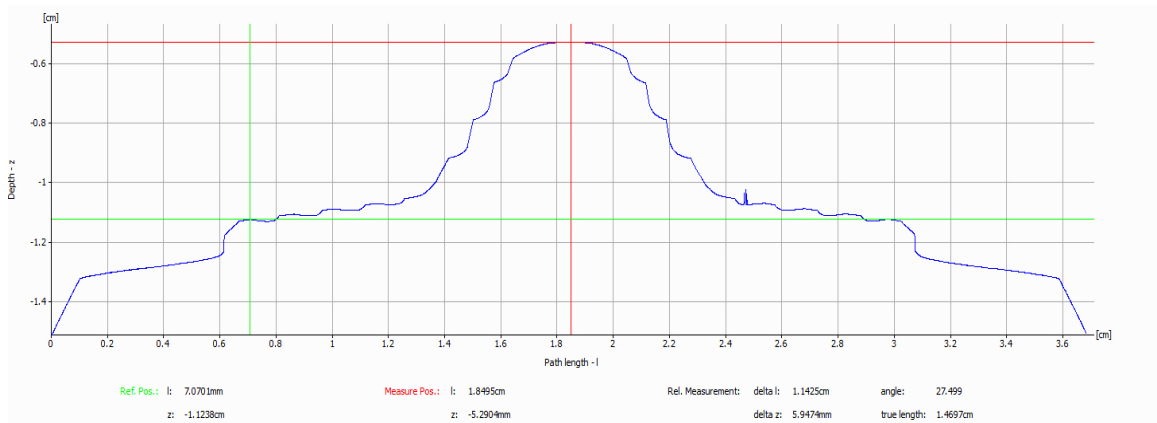
Figure 3.18: 2 dimensional cross section produced by IFM showing the dimensions of the PCBN tool as shown in figure 3.17.

The CAD model for the tool is shown in Figure 3.19 -a- compared to the real image in -b-. The same tool parts (shoulder, probe side and probe end) and dimensions have been applied to design the plate keyhole before assembling the whole parts where the tool is plunged into the workpiece as shown in figure 3.20 and 3.21.

-a-   -b-
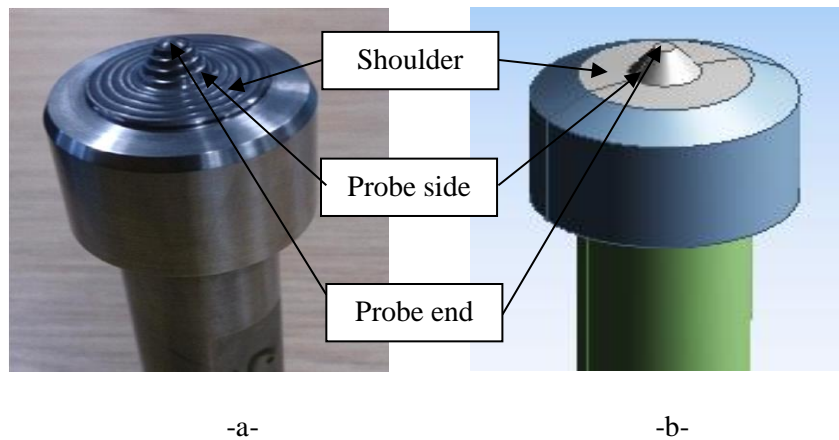
Figure 3.19: The PCBN Tool .-a-Real Image. -b- CAD model.

The DH36 (6mm thickness) and EH46 (14.8 mm thickness) plates were designated as a disc centred on the tool rotational axis (Eulerian frame work) with a 200mm diameter. Due to the low thermal conductivity of steel and also low heat input in FSW process, the dimension of regions affected by heat generated from the tool is expected to be small. Thus part of plate's geometry was suitable for the local Eulerian framework and there was no need to design the whole length of the workpiece [16], [147], [148], [149].

98

The tool and the plate were considered in the designed geometry with the flexibility of applying the sticking-slipping conditions. The tool probe and shoulder are assumed to be fully inserted into the workpiece. The backing plate and the anvil were not designed but instead a thermal convection coefficient with a high value (2000 W/m^2.K) was applied on the bottom surface of the plate [61].

All tool parts including the shoulder, probe side, probe end, collar and shank have been assigned in the geometry in the software Mesher by using "*Named Selection*". The same procedure has been carried out on the plate where the inlet, outlet, top and bottom have been assigned.
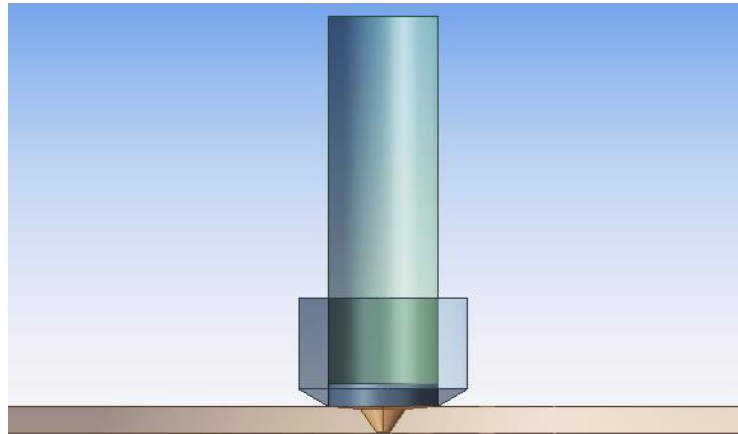
Figure 3.20: Geometry of 6mm DH36 steel plate and PCBN FSW tool.
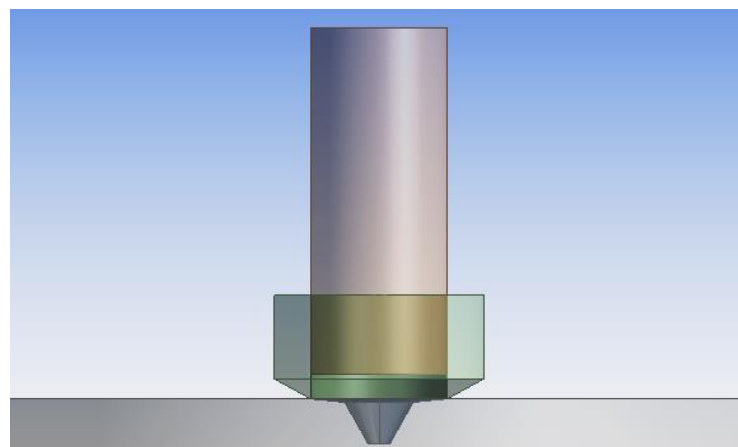
Figure 3.21: Geometry of 14.8mm EH46 steel plate and PCBN FSW tool.

.

Factors affecting mesh quality include small edges, gaps between parts and sharp angles. These issues have been controlled by geometry clean-up in "Design Modeller" or by Virtual topology and pinch in "Meshing" [150].

3.5.4.2 Mesh of the Designed Geometry of the FSW Tool and Workpiece

By definition, mesh is a method in which the geometry designed in CAD is approximated by a network of wire mesh (discrete cell). The geometry of single parts can be meshed easily using software like ANSYS Workbench. For assembled parts, meshing was applied in a way that nodes between two different parts are connected. Multiple part connections can be achieved in ANSYS Design Modeller by converting different designed parts into one part using the function (*Form new part*). The patch confirming method has been used in order to control the growth and smoothness of the mesh and to obtain an accurate surface.

Tetrahedron assembly meshing has been employed to cope with the complex connection between the tool and workpiece. A face sizing minimum of 0.1mm has been applied in the tool/workpiece contact region to obtain a very fine mesh thus all the physical and non-linear properties can be captured. Coarser mesh (larger cell) has been represented elsewhere in geometry where only heat transfer is occurring.

To obtain a fine surface transition mesh on curved and normal angles, the advanced size function curvature has been employed with a growth rate of 1.1.

3.5.4.3 Mesh Quality

The solution convergence and stability are highly dependent up on the mesh quality, unsuitable mesh can cause an unexpected description for the model physics outputs. For checking mesh quality several metrics should be addresses before proceeding to model boundary conditions. The most important mesh metrics in which any deviation from the standard can significantly affect the numerical analysis are: Aspect ratio, Skewness and Orthogonal quality.

Aspect ratio is the ratio of an element area in one direction to another area in a different direction [151].

Skewness is the deviation of actual cell from the optimal cell and can be represented from the following equation [151]

$$Skewness = \frac{optimal\ cell\ size - cell\ size}{optimal\ cell\ size} \qquad (3.49)$$

Highly skewed elements are not desirable in meshing as they can cause solution divergence.

<u>Orthogonal Quality</u> for the element face can be represented by the following equation [151]:

$$\frac{A_i.e_i}{[A_\iota][\overrightarrow{e_\iota}]} \qquad (3.50)$$

Where A_i is the face normal vector

e_i- vector measured from face centroid to the edge centroid.

Low orthogonal quality less than 0.15 can cause solution divergence.

Table 3.3 shows the standard of mesh metric and the "*very good*" accepted range [151].

Table 3.3: The standard of mesh metrics and the "very good" accepted range [151].

Mesh Metric	Min	Max	Average	Standard Deviation	Accepted Standard range (*Very Good*)
Aspect ratio	1.1575	9.7184	1.8137	0.44382	5-10
Skewness	1.0132e-008	0.79981	0.21356	0.11432	0.25-0.5
Orthogonal Quality	0.24622	0.9979	0.86671	8.0851e-002	0.6-0.95

The mesh metrics result for 6mm and 14.8mm thick plates including the aspect ratio, skewness and orthogonality are shown in Figure 3.22 and Figure 3.23 respectively. According to the standard range mentioned in Table 3.3, the mesh quality can be represented as "very good".
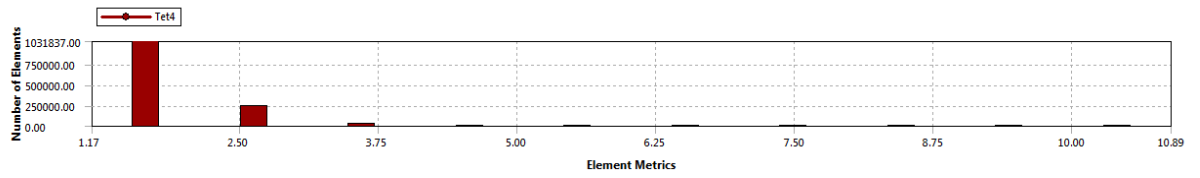
-a- Aspect Ratio.
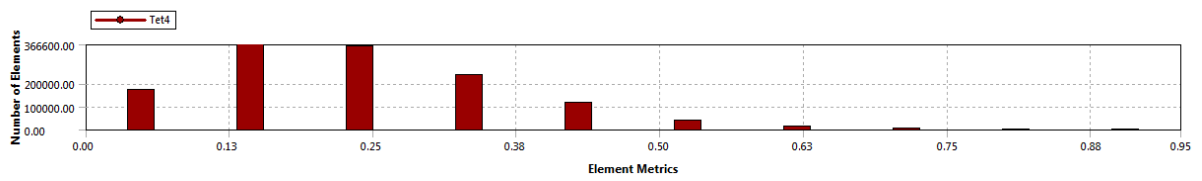
-b- Skewness.
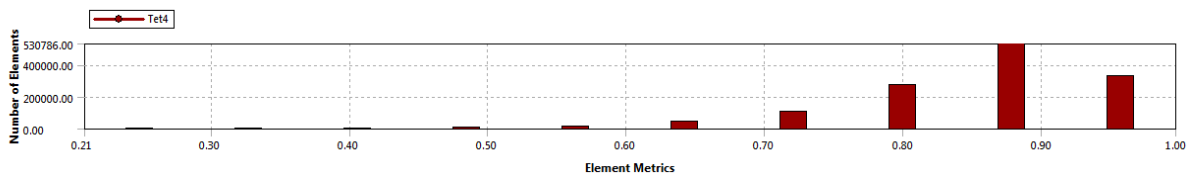
-c-Orthogonal Quality mesh.

Figure 3.22: Mesh metric of the 6mm plate thick -a- Aspect Ratio, -b- Skewness. and -c- Orthogonal Quality mesh.
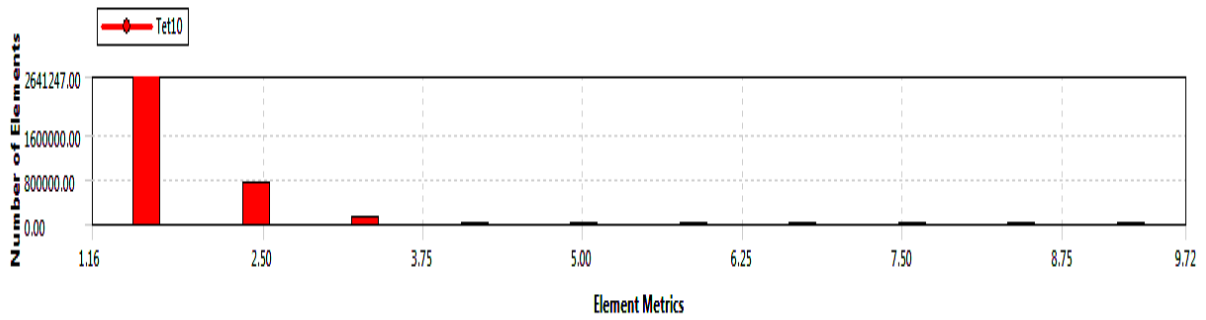
-a- Aspect Ratio.
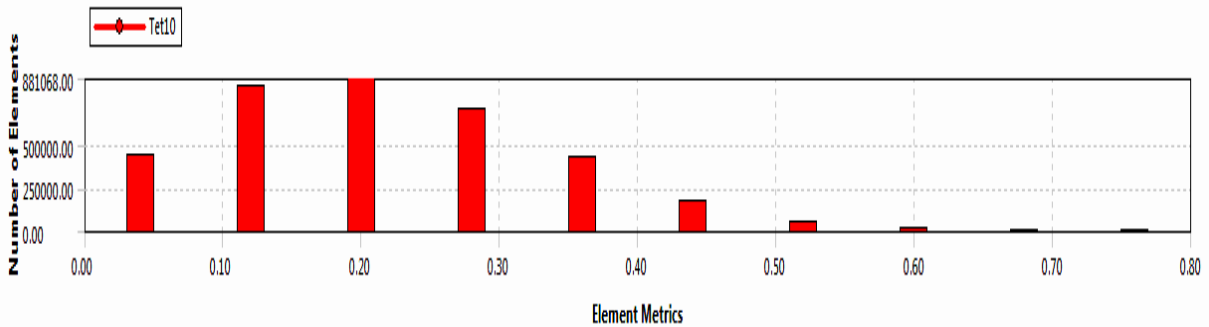
-b- Skewness.
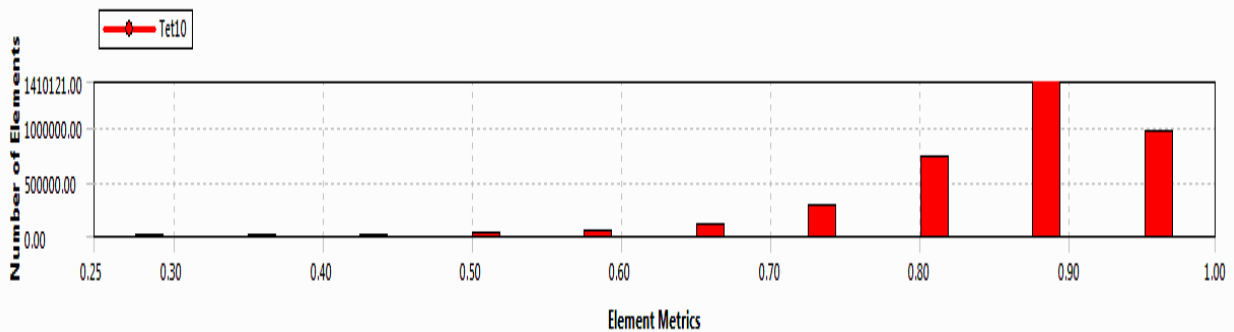
-c-Orthogonal Quality mesh.

Figure 3.23: Mesh metric of the 14.8mm plate thick -a- Aspect Ratio, -b- Skewness. and -c-Orthogonal Quality mesh.

The mesh quality has also been checked in FLUENT by using the *tools "Check" and "report Quality"* to list the minimum values of orthogonal quality, maximum Ortho Skew and maximum Aspect Ratio. The checked mesh has showed no issues that can affect the calculation process.

3.4.6 Boundary Conditions

3.4.6.1 Representing the Material Flow in the tool/workpiece interface

It is assumed that, as the tool moves and rotates, a specified node in the simulation shown in Figure 3.24 is transferred from location 1 to location 2 and its coordinates may be represented as [55]:

$$X = U\,t + r(\cos(\theta_2) - \cos(\theta_1)) \qquad (3.51)$$

$$Y = r(sin(\theta_2) - \sin(\theta_1)) \qquad (3.52)$$
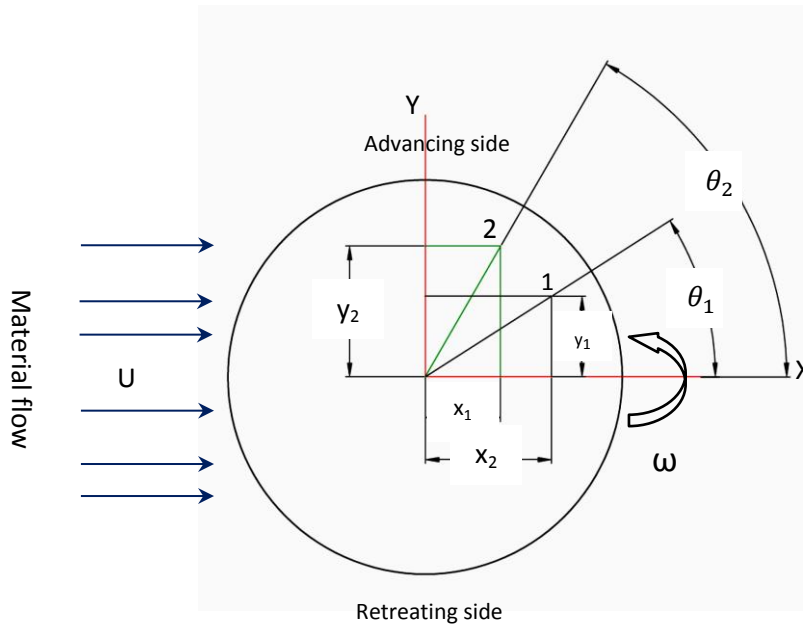
Figure 3.24: The material flow around the tool in FSW (steady state), material is moved from point 1 to point 2.

And by driving these coordinates equations the velocities (u,v) in x and y directions can be obtained as:

$$u = \frac{dX}{dt} = U - r\omega\sin(\theta)$$

(3.53)

$$v = \frac{dY}{dt} = r\omega\cos(\theta)$$

(3.54)

Another velocity in the vertical Z direction may be represented as [152]:

$$w = \gamma\frac{R_p\omega}{2\pi}$$

(3.55)

γ, R_p are the pitch and radius of the pin respectively.

the total magnitude of the velocity as [152]:

$$V = \sqrt{u^2 + v^2 + w^2}$$

(3.56)

and the two dimensional velocity can be represented as:

$$V = \sqrt{r^2\omega^2 - 2Ur\omega\sin(\theta) + U^2}$$

(3.57)

The asymmetry of the velocity distribution in FSW simulation is represented by the term $-2Ur\omega\sin(\theta)$ and thereby the heat flux asymmetry in the weld line.

Laminar flow has been chosen as the viscose forces are the most dominant during FSW process [16], viscous heating has been enabled during the solution.

3.4.6.2 Calculating Heat Transfer From the FSW Tool and Workpiece

The temperature of the workpiece was set to room temperature (25°C). The heat loses from the tool-workpiece can be divided as:

A-Calculating Heat Fraction lost between the Tool and the Workpiece:

Due to the low thermal conductivity of DH36 steel (as received from the manufacturer = 50 W/m. $^{\circ}$C) compared to the tool types (PCBN) which is about three times that of steel, the heat generated in the FSW process will be divided between the tool and work piece.

Other researchers [152] [55] calculated this fraction (*f*) as follows:

$$f = \frac{J_{WP}}{J_{WP}+J_{TL}} = \frac{\sqrt{(k\rho C_p)_{WP}}}{\sqrt{(k\rho C_p)_{WP}}+\sqrt{(k\rho C_p)_{TL}}} \qquad (3.58)$$

$$q \;\; = h(T - T_\circ) + \epsilon\sigma(T^4 - T_\circ^4) \qquad (3.59)$$

f - Heat fraction between the tool and workpiece, k:thermal conductivity in (W/m.K) , ρ - material density (Kg/m^3) , C_p - specific heat capacity (J/Kg. K) , ϵ :emissivity of the plate surface , β is Stefan-Boltzmann constant ($5.670373(21)\times10^{-8}$ W m^{-2} K^{-4}). T_o - Initial temperature $^{\circ}$C. *h* - thermal convection coefficient (W/m^2.K) The abbreviation *wp* and *TL* refer to the workpiece and the tool respectively.

So the heat transfer at the tool/shoulder interface is determined as follow:

$$k \frac{\partial T}{\partial z} \;]_{top} = \frac{\sqrt{(k\,\rho C_p)_{wp}}}{\sqrt{(k\,\rho C_p)_{wp}}+\sqrt{(k\,\rho C_p)_{TL}}}\, Q_i \qquad (3.60)$$

The estimated heat fraction transformed into heat to the workpiece was determined between 0.4- 0.45 for welding using a tungsten based tool and workpieces of stainless steel 304L [152]. However, for welding other types of steel such as DH36 and EH46 using (Poly Crystalline Boron Nitride) PCBN tool with a cooling system as in this work, equation 3.60 cannot accurately represent the heat fraction between tool and workpiece because:

1-The PCBN tool is a hybrid tool includes three types of material with different thermal properties (as shown in Table 3.5).

2-The presence of the cooling system and gas shield will affect this heat fraction.

[153] Subrata and Phaniraj agreed that equation 3.58 is only valid when the tool and plate are considered as an infinite heat sink with no effects of heat flow from air boundary of the tool and they found that the heat partitioned to the tool is less than calculated from equation 3.60.

So in the present simulation the tool has been represented in the geometry to estimate the heat fraction numerically.

B. Calculating Heat removed from the tool shank during FSW process by the cooling system[154]**:** $Q_{cooling} = \overset{o}{m} C_p \Delta T$ 　　　　　　　　　　(3.61)

m^o - is the flow rate of fluid (L/sec for liquid and m^3/sec for gas).

Table 3.4 shows the various coolants types for shank and collar parts of the tool with associated characteristics [21]. The calculated heat has been distributed on the exposed area and then represented on the tool shank as a negative heat flux. In previous work, on the same materials (workpiece of DH36 and PCBN tool) [16] the cooling system was implemented under heat convection conditions on the side of the shank by applying a heat convection coefficient. Given that the maximum temperature on the tool cannot be measured with high precision, the calculated value of heat convection coefficient will not be accurate. Hence, using a negative heat flux on the tool surface seems to be more appropriate.

Table 3.4: The various coolants types for shank and collar parts of the tool with associated characteristics [21].

coolant	flow rate m^o	specific heat C_p	inlet coolant temperature ^oC	outlet coolant temperature ^oC	tool surface area exposed $m^2 \times 10^6$	heat flux W/m^2 $\times 10^{-6}$
50% Ethanol glygol+50%distill water	5.3-13.3 L/min	3.41 KJ/Kg. K	15	17	4241.15	0.217
Air	5.7 m^3/hr	1.2 KJ/m^3. K	15-20	100-125	2760.67	0.0688

Using a range of flow rates may affect dramatically the values of outlet temperature and in turn the heat flux values. However an average value of fluid flow rate has been adopted.

C- Calculating Heat Losses from the Workpiece Surfaces (Top and Sides)

Convection and radiation in heat transfer are responsible for heat loss (Q) to the ambient and can be represented as [152]:

$$Q = hA(T - T_o) + \varepsilon\beta A(T^4 - T_o^4) \qquad (3.62)$$

And

$$k \frac{\partial T}{\partial n} \Big]_\Gamma = q = h(T - T_o) + \varepsilon\beta(T^4 - T_o^4) \qquad (3.63)$$

T_o - is the ambient temperature (25°C), n is the normal direction of boundary Γ.

H - is the convection coefficient (W m^{-2}. K^{-1})

In the current model radiation will not be taken into consideration as its effect is considered to be small and it will add more complexity to the model. The value of heat transfer coefficient (h) around the tool has been increased to compensate the effect of radiation [61].

D-Calculating Heat loss from the Workpiece Bottom Surface

The lower surface of the plate is in contact with the steel backing plates (usually mild and O$_1$ steel grades) and the anvil. Previous workers [155] have suggested representing the backing plates effects by a convection heat condition with a higher coefficient of heat transfer values (500-2000 W/m^2. K). In the current model a value of 2000 W/m^2.K has been used as it was found to give a suitable distribution for temperature at the workpiece bottom.

3.4.6.3 The "*Named Selection walls*" surfaces and interior of the plate: The interior material of the plate was allowed to move by assigning an inlet velocity at one side. The other side of the plate was assigned with zero constant pressure to ensure there was no reverse flow at that side [58]. All plate walls were assumed to move with the same speed as the interior (no slip conditions) with zero shear stress at the walls. The normal velocity of the top and bottom of the plate was constrained to prevent outflow.

3.4.6.4 FSW Tool Rotational/Traverse Speeds: Tool rotational speed (rad/s) was effectively applied in the contact region between the tool and the workpiece. This gave the material in the

contact region asymmetry from the advancing to the retreating side as the material flows (the traverse speed in m/s) from the inlet to the outlet.

3.4.6.5 Gravitational Forces: Gravitational forces were neglected here due to the very high viscous effect of the material [147].

Figure 3.25 shows the boundary conditions applied on the tool and workpiece.
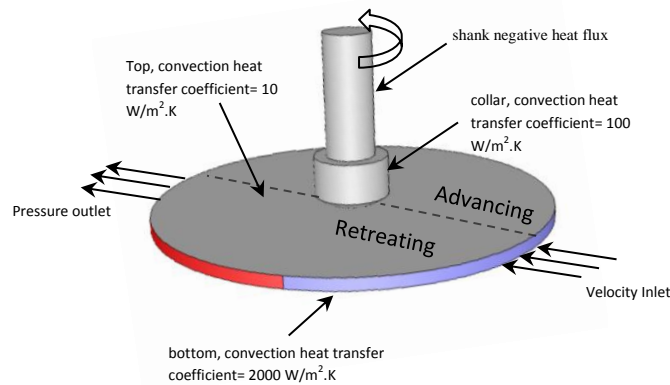
Figure 3.25: The Boundary Conditions applied to the workpiece and FSW tool.

3.4.7 CFD Solution Method

A Pressure-based Navier-Stokes solution with pressure-velocity coupling [58] has been employed, this enables solving the problem in a coupled manner by obtaining a robust and effective single phase application for steady-state flows. Thus the pressure-based continuity (equation 3.39) and momentum (equation 3.40) equations are solved together. The spatial discretization including energy, momentum and pressure are solved using second order to increase the accuracy.

The model case analysis has been solved using the series procedure in order to override the problems of errors related to read and write files such as the User Defined Function (UDF) accompanied with the parallel solution. The Double Precision solver has been chosen in order to increase the results accuracy. About five hours were required to solve the case of 6mm plate thickness while about 7 hrs were required for the 14.8mm plate thickness.

3.4.8 User Defined Function (UDF)

UDF is a C language function which can be compiled, interpreted and works dynamically with FLUENT. By using UDF; the features which are not found in standard FLUENT can be represented effectively. UDF has been used in the current work to represent the material properties including thermal conductivity and non-Newtonian viscosity. Sticking/Slipping velocity and heat generation have been also represented by a UDF. Appendix A includes the forms of C language used in the UDF.

3.4.9 Materials Data Input for Modelling

The chemical composition of the DH36 and EH46 steel grades used for this study were given in Table 2.5 and Table 2.6 respectively. Thermal properties (density, specific heat and thermal conductivity) adopted from previous work carried out on low carbon manganese steel, are given as follows [156]:

$$k = 23.16 + 51.96 . e^{-2.03T/1000} \tag{3.64}$$

$$Cp = 689.2 + 46.2 . e^{3.78T/1000} \qquad \text{for T<700}^{o}\text{C} \tag{3.65}$$

$$Cp = 207.9 + 294.4 . e^{1.41T/1000} \qquad \text{for T>700}^{o}\text{C} \tag{3.66}$$

$$\rho = 7850 \, Kg/m^3$$

Where k, C_P and ρ are thermal conductivity, the specific heat and density, respectively.

The thermal properties for the PCBN hybrid tool are given in Table 3.5 [21], [157].

Table 3.5: Thermal properties of the PCBN tool [21], [157]

Tool part	k (W.m⁻¹.K⁻¹)	C_p (J.Kg⁻¹.K⁻¹)	ρ (Kg.m⁻³)	Ref.
Shoulder and probe (PCBN-WRe)	120	750	3480	[21]
Shank (WC)	92	500	14900	[21]
Collar	11	440	8900	[157]

Tool parts have been treated to behave as a solid while the workpiece has been treated as a fluid during the analysis. Thus a shadow surfaces "*Walls*" in the tool/workpiece have been created automatically with the thermal conditions chosen as "*Coupled*" to allow the heat generated to transfer between the tool and workpiece. Tool properties have been input to the software as constants whereas, the workpiece properties are a function of temperature. The density of steel has been treated as constant, the thermal conductivity has been entered as a function of temperature by the aid of UDF, specific heat also was included as a function of temperature using piecewise-linear function and finally the viscosity was included as a function of temperature and strain rate by using a UDF.

3.4.10 The Independence of the CFD solution on Mesh size

The CFD analysis should be independent of the variation in mesh size, so that a mesh study has been carried out including refining the mesh and monitoring the FLUENT output. Peak temperature was chosen to be monitored with mesh refinement and a difference of 10°C was determined as the limit of mesh refinement.

The first step was to run the FLUENT for a specific mesh size until obtaining the solution convergence including the residual error below 10^{-6} and also monitoring the tool shoulder torque until it reaches a steady state value. Figure 3.26 -a- and -b- show the convergence in term of residuals and torque respectively.

The second step is to refine the mesh and monitor the solution convergence as mentioned in the first step. The obtained results will be compared with the results obtained from the mesh in step number one, when the values is the same or very close, the mesh in step number one will be assumed suitable and the mesh independent solution has been achieved otherwise the mesh will need more refinement.

A chart between temperature output and elements cell numbers can be found in the results section.

-a-   -b-
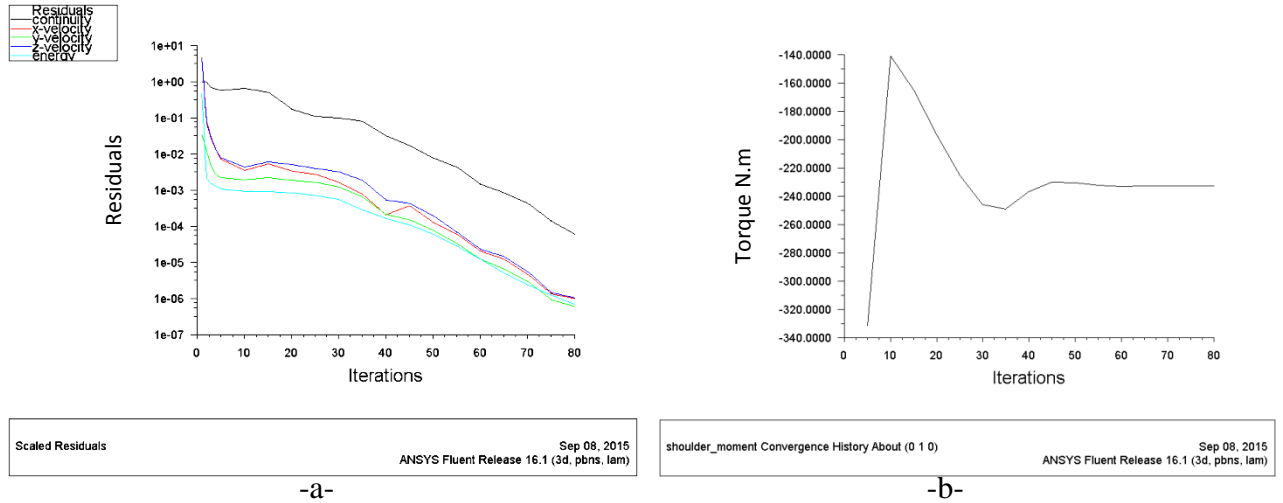
Figure 3.26: Convergence in FLUENT analysis, -a- Residual convergence, -b-Torque N.m convergence.

Figure 3.27 –a- and –b- show transverse section to the mesh of 6mm and 14.8mm plates respectively, mesh is very fine at the tool/workpiece contact region. 1,300,460 tetra elements were used in 6mm plate case while 3,487,632 were used in14.8mm plate.

-a-   **-b-**
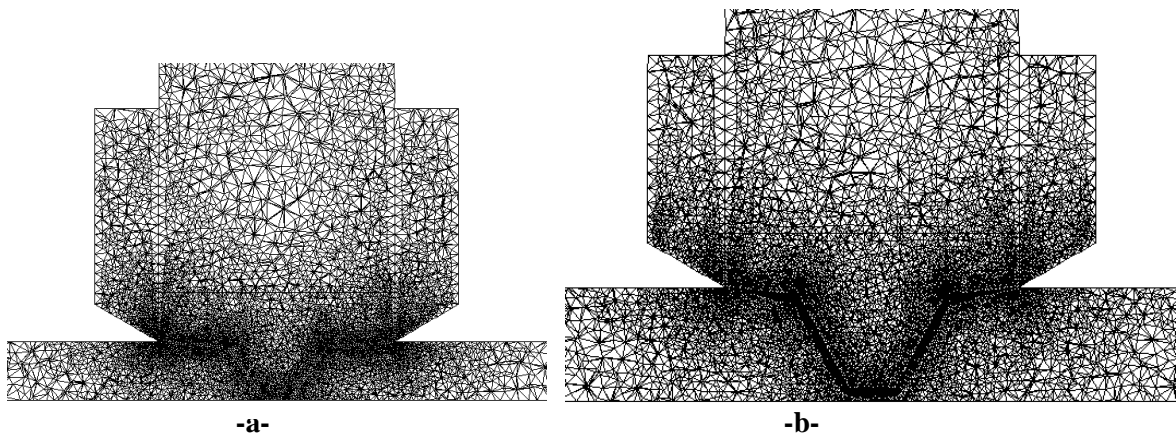
Figure 3.27: Transverse section showing the mesh of -a-6mm plate with PCBN FSW tool of 5.5mm probe length and -b- 14.8 mm plate with PCBN FSW tool of 12mm probe length.

4   Results and Analysis

The following section outlines the results and analysis of the experimental work and numerical analysis of the research.

4.1 FSW Process Parameters Graphs

4.1.1FSW Samples W1 to W8 (DH36) 6mm plate thick.

Table 4.1 shows a decrease in the average tool torque when the tool rotational speed increases. This finding is in agreement with previous work [67] and is thought to be as a result of the decrease in the contact shear stress between the workpiece and the tool, and thus the torque. The relationship between the torque and the flow shear stress is described in equation 3.2. Figure 4.1 to Figure 4.12 shows the relationship between welding parameters with time and the distance travelled. In W4, figures 4.3 and 4.4, the axial force increases gradually with the distance travelled whereas in W5 it decreases with the distance travelled as shown in figure 4.4 and figure 4.6 respectively. This increase and decrease in axial forces may be related to a change in plunge depth, plate thickness or it can be attributed to a deflection in the machine. This variation in axial forces has been reported to TWI and needs an extensive separate study to investigate it.

In DH36 W6, figures 4.7 and 4.8, it can be shown that there are three points where axial force decreases. This reduction in axial force was in the location of the thermocouples as shown in figure 4.8. This suggests that any change in the plate thickness even parts of millimetres can cause a significant decrease in the axial forces.

Considering torque showed fluctuations with time and distance travelled, the fluctuations increase as the tool traverse speed increases. As mentioned in the literatures review (section 2.10), torque fluctuation can be attributed to two sources: -a- Process effects - as the material warms up and becomes plasticised (on the advancing-trailing side), it will generate less torque than cooler material (on the leading-retreating side). -b- Measurement variation: the FSW machine such as (PowerStir) is large and the torque sensors are relatively insensitive in so much as they need to cover a wide range of torque. Some fluctuation will be present in the form of signal noise, and overlaying these variations may be due to the size and inertia of the spindle as the control system seeks to keep it running at a constant pre-set speed as the workpiece material softens.

4.1.2 FSW Process Parameters Graphs for Sample W9 (DH36), 8mm thick steel plate which is 1m long.

Figure 4.13 and figure 4.14 show that the weld was started with the tool plunging to an indicated depth of 8.5mm. Although the PowerStir machine, used to carry out the weld, is large and "stiff", it isn't infinitely stiff and so deflection upwards is expected as the tool is pushed down - the tool penetration depth will not therefore be exactly 8.5mm. The actual plunge depth measured by the IFM technique was 7.7mm. After plunging into the steel, the tool, rotating at 200 RPM, was accelerated to a welding speed of 100 mm / min over a distance of 50 mm. At approximately 460 mm into the weld, the tool was withdrawn to an indicated depth of 8.45mm (note the fall in the axial force Fz, at that point) and at about 720 mm into the weld the tool was withdrawn to an indicated depth of 8.4 mm; as recorded by the machine. The average values of torque and forces shown in table 4.2 have been calculated from the maximum and minimum values of the data recorded by the FSW machine.

Table 4.1: Eight welding conditions provided by TWI and used in the CFD analysis

Weld No.	Tool rotational speed RPM	Traverse speed mm/min	Rotational/Traverse speeds (rev/mm)	Average Spindle Torque N.m	Average Tool Torque N.m	Axial Force (average) KN	Longitudinal Force (average) KN
W1	160	100	1.6	308	117	54.47	6.99
W2	200	100	2	278	105	57.55	12.8
W3	300	250	1.2	237	90	50	9
W4	325	400	0.8125	247	94	55	9
W5	500	400	1.25	202	77	45	8.3
W6	550	400	1.375	163	62	47	12
W7	550	400	1.375	179	68	52	12
W8	550	400	1.375	168	64	50	9
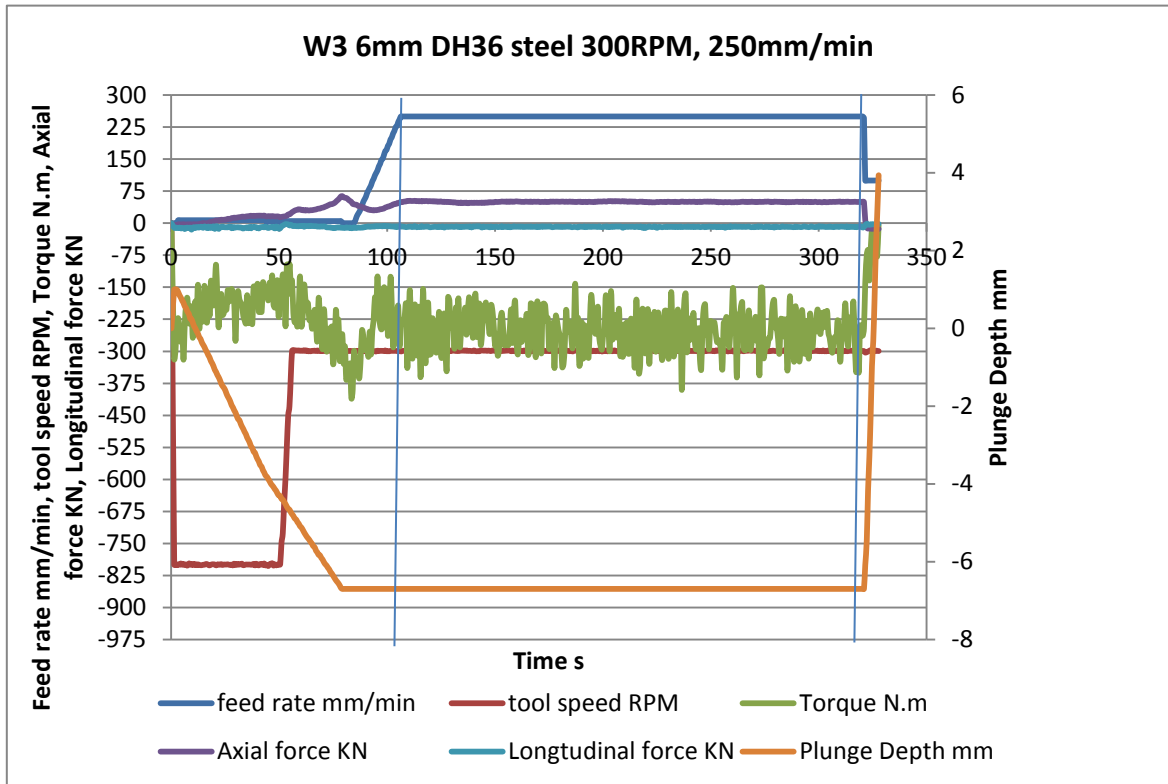
Figure 4.1: Welding parameters with time for 6mm FSW DH36 steel (W3) recorded on the PowerStir FSW machine.
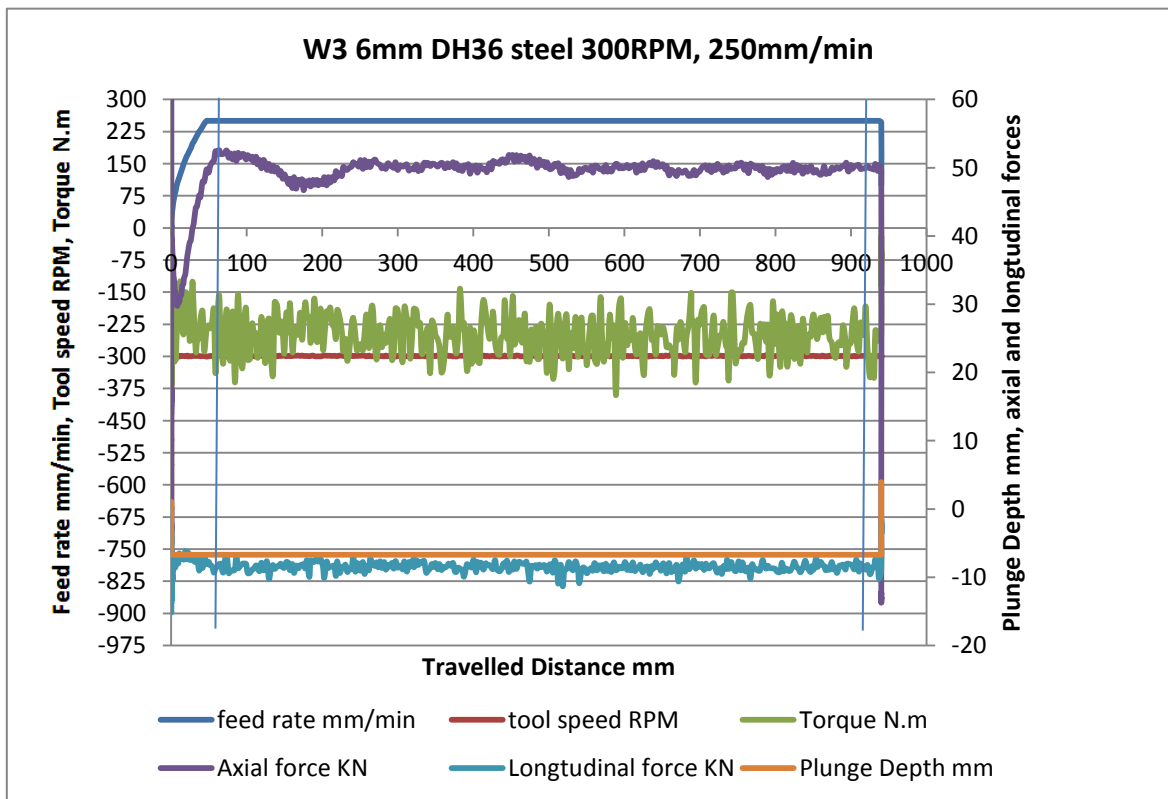
Figure 4.2: Welding parameters with travelled distance for 6mm FSW DH36 steel (W3) recorded on the PowerStir FSW machine.

115
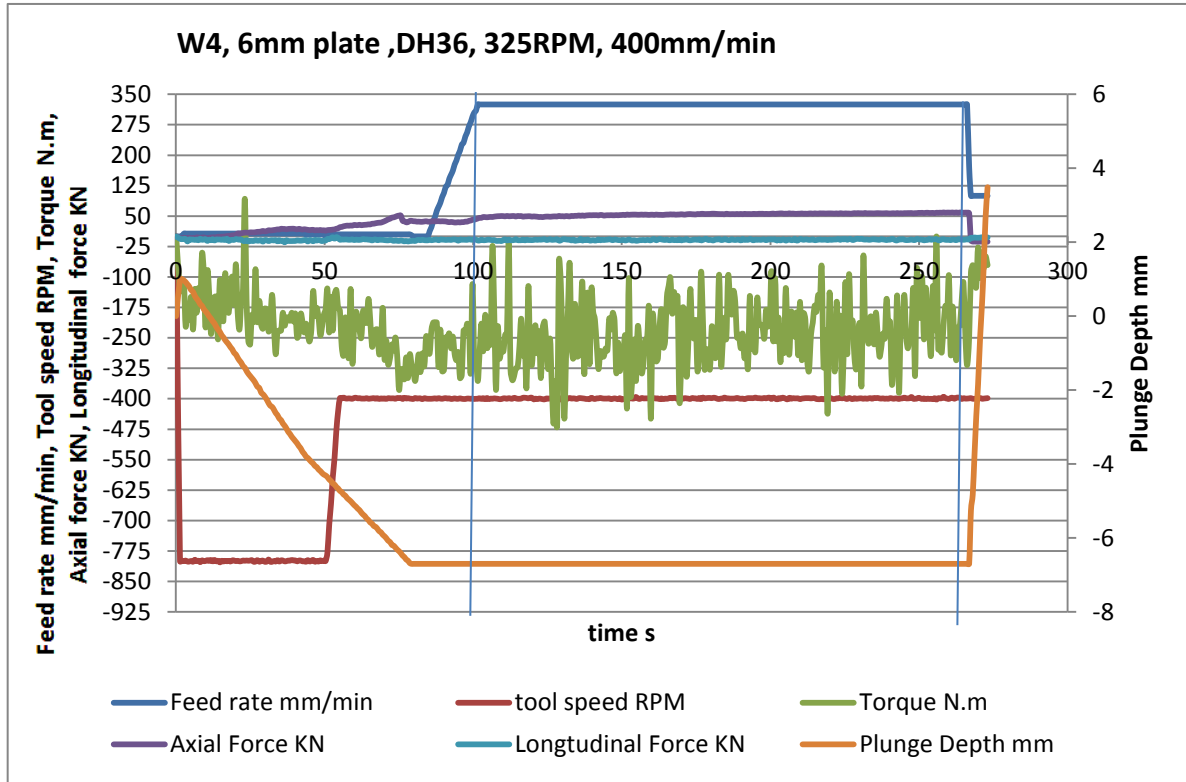
Figure 4.3: Welding parameters with time for 6mm FSW DH36 steel (W4) recorded on the PowerStir FSW machine.
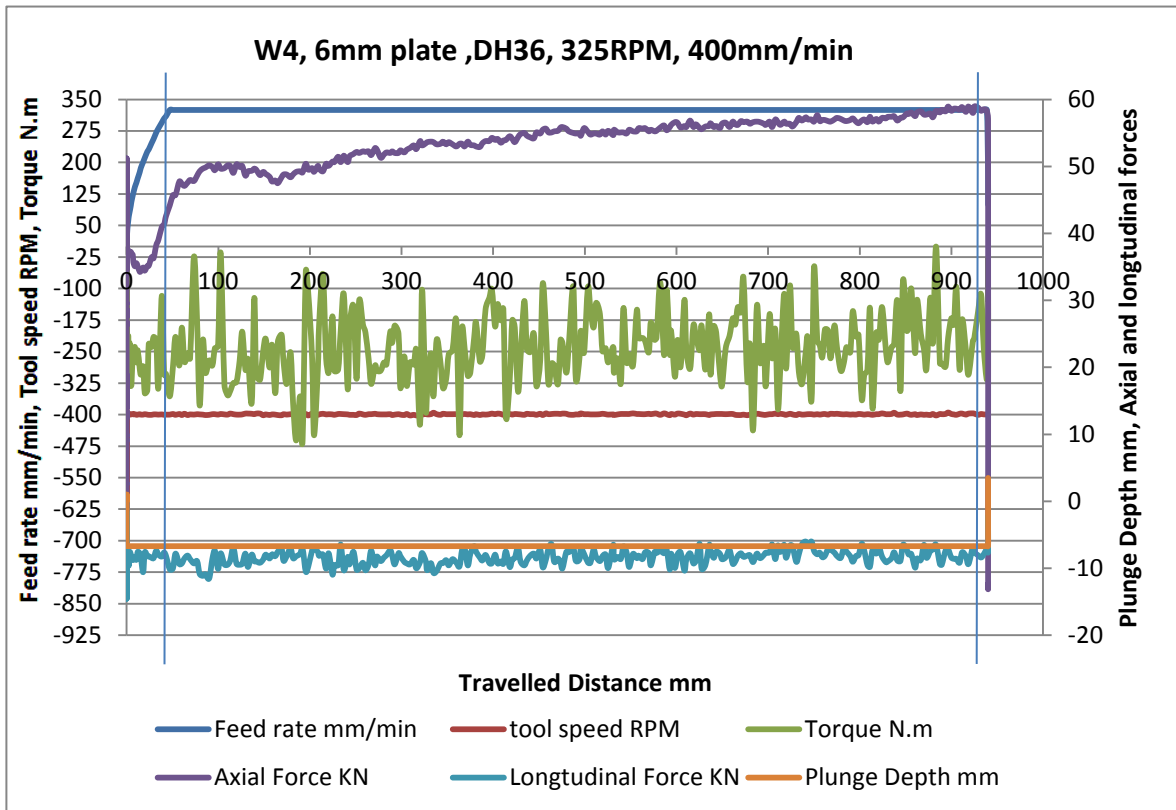
Figure 4.4: Welding parameters with travelled distance for 6mm FSW DH36 steel (W4) recorded on the PowerStir FSW machine.
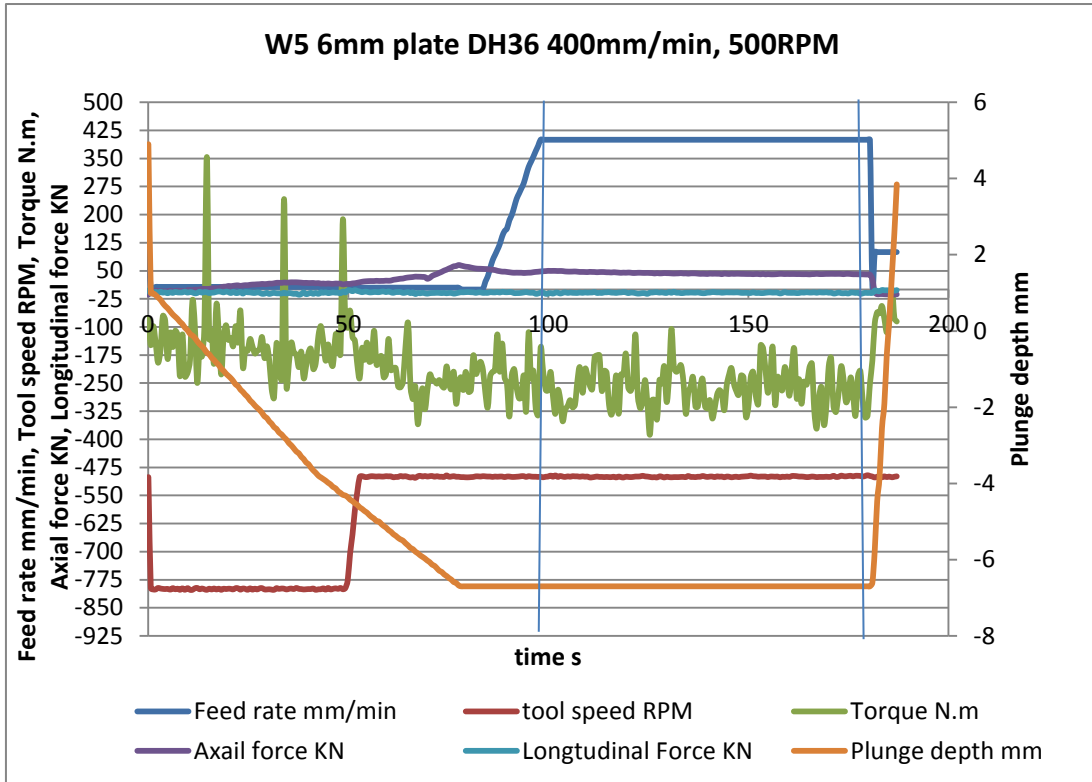
Figure 4.5: Welding parameters with time for 6mm FSW DH36 steel (W5) recorded on the PowerStir FSW machine.
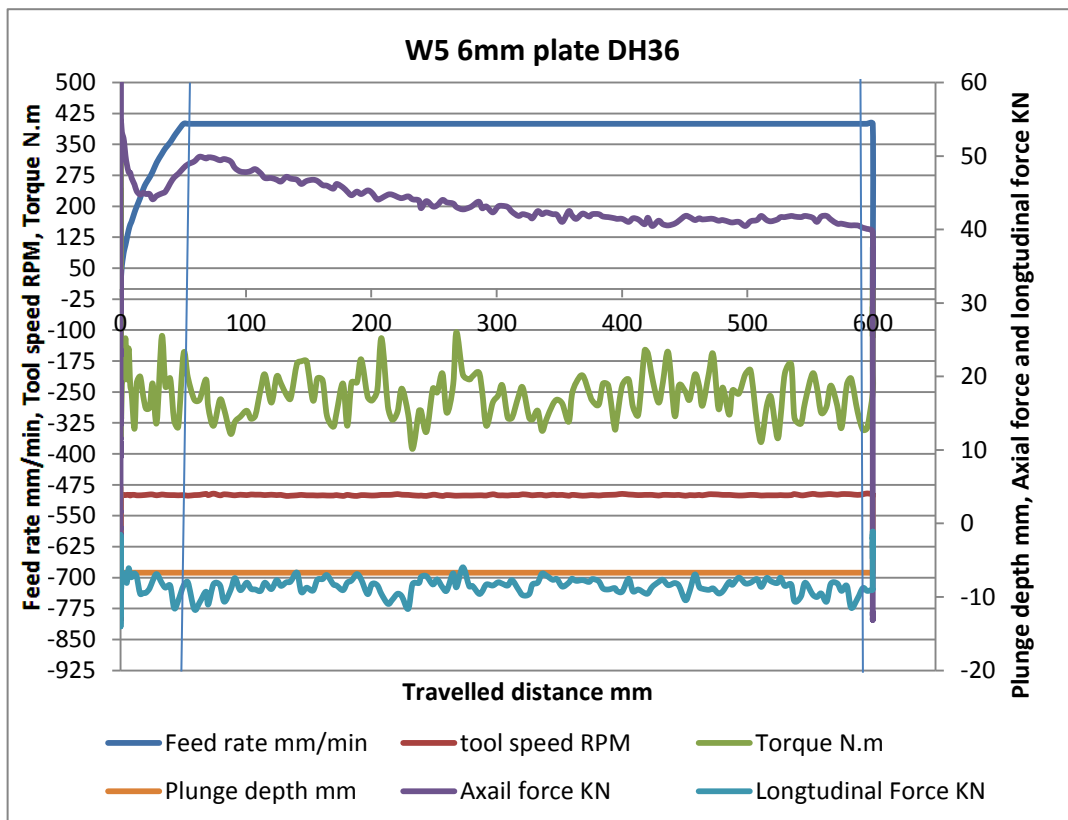
Figure 4.6: Welding parameters with travelled distance for 6mm FSW DH36 steel (W5) recorded on the PowerStir FSW machine.
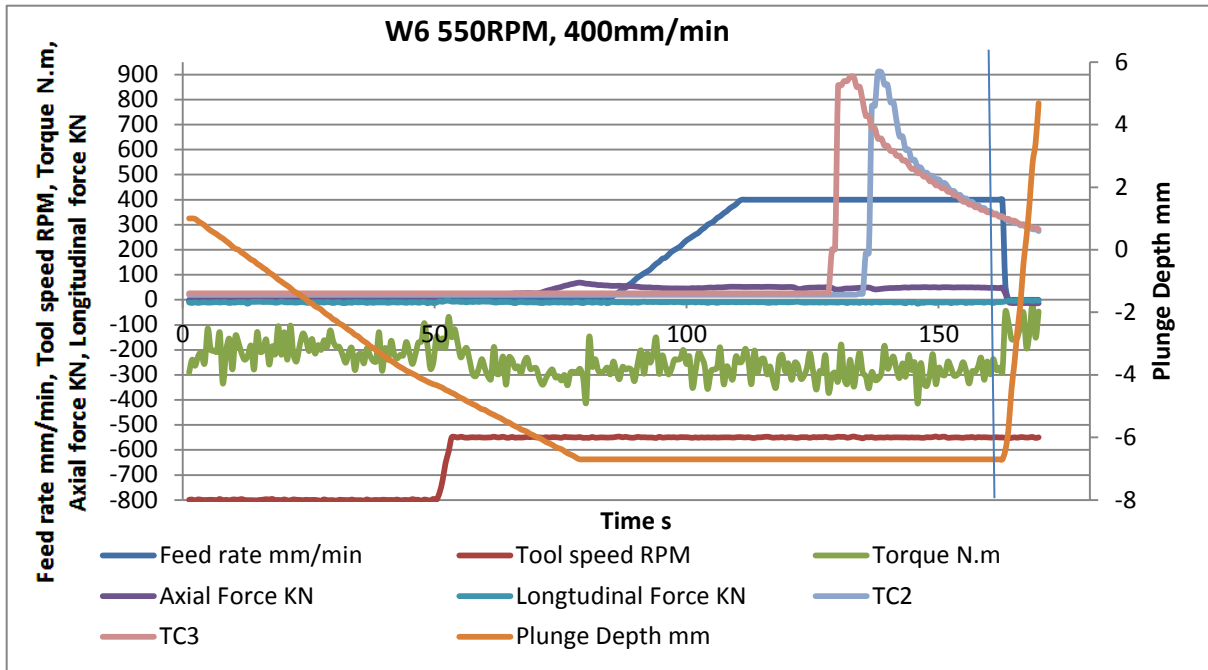
Figure 4.7: Welding parameters with time for 6mm FSW DH36 steel (W6) recorded on the PowerStir FSW machine.
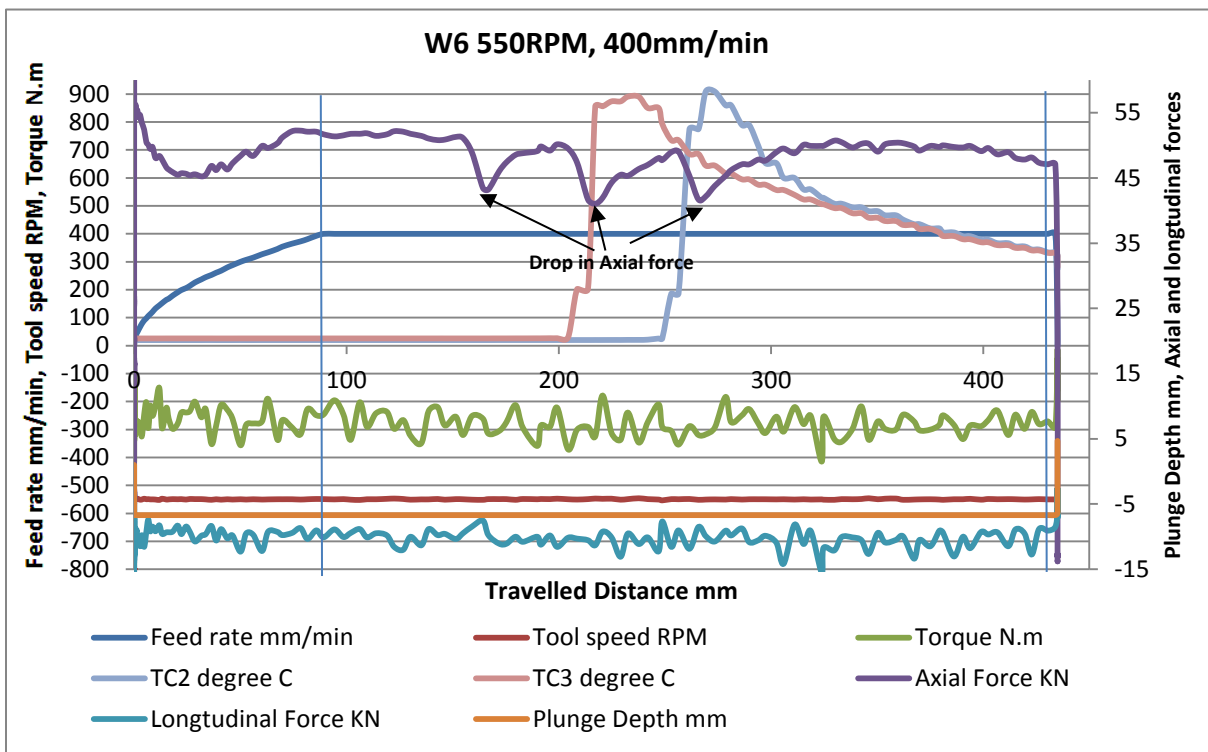
Figure 4.8: Welding parameters with travelled distance for 6mm FSW DH36 steel (W6) recorded on the PowerStir FSW machine.
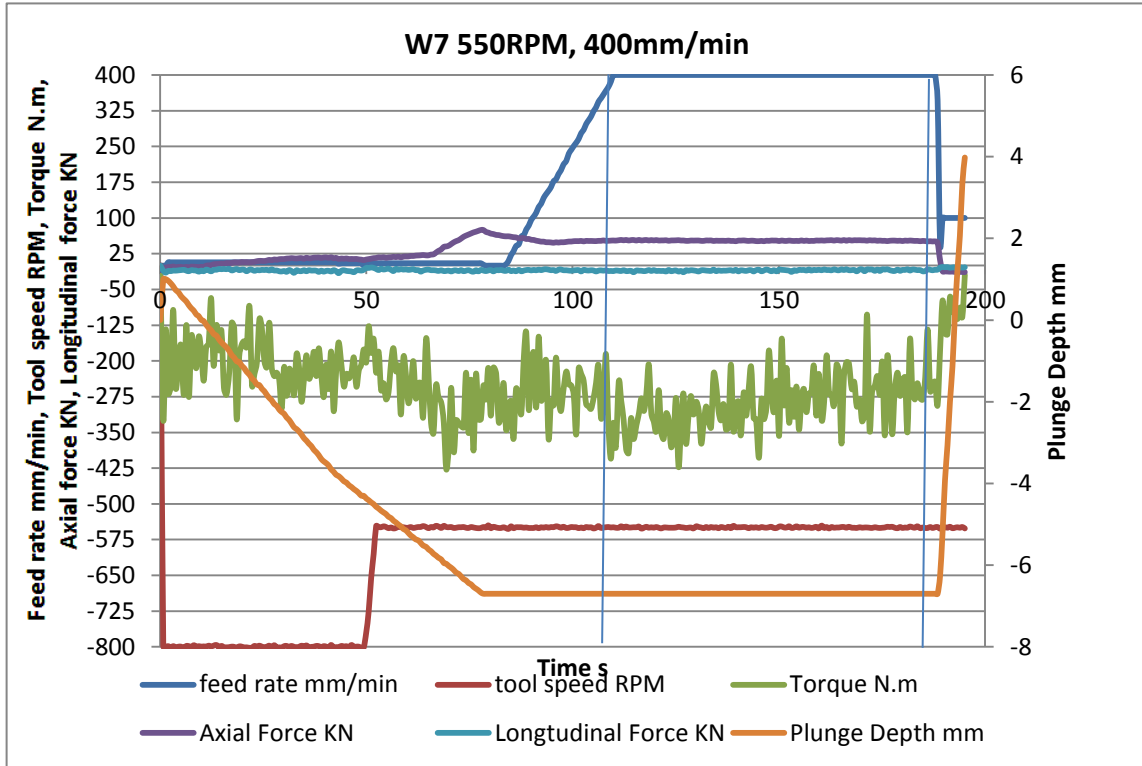
Figure 4.9: Welding parameters with time for 6mm FSW DH36 steel (W7) recorded on the PowerStir FSW machine.
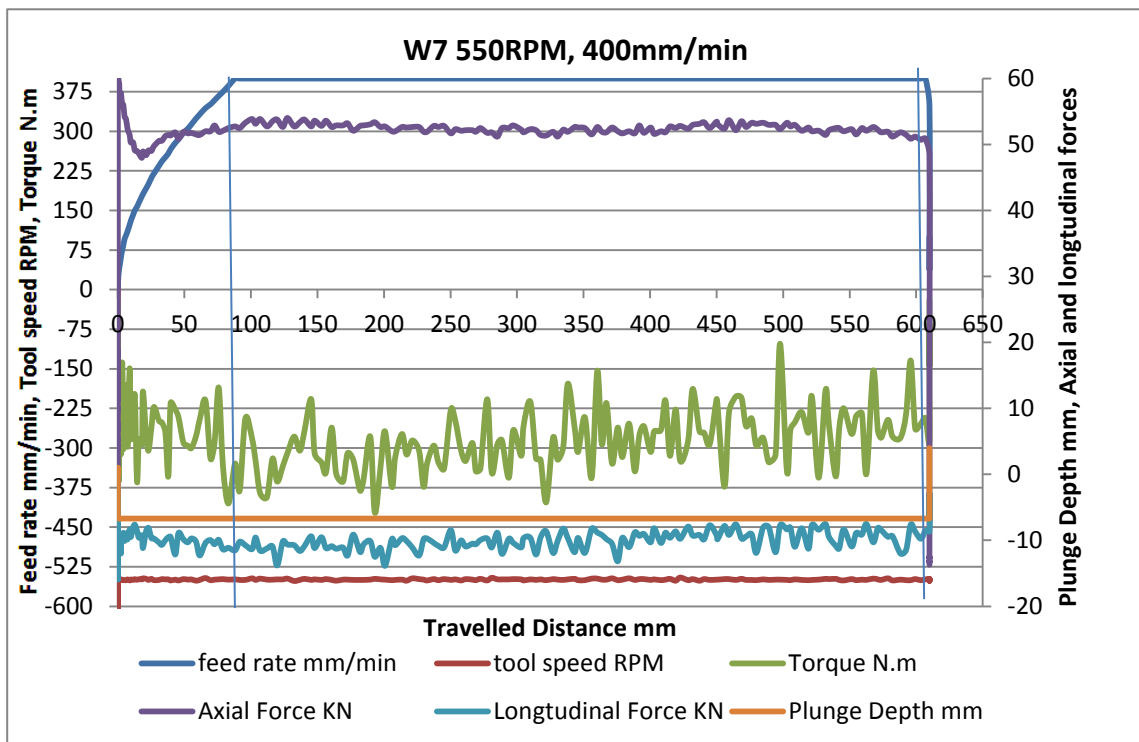
Figure 4.10: Welding parameters with travelled distance for 6mm FSW DH36 steel (W7) recorded on the PowerStir FSW machine.
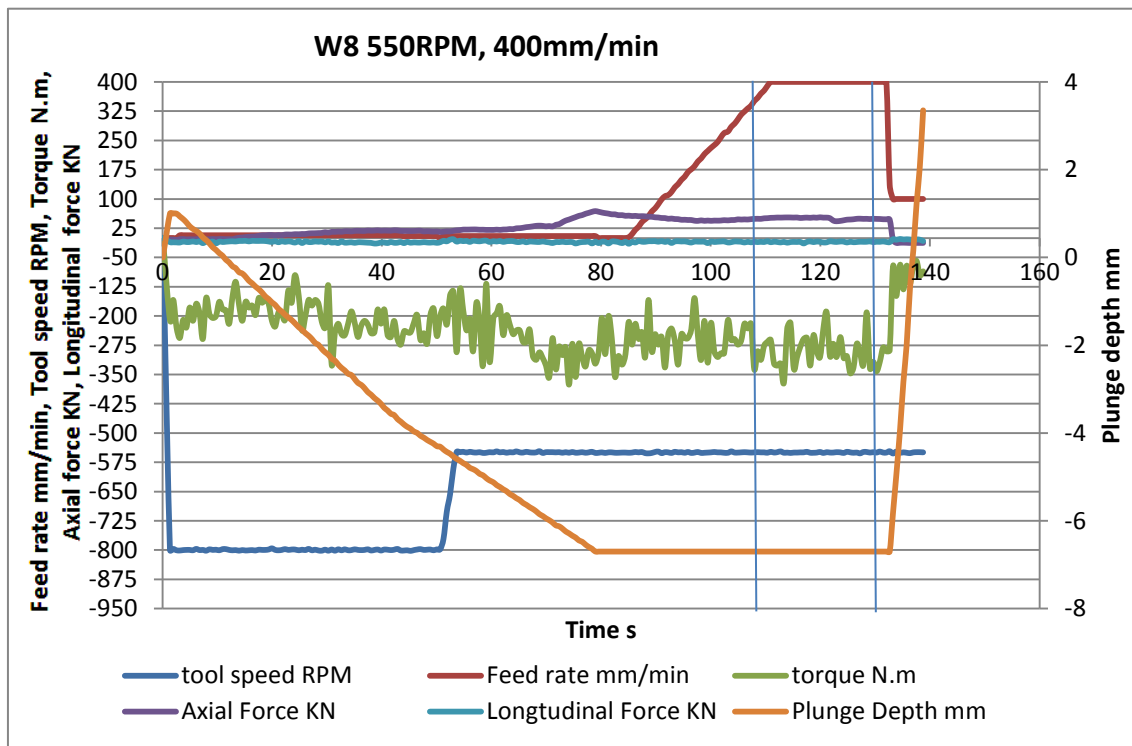
Figure 4.11: Welding parameters with time distance for 6mm FSW DH36 steel (W8) recorded on the PowerStir FSW machine.
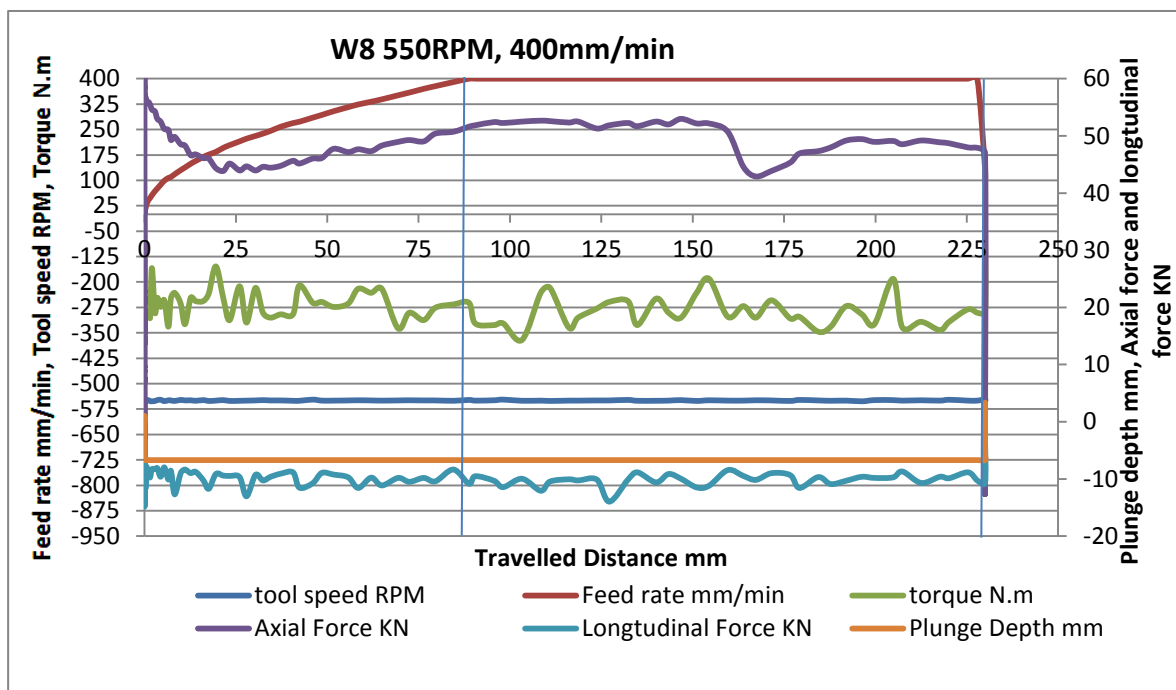
Figure 4.12: Welding parameters with travelled distance for 6mm FSW DH36 steel (W8) recorded on the PowerStir FSW machine.
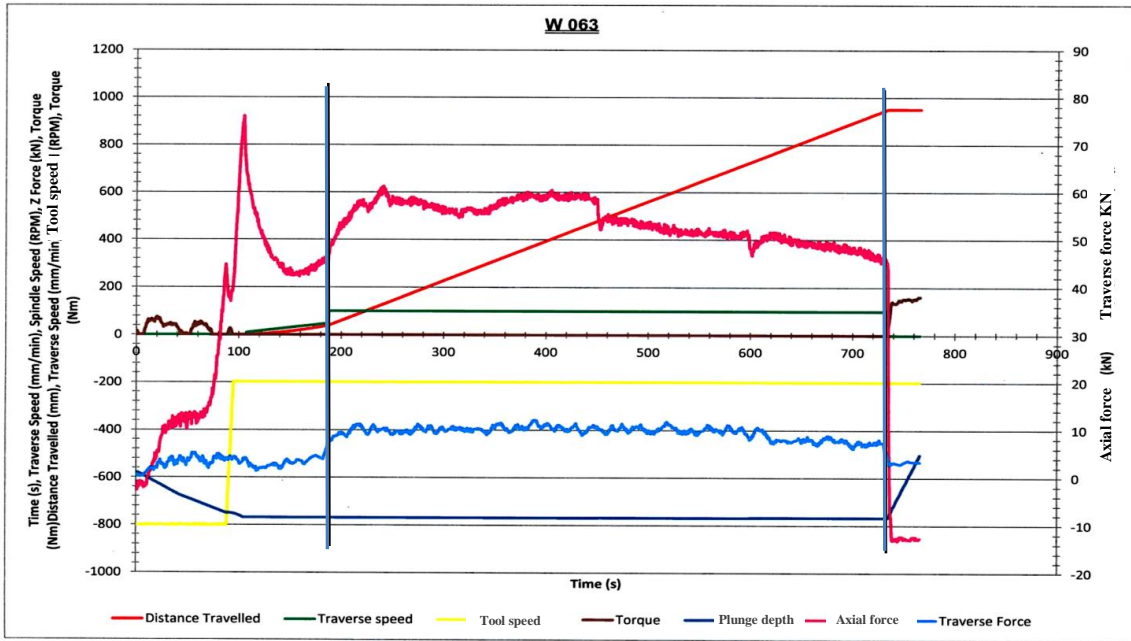
Figure 4.13: Welding parameters with time of 8mm FSW DH36 steel (W9) recorded on the PowerStir FSW machine.
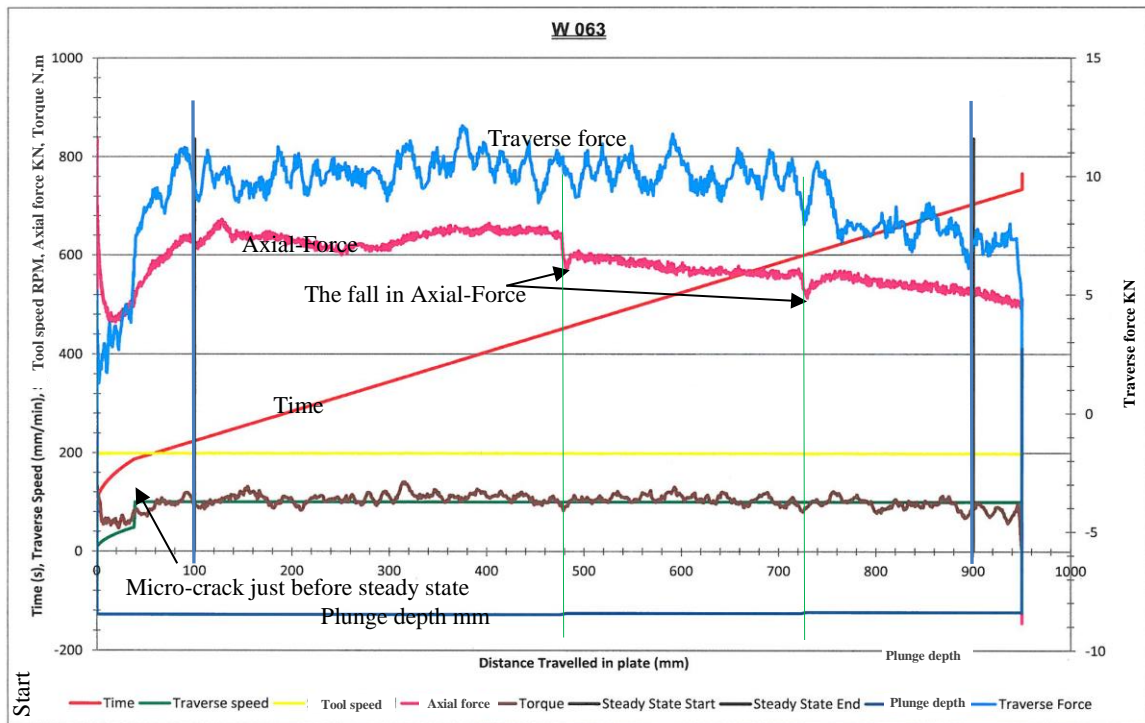
Figure 4.14: Welding parameters with distance travelled for 8mm FSW DH36 steel (W9) recorded on the PowerStir FSW machine.

Table 4.2: The maximum, minimum and average axial force (Z-force) and longitudinal force (X-force) and torque for FSW 8mm DH36 steel (W9)

	AVERAGE	MAXIMUM	MINIMUM
X-FORCE (kN)	9.71	12.14	6.10
Z-FORCE (kN)	596.46	673.20	512.71
TORQUE (N m)	104.76	140.58	67.59

4.1.3 FSW Process Parameter Graphs for FSW 14.8mm thick EH46 steel during the Plunge/dwell period (W1-W7).

In the EH46 plunge/dwell experiments, Figure 4.15 to Figure 4.21, it is evident that the feed-rate has decreased as the tool is depressed into the surface of the material. For W1 and W2 the plunge depth feed-rate starts at 10mm/min and decelerates to 5mm/min and finally 3mm/min before reaching the maximum plunge depth. For EH46, W3 to W7, the plunge depth feed-rate decreases from a maximum of 7mm/min to 3mm/min before reaching the maximum plunge depth. The plunge depth recorded by the machine has not been used in this work because of concerns over a possible error due to machine deflections during processing. For this reason resulting plunge depths, following each of the trials, have been measured using the Infinite Focus Microscope (IFM) which can be found in the IFM section of the results. In all experiments the torque and axial force reached its maximum values at the start of the dwell time when reaching the maximum plunge depth (region assigned between the two vertical blue lines) and decreases slightly after several seconds from the start of the dwell stage. Table 4.3 and Table 4.4 summarize the welding conditions and also provide the peak temperatures recorded by Thermo-Couples respectively. It can be noticed in all curves that the torque reaches a maximum value at the dwell period when the tool shoulder "fully stick" into the workpiece. Previous work on FSW showed that the torque generated from the tool shoulder represents the major part of the total torque [67]. Torque, as shown in table 4.3, decreases when the tool rotational speed increases as a result of an increase in parent metal temperature and thus material softening.
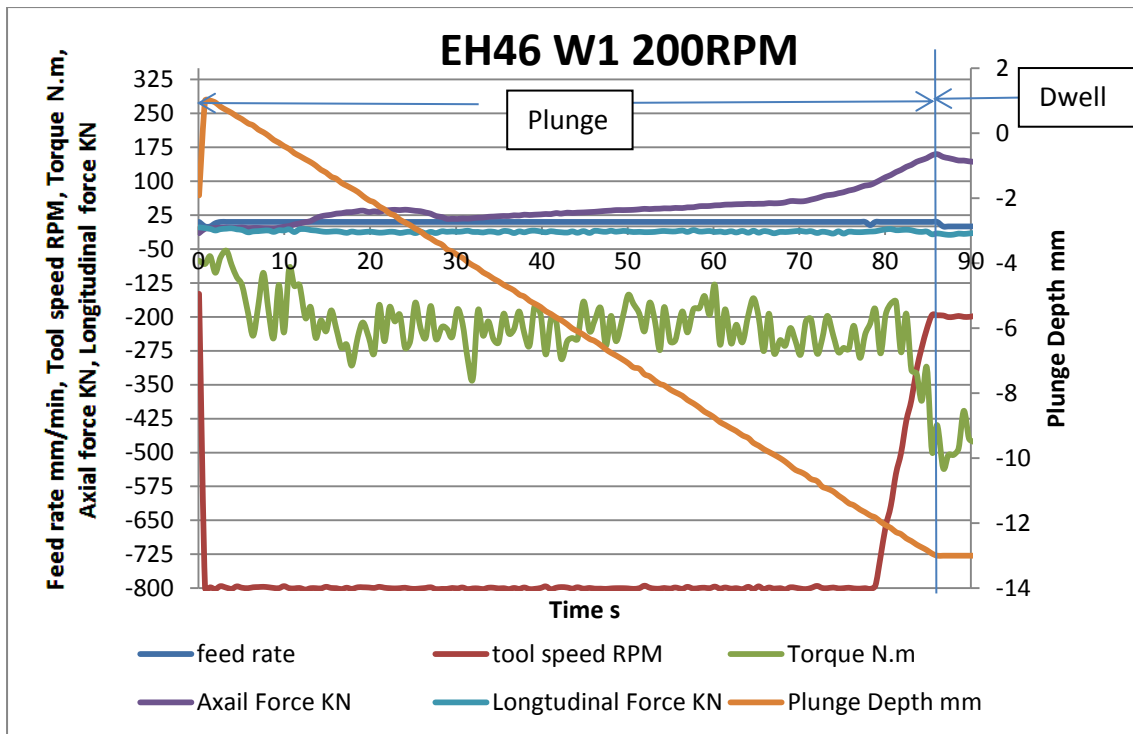
Figure 4.15: Welding parameters with time (W1 the 14.8mm EH46 steel, plunge experiment), recorded on the PowerStir FSW machine.
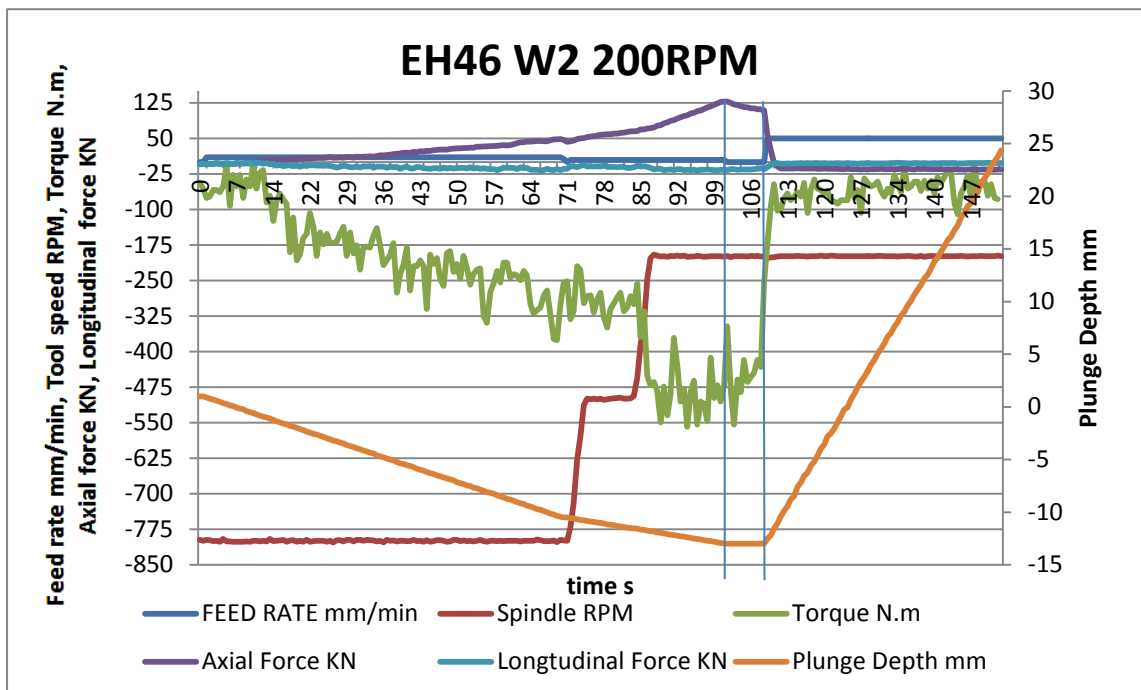
Figure 4.16: Welding parameters with time (W2 the 14.8mm EH46 steel plunge, experiment), recorded on the PowerStir FSW machine.
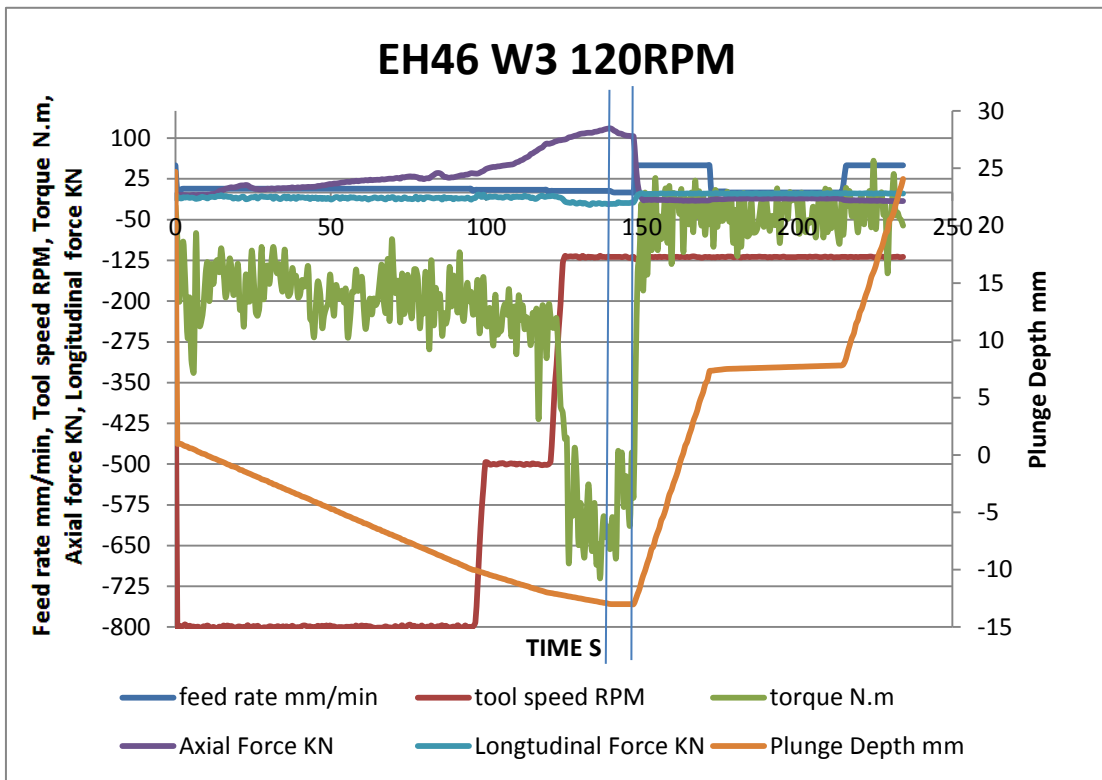
Figure 4.17: Welding parameters with time (W3 the 14.8mm EH46 steel plunge, experiment), recorded on the PowerStir FSW machine.
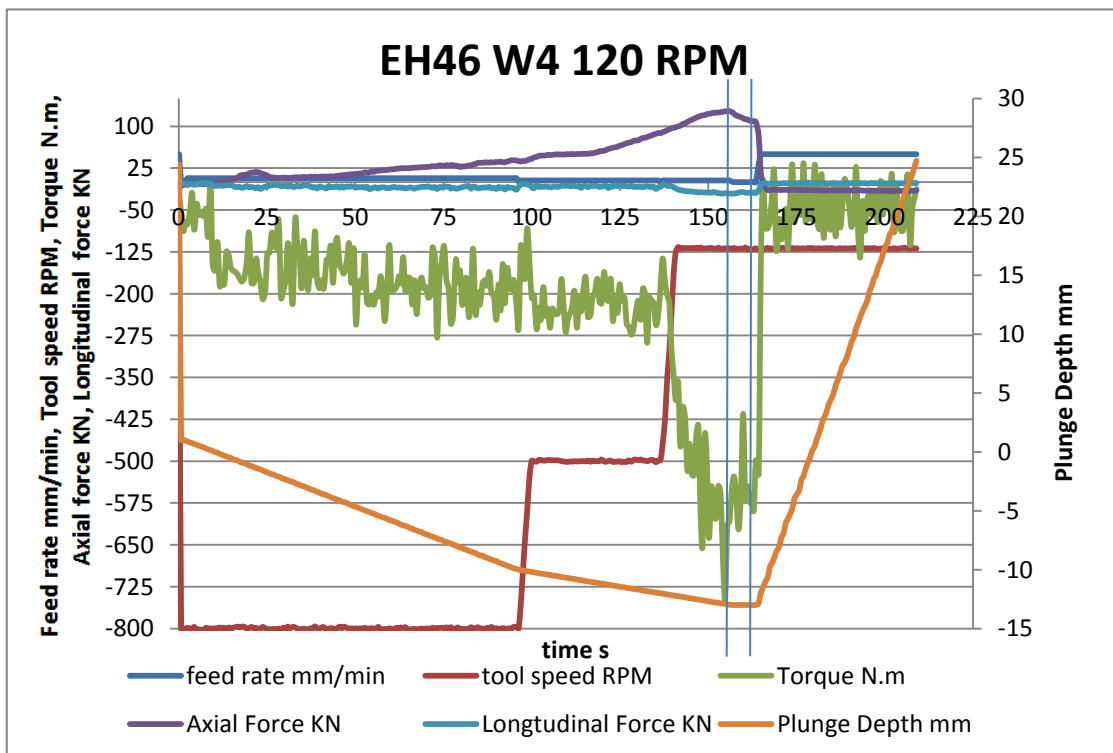
Figure 4.18: Welding parameters with time (W4 the 14.8mm EH46 steel, plunge experiment), recorded on the PowerStir FSW machine.
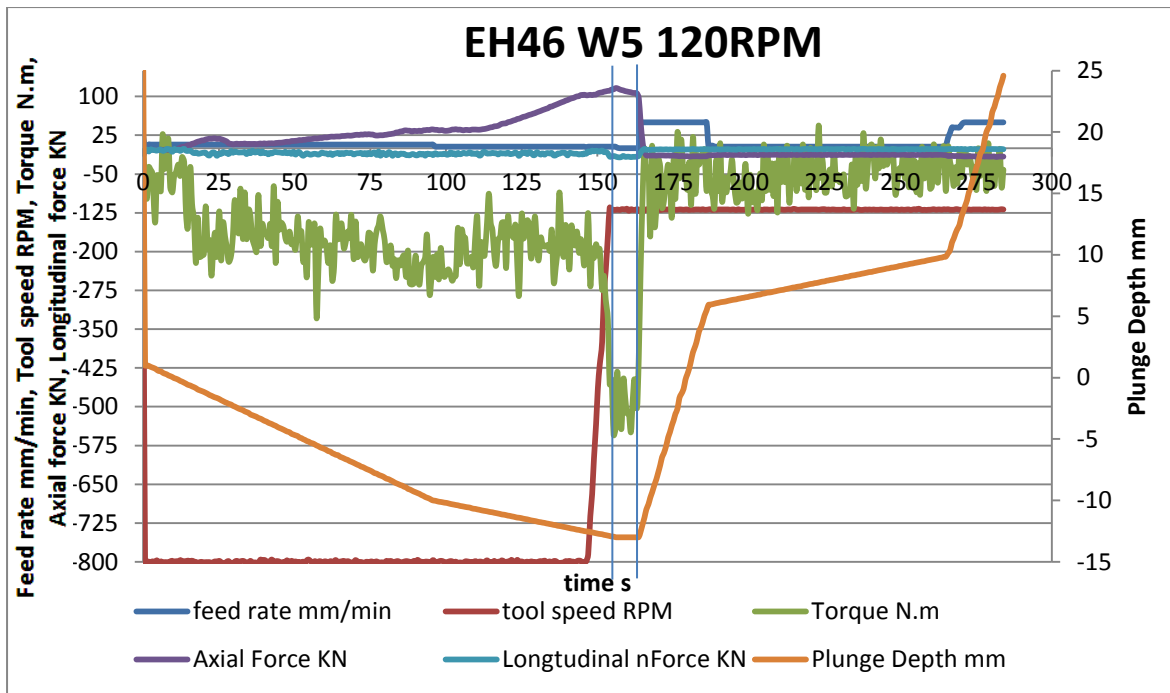
Figure 4.19: Welding parameters with time (W5 the 14.8mm EH46 steel, plunge experiment), recorded on the PowerStir FSW machine.
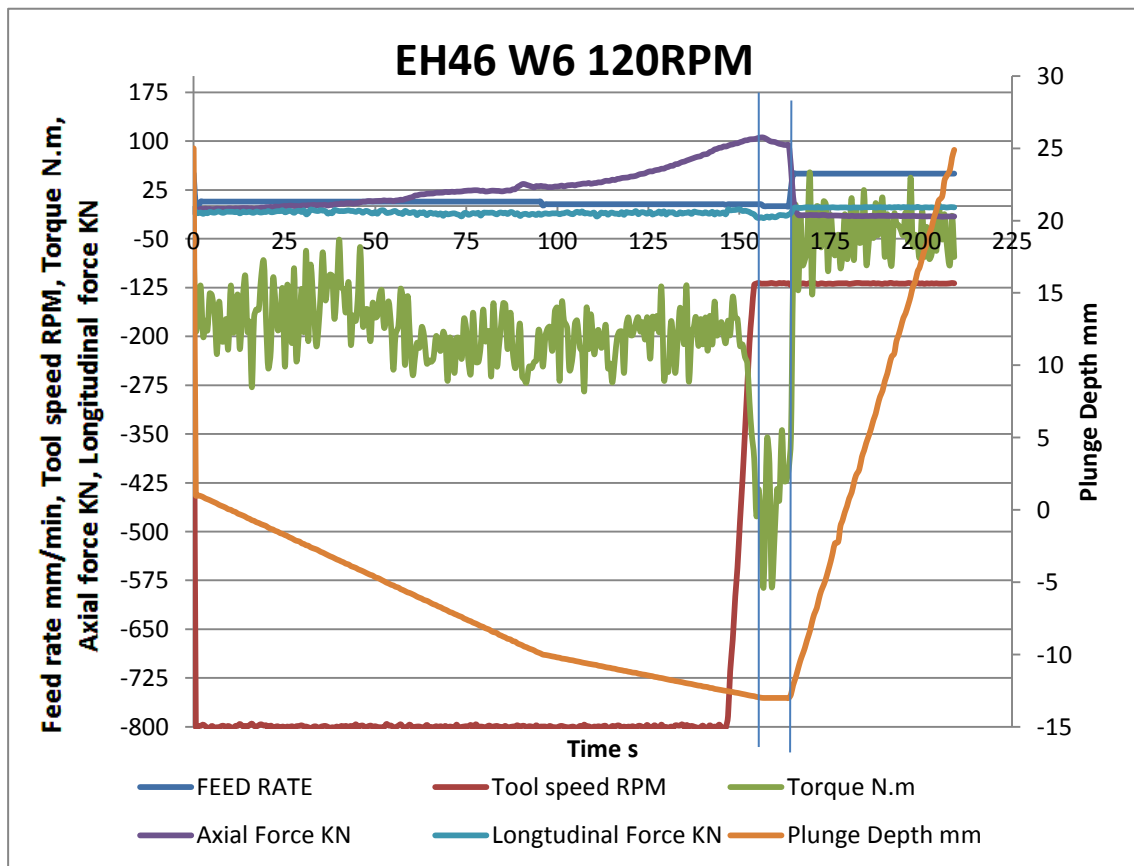
Figure 4.20: Welding parameters with time (W6 the 14.8mm EH46 steel, plunge experiment), recorded on the PowerStir FSW machine.

125
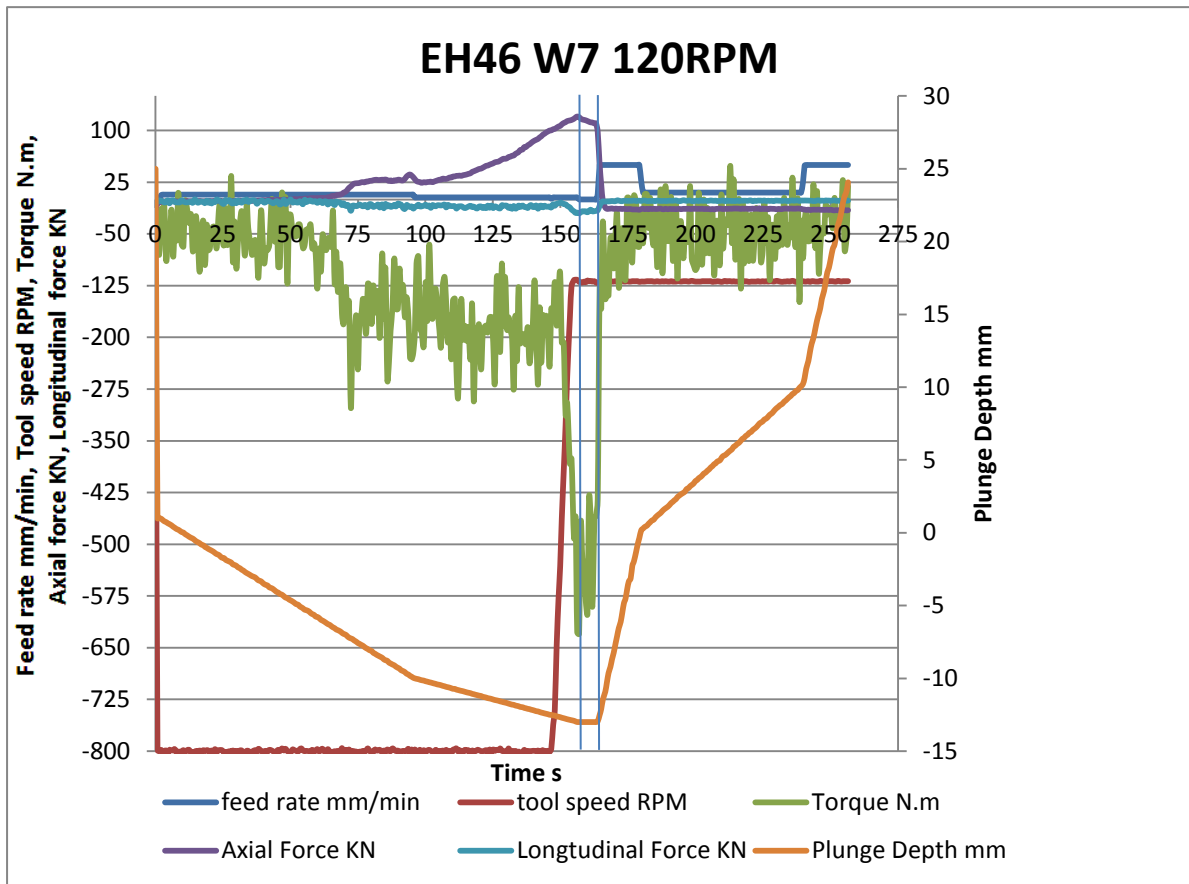
Figure 4.21: Welding parameters with time (W7 the 14.8mm EH46 steel, plunge experiment), recorded on the PowerStir FSW machine.

Table 4.3: The welding conditions for FSW EH46 plunge/dwell period (W1-W7).

Weld Trial No.	Tool rotational speed ω (RPM) at dwell period	Max. Axial (Plunge) force (F_z) KN	Max. longitudinal force (F_x) KN	Max. Torque (M) N.m	Plunge Depth (Z) mm from FSW machine	Dwell Time (t) sec at (dwell) period
W1	200	157	17	498	13	6
W2	200	127	17	471	13	8
W3	120	116	21	598	13	7
W4	120	126	20	549	13	6
W5	120	115	17	532	13	7
W6	120	105	18	583	13	7
W7	120	119	20	548	13	7

Table 4.4 shows the peak temperatures measured by the thermocouples for each of the welding trials.

Table 4.4: Thermocouple measurements for the seven plunge trials (W1 - W7)

Weld No.	Maximum recorded Temp. T °C TC 1	Maximum recorded Temp. T °C TC 2	Maximum recorded Temp. T °C TC3	Maximum recorded Temp. T °C TC 4	Maximum recorded Temp. T °C TC 5	Maximum recorded Temp. T °C TC 6
W1	430	630	430	422	600	421
W2	444	650	-----	427	620	432
W3	380	550	381	382	545	---
W4	400	580	-----	402	581	405
W5	----	544	375	380	553	381
W6	----	----	420	410	----	----
W7	400	554	----	----	----	----

Some thermo-couple data is missing because the thermo-couple had either been displaced by the FSW flash or it failed to record the temperature.

4.1.4 FSW Process Parameters Graphs of EH46 W8-W10 including tool travelling.

Figure 4.22 to Figure 4.27 show the welding parameters as a function of time and distance travelled for samples W8 to W10 (EH46) . The torque measured in W10 (450 N.m) is 50 % higher than in W8 (300 N.m) as a result of the increase in the tool traverse speed. This finding is in agreement with the work of Atharifar et. al. [147] which reported a decrease in torque with decreasing tool traverse speed as a result of a low viscosity field resulting from an accumulation in thermal energy. The increase of tool torque can result in increasing tool wear due to the increase in thermo-mechanical action on the tool surface as will be discussed in the tool wear section. The axial and traverse forces were nearly stable while the torque experienced fluctuations in all welds.

TCs reading for W8 and W10 are stable along the steady state portion of the weld with a maximum average temperature of 325°C in both welds as they have the same tool rotational speed and plunge depth. However, sample W8 shows a slower cooling rate than W10 as the former has experienced a slower tool traverse speed, the effect of cooling rate on the microstructure evolution will be discussed in section 5.8. W9 showed a decrease in temperature from 339°C to 221°C (118°C difference) when the plunge depth decreased by 0.22mm. The sensitivity to heat generation with plunge depth has been studied by Fehrenbacher, et al. [139] who reported that increasing plunge depth in FSW of aluminium from 4.6mm to 5mm has caused the peak temperature to increase from 400°C to 580°C.
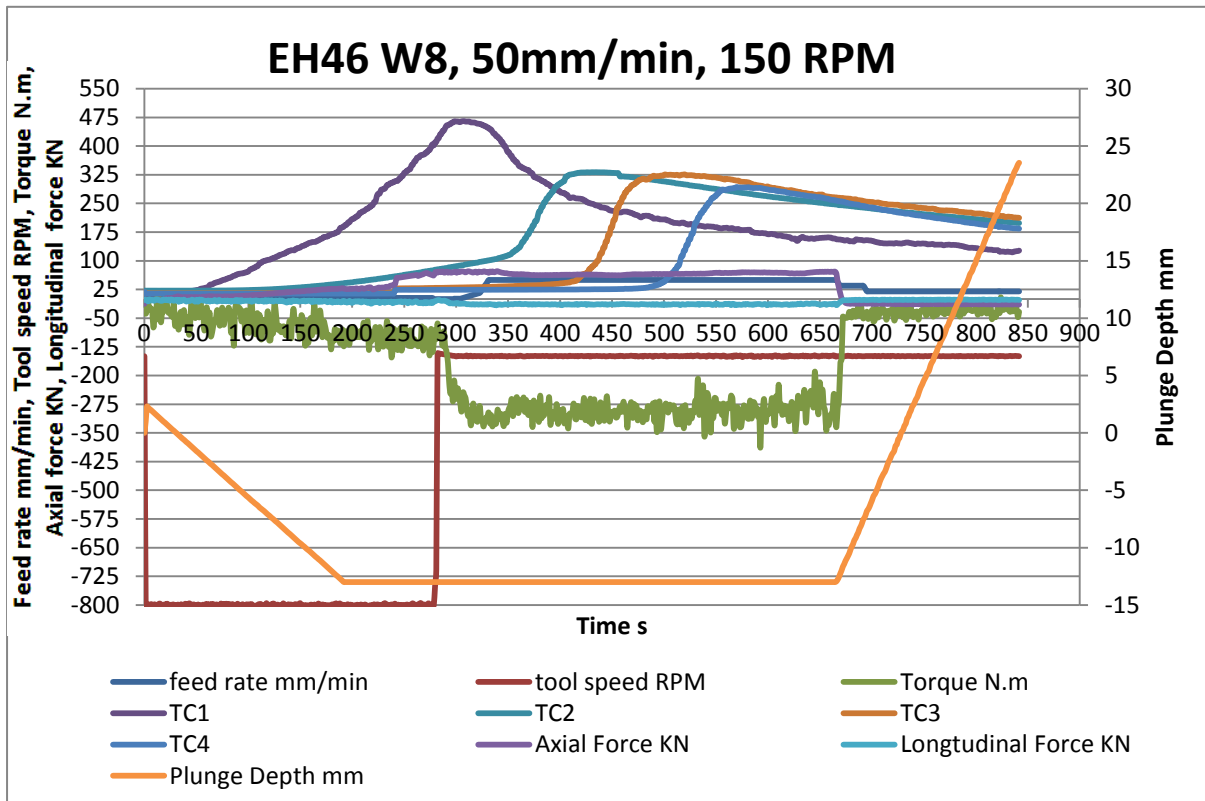
Figure 4.22: Welding parameters with time recorded on the PowerStir FSW machine, 14.8mm FSW EH46 steel (W8). TCs are located at 29mm from the tool centre, the average TCs peak temperature at steady state is 330°C.
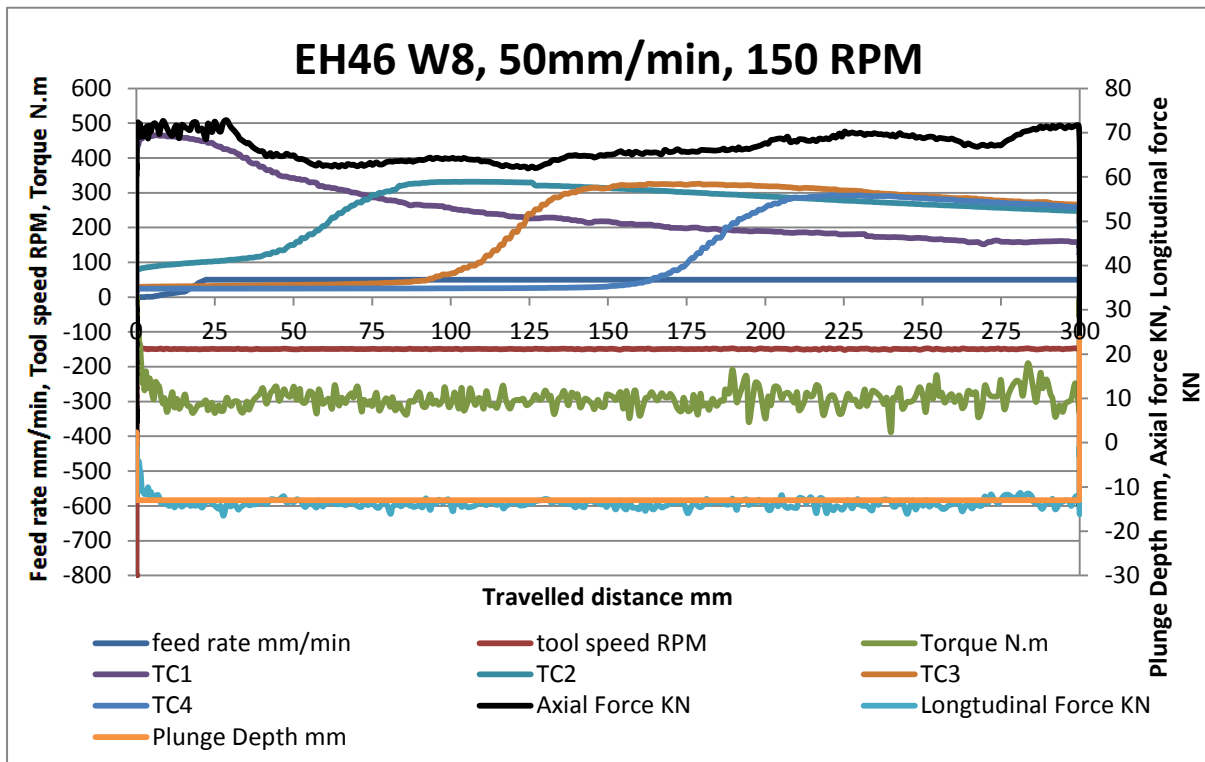
Figure 4.23: Welding parameters with travelled distance recorded on the PowerStir FSW machine, 14.8mm FSW EH46 steel (W8).
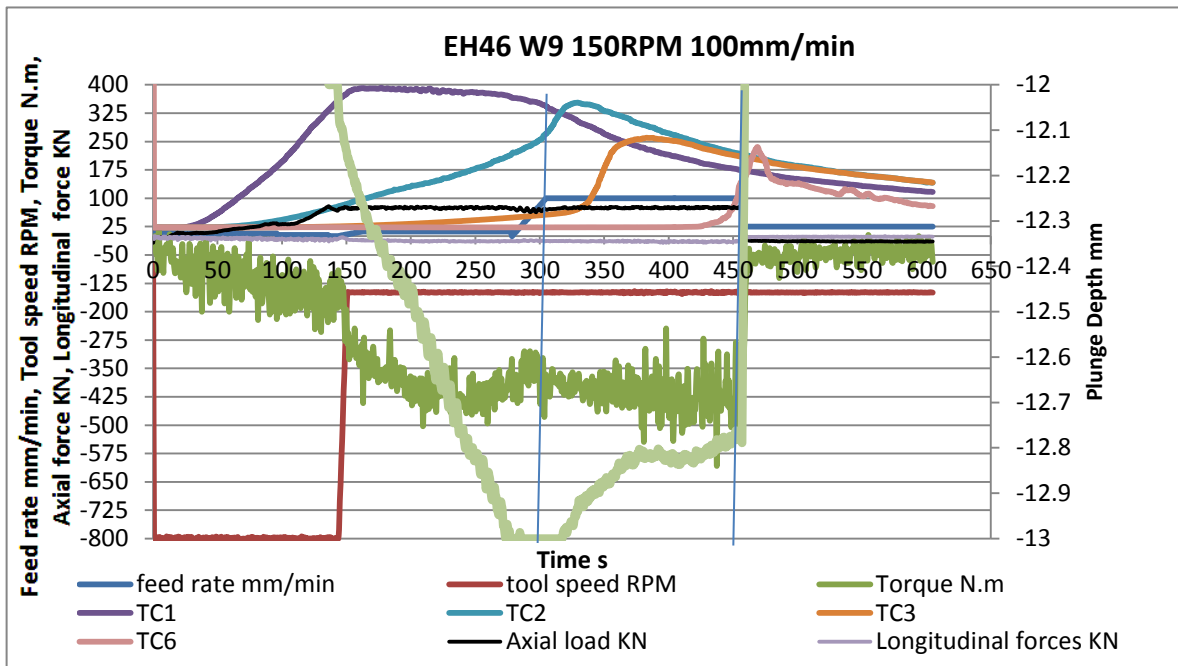
Figure 4.24: Welding parameters with time recorded on the PowerStir FSW machine, 14.8mm FSW EH46 steel (W9). TCs are located at 29mm from the tool centre, average TC peak temperature is 280°C. This temperature has dropped from 339°C to 221°C (118°C difference) when the plunge depth decreased by 0.22mm.
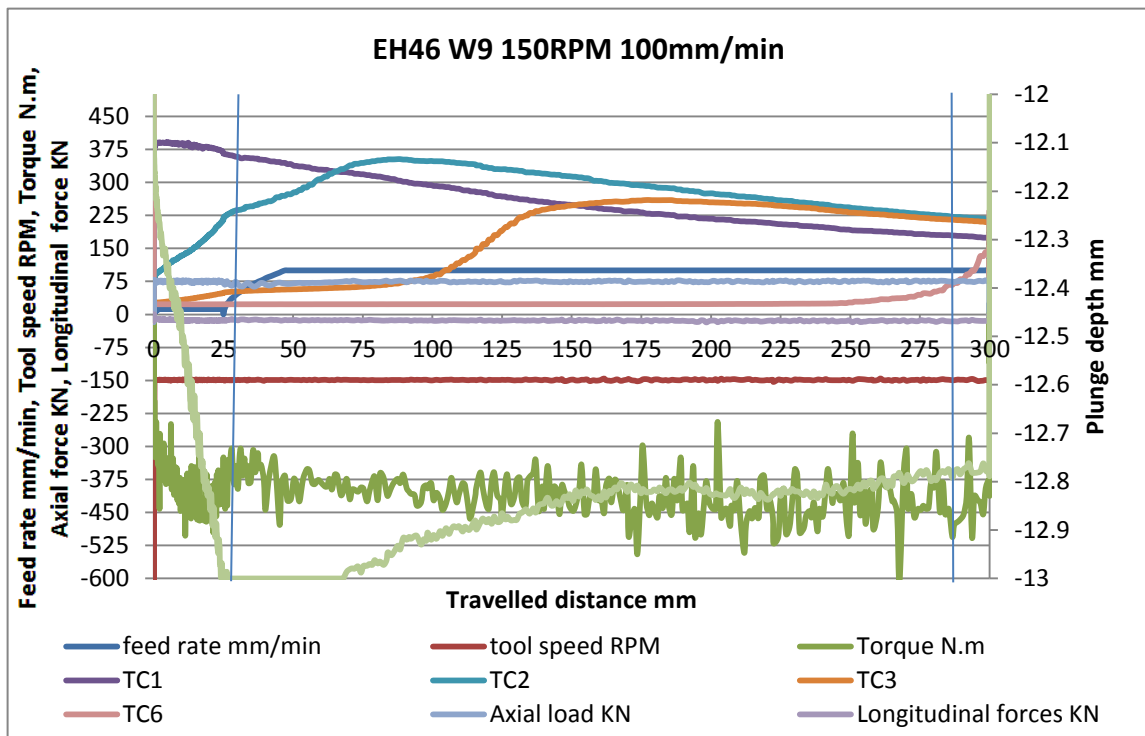
Figure 4.25: Welding parameters with travelled distance recorded on the PowerStir FSW machine, 14.8mm FSW EH46 steel (W9).
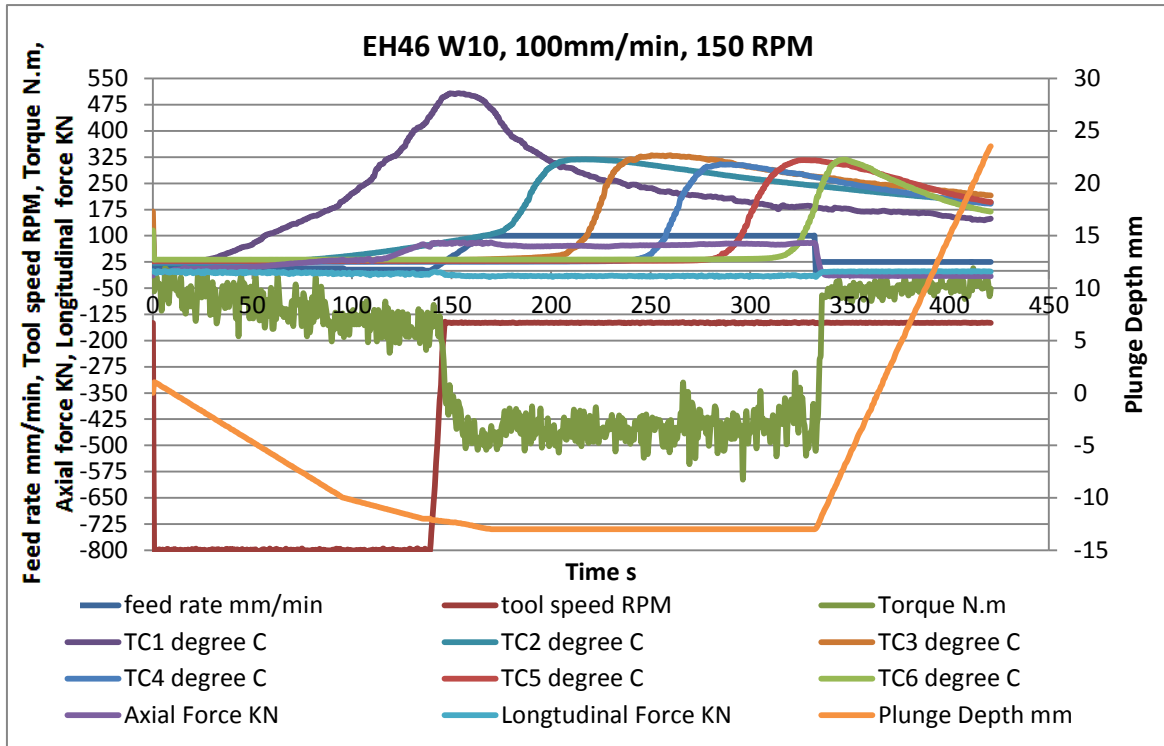
Figure 4.26: Welding parameters with time recorded on the PowerStir FSW machine, 14.8mm FSW EH46 steel (W10). TCs are located at 29mm from the tool centre, average TC peak temperature at steady state is 320°C.
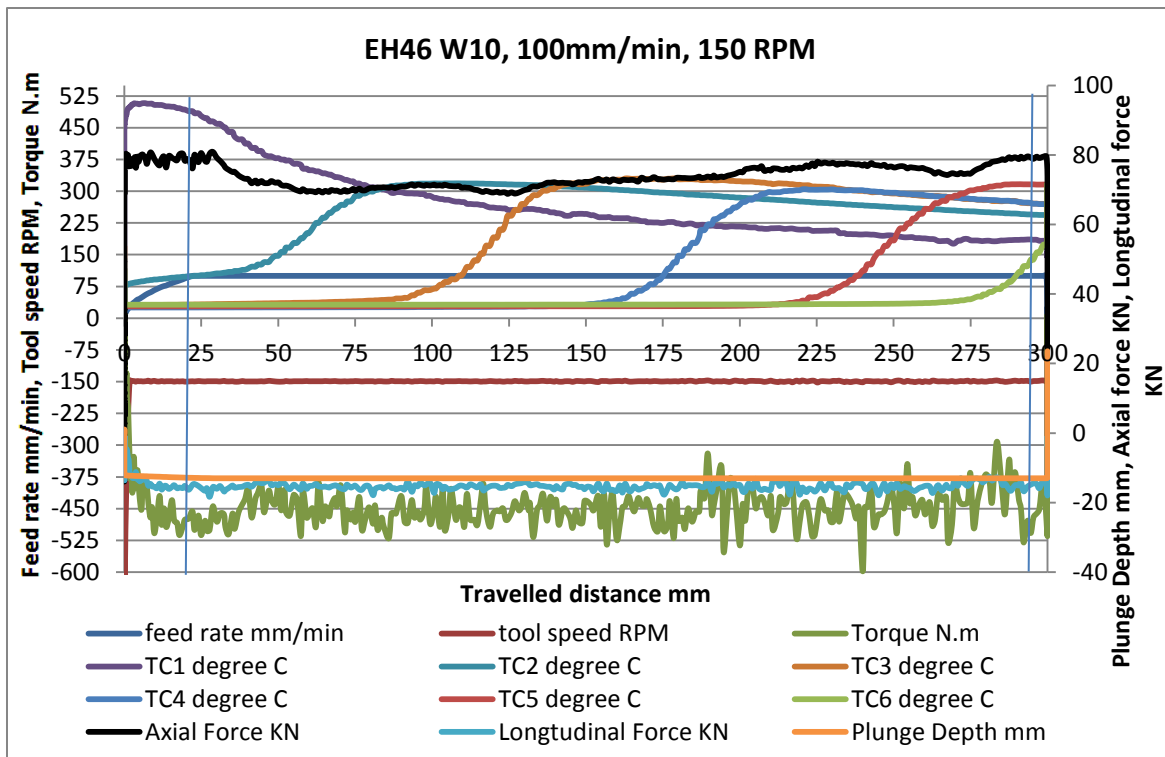
Figure 4.27: Welding parameters with travelled distance recorded on the PowerStir FSW machine, 14.8mm FSW EH46 steel (W10).

131

Table 4.5: Welding conditions of FSW EH46 steel at steady state (W8-W10)

Weld No.	Tool rotational speed RPM	Traverse speed mm/min	Rotational/ Traverse speeds	Average Spindle Torque N.m	Average Tool Torque N.m	Axial Force (average) KN	Longitudinal Force (average) KN	Heat Input ($\frac{\omega \times torque}{v}$)
W8	150	50	3	300	114	66	13	342
W9	150	100	1.5	450	171	76	14	256.5
W10	150	100	1.5	450	171	72	14	256.5

4.2 Infinite Focus Microscopy (IFM) Measurements.

The IFM has been employed in order to measure the actual plunge depth of the welded joints and to compare them with the ones recorded by the FSW data acquisition. The size and length of HAZ and SZ have also been measured by the IFM technique in order to understand the effect of different welding parameters on the heat generated in the welded joints during the FSW process.

4.2.1 IFM Measurements of Samples W1-W7 (EH46).

Figures 4.28 to figure 4.34 show the 3D images and 2D diagram of samples W1 to W7 (EH46) plunge/dwell experiment respectively which were produced using the IFM. The polished and etched half sections of sample W1 to W7 have been scanned by the IFM as shown in figure 4.35 in order to measure the size and length of the SZ and HAZ. The actual plunge depth, SZ and HAZ of W1 to W7 have been listed in table 4.6.

Figure 4.35 shows a longitudinal cross section macrograph of W1-W7, polished, etched by 2% Nital and scanned by the IFM technique. All samples show flash forming on the top surface of the workpiece, it is also shown that hooking defects are present; this can be a result of un welded material pushed upward forming a hook [19]. The spiralling shape found in the upper region between shoulder and probe side, as shown in Figure 4.35 (W5), is the results of thermo-mechanical deformation caused by the tool shoulder-probe parts [36].

A slight asymmetry in term of TMAZ and HAZ size between the right and left hand sides of the plunge/dwell is noted in samples W1, W5 and W6, while W2 shows an increase in asymmetry between the right and left sides as measured by IFM with a deformation on the right hand side of the plate bottom. W6 also shows deformation at the plate bottom as shown in figure 4.35. The asymmetry may be attributed to the tools deviation from its normal axis which in turn can produce extra heat on that side compared to the other.. Table 4.6 shows the welding conditions, the surface area of affected zones and plunge depth measurements while Table 4.4 shows the peak temperatures measured by TCs. From Table 4.6 it can be shown that despite the high rotational speed and the highest plunge force in sample W1, it recorded the smallest TMAZ, IHAZ and OHAZ zones compare to other welds. This can be attributed to insufficient plunge depth which in turn can produce insufficient heat generation in the Z-direction during the FSW process. Sample EH46 W2, which has a plunge depth similar to the group of welds produced at 120RPM (W5, W5 and W7 but excluding W6), shows a larger

TMAZ. This can be related to the higher tool rotational speed which produces more heat and encourages the material layers adjacent to the tool to thermo-mechanically stir. From Table 4.4 it can be shown that W1 and W2 have recorded temperatures of 630 $^{\circ}$C and 650 $^{\circ}$C respectively on the top surfaces at TC2. The higher temperature of W2 at the top surface can be related to the higher plunge depth despite the higher plunge force of W1. This can give an indication that the plunge depth effect can override the effects of plunge force in terms of heat generation. Unfortunately, there is no clear relationship between plunge force and plunge depth in this work. The asymmetry in temperatures between TC2 and TC5 may be due to tool deviation from the normal centre of the FSW tool. W3, W5 and W7 have nearly equal plunge forces and showed almost equal TMAZ despite the slight difference in plunge depth. Temperatures of TC2 of W3, W5 and W7 were 550 $^{\circ}$C, 544 $^{\circ}$C and 554 $^{\circ}$C respectively which indicates that welding with the same plunge forces, rotational speed and slight difference in plunge depth can generate almost equal peak temperatures.

Sample W6 has recorded the highest plunge depth and the TMAZ was almost equal to W2 although rotational speed was less than the former. The IHAZ and OHAZ were also larger than all the other plunge cases. The interpretation of this is that a higher plunge depth can generate more heat towards the workpiece depth because more material will be in contact with the tool and thus the sticking conditions is increased especially around the probe. These findings are in accordance with previous work carried out on FSW of DP590 steel grade [36]. Nagasaca and Nishihara 2003 [158] also found that the temperature of the tool and backing plate were increased when the plunge depth increases. Fehrenbacher et al. reported that increasing plunge depth in FSW of aluminium from 4.6mm to 5mm has caused the peak temperature to increase from 400 $^{\circ}$C to 580 $^{\circ}$C [139]. Unfortunately, for W6 the thermocouples located at the plunge centreline (TC2 and TC5) were highly affected by the produced flash so the readings for temperatures were excluded. However, TC3 and TC4 recorded temperatures higher than other welds of the 120 RPM group. Table 4.6 shows that the torque of the 120 RPM group was higher than the group of 200 RPM, it is known that most of the torque comes from the tool shoulder [67], so more rotational speed will produce more heat on the top surface of the workpiece and will result in a reduction in the torque value. This can give an indication that plunge depth is more dominate in producing heat in the workpiece depth than rotational speed but increasing tool rotational speed produces more heat on the top surface of the workpiece thus reducing the generated torque.

W4 and W5 was carried out with the same plunge depth, however, the TMAZ of W5 was smaller and the reason might be due to the lower plunge force of W5 as recorded by the FSW data acquisition. High plunge force can reduce the gaps between the tool and workpiece and thus will result in more sticking conditions and also in producing more heat. Upadhagay and Reynold 2011 [159] reported that lower axial forces (plunge forces) can lead to a reduction in heat input and material flow which in turn causes a reduction in the size of the TMAZ. TC readings for sample W4 recoded a temperature higher than in W5 because of the effects of higher plunge force.

In general, for all cases under study, the TMAZ around the probe seems to be bigger than under shoulder (Fig. 2 W1-W7). Although it is not easy to calculate the TMAZ separately for the shoulder and probe side, a measurement by IFM of the TMAZ for sample W2 showed that the size of the affected zone under the shoulder was 17.5 mm^2 whereas, 50 mm^2 was affected by the probe side. This finding can give an indication that a tool with a rotational probe and stationary shoulder can generate the heat required for welding. This in turn can reduce the cost of the tool by reducing the amount of PCBN material required for manufacturing the tool. Also, it was found for all cases under study that the probe end did not show a significant contribution in stirring the material in contact, so less heat input can be expected from this part of the tool. This is in agreement with Schmidt and Hattel [50][51][52] who showed that the probe end contribution in heat generation and material stirring is insignificant. However, some workers [6] have investigated the material flow of light alloys (Mg alloy) during Friction Stir Spot Welding (FSSW) and recognised a torsional flow zone under the probe. This difference in flow between steel and light alloys can be related to the high density and viscosity of steel compared to Mg. Steel was shown experimentally using W traces to be harder to cause to flow compared to light alloys such as aluminium [34]. No comparison will be carried out regarding plunge time as the difference between all cases in plunge time was not significant.

4.2.2 IFM Measurements of 6mm and 8mm DH36 Keyholes.

Figure 4.36 and figure 4.37 shows the 3D IFM images of the keyholes produced following FSW., The 2D macrographs of W1 [61], W6, W8 and W9 are shown in figure 4.38 to figure 4.40. Table 4.7 summarize the results of measurements made using the IFM for figure 4.36 to figure 4.40 which includes the plunge depth, SZ and HAZ size and length. It can be shown that the size of SZ of sample W1 is smaller than W6 and W8; this can be attributed to the higher rotational speed of the FSW tool in W6 and W8 which caused more thermo-mechanical action leading to stirring more material in contact with the tool. The length of the HAZ of W1 is bigger than in W6 and W8 despite the lower tool rotational speed which generates less heat, this can be attributed to the higher heat input ($\frac{\omega \times torque}{V}$) in W1 compare to W6 and W8 as shown in table 4.1. The sample W8 macrograph shows two types of defects including weld root and kissing bond which will be discussed extensively in the defect section.

4.2.3 IFM Measurements Taken from Samples W8 and W10 (EH46) steady state Conditions.

Figure 4.44 and figure 4.45 show the macrographs of sample W8 and W10 (EH46) at the plunge location. In both welds, the total TMAZ consists of two parts, nugget (SZ) in the middle of the weld (the dark colour) and shear layer around the SZ. The nugget region is believed to have experienced higher temperatures than the shear layer as will be discussed later in the elemental precipitation section. In the steady state region the nugget zone is not clear because the thermo-mechanical effect of the tool was not enough to separate it from the shear layer. This finding is in agreement with Pradeep [17] who reported the difficulty of observing the shear layer in FSW joints in the steady state period. The size of SZ and the length of HAZ of W8 (EH46) are bigger than in W10 (EH46) due to the lower tool traverse speed which caused high heat input as shown in table 4.5. A void at the AS of W10 has been detected with a length of 3.4mm starting at 9mm from the top surface of plate. The voids formation will be discussed extensively in the FSW defect section.

4.2.4 IFM of the PCBN Tool.

IFM has been applied on the PCBN FSW tool used for welding the 6mm plates of grade DH36 steel in order to calculate the exact surface area which will be used for designing the CAD geometry of the FSW tool. The calculated surface areas of the differennt parts of the tool, using the IFM technique, were as follows: $A_{shoulder} = 1499.2$ mm^2, $A_{probe\_side} = 373.2$ mm^2, $A_{probe\_end} = 50.3$ mm^2.

4.2.5 Comparison of the Distortion produced following FSW and MIG Welding 8mm thick (DH36) steel plate.

Two plates of 8mm thick DH36 steel have been welded by FSW (W9) and by the MIG welding technique in order to compare the distortion which occurs after welding. The FSW sample showed a deflection angle of 1.25 ^{o} whereas the sample welded by the MIG technique showed a higher deflection angle equal to 2.5 ^{o}. The low distortion in FSW sample can be attributed to the lower heat input compared to the MIG fusion welding.

4.2.1 IFM Plunge Depth Experiments using EH46 steel (W1-W7) to compare actual plunge depths to the process data recorded plunge depth.
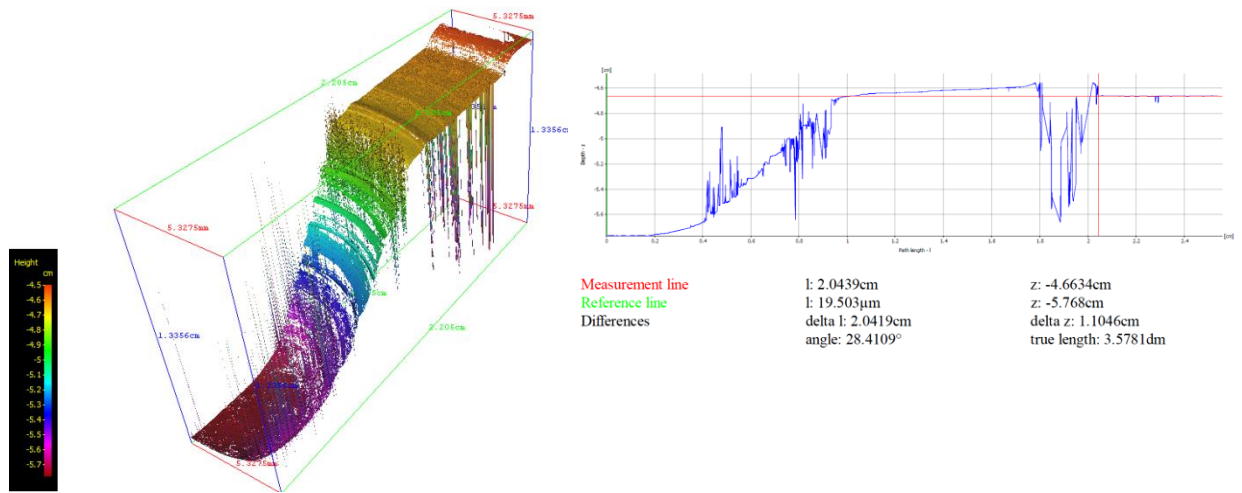
Figure 4.28: IFM 3D image and surface profile of weld tool plunge depth for sample W1 EH46 steel grade.
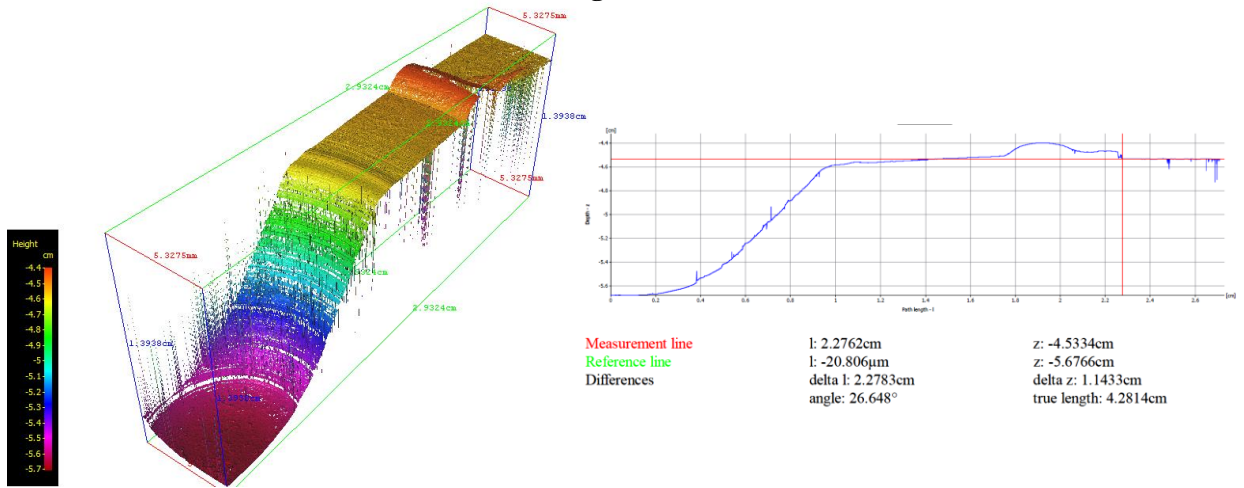
Figure 4.29: IFM 3D image and surface profile of weld tool plunge depth for sample W2 EH46 steel grade.
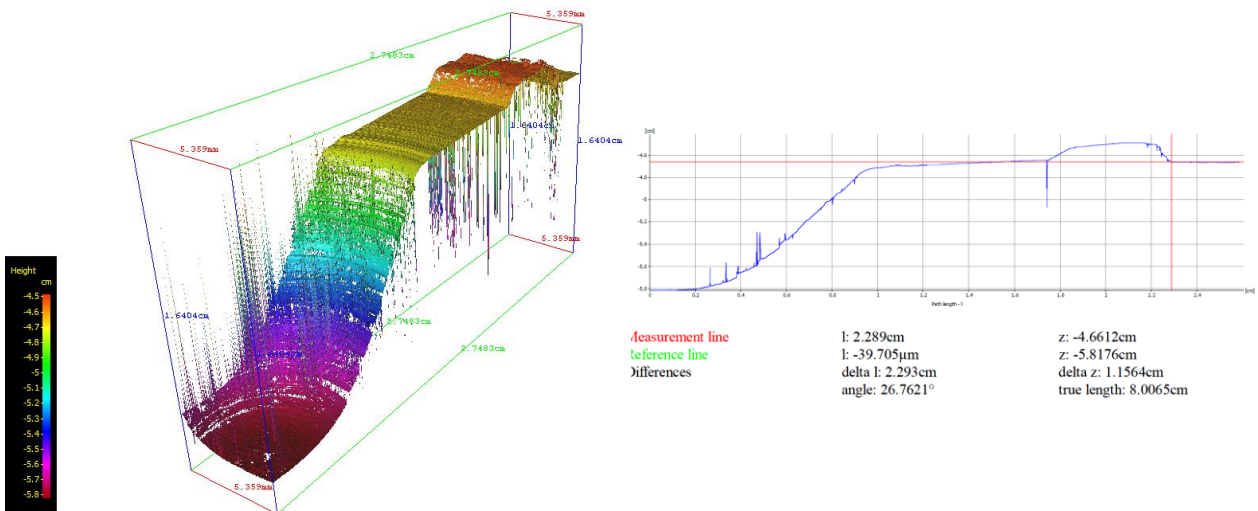
Figure 4.30: IFM 3D image and surface profile of weld tool plunge depth for sample W3 EH46 steel grade.

138
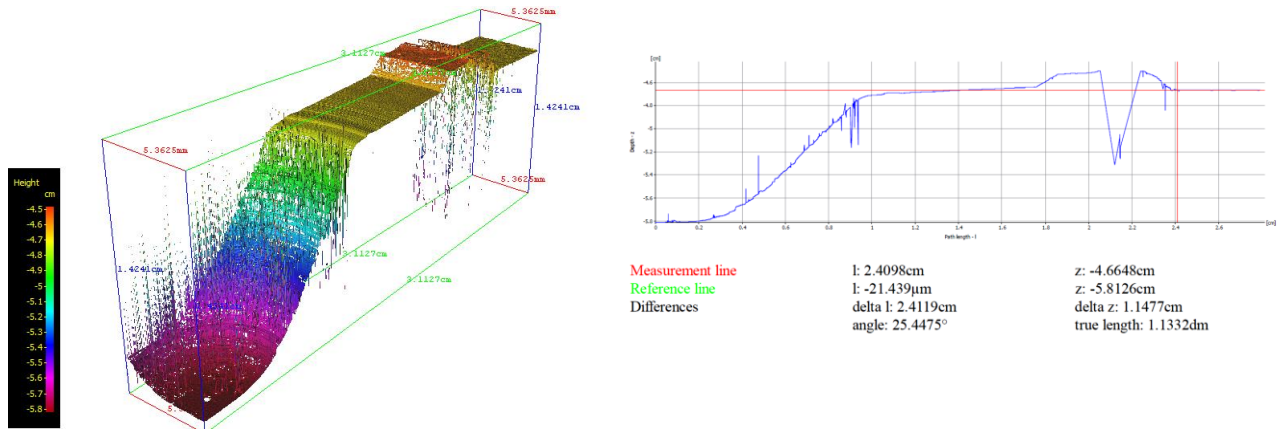
Figure 4.31: IFM 3D image and surface profile of weld tool plunge depth for sample W4 EH46 steel grade.
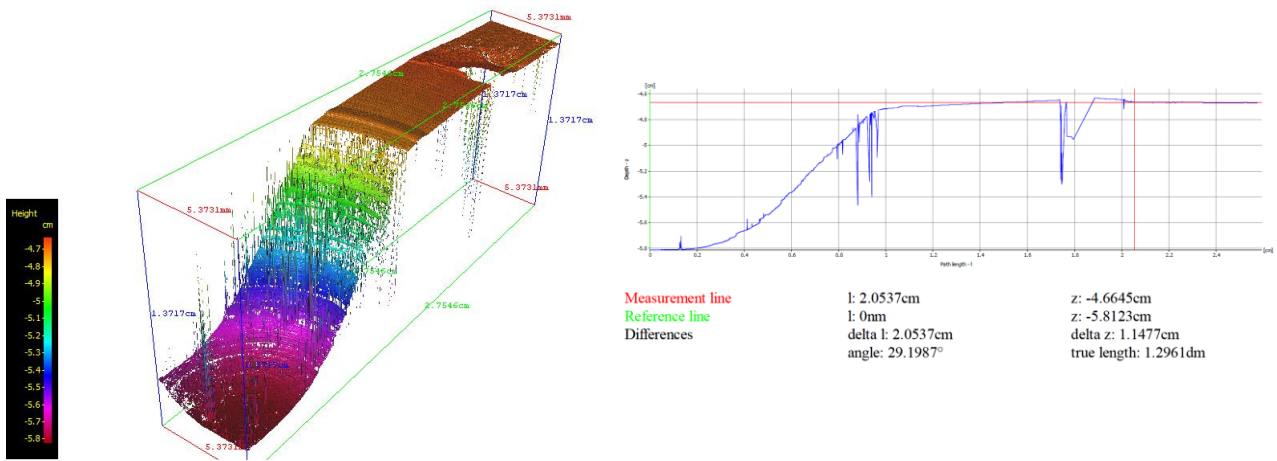
Figure 4.32: IFM 3D image and surface profile of weld tool plunge depth for sample W5 EH46 steel grade.
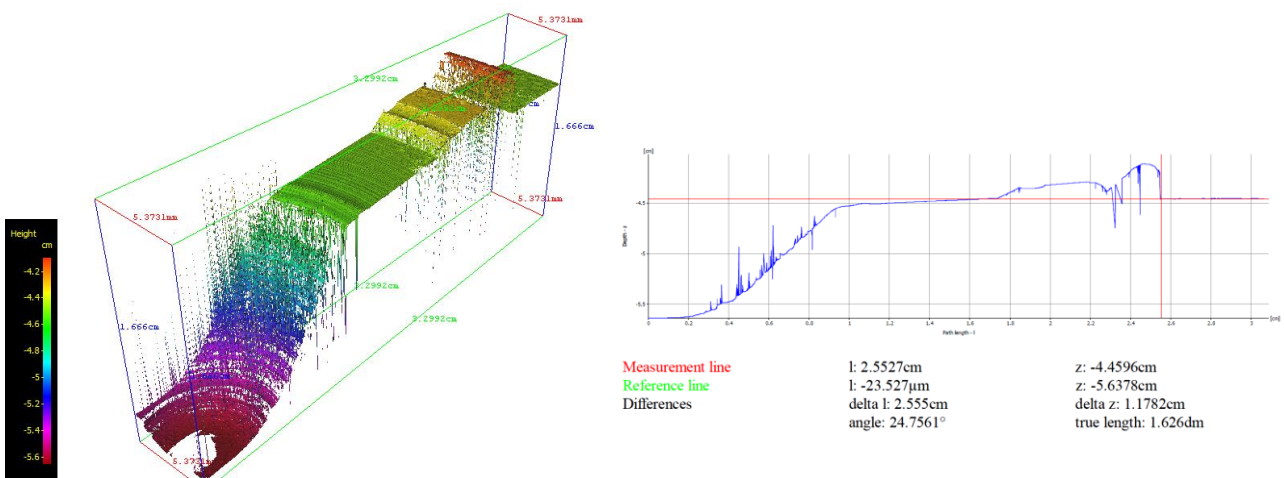
Figure 4.33: IFM 3D image and surface profile of weld tool plunge depth for sample W6 EH46 steel grade.

139
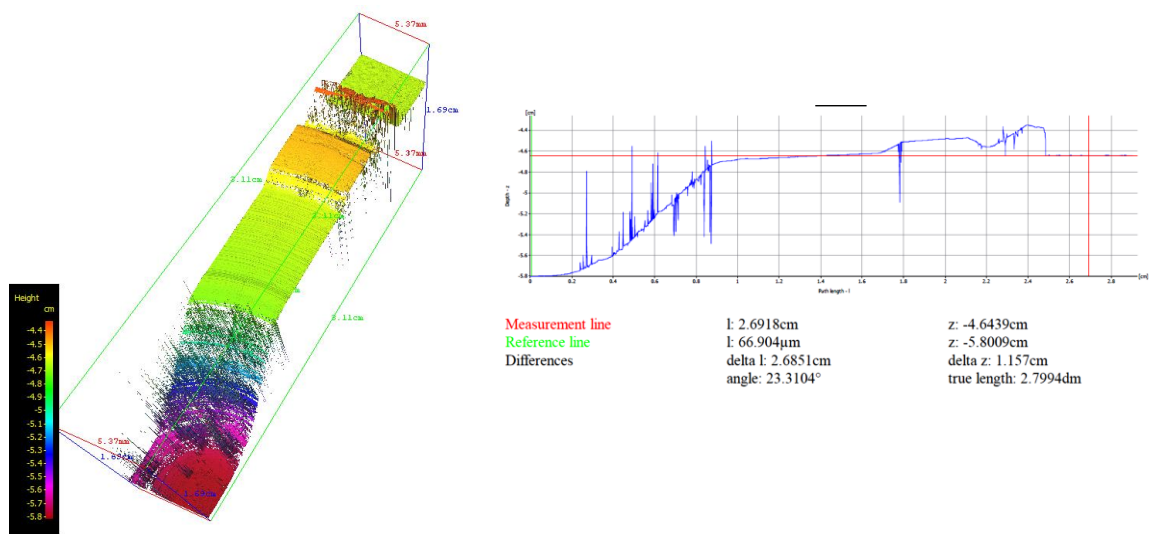
Figure 4.34: IFM 3D image and surface profile of weld tool plunge depth for sample W7 EH46 steel grade.

4.2.2 IFM macrograph images of cross sections of EH46 welded samples W1-W7 examining the effect of Plunge depth and /Dwell cases
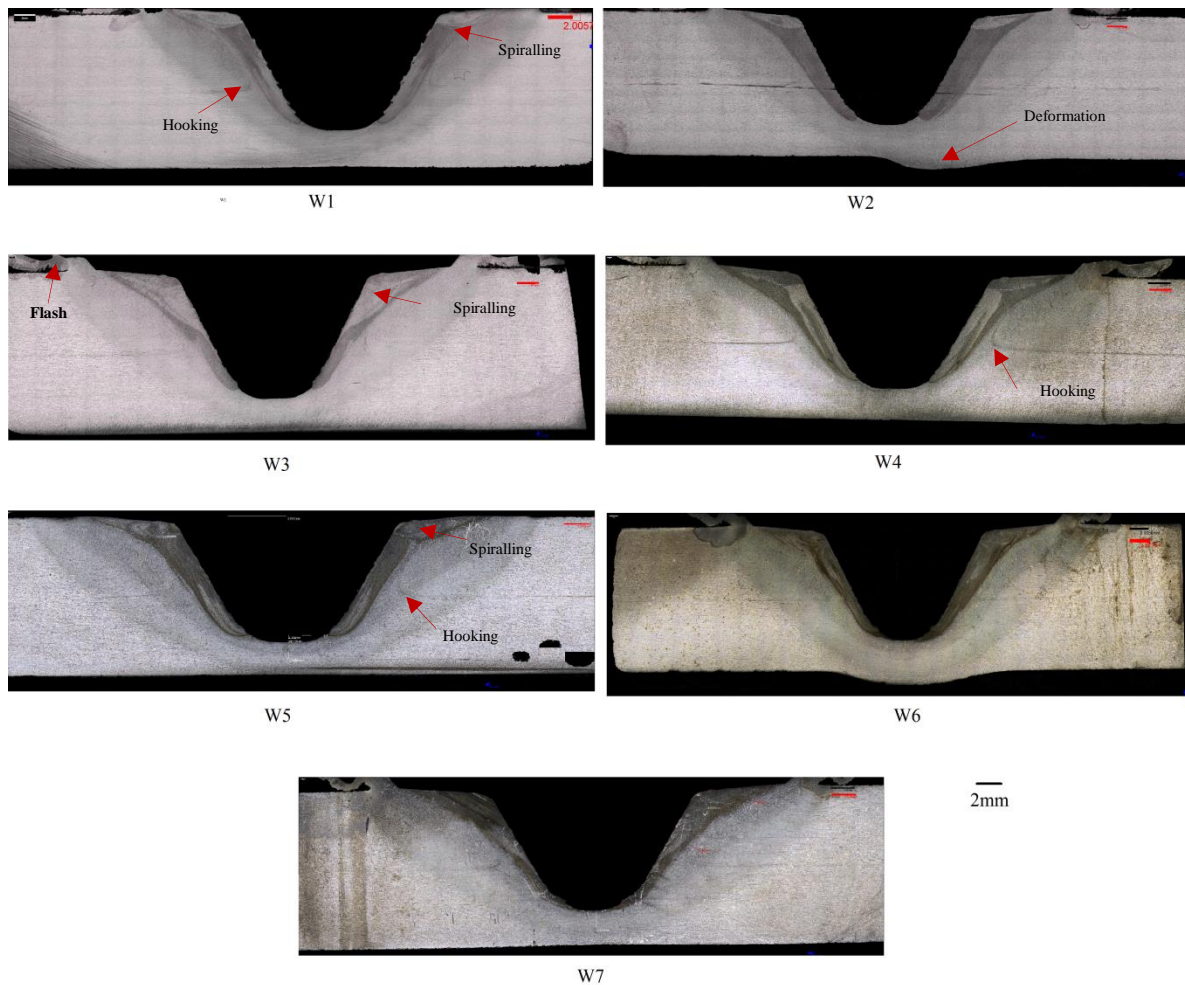
Figure 4.35: Micrographs of longitudinal cross section taken from samples of EH46 W1-W7, polished and etched by 2%Nital.

Table 4.6: The welding conditions, the IFM measurements of plunge depth and area of affected zones W1-W7 EH46 steel.

Weld No.	Tool rotational speed ω (RPM) at maximum plunge depth	Max. Plunge force (F_z) KN	Max. traverse force (F_x) KN	Max. Torque (M) N.m	Plunge depth (Z) mm (IFM)	time (t) sec at (dwelling)	Total TMAZ (region 1+2) area mm² (IFM)	(Region 3) IHAZ mm² (IFM)	(Region 4) OHAZ mm² (IFM)	Length of the HAZ measured from the end of TMAZ directly under shoulder (mm)
W1	200	157	17	498	11.05	6	47.46	64.7	82	4.1
W2	200	127	17	471	11.43	8	67.5	78.5	102	4.6
W3	120	116	21	598	11.56	7	58	69.6	112.6	3.1
W4	120	126	20	549	11.47	6	66	64.25	118	3.2
W5	120	115	17	532	11.47	7	55	93.5	120.4	3.2
W6	120	105	18	583	11.78	7	68	99.5	143.8	3.8
W7	120	119	20	548	11.57	7	57.2	91	120	3.5

4.2.3 IFM measured depths of 6mm and 8mm thick DH36 steel plate keyholes, SZ and HAZ following FSW.

Measurement line	l: 1.4822cm	z: -5.4149mm
Reference line	l: 1.0888mm	z: 2.322mm
Differences	delta l: 1.3733cm	delta z: -7.737mm
	angle: -29.3958°	true length: 3.903cm
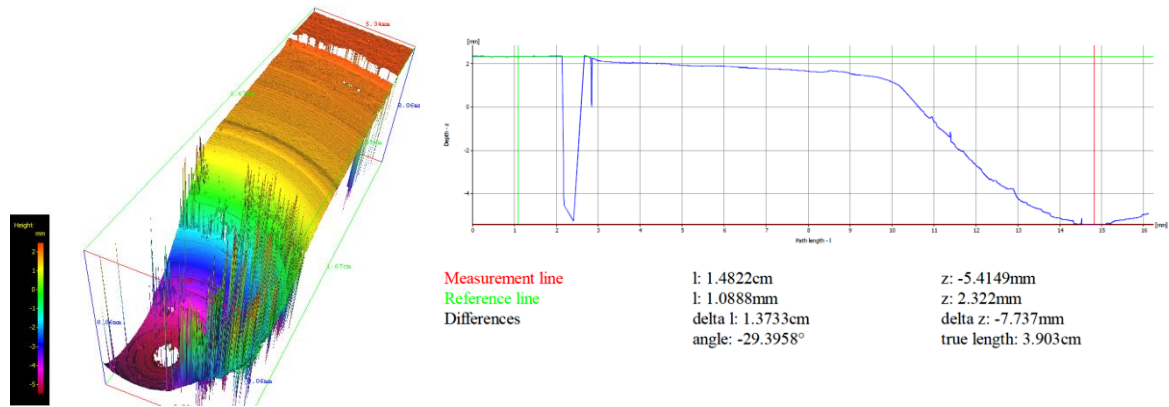
Figure 4.36: IFM 3D image of 8mm thick FSW DH36 steel, keyhole plunge depth 7.7mm

Measurement line	l: 1.3077cm	z: 311.55µm
Reference line	l: 20.529µm	z: -5.5216mm
Differences	delta l: 1.3056cm	delta z: 5.8331mm
	angle: 24.0734°	true length: 1.6403cm
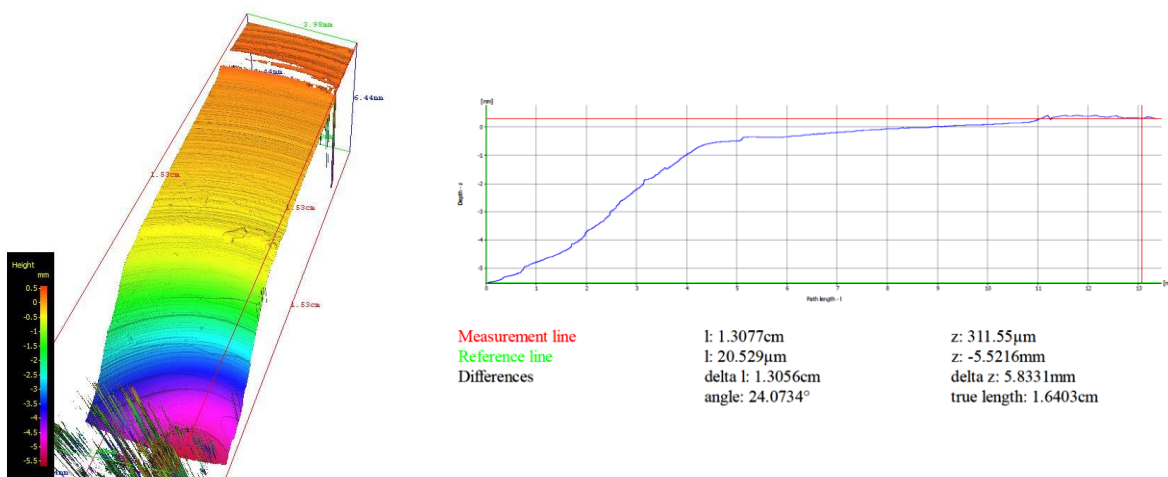
Figure 4.37: IFM 3D image of 6mm thick FSW DH36 steel, keyhole plunge depth 5.8mm

142

4.2.4. IFM of 6mm thick DH36 steel plate samples W6 and W8, (550RPM, 400mm/min) and 8mm thick DH36 steel plate sample W9(200RPM, 100mm/min).
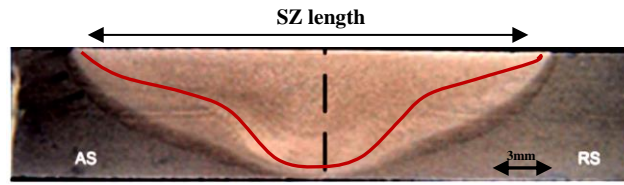
Figure 4.38: Sample W1 DH36 macrograph of a cross section through a FSW [61p596]
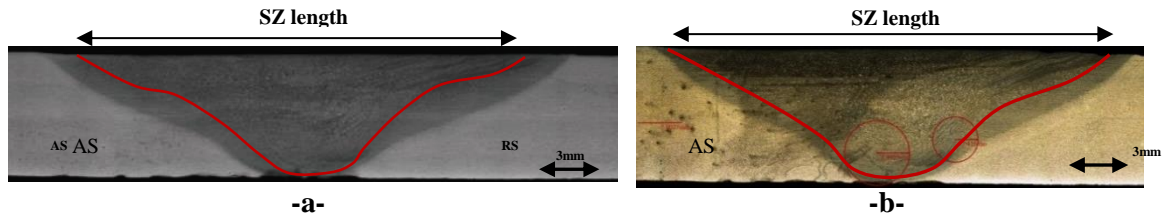
Figure 4.39: Samples W6 -a- and W8 -b- (6mm thick DH36 steel plate) macrographs of cross sections of FSW measured by IFM.
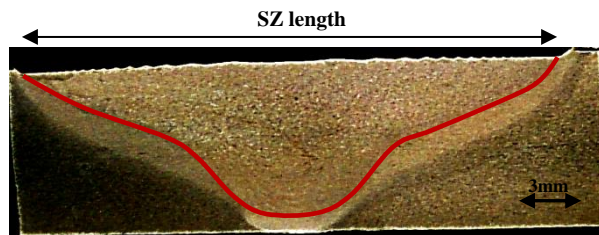
Figure 4.40: 8mm thick DH36 steel plate (DH36 W9) macrograph of a cross section taken through a FSW and measured by IFM, (200RPM, 100mm/min).

Table 4.7: Welding conditions and IFM measurements of DH36 steel 6mm and 8mm plate thickness.

Weld No.	DH36 Welding conditions	SZ length at the top surface, mm	SZ size, mm^2	HAZ length at the top surface, mm	Keyhole depth, mm
W1	200RPM, 100mm/min, 6 mm thick plate	21	58	24.5	5.8
W6	550RPM, 400mm/min, 6mm thick plate	20.8	63	22.3	5.8
W8	550RPM, 400mm/min, 6mm thick plate	20.9	64	22.15	5.8
W9	200RPM, 100mm/min, 8 mm thick plate	24.3	83	25.3	7.7

4.2.5 IFM images and measurements of EH46 steel plate samples W8 and W10 - Keyhole depths,

Measurement line	l: 2.0447cm	z: -4.6134cm
Reference line	l: 0nm	z: -5.7807cm
Differences	delta l: 2.0447cm	delta z: 1.1673cm
	angle: 29.7222°	true length: 2.0635dm
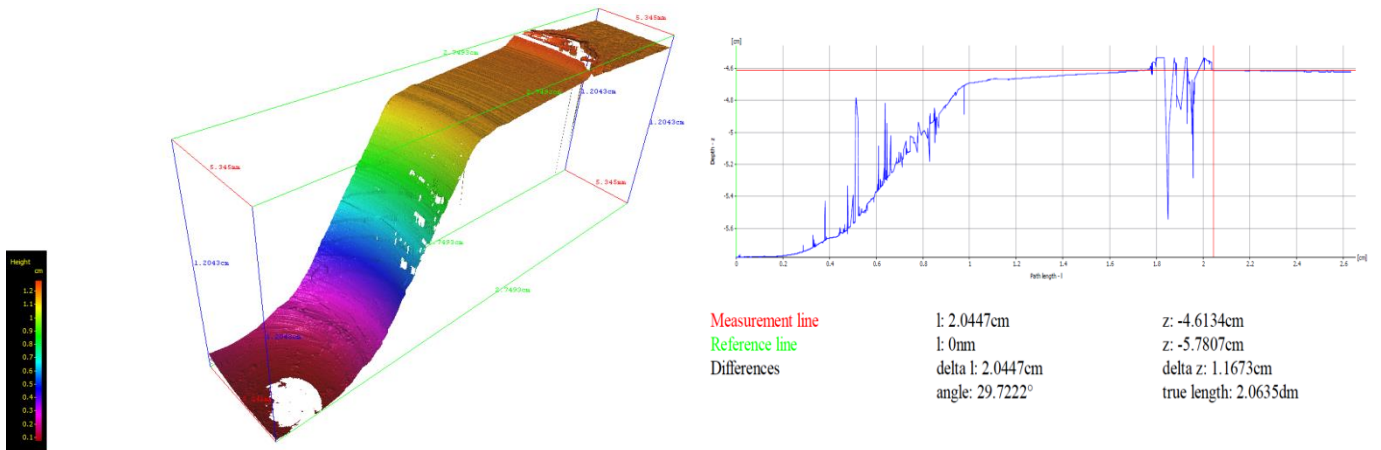
Figure 4.41: IFM 3D image and surface profile for keyhole of W8 EH46 steel grade, 11.67mm keyhole depth.

Measurement line	l: 1.928cm	z: 1.2253cm
Reference line	l: 1.7124mm	z: 817.82μm
Differences	delta l: 1.7568cm	delta z: 1.1436cm
	angle: 33.062°	true length: 2.5209cm
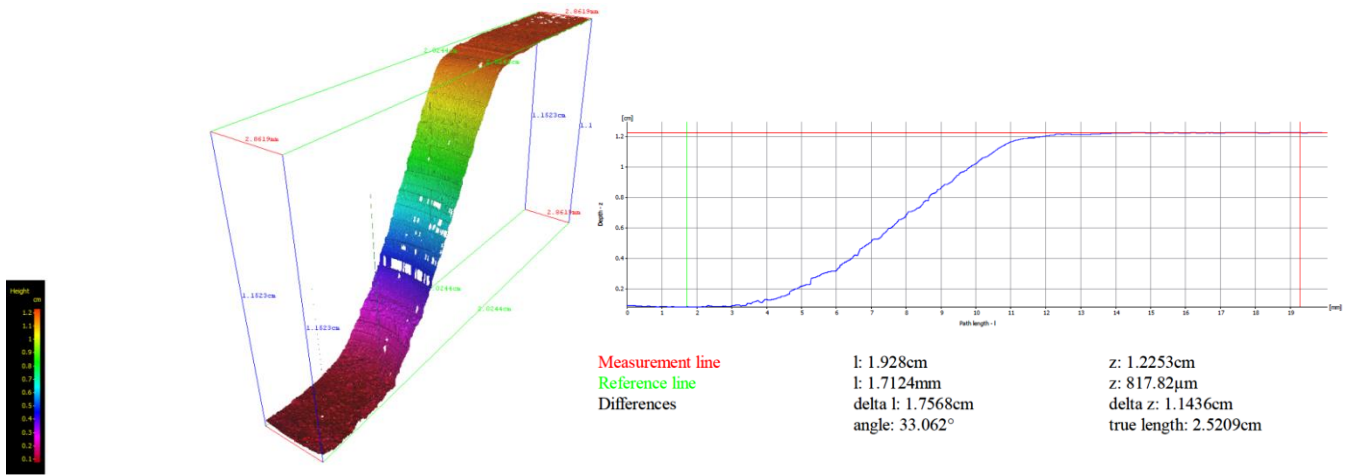
Figure 4.42: IFM 3D image and surface profile for keyhole of W9 EH46 steel grade,11.43mm keyhole depth.

Measurement line	l: 866.62μm	z: 1.3208cm
Reference line	l: 1.854cm	z: 1.7993mm
Differences	delta l: -1.7673cm	delta z: 1.1673cm
	angle: 147.157°	true length: 2.4898cm
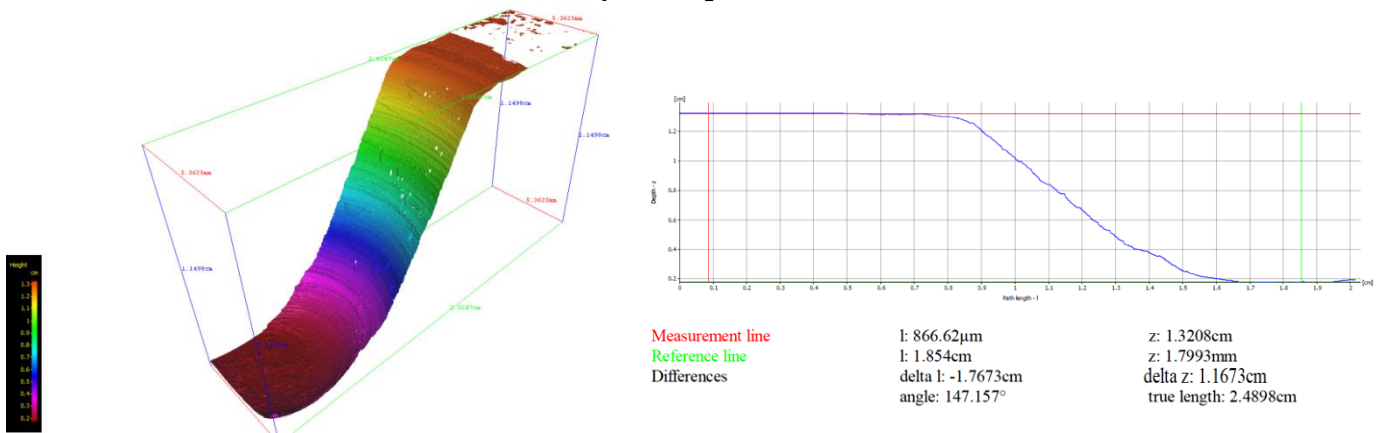
Figure 4.43: IFM 3D image and surface profile for keyhole of W10 EH46 steel grade, 11.67mm keyhole depth.

144

4.2.6 IFM macrographs of EH46 W8 and W10
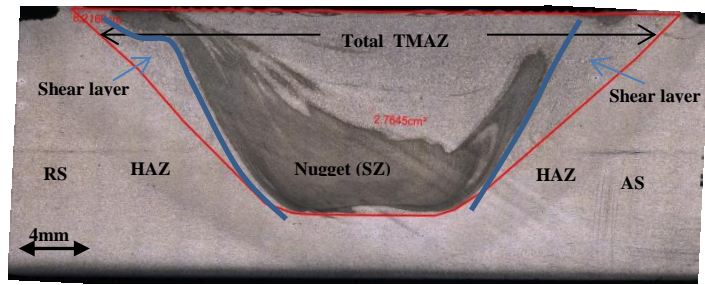
Figure 4.44: EH46, W8 macrograph showing a cross section of the weld macrostructure at the plunge stage of FSW measured by IFM
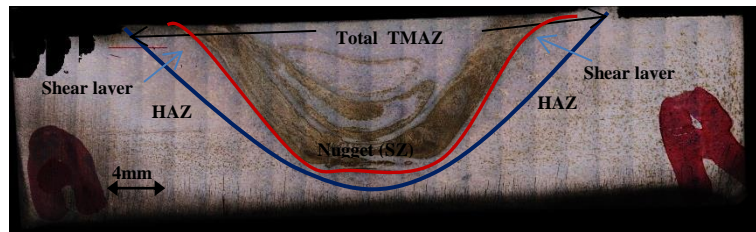
Figure 4.45: EH46, W10 macrograph showing a cross section of the weld macrostructure at the plunge stage of FSW measured by IFM
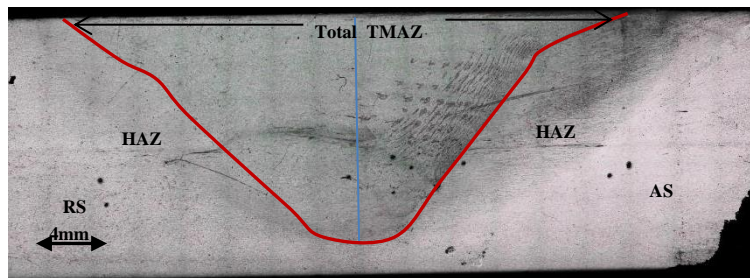
Figure 4.46: EH46, W8 macrograph showing a cross section of the FSW taken from the steady state portion of the weld.
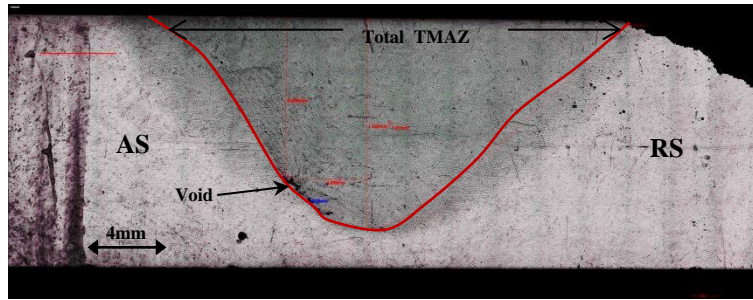
Figure 4.47: EH46 W10, macrograph showing a cross section of the FSW taken from the steady state portion of the weld and measured by IFM

Table 4.8: Welding conditions (Steady State) and IFM measurements of FSW EH46 W8 and W10.

Weld No.	Welding conditions	SZ length at the top surface (mm)	SZ size (mm^2)	HAZ length at the top surface (mm)	HAZ under the probe (mm)	Keyhole Plunge depth (mm)
W8	150RPM, 50mm/min	31.2	199 (90.6 AS, 108.4 RS)	37.6	1.6	11.67
W10	150RPM, 100mm/min	28	181	31	1.4	11.67

Void on the AS of W10 has been detected with a length of 3.4mm starting at 9mm from the top surface of plate.

4.2.7 IFM image and measurements of the PCBN FSW tool.
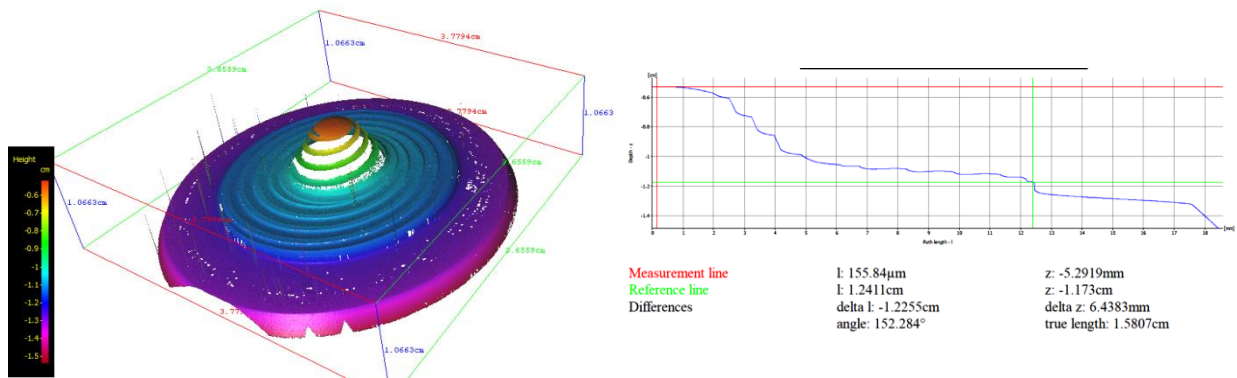
Figure 4.48: IFM 3D image and surface profile for PCBN FSW tool (24mm diameter, 5.5mm probe length which was used to produce the 6mm weld joints).

4.2.8 Distortion comparison between FSW and MIG welded 8mm thick DH36 steel plates, measured by using IFM.
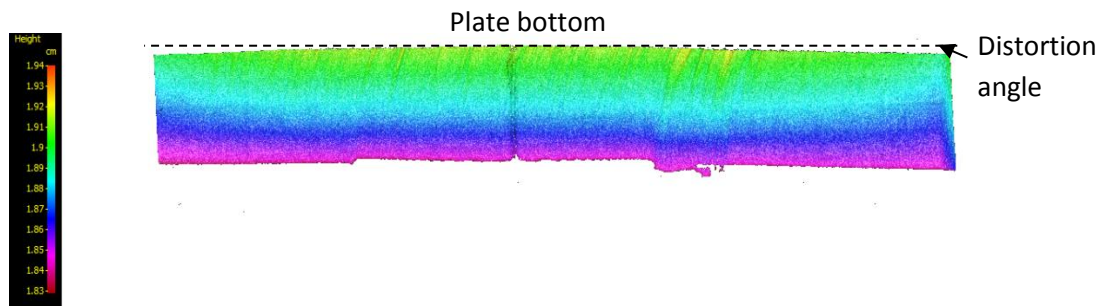
Figure 4.49: IFM 3D image and surface profile for DH36, sample W9 (section through the transverse welding direction), 8mm thick plate, FSW at 200RPM and traverse speed 100mm/min showing a distortion angle = 1.25^{o}.
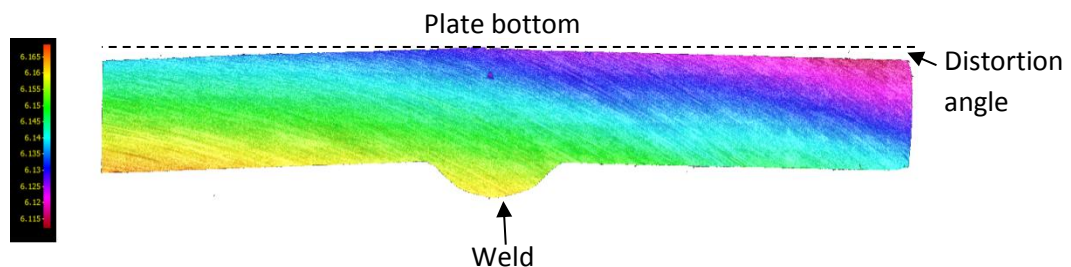
Figure 4.50: IFM 3D image and surface profile for DH36 (section through the transverse direction), DH36, 8mm plate, *MIG* welding technique, distortion angle=2.5^{o}.

4.3 Discussion of XRD Results.

4.3.1 XRD scans of the top surface of as-received Galvanised DH36 steel sample and polished DH36 and EH46 Parent Material.

Figure 4.52 shows the results from XRD analysis using a Co-tube of the top surface of as-received DH36 steel; four ferrite peaks (assigned by red lines) and 11 Zn peaks (assigned by blue lines) were detected. Figures 4.52 and figure 4.53 show the results of XRD analysis of as-received polished samples of DH36 and EH46 steel respectively; ferrite was the predominant phase found in both steel grades.

4.3.2 XRD Analysis of FSW samples of DH36 Steel.

The results of the XRD analysis of DH36 steel after the FSW process are shown in figure 4.54 for low tool speeds (W9 200RPM, 100mm/min) and figure 4.55 for high tool speeds (W6 550RPM, 400mm/min). The XRD scan was taken at the top surface of the SZ. The XRD scan results of low tool speeds (DH36 W9) shows only ferrite peaks, whereas for high tool speeds (DH36 W6), the BN peaks are also present. In both welded joints, there is no phase change compared to the peaks from the parent material (PM) shown in figure 4.52, however, BN peaks in W6 indicate that the FSW tool has experience a certain level of wear.

4.3.3 XRD Analysis of FSW samples of EH46 Steel.

Figure 4.56 shows a combination of XRD peaks from samples W1 to W7 (EH46), the main phase is still ferrite, but BN peaks are also present. As expected, the region between the shoulder and probe is the one most affected by the thermo-mechanical action due to the combination between both parts of the FSW tool. Figure 4.57 shows peaks of ferrite (4 peaks assigned with red colour) and also BN (4 peaks assigned with blue colour) for sample W2 (EH46) using Co-tube.

Sample W8 and W10 (EH46) steel XRD scan on the top surface of the SZ and also at the probe end is shown in Figure 4.58. Ferrite and BN peaks are present in both welds. Figures 4.59 and 4.60 show a comparison between W8 and W10, BN peaks in W10 are stronger than in W8 which suggests that more tool wear has been experienced by the tool in W10 due to the higher traverse speeds.

Tool wear will be discussed extensively later in tool wear section and also in CFD modelling section.

4.3.4 Residual Stresses in FSW Samples.

Table 4.9 provides the result for the measurement of the range of $\psi, \Omega, 2\theta$ and d-space obtained from XRD procedure as described in the experimental section (3.3.9). The range of Ω angle (the angle between sample surface and the X-Ray incident beam) for the same 2θ peak is shown in Figure 4.61. The the data taken following calculations made using an Excel spreadsheet for ψ angle and lattice space taken from table 4.9 is shown in Figure 4.62. The linear regression $R^2=0.8172$ is acceptable; however, some attempt was done previously to improve the linear regression by using a parabolic approach assuming the top part of the curve as a parabolic equation [128]. As described in previous work it is common in the literature to do a correction for the XRD-lab peaks in order to increase the linear regression (R^2) value. However, this may lead to a shift in the 2θ peak location leading to inaccuracy of measuring residual stresses.

The results of longitudinal residual stress measurements taken along the traverse welded joint sides are shown in figure 4.63 for two samples; one from low tool speeds (W9) and one from high tool speeds (W6). Tensile longitudinal residual stresses in the SZ in both weld joints were found below the yield stress values with compressive stresses in the surrounding regions to balance the tensile stress. These results coincides with other work [122] done on FSW samples of DH36 steel which concluded that residual stresses were below the yield stress. [122] Camilleri et. al. 2015 used a strain gauge to estimate the residual stresses of 6mm thick DH36 steel and found that maximum longitudinal residual stresses (380 MPa) occurred below the tool shoulder and was less than the yield stress. It was also shown that residual stresses decreased with reducing plate thickness and the maximum longitudinal stress was on the top surface at the edge of the SZ. [133] Steuwer et. al. (2012) showed that the peak residual stress of HSLA-65 steel at the tool shoulders remained largely unchanged (approximately equal to the nominal yield stress (450 MPa)) but it can increase slightly with increasing traverse speed. This finding agrees with the current work which showed an increase in longitudinal residual stress for sample W6 (DH36) which was welded using a higher traverse speed than W9 (DH36). Also it is shown that residual stresses on the AS is higher than the RS, this can be attributed to the higher peak temperatures during the FSW at the (AS) as will be discussed in the modelling section, later.

Measuring of the strain-lattice free parameter (d_o) in the welded joints was not necessary because there was not any phase change that could lead to varying the crystal structure (as bainite and acicular ferrite crystal structure is BCC) or any variation in chemical composition which can be misunderstood as residual stresses. The phase of DH36 steel before and after welding was as detected by XRD shown in figure 4.52, figure 4.54 and figure 4.55 which showed a ferritic (BCC) crystal structure. So the need to cut small cubes or producing combs from welds section by wire electro discharge machine in order to detect the free lattice space was avoided [129]. The strength of the $Sin^2\psi$ technique can be attributed to the fact that it does not require a knowledge of the strain-free lattice spacing, since d_o can be replaced in the denominator by $d_{\psi\rightarrow0}$ (lattice space when ψ angle equal zero) without significant error because elastic strains are typically less than 0.1%, so that $d_o \cong d_{\psi\rightarrow0}$.

4.3.1 XRD scan of the top surface of Galvanised as received DH36 sample and polished DH36 and EH46 Parent Material.
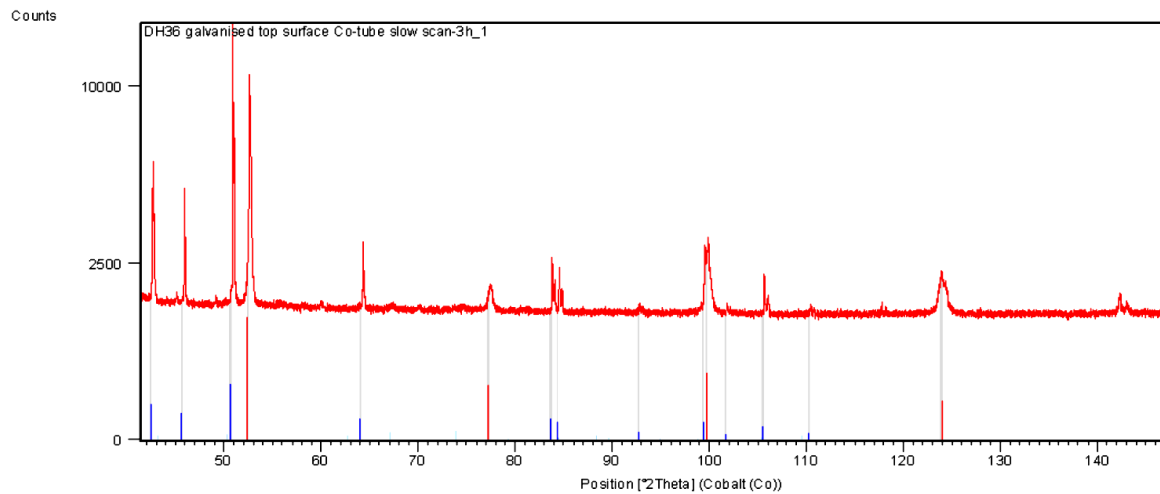
Figure 4.51: XRD scan of the Galvanised DH36 top surface, Ferrite peaks are in red, Zn peaks are in blue.
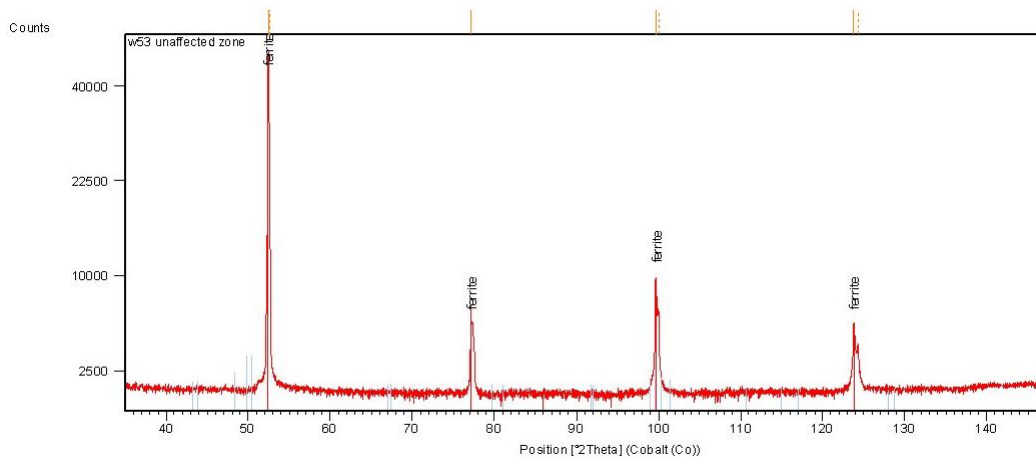
Figure 4.52: XRD scanning of DH36 grade as received shows that microstructure is mainly ferrite phase, a Co target (Kα 1.79 (Å)) was used. .
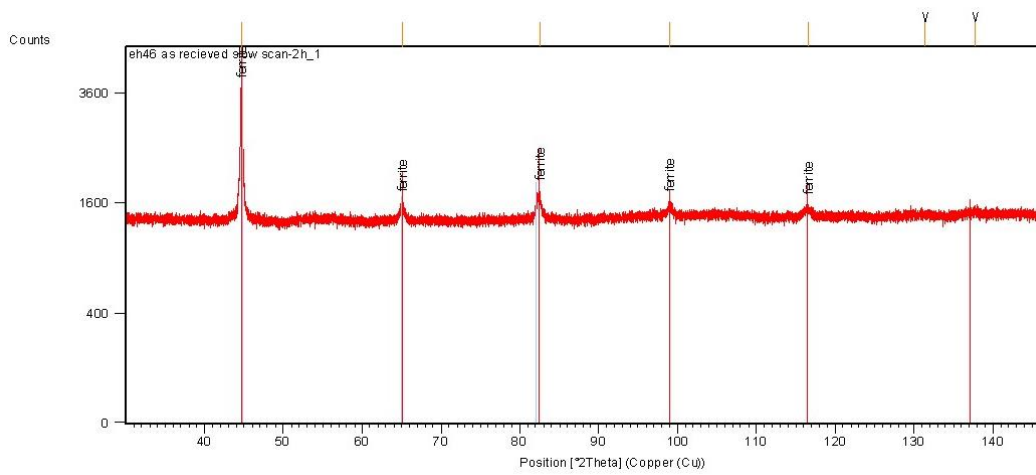
Figure 4.53: XRD scan of as received grade EH46 steel shows that the microstructure is ferritic (BCC), a Cu-target Kα 1.54 (Å) was used.

4.3.2 XRD scans of FSW of DH36 steel samples

- **DH36 200RPM, 100mm/min**
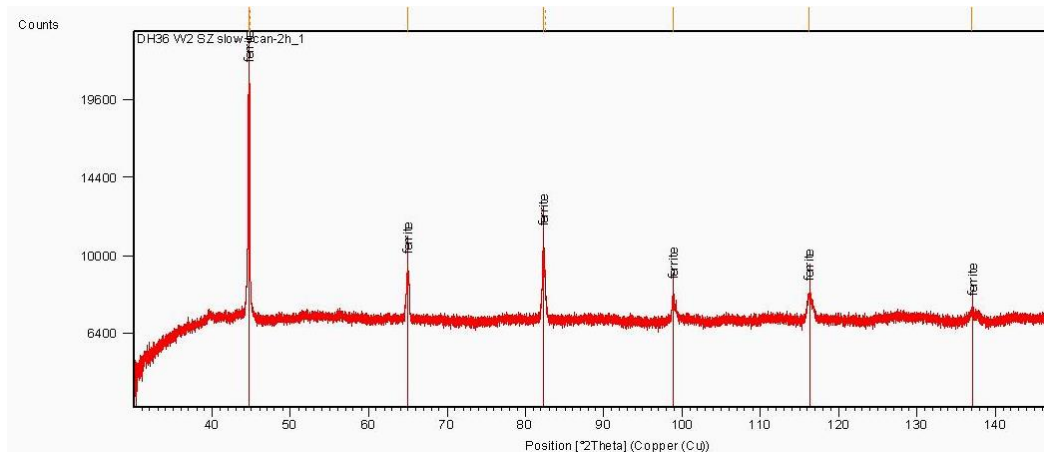
Figure 4.54: XRD scanning of FSW of DH36 grade (200RPM, 100mm/min), the microstructure is ferritic without any change following the FSW process. A Cu-target Kα 1.54 (Å) was used.

- **DH36 550RPM, 400mm/min**
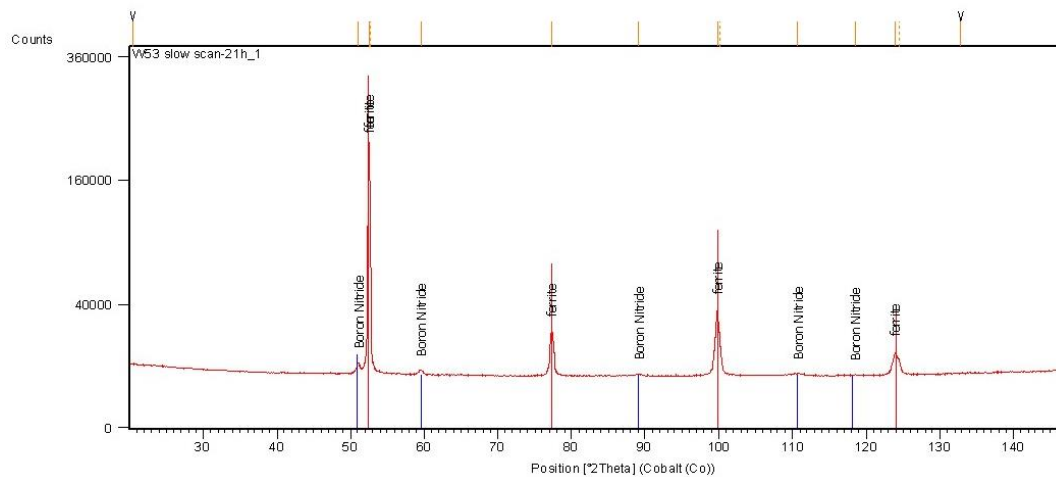
Figure 4.55: XRD scan of FSW of DH36 grade (550RPM, 400mm/min), the microstructure is mainly ferrite; BN peaks are also present. A Co target (Kα 1.79 (Å)) was used.

4.3.3 XRD scan of FSW samples of EH46 W1-W10
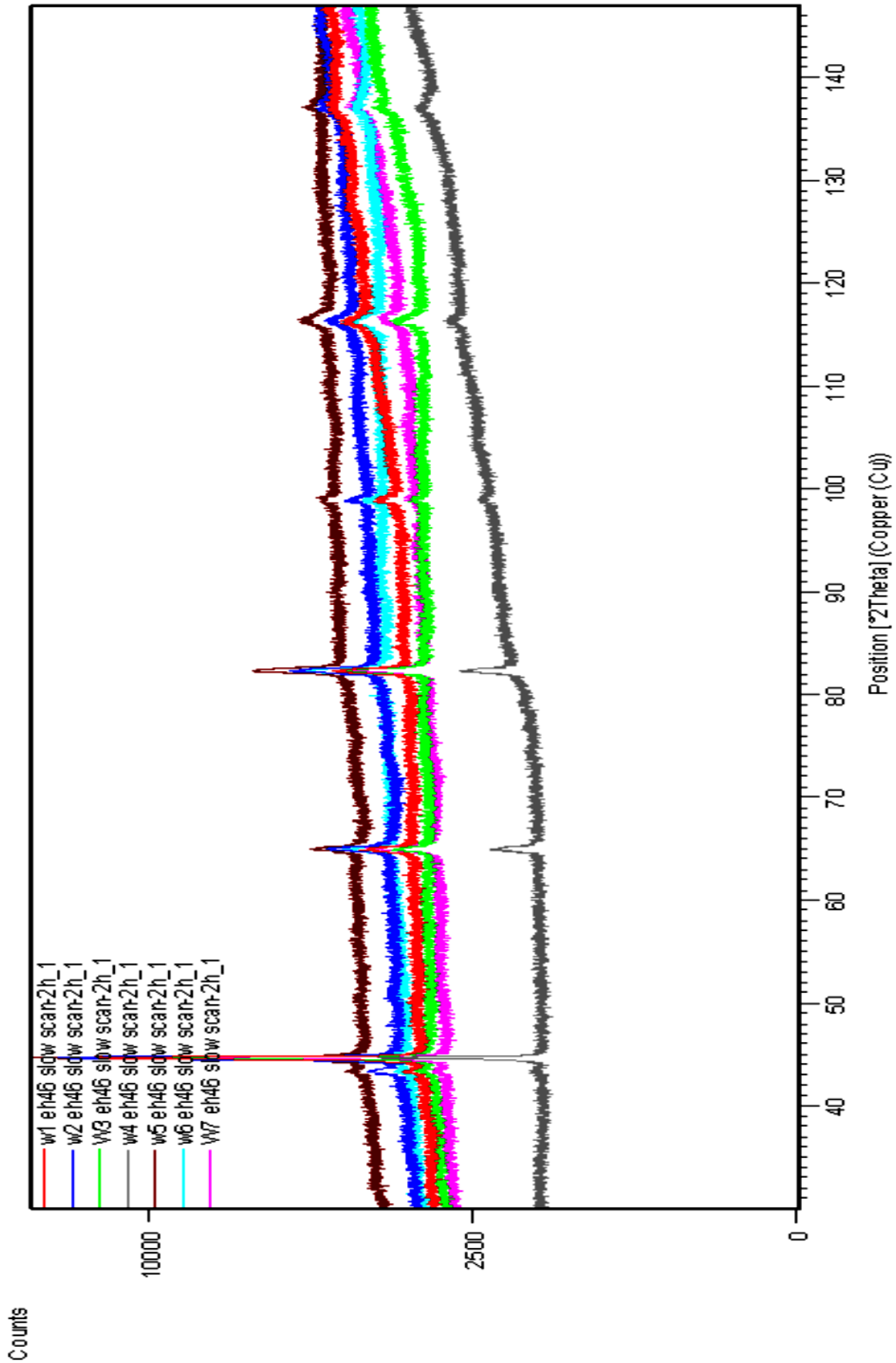
Figure 4.56: XRD scan of FSW of EH46 grade (Plunge experiments from W1-W7 at region 1 under shoulder), microstructure is mainly ferritic BCC phase; BN peaks are also present, Cu-target Kα 1.54 (Å) was used.
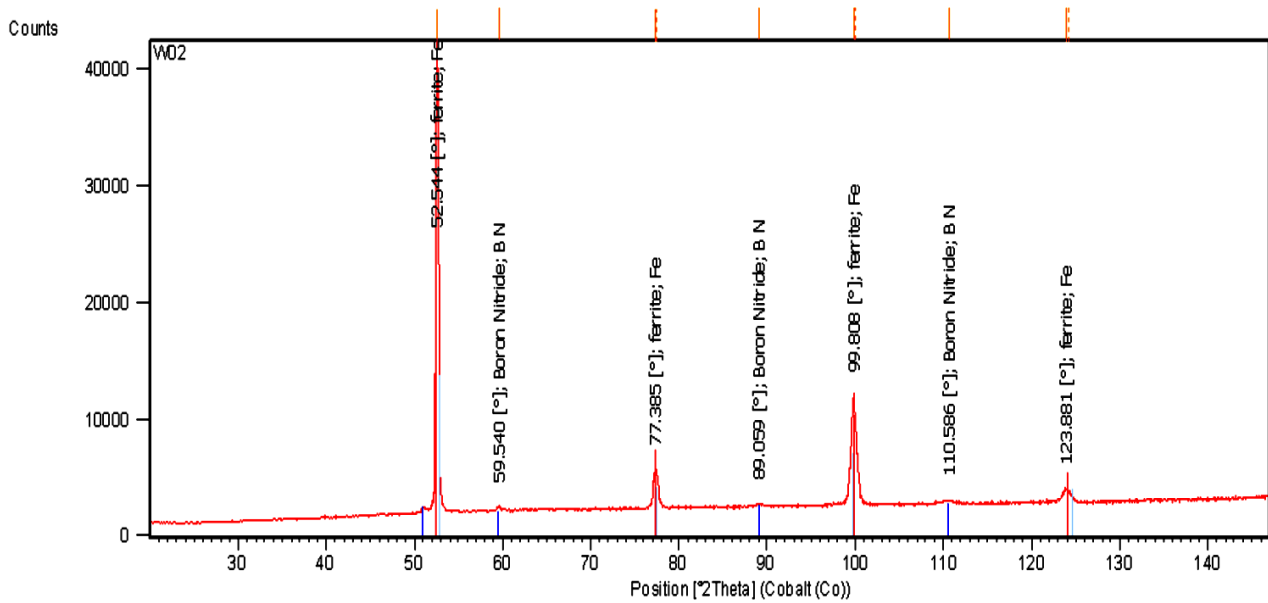
Figure 4.57: XRD scan of FSW of EH46 grade (W2 Plunge under shoulder), the microstructure is mainly BCC ferrite; BN peaks are also present. A Co target (Kα 1.79 (Å)) was used.
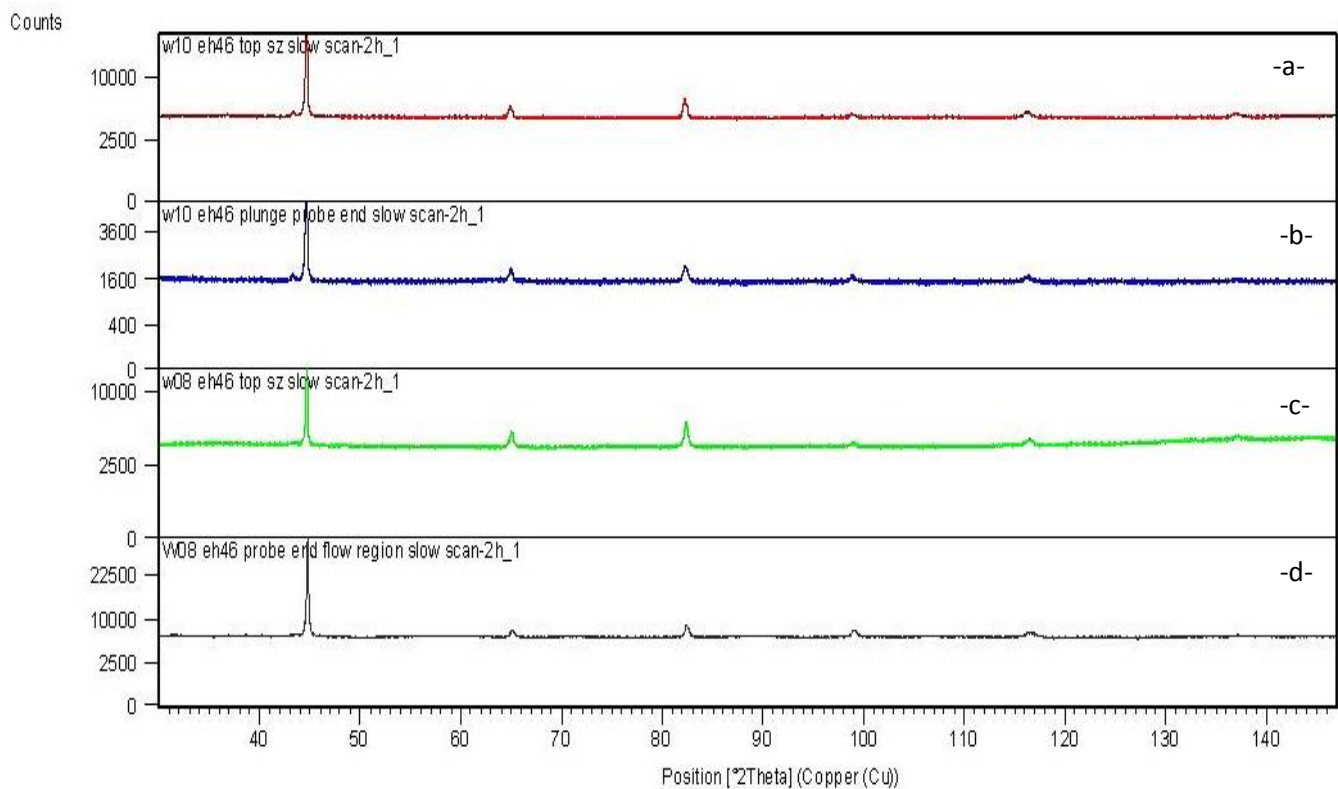
Figure 4.58: XRD scan of FSW of EH46 grade -a- W10 top of SZ, -b- W10 probe end, -c- W8 top of SZ and -d-W8 at the probe end. Microstructure is ferritic phase; BN peaks are present. A Cu-target Kα 1.54 (Å) was used.
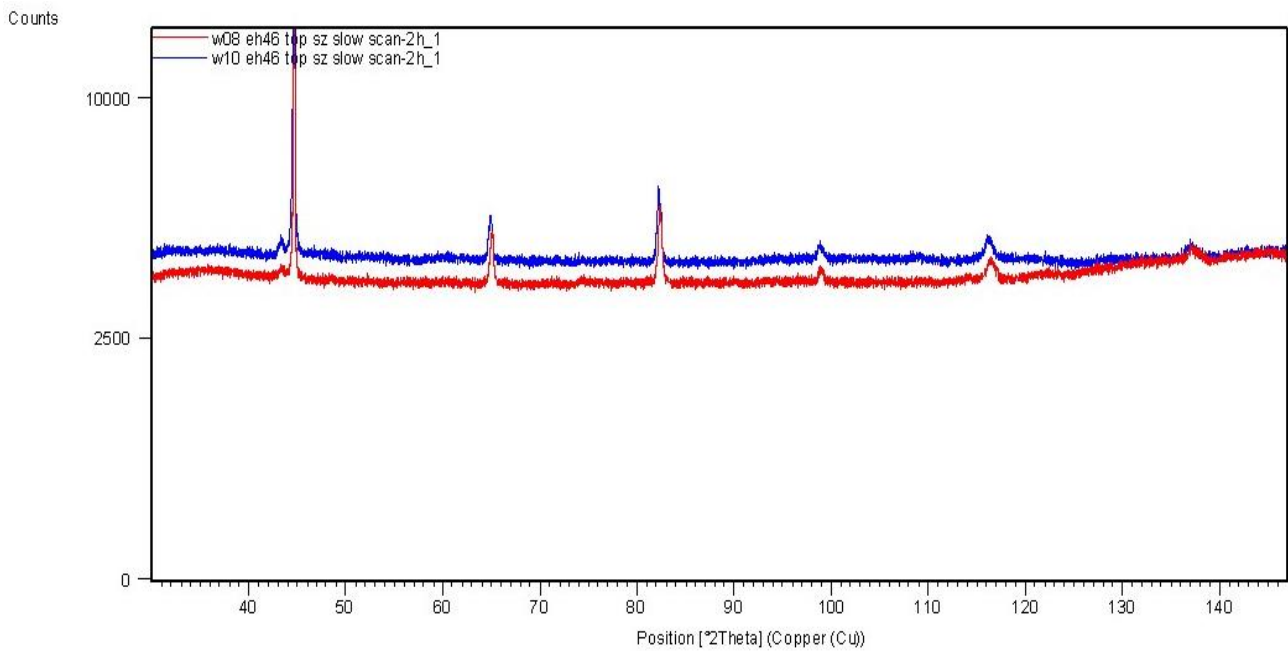
Figure 4.59: XRD scan of FSW of EH46 grade (comparison between W8 and W10 at the top of SZ), W10 shows stronger peak of BN than W8. A Cu-target Kα 1.54 (Å) was used.

BN peak, W10 shows (blue) a stronger peak.
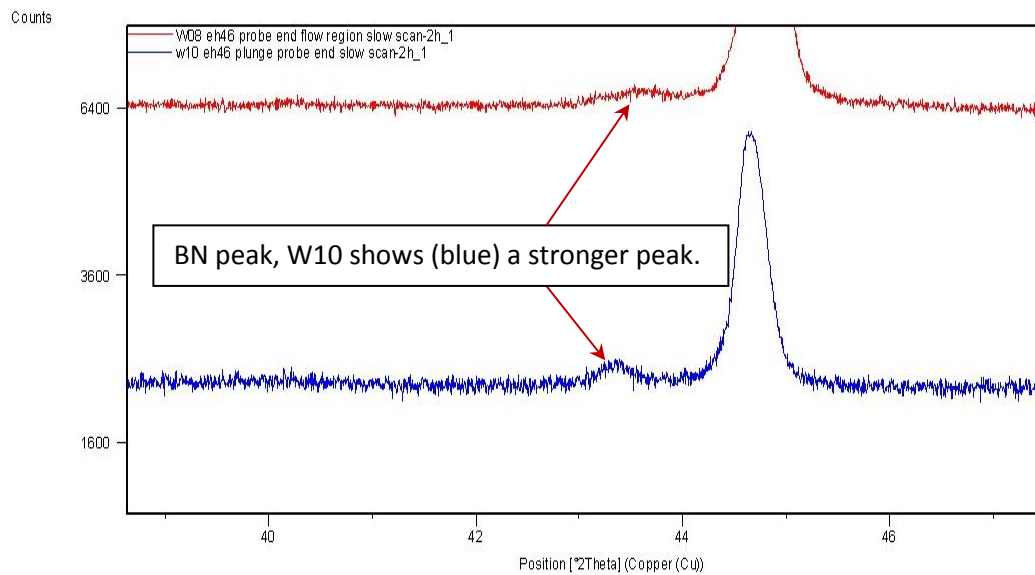
Figure 4.60: XRD scan of FSW of EH46 grade (comparison of the first peaks of W8 and W10 at the probe end), W10 shows a stronger peak for BN than W8. A Cu-target Kα 1.54 (Å) was used.

4.3.4 Residual Stresses
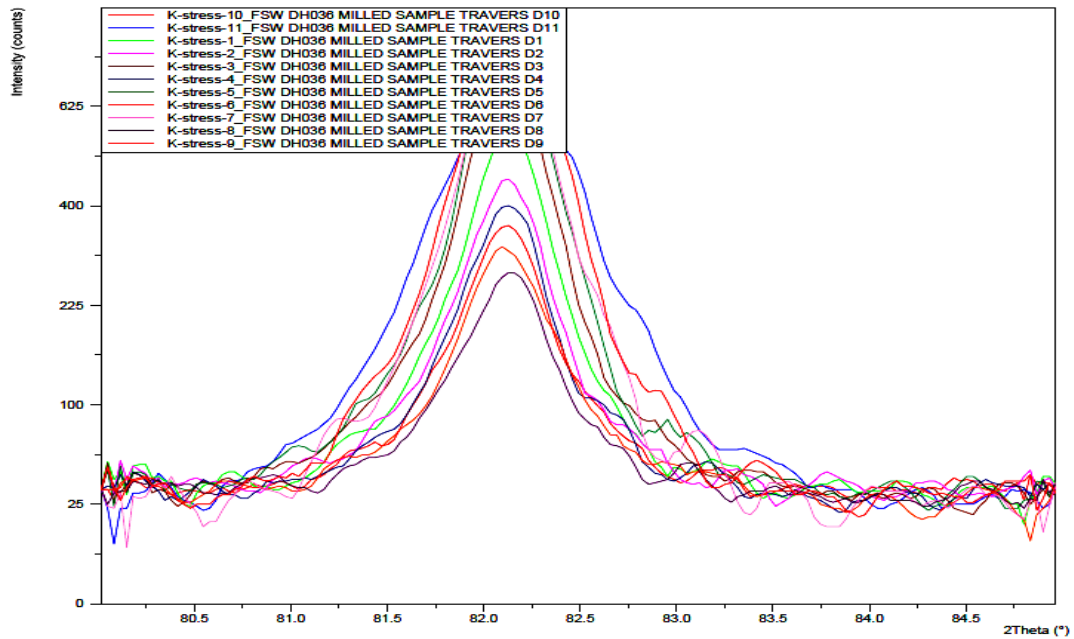
Figure 4.61: Combination of $(\Omega - 2\theta)$ curves taken directly from the XRD-machine and as explained in Table 17.

Table 4.9: The data required in order to estimate residual stresses.

Ω^0	$2\theta^0$	θ^0	ψ^0	θ rad	Ω rad	ψ rad	d-space	[-2υ+(1+υ)Sin²ψ]/E	Sin²ψ
40	82.09	41.045	1.045	0.7163720	0.6981333	0.0182387	0.1172613	-0.002767171	0.0003326
57	82.09	41.045	-15.95	0.7163720	0.99484	-0.2784679	0.1172613	-0.002301336	0.0755606
28	82.1	41.05	13.05	0.7164593	0.4886933	0.227766	0.1172496	-0.002453507	0.0509864
63	82.11	41.055	-21.94	0.7165466	1.09956	-0.3830134	0.1172378	-0.001904385	0.1396645
22	82.11	41.055	19.055	0.7165466	0.38397333	0.332573267	0.11723785	-0.002109212	0.10658682
68	82.11	41.055	-26.94	0.7165466	1.18682666	-0.47028006	0.11723785	-0.001497751	0.20533220
16.5	82.11	41.055	24.555	0.7165466	0.28798	0.4285666	0.11723785	-0.001699842	0.17269631
70.5	82.12	41.06	-29.44	0.71663386	1.23046	-0.51382613	0.11722610	-0.001273263	0.24158493
12	82.11	41.055	29.055	0.7165466	0.20944	0.5071066	0.11723785	-0.001308738	0.23585593
66	82.12	41.06	-24.94	0.71663386	1.15192	-0.43528613	0.11722610	-0.001668205	0.17780547
8	82.12	41.06	33.06	0.71663386	0.13962666	0.5770072	0.11722610	-0.000926462	0.29759002
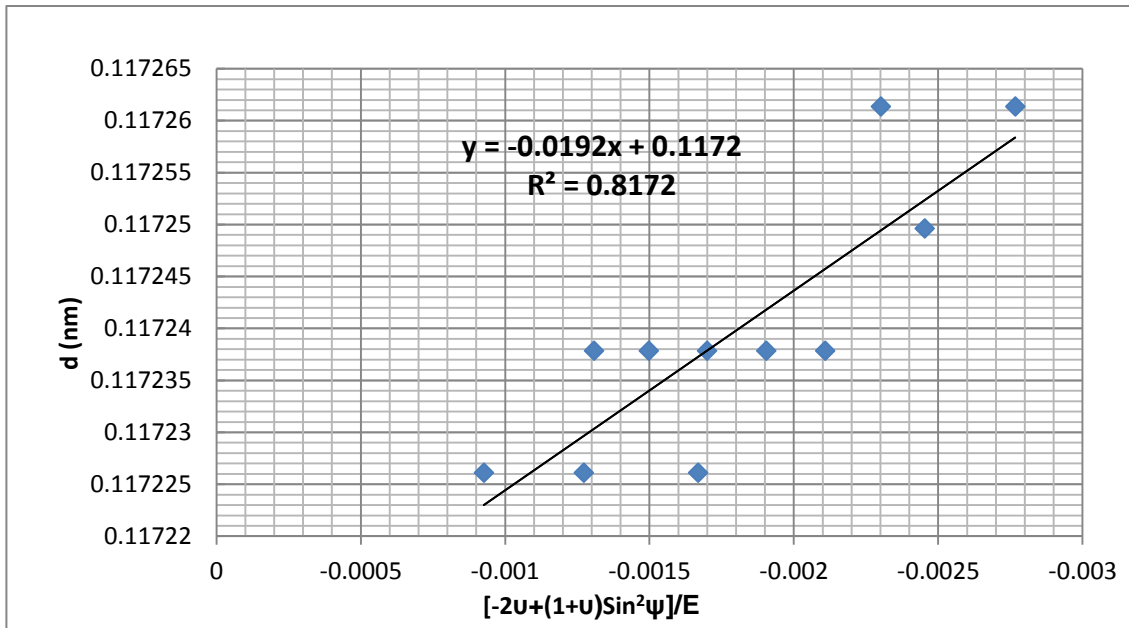
Figure 4.62: Linear relationship between d-space and $\sin^2\psi$ in order to determine the residual stresses and free lattice space (d_o).
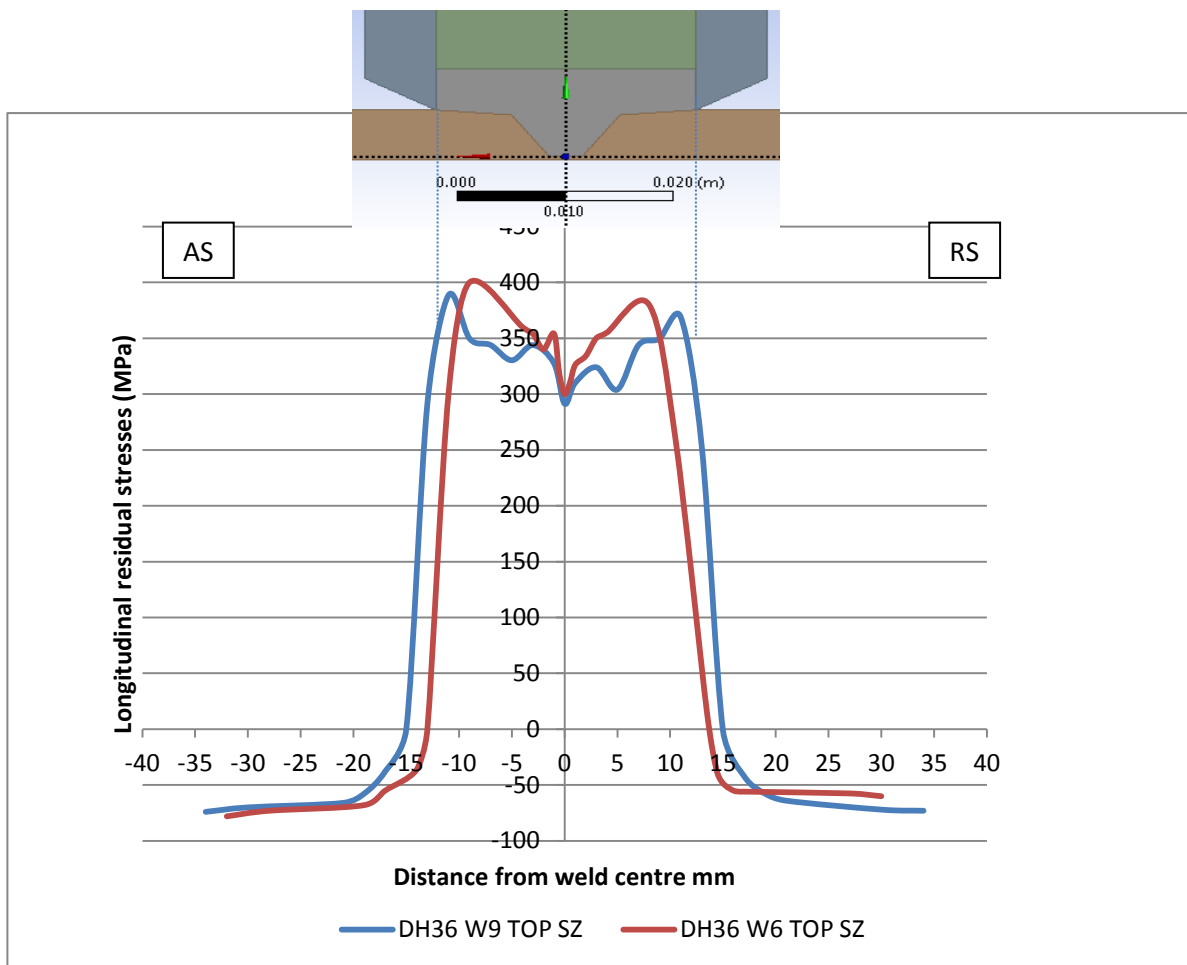
Figure 4.63: Longitudinal residual stresses distribution along the W9 and W6 DH36 FSW joints.

4.4 Mechanical Testing

4.4.1 Tensile test results.

Figure 4.64 shows photographs of the broken samples of 8mm FSW DH36 steel (W9) after tensile testing. It shows that all the tensile samples failed outside the welded region; this means that the strength of the SZ was higher than the PM and the possible defects present did not affect the strength of the SZ. Figure 4.65 shows the stress-strain curves for six FSW samples and 2 parent metal (PM) samples. The PM samples have shown higher elongation but lower tensile strength when compared to the as-welded samples. Table 4.10 lists the calculated data of the tensile test including: E-Young modulus, $\sigma_{y0.2}$-0.2% Yield stress , σ_{UTS}-Ultimate stress, F_m-Normal applied force, A_g-reduction in area%, A_{40}-Reduction in area at 40%, a_o, b_o, and S_o are the cross section dimension. The 0.2% proof stress was 475 MPa for the parent metal whereas for the FSW samples it was slightly higher. The tensile strength (σ_{UTS}) for the FSW sample has also increased compared with the PM; this increase was also reported by [79] Reynolds et al 2003. In this work, the average ultimate strength of the welded samples was 580 MPa, similarly [8] Cater et. al. 2013 reported a tensile strength of 570 MPa for the same grade of steel which is slightly lower than the findings of the current work. [78] Toumpis et. al. 2014 reported a yield stress 408 MPa and 540 MPa ultimate stress for the same grade and welding conditions, which are in agreement with the current work results. The increase in tensile strength of the FSW samples can be attributed to the refinement in the microstructure of the SZ which will be discussed in the SEM results section.

Figure 4.66 shows the broken samples of 6mm FSW (DH36) steel plate (W6), the force displacement curve is shown in figure 4.67 and the results from the analysis of the curve in table 4.11. As with sample W9 (DH36) the samples have failed outside the SZ and the ultimate tensile strength has increased compared to the ultimate tensile strength of the PM.

Figure 4.64: 8mm DH36 FSW and PM samples after Tensile test.
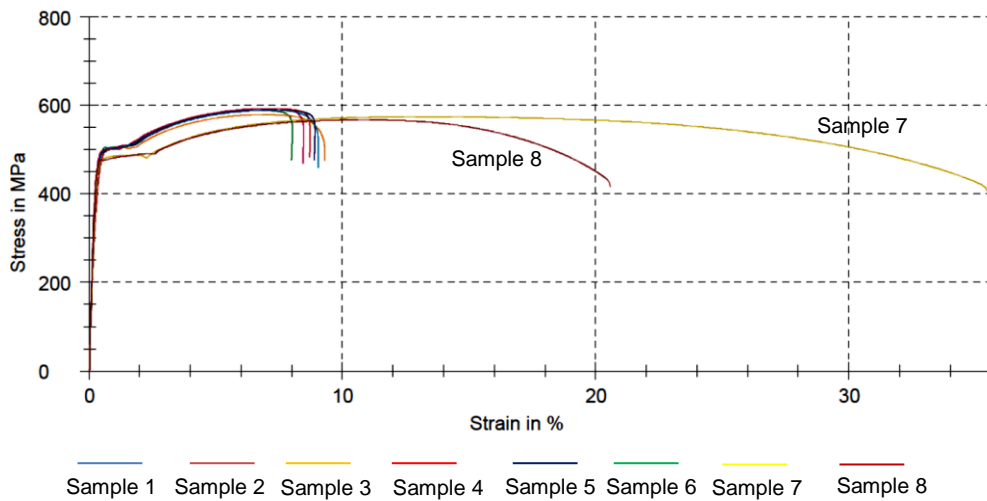
Figure 4.65: The Engineering Stress Strain curves for the tensile tests of 8mm thick DH36 FSW and PM samples.

Table 4.10: A comparison of the results of uniaxial tensile testing 8mm thick DH36 plate which has been FSW at 200RPM/ 100mm/min, and compared with un-welded PM samples.

No.	Specimen No.	E GPa	$\sigma_{y0.2}$ MPa	σ_{ult} MPa	F_m KN	A_g %	A_{40} %	a_o mm	b_o mm	S_0 mm^2	Break
1	1	159	476	592	127.13	6.87	8.41	8.481	25.35	214.74	out of gauge length
2	4	183	492	589	126.32	6.34	7.73	8.467	25.34	214.55	out of gauge length
3	8	186	485	589	126.69	6.86	8,63	8.479	25.36	215.03	out of gauge length
4	2	202	487	579	126.24	6.61	9.07	8.579	25.41	217.99	out of gauge length
5	11	207	493	593	126.71	6.85	8.21	8.444	25.31	213.72	out of gauge length
6	12	202	482	589	126.85	6.83	8.81	8.46	25.44	215.22	out of gauge length
7	15 unwelded sample	167	473	574	120.76	12.89	35.22	8.28	25.39	210.23	between gauge length
8	16 unwelded sample	189	477	567	124.27	10.40	20.37	8.403	26.07	219.07	between gauge length

E.Young modulus, $\sigma_{y0.2}$-0.2% proof stress , σ_{UTS}-Ultimate stress F_m-Normal applied force , A_g-reduction in area %, A_{40}-Reduction in area at 40%, a_o, b_o and S_o are the cross sectional dimensions.

159

Figure 4.66: Photographs of tensile testing samples, the broken FSW sample and also a sample of the parent metal.
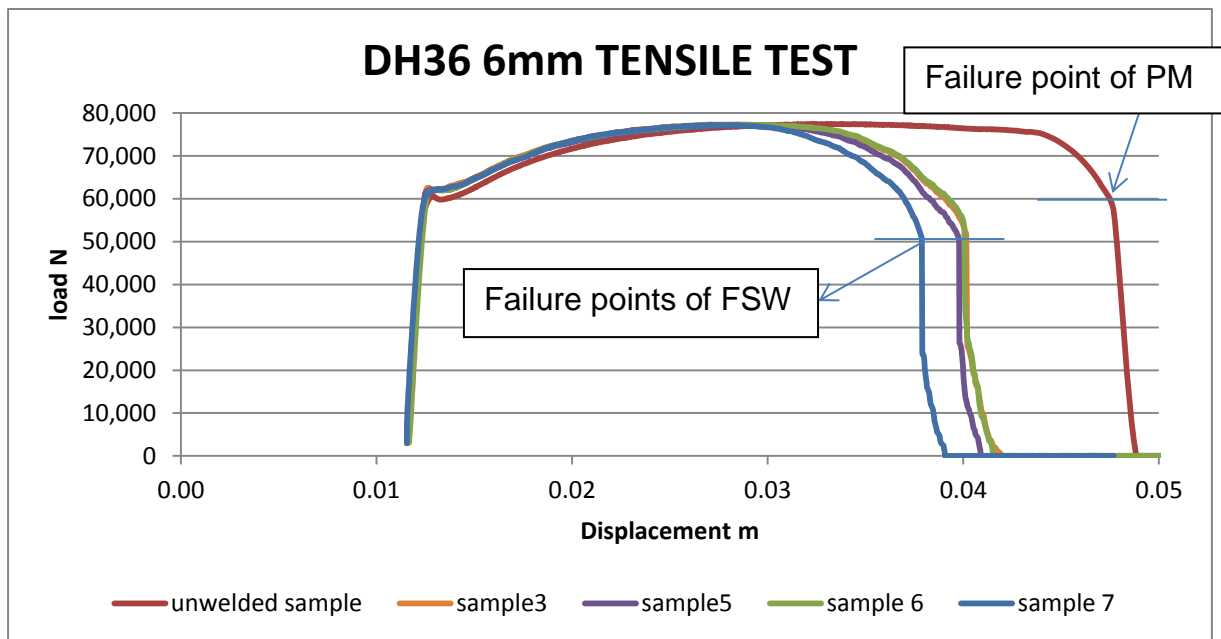
Figure 4.67: The load/displacement graph of the tensile test of welded and unwelded 6mm DH36 steel plate samples.

Table 4.11: The results of the tensile test (6mm plate thickness with FSW 550 RPM/ 400mm/min).

No.	Specimen No.	E GPa	$\sigma_{y0.2}$ MPa	σ_{UTS} MPa	F_m KN	a_o mm	b_o mm	S_0 mm^2	Break
1	3	166	439	547	77.2	6.1	23.12	141.032	out of gauge length
2	5	201	440	546	77	6.1	23.09	140.849	out of gauge length
3	6	201	440	551	77.6	6.1	23.08	140.788	out of gauge length
4	7	201	440	546	77	6.1	23.09	140.849	out of gauge length
5	Unwelded sample	190	425	532	75	6.1	23.11	140.971	between gauge length

4.4.2 Fatigue Test Results

Figure 4.68 shows images of failed fatigue specimens from:, -a- DH36 8mm thickness (W9 200RPM, 100mm/min) and -b-DH36, 6mm thick (W6, 550RPM, 400mm/min). Table 4.12 and table 4.13 show the number of cycles required to failure for each sample of DH36 W9 and W6 respectively. Samples of W6 (DH36) have failed in the welding zone at an average of 115,078 cycles and the crack initiated from the back middle of the plate towards the advancing side. This could be associated with defects (cracks) found in the SZ (this will be discussed in the SEM and defects sections). However, for specimens taken form sample W9, the slow tool speed samples; the failure occurred just outside the SZ in the advancing side and the average sampled failed limit was 642,935.5 cycles. The high fatigue strength in the low welding speed samples can be attributed to its defect free and fine microstructure formed in SZ during FSW process (this will be shown and discussed in the SEM and defects sections).

.

-a-   -b-
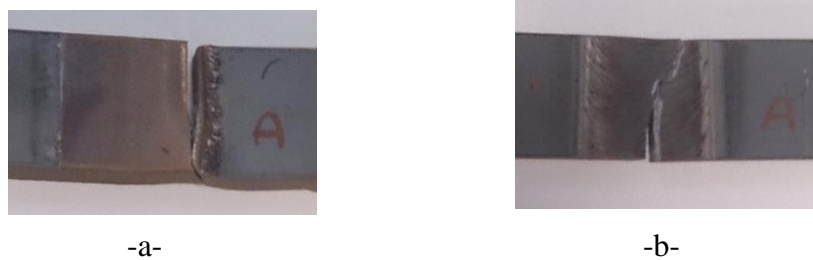
Figure 4.68: Fatigue test of a- DH36 8mm thickness W9 (200RPM, 100mm/min) and b-DH36 W6 (6mm 550RPM, 400mm/min).

Table 4.12: Fatigue test results of DH36 8mm thickness (200RPM, 100mm/min)

No.	Sample No.	Maximum stress MPa	Minimum stress MPa	Number of cycles to failure
1	3	305.6	30.65	644128
2	6	305.6	30.65	635767
3	7	305.6	30.65	651001
4	10	305.6	30.65	640023
5	18	305.6	30.65	643378
6	19	305.6	30.65	643316

Average cycles to failure=642,935.5

Table 4.13: Fatigue test results of DH36 6mm thickness (550RPM, 400mm/min)

No.	Sample No.	Maximum stress MPa	Minimum stress MPa	Number of cycles to failure
1	1	305.6	30.65	111,736
2	2	305.6	30.65	112024
3	4	305.6	30.65	124001
4	8	305.6	30.65	112551

Average cycles to failure=115,078

4.4.3 Micro-hardness Test of FSW Samples.

Figure 4.69 and figure 4.70 show the result of Vickers micro-hardness (300gf HV Kg/mm^2) measurements along the weld line of FSW DH36 steel samples W9 and W6 respectively. The hardness of the base metal was equal to about 170-180HV; however, it increased toward the SZ with a maximum value equals to 260HV in W9 and 285HV in W6. The reason for the increase in hardness can be attributed to grain refinement and phase transformation occurring in the SZ after the FSW process - as reported by the previous works [76] [78]. [78] Toumpis et.al. 2014 reported the same increase in the hardness values after FSW of 6mm DH36 steel. [76] Failla et al. 2009 explained this increase in hardness corresponded to a bainite/Widmanstatten ferrite microstructure. The hardness in DH36 W9 seems relatively evenly distributed from the AS to the RS of the SZ, however, a slight decrease in the middle of the weld as shown in figure 4.69 and can be related to a slight difference in the microstructure as will be discussed later. The microhardness in DH36 W6 showed an uneven distribution in the SZ as a result of an inhomogeneous microstructure produced following a high traverse speed. The higher values of hardness are located in a bainitic microstructure and the lower values were located in acicular ferrite microstructure. [77] Martino and Thewlis 2013 showed that microhardness in mild steel can increase to 300HV with lower bainite and to 240HV with upper bainite phase transformation. The difference in microhardness in the SZ was also reported by [76] Failla et al. 2009 and has been interpreted as a result of the difference in cooling cycles inside the SZ. The asymmetry in hardness was also investigated by [92] MC Pherson et. al. 2013, they relate it to the difference in relative material movement causing   localised strain rates with different values between the tool sides.

Figure 4.71 and figure 4.72 show the microhardness distribution from the top of SZ towards the plate bottom. The microhardness in sample W9 decreases towards the plate bottom and

the maximum hardness (260HV) was associated with a bainite phase at 2mm from the top of the SZ. W6 shows fluctuations in microhardness values as a result of the inhomogeneous microstructure resulting from using high tool speeds. The maximum hardness value associated with the bainite microstructure was 280HV located at 3mm from the top of the SZ. Sample W8 and W10 (EH46) also showed improvement in the microhardness as a result of the finer microstructure resulting from the phase transformation in the SZ compared to the PM microstructure (as will be shown in 5.8). Figure 4.73 shows the distribution of microhardness in the top surface of the SZ and HAZ between AS and RS. Sample W8 (EH46) shows more symmetry in microhardness between AS and RS compared to W10 as a result of slower tool traverse speed and the maximum HV in both welded joints was associated with the bainite phase. Figure 4.74 shows the microhardness distribution from the top of SZ towards the bottom of the plate. In both welded joints the microhardness decreases towards the plate bottom which indicates that the SZ microstructure has significantly improved in terms of microhardness. Sample W10 shows a higher microhardness value than W8 as a result of the higher traverse speed which in turn caused a higher cooling rate so more bainite phase is expected as will be discussed later in the SEM images section.
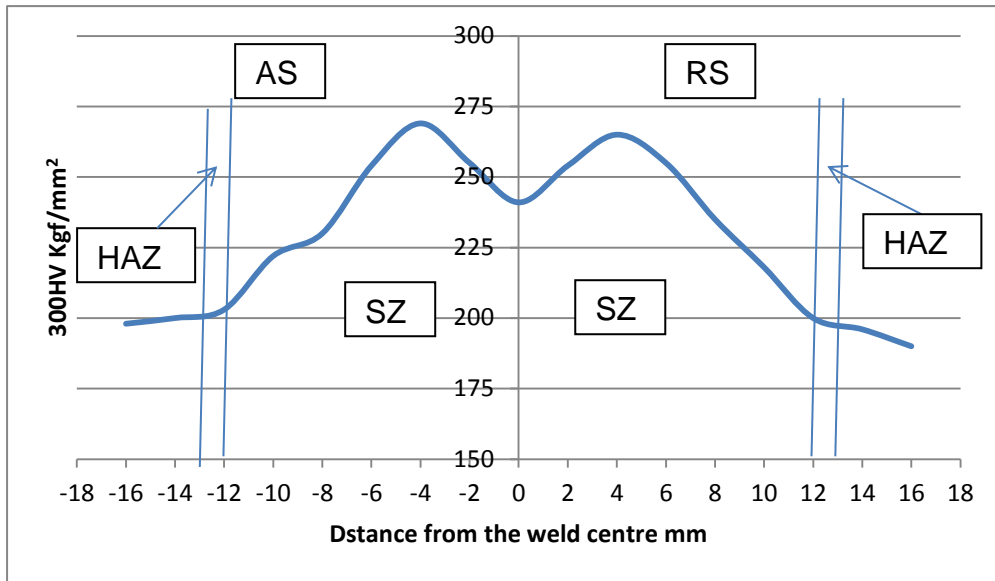
Figure 4.69: HV micro-hardness distribution between AS and RS of DH36 8mm plate (200RPM, 100mm/min).
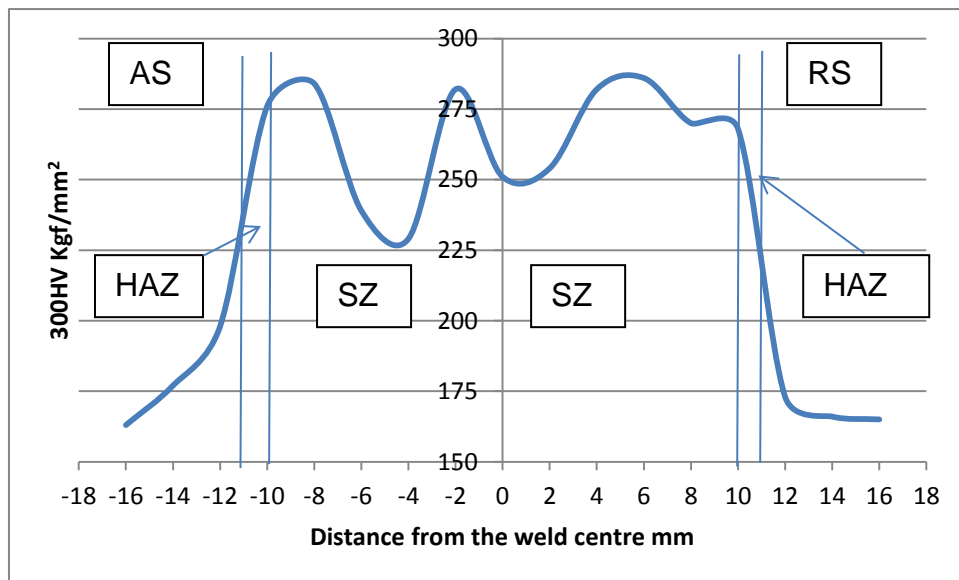
Figure 4.70: HV micro-hardness distribution between AS and RS of W6 DH36 6mm plate (550RPM, 400mm/min).
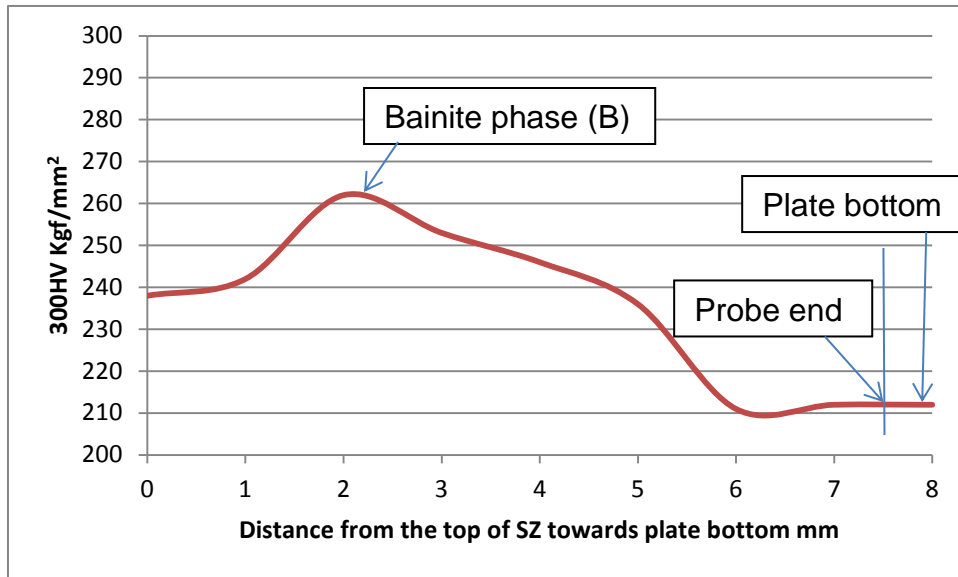
Figure 4.71: HV micro-hardness distribution from the top of SZ towards the plate bottom of DH36 8mm plate (200RPM, 100mm/min). The peak hardness is associated with the formation of Bainite in the microstructure.
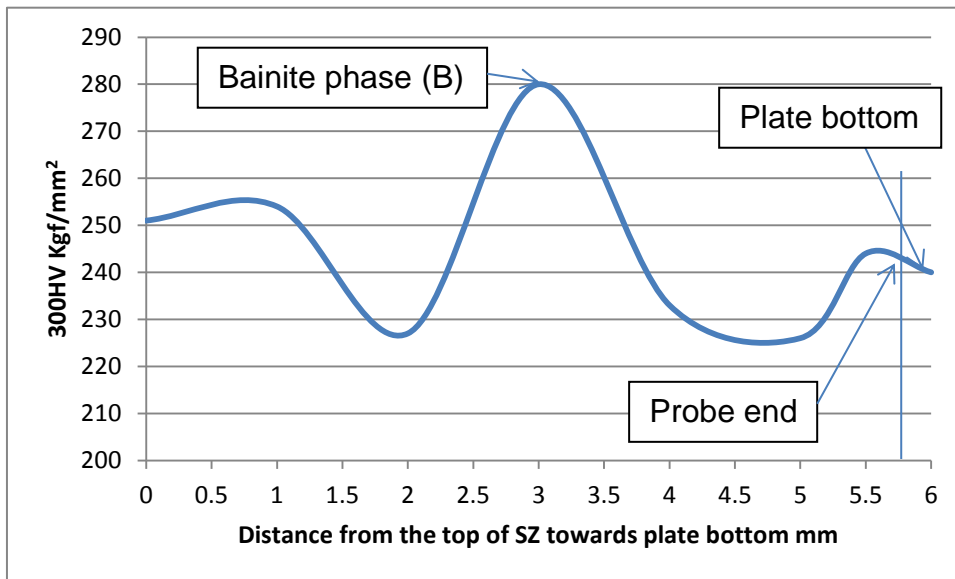
Figure 4.72: HV micro-hardness distribution from the top of SZ towards the plate bottom of W6 DH36 6mm plate (550RPM, 400mm/min). Peak hardness is associated with the formation of Bainite in the microstructure.
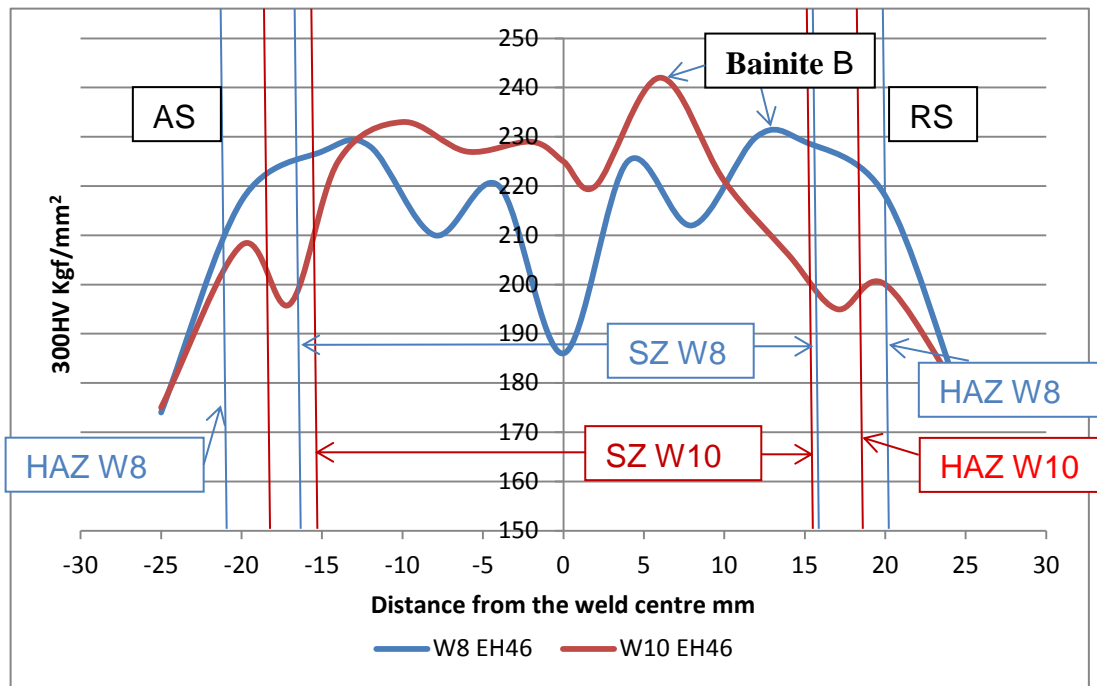
Figure 4.73: Micro-hardness distribution (300HV) between AS and RS of EH46 W8 (150RPM, 50mm/min) and EH46 W10 (150RPM, 50mm/min) 14.8mm plate. (300HV used 300g load).
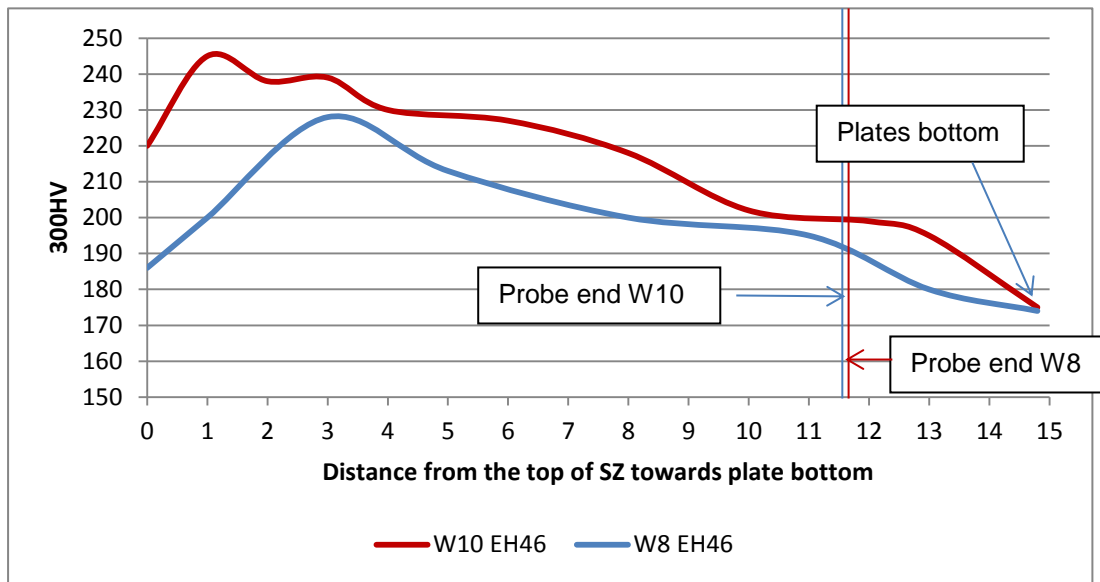
Figure 4.74: Micro-hardness distribution (300HV) from the top of SZ towards the plate bottom of FSW W8 and W10 EH46 steel.

166

4.5 SEM Analysis of DH36 and EH46 Steel in the as Received Condition.

The microstructure of grade DH36 steel as shown in figure 4.75 -a- and -b- shows an average ferrite grain size of 15µm with long narrow bands of pearlite. Precipitates which consist of Ti, Nb and Ti-Nb combination are shown in figure 4.76 and figure 4.77 respectively. These precipitates are small (less than 10nm) and act to pin the austenite grain boundaries thus preventing grain coarsening and improving the final as-welded material mechanical properties [83]. MnS, MnS-CaS compound and MnS-Al stringers are also present with a maximum width of 1µm and a length of 10µm as revealed by the SEM-EDS when examining polished un-etched PM samples shown figure 4.78 to figure 4.80 respectively.

The EH46 steel PM microstructure shown in figure 4.81 -a- and -b- shows an average ferrite grain size of 20µm with bands of pearlite which appear shorter and wider than in the grade DH36 parent metal sample. Ti and Ti-Nb precipitates as shown in the high magnification SEM image, figure 4.82 and in the SEM-EDS images figure 4.83 and 4.84 are small and act to pin the austenite grain boundaries thus preventing grain coarsening and improving the final as-welded material mechanical properties [83]. Alumina-calcium sulphide was also identified in the microstructure. It appeared as a spherical compound which achieved a maximum size of 3µm whereas the MnS-calcium sulphide compound formed as an irregular spherical shape with maximum size of 3µm.

The information provided above will be used to inform the discussion regarding:

- Phase transformation which occurs during the FSW process.
- Elemental precipitation/segregation which occurs during the FSW process.
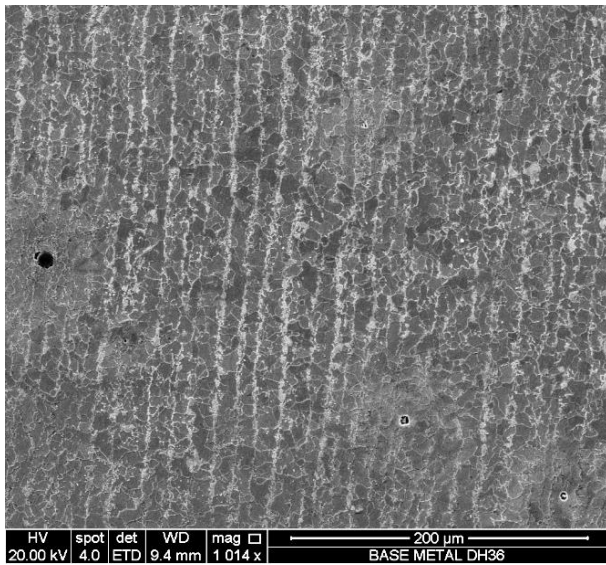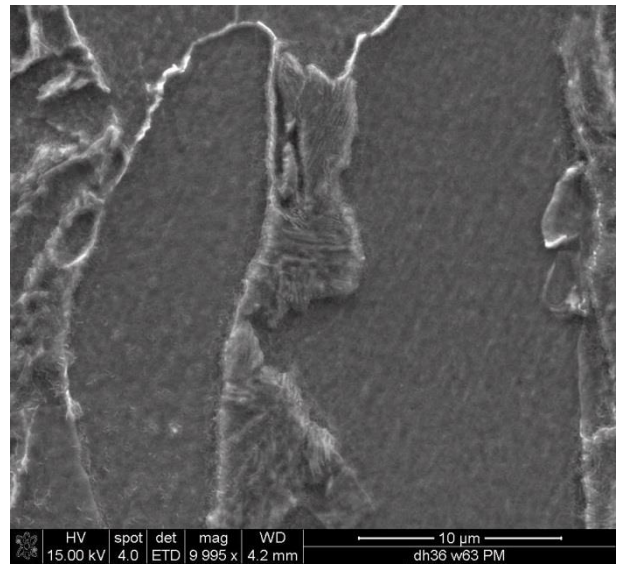
-a-   -b-

Figure 4.75: DH36 steel in the as received condition shows 15µm ferrite grains and bands of pearlite, -a- low magnification, -b-high magnification.
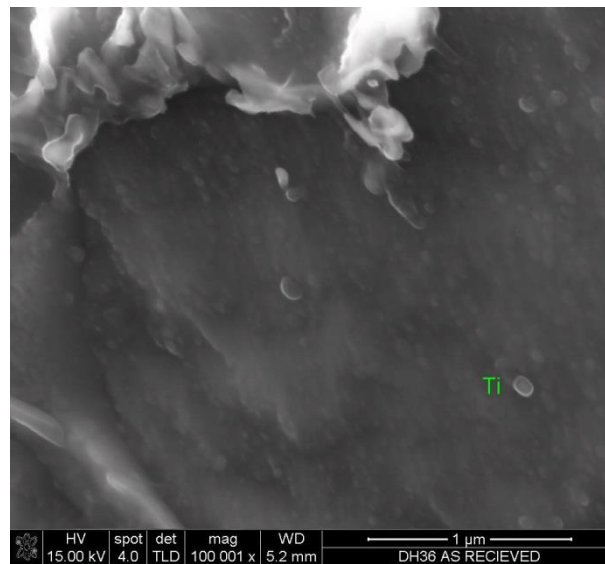
Figure 4.76: Higher magnification SEM image of DH36 grade showing Ti rich particles.
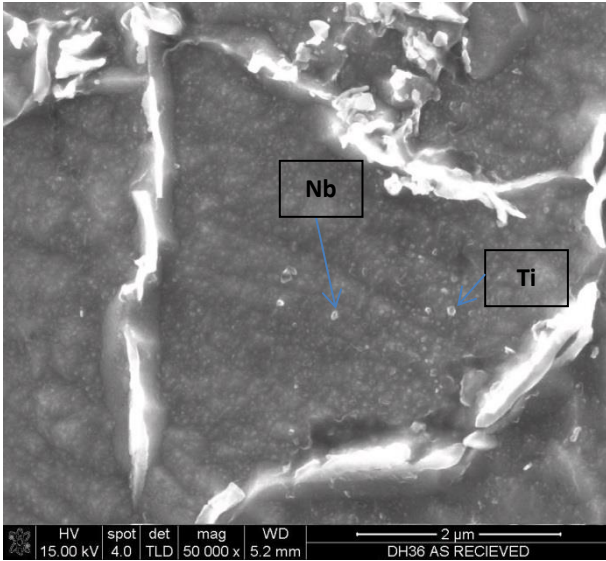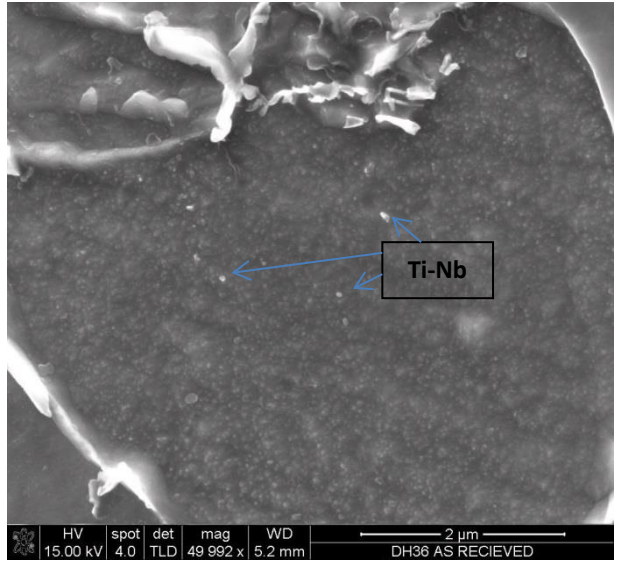
Figure 4.77: DH36 as received steel samples, high magnification showing Nb and Ti rich particles and particles which are both Ti-Nb rich.
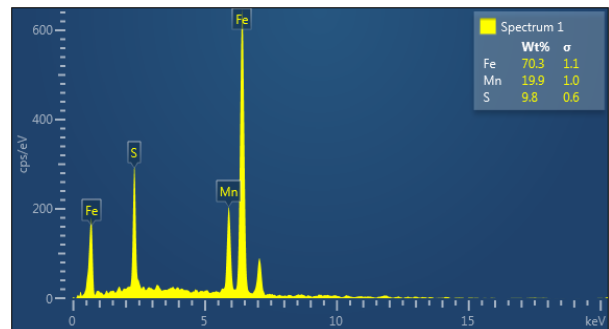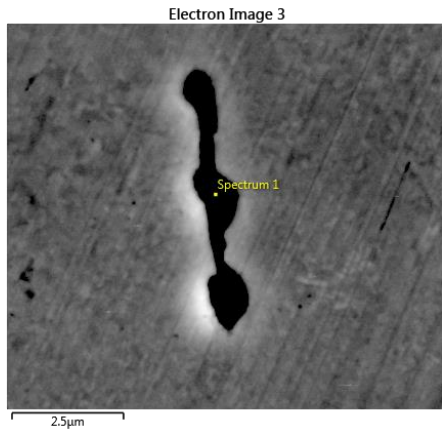
Figure 4.78: SEM-EDS of DH36 as received steel sample polished but in the un etched condition showing a MnS stringer.
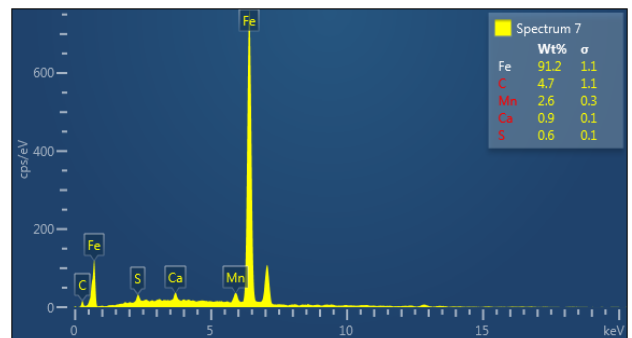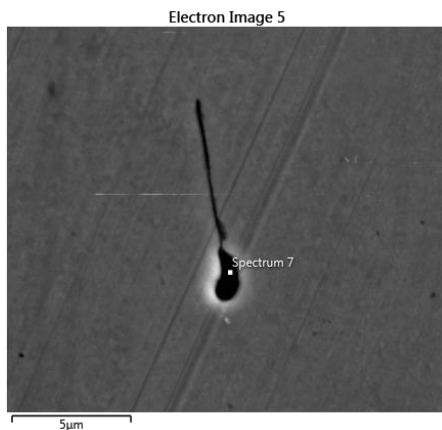
Figure 4.79: SEM-EDS of DH36 as received steel showing a MnS-CaS non-metallic inclusion.

169
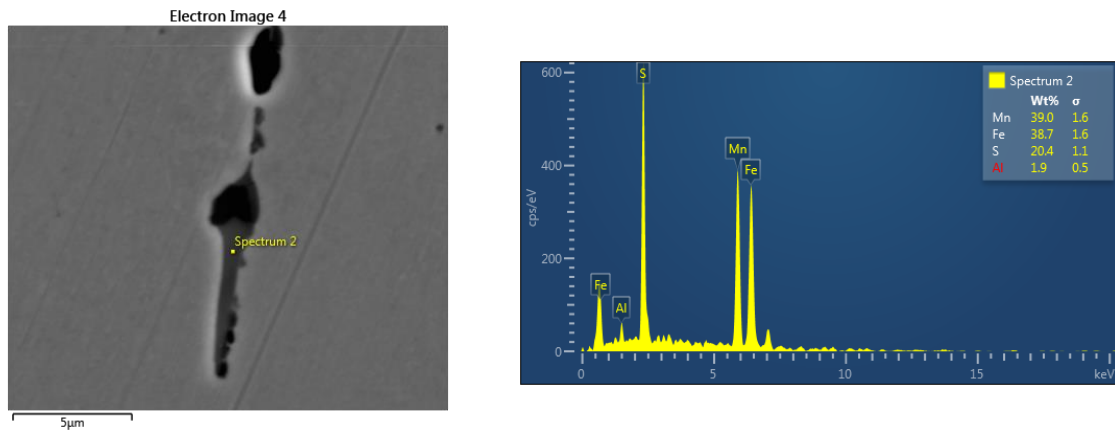
Figure 4.80: SEM-EDS of DH36 steel as received showing MnS-Al stringer like particle. .
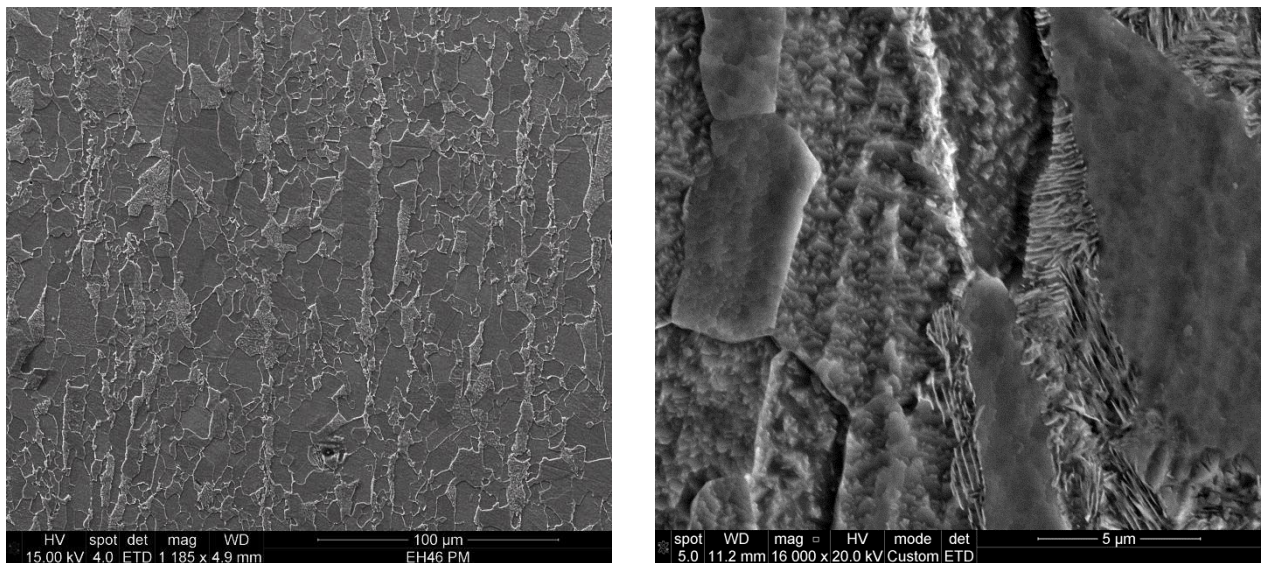
-a-   -b-

Figure 4.81: EH46 as-received steel polished and etched in 2% Nital showing -a- 20 μm ferrite grains and bands of pearlite, -a-low magnification. -b-higher magnification.

Figure 4.82: Ti and Ti-Nb rich particles in the as received EH46 steel.
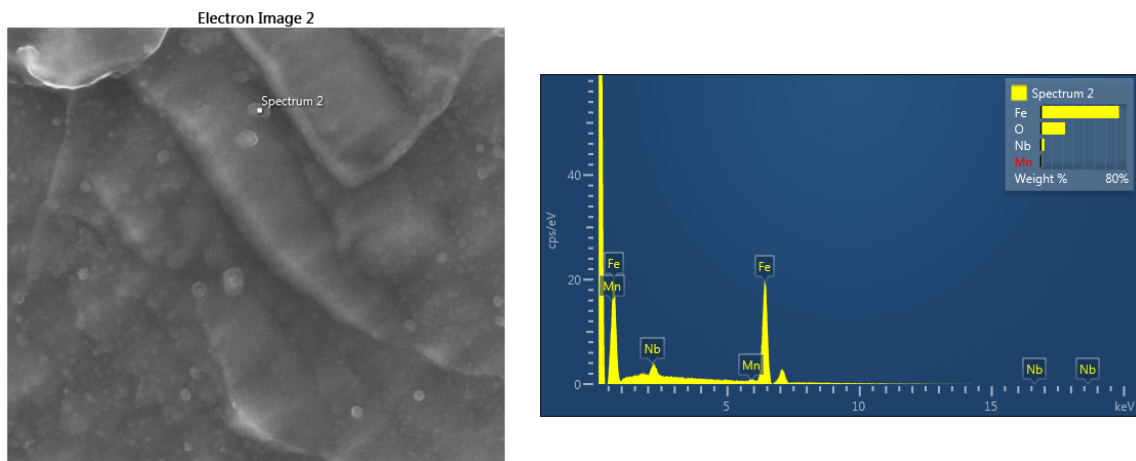
Figure 4.83: SEM-EDS of EH46 steel as received showing Nb rich particles.
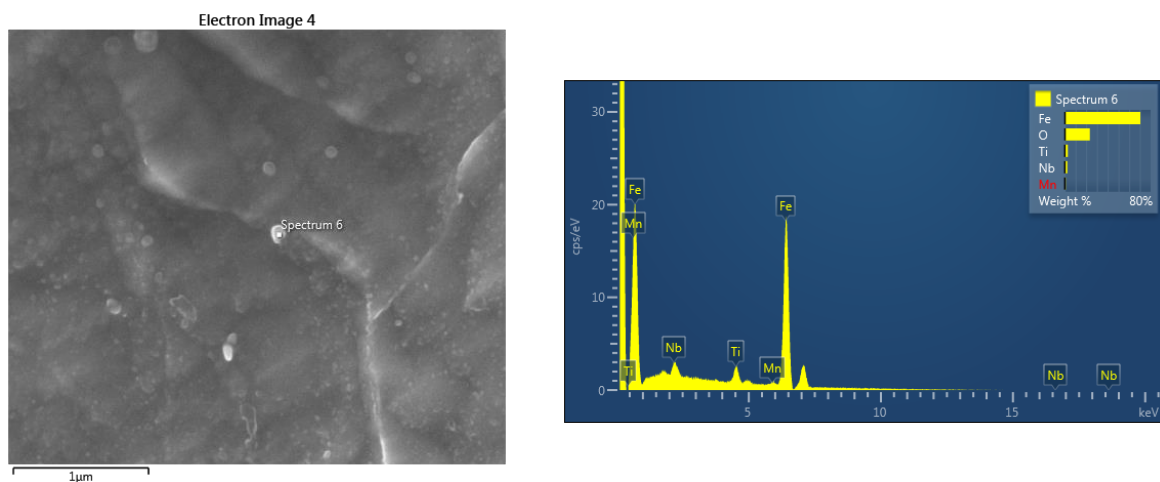
Figure 4.84: SEM-EDS of EH46 steel as received showing a Nb-Ti rich particle elements.

171
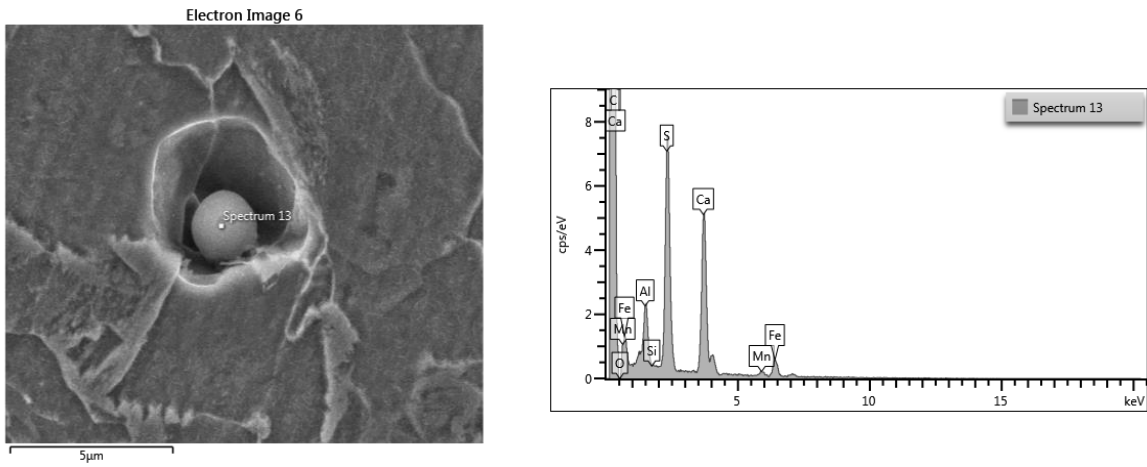
Figure 4.85: SEM-EDS of EH46 steel as received showing an alumina-calcium sulphide particle.
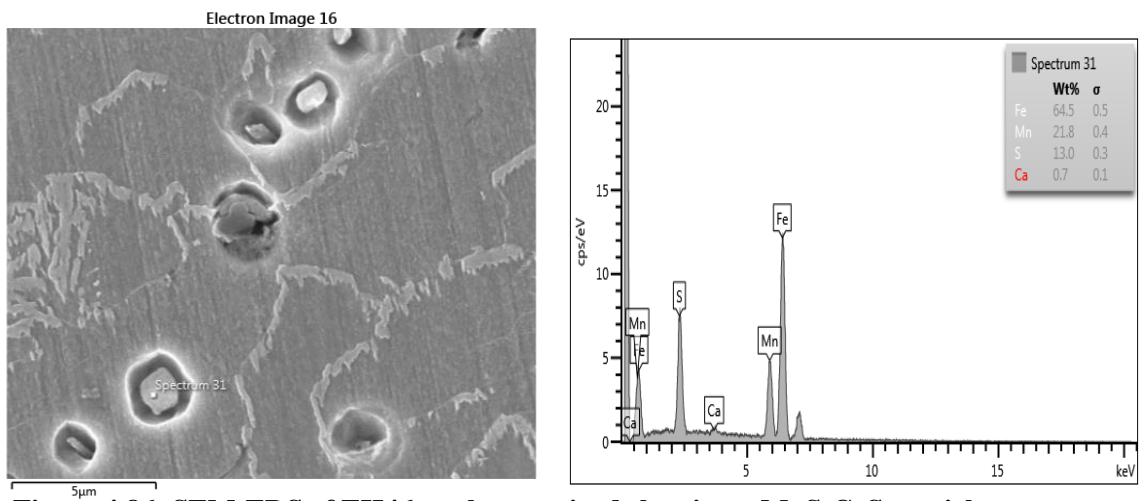
Figure 4.86: SEM-EDS of EH46 steel as received showing a MnS-CaS particles.

172

4.6 SEM FSW of DH36 Steel Samples at Low (W9) and High (W6) Tool Speeds.

4.6.1 Microstructure Evolution of Sample W9 (DH36) Steel.

A microstructural examination of the stirred zone of the as-welded DH36 steel sample (W9) revealed that the ferrite grains and pearlite bands of the parent material had disappeared and have been replaced by a mixed microstructure of bainite (B) and acicular ferrite (α_a), starting from the top of the SZ until 4mm from the probe end as shown in Figure 4.87. [78] Toumpis et. al. 2014 reported the same microstructure evolution in the SZ for welding DH36 with the same welding parameters and an increase in the presence of bainite when increasing the traverse speed due to the increase in cooling rate. However, they found, when keeping a balance of both the traverse and rotational speed (the same heat input), that the acicular ferrite/bainite mix reappeared. [92] McPherson et al. 2013 and [93] Lienert 2004 also reported an acicular ferrite microstructure formation in the SZ of welded steel (DH36) joints with a wide range of tool rotational/traverse speeds. [79] Reynolds et al. 2003 explained that a bainite and acicular ferrite microstructure evolved in the SZ of the same grade of (DH36) steel. They concluded that it was a consequence of the phase transformation of austenite during fast cooling and since no ferrite was observed in this region, it was evidence that FSW elevated the steel's temperature above the upper transformation temperature (A3). However, the rotational speed used for this weld was different from the current study, so a direct comparison has not been possible.

Figure 4.88 shows fine grains of ferrite (2µm average size) at the weld root (tool probe end). The refining in the ferrite grains from 15 µm in the PM to 2 µm in and near the probe end is reported previously by Failla [76] who explained that the ferrite grain refinement indicates that the material experienced dynamic recrystallization (DRX) as a result of high strain. The fine granular ferrite formation in the weld root instead of bainite/acicular ferrite was interpreted as a result of experience lower temperatures than the SZ and high strain rate leading to promoting the formation of ferrite by DRX. [8] Cater et. al. 2013 also reported the same grain refinement after welding 4mm, 6mm and 8mm thick DH36 plates as a result of DRX. [94] Fowler et al. 2016 reported that the weld root microstructure consisted of fine grains of ferrite which were attributed to the lower temperature and slower cooling rate compared to the top surface of the SZ. The grain size of ferrite in the weld root was finer than those in the PM due to the effects of high strain rate coming from material stirring. [92] McPherson et. al.

2012 suggested a dynamic recrystallization which in turn led to fine grains of ferrite in the probe region.

The HAZ as shown in figure 4.89 is 5μm ferrite grains with nodular cementite and some islands of pearlite. This results coincides with previous work on FSW DH36 [93][78] which reported a microstructure of ferrite grains, cementite and partially "shredded" pearlite as a result of the heat experienced but without the effect of strain rate.

4.6.2 Microstructure Evolution of Sample W6 (DH36).

The microstructure of welded sample W6 (DH36) showed heterogeneity (different types of microstructure) at the top of the SZ as a result of the higher tool speeds. In the middle of the stir zone the microstructure consisted mainly of acicular ferrite on both the AS and RS but there was some evidence of bainite (B) towards the RS as shown in figure 4.90 to 4.91 -a- and -b- respectively. The lower peak temperature experience on the RS and the higher traverse speed of the tool (than in W9 (DH36)) has resulted in a faster cooling rate than on the AS and thus more bainite has formed. The probe end, as shown in figure 4.92, consists of 4μm ferrite grains with short cementite plates; a higher temperature is expected in this region compared to the weld root of W9 (DH36) [77]. The HAZ on the AS and RS are shown in figure 4.93, bainite with 20μm average prior austenite grains is shown in the HAZ of AS compared to a matrix of ferrite with short plated cementite which indicate that AS has experienced a higher temperature and above the A_3 line [77]. The heterogeneity in microstructure has been reported in previous work carried out on DH36 steel [78] and interpreted as a result of higher tool rotational/traverse speeds which caused the material to experience different temperatures and cooling rate.
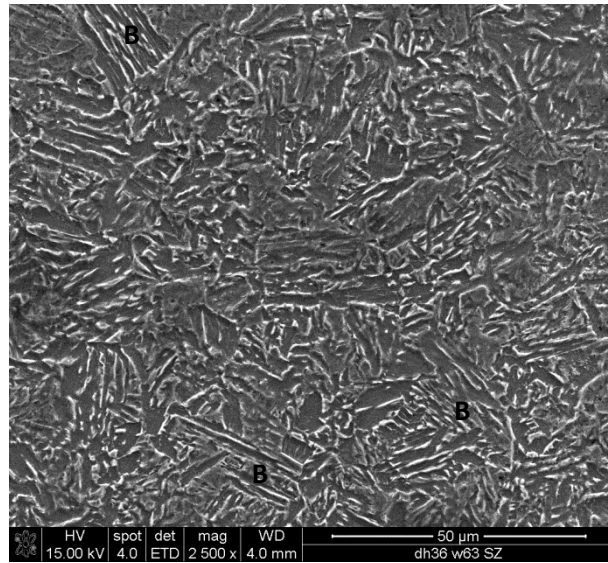
Figure 4.87: An SEM micrograph of the middle of the SZ of the low tool rotational/traverse speed (200RPM, 100mm/min) FSW. The SZ shows a mixture of bainite and acicular ferrite.
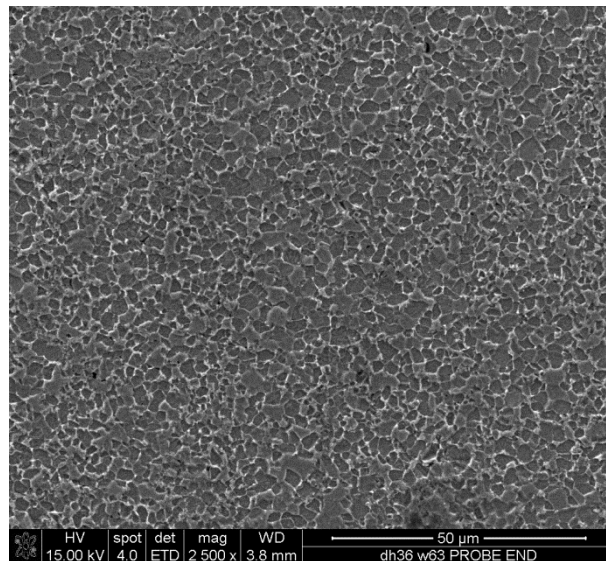
Figure 4.88: An SEM micrograph of low FSW tool rotational/traverse speeds (200RPM, 100mm/min) at the weld root, showing 2μm average ferrite grain size.
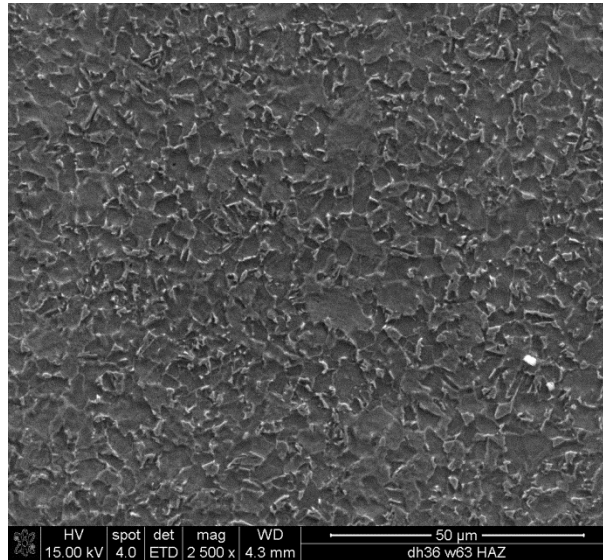
Figure 4.89: An SEM micrograph of the HAZ of low FSW tool rotational/traverse speeds W9 (200RPM, 100mm/min), 5μm ferrite grains (dark phase) with nodular cementite (bright phase).
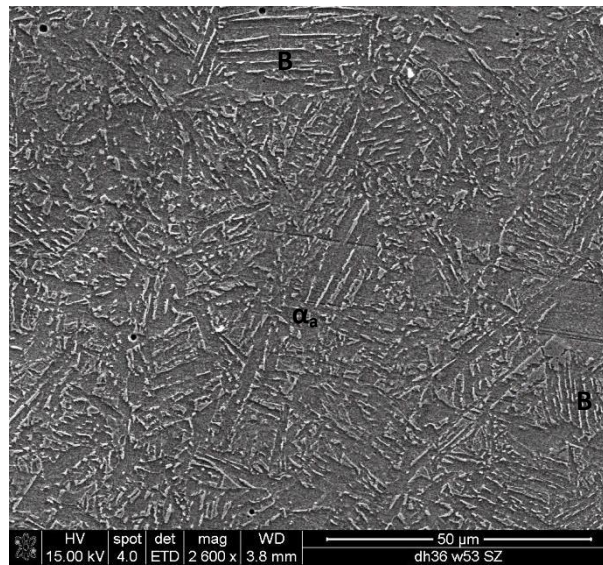
Figure 4.90: An SEM micrograph of the high FSW tool rotational/traverse speeds (W9) (550RPM, 400mm/min). The middle of SZ is a mixture of bainite and acicular ferrite.
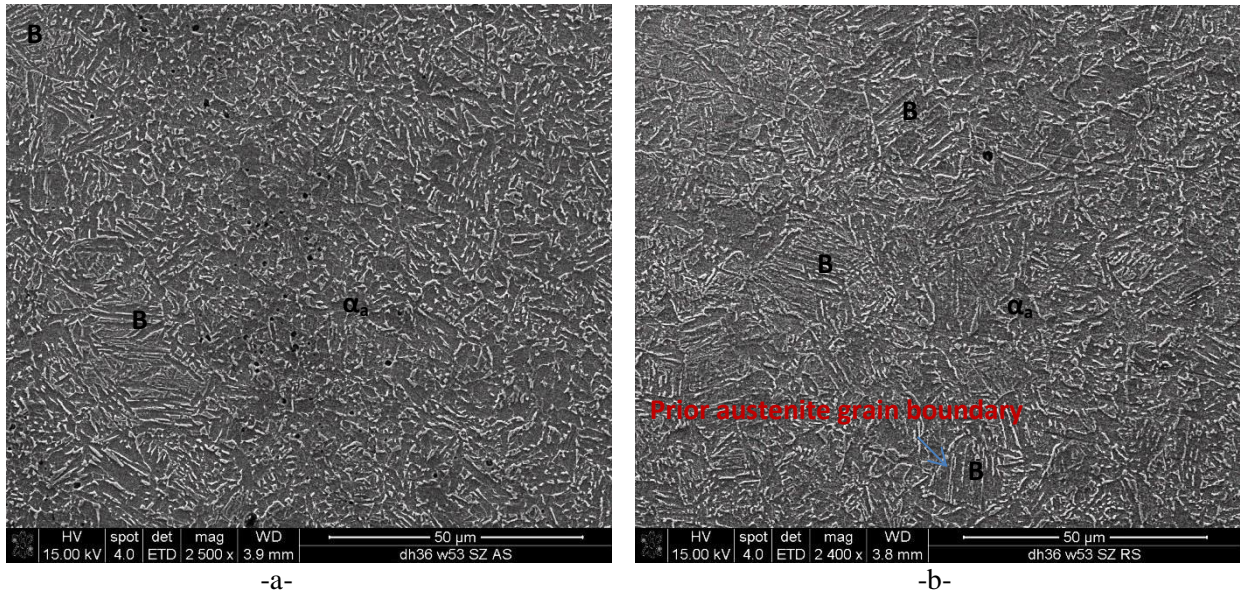
Figure 4.91: SEM micrographs of the high tool rotational/traverse speed FSW (W6) (550RPM, 400mm/min), showing the difference in microstructure of the SZ on the AS and RS.-a- AS showing more acicular ferrite, -b- RS showing more bainite with 25 μm average prior austenite grains.
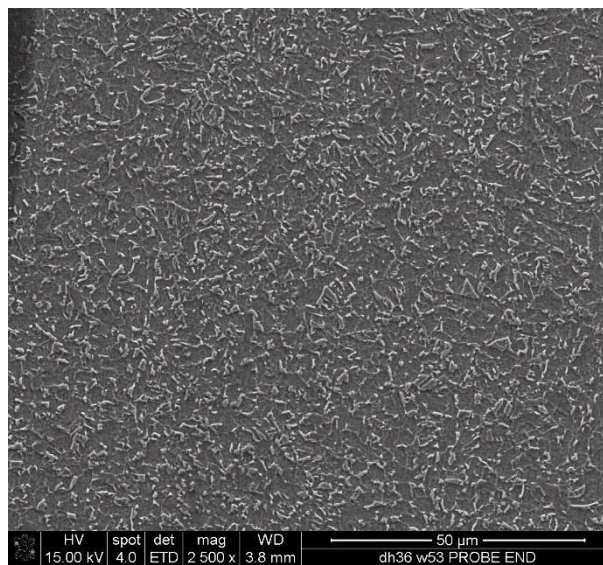
Figure 4.92: An SEM micrograph of the high tool rotational/traverse speeds (550RPM, 400mm/min) FSW (W6). The image shows the weld root with 4μm ferrite grains (dark phase) and short cementite plates (bright phase).
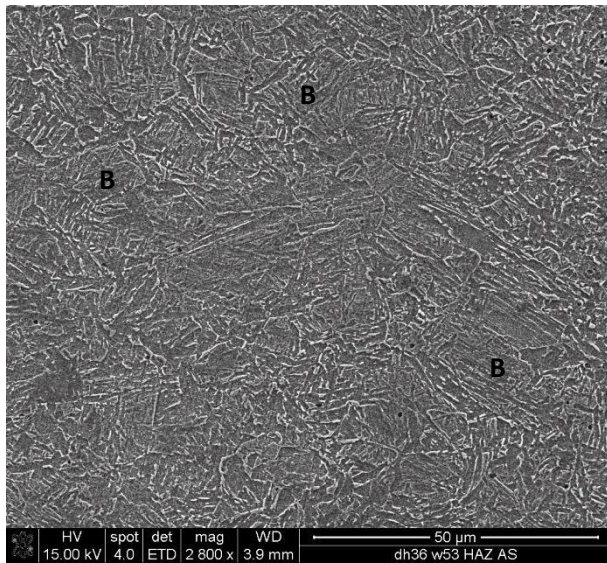
-a-
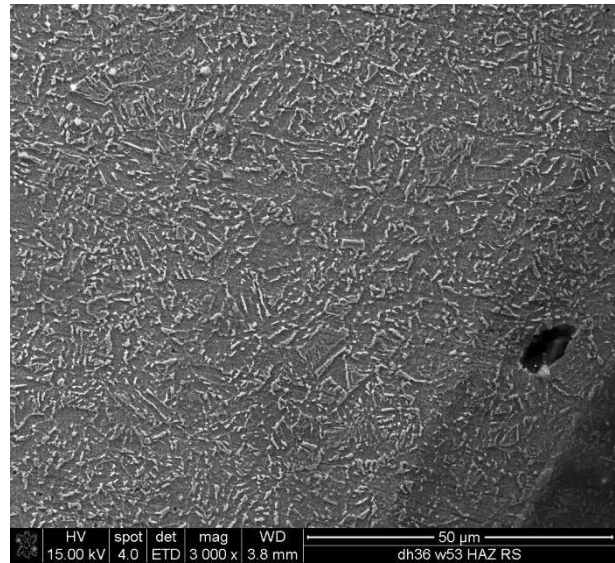
-b-

Figure 4.93: SEM micrographs of the high tool rotational/traverse speed FSW (W6) (550RPM, 400mm/min). The images show -a- the HAZ at the AS with Bainite and prior austenite grains with an average size of 20μm and -b- RS ferrite (dark phase) with some cementite precipitated at ferrite grains boundaries (bright phase).

4.7 SEM Analysis of Sample W1-W7 (EH46) Plunge Trials Experiment.

Following the plunge trials; it is evident that the microstructure of EH46 steel grade has experienced phase changes which will now be discussed for each of the affected regions. The locations of regions affected by tool plunge and rotation are shown in Figure 4.94; the red points refer to the location of SEM images as shown in Figure 4.95 to Figure 4.98. According to plunge depth and thermocouples measurements, samples W3, W4 and W5 are very similar and will be considered together. For this microstructural analysis welded sample W5 was chosen. Other welds including W1, W2, W6 and W7 have been considered separately.

Welded sample W1 region1 (TMAZ under the shoulder) (Figure 4.95 -a-) shows a mixed microstructure which consists of bainite (B) inside prior austenite grains as well as some acicular ferrite phase (α_a). The prior austenite grains have an average diameter of 55µm. Sample W2 region 1(under the shoulder) (Figure 4.96 -a-) shows bainite (B) with an average of 80µm prior austenite grains and some acicular ferrite (α_a). The difference in prior austenite grain size between samples W1 and W2 can be explained by examining the reading from the thermocouple (Table 4.4) which shows a higher temperature at W2 probably due to the higher plunge depth and significantly longer dwell time (Table 4.3). For both W1 and W2 the cooling rate at region 1 was high enough to form bainite and limited acicular ferrite α_a. Region 2 (probe side) at the top of W1 (Fig. 6 -b-) is bainite inside prior austenite grains of 40µm, some acicular ferrite phase α_a is also found. Region 2 (probe side) at the top of W2 (Figure 4.96 -b-) shows mainly acicular ferrite α_a with limited bainite, so the peak temperature is expected to be higher, and the cooling rate to be slower, than in W1. The finding from W1 and W2 welded samples suggests that controlling the plunge depth is important when considering the generation of heat in FSW under constant rotational speed and thus W2 has the higher plunge depth and has a higher percentage of acicular ferrite. Increasing the plunge depth even by parts of a millimetre inside the workpiece can make a significant difference to the heat generation and microstructural evolution. This finding is in accordance with Nagasaka and Nishihara [158] who showed that increasing the plunge depth has caused an increase in workpiece temperature. Fehrenbacher, et al. [139] reported that increasing plunge depth in FSW of aluminium from 4.6mm to 5mm caused the peak temperature to increase significantly from 400°C to 580 °C. Example of plunge depth effect on the heat generation during the FSW is shown in figure 4.24 (EH46 W9) where the temperature recorded by TCs has dropped by 118°C when the plunge depth decreased by 0.22mm.

Region 2 at the bottom of W1 (Figure 4.95 -c-) shows a ferrite-cementite aggregate (FCA) with nodular ferrite of 5 μm grain size. Region 2 at the bottom of W2 (Figure 4.96 -c-) shows a mix of bainite with prior austenite of 20 μm grain size and some acicular ferrite α_a. As discussed previously, the effect of plunge depth was apparent in generating more heat towards the sample depth in W2 compared to W1. Region 3 IHAZ top of W1 (Figure 4.95 -d-) showed a mix of bainite with prior austenite grains of 20μm and also some acicular ferrite α_a. Region 3 Inner Heat Affected Zone (IHAZ) at the top of W2 (Figure 4.96 -d-) showed mainly acicular ferrite α_a. These microstructures of both W1 and W2 indicate that the temperature at the IHAZ top (Region 3 top) is still high and above the A_3 line in the Fe-C equilibrium phase diagram which is enough for a phase transformation in this type of steel. The bottom of region 3 in W1 showed coarse FCA microstructure, whereas a matrix of ferrite with short plated cementite microstructure was found in W2 (as shown in Figure 4.95 -e- and Figure 4.96 -e- respectively). Again, from the microstructure evolution, the expected temperature of W1 at this location is less than in W2 due to the difference in plunge depth and/or dwell time. Figure 4.95 -f- and -g- show the microstructure of W1 region 4 (OHAZ) top and bottom respectively. They show nodular ferrite with 6 μm grain size in the top of region 4 (OHAZ) while the ferrite grain size at the bottom of this zone was 7-8 μm. Region 4 (OHAZ) of W2 shown in Figure 4.96 -f- also contained a nodular ferrite microstructure but with an average grain size of 10 μm, also cementite was precipitated on the grain boundaries of ferrite. The bottom of the former region as shown in figure 4.96 -g- is a 9 μm ferrite grain decorated by cementite. The region just under the probe end of W1 and W2 as shown in Figure 4.95 -h- and Figure 4.96 -h- respectively shows a similarity in microstructure which is a ferrite-cementite aggregate (FCA) and some islands of bainite with 15 μm prior austenite grains. This similarity in microstructure in W1 and W2 at the probe end is a sign of the close/similar amount of heat generation in that region and thus similar temperatures range experienced by the material in contact with that part of the tool is expected. This finding indicates that although the W1 microstructure experienced slightly lower temperature at the shoulder and around the probe side compared to W2, the probe end for both cases (W1 and W2) shows no evidence of a significant heat difference. Schmedit et al. 2005 [28] [51] showed analytically that the probe end contribution in heat generation for the hybrid PCBN FSW tool was less than 3% because of the smaller probe end/workpiece contact area compared to other tool parts.

Samples W3, W4, W5 and W7 showed similarity in microstructure and thus their description was organised in Table 4.14. Figure 4.97 shows the macrograph of W5 and the microstructure of the regions of interest. A comparison in microstructure of these welds with W1 and W2 are carried out here. The microstructure at region 1 (under shoulder) of W1 and W2 showed a bainite phase with prior austenite grains larger than for the 120 RPM group as reported in Table 4.14. This in turn suggests that the peak temperatures at the shoulder/workpiece contact region were higher in W1 and W2. This finding is in accordance with other work [51], [160] and [161] which shows that the heat input increases with the increase in tool rotational speed. Region 2 (probe side) top and bottom of W2 also showed a microstructure evolution with an expected temperature higher than the 120 RPM group because of the higher rotational speed (readings of TC2 and TC5 in Table 4.4). This indicates that in W2 the rotational speed effect was overriding the slight increase in plunge depth of the 120RPM group. W1 showed some similarity in microstructure of the 120RPM group recorded in Table 4.14 at region 2 top and bottom, however, the size of the prior austenite grains of W1 at region 2 top was double. This similarity in microstructure despite the higher rotational speed of W1 compared with the group of samples produced at 120RPM, can be attributed to the lower plunge depth of W1 (about 0.5mm as reported in Table 4.6). The plunge depth which exceeds 11mm in 120RPM group has caused an increase in the contact area between the tool and the workpiece which in turn produced more heat towards the plate thickness. The microstructure for sample W7 region 1 under the tool shoulder shows more acicular ferrite compared to W3, W4 and W5 while the probe end showed coarser ferrite grains as shown in figure 4.99 which indicates that more heat is produced during the FSW process as a result of increasing the plunge depth by about 0.1mm.

Figure 4.98 shows the microstructure of sample W6 for all regions of interest. Although the rotational speed of sample W6 was the same as for W3, W4, W5 and W7, it shows some difference in microstructural evolution especially in the direction towards the probe side/end. A mix of acicular ferrite microstructure and bainite with prior austenite grains of 35 μm was found under the shoulder in region 1. This microstructure is similar to the one found in the 120RPM group. This finding supports the assertion that increasing plunge depth greatly affects the microstructure towards the sample depth but less so on the top. Region 2 top (Figure 4.98 -b-) showed higher amount of acicular ferrite microstructure similar to that found in W2. Compared to other cases of the 120 RPM group which showed a mix of bainite and acicular ferrite, region 2 top of W6 seems to have experienced higher temperatures and a

slower cooling rate and thus a microstructure of acicular ferrite was dominant. Region 2 bottom (Figure 4.98 -c-) showed ferrite grains (7 μm) with cementite precipitated at their grain boundaries. Region 3 (IHAZ) showed acicular ferrite in the top and a mix of acicular ferrite and nodular ferrite in the bottom. This microstructural evolution gives evidence of higher temperature experienced by W6 compared to the microstructure of the other 120 RPM group which shows a mix of bainite and FCA because of the difference in plunge depth. The microstructure of W6 region 3 (IHAZ figure 4.98 -d- and -e-) is also similar to that found in W2, however, W6 region 3 bottom (figure 4.98 -e-) has showed some nodular ferrite in addition to short plated cementite. Region 4 OHAZ showed ferritic grains of (7-8 μm) with a mix of short plated and nodular cementite. The Probe ends showed a ferritic matrix with a short plated cementite (FCA) microstructure which was similar to other 120 RPM welds. It was also similar to 200 RPM group, however, some bainite was found in samples W1 and W2.
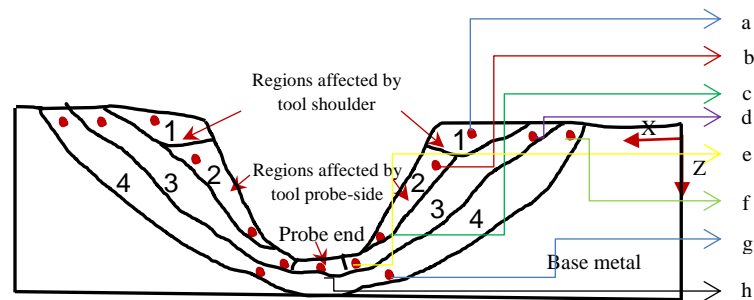
Figure 4.94: Affected regions identified following the weld tool plunge trials. TMAZ under the shoulder (region 1), TMAZ around the probe side (region 2), Inner Heat Affected Zone, (IHAZ) (region 3), Outer Heat Affected Zone, (OHAZ) (region 4) and probe end. The red dots refer to the location that SEM images were taken for each region (-a- to -h-).
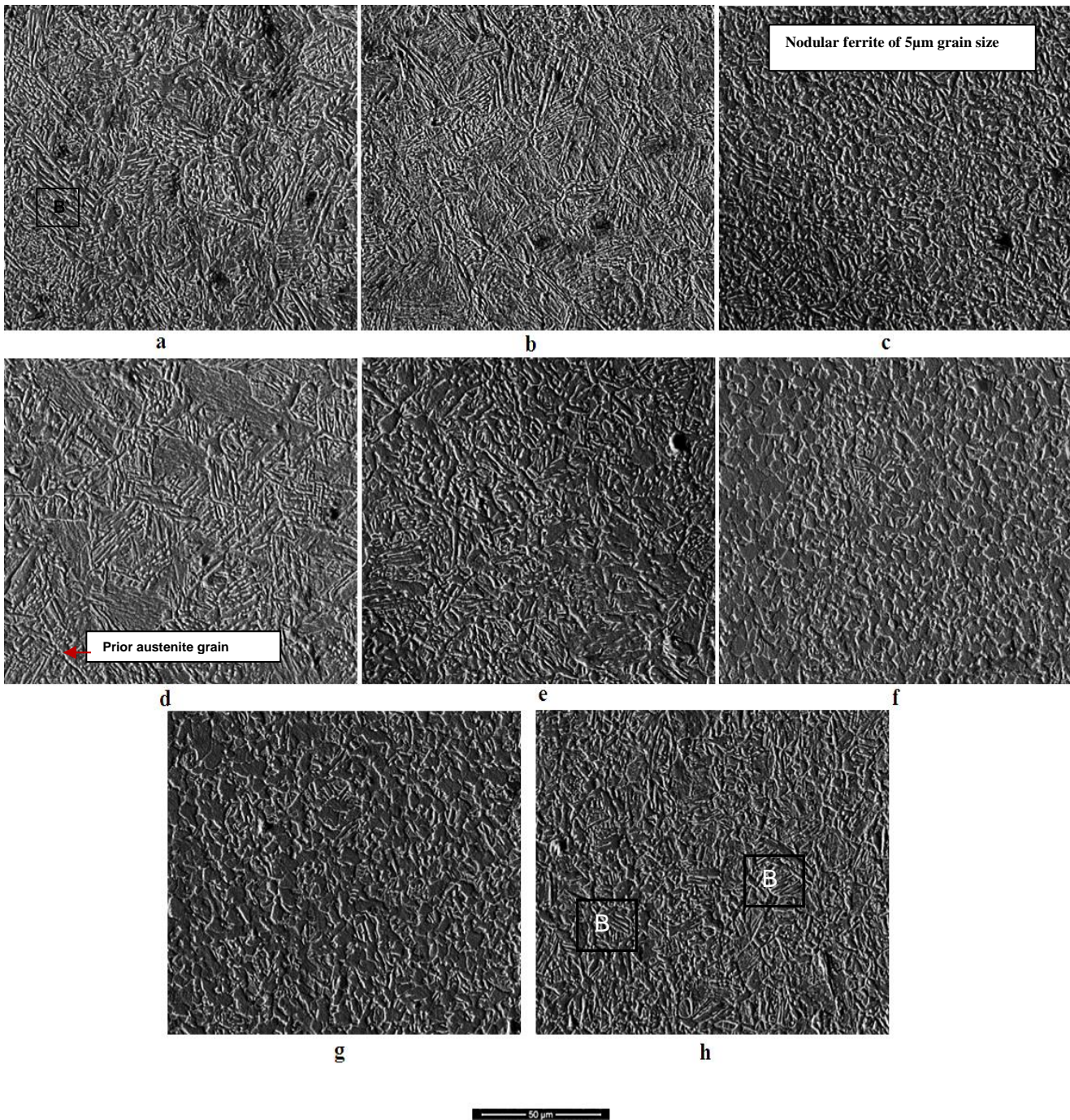
Fig. 4.95: SEM micrographs of EH46 sample W1 for all regions of interest: -a- W1 (Region 1) under shoulder bainite with 55µm prior austenite size and some acicular ferrite. -b- W1 (Region 2) Probe side top region contains bainite with 40µm prior austenite and some acicular ferrite. -c- W1 (Region 2) probe side bottom region showing fine ferrite-cementite aggregate (FCA) with some nodular ferrite of 5m grain size. -d- W1 (Region 3) IHAZ top region showing a mixture of acicular ferrite and bainite phase with prior austenite of 20µm. -e- W1 (Region 3) IHAZ bottom region showing a coarser ferrite-cementite aggregate (FCA), -f- W1 (Region 4) OHAZ top region contains nodular ferrite with 6µm grain size. -g- Region 4 OHAZ bottom showing a nodular ferrite phase of 7-8 µm grain size with cementite precipitations at ferrite grains boundaries. -h-probe end ferrite-cementite aggregate (FCA) and some islands of bainite in 15 µm prior austenite grains.
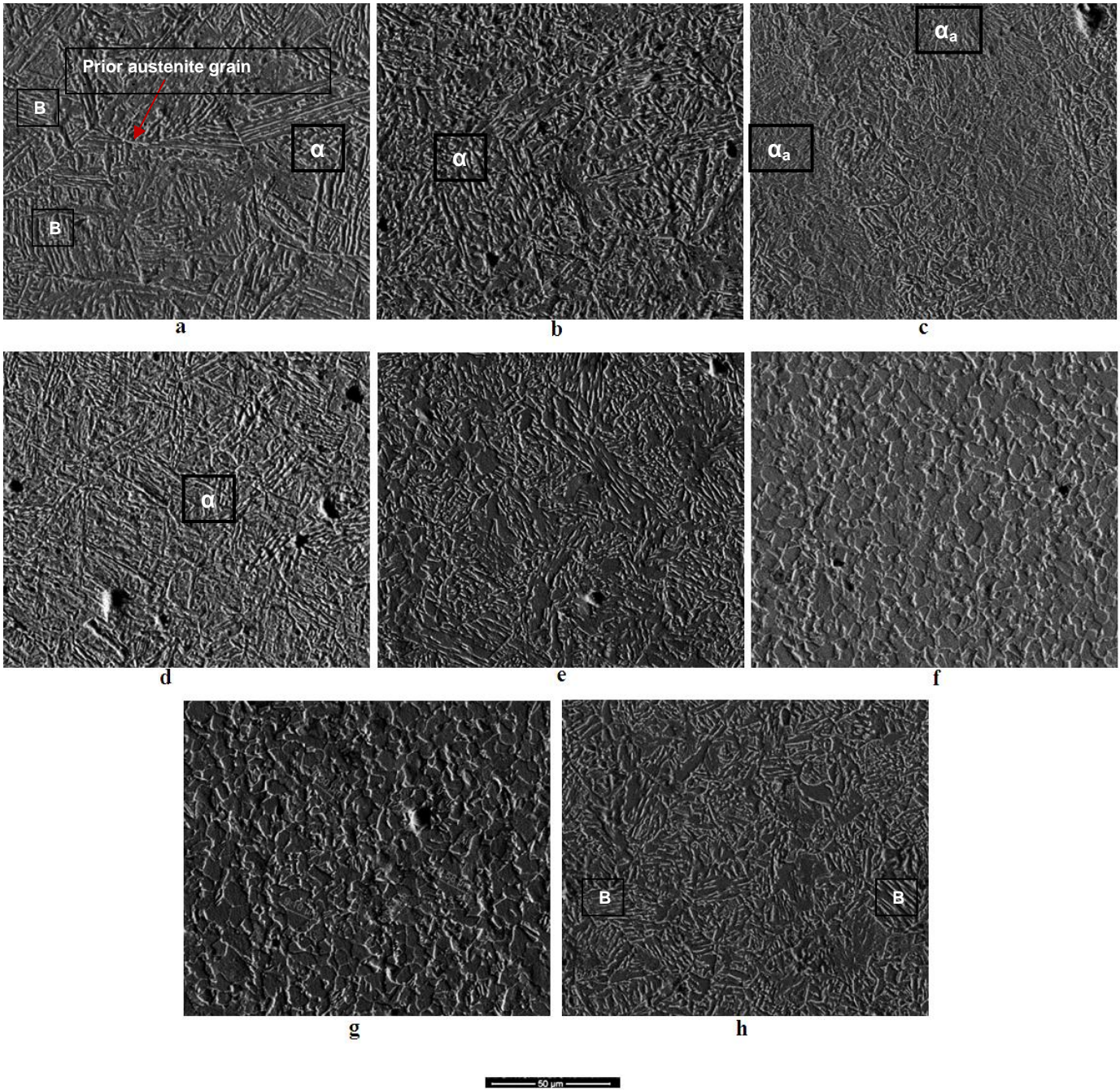
Fig. 4.96: An SEM micrographs of sample W2 (EH46) for all regions of interest. -a-W2 (Region 1) under shoulder region contains bainite inside prior austenite grains of 80 µm) and α_a. -b-W2 (Region 2) probe side top mainly α_a. -c-W2 (Region 2) probe side bottom contains bainite inside prior austenite grains of 20 µm and α_a. -d-W2 (Region 3) IHAZ-top is mainly α_a. -e-W2 (Region 3) IHAZ-bottom is a matrix of ferrite with short plated cementite. -f-W2 (Region 4) OHAZ-top, nodular ferrite microstructure with average of 12 µm grain size. -g-W2 (Region 4) OHAZ-bottom, nodular ferrite microstructure with average of 12 µm grain size. -h-W2 Probe end, ferrite-cementite aggregate (FCA) and some islands of bainite in 15 µm prior austenite grains.
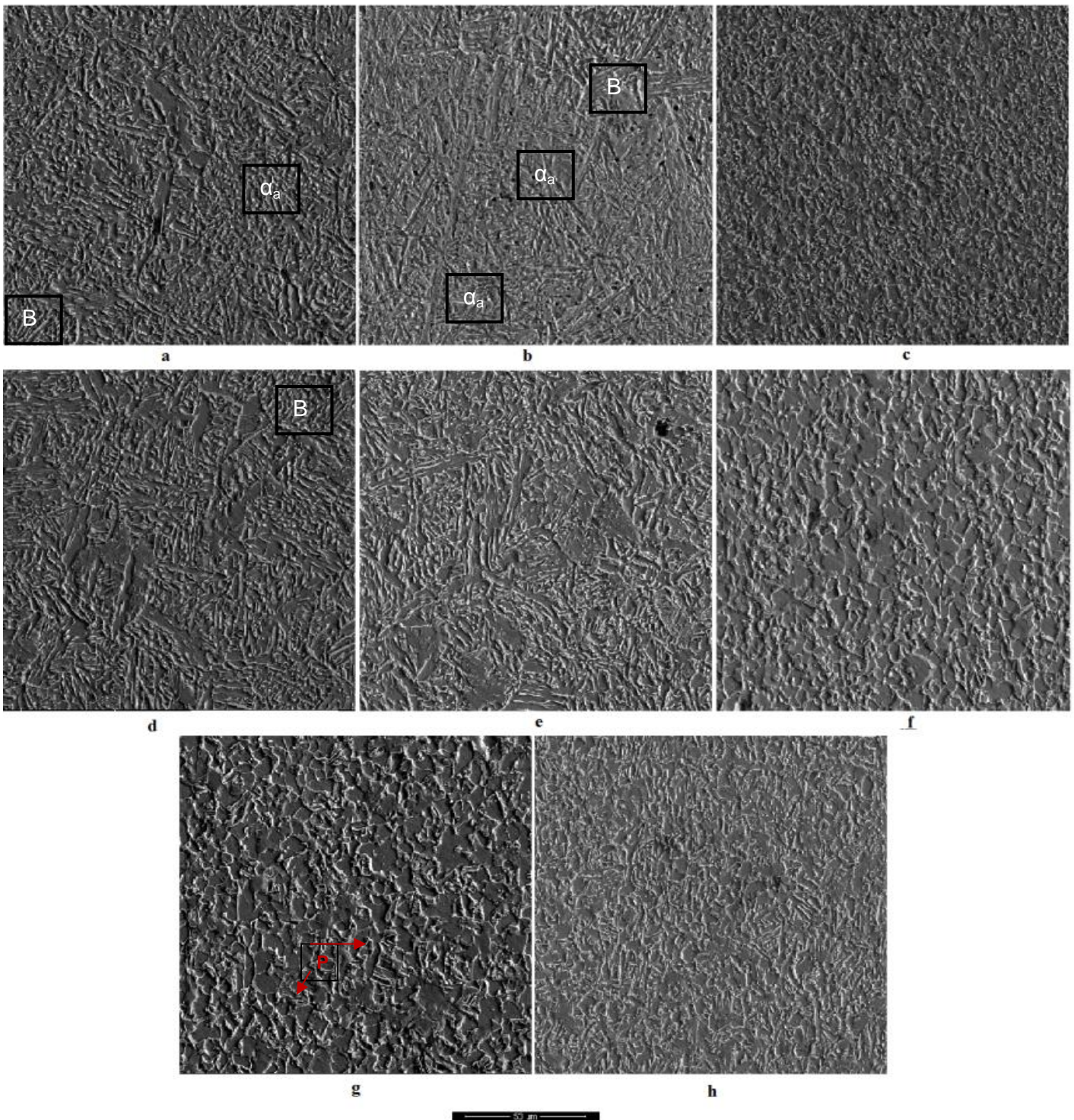
Fig. 4.97: SEM Micrographs of sample W5 (EH46) for all regions of interest. -a-W5 (Region 1) under shoulder, contains mix of bainite inside prior austenite grains of 40 μm and α_a. -b-W5 (Region 2) probe side top, contains mix of bainite inside prior austenite grains of 20 μm and α_a. -c-W5 (Region 2) probe side bottom, fine ferrite grains with average of 5 μm grain decorated by cementite. -d-W5 (Region 3) IHAZ-top, mix of bainite inside 15 μm prior austenite grains and ferrite cementite aggregate. -e-W5 (Region 3) IHAZ-bottom, Longitudinal ferrite matrix with a mix of longitudinal and nodular cementite. -f-W5 (Region 4) OHAZ-top, ferrite matrix with cementite precipitated on the grain boundaries, [nodular ferrite grain measured 7-8 μm]. -g-W5 (Region 4) OHAZ- bottom, ferrite grains (9 μm) decorated by cementite with some islands of pearlite. -h-W5 Probe end, ferritic matrix with fine (0.3 μm) short plate-like cementite.

185
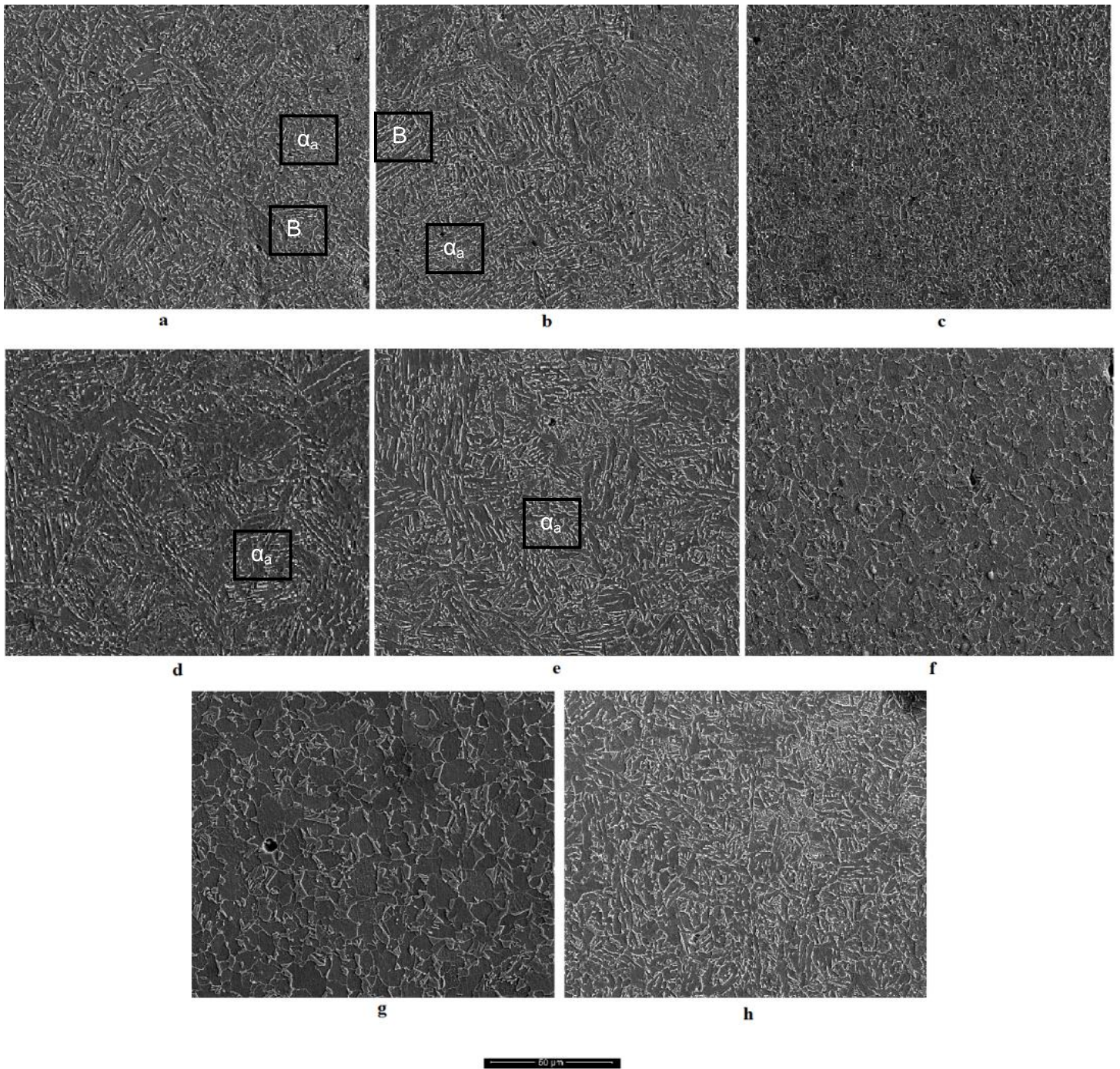
Fig. 4.98: SEM micrographs of EH46 W6 for all regions of interest. -a-W6 (Region 1) showing A mix of acicular ferrite microstructure and bainite phase with prior austenite grains of (35 μm). -b- W6 (Region 2) top is mainly acicular ferrite -c-W6 Region 2-bottom, ferrite grains (7 μm) with cementite precipitate at the grain boundaries. -d-W6 Region 3 IHAZ top, acicular ferrite . -e- W6 Region 3 IHAZ bottom, mix of acicular ferrite and nodular ferrite., -f- W6 region 4 top, ferrite grains of (7-8 μm) with a mix of short plated and nodular cementite. g- W6 region 4 OHAZ bottom ferrite grains of 8 μm with nodular cementite. -h-W6 probe end, ferritic matrix with short plated cementite (FCA) microstructure.

Table 4.14: Microstructure of the different affected regions of samples W3, W4, W5 and W7, (EH46).

Region No.	Affected Region	Main microstructure	Average prior Austenite grains size (µm) of B phase	Estimated temperature range (°C) (Using Di Martino et al 2014 assumption) [77]	Estimated cooling rate °C/s (using Di Martino et al 2014 assumption) [77]
1	Under the shoulder	Mix of bainite and acicular ferrite. More acicular ferrite in W7.	W03(33±2) W04(35±2) W05(40±3) W07(35±2)	1200-1300°C in the top surface and 1000-1100°C for the bainite phase	20-30°C/s for FCA and 30-40°C /sfor B phase
2	Probe side	Top of the probe side is a mix of bainite and acicular ferrite, bottom of the probe side is a fine ferrite (4-5 µm) decorated with cementite.	W03(18±1) W04(19±2) W05(20±2) W07(25±2)	1200-1300°C	30-40°C/s
3	IHAZ (Top) IHAZ (bottom)	Bainite with a coarser ferrite (2.5 µm) and cementite (1 µm) bands, the cementite bands are shorter than in regions 1 and 2. Longitudinal ferrite matrix with a mix of longitudinal and nodular cementite.	15±2	1100-1000°C	20-25°C/s
4	OHAZ	Ferrite matrix with cementite precipitated on the grain boundaries, [nodular ferrite grain measured 7-8 µm] the microstructure in welds tends to be ferrite grains (9 µm) decorated by cementite with some islands of pearlite toward the bottom of this region.	not clear	1000-900 °C	25-30°C/s
----	Probe end	Ferritic matrix with fine (0.3 µm) short plate-like cementite. Coarser grains in W7	not clear	1000-1100 °C	20-30°C/s for FCA and 30-40 °C/s For B

| Region 1 under shoulder | Probe end |
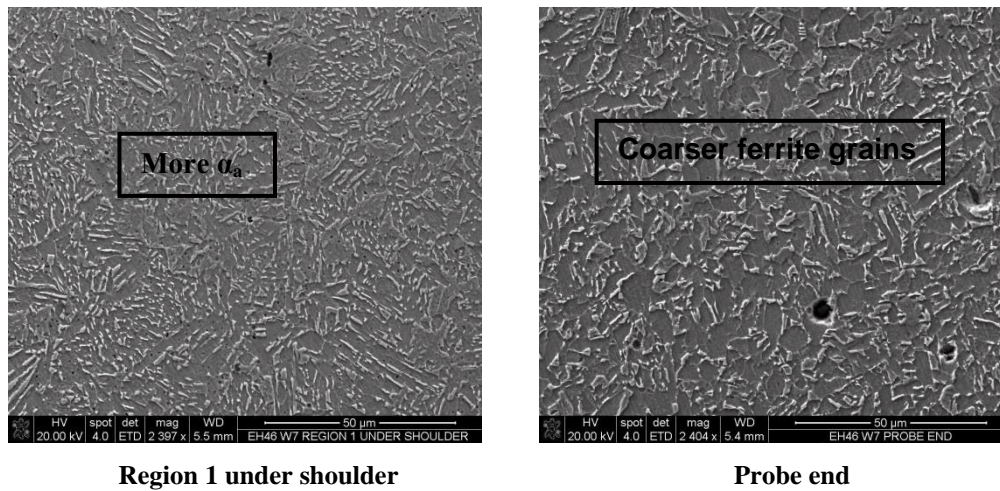
Figure 4.99: SEM Micrographs of sample W7, (EH46), Region 1 under the shoulder, the microstructure is mainly α_a and at the probe end, coarser ferrite grains.

From all the studied cases (Samples W1-W7 (EH46) it can be inferred that the microstructure evolution was spatial (as a function of the distance from tool radius). Regions in contact with the FSW tool have undergone phase transformations commensurate with the fact that they had experienced higher temperatures. It is also shown from the macrographs of Figure 4.35 which measured the TMAZ by the IFM as reported in table 4.6 that the regions affected by the tool probe is bigger (represent about 70% from the total TMAZ and HAZ) than those affected by the tool shoulder, thus it is proposed that a FSW tool with a stationary shoulder and slightly higher rotational speed can generate enough heat required for friction stir welding. This finding will be represented and discussed in the modelling and simulation section.

It can be noted from the microstructural evolution for all the plunge/dwell samples under study that the total TMAZ (region1 and region 2) has experienced phase transformation and thus are assumed to be fully austenitic during FSW. This region which is also called *the shear layer* is believed to experience metal flow at a minimum temperature which is above the A_3 of the Fe-C equilibrium phase diagram. This finding will also be represented and discussed in the modelling and simulation section.

4.8 SEM Images of FSW Samples W8 and W10 (EH46) Showing the SZ and HAZ.

The microstructures of samples W8 (150RPM, 50mm/min) and W10 (150RPM, 100mm/min) (EH46) steel have been examined using the SEM in order to understand the phase transformations that have taken place for each weld. It is expected that both welds have experienced almost the same heat generation as the rotational speed are same, however, the cooling rate of W10 will be higher as it experienced higher tool traverse speed than in W8. The difference in cooling rate between the two welds is clear when examining the microstructure especially in the top of the SZ as shown in figure 4.100 to figure 4.102. The top-middle of SZ of W8 and W10 are shown in figure 4.100 -a- and -b- respectively. Welded sample W8 shows a ferrite matrix with a mix of short plated and granulated cementite while welded sample W10 consists of a ferrite matrix with short plated cementite and some bainite which indicates that faster cooling rate has occurred in W10.

The RS and AS of welded sample W8 shown in figure 4.101 low magnification and figure 4.102 higher magnification -a- and -b- respectively shows evidence of acicular ferrite (α_{ac}) with some bainite inside large prior austenite grains (150 micron). There are also some ferrite grains (20μm) and, on the AS, acicular ferrite with some nodular ferrite of 20 μm. Allotriomorphic (α_{all}) ferrite appears in both the AS and the RS of the SZ with more bainite on the RS. The presence of α_{all} indicates a low cooling rate (less than (30°C/s) [162]) and high homologous temperature.

The RS and AS of the welded sample W10 (EH46), shown in figure 4.103 low magnification and figure 4.104 higher magnification -a- and -b- respectively, shows a mixture of acicular ferrite with bainite with a finer microstructure on the AS. Compared to sample W8, the cooling rate in W10 was higher as the microstructure includes more bainite and the α_{all} was absent

The probe end (weld root) of samples W8 and W10 are shown in figure 4.105 -a- and -b- respectively, a microstructural examination of the weld root of W8 revealed fine ferrite grains (4 μm). As described earlier this is attributed to the effects of high strain rate and slower cooling rate (dynamic RX) [76] [8] [94]. A similar examination of the microstructure of FSW sample W10 (EH46) probe end revealed larger ferrite grains (10μm) with mix of nodular ferrite and short plates of cementite.

Figure 4.106 -a- and -b- show the microstructures of the HAZ on the RS of FSW sample W8 and W10 respectively. 15µm ferrite grains with nodular and short plated cementite and some island of pearlite was in the HAZ of W8 at RS while 12 µm ferrite grains with nodular and short plated cementite and some islands of pearlite was in the HAZ of W10 at RS. The previous work on DH36 [93][78] reported a similar microstructure of ferrite grains, cementite and partially shredded pearlite as a result of thermal history experienced without the effect of strain rate. The AS in W8 and W10 showed clear IHAZ and OHAZ which are shown in figure 4.107 and figure 4.108 -a- and -b- respectively. The microstructure of as welded sample W8 IHAZ on the AS revealed 20µm ferrite grains with short plated cementite and some bainite, the OHAZ on the AS showed 10 µm ferrite grains with nodular and short plated cementite as shown in figure 4.107 -a- and -b- respectively. The absence of pearlite in the IHAZ and OHAZ on the AS of W8, is an indication that a higher temperature has been experienced at the AS compared to the IHAZ and OHAZ at the RS of W8. The IHAZ W10 on the AS included a ferrite matrix with plates of cementite as shown in figure 4.108 -a-; this indicates a faster cooling rate has occurred compared to the IHAZ on the AS of W8 as shown in figure 4.107 -a-.

-a-

-b-
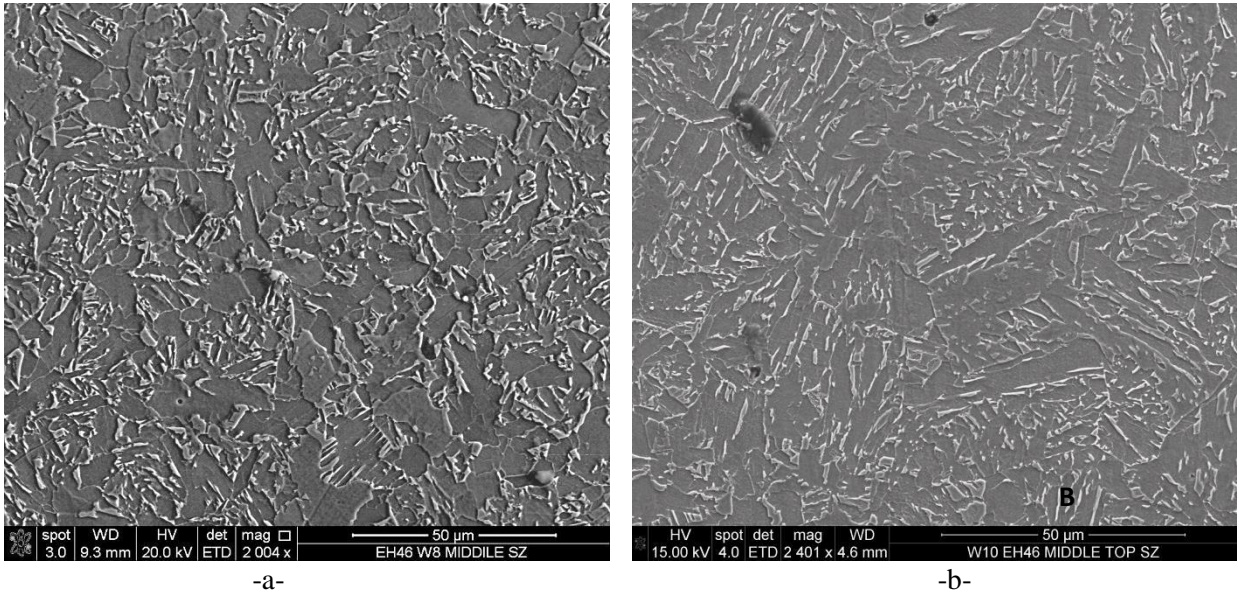
Figure 4.100: SEM micrographs of -a- FSW sample W8 (EH46) showing that the top-middle of the SZ consists of a ferrite matrix with a mixture of short plated and granulated cementite. -b-FSW sample W10 (EH46) showing that the middle of the SZ consists of a ferrite matrix with short plated cementite and some bainite phase.

-a-

-b-
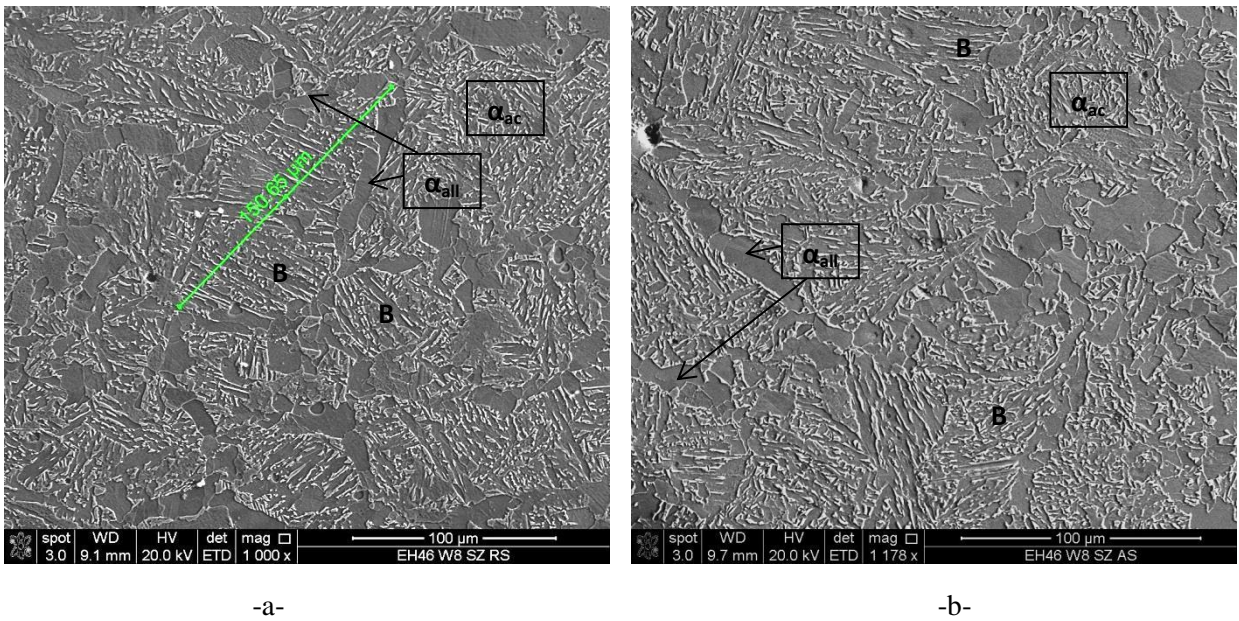
Figure 4.101: SEM micrographs of -a- FSW sample W8 (EH46) SZ, RS showing acicular ferrite with some bainite (B) inside 150 micron prior austenite and some 20µm ferrite grains. -b- FSW EH46 W8 SZ, AS showing acicular ferrite with some nodular ferrite of 20 µm. Allotriomorphic (α$_{all}$) ferrite also appears in both SZ of AS and RS.

191

-a- -b-
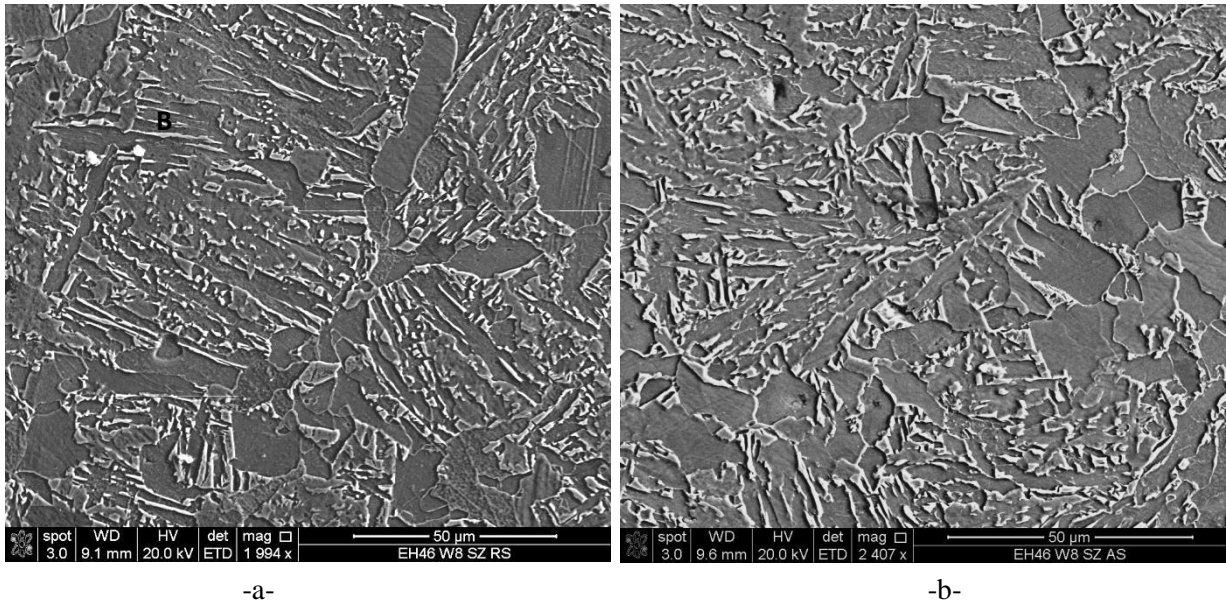
Figure 4.102: SEM micrographs of -a- FSW sample W8 (EH46) SZ, RS showing higher magnification, acicular ferrite with some bainite (B) inside 150 micron prior austenite and some 20µm ferrite grains. -b- FSW sample W8 (EH46) SZ, AS showing higher magnification, acicular ferrite with some nodular ferrite of 20 µm. Allotriomorphic (α_all) ferrite is also present in both SZ of AS and RS.

-a- -b-
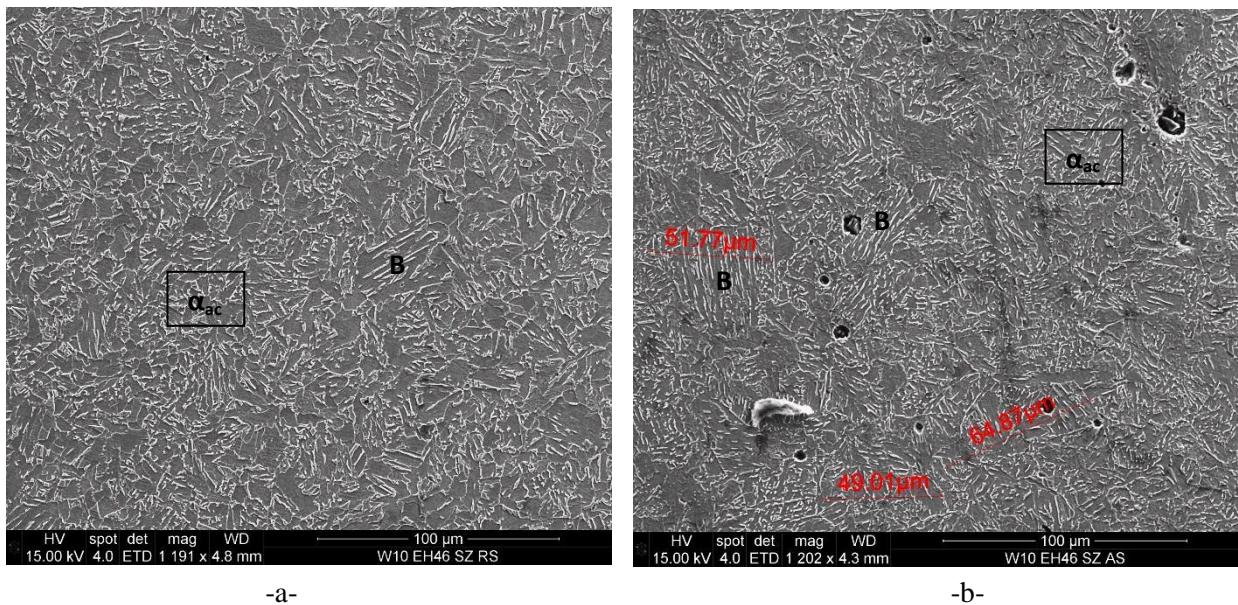
Figure 4.103: SEM micrographs of -a- FSW sample W10 (EH46) SZ, RS showing a mixture of acicular ferrite with bainite (B) phase. -b- FSW sample W10 (EH46) SZ, AS shows a mixture of acicular ferrite with bainite B.

192
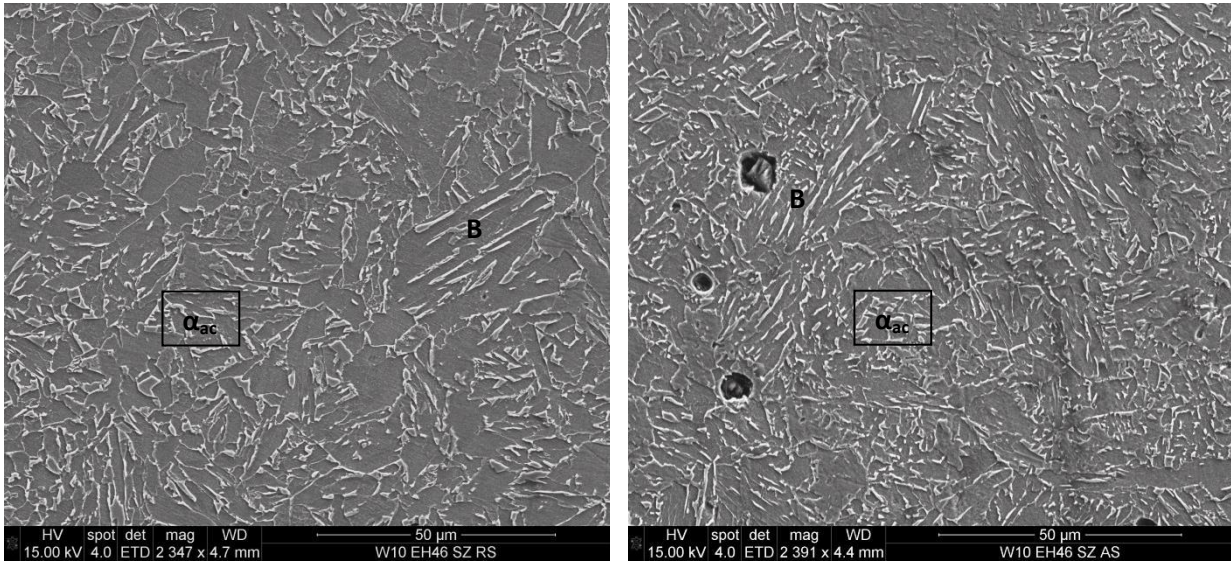
<center>-a-</center>

<center>-b-</center>

Figure 4.104: SEM micrographs showing -a-FSW sample W10 (EH46) SZ, RS showing at higher magnification, a mixture of acicular ferrite with bainite (B) phase, -b- FSW sample W10 (EH46) SZ, AS showing, at higher magnification, a mixture of acicular ferrite with bainite (B) .
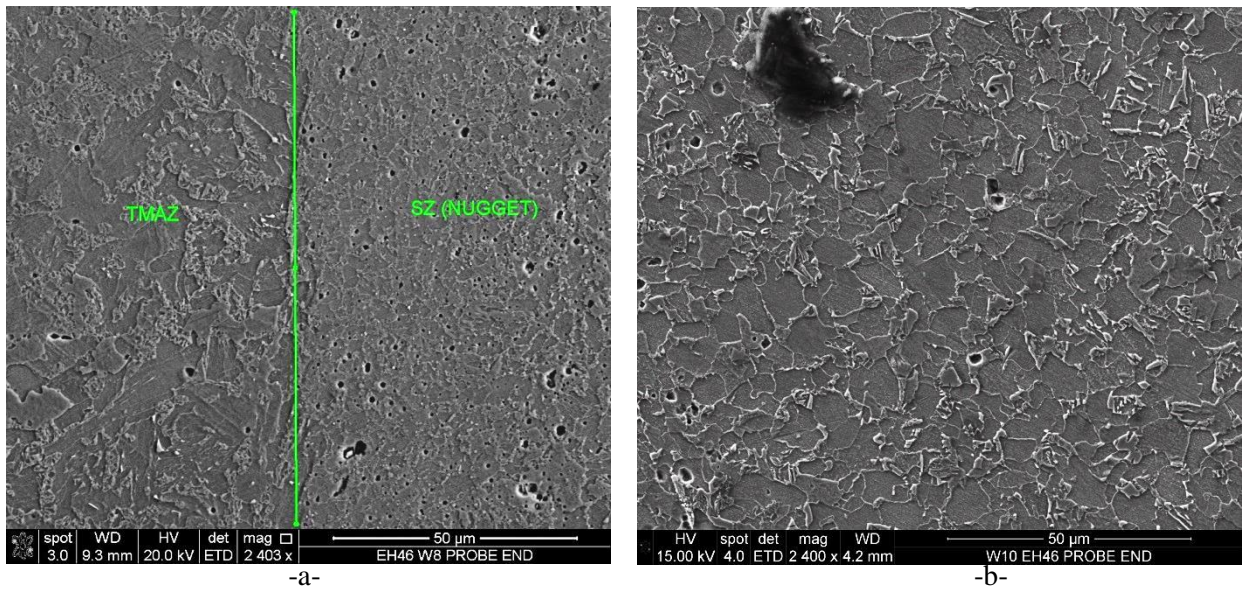
<center>-a-</center>

<center>-b-</center>

Figure 4.105: SEM micrographs showing -a- FSW sample W8 (EH46) probe end shows the weld nugget and TMAZ. The weld nugget consists of fine ferrite grains (4 µm) due to the effects of high strain rate and slower cooling rate (dynamic RX), the region affected by tool rotation TMAZ shows larger ferrite grains. -b- FSW sample W10 (EH46)probe end shows 10µm ferrite grains with a mixture of nodular ferrite (dark phase) and short plate cementite (bright phase).

<center>193</center>
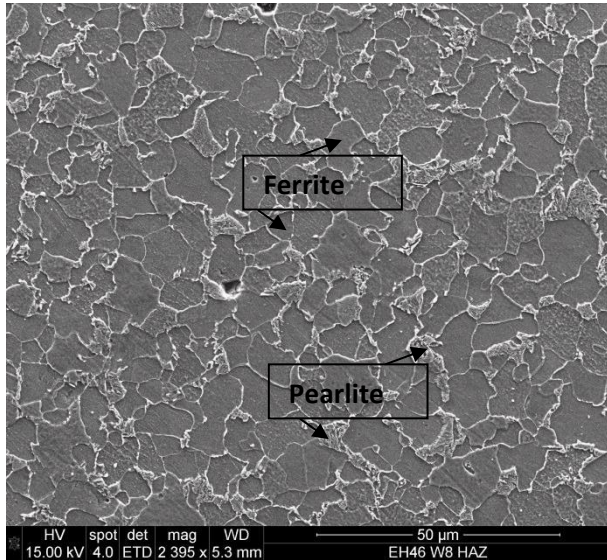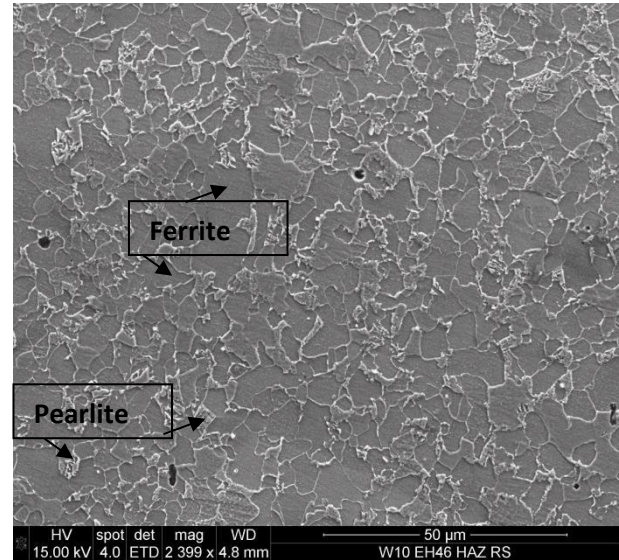
-a-   -b-

Figure 4.106: SEM micrographs showing -a- FSW sample W8 (EH46) HAZ, RS shows 15µm ferrite grains with nodular and short plated cementite and some island of pearlite. -b- FSW sample W10 (EH46) HAZ, RS shows 12 µm ferrite grains (dark phase) with nodular and short plated cementite (bright phase) and some island of pearlite.
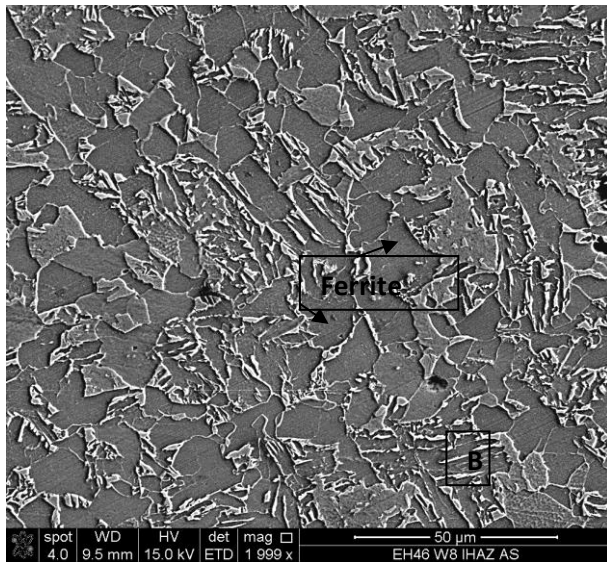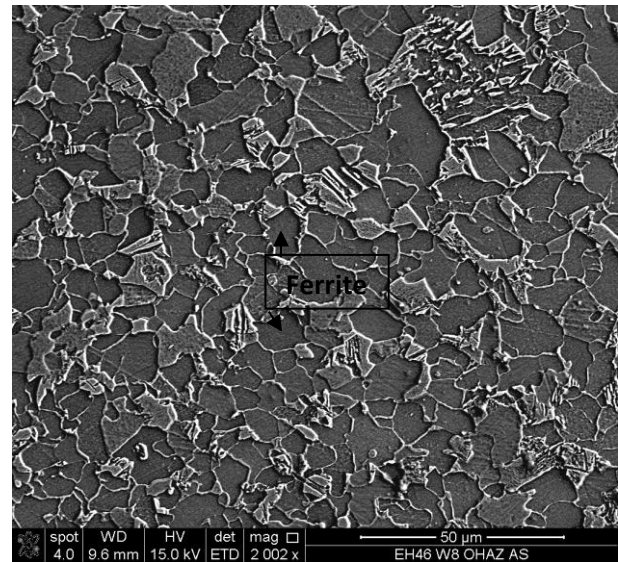
-a-   -b-

Figure 4.107: SEM micrographs showing -a- FSW sample W8 (EH46) IHAZ, AS shows 20µm ferrite grains (dark phase) with short plated cementite (bright phase) and some bainite (B). -b- FSW sample W8 (EH46) OHAZ, AS 10 µm shows ferrite grains (dark phase) with nodular and short plated cementite (bright phase).

194

-a-   -b-
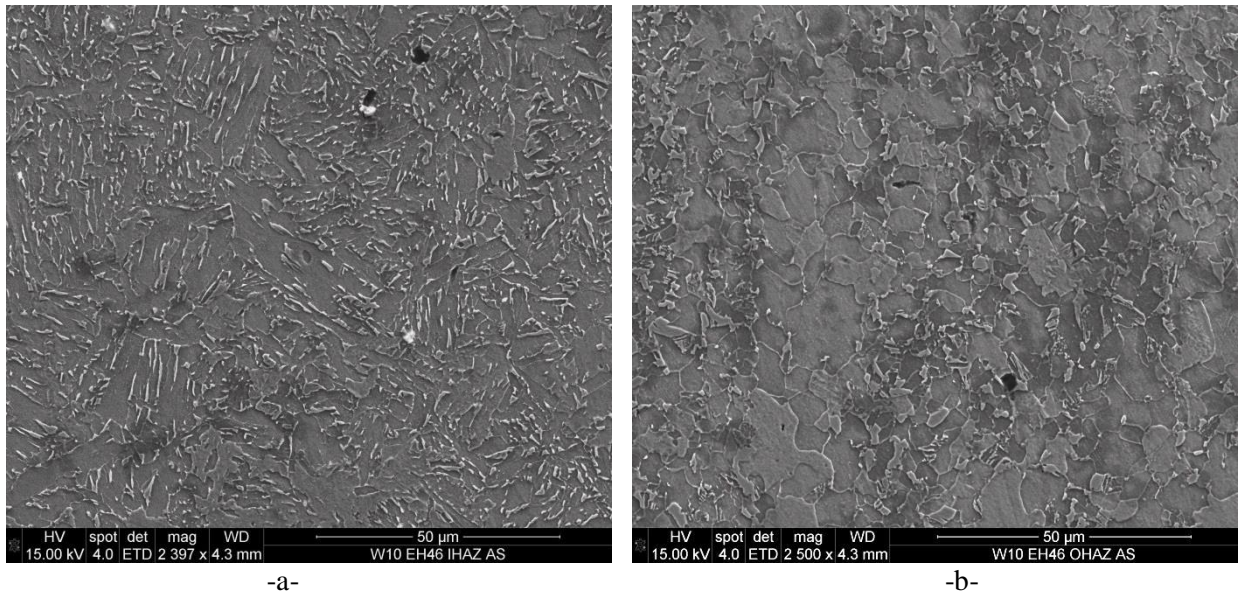
Figure 4.108: SEM micrographs showing -a-FSW sample W10 (EH46) IHAZ, AS shows ferrite matrix with plates of cementite. -b- FSW sample W10 (EH46) OHAZ, AS shows 10µm ferrite grains with nodular cementite.

4.9 SEM images of the Effect of Heat Treatment on the Prior Austenite Grain Size of DH36 and EH46 Steel Samples.

Figure 4.109 and 4.110 show SEM images of the microstructure of DH36 and EH46 heat treated samples in a temperature range of 1000 ^{o}C -1450°C and 10 min holding time followed by oil quenching. The increase in temperature in general has led to an increase in the Prior Austenite Grains Size (PAGS). Figure 4.111 and Figure 4.112 shows the relationship between PAGS and temperature for the heat treated samples at holding times of 1min and 10 mins respectively. DH36 shows a greater increase in the PAGS when temperature increase than the EH46 steel grade. This can be attributed to the lower percentage of alloying elements exist in DH36 compared to EH46 grade (chemical composition are shown in table 2.5 and table 2.6). Ti is a very effective element, when considering grain size control, due to its affinity for carbon and nitrogen. Ti readily forms Ti (CN) which acts to pin austenite grain boundaries and therefore impedes high temperature austenite grain growth [84] [85] [86]. Figure 4.111 and figure 4.112 show how the prior austenite grain size are increased significantly once a temperature of 1300°C is exceeded which indicates that most of grain boundary pinning precipitates responsible for grain refining have either coarsened beyond the critical diameter for grain boundary pinning or been taken into solution. The effects of micro-alloyed elements on the PAGS have been studied by Karmakar et al. 2014 [163] in which Ti and Nb were identified as the most effective elements for pinning austenite grains during heating. The author reported that grain growth of austenite can occur when the temperature exceeds 1150 ^{o}C as a result of the start of Ti-Nb coarsening. However, abnormal grain growth in austenite was reported to occur after reaching a temperature of 1400 ^{o}C due to higher coarsening of Ti element. Gong et al. 2015 [144] reported a reduction in the pinning force of Ti-Nb steel after reaching a temperature of 1200 ^{o}C as a result of coarsening /dissolving of Ti-Nb rich precipitates in austenite.
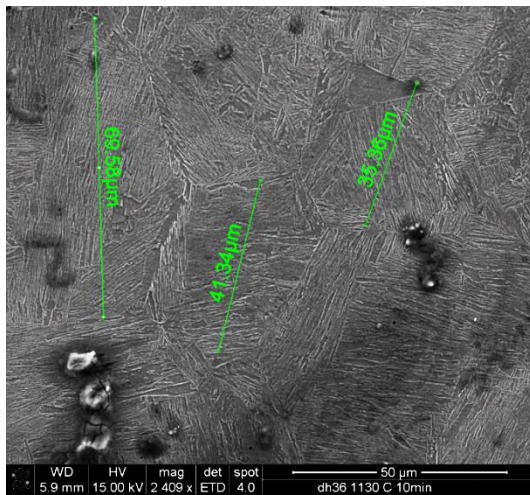
-a- 85µm prior austenite grains
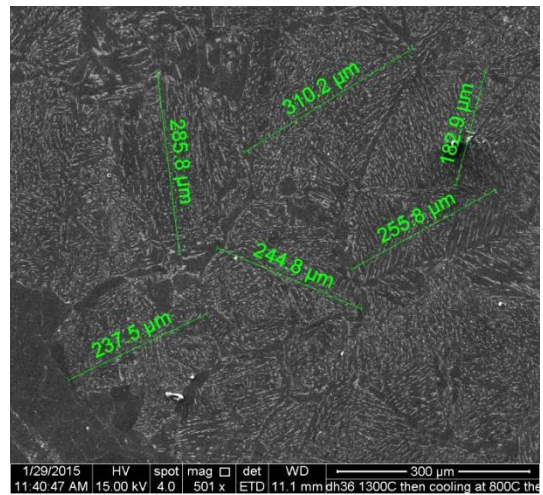
-b- 250µm prior austenite grains
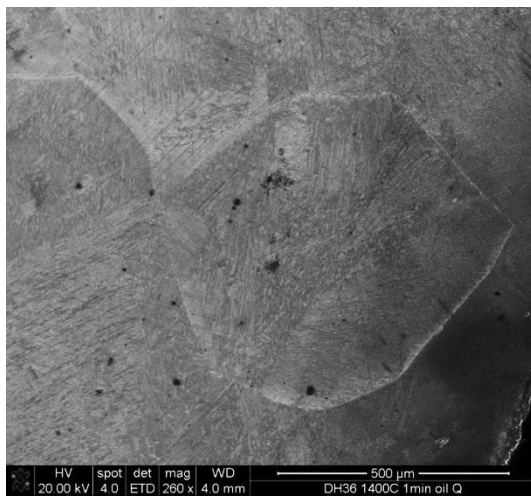
-c- 600µm prior austenite grains
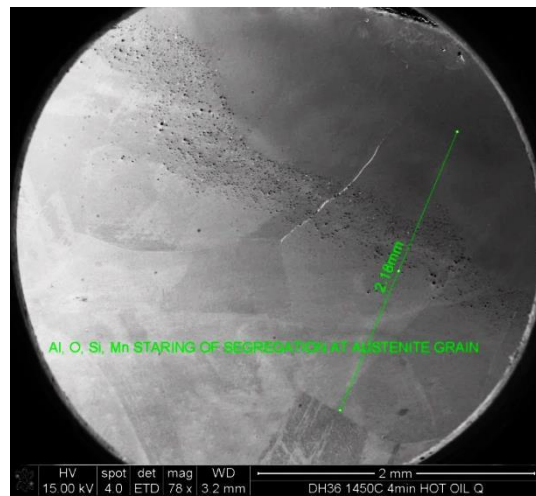
-d- 2000µm prior austenite grains
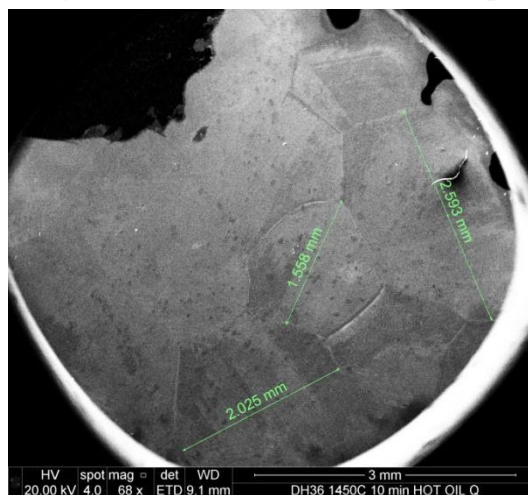
-e- 2000µm prior austenite grains

Figure 4.109: SEM micrograph images showing prior austenite grain size of grade DH36 steel when heat treated with different peak temperatures. -a- (1130°C), 85µm prior austenite average grain size, -b-1300°C, 250 µm prior austenite average grain size, -c- 1400°C, 600µm prior austenite average grain size, -d- 1450°C for 4min holding time, 2000µm prior austenite average grain size, -e- 1450°C and 10 min holding time, 2000µm prior austenite average grain size.
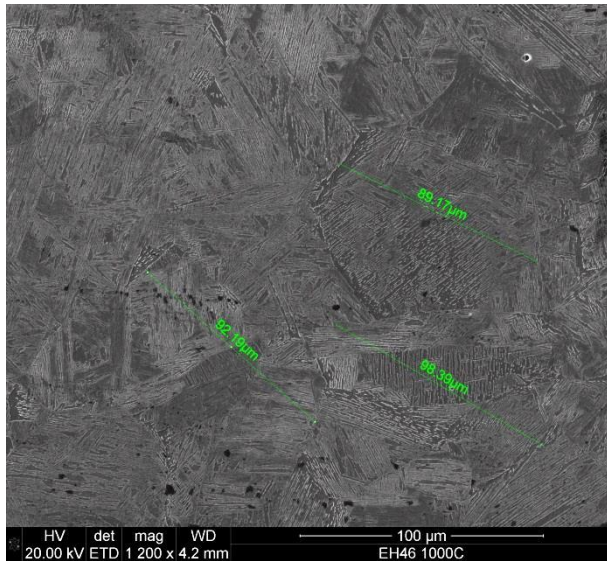
-a- 90µm prior austenite grains
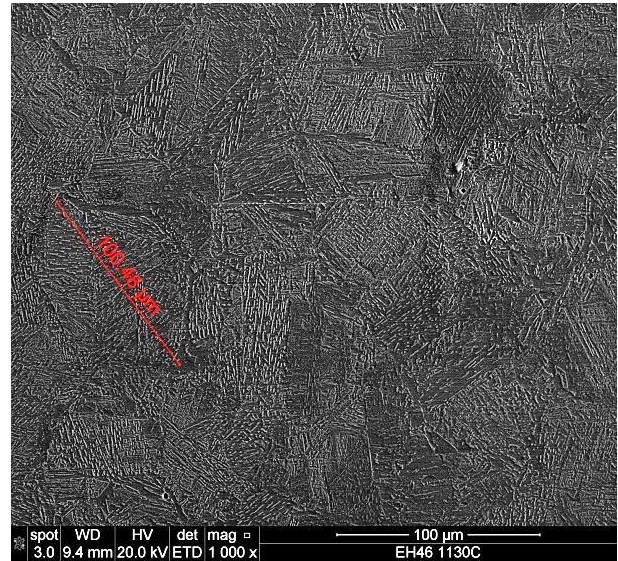
-b- 100µm average prior austenite grains
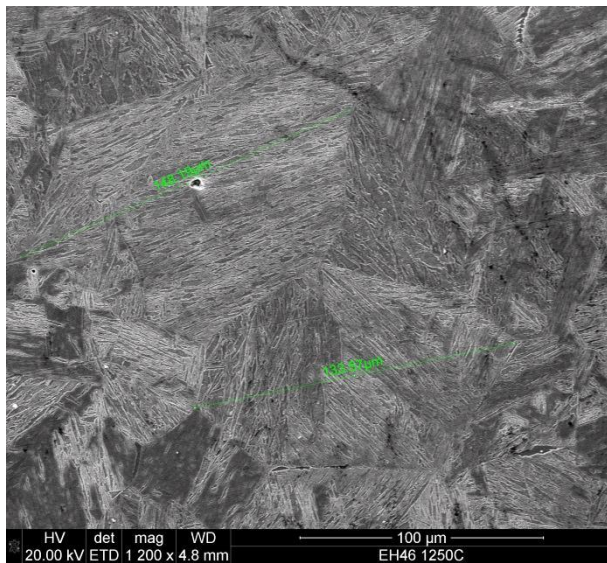
-c- 110µm prior austenite grains
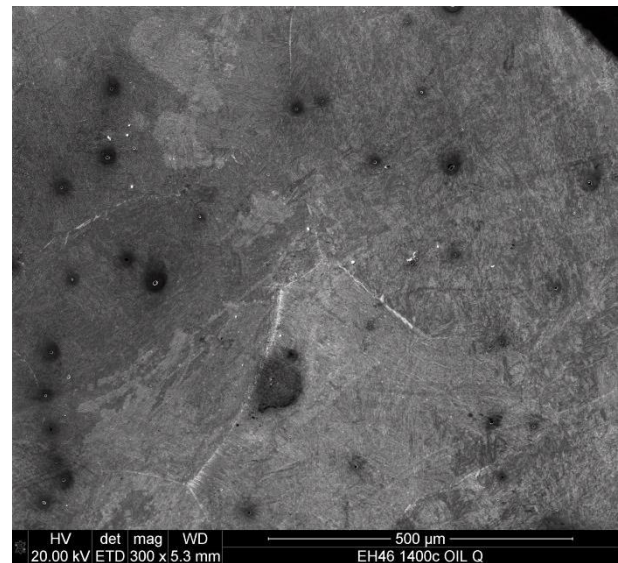
-d-400µm prior austenite grains

Figure 4.110: SEM micrograph images showing prior austenite grain size of grade EH46 steel when heat treated with different peak temperatures and a 10min holding time.-a- (1000ᵒC), 90µm prior austenite average grain size, -b- 1130ᵒC, 100 µm prior austenite average grain size, -c- 1250ᵒC, 110µm prior austenite average grain size, -d- 1400ᵒC, 400µm prior austenite average grain size,
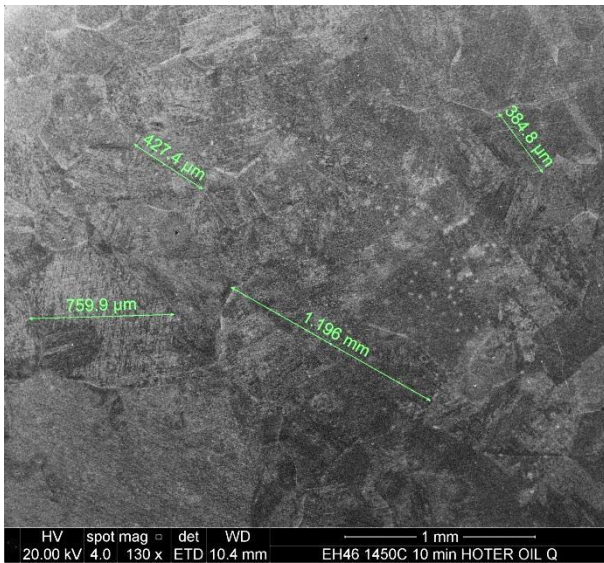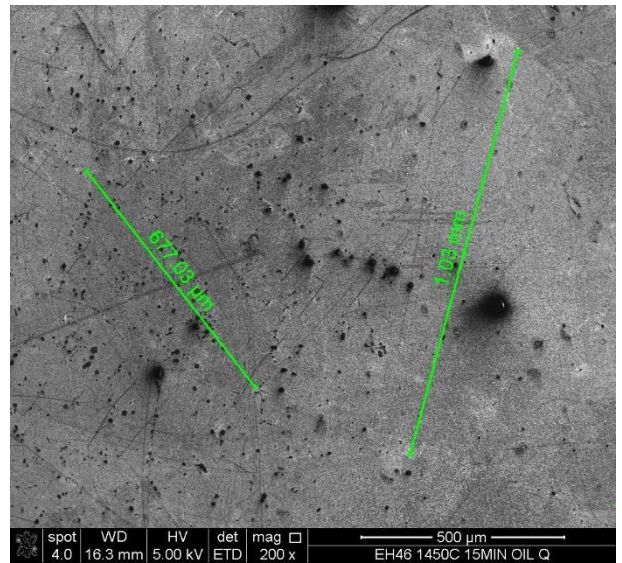
-e-700µm prior austenite grains **-f-1000µm average prior austenite grains**

Figure 4.110 cont.: SEM images showing prior austenite grain size of grade EH46 steel when heat treated with different peak temperatures and 10min holding time. -e- 1450°C and 10 min holding time, 700µm prior austenite average grain size, -f- 1450°C for 15 min holding time, 1000µm prior austenite average grain size.
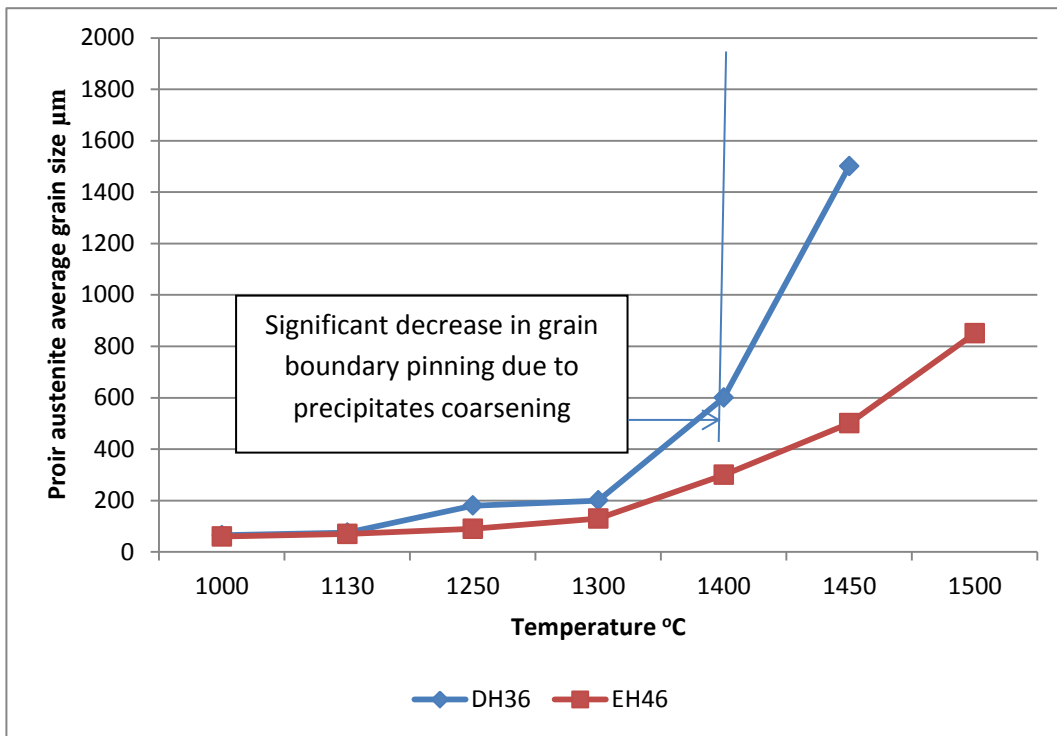
Figure 4.111: The effect of temperature on prior austenite grain size for heat treated samples of DH36 and EH46 steel in the temperature range 1000°C-1450 °C for DH36 and 1000°C-1500 °C for EH46 with a holding time of 1min.
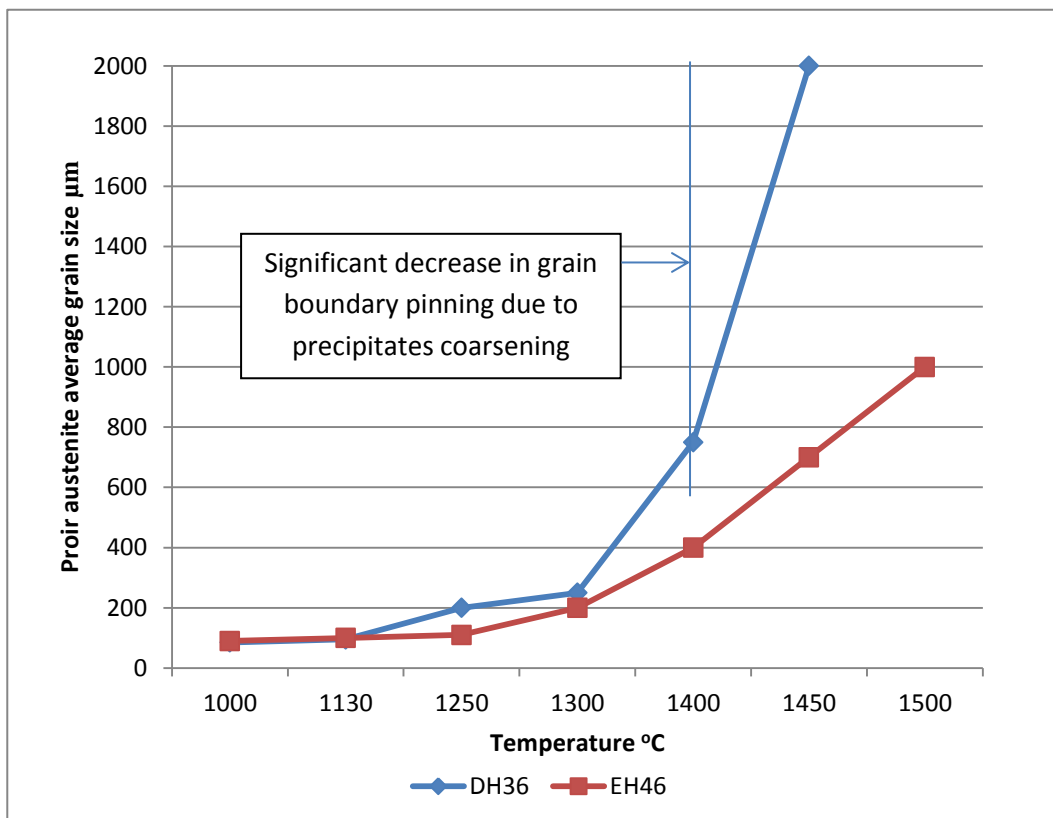
Figure 4.112: The effect of temperature on prior austenite grain size for heat treated samples of grade DH36 and EH46 steel in the temperature range 1000°C-1450 °C for DH36 and 1000°C-1500 °C for EH46 with a holding time of 10mins.

4.10 TiN Precipitates in As-Received EH46 Steel.

Ti as an alloying element in the grade EH46 steel is usually found as Ti or alloyed with other elements such as Nb as shown in figures 4.82, 4.113 and 4.114. During the FSW process the material in the SZ will experience high temperatures and also high strain rates which can cause a phase change in the PM microstructure and also in elemental composition of precipitates/segregates. The effect of strain rate was not included in the heat treatments used to simulate phase change and elemental precipitation/segregation as the maximum temperature on Gleeble simulator hot compression test will not exceed 1100°C and the current heat treatments reach up to1500^{o}C. However, it is expected that strain rate will affect the incubation time of phase transformation and elemental precipitation/segregation. Previous work carried out on steel including heat treatments and strain rate (such as hot compression, rolling and FSW) has shown that the phase changes and elemental precipitation occur faster when the process includes strain rate in addition to heating [76] [140] [141] [142] [143] and [144]. Failla et al [76] studied the effect of deformation on the phase transformation of ferrite and bainite of HSLA-65 during the FSW process and found that the phase transformation occurs faster when deformation is increased. This was attributed to the reduction in austenite grain size during the FSW process. The incubation time for the precipitation of Nb(C, N) has also studied by Zhu and Qiu [142] who found that an increase in strain resulted in a decrease in incubation time. The precipitation time was reduced from 6000 sec to 3548 sec with the casting speed increasing from 0.9m/min to 2.4m/min whereas, the temperature of precipitation was constant [142].

4.10.1 TiN Precipitates in the Heat Treated EH46 Steel Samples.

Samples which have been heat treated at 1000°C did not show evidence of TiN precipitates under the SEM investigation. This may be due to the fact that, for the chemical composition, the TiN precipitation process may not occur at temperatures below 1000°C [83]. Other samples which experienced higher temperatures (than 1000°C) have shown different sizes of Ti precipitates including TiN as shown in SEM images and EDS spectrum as shown in figure 4.115 to figure 4.117. Generally speaking, heating to 1130°C with different cooling rates has resulted in precipitation of Ti with other elements including Al, Nb, S, O, V, and P as shown in figure 4.115. The current work only deals with TiN precipitates so other Ti precipitates will not be discussed but a work has been carried out can be found in [90] [164] [165] [166] and [167]. Samples heated at 1240°C (Figure 4.116) shows Ti/Nb Nitrides precipitates with an average

size of 100nm whereas; heating to 1400°C has resulted in coarser precipitates forming of 0.5-1μm TiN as shown in Figure 4.117. The samples shown in Figure 4.115 to Figure 4.117 were quenched in hot oil (30°C/sec). This cooling rate is expected to produce an acicular ferrite microstructure similar to that in FSW samples as shown in Figure 4.110. Ti usually has a strong affinity to form nitrides, oxides and even sulphides before forming carbides [168] [169]. It is known that TiN precipitate requires a low amount of Ti in the steel matrix (less than 0.025wt%) and also a low carbon content otherwise Ti (C,N) will be more dominant [164] [170].

4.10.2 The Effects of the Cooling Rate on TiN Particle Size Found in the Heat Treated Samples of EH46 Steel.

Figure 4.119 -a- to -d- show SEM images of TiN precipitates heat treated at 1400°C and held at this temperature for 30 sec followed by cooling to produce four different cooling rates, oil quench, hot oil quench, air cool and furnace cooled. Samples were then examined on the SEM to show the effect of cooling rate on TiN precipitate size. It was found that the TiN particle size increases significantly when the cooling rate decreases, especially when cooling inside the furnace. It is also shown that TiN can precipitate even at a fast cooling rate such as oil quenching as shown in Figure 119 -a-. Recent work carried out on low carbon steel (0.12-0.14%C) with a Ti content between 0.006%-0.013% [171] showed that cubic TiN can precipitate at very high temperatures (1400°C) and the size of the precipitate was controlled by the cooling rate. It has also been shown that TiN cubic precipitates can be formed even at fast cooling rates (water quenching) but with a smaller size and that the peak temperature was the driver for the precipitation of TiN in these circumstances. [171]

Figure 4.120 -a- and -b- shows the relationship between the cooling rate and the average TiN particle size for two temperatures (1250°C and 1400°C) and two holding times (10 seconds and 30 seconds). The slower cooling rate means that the TiN precipitates could form over a longer period of time at a higher temperature thus increasing coarsening of the precipitation [88]. Increasing the holding time to 30 sec at 1400°C with a very slow cooling rate (cooling inside furnace) has resulted in a coarsening of TiN particles to reach a size exceeds 3μm as shown in figure 4.119 -d- and figure 4.120 -b-. The faster cooling rate can lead to larger undercooling and higher supersaturating of solute for precipitation and thus a larger driving force, so more fine particles will form at lower temperatures (insufficient diffusion time with increasing cooling rate so less Ti precipitates). Figure 4.121 shows the frequency (%) of TiN

particles sizes when heating to -a- 1250 $^{\circ}$C for 10sec, -b- 1400 $^{\circ}$C for 10sec, -c- 1250 $^{\circ}$C for 30sec and -d- 1400 $^{\circ}$C for 30sec. TiN particle size increases with the increase in peak temperature, the frequency of large particles also increases when soaking time increases due to the samples experiencing a high temperature for more time . The above discussion about TiN formation during heat treatments can be helpful in estimating peak temperature and cooling rate of the FSW joints of EH46 steel and thus can help in estimating the suitable rotational and traverse speeds of the tool which can give the best welding conditions without the need for using TCs or a thermal imaging camera.

4.10.3 TiN precipitates in FSW of EH46 Steel Samples.

The SEM images of FSW samples W8 (EH46) and W10 show precipitation of TiN in the top of the SZ with average size of 0.6 μm and 0.5 μm in the steady state period as shown in figure 4.122 -a- , -b-, -c- and -d- respectively. The TiN particle size has exceeded 1μm in the plunge period (the start of welding where the tool is rotating but not moving) as shown in Figure 4.123 -a- and -b- low and high magnification respectively. In this figure there are eight TiN particles (size is 0.7μm to 1.5μm) inside a 10 μm ferrite grain. This coarsening of TiN particles can be the result of higher temperatures and slower cooling rates, more discussion about the precipitation size and cooling rate is in the following section.

The study of the plunge/dwell period for grade EH46 steel, samples W1 to W7 have also been examined for TiN precipitates. Figure 4.124 -a- and -b- shows TiN precipitates present in samples W2 and W3 respectively at region 1 under the tool shoulder (see figure 4.94). An average particle size of 0.7 μm in W2 and 0.5 μm in W3 has been measured. Figure 4.125 shows TiN particles present in sample W6, which have an average size of 0.5 μm detected under the tool shoulder (region 1). The frequency and TiN particle size are shown in figure 4.126 -a- Sample W8 and W10 and -b- sample W1 to W7 plunge/dwell trial. The average size of TiN particles are calculated and listed in table 4.15.

4.10.4 Comparison of the TiN Precipitates in FSW and Heat Treated Samples.

From figure 4.120 -a- and -b-,which shows the relationship between the average size of TiN precipitates and the cooling rate compared to water, it is shown that the heat treatment at 1250 ^{o}C followed by a hot oil quenching resulted in TiN precipitates with an average size of 0.2-0.5 µm (soaking time 10-30sec) which coincides with the average size and frequency of precipitate found in sample W10 (EH46) (Figure 4.122 -c- and -d-). Sample W8 (EH46) shows coarser TiN particles with an average size of 0.6µm which suggests a slower cooling rate than the sample W10 (EH46). This, in turn, is supported by the fact that the tool traverse speed for W8 was 50% slower than for W10. The cooling rate can be in the range of 10 ^{o}C/s - 30 ^{o}C/s according to the implemented heat treatments with a minimum peak temperature of 1250 ^{o}C. The ferrite grain shown in Figure 4.123, with average grain size of 10 µm, contains eight large cubic precipitates of TiN with a size range from 0.7µm to 1.5 µm. The large size of these precepitates indicate that the material has been exposed to a very high temperature (may have reached 1400 ^{o}C), the cooling rate was also slow enough to form these precipitates and expected to be less than 10 ^{o}C/s. It is, however, unlikly these large precipetates can play any useful role in pinning the austenite grain during heating (see figure 4.111 and figure 4.112). The reduction in pinning forces due to temperature increase higher than 1200 ^{o}C was reported by Gong et al. 2015 [144] and also by Karmaker et al. 2014 [163] where the austenite grains have experienced coarsenning resulted from Ti-Nb dissolving. The coarse ferrite grain at the probe end of W10 during the plunge period shown in figure 4.123 which exceeds 10µm can be attributed to the inability of the larger precipitates to exert a pinning force on the grain boundaries.The high temperature generated during welding will have the effect of slowing down the cooling rate, allowing precipitate disolution ,as well as, precipitate growth - all of which will result in austenite grain growth - as seen in figure 4.123.

With regards to samples W1 to W7 (EH46) the shoulder-probe region shows evidence of precipitation of TiN particles, as shown in figure 4.124 and figure 4.125. Table 4.15 shows the average size of TiN particles of W1 to W7 at the shoulder-probe region (shown previously in figure 4.35). Sample W1 and W2 (EH46) shows bigger average size of TiN particles (0.6-0.7 µm) than samples W3-W7 (0.5µm) as the result of higher tool rotational speed (200 RPM) of W1-W2 compare to the other welded joints which have a lower tool rotational speed (120 RPM). The higher tool rotational speed has resulted in a higher peak temperature and thus a slower cooling rate is expected which in turn can cause TiN particle coarsening as discussed previously. The temperature of W1 and W2 at the shoulder-probe is

expected to have exceeded 1250 ^{o}C but not to have reached 1400 ^{o}C according to the heat treatments results shown in figure 4.120 -a- and -b-. Sample W3 to W7 (EH46) peak temperatures are expected to have reached 1250 ^{o}C with a cooling rate range of 20 ^{o}C/s-30 ^{o}C/s.

Figure 4.127 shows TiN particle at region 2 under the tool probe of sample W2 (EH46) with average size of 0.35μm. This decrease in TiN particle size from 0.7 μm to 0.35 μm can be attributed to a lower peak temperatures under the probe (region 2) compared to the region under the shoulder (region 1). This finding is in agreement with previous work [28][52][57] which showed that heat generation in FSW process is spatial (i.e. the maximum temperature is always at the tool/workpiece contact region TMAZ and it decrease towards the HAZ).

-a-   -b-
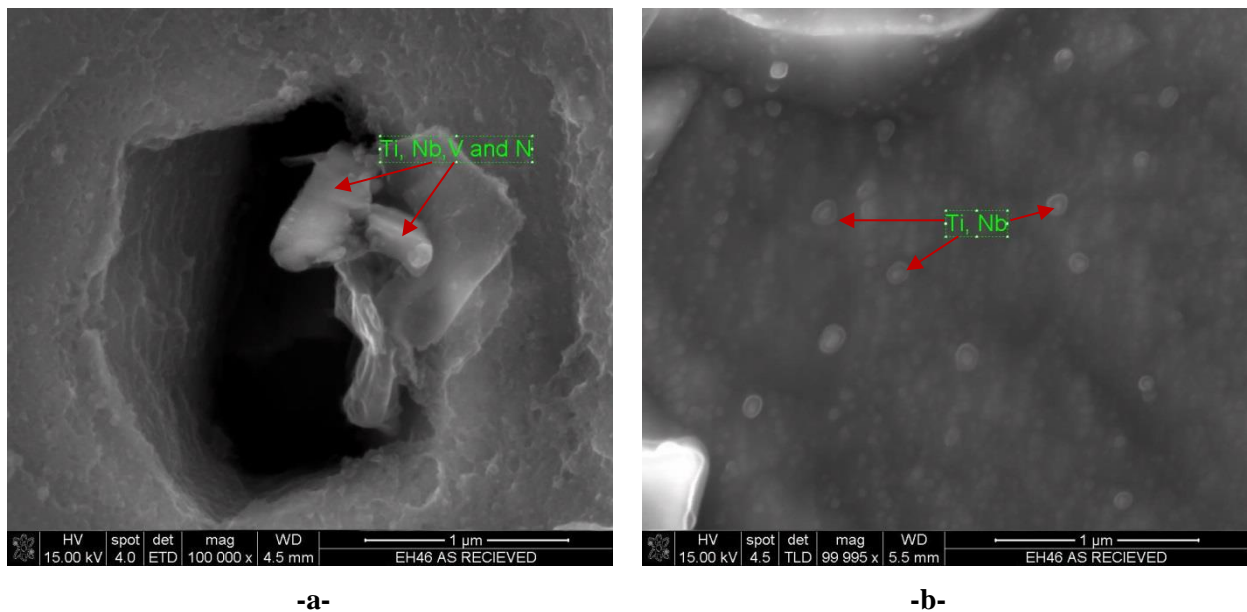
Figure 4.113: SEM micrograph image for the grade EH46 steel as received material showing -a-Ti, V and Nb rich precipitates and -b- very small Ti-Nb rich precipitates.

205
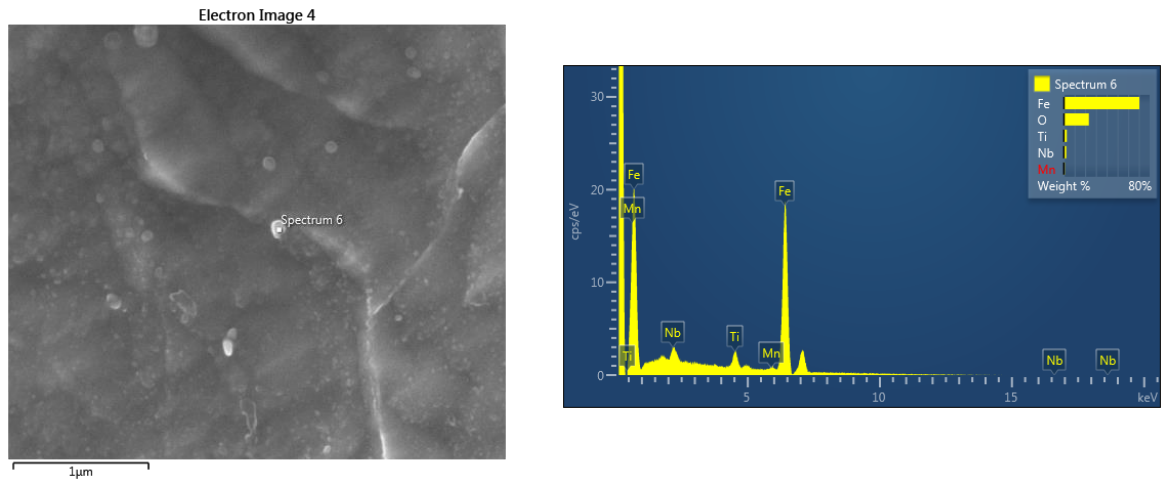
Figure 4.114: SEM-EDS high magnification of as received grade EH46 steel showing Ti spectra.

4.10.1 TiN precipitates in the heat treated samples
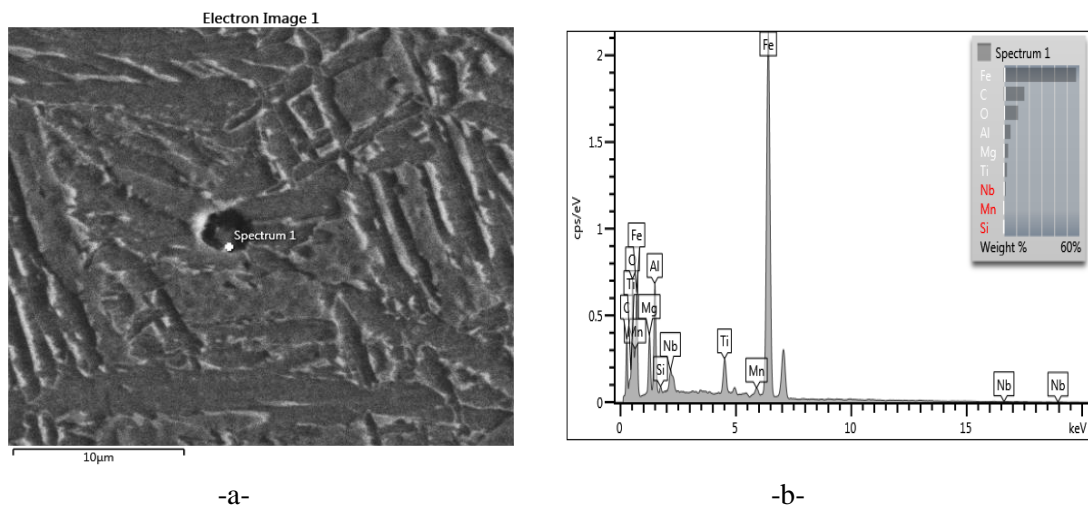
-a-   -b-

Figure 4.115: Grade EH46 steel, heat treated at 1130 ^{o} C for 1min, hot Oil quenched, -a-SEM micrograph image, -b-EDS spectra
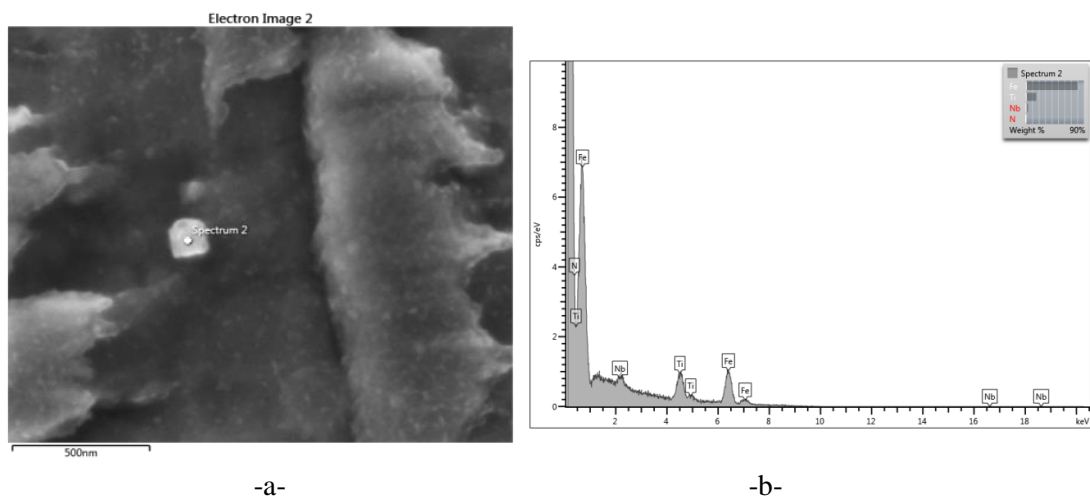
-a-   -b-

Figure 4.116: Grade EH46 steel heat treated to 1240°C for 1min, hot oil quenched, -a-SEM image, -b- EDS spectra

206

-a-   -b-

Figure 4.117: Grade EH46 steel, heat treated to 1400°C for 1min, oil quenched, -a-SEM image, -b-EDS spectra
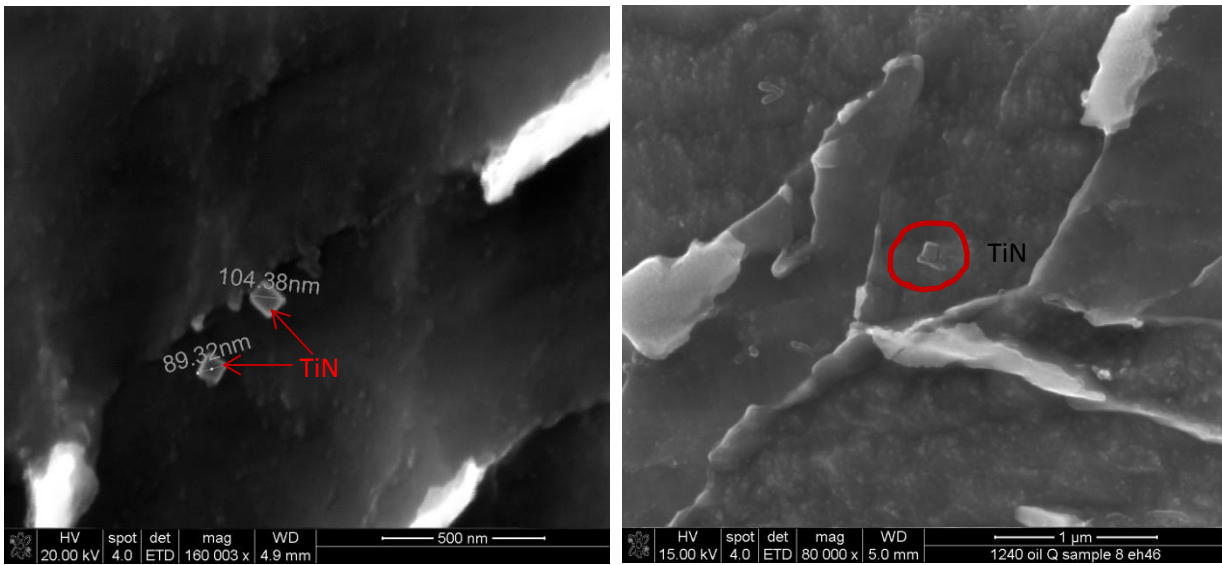
Figure 4.118: Grade EH46 steel heat treated to 1240 °C for 1min followed by oil quenching. TiN particles sizes range for 90 to300nm.

4.10.2 The Effects of the cooling rate on TiN particle size
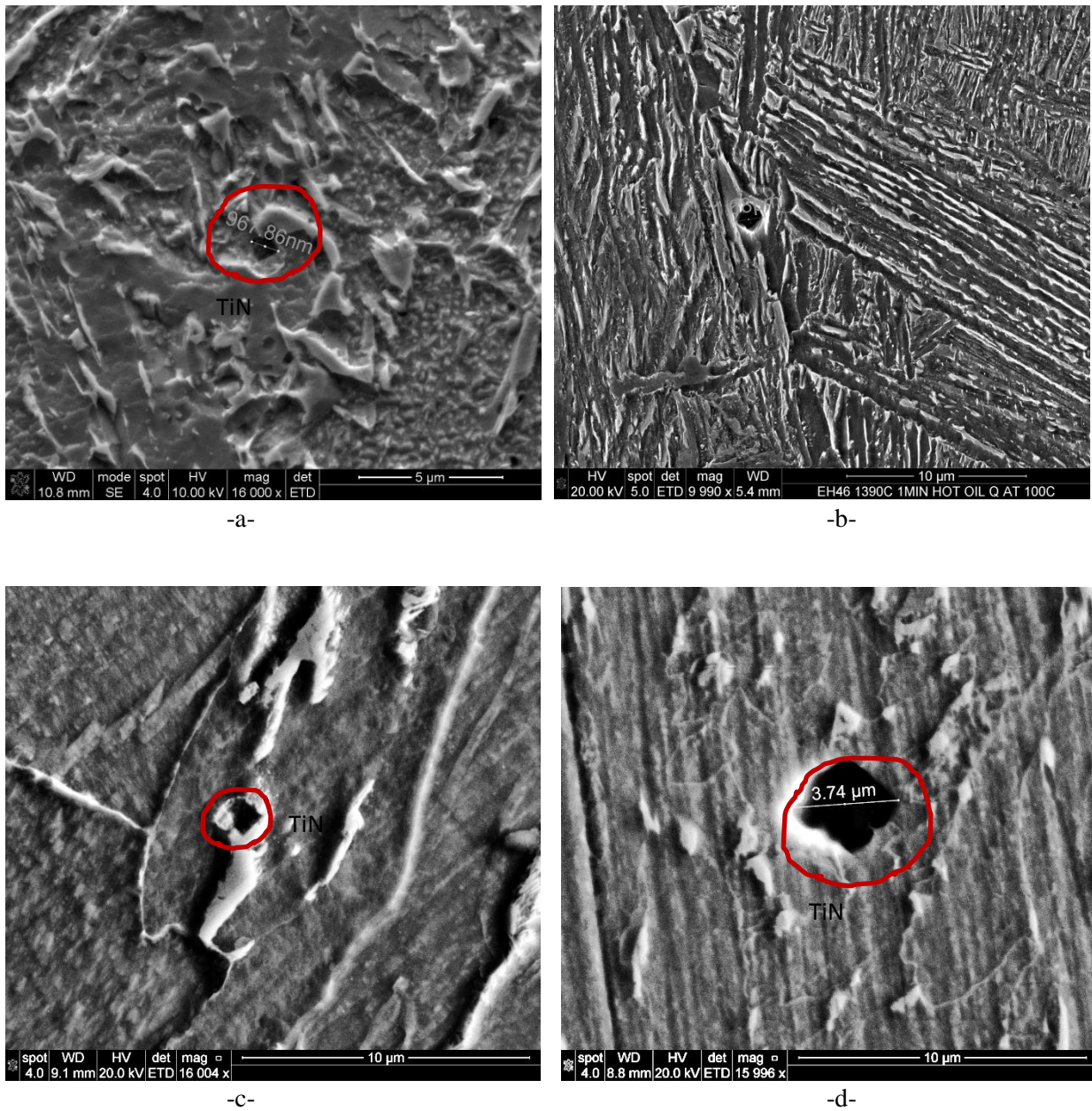
Figure 4.119: SEM images of a heat treated samples of EH46 at (1400°C) for 30 sec followed by quenching at four different cooling rates. -a- oil Q, -b-hot oil Q, -c- air cooling, -d- cooling inside furnace.
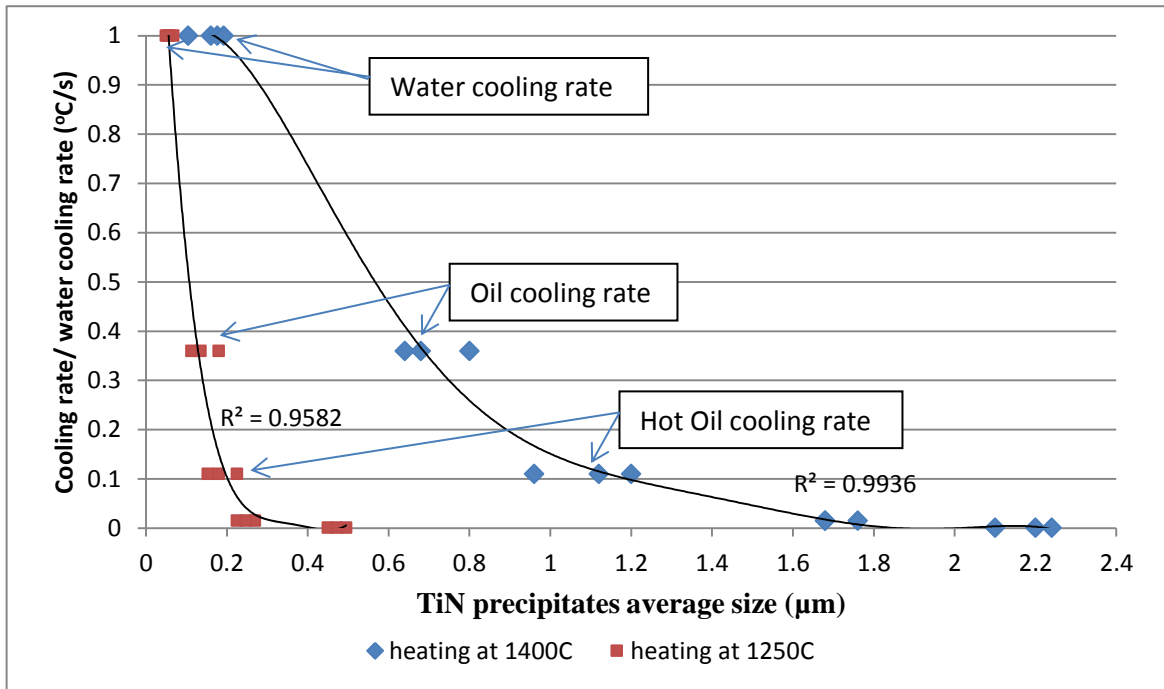
Figure 4.120: -a-The relationship between TiN precipitates size (µm) and the cooling rate °C/s (holding time is 10 sec), the precipitates size increases with decreasing cooling rate.
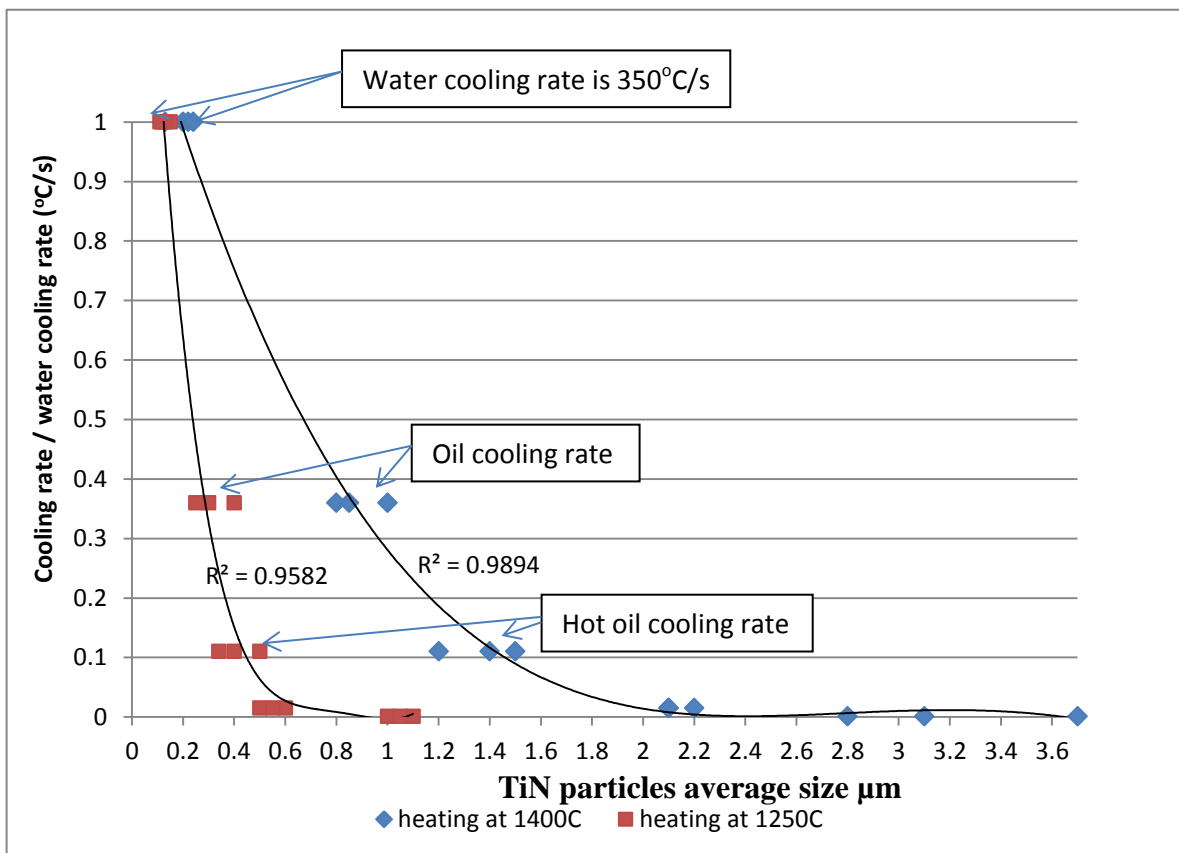
Figure 4.120: -b-The relationship between TiN precipitates size (µm) and the cooling rate °C/s (holding time is 30 sec), the precipitates size increases with decreasing cooling rate.
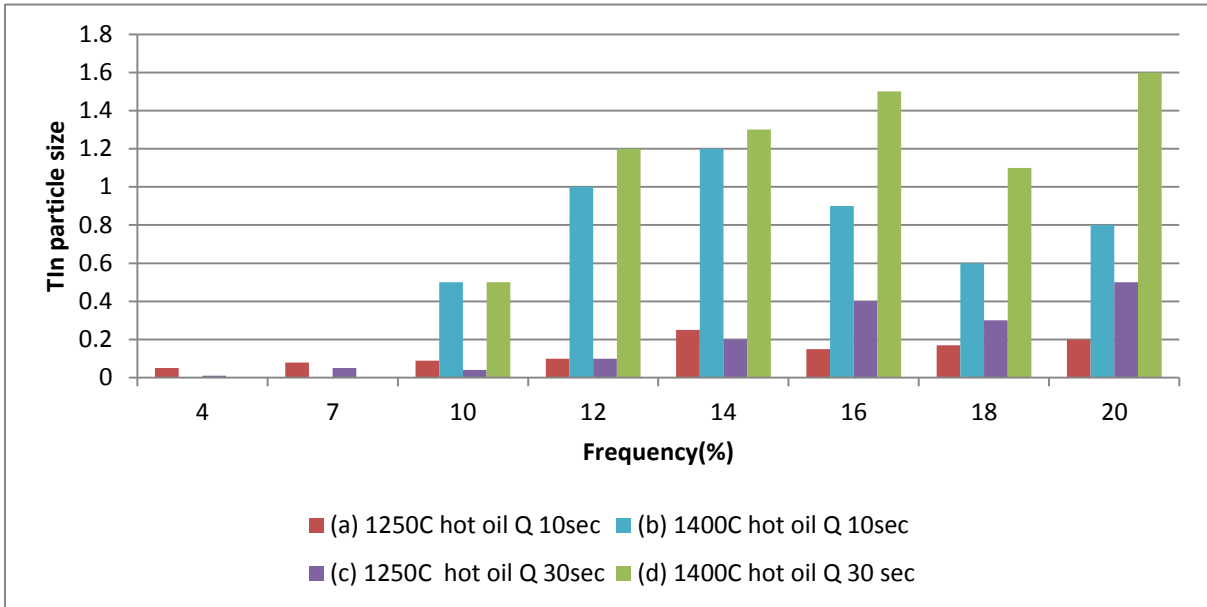
Figure 4.121: Frequency Distribution (%) of the TiN particle size (μm) observed in the heat treated samples with hot oil quenching -a- 1250°C for 10 sec, -b- 1400°C for 10 sec, -c- 1250°C for 30 sec and -d- 1400°C for 30 sec.

-a-
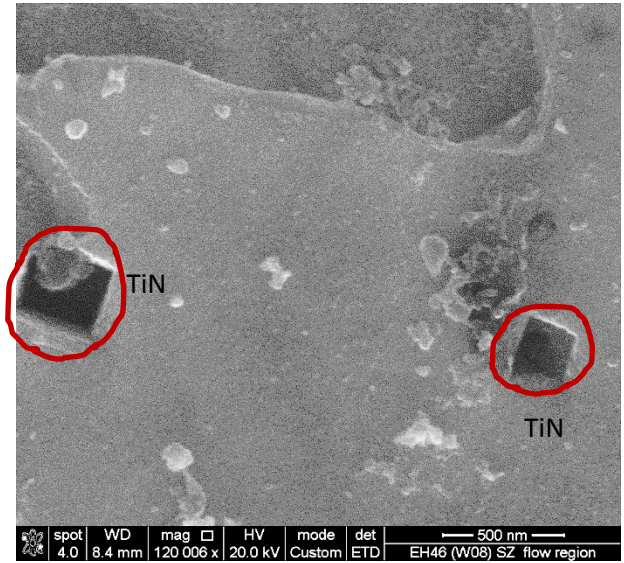
-b-
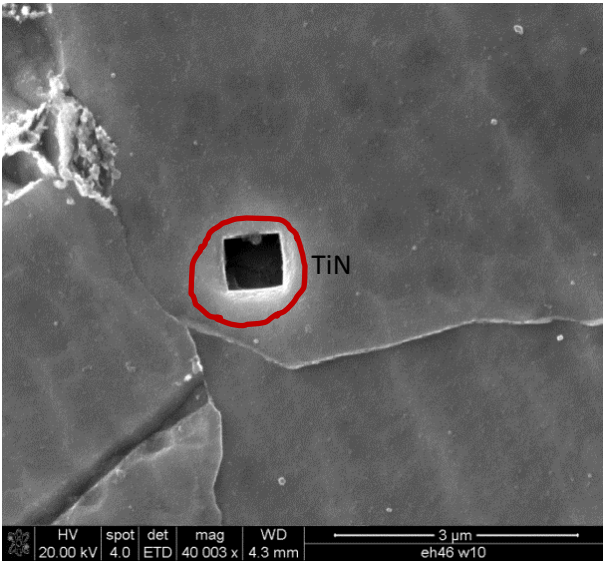
-c-
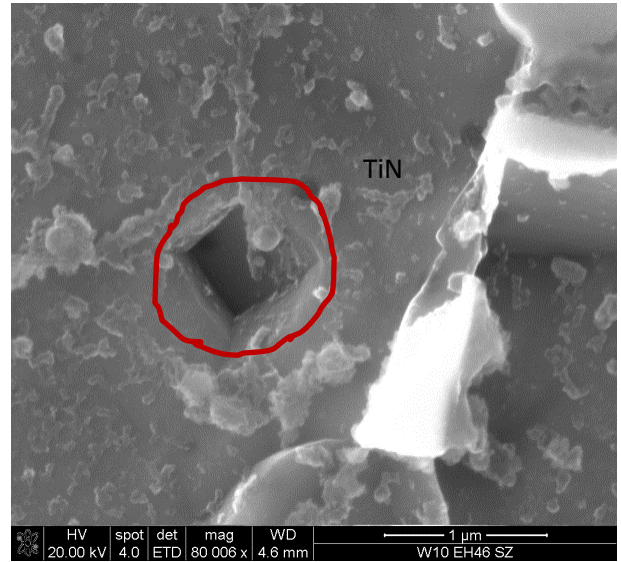
-d-

Figure 4.122: SEM microsgraphs of: -a- and -b- TiN particles in FSW sample W8 (EH46) (150RPM, 50mm/min), average size is 600nm, and -c- and -d- TiN particles in FSW sample W10 (EH46) (150RPM, 50mm/min), average size is 500nm.
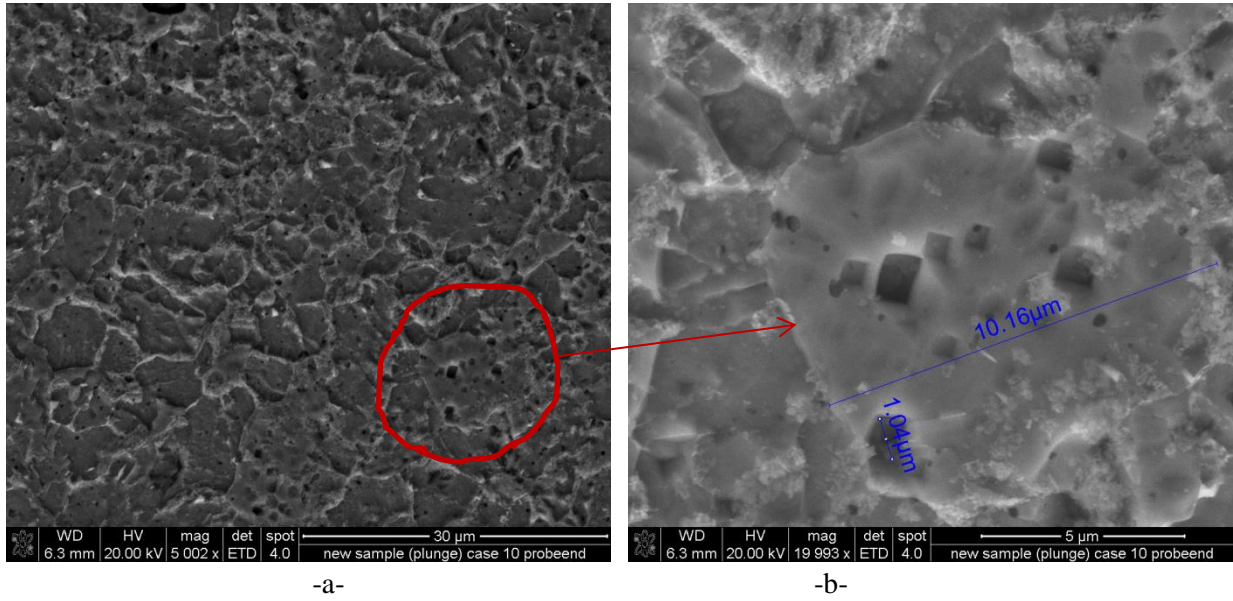
Figure 4.123: SEM micrographs of sample W10 (EH46) (plunge/dwell period) taken at the probe-end, -a-low and -b- high Magnifications, showing a significant number of TiN precipitates (size is 0.7-1.5μm).
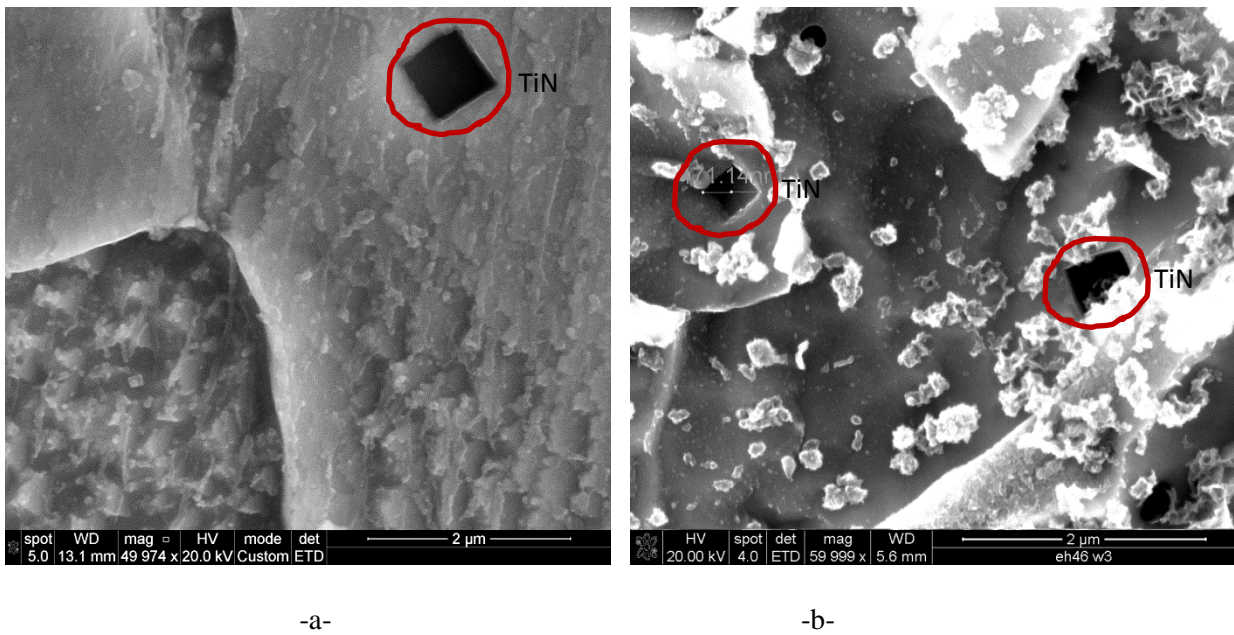
Figure 4.124: SEM micrographs examining region 1 under the tool shoulder during the plunge /dwell period (EH46)   -a- Sample W2 average of 0.7μm TiN particles, -b- Sample W3,   average of 0.5μm TiN particles.
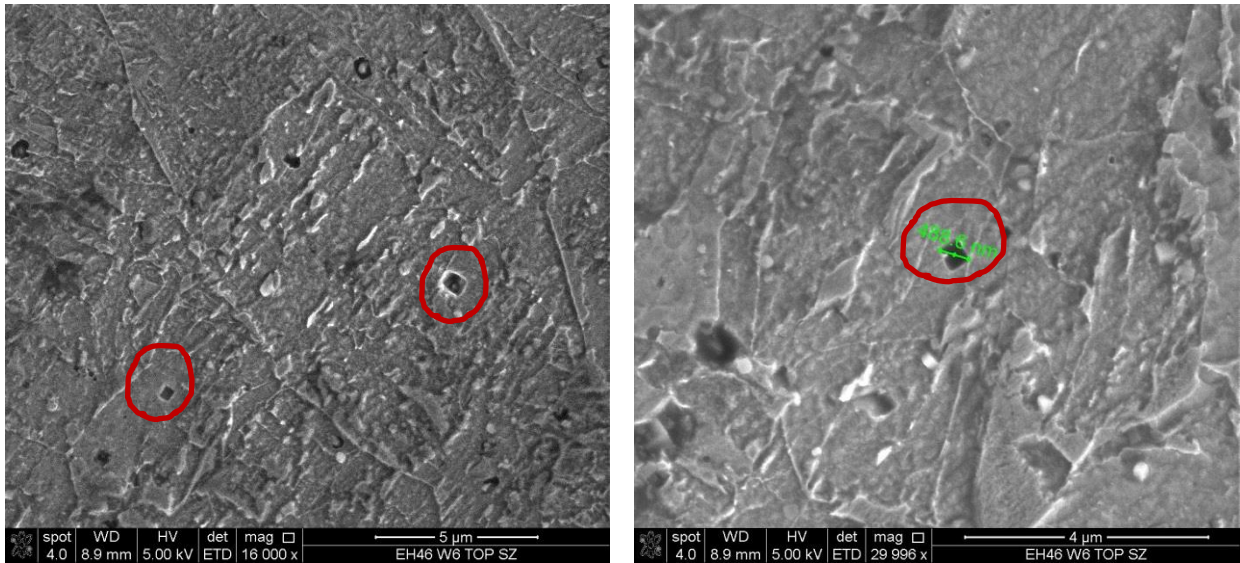
Fig. 4.125: SEM micrograph of sample W6 (EH46) (plunge/dwell period) under the shoulder, average of 0.5µm TiN particles.

-a-   -b-
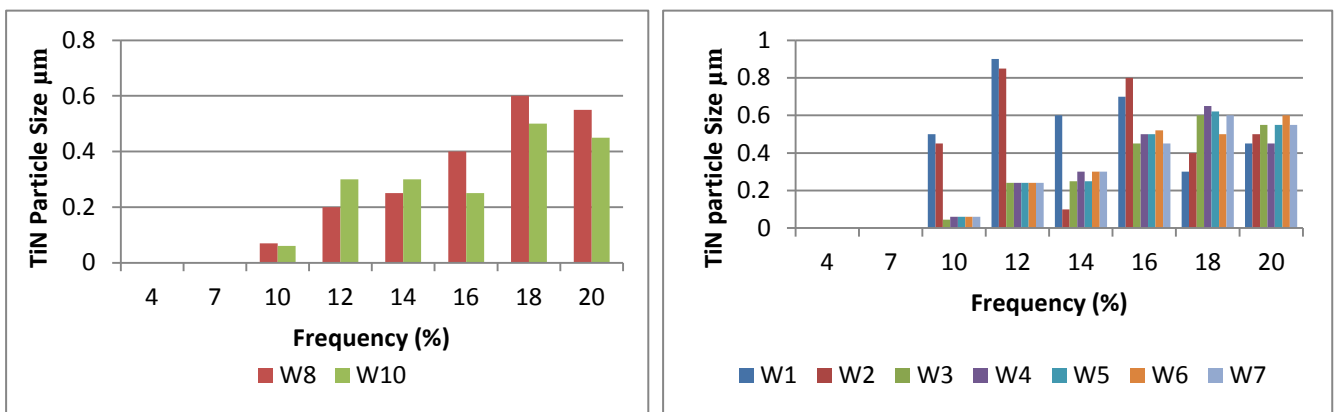
Figure 4.126: The Frequency Distribution (%) of the TiN particle size (µm) observed in -a- FSW sample W8 and sample W10 (EH46), -b- FSW samples W1toW7 (EH46) (Plunge/Dwell case).

Table 4.15: TiN average particle size of EH46 W1 to W7 at the shoulder-probe region

Weld No.	W1	W2	W3	W4	W5	W6	W7
TiN average particle size µm	0.6	0.7	0.5	0.5	0.5	0.5	0.5
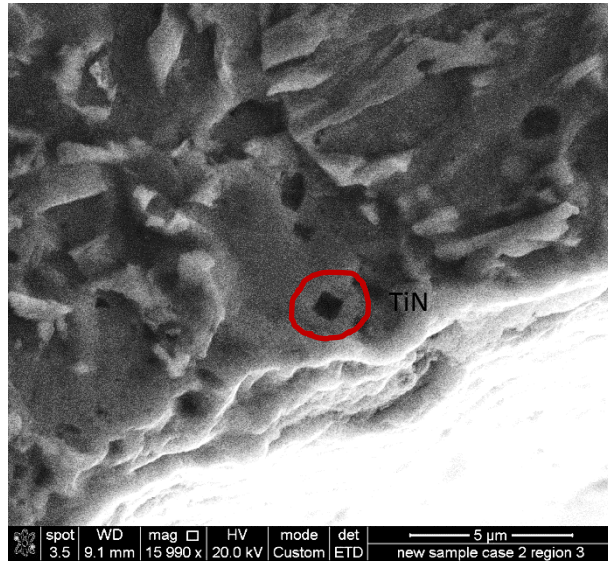
Figure 4.127: SEM micrograph of sample W2 (EH46) (plunge/dwell case) under the probe. Average TiN particles size 0.35μm.

To conclude, the technique of estimating the peak temperature and cooling rate of a FSW based upon the size and distribution of TiN precipitates can be represented as a valid and inexpensive alternative to other techniques such as using TCs or a thermal imaging camera.

4.11 Segregation/Precipitation Analysis using SEM-EDS of DH36 and EH46 Heat Treated Samples in the Temperature Range of 1400°C to 1500°C.

The microstructure of the PM of DH36 steel consists of ferrite grains with an average size of 15μm and elongated bands of pearlite as shown in figure 4.75 -a- and -b-. Ti and Nb rich particles were found on a nano-scale size either as a Ti, Nb or as a compound with each other (Figure 4.76 and figure 4.77). MnS is present as stringers in the microstructure, either as MnS or as a compound with Ca and Al as shown in figure 4.78 to figure 4.80. Grade EH46 steel parent materials microstructure also consists of ferrite grains with average size of 20μm with shorter but wider bands of pearlite compared to DH36 grade as shown in figure 4.81 -a- and -b-. Nano-scale sized alloying elements such as Ti and Nb are shown in figure 4.82 to 4.84. Ca, which has a strong affinity to form sulphides and oxides, was found as a compound of calcium aluminates (CaO-Al$_2$O$_3$) and also calcium-manganese-sulphide (MnS-CaS) as shown in figure 4.85 and 4.86 respectively. The melting point of (CaO-Al$_2$O$_3$) is in the range of 1450-1850°C depending on the amount (wt%) of CaO compound with Al$_2$O$_3$ [172]. MnS melts at 1600°C [164], however, the melting point is lower when it forms compounds with other elements such as Ca and Al [164]. Hence, it is expected that some melting/softening of the CaO-Al$_2$O$_3$ and also MnS-CaS will occur when the temperature exceeds 1400°C.

It is recognised that the samples heat treatments are non-equilibrium. The samples are heated between 1 to 10 min which is insufficient time for the whole sample to reach the same temperature. The heating temperature is designed to simulate the non-equilibrium surface temperature conditions that a FSW sample might experience.

4.11.1 Heat treatments of DH36 and EH46 steel grades at 1400°C.

Heat treatments of DH36 steel up to a temperature of 1400°C for 1min followed by a hot oil quench showed significant segregation of Mn, S and Nb at prior austenite grain boundary (PAGB) as shown in figure 4.128 and figure 4.129. This type of segregation can affect negatively the mechanical properties of the welded joints. The segregation of MnS, and its detrimental effects on hot tensile fracture was studied by Santillana et al. 2012 [173]. They found that segregation of MnS occurs at a temperature range up to 1440°C which in turn had significantly reduced the tensile strength of the samples under study. Heat treatments of DH36 steel at 1400°C for 10 minutes have caused segregation of MnS at PAGB and within the PAG. Some other elements such as Al, O$_2$ and P are also identified with MnS as shown in figure 4.130 and figure 4.131. It is also shown that the segregated elements' morphology has

been converted from plate-like to a spherical shape when the holding time increased from 1 to 10 minutes.

Grade EH46 steel heated to 1400°C for 1min showed no significant segregation of MnS or alumina, however, the % of P in these segregates has increased slightly as shown in figure 4.132. Extending the holding time to 10 mins has caused segregation of other elements such as Ti and Nb with Al compounds as shown in figure 4.134 and figure 4.135.

4.11.2 Heat treatments of DH36 and EH46 Steel at 1450°C.

Figure 4.136 shows the microstructure of DH36 sample heat treated at 1450°C for 1min followed by hot oil quenching. It shows that significant segregation of Mn, S, Al and O has occurred and was associated with acicular ferrite formation. Figure 4.136 shows segregation which contains Mn, Si, Al and O within and at the boundary of PAG when the holding time was prolonged to 4mim. In this stage sulphur has started to disappear and is replaced by Si. The mechanism of Mn, Si, Al and O segregation will be discussed separately later in this section. Figure 4.138 shows SEM-EDS mapping of a Mn, Si, Al and O spinel compound, which contain a high percentage of O and Si. Extending the holding time from 4 min to 10 min did not change the elemental segregation of Mn, Si, Al and O, some regions shows the presence of Ca and S elements among the compound as shown in figure 4.139.

The microstructure of grade EH46 steel heat treated at 1450°C for 1min followed by hot oil quenching is shown in Figure 4.140. This image shows segregation of Mn, S, Al and Nb to PAG boundaries whereas figure 4.141 shows segregation of Nb, P and S to PAG boundaries. Heating the samples of EH46 steel to 1450°C for 4min has caused different types of elemental segregation as listed in table 4.17. MnS has joined with other elements including Ti, V, Nb, Mn, P and O whereas sulphur has joined mainly with Nb. The different types of elemental segregation are shown in SEM images at higher magnification in figure 4.142 -a- to -l-. Increasing the holding time to 10min at 1450°C has caused the coalescence of Si into Mn compounds and also more sulphide forming such as NbS and CaS as reported in table 4.17 and as shown in figure 4.144. Mn, Si, Al and O spinel has been formed and completed when the holding time increase to 15min as shown in the SEM-EDS mapping in figure 4.145 and in the SEM images of figure 4.146 and figure 4.147. In these figures the segregation of Mn, Si, Al and O spinel occurs within and at the boundary of the PAG.

4.11.3 Heat treatments of DH36 and EH46 steel grades at 1500 °C

Heating samples of DH36 steel to 1500°C for only 1 minute has caused segregation of a Mn, Si, Al and O spinel in the regions near the sample surface to a depth of 1.14 mm as shown in figure 4.148. A small amount of Nb is present with the spinel at regions away from the outer surface of the sample as shown in figure 4.149. Figure 4.150 shows a higher magnification image of Mn, Si, Al and O spinel which takes a spherical shape. The size of the spinel in all previous figures varies from less than 1μm to 20 μm. Phosphorus sulphide is also segregated to the boundary of PAG as shown in figure 4.150 -b- which give an indication about the separation of sulphur from MnS and subsequent reformation with other elements such as P and Nb.

Grade EH46 also showed segregation and precipitation to a Mn, Si, Al and O spinel as shown in the SEM-EDS spot analysis (point and ID) and also mapping in figure 4.151 and figure 4.152 respectively.

It is evident from the previous results and discussion that the segregation of spinel elements of Mn, Si, Al and O only occurs at temperatures equal or exceeding 1450°C. It is also worth highlighting that a holding time of 1min at 1500°C in both steel grades was enough for Mn, Al, Si and O spinel segregation at the sample surface and thus it is expected that the time required for segregation is decreased with increasing temperature. It is also expected that the high strain rate which exists in the FSW process will also reduce the time required for elemental segregation/precipitation as shown by previous work [76] [140] [141] [142] [143] and [144].

4.11.4 Segregation/Precipitation Analysis using SEM-EDS to Identify Elemental Segregation in FSW Samples of DH36 Steel at High Tool Speeds (550RPM, 400mm/min) (Samples W6 and W8).

A microstructural examination of two FSW (Samples W6 and W8 (DH36)) which were produced using high tool speeds (550RPM, 400mm/min) revealed the existence of a significant volume fraction of a Mn, Si, Al and O spinel in the microstructure of the SZ as shown in figure 4.153 to figure 4.162. Zn was also found associated with the spinel as revealed by the SEM-EDS spot analysis and also elemental mapping techniques as shown in figure 4.156 and figure 4.157.

The Zn present in the spinel 2nd phase particle will have originated from the galvanised surface of the DH36 steel. Al-moussawi et al. 2017 [173] suggested from CFD modelling that the maximum peak temperature in FSW of DH36 steel is localised at the tool/workpiece top contact surface on the advancing trailing side and it can reach close to the melting point of steel when the tool speed exceeds 500 RPM. The melting and boiling temperatures of Zn are 420°C and 1907°C respectively. The welding peak temperature especially at the tool/workpiece contact region is expected to be higher than the melting temperature of Zn and thus the possibility of Zn present in the stirred zone (SZ) should be low. Beak et al. 2010 [174] explained the existence of Zn in the stirred zone as a result of the FSW tool effect, whereby Zn will melt and evaporate during FSW but because there is no way for it to escape outside the tool/workpiece contact region it will trap and explode into the SZ. In this thesis the mechanism to coalesce Zn with other elemental segregation in samples W6 and W8 FSW DH36 steel is proposed as follow: (a) The centrifugal forces from FSW tool pushes the steel including the Zn coated layer at the tool/workpiece contact surface to the advancing trailing side during the FSW process. (b) Heat generated during the FSW process results in a peak temperature at the advancing-trailing side which exceeds 1400°C. (c) at a cooling rate in the range of 10-30°C/sec, segregation of the Mn, Si, Al and O spinel including Zn occurs as shown previously by heat treatments for the peak temperature and cooling rate required for segregation (section 5.11.2 and 5.11.3). (d) The segregated elements are moved from the top surface of advancing-trailing side and distributed downward into the SZ under the effect of tool rotational and traverse speeds. This finding is in agreement with Arbegast et al. 2003 [45] who showed that material during FSW experiences upward flow into the shoulder and then downward flow into the extrusion zone around the tool.

The difference in the shape of the segregated elements following the FSW process when compared to those following the heat treatments is as a result of the thermo-mechanical effect of the tool on the material during stirring. Figure 4.153 to figure 4.161 show a deformed longitudinal shape of the spinel which has a larger size than is shown in the heat treated samples. The increase in spinel size in FSW samples may be a result of joining small spinel's together under the effect of stirring. It is also shown that other elements such as Ca and P appear in the spinel in some locations of the SZ as in figure 4.155; sulphur is also found to exist in the spinel as shown in figure 4.156 and figure 4.162. This can give an indication that the SZ has experienced localised heating including a higher peak temperature which reaches or exceeds 1450 ^{o}C and which can cause complete segregation of the spinel whereas some locations in the SZ have experienced lower temperatures.

4.11.5 Experimental Heat Treatments to help understand the Segregation/Precipitation Process.

In an effort to understand the formation of the complex spinel of Mn, Si, Al and O which have been identified in the FSW joints of DH36 samples W6 and W8 and in the heat treatments of unwelded samples of DH36 and EH46, a series of heat treatments were carried at 1450°C with holding times of between 1 min and 15 minutes. The temperature of 1450°C was chosen because it showed the lower limit of elemental segregation and below this limit no segregation of Mn, Si, Al and O is likely to occur as mentioned in the heat treatments previous sections. The purpose of varying the soak time in the furnace was to establish knowledge of the segregation progress with increasing time. Following heat treatment all the samples were quenched in hot oil which gives a cooling rate of approximately 30°C/sec. Following oil quenching, all samples were sectioned, polished and etched in preparation for microscopic examination of the microstructure. The results of the microstructural examination of the segregation steps are presented in figures 4.163 to figure 4.167 -a- and -b- and the final step of segregation is shown in figure 4.168.

It can be seen in figure 4.163 -a- and -b- (1 min and 2 min soaking time respectively) that segregation appears to be starting with the coalescing of MnS-CaS with Al_2O_3-CaO to form a complex compound as in figure 4.164 -a- which is an example of the chemical composition of the predominate second phase particles in the matrix after 3 minutes soak time. The segregation appears to advance with time by more elements joining the complex compound

such as Si, Nb and P as shown in figure 4.164 -b- (4 min soaking time). During this stage separation of sulphides from the main compound occurs including the formation of 2nd phase particles which are rich mainly with niobium and sulphur. Other elements such as Ti, P and V are also found to join with the niobium sulphide as shown in figure 165 -a- and -b- and figure 4.166 -a-. Calcium sulphide, as shown in figure 4.166 -b-, exists once the soaking time is increased to 5 min. During the period of increasing the soaking time up to 10 minutes the separation of sulphur from the complex compound is almost completed leaving the Mn, Si, Al and O with some other elements such as Ti and Nb as shown in figure 4.167 -a- and -b-. The final spinel compound with increasing holding time to 15 min elementally consists of Mn, Si, Al and O as shown in 4.168.

This elemental segregation is expected to have a detrimental effects on the final welding joint' mechanical properties as these elements can be a source of microcracks and residual stresses. Also the main matrix of steel has lost the benefit of uniform elemental distribution which was mainly added to the steel during manufacturing in order to improve the physical properties. The effect of elemental precipitation/segregation on the mechanical properties will be discussed in the defect section.

1. SEM-EDS of DH36 heat treated samples for 1min at 1400°C and oil quenched
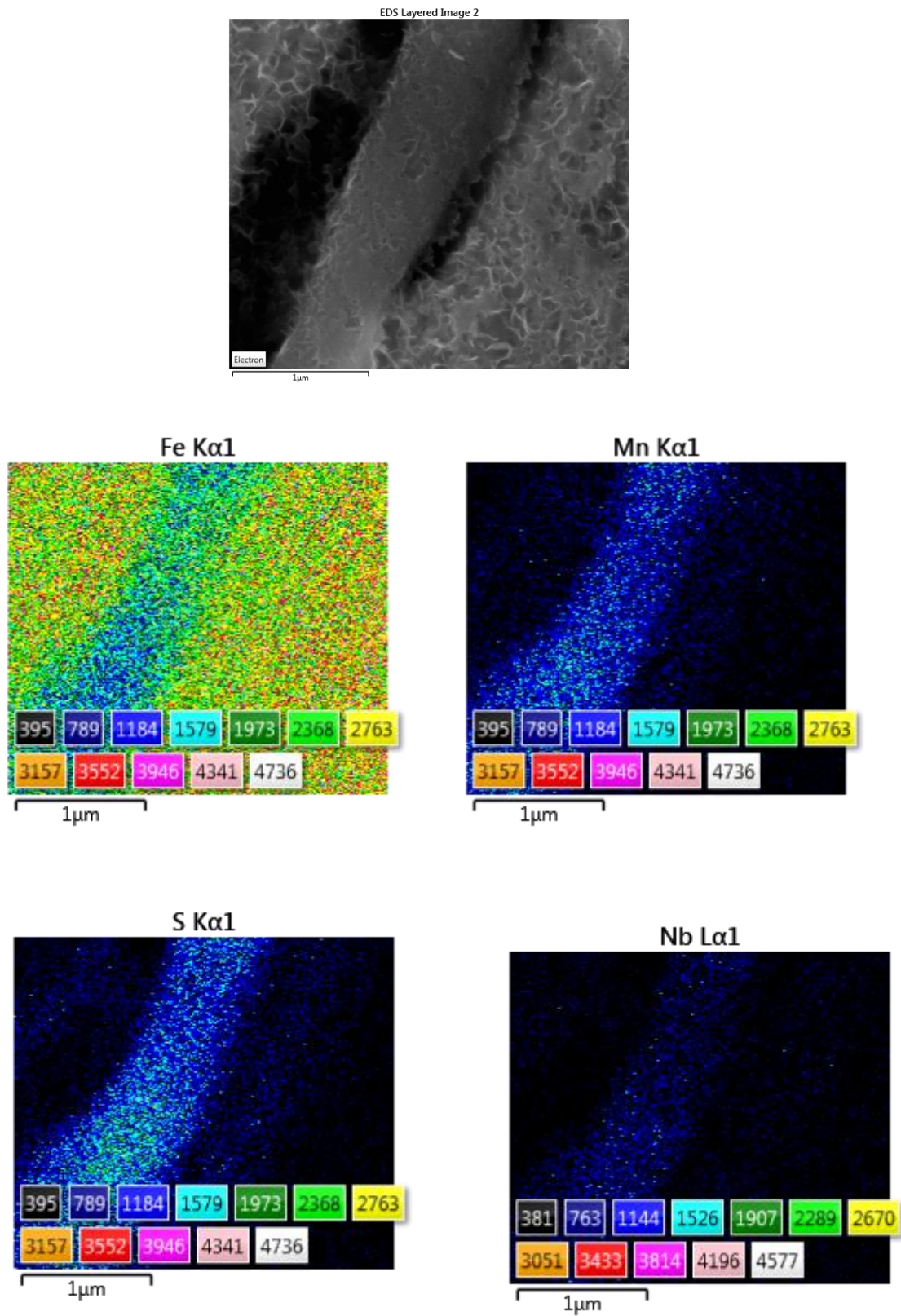
Figure 4.128: SEM-EDS mapping of DH36 steel heat treated for 1 min at 1400°C, oil quenched showing precipitation/segregation of Mn, S and Nb at the prior austenite grain boundary (PAGB).
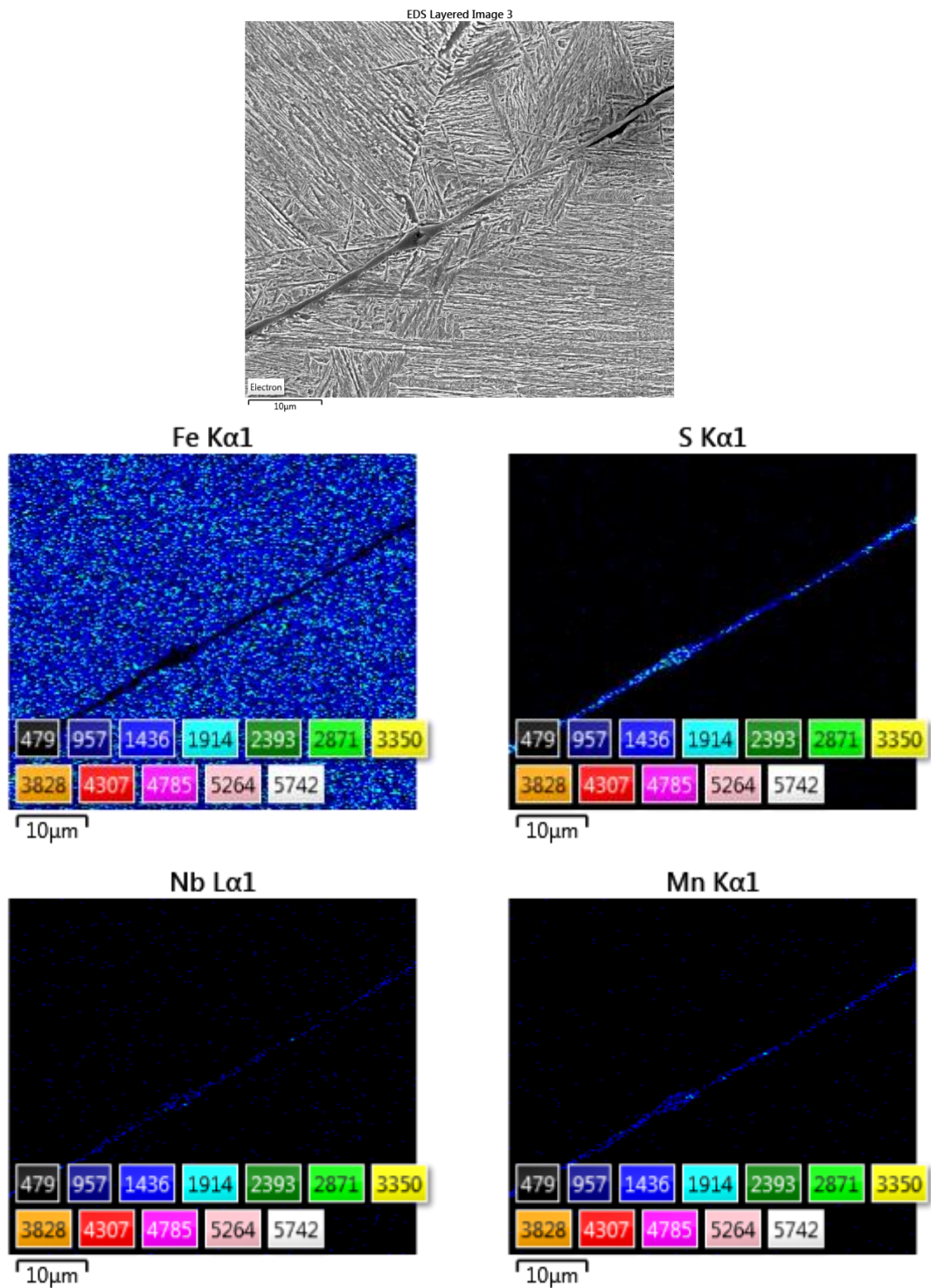
Figure 4.129: SEM-EDS mapping of DH36 steel heat treated at 1400ᵒC for 1 min and quenched showing precipitation/segregation of Mn, S and Nb at prior austenite grain boundary (PAGB).

2. SEM-EDS of DH36 steel sample heat treated at 1400°C for 10min and oil quenched
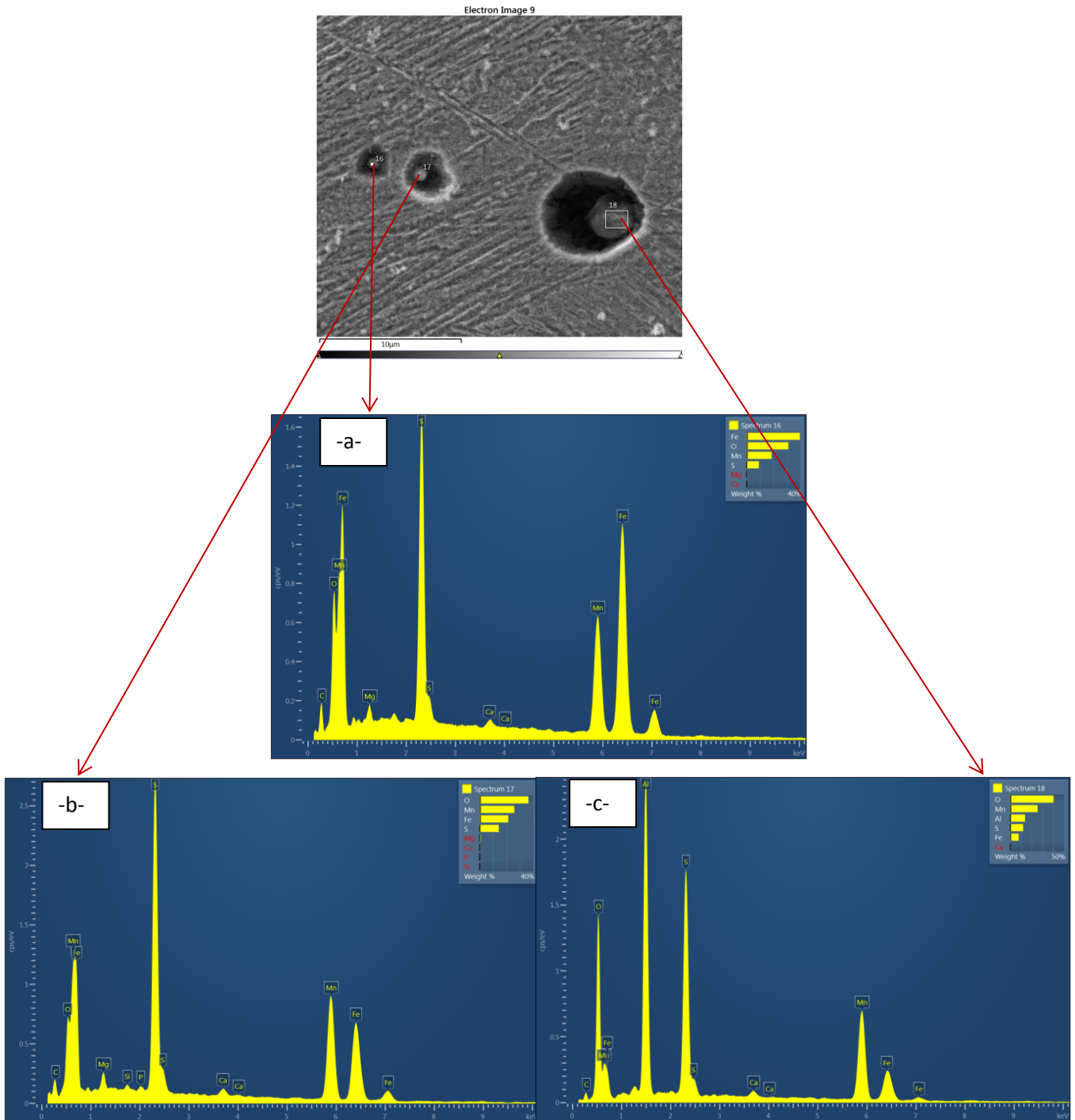
Figure 130: SEM-EDS Point and ID of DH36 steel heat treated at 1400°C for 10 mins and oil quenched showing precipitation/segregation of different types of elements -a- Mn, S, Ca and O. -b- Mn, S and P. -c- Mn, Ca, Al and O.
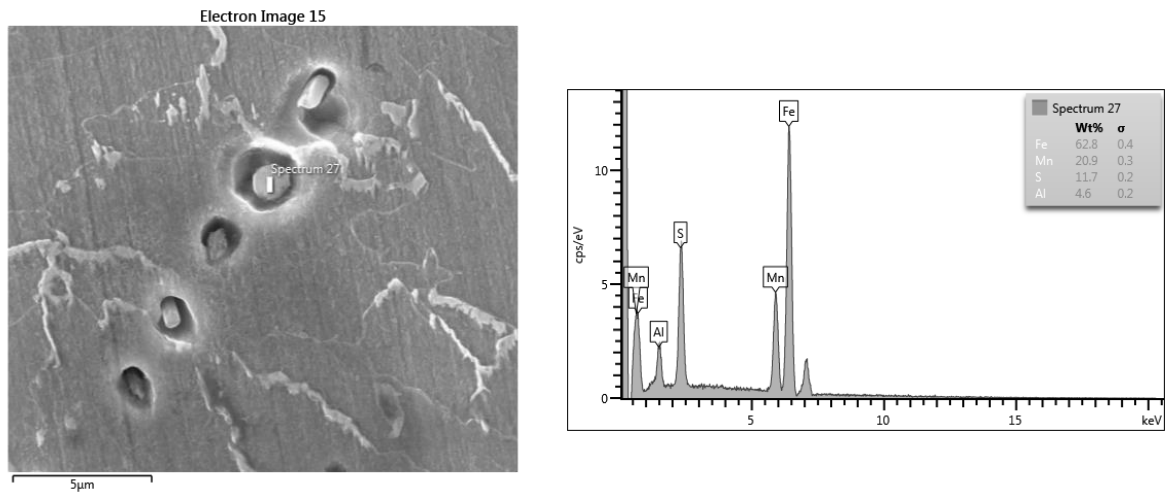
Figure 4.131: SEM-EDS Point and ID of DH36 steel sample heat treated at 1400°C for 10 mins and oil quenched showing precipitation/segregation of elements mainly Mn, S and Al.

3. SEM-EDS of EH46 steel samples heat treated at 1400°C for 1min and oil quenched.
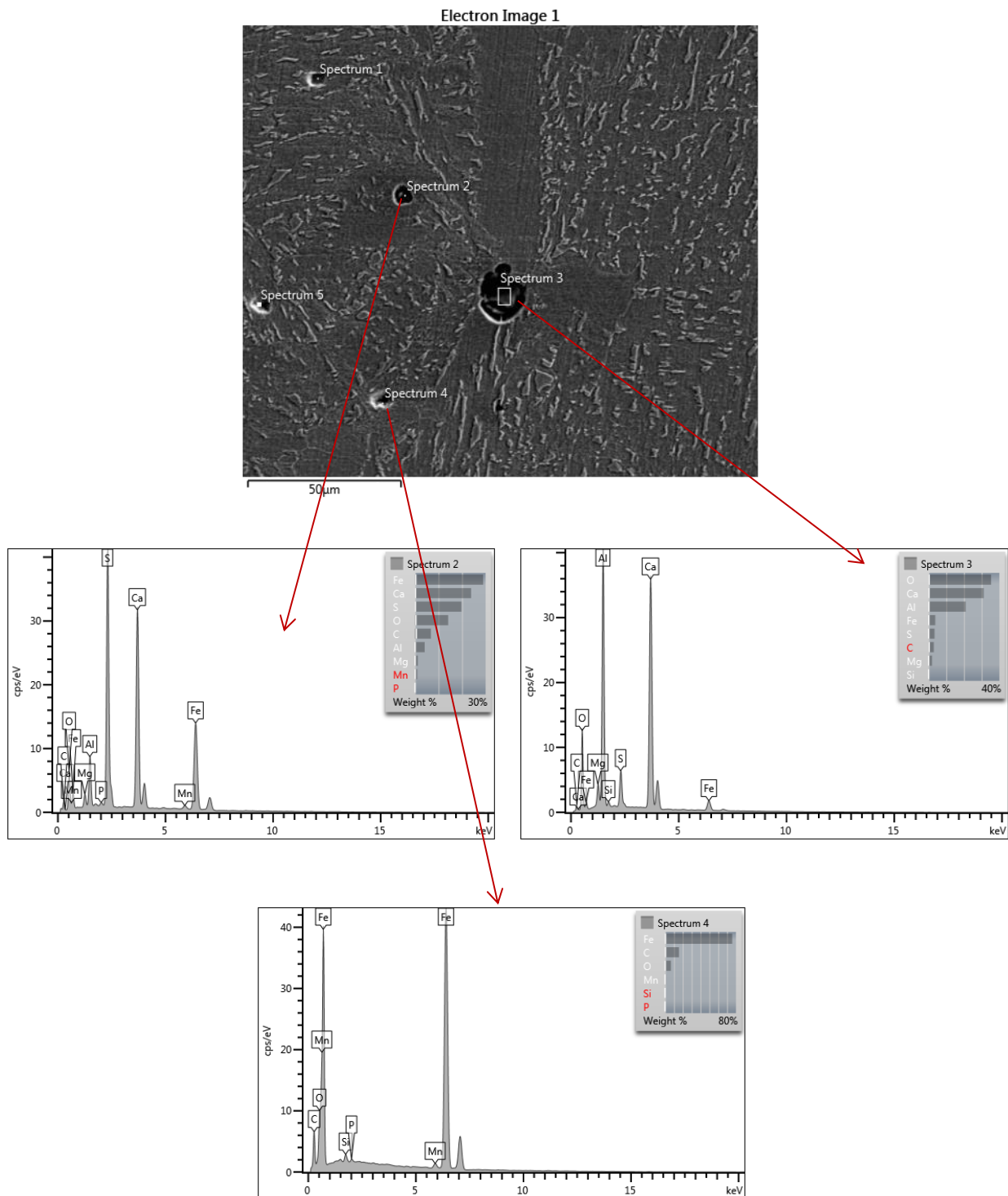
Figure 4.132: SEM-EDS Point and ID of EH46 heat treated at 1400°C for 1 min and oil quenched showing precipitation/segregation of Al,S and P rich particles .

4. SEM-EDS of EH46 steel samples heat treated at 1400°C for 10min and oil quenched
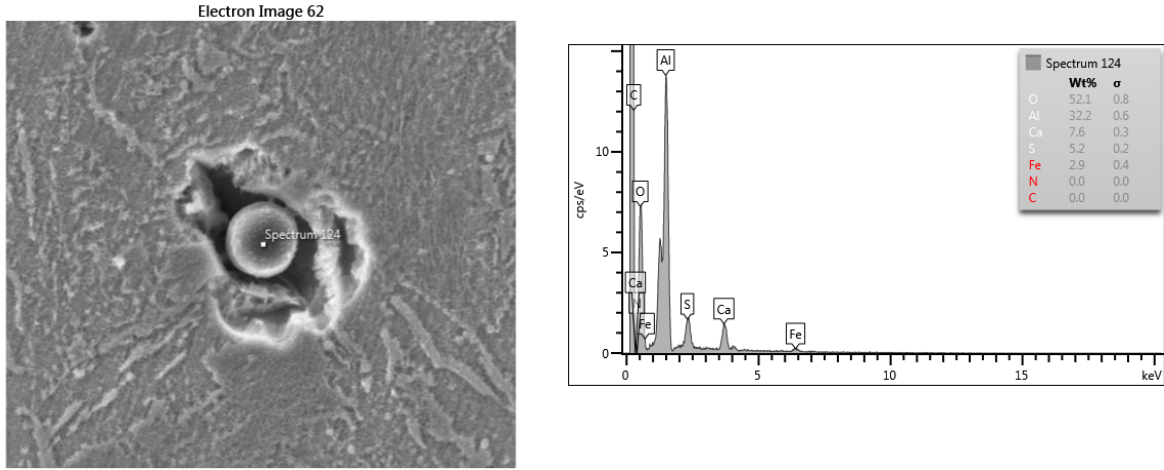
Figure 133: Possibly alumina-CaS precipitation in the EH46 heat treated at 1400 °C for 10min and oil quenched.
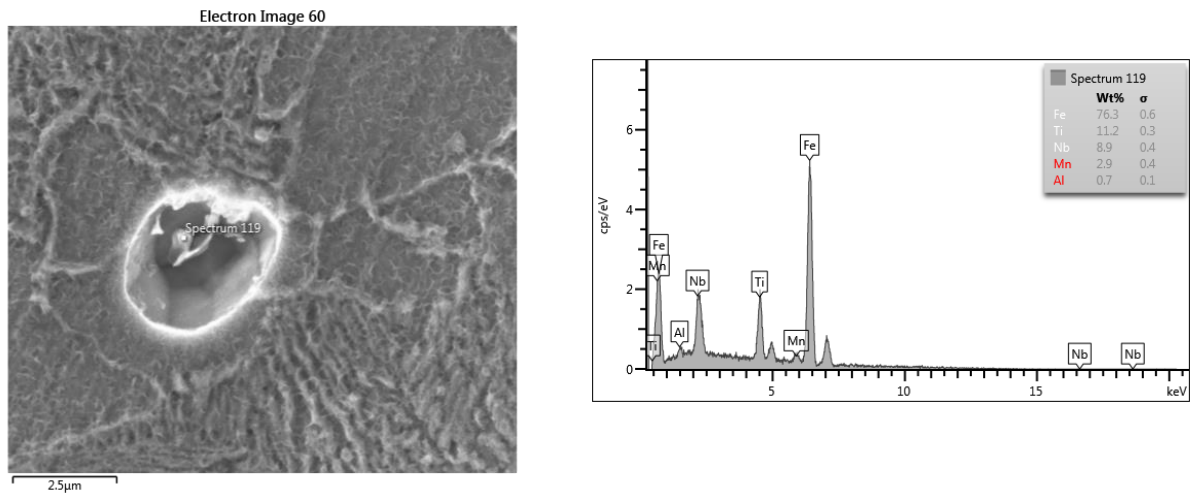
Figure 4.134: Ti, Nb and Al precipitation in the EH46 heat treated at 1400 °C for 10min and oil quenched.
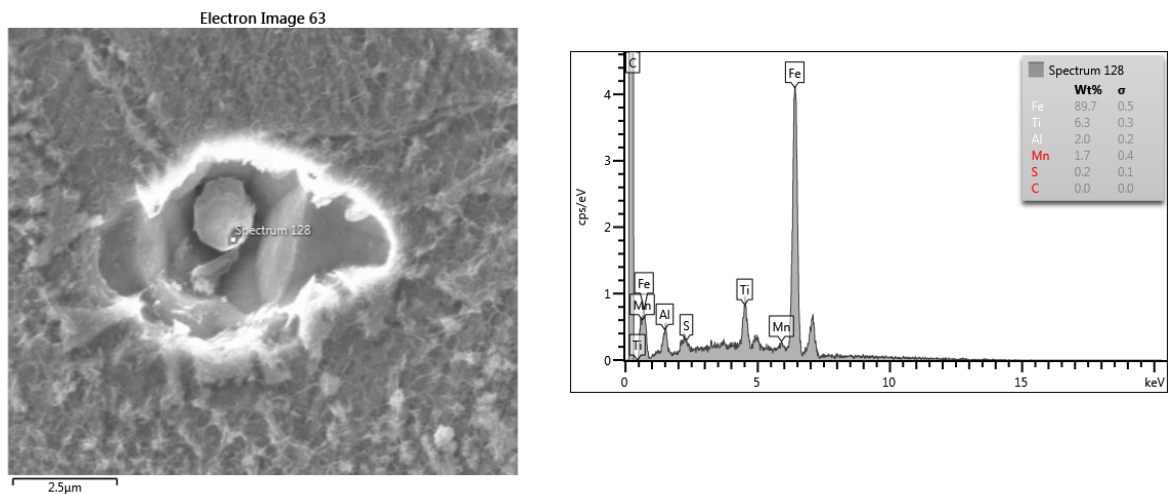
Figure 4.135: SEM-EDS shows Ti, S and Al precipitation in the EH46 heat treated at 1400 °C for 10min and oil quenched.

5. SEM-EDS of DH36 steel samples heat treated at 1450°C for 1min and oil quenched.
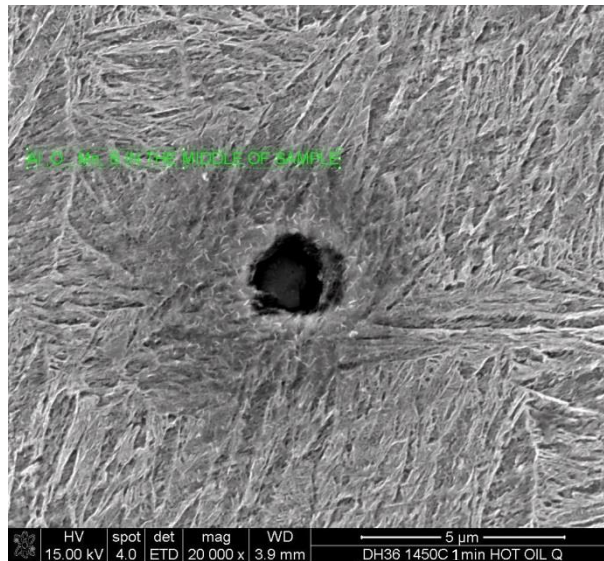
Figure 4.136: SEM image of DH36 steel heat treated at 1450°C for 1 min and oil quenched showing precipitation/segregation of Mn, Al, S and O elements as identified by EDS.

6. SEM-EDS of DH36 steel samples heat treated at 1450°C for 4min and oil quenched.

-a-   -b-
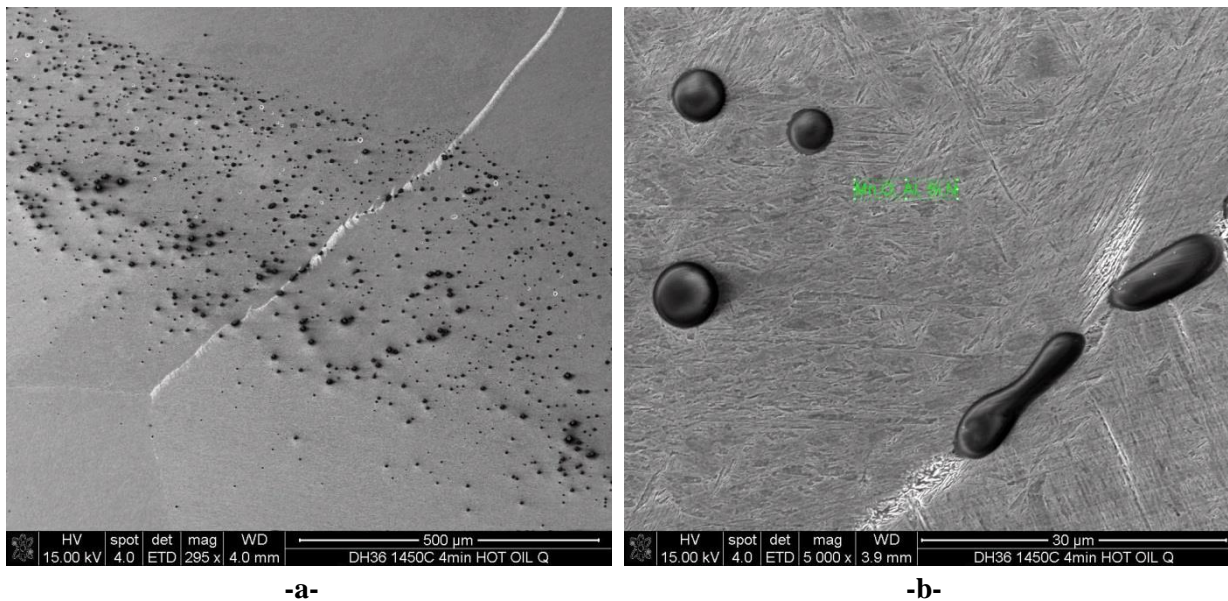
Figure 4.137: SEM images -a- low and -b- high magnification of DH36 steel heat treated at 1450°C for 4 mins and hot oil quenched showing precipitation/segregation of Mn, Al, Si and O elements as identified by EDS.
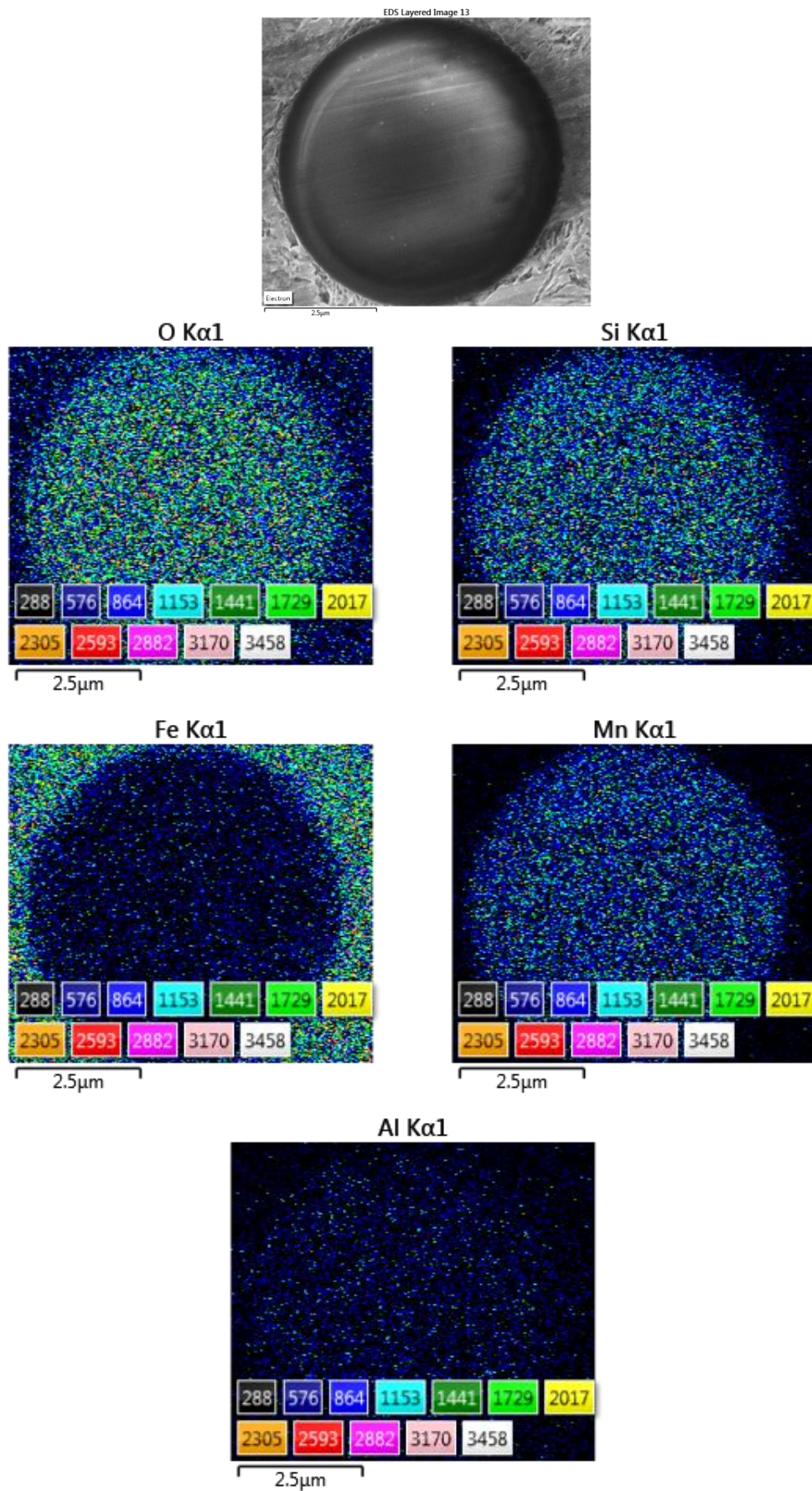
Figure 4.138: SEM-EDS mapping of DH36 steel heat treated at 1450°C for 4 mins and oil quenched showing Mn, Si, Al and O segregation.

7. SEM-EDS of DH36 steel samples heat treated at 1450ºC for 10mins and oil quenched.
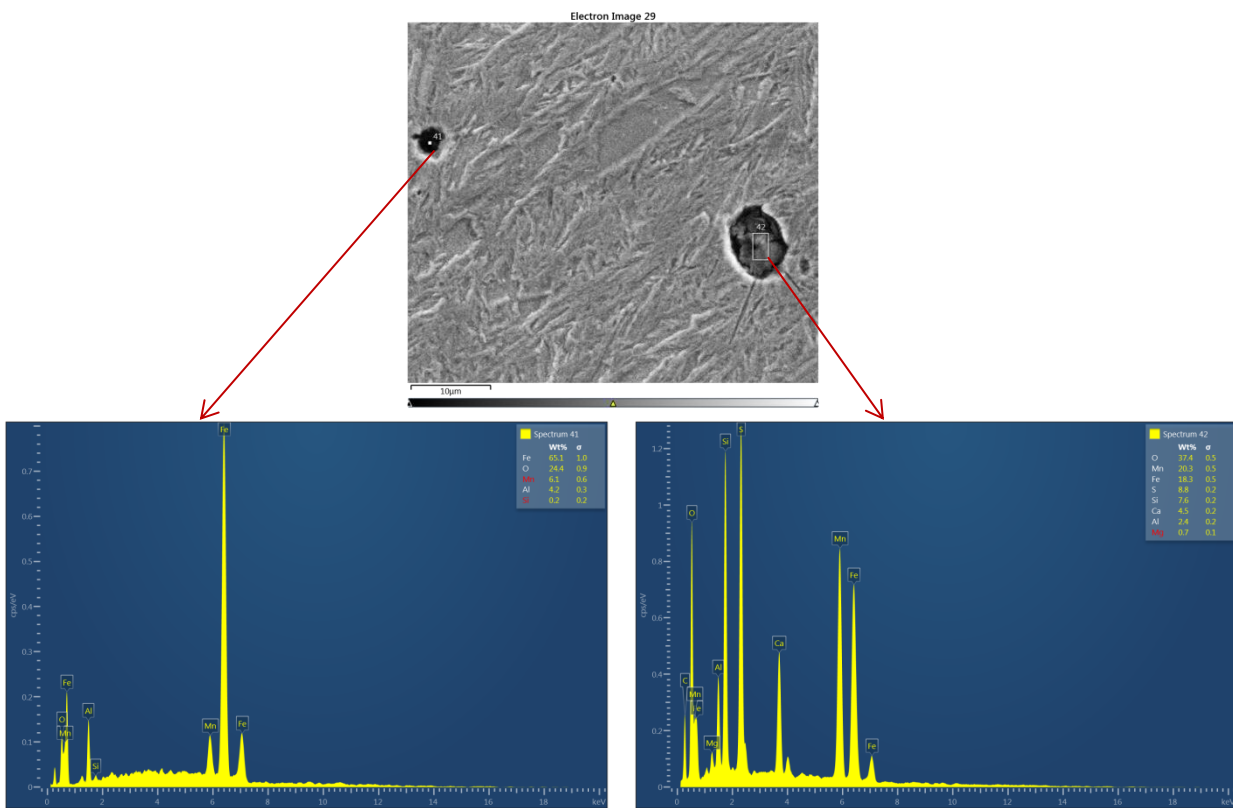
Figure 4.139: SEM-EDS of DH36 steel samples heat treated at 1450ºC for 10mins and oil quenched showing the composition of the precipitates are mainly Mn, Si, Al and O. Ca and S are also present in some regions.

8. SEM-EDS of EH46 steel samples heat treated at 1450°C for 1min and oil quenched.
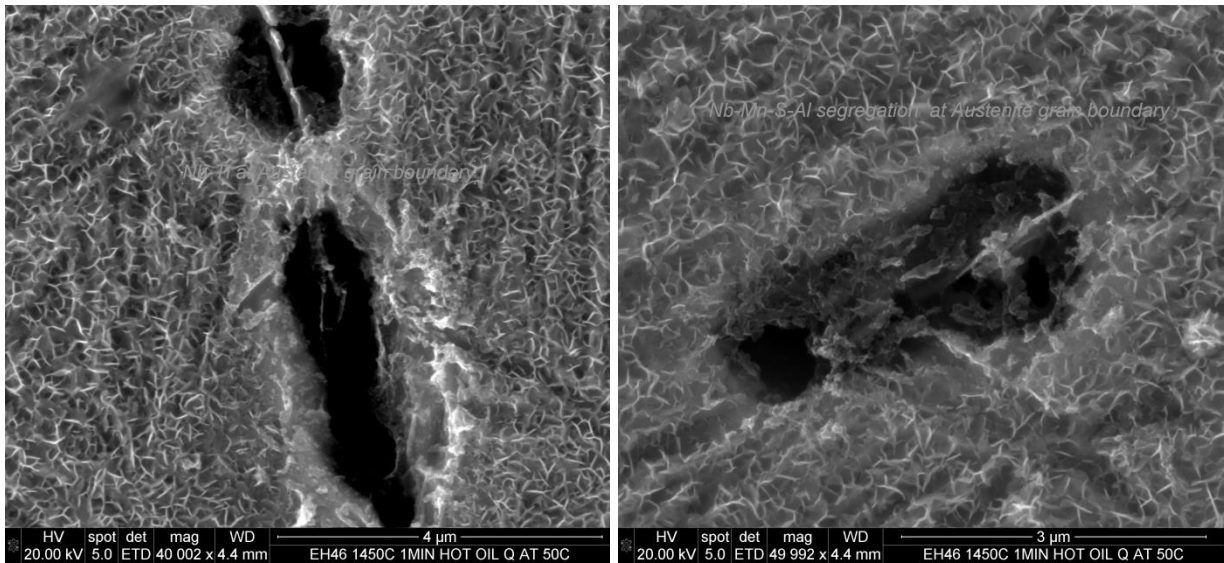
Figure 4.140: SEM images of EH46 steel heat treated at 1450°C for 1min and oil quenched, EDS shows the precipitates are rich is Mn, S, Al, Nb.
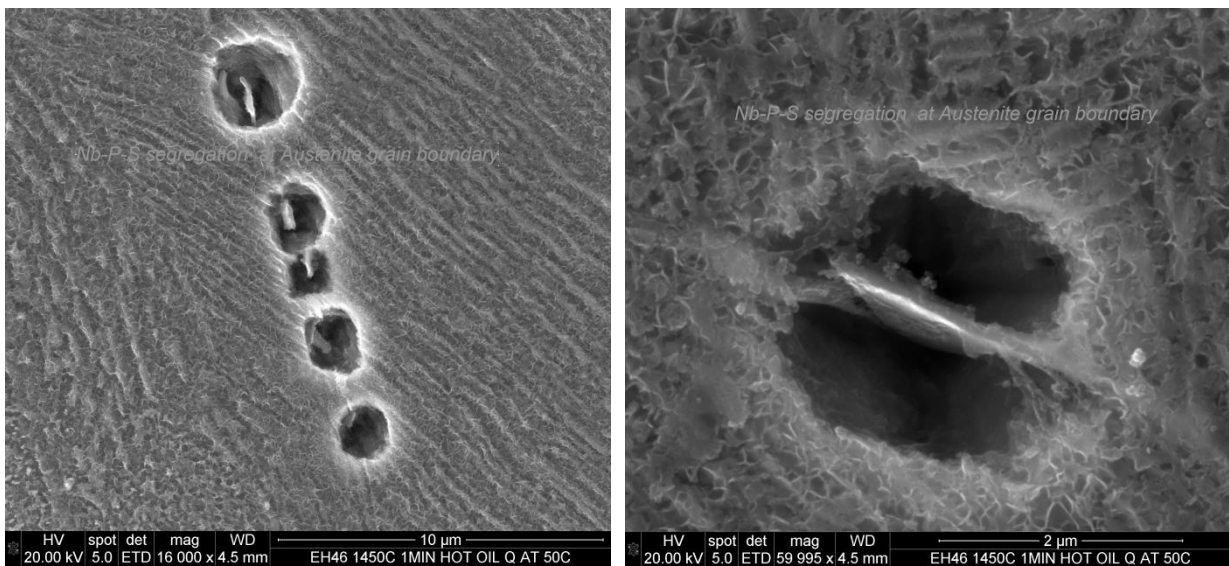
Figure 4.141: SEM images low and high magnification of EH46 steel heat treated at 1450°C for 1min and oil quenched. EDs analysis revealed that the segregation at prior austenite grain boundaries consists of Nb, P and S.

9. SEM-EDS of EH46 steel samples heat treated at 1450°C for 4min and oil quenched.

-a-

-b-

-c-
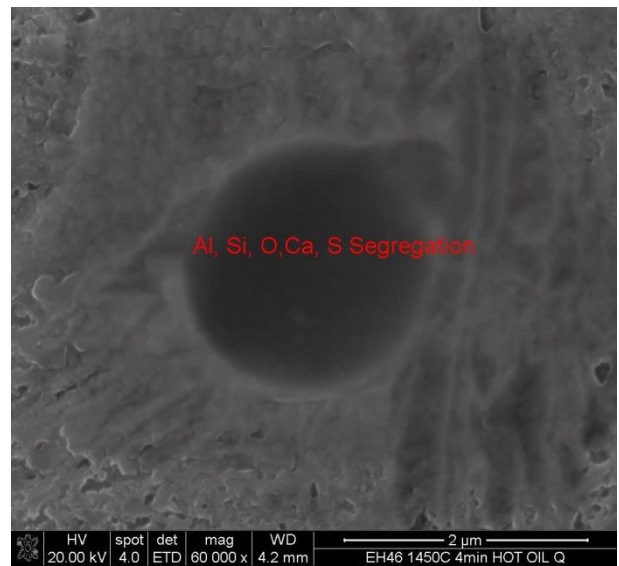
-d-
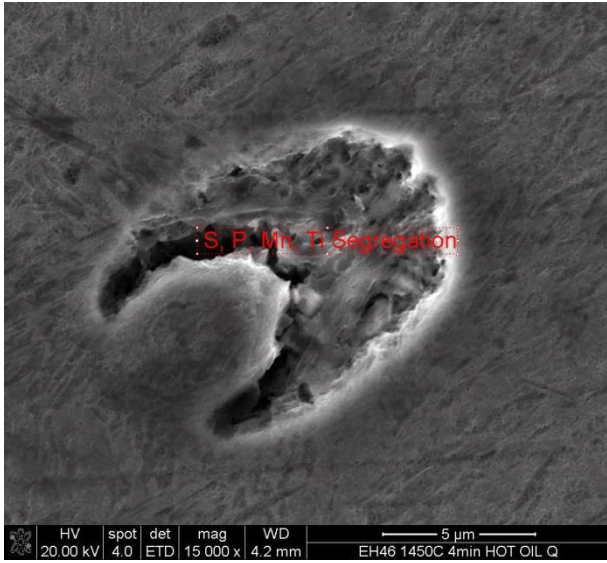
-e-
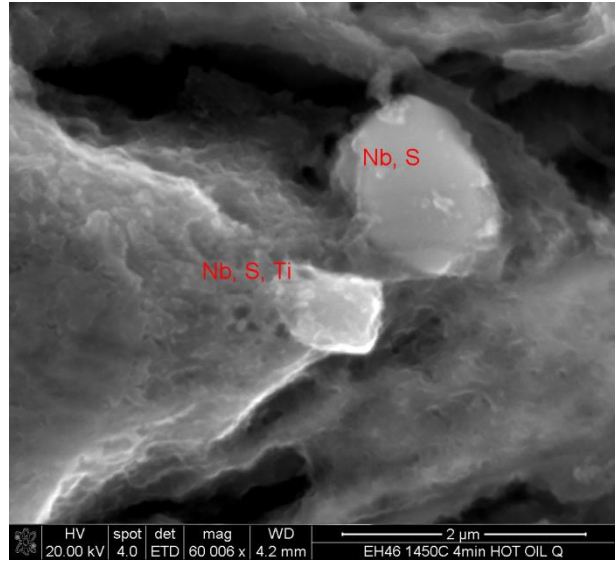
-f-
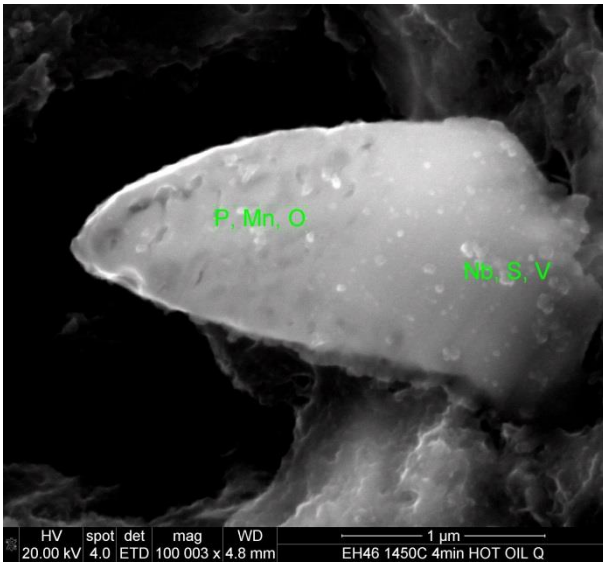
-g-
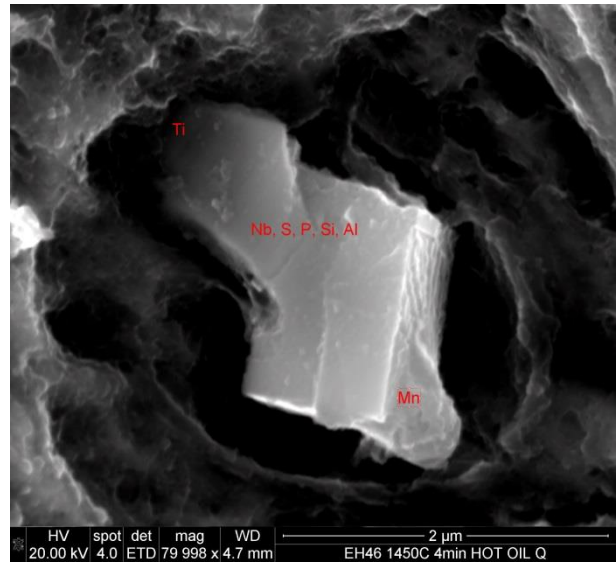
-h-
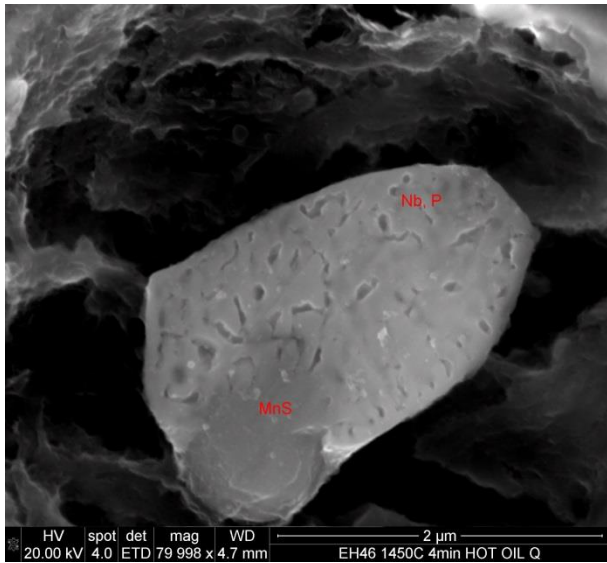
-i-
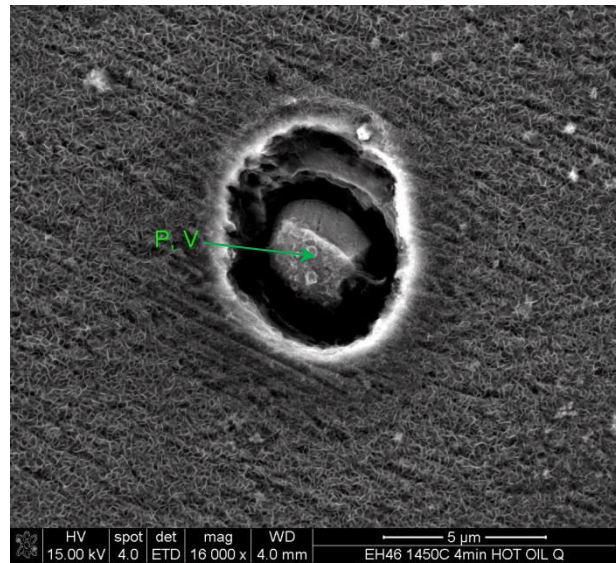
-j-
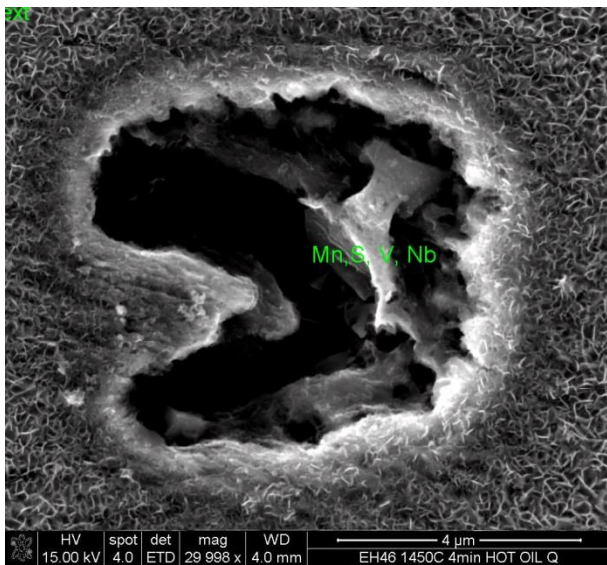
-k-
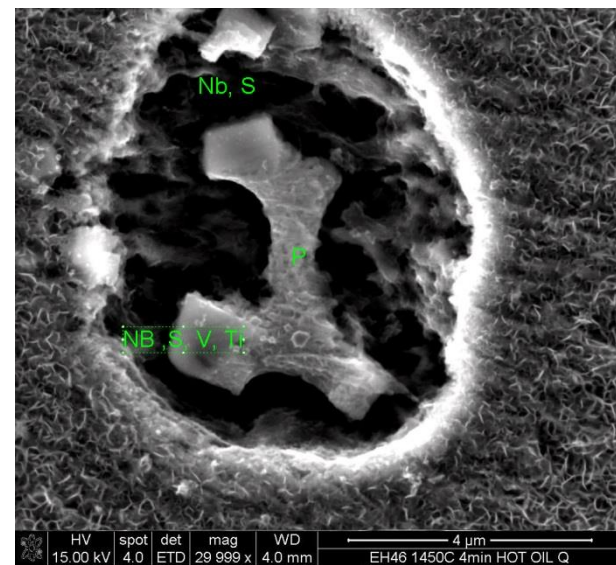
-l-

Figure 4.142: -a- to -l- Show different types of elemental segregation/precipitation as identified by EDS including (Mn, P, V, S, Al, O, Si, Ti and Ca), samples are EH46 steel heated at 1450°C for 4mins followed by oil quenching.

10. SEM-EDS of EH46 steel samples heat treated at 1450°C for 10min and oil quenched.
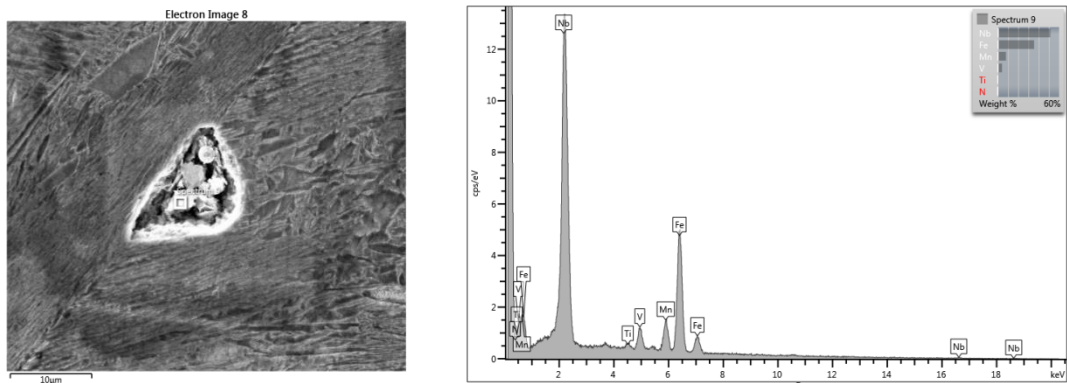
Figure 4.143: SEM-EDS of EH46 steel samples heat treated at 1450°C for 10mins and oil quenched showing segregation/precipitation of Mn, V, Ti and Nb rich particles.
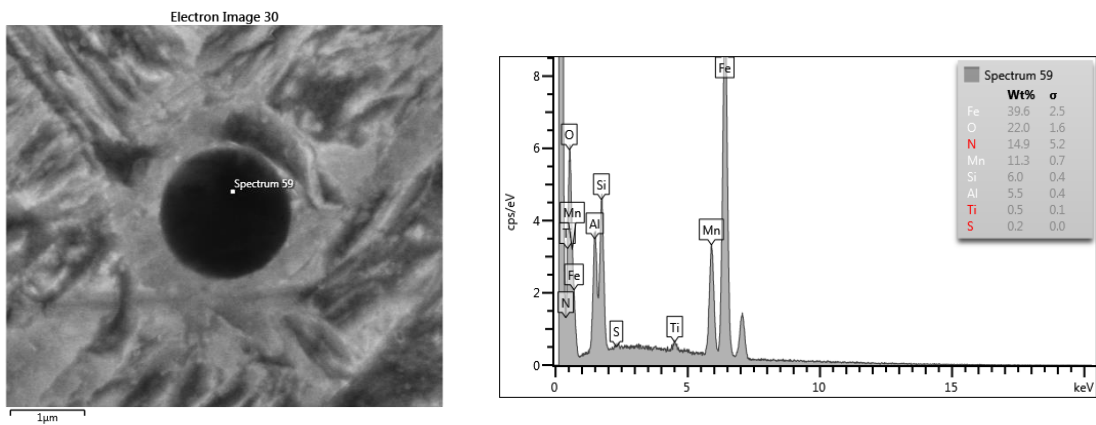
Figure 4.144: SEM-EDS of EH46 steel samples heat treated at 1450°C for 10min and oil quenched showing segregation/precipitation of Mn, Ti, Al, Si and O rich particles.

11. SEM-EDS of EH46 steel samples heat treated at 1450°C for 15min and oil quenched.
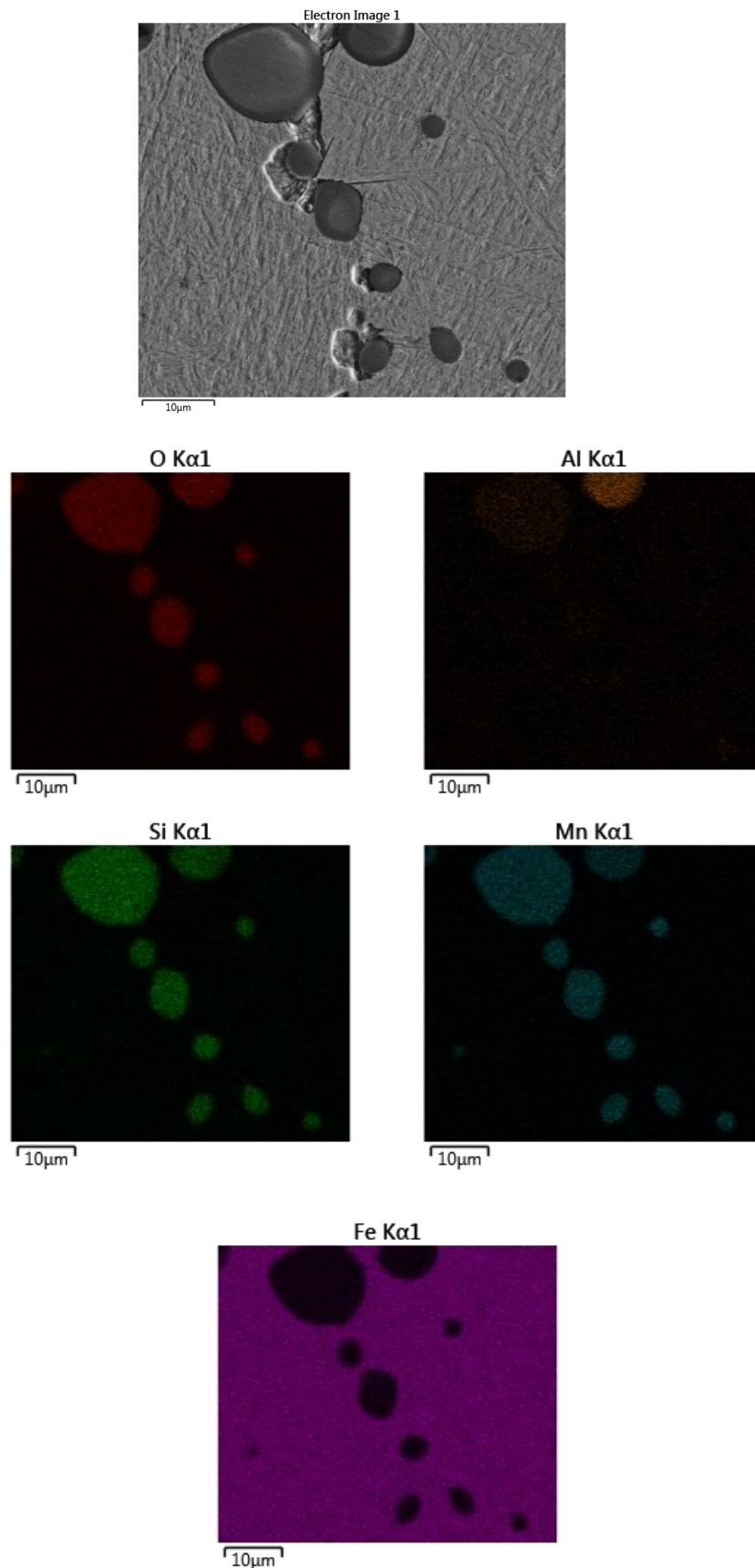
Figure 4.145: EDS mapping EH46 steel heat treated at 1450°C for 15min and oil quenched showing the segregation/precipitation of Mn, Si, Al and O rich particles.
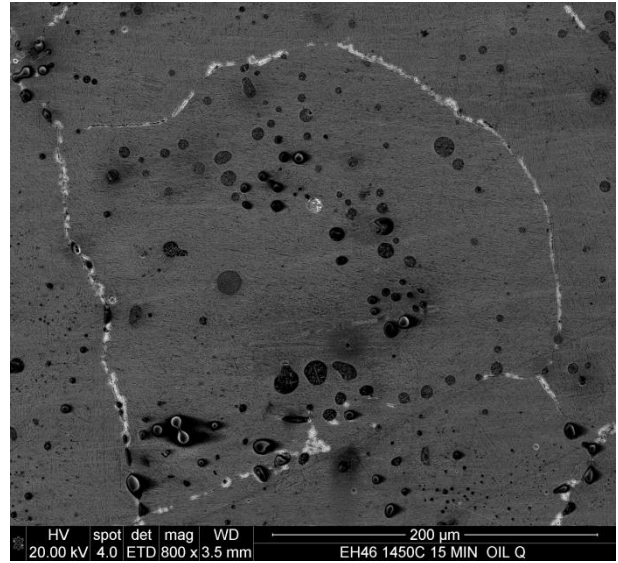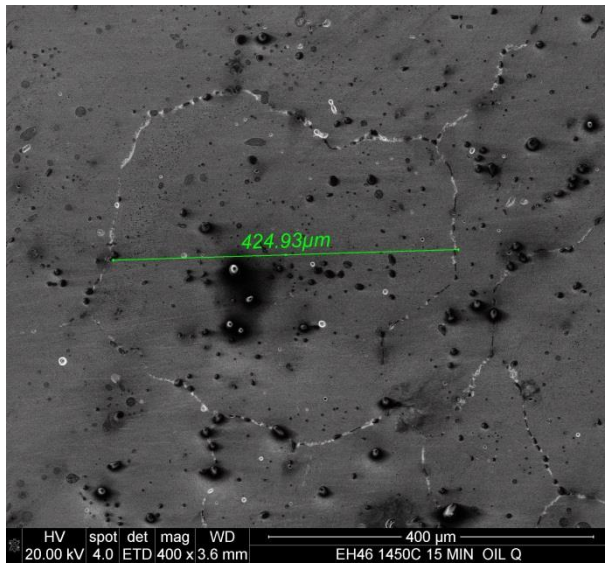
Figure 4.146: SEM of EH46 steel samples heat treated at 1450°C for 15min and oil quenched showing segregation/precipitation of Mn, Si, Al and O rich particles as identified by EDS.
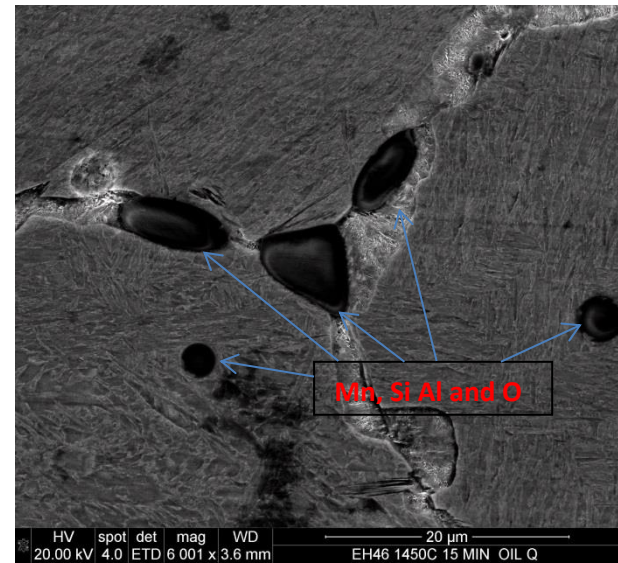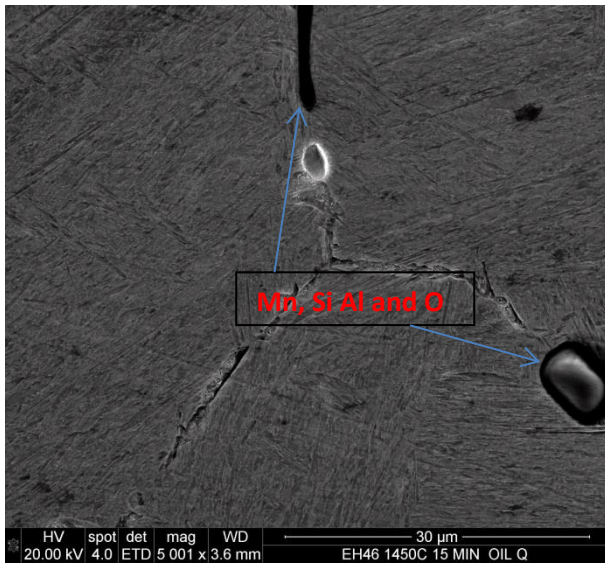
Figure 4.147: SEM high magnification of EH46 steel samples heat treated at 1450°C for 15min and oil quenched, showing segregation/precipitation of Mn, Si, Al and O rich particles as identified by EDS.

12. SEM and EDS of DH36 steel samples heat treated at 1500°C for 1min and oil quenched, showing precipitation of Mn, Si, Al and O particles.

-a-
-b-
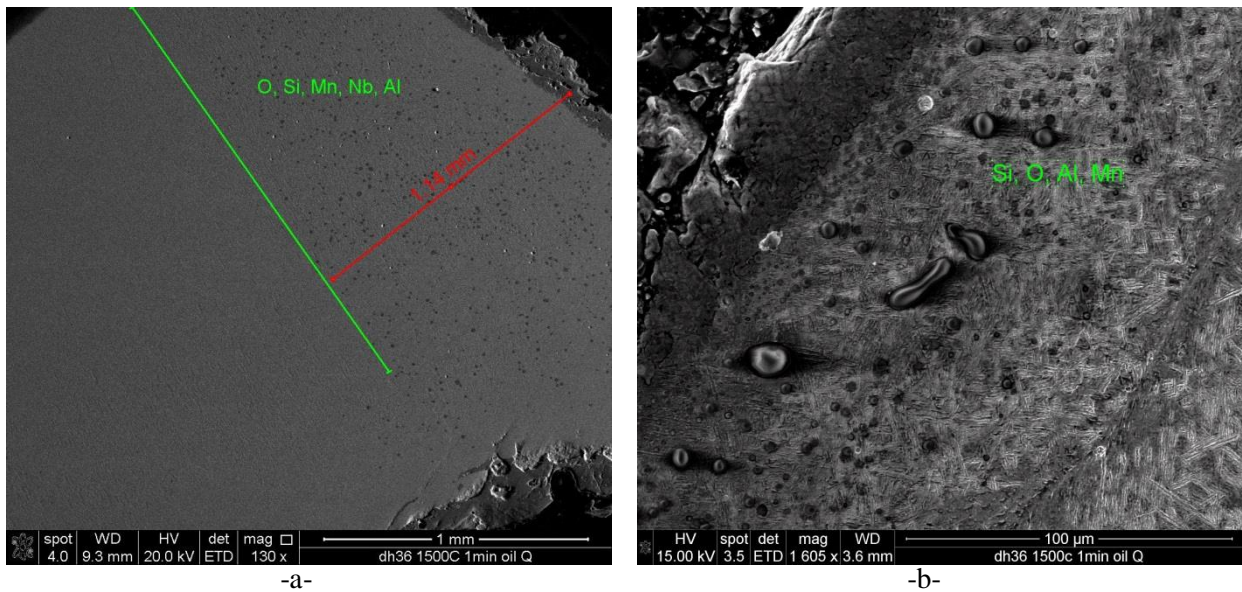
Figure 4.148: SEM (-a- low and -b- high magnification) of DH36 steel samples heat treated at 1500°C for 1min and oil quenched, showing precipitation of Mn, Si, Al and O rich particles as identified by EDS.
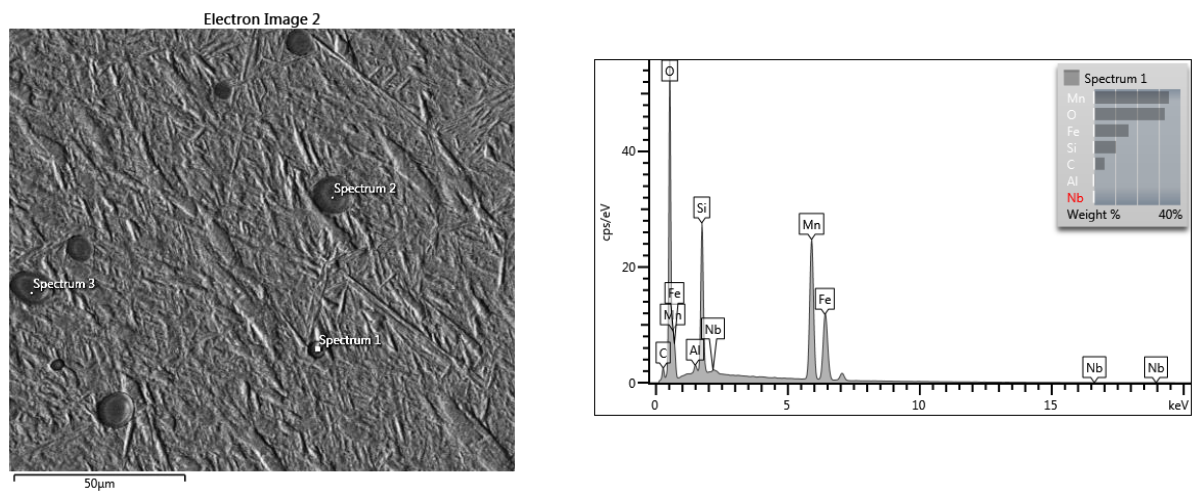
Figure 4.149: SEM-EDS of DH36 steel sample heat treated at 1500°C for 1min and oil quenched, showing segregation/precipitation of Mn, Si, Al and O rich particles segregation. Region is 1mm away from the outer sample surface.

Electron Image 1

-a-

-b-

Figure 4.150: DH36 steel sample heat treated at 1500ᵒC for 1min and oil quenched,-a- SEM (high magnification) shows Mn, Si, Al and O spinel segregation, -b- P and S segregation as identified by EDS.

13. SEM and EDS of EH46 steel samples heat treated at 1500ᵒC for 1min and oil quenched, showing Mn, Si, Al and O segregation.

Electron Image 4

Spectrum 13

	Wt%	σ
O	29.5	0.5
Mn	26.7	0.4
Fe	16.2	0.3
Al	15.4	0.2
Si	12.2	0.2

Figure 4.151: SEM-EDS of EH46 steel sample heat treated at 1500ᵒC for 1min and oil quenched, showing segregation/precipitation Mn, Si, Al and O rich particles. .

Figure 4.152: EDS mapping of EH46 steel sample heat treated at 1500°C for 1min and oil quenched, showing segregation/precipitation Mn, Si, Al and O rich particles.

239

Table 4.16: Heat treatments of DH36 steel grade from 1400 °C-1500 °C

Heating Temperature °C	Holding Time (minutes)	Elemental Segregation/Precipitation	Location of Segregation
1400	1	Mn, S, Nb	At austenite grains boundaries
1400	10	Mn, S, Ca and O Mn, S, Ca, P and O Mn, S, Ca Al and O Mn, S and Al	Within austenite grains and at austenite grains boundaries
1450	1	Mn, Al, S and O	Within austenite grains and at austenite grains boundaries
1450	4	Mainly Mn, Al, Si and O Mn, S, Ca Al and O	Within austenite grains and at austenite grains boundaries
1450	10	Mainly Mn, Al, Si and O Mn, S, Ca Al and O	Within austenite grains and at austenite grains boundaries
1500	1	Mainly Mn, Al, Si and O	Within austenite grains and at austenite grains boundaries

Table 4.17: Heat treatments of EH46 steel grade from 1400 °C-1500 °C

Heating Temperature °C	Holding Time (minutes)	Elemental Segregation/Precipitation	Location of Segregation
1400	1	Ca, S Al and O	Within austenite grains and at austenite grains boundaries
1400	10	Ti, Nb and Al Al, Ca ,S and O Ti, S and Al	Within austenite grains
1450	1	Mainly Mn, Al, S and Nb Nb, P and S Nb, S S,Al,O Al, O, Si, Ti, Mn	At austenite grains boundaries within austenite grains
1450	4	Nb ,S Mn, P Mn, Al, Si, S and Ti P, Mn, O, Al Nb, V, S Ti,Nb, Al, O Al, Nb, O Al, Si, Ca, O, S S, P, Mn, Ti Nb, S, Ti P, Mn, O Nb, S, P, Si ,Al Nb, P P, V Mn, S, V, Nb Nb, S, V, Ti	Within austenite grains at austenite grains boundaries
1450	10	Mn, Ti, Al, Si and O Ca, S Nb ,S Mn, P Mn, Al, Si, S and Ti P, Mn, O, Al Nb, V, S Ti,Nb, Al, O Al, Nb, O Al, Si, Ca, O, S S, P, Mn, Ti Nb, S, Ti P, Mn, O Nb, S, P, Si ,Al Nb, P P, V Mn, S, V, Nb Nb, S, V, Ti	Within austenite grains and at austenite grains boundaries
1450	15	Mainly Mn, Al, Si and O Al, O, Mn, Ti, Si Mn, S, Nb, Si, P, O P, S, Mn, V, Nb Nb, S C, P, S, V, Mn, Nb C, P, Mn, V	Within austenite grains and at austenite grains boundaries
1500	1	Mainly Mn, Al, Si and O	Within austenite grains and at austenite grains boundaries

14. FSW samples from samples W6 and W8 (DH36) welded at high tool speeds (550RPM, 400 mm/min)
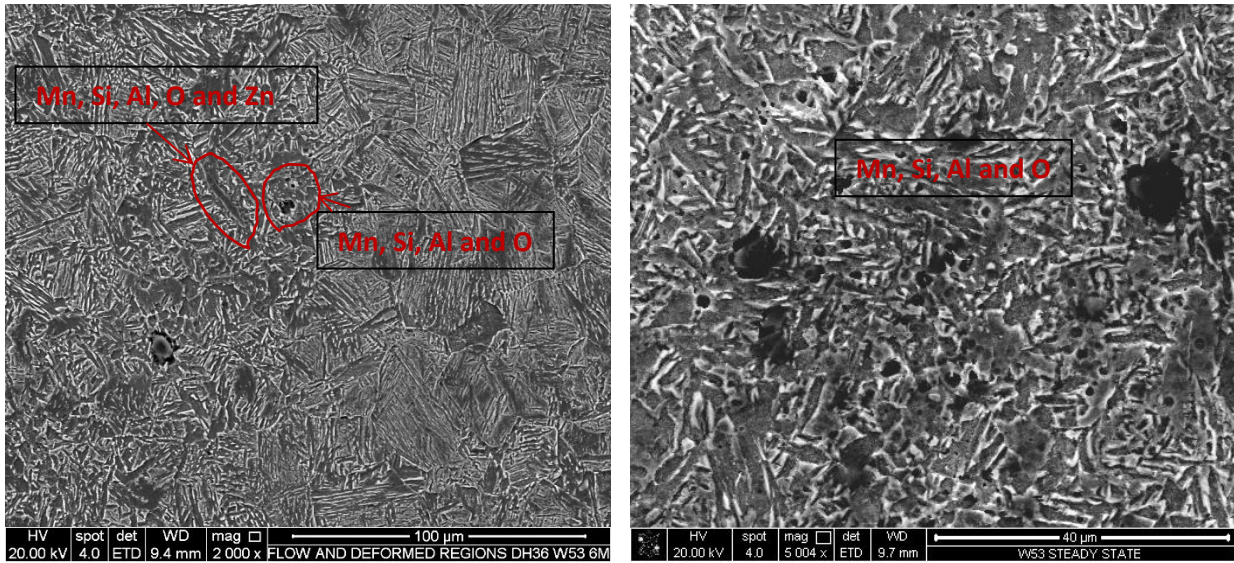
Figure 4.153: SEM images taken at low and high magnification of FSW of W6 (DH36) showing elemental segregation/precipitation of Mn, Si, Al, O and Zn rich particles as identified by EDS.
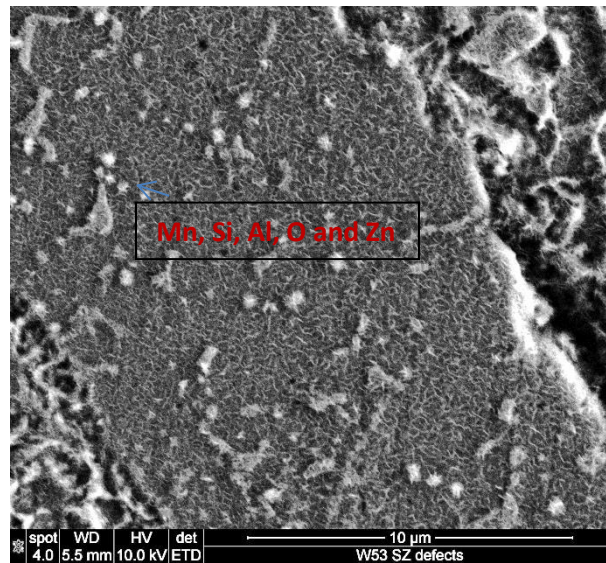
Figure 4.154: SEM image high magnification of FSW of sample W8 (DH36) shows elemental segregation/precipitation of Mn, Si, Al, O and Zn rich particles as identified by EDS.
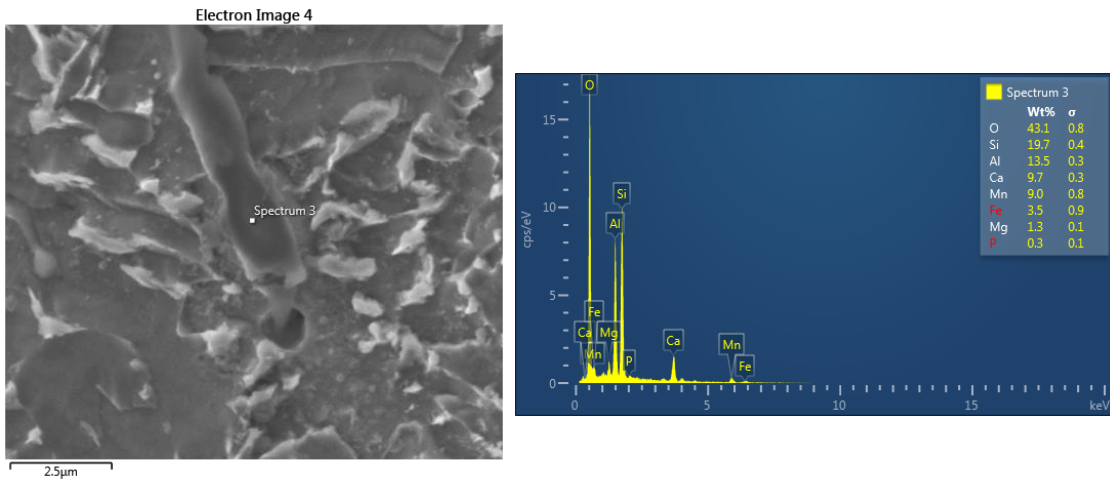
Figure 4.155: SEM-EDS at high magnification of FSW of sample W6 (DH36) show elemental segregation/precipitation of Mn, Si, Al, O and Ca rich particles as identified by EDS.
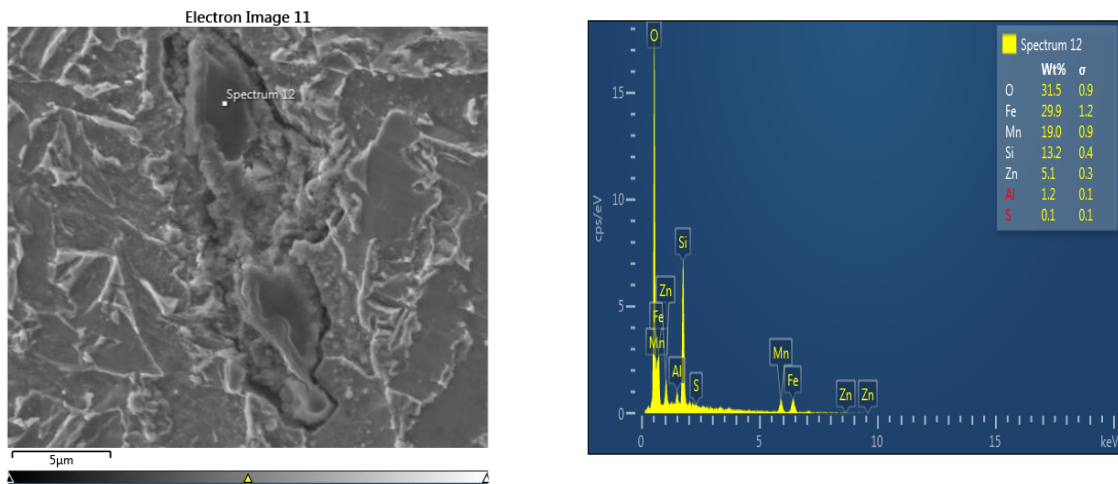
Figure 4.156: SEM-EDS showing elemental segregation of Mn, O, Si, Al and Zn in the SZ of the high tool speed welded sample W6 (DH36).
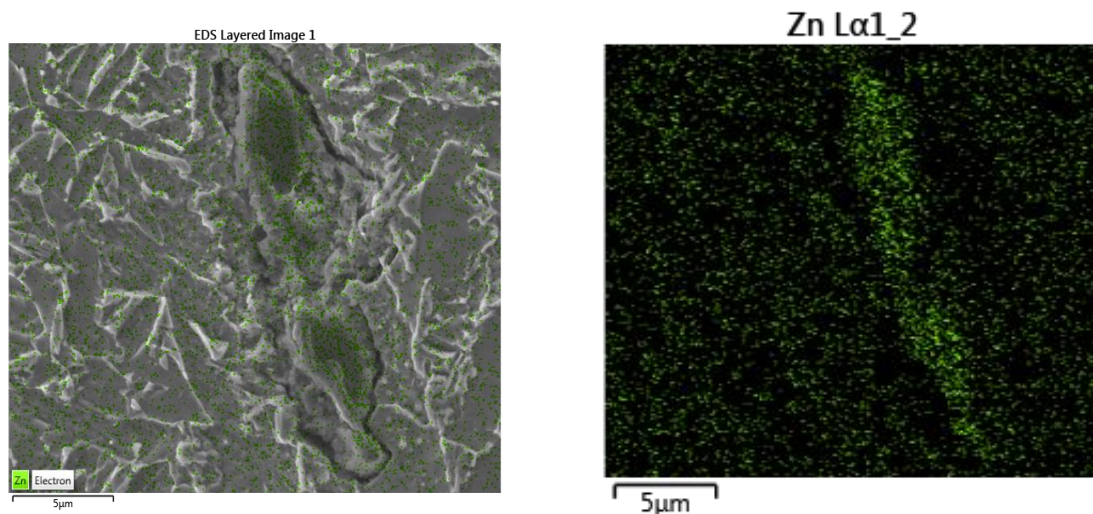
Figure 4.157: EDS mapping of Zn in the elemental segregation of the SZ of sample W6 (DH36) as identified by EDS.
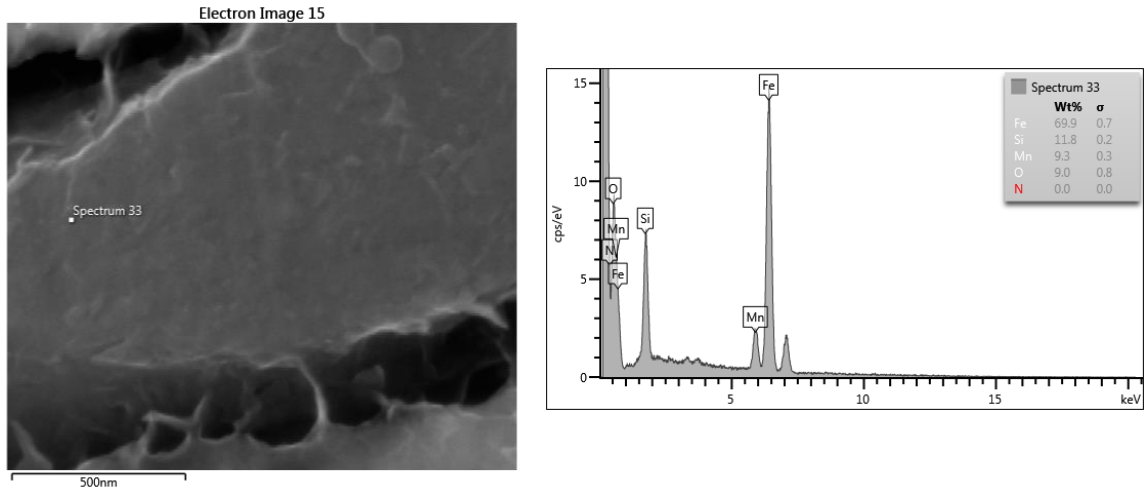
Figure 4.158: SEM-EDS shows elemental segregation of Mn, O and Si in the SZ of FSW sample W6 (DH36) welded at high tool speeds ().
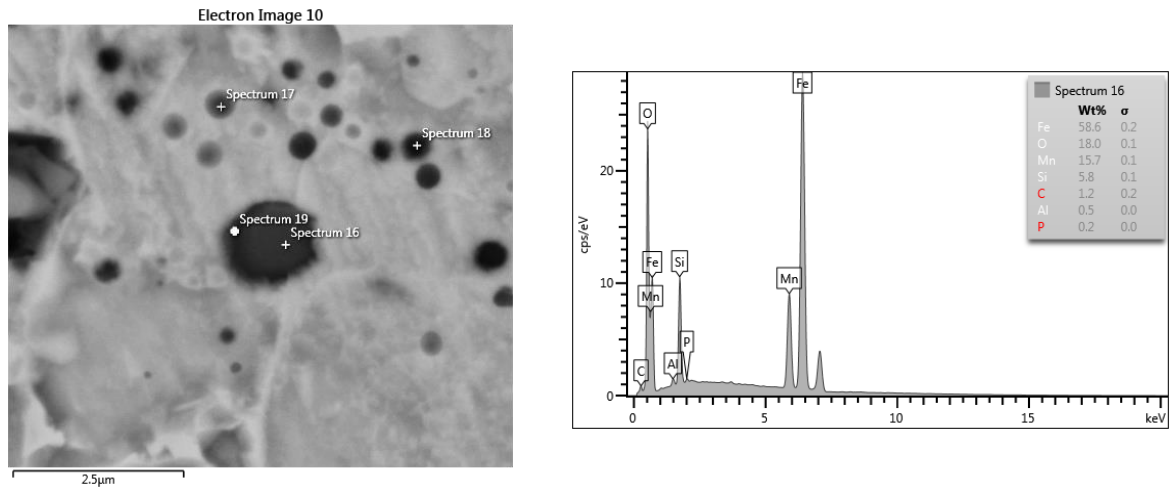
Figure 4.159: SEM-EDS shows elemental segregation/precipitation of Mn, O and Si in the SZ of FSW sample W8 (DH36) welded at high tool speeds ().
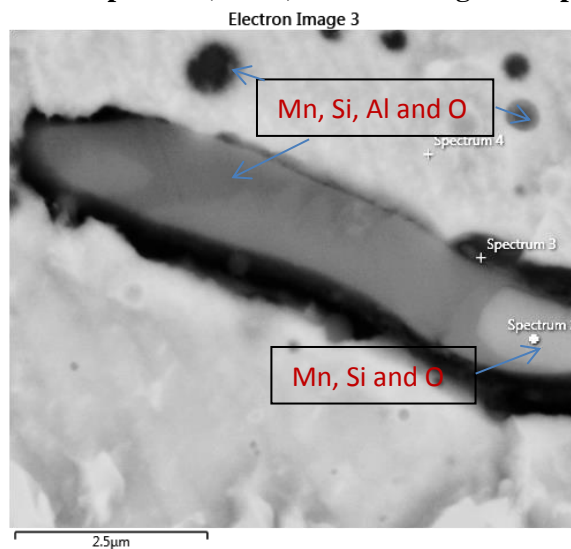
Figure 4.160: SEM image at the SZ of FSW sampleW8 (DH36) showing elemental segregation/ precipitation of Mn, Si, Al and O as identified by EDS.
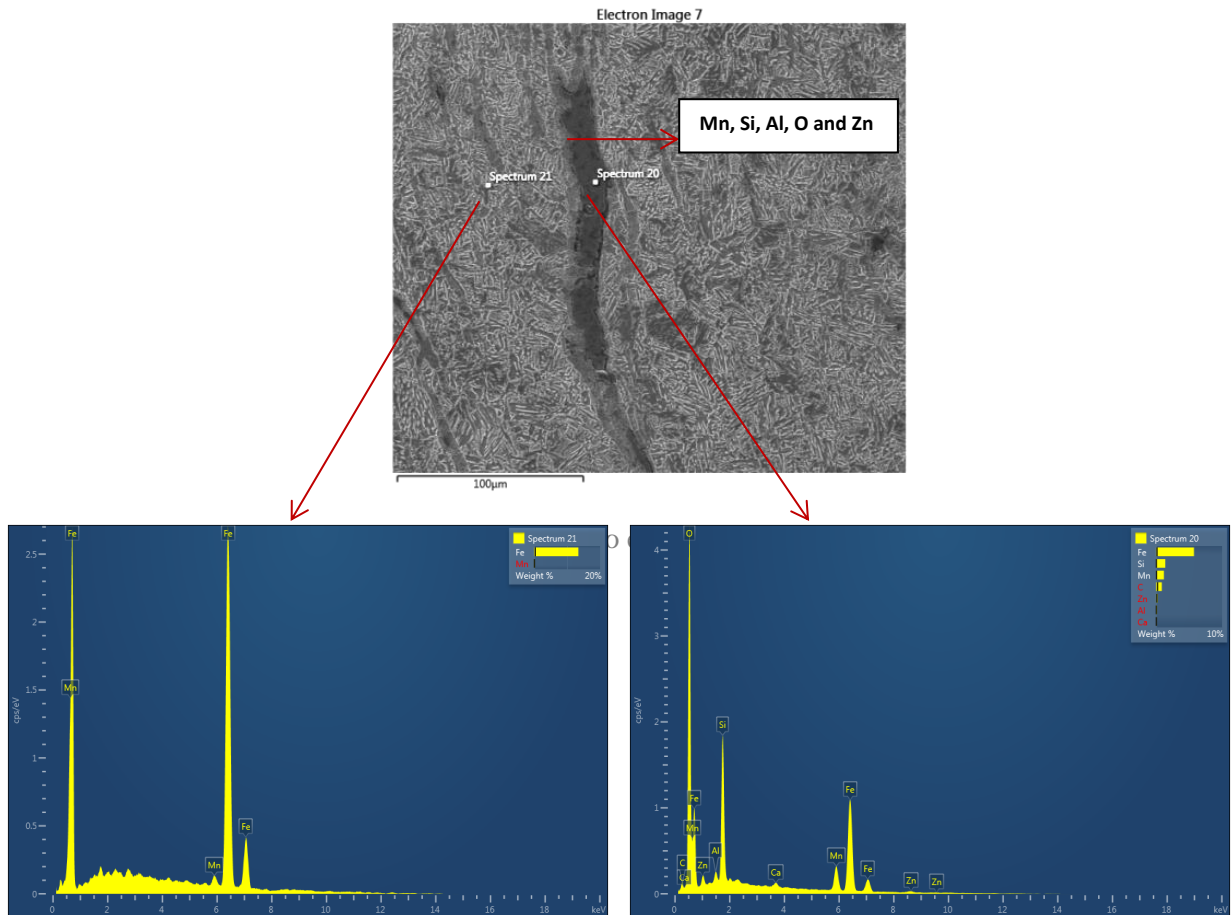
Figure 4.161: SEM-EDS showing a large (300 μm X 20μm) precipitate consisting of Mn, O, Si, Al and Zn in the SZ of a high tool speed weld,W6, (DH36.
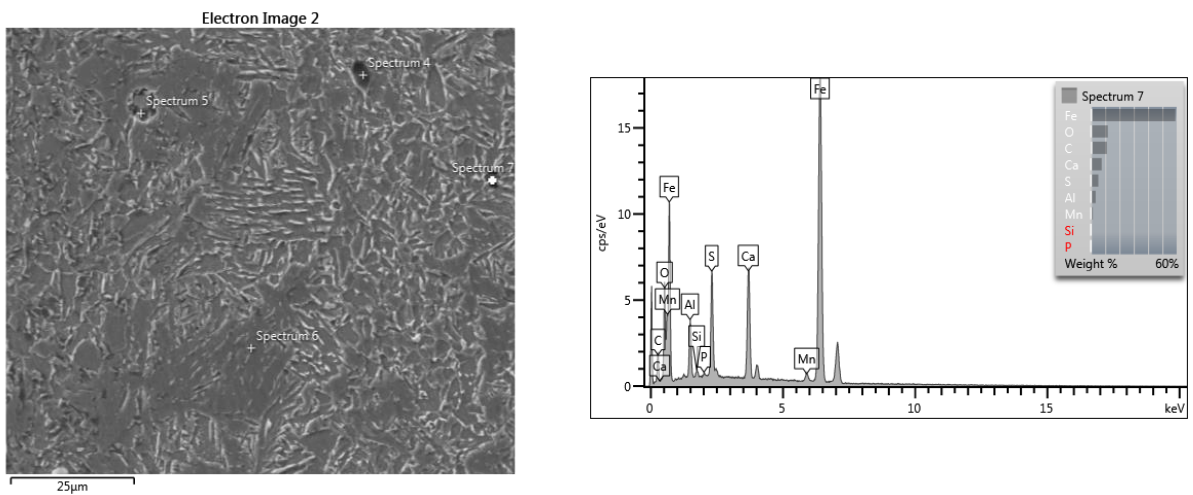
Figure 4.162: SEM-EDS showing segregation/precipitation of Al O, Ca and S in the SZ of a high tool speed weld W8 (DH36).

15. Understanding the Mechanism of Segregation by heating samples of EH46 at 1450°C and changing the soaking time.

- **Alumina-CaO and MnS-CaS reaction**

-a-   -b-
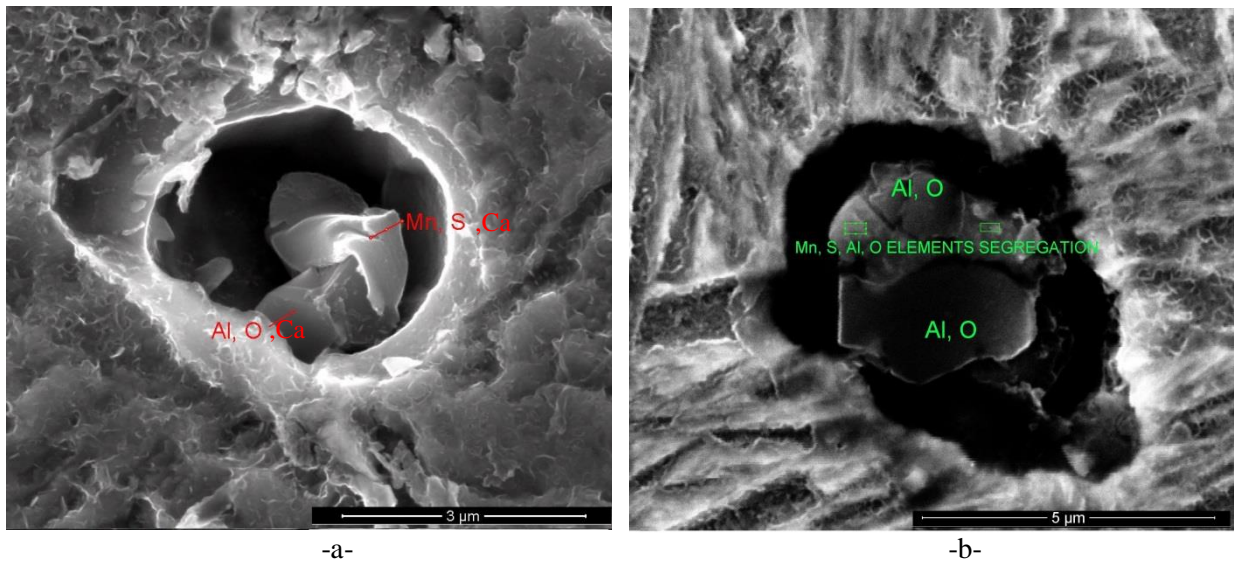
Figure 4.163: -a- SEM micrograph showing Alumina-CaO and MnS-CaS reaction heating to 1450°C, holding time 1min, oil quenching. -b- Alumina-CaO and MnS-CaS reaction heating to 1450°C, holding time 2min, oil quenching.

-a-   -b-
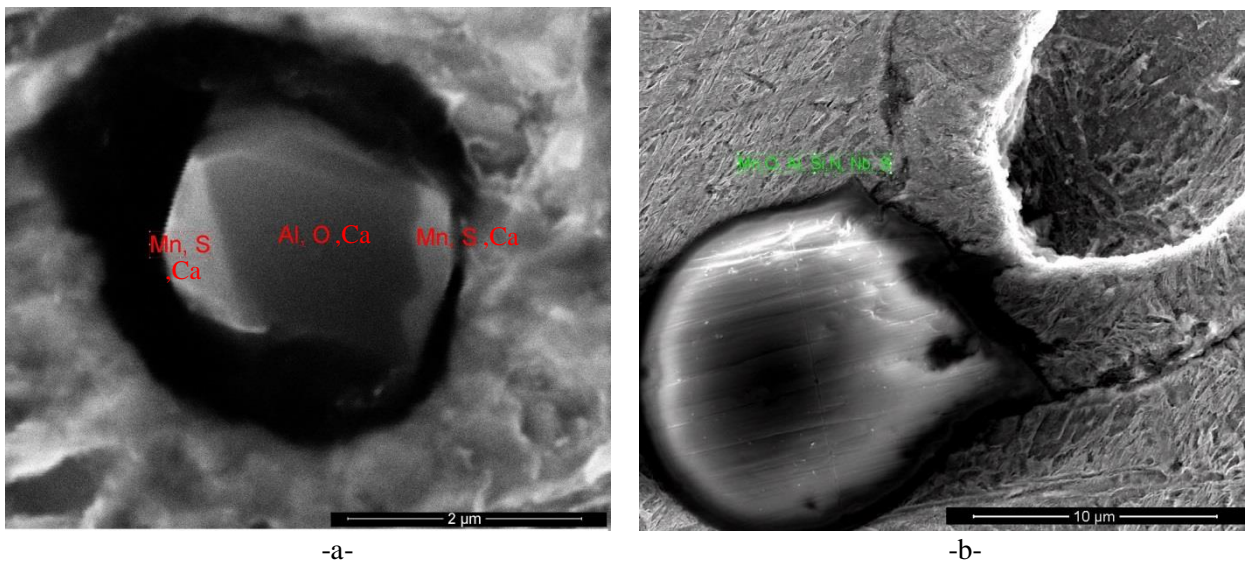
Figure 4.164: The effect of soaking time at temperature on the development of precipitates (chemical composition, size and morphology) in the microstructure -a- SEM micrograph showing Alumina-CaO-MnS-CaS reaction, Heating to 1450°C, holding time 3min, oil quench. -b-Alumina-CaO-MnS-CaS reaction with joining other elements such as Si, Nb and P when heating to 1450°C, holding time 4min, oil quenching.

246

- **Sulphides formation**

-a-   -b-
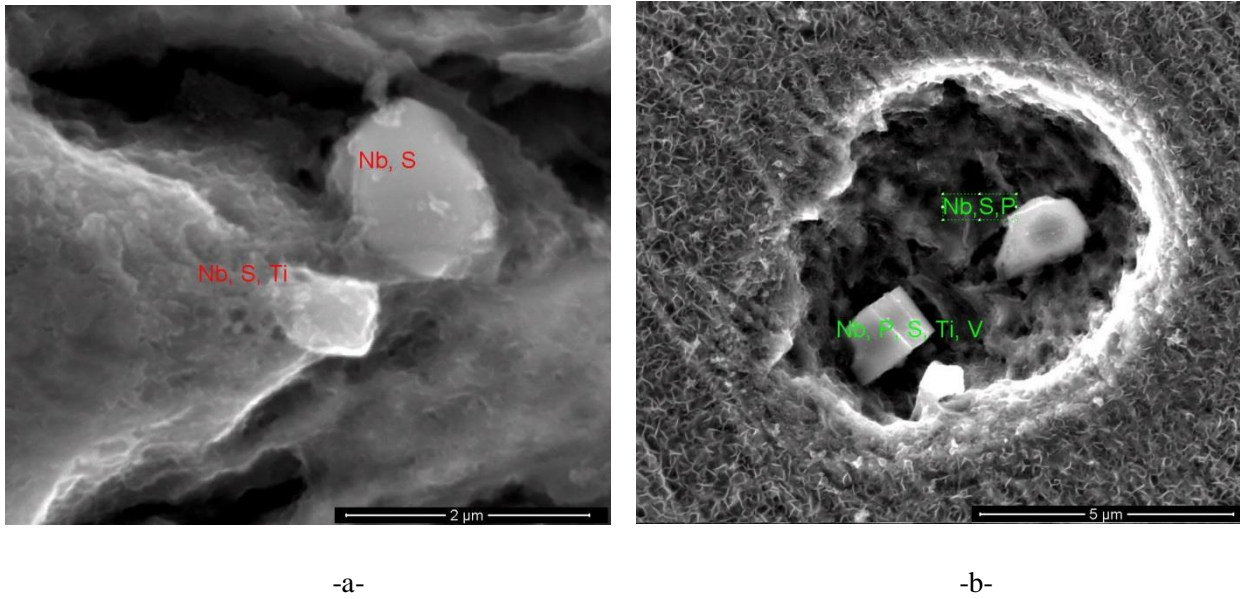
Figure 4.165: -a- SEM microgrpah showing the development of Nb Sulphide and Ti sulphide heating to 1450°C, holding time 4mins, oil quenching. , -b- Forming Nb, P Sulphide and Nb, P, Ti and V sulphide, heating to 1450°C, holding time 4min, oil quenching.

-a-   -b-
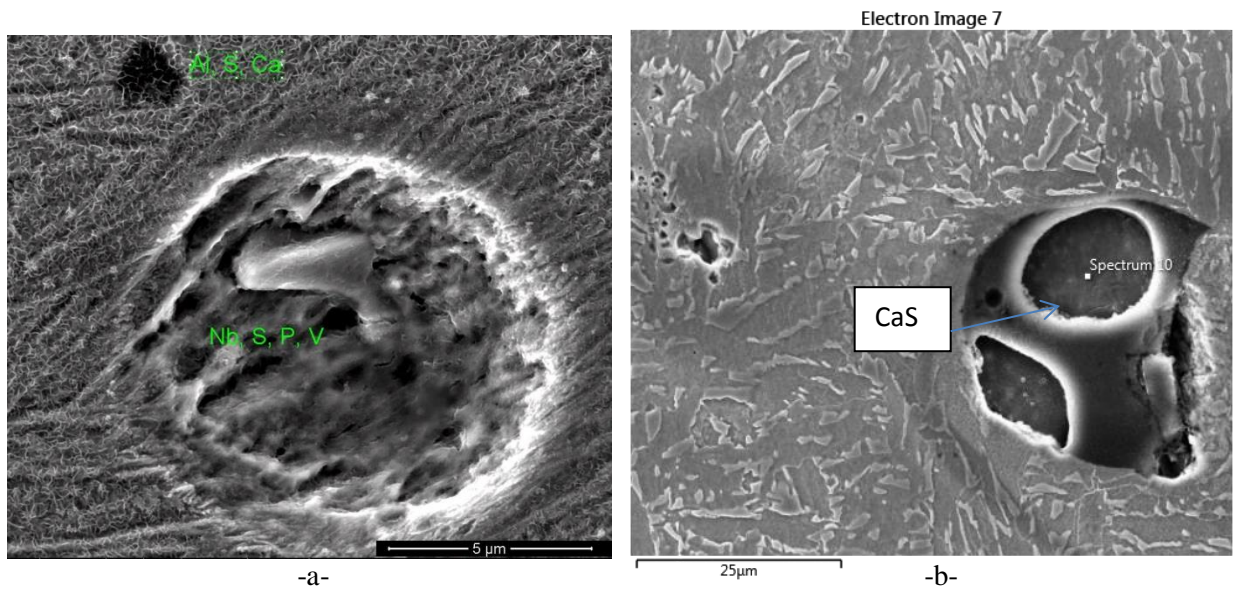
Figure 4.166: -a- SEM micrograph showing the development of Nb, P and V sulphides heating to 1450°C, holding time 4min, oil quench., -b- Development of calcium sulphide heating to 1450°C, holding time 5mins,oil quench.

-a-   -b-
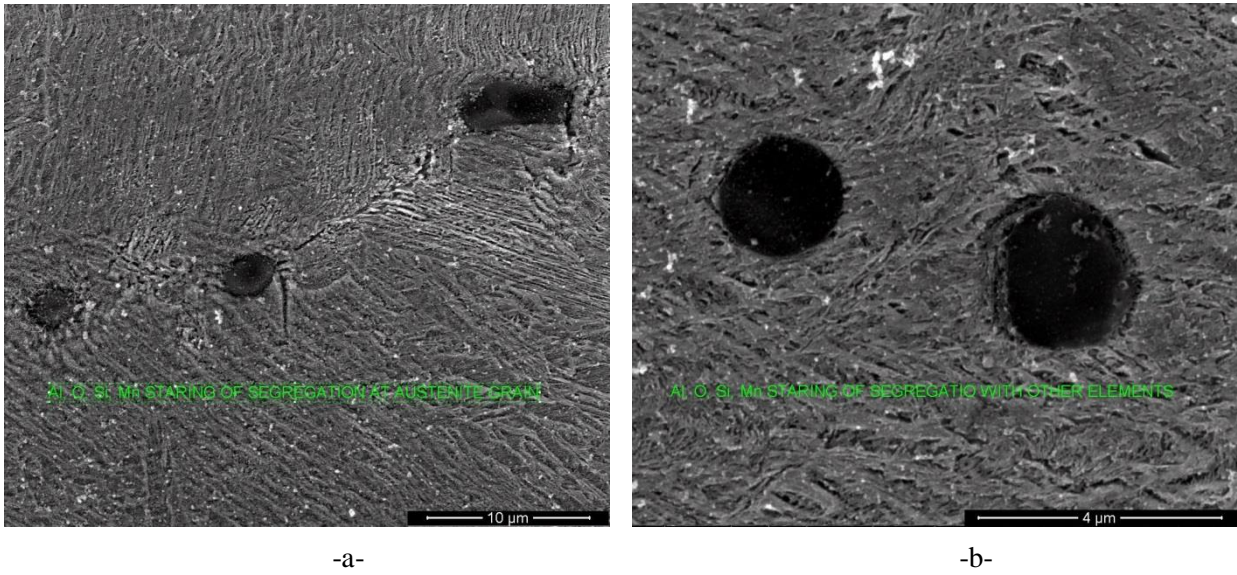
Figure 4.167: SEM micrograph showing the early stage development of a Mn, Si, Al and O rich precipitate which also contains small amounts of other elements such as Ti and Nb -a-low and -b- high magnifications images. Heat treated to 1450°C, holding time 10mins, oil quenching.
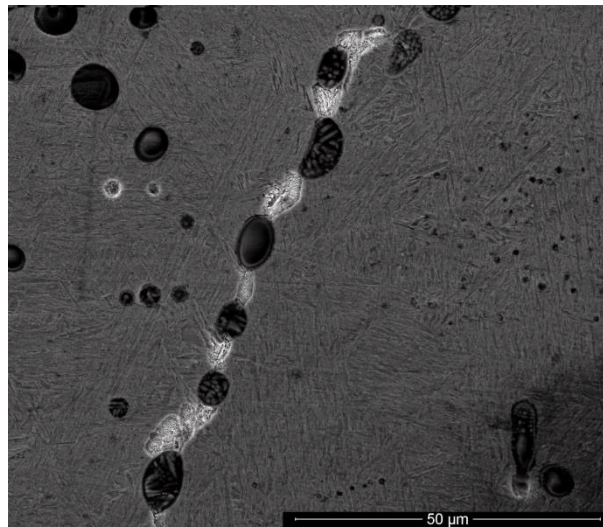
Figure 4.168: Formation of Mn, Si, Al and O rich precipitates as identified by EDS, heating to 1450°C, holding time 15min and oil quenching.

248

4.12 Wear of Friction Stir Welding Tool.

4.12.1 Tool Wear in FSW sample W6 and W8 (DH36) at High Tool Rotational/Traverse Speeds.

SEM-EDS of FSW samples W6 and W8 (DH36) steel joints (550RPM, 400mm/min) in figure 4.169 to figure 4.171 show different sizes of BN particles in the SZ. Tool wear is expected to be a result of the parent materials resistance to the thermo-mechanical process that is friction stir welding. Although the tool torque of sample W6 and W8 (table 4.1) was lower than of W9 (table 4.2), W9 did not show significant presence of BN particles in the microstructure (as revealed by X-ray diffraction figure 4.54 and figure 4.55 and also as shown in SEM images of section 4.6). The W-Re binder softening [24] as a result of temperature increase coming from the increase in tool rotational speed is highly likely to be the interpretation of the higher PCBN tool wear in samples W6 and W8 than in W9. Also the higher traverse speed of the FSW tool in W6 and W8 accompanied with higher temperature generation can exacerbate the tool wear, leading to disastrous damage of the tool. The top surface of the SZ as shown in figure 4.171 showed the maximum presence of BN particles. This result is in agreement with the published work of the authors [173] in which they found from modelling the FSW of DH36 that maximum temperature can approach the melting point of DH36 steel (1450°C) when applying tool speeds of 550RPM/400mm/min. W-25Re hardness was found in previous work to reduce by about 50% when the temperature increases from room temperature to 1450°C [24].

4.12.2 Tool Wear in FSW samples W1-W7 (EH46) Plunge/Dwell Experiment.

Figure 4.172 to figure 4.178 are SEM images (low and high magnification) of samples W1-W7 respectively from the plunge/dwell experiment. The images are taken from the shoulder-probe region and show the different sizes and amounts of BN particles present. BN particles sizes were detected between 0.5-13 μm and the percentage (%) of BN was calculated [145] and reported in table 4.18. Depending on the welding conditions and the calculated results of TMAZ size and plunge depth mentioned in table 4.6, the calculated percentage (%) of BN particles has varied as shown in table 4.18. Sample W6 (EH46) showed the maximum percentage (%) of BN particles in the shoulder-probe region as a result of maximum plunge depth and TMAZ size. Samples W3, W4, W5 and W7 showed the lowest % of BN particles which can be attributed to the low tool rotational speed and also low plunge depth. Sample W2 also showed a high percentage of BN in the shoulder-probe region compared to W1

which can be a result of the higher plunge depth despite the fact that the same tool rotational speeds were applied. BN percentage in W2 was also higher than W3, W4, W5 and W7 which have almost the same plunge depth as W2. This finding can be attributed to the higher tool rotational speed of W2 (200RPM) which in turn can cause an increase in the temperature at the tool/workpiece contact region and thus high softening of the W-Re binder is expected.

Figure 4.179 -a- and -b- are SEM images of the probe side bottom (region-2 bottom) of samples W2 and W6 respectively which show significant amounts of BN particles; particularly in W6 and less in W2. The higher plunge depth in W6 may be the reason for this increase in tool wear.

It can be concluded from the above discussion that increasing the plunge depth is associated with higher increase in tool wear as a result of increasing the contact surface area and thus the temperature in the tool/workpiece contact region. Increasing the tool rotational speed also increases the PCBN tool wear under the shoulder as a result of temperature increase and binder softening as shown in figure 4.18.

4.12.3 Tool Wear in FSW Sample W8 and W10 (EH46) during Steady State Welding Conditions.

Figure 4.181 is an SEM image with high magnification which shows a 13 μm BN particle in the SZ of the FSW sample W8; the binder of W-Re was also detected by SEM-EDS and is shown in the image. Softening of the binder accompanied by mechanical action (tool rotational/traverse speeds) can be the reason for separation of the BN particles from the PCBN FSW tool which is then followed by those released particles becoming attached and entrapped in the SZ microstructure of the workpiece during the FSW process. Figure 4.182 and figure 4.183 show the SEM-EDS spot analysis of BN particles in a FSW of sample W8 at the top surface of the SZ and at the probe end respectively. Figure 4.184 and figure 4.185 show the SEM-EDS of BN of FSW sample W10 at the top surface of the SZ and at the probe end respectively. More BN particles were shown in sample W10 at the top and bottom of the SZ rather than in sample W8 which is the result of increasing the tool traverse speed from 50mm/min to 100mm/min. More SEM images of the top surface of SZ and in the probe end of sample W8 and W10 are shown in figure 4.186 to figure 4.189 respectively. Figure 4.188 -a- shows a significant amount of BN particles at the top surface of the SZ of sample W10 until 250μm depth whereas, figure 4.188 -b- is a higher magnification SEM image of the SZ which shows BN particles. The middle of the SZ of sample W8 and W10 did not show

significant presence of BN as shown in figure 4.187 -a- and figure 4.189 -a- respectively whereas BN at the probe end of both welds is clearly evident in figure 4.187 -b- and figure 4.189 -b-. The significant existence of BN in the top and bottom of the SZ but less in the middle of the SZ can be attributed to the fact that the tool edges (top and bottom) are the most vulnerable locations with regards to wear as a result of experiencing higher temperatures or higher shear stress. Al-Moussawi et al. 2017 [173] showed by simulation that the tool shoulder periphery experiences the maximum peak temperature at the advancing-trailing side and the maximum shear stress was on the leading-retreating side. They also showed that at higher traverse speed, the maximum value of shear stress was at the shoulder periphery and probe end. This can be noticed in figure 4.190 where BN particles are found at the probe end of sample W10 as a result of higher traverse speed. Table 4.19 shows the calculated percentage (%) of BN in 1mm^2 at the middle top of SZ and at the probe end of sample W8 and W10. Wear at the tool shoulder periphery in W10 is about 3 times that in W8 whereas, at the probe end it is approximately double.

I. SEM-EDS W6 and W8 (DH36)
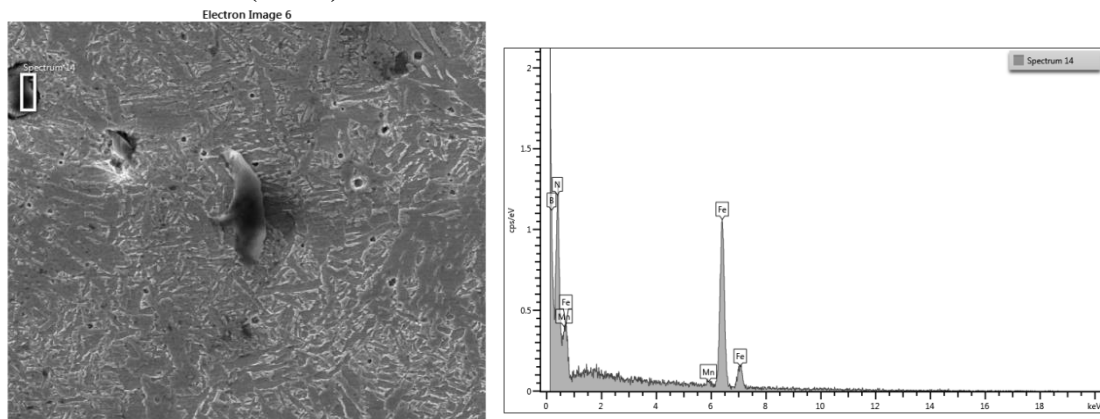
Figure 4.169: SEM-EDS showing 8-12µm BN particles in the SZ of FSW sample W6 (DH36), (550RPM, 400mm/min).

Electron Image 6
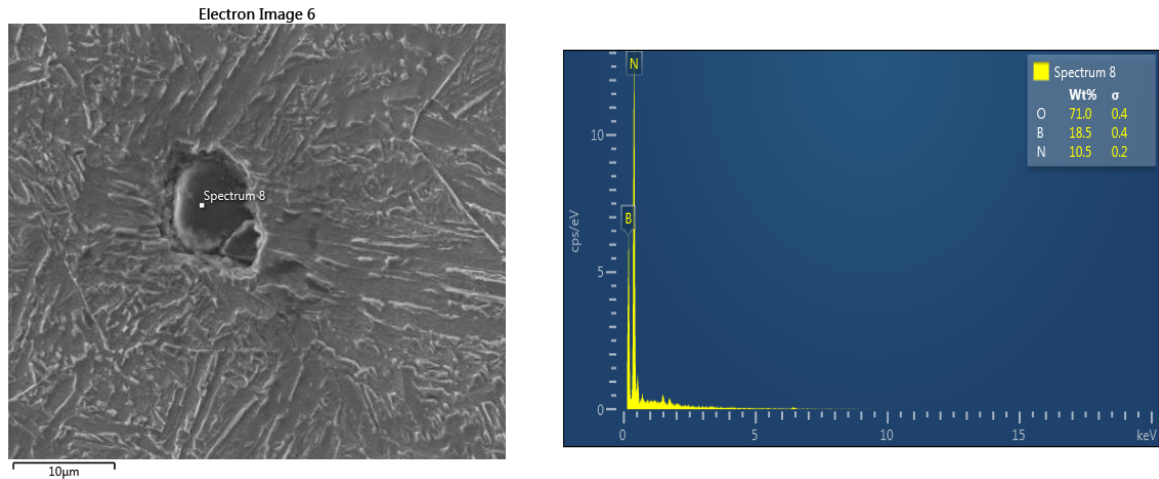
Figure 4.170: SEM-EDS showing 10μm BN particles in the SZ of FSW sample W8 (DH36) , (550RPM, 400mm/min).
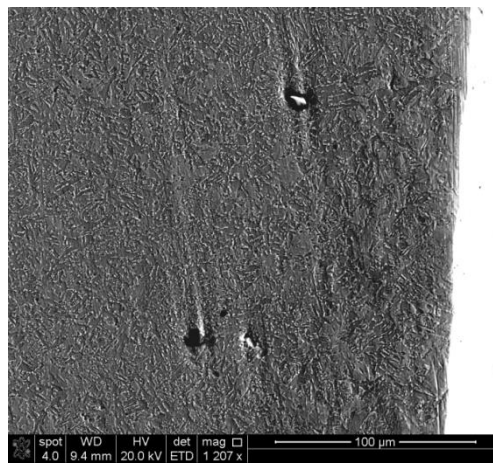
Figure 4.171: SEM image at the top of the SZ of sample W6 (DH36) () which clearly shows the existence of BN particles.

II. SEM images of FSW samples W1-W7 (EH46) Plunge/Dwell Experiment to reveal BN
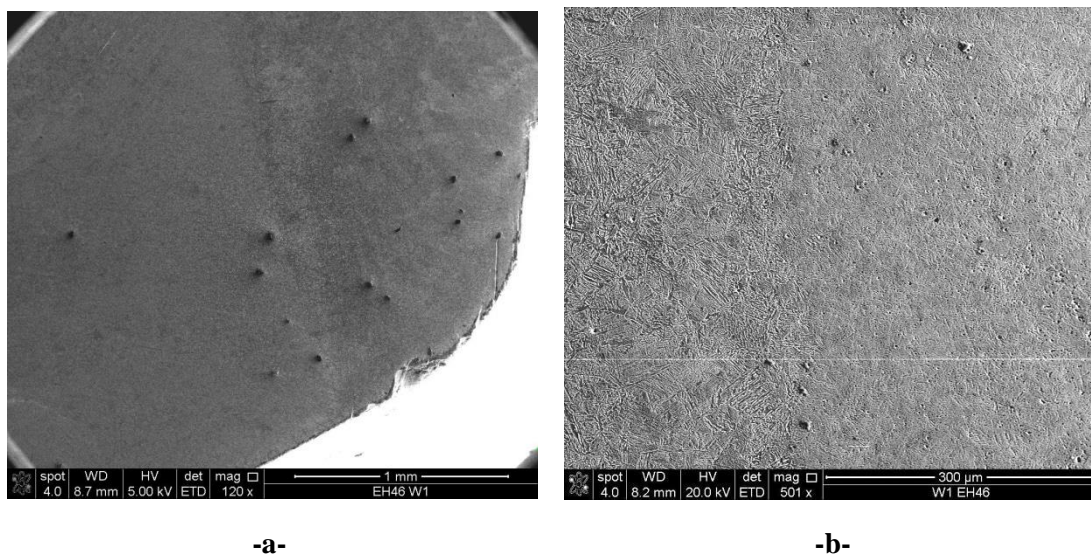
-a-

-b-

Figure 4.172: SEM images of sample W1 (EH46) at plunge/dwell stage showing BN particles (dark spots) ranging from 0.5 μm -13μm. -a- low magnification and -b-high magnification.
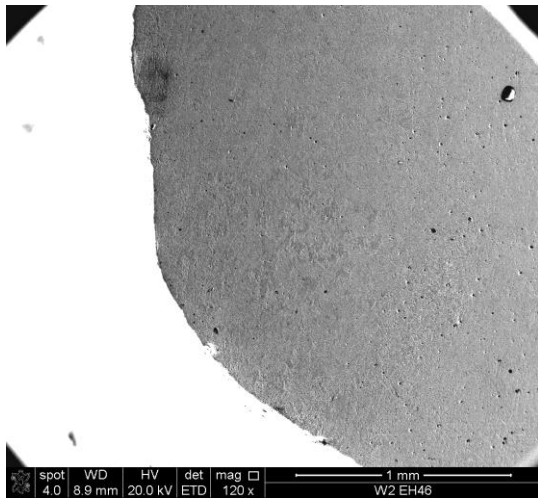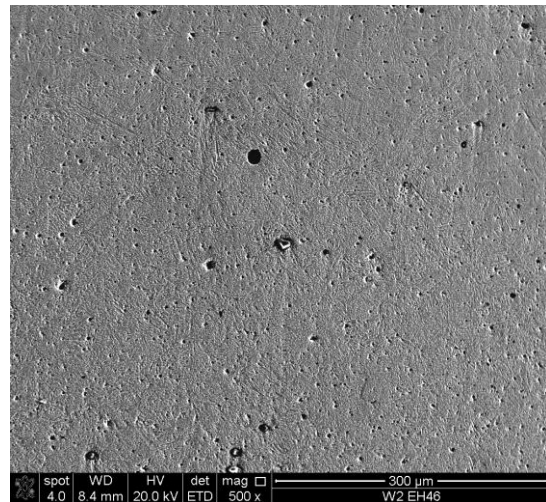
-a-
-b-

Figure 4.173: SEM images of sample W2 (EH46) () at plunge/dwell stage showing BN particles (dark spots) ranging from 0.5 μm -13μm. -a-low magnification and -b-high magnification.
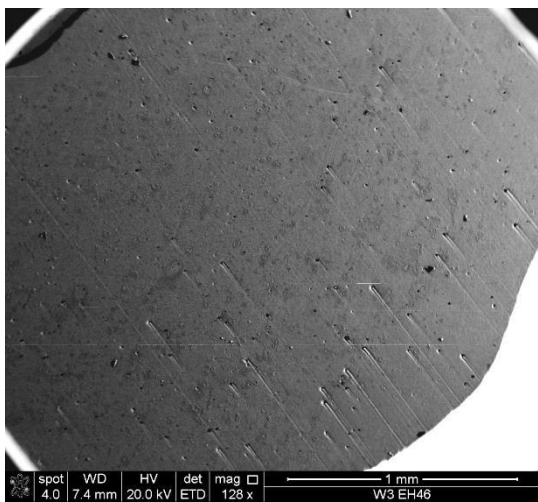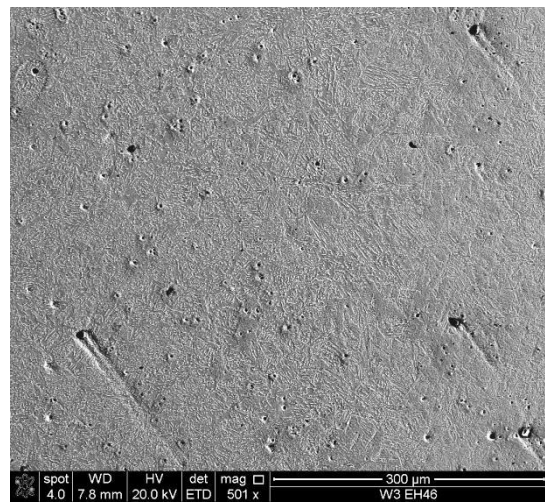
-a-
-b-

Figure 4.174: SEM images of sample W3 (EH46) () at plunge/dwell stage showing BN particles (dark spots) ranging from 0.5 μm -13μm. -a-low magnification and -b-high magnification.
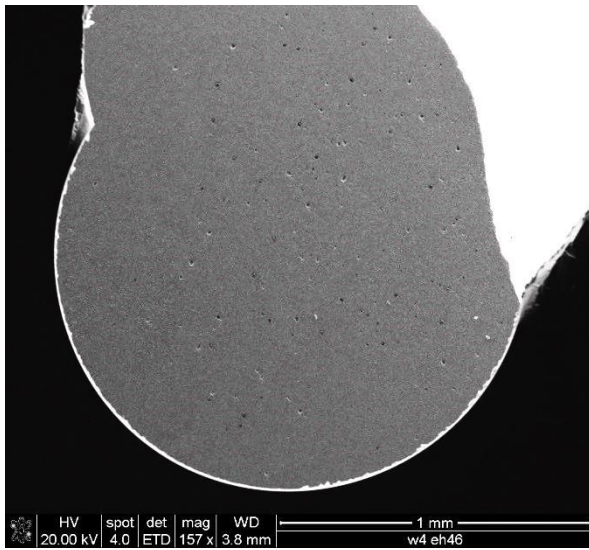
-a-
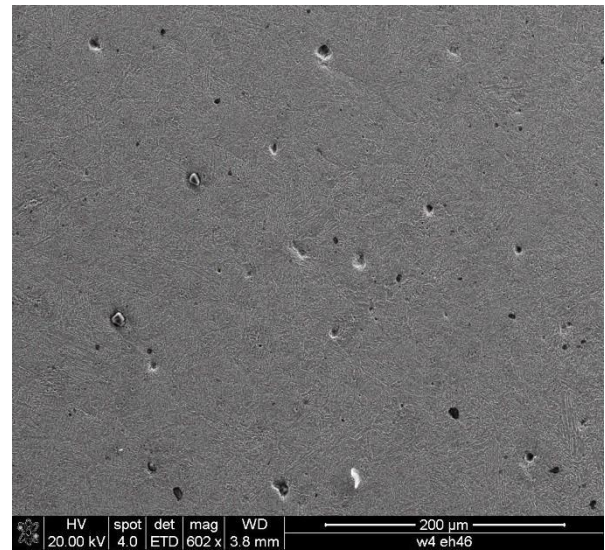
-b-

Figure 4.175: SEM images of sample W4 (EH46) () at plunge/dwell stage showing BN particles (dark spots) ranging from 0.5 µm -13µm. -a-low magnification and -b-high magnification.
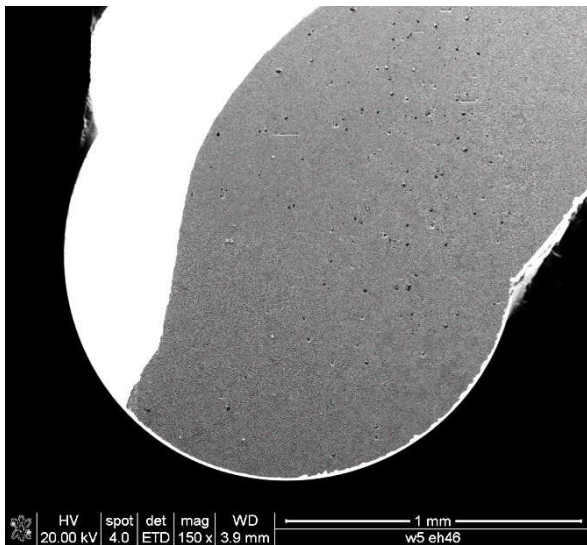
-a-
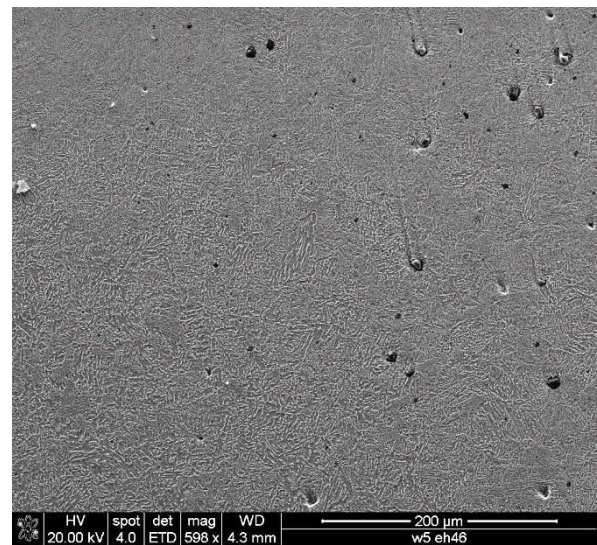
-b-

Figure 4.176: SEM images of sample W5 (EH46) () at plunge/dwell stage showing BN particles (dark spots) ranging from 0.5 µm -13µm. -a-low magnification and -b-high magnification.
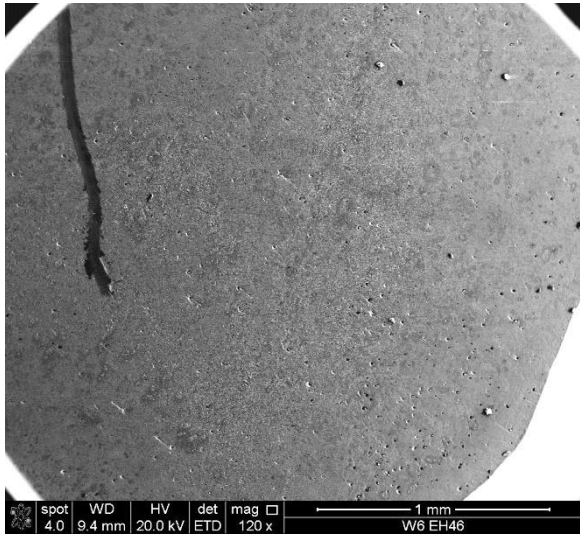
-a-
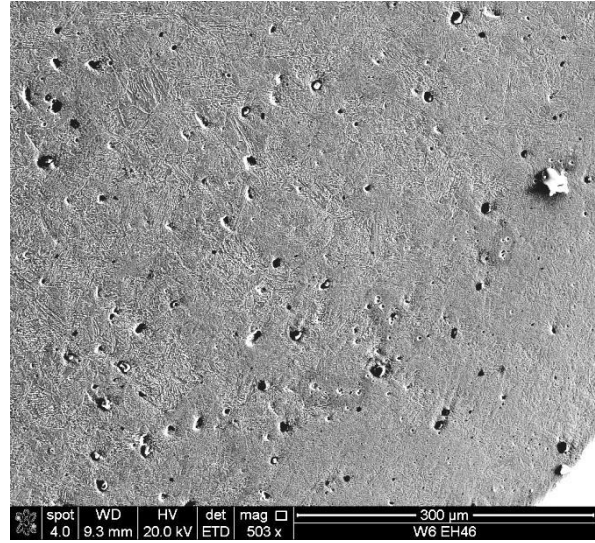
-b-

Figure 4.177: SEM images of sample W6 (EH46) () at plunge/dwell stage showing BN particles (dark spots) ranging from 0.5 μm -13μm. -a-low magnification and -b-high magnification.
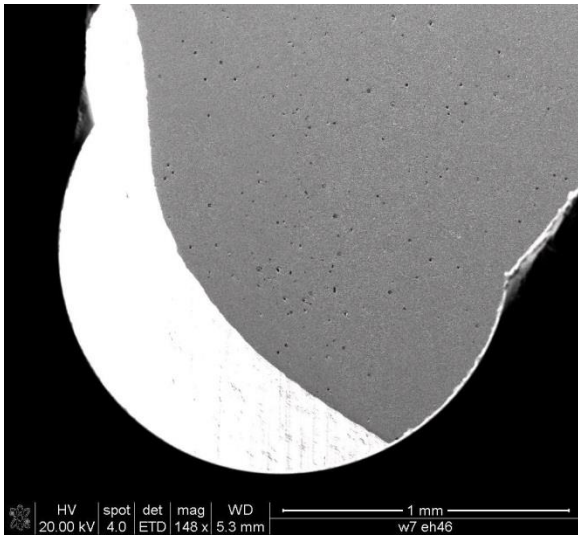
-a-
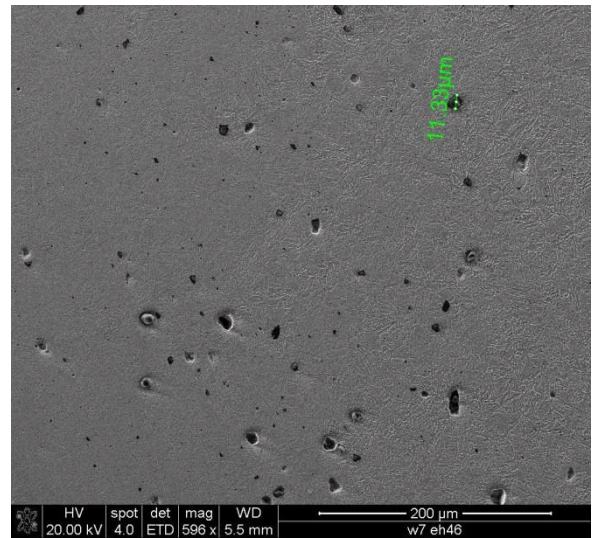
-b-

Figure 4.178: SEM images of sample W7 (EH46) () at plunge/dwell stage showing BN particles (dark spots) ranging from from 0.5 μm -13μm. -a-low magnification and -b-high magnification.
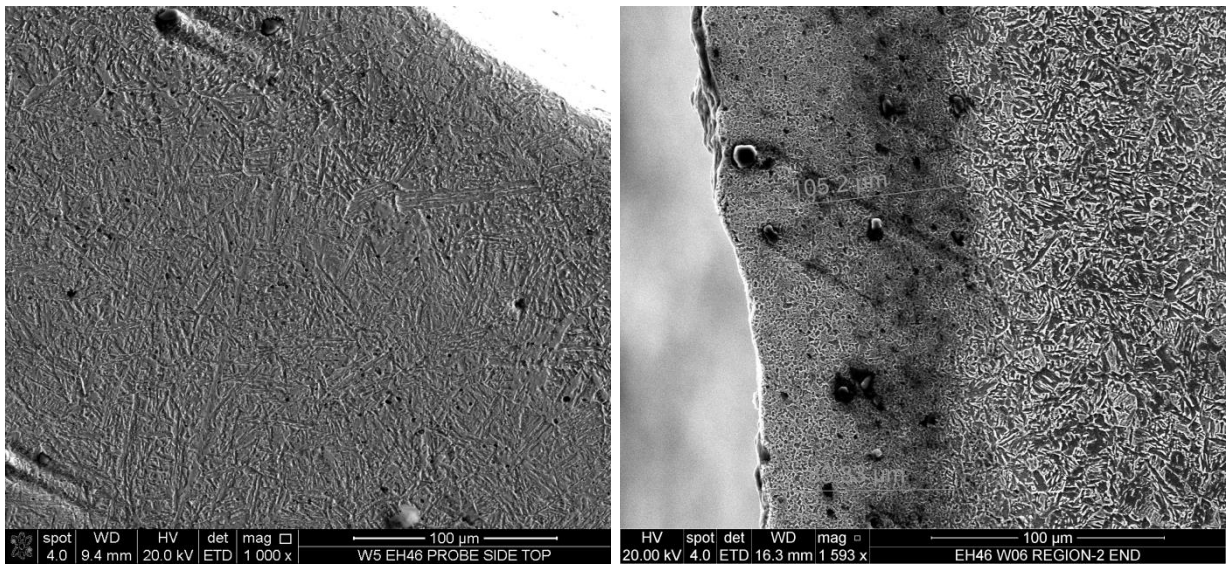
-a-   -b-

Figure 4.179: SEM images of samples W2 and W6 (EH46) at Plunge/dwell period, Probe side bottom (region-2 bottom), -a-W2 and -b-W6.
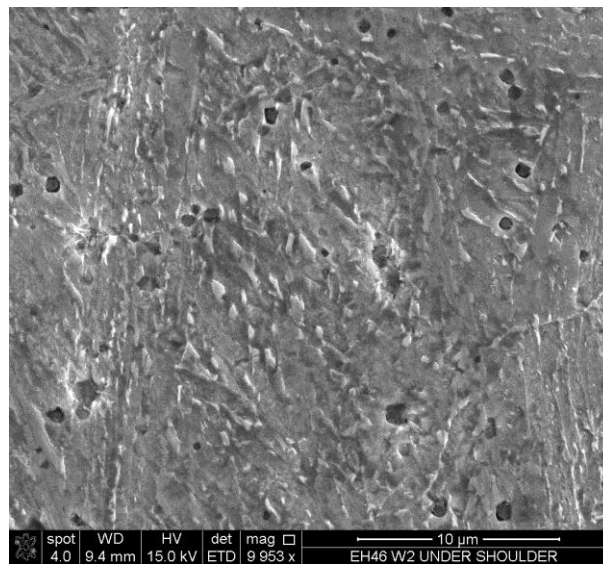
Figure 4.180: SEM higher magnification micrograph of sample W2 (EH46) at Plunge/dwell stage under the tool shoulder (region-1).

Table 4.18: BN percentage (%) in samples W1 to W7 (EH46) plunge/dwell stage at shoulder/probe side region, the scanned area is 1mm^2

Weld No.	W1	W2	W3	W4	W5	W6	W7
%BN	1.4	2.8	0.65	0.7	0.9	3.3	1.2

III. Sample W8-W10 (EH46) steady state welding conditions.
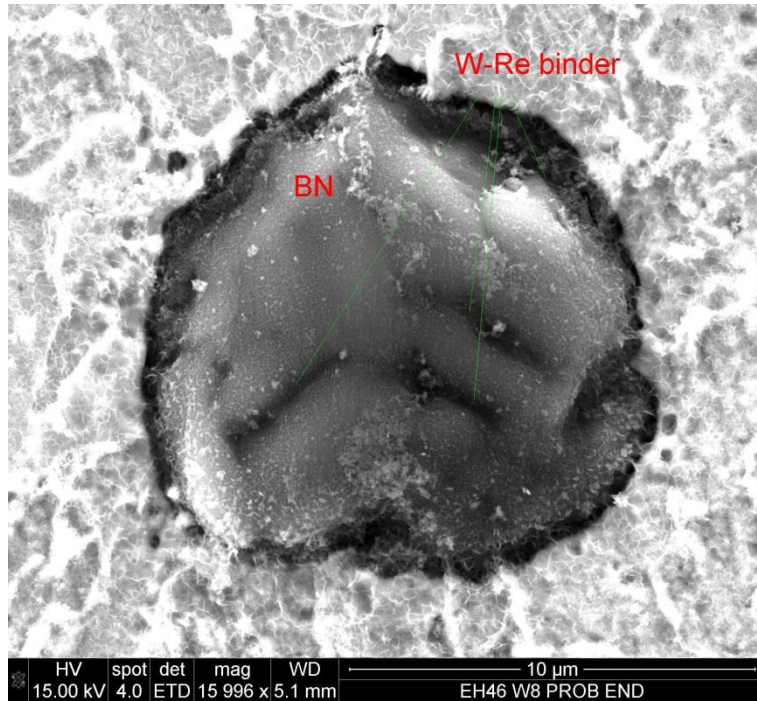
Figure 4.181: BN particle in the top of the SZ of FSW sample W8 (EH46)
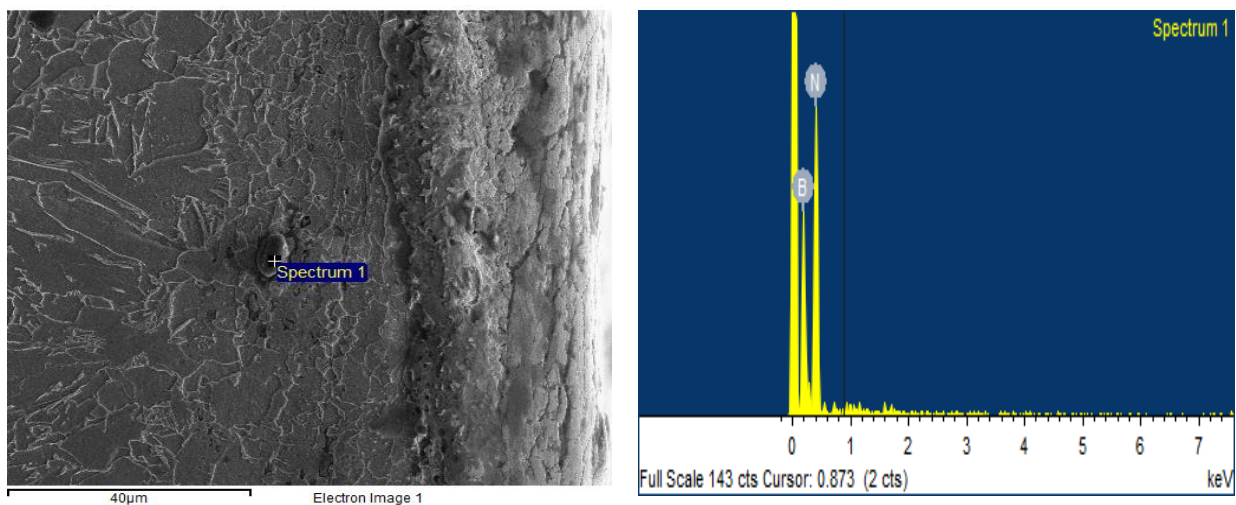
Figure 4.182: SEM-EDS showing BN particles with different sizes at the top of the SZ of FSW sample W8 (EH46).

257
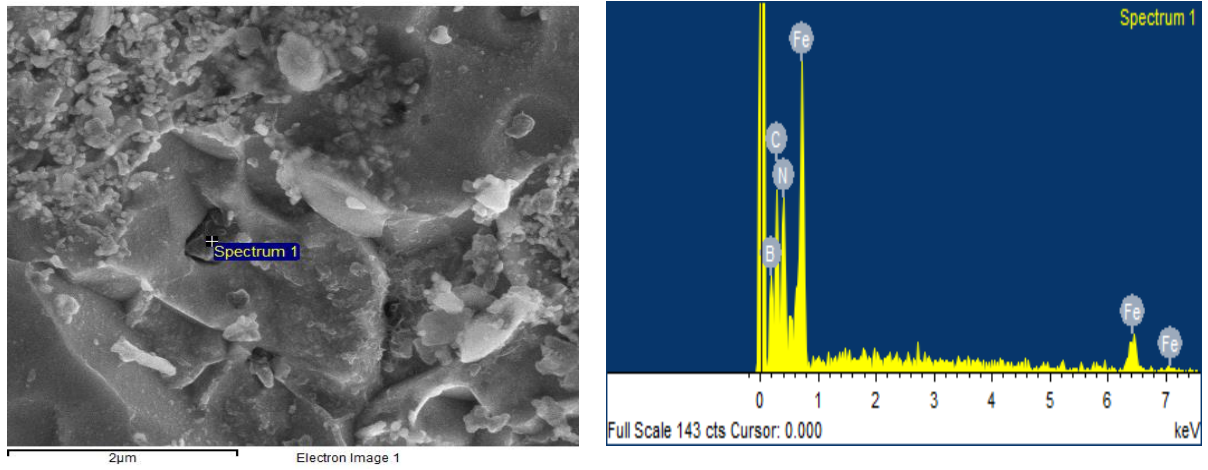
Figure 4.183: SEM -EDS showing a small 0.5 μm BN particle at the probe end of FSW sample W8 (EH46).
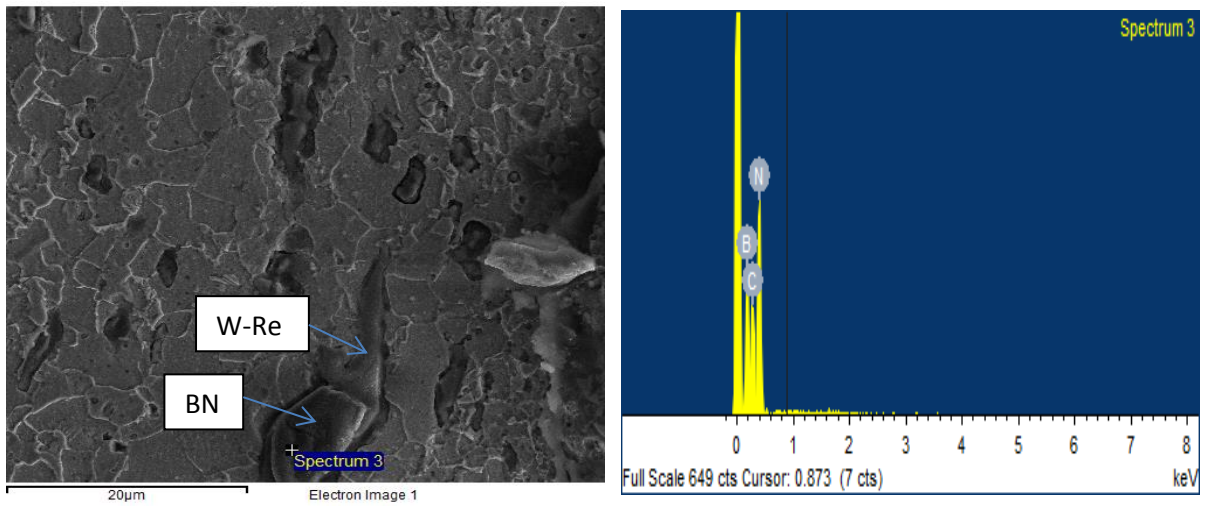
Figure 4.184: Top surface of SZ (steady state) full of different sizes of BN particle in the (EH46 W10)
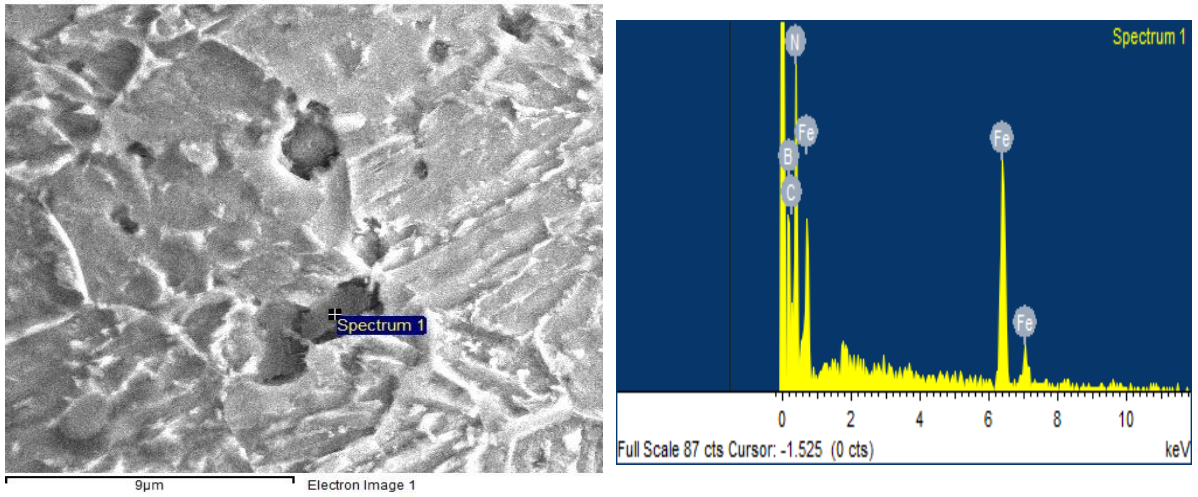
Figure 4.185: SEM microgrpah of BN particle in the SZ at the probe end region of FSW sample W10 (EH46).

-a-   -b-
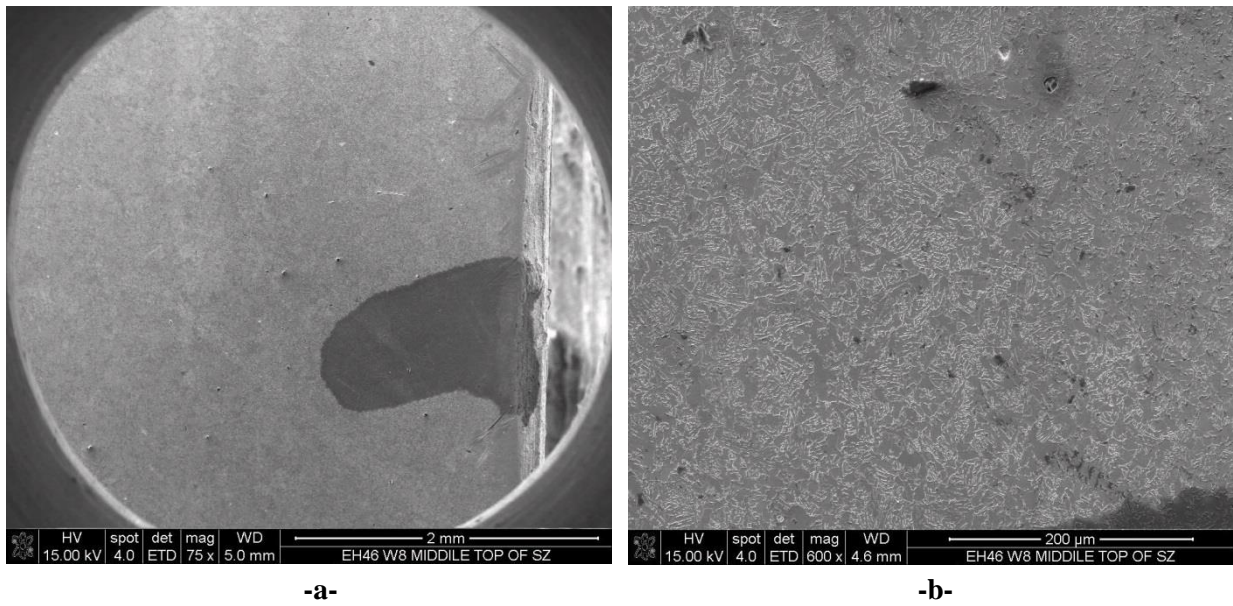
Figure 4.186: Top centre of SZ of sample W8 (EH46) (steady state), showing BN particles, -a-low magnification and -b- high magnification etched.
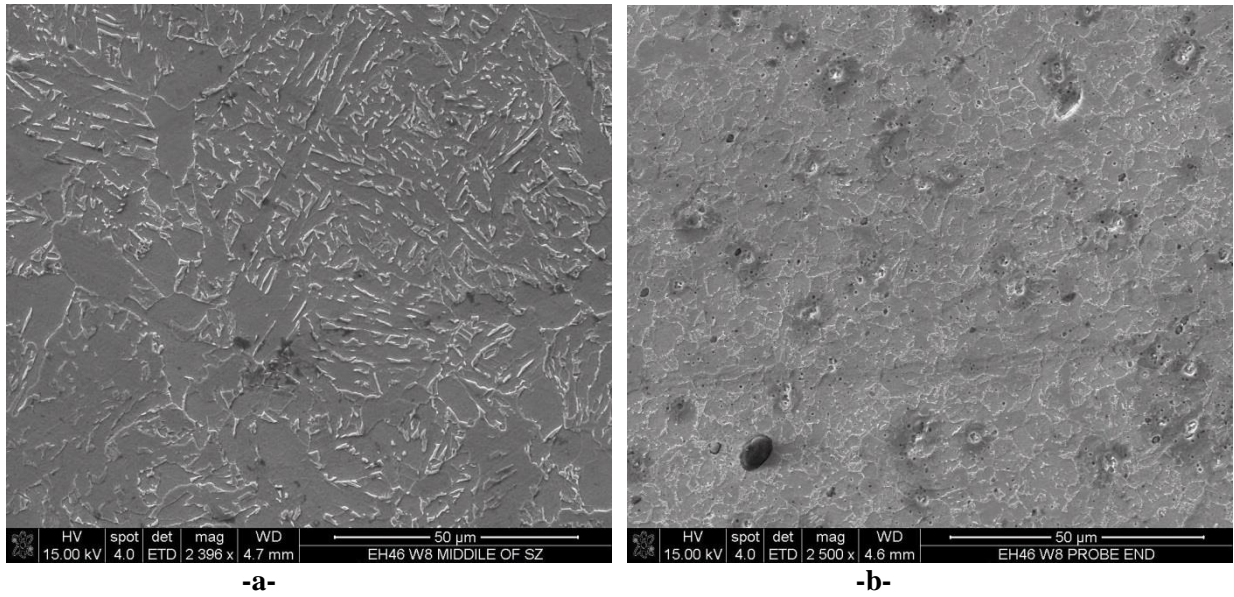
Figure 4.187: SEM microgrpah of sample W8 (EH46) (steady state),-a- The middle of SZ (no BN particles), microstructure is mainly acicular ferrite, b- Probe end SZ (BN particles are present), microstructure is mainly granular ferrite and some short plated cementite.
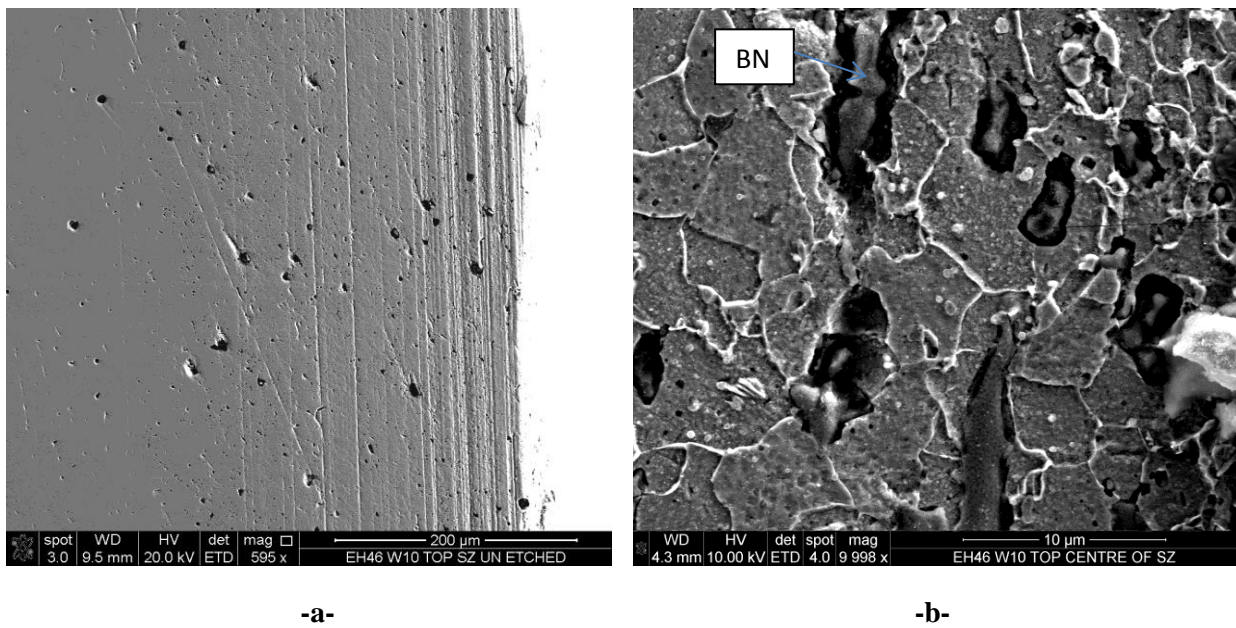
Figure 4.188: SEM micrograph of the top middle centre of the SZ of sample W10 (EH46)(steady state) heavily populated with BN particles , -a- low magnification (un-etched) and -b- high magnification (etched).
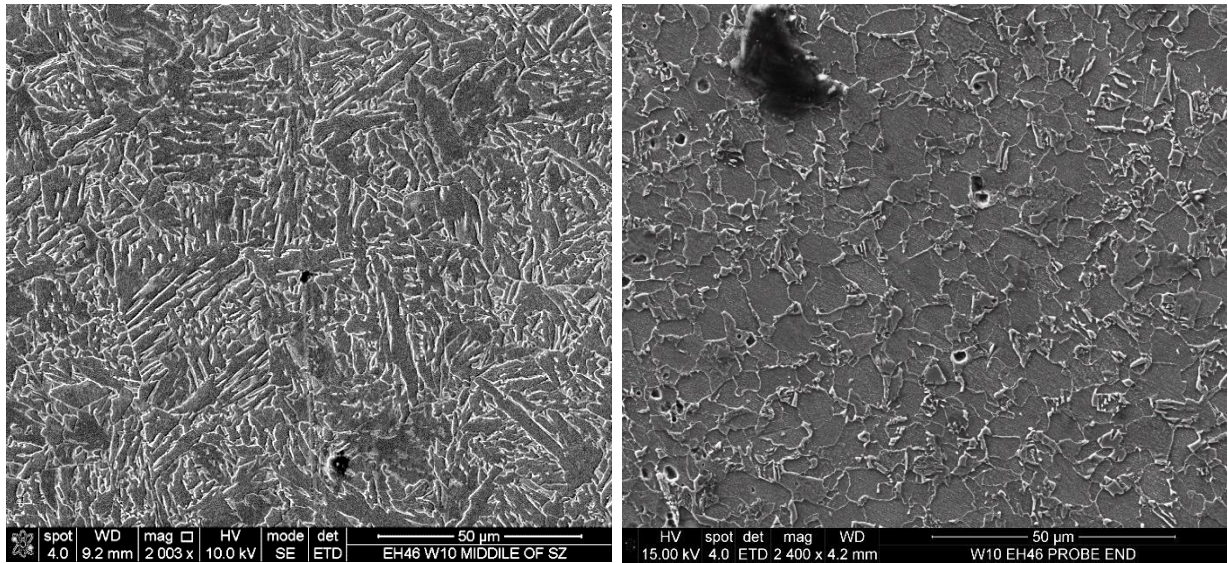
Figure 4.189: SEM micrograph of sample W10 (EH46) (steady state),-a- The middle of SZ (no BN particles), microstructure is mainly acicular ferrite, -b- Probe end (BN particles are present), microstructure is mainly granular ferrite and cementite.
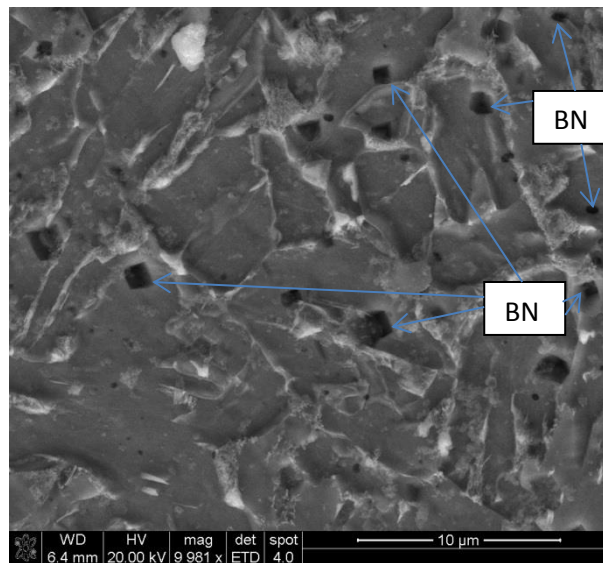
Figure 4.190: High magnification SEM image sample W10 (EH46) (steady state) at probe end showing evidence of BN particles.

Table 4.19: BN percentage (%) in samples W8 and W10 (EH46) steady state at the middle top of the SZ and at the probe end. The scanned area is 1mm^2

Weld No. and region	W8 top SZ	W8 probe end	W10 top SZ	W10 probe end
BN%	1.1	1.3	4.4	2.8

4.13 Defects Found in Friction Stir Welding of Steel.

As described in the results section; FSW sample W9 (DH36) showed a microcrack of 2-5 µm width (Figure 4.191 -a- and -b-) when the tool had travelled a distance 38-42mm in the plate weld line just before achieving steady state. Figure 4.192 compared curves of feed rate with the distance travelled by the FSW tool just before the start of steady state welding of sample W9 (DH36) with sample W6 and W8 (DH36). The fact that there was insufficient heat coming from the low tool rotational speed and the sudden increase in traverse speed has caused a lack of material flow in the critical position of the microcrack in sample W9 (DH36) which in turn resulted in crack initiation. The crack is initiated from the top surface of the weld toward the steady state of the SZ depth. This type of defect will weaken the welded joint and thus poor mechanical properties are expected. SampleW6 and W8 samples have shown different types of microcracks created inside the SZ in the direction of the welding line between the plunge and steady state region as shown in figure 4.193 -a- and -b- respectively. Despite the higher rotational speed of the tool (500RPM) compared to sample W9, the higher traverse speed (400mm/min) seems to override the effect of the rotational speed. The lack of material flow due to low heat input appears to be the main reason for these defects as reported in previous work [173] [107] [14].

Figure 4.194 shows sample W8 (DH36) macrograph scanned by the IFM technique. Two types of defects have been detected including a weld root defect at the weld joint bottom and a kissing-bond defect on the AS of the weld. The first macro crack (weld root defect) which appears from the bottom of the plate with a length of 2 mm towards the SZ as shown in figure 4.195 -a- can be attributed to the lack of material flow as a result of high traverse speed. This type of defect was investigated previously by Stevenson et al. [14] where it was identified as a weld root flaw attributed to insufficient tool plunge depth or a deviation of the tool from its centreline. As this type of defect was found along all the weld line, it is unlikely that the tool deviation was the main cause for the defect here. This macro crack may be due to the lack of velocity and plasticity under the probe end which causes a stagnant zone formation as demonstrated by CFD modelling [173]. The material in this region will be vulnerable to crack formation under the normal plunge force, so any uneven surface or sharp edge will act as a stress concentration point as labelled in figure 4.195 -a-.

The second crack on the AS of sample W8 (DH36) at the weld root as shown in figure 4.195 -b- can be classified as a "kissing-bond" which is material in close contact but which has a lack of chemical and mechanical bonding. This type of defect is difficult to identify by using

the non-destructive tests such as ultrasound and thus needs to be investigated carefully using optical or SEM analysis of a polished and etched sample which is clearly not a non-destructive technique. Depending on the size of kissing bond defect, it can affect the mechanical properties of the weld joints especially the fatigue strength.[108]

Figure 4.196 -a- and -b- show a non-metallic layer of (Fe, Mn, Si, Al and O) as identified by SEM-EDS between the SZ and HAZ of sample W6 and W8 (DH36) at -a- plunge period with 10µm width and -b- at the steady state period with a width of 1.3µm. This type of defect can be caused by higher tool rotational speed which results in the parent material reaching a temperature which is close to the local melting point of the parent metal causing elemental segregation/precipitation (see section 4.11). It is proposed that the tools centrifugal forces act to push these elements towards the edge of the SZ and thus they deposited in the region between the SZ and HAZ.

Void on the AS of FSW sample W10 (EH46) has been found at 9.8mm distance from the top surface of the weld joint between the SZ and HAZ as shown in figure 4.197. Figure 4.198 -a- shows SEM image of the void which has a diameter of about 250µm, a high percentage of BN particles which have separated from the PCBN FSW tool were also found near and around the void as shown in figure 4.198 -b-. The void defect is likely to have resulted from a lack of material stirring caused by high tool traverse speed. Schmidt and Hattel 2005 [25] included the formation of the void in modelling the FSW by establishing the dwell and weld periods. They interpreted the formation of the void at the lower advancing trailing side of the probe/workpiece interface as a lack of contact between the tool and matrix interface because of the high traverse tool speed, whereas, Toumpis et. al. 2015 [9] explained the formation of voids experimentally; they showed that the interruption in the surrounding phase has led to a minor cavity caused by non-metallic inclusions. Failla 2009 [76] related the void defect formation to the FSW tool travel speed. The increase in travel speed was found to cause rapid cooling of the material before the region becomes filled with stirred material leading to the void formation.

Figure 4.199 -a- and -b- shows SEM image including TiN and Al, P, S precipitates respectively in the SZ microstructure of FSW sample W6 (DH36) as identified by SEM-EDS technique. This weld also showed a microcrack which initiated from a cuboid TiN particle and also Al, P, and S. These elemental precipitations especially TiN in the SZ microstructure are usually the result of a high peak temperature which exceeds 1200$^{\mathrm{o}}$C as discussed in

section 5.10 (TiN precipitate). Defects resulting from precipitation of TiN are known as cleavage cracks which can reduce the mechanical properties of the welds such as the fatigue and impact resistance [166]. Orlando et al. 2010 [174] showed by the aid of an optical microscope and an SEM that cuboid TiN particles can cause voids during the tensile test of IF steels. They interpreted this type of defect as a fragmentation of weak particles coming from stresses generated from TiN particles corners. An extensive study concerning the microphysical process of cleavage fracture in steel can be found in Chen and Cao [175] which focus on steps of crack initiation, nucleation and propagation under internal residual stresses caused by TiN precipitation. Figure 4.200 -a- and -b- show microcracks caused by TiN particles (exceeds 1µm) in FSW sample W10 (EH46) SZ at steady state and a DH36 sample heat treated to 1300°C with slow cooling (cooling inside furnace) respectively. Figure 4.201 shows elemental segregation of Mn, Si, Al and O in the SZ of FSW sample W6 (DH36) which can also act as a stress concentration and microcrack initiation site as discussed previously in the elemental segregation section.

Mechanical properties of FSW joints are expected to decrease with the existence of the above mentioned defects. As discussed earlier in section 5.4 (Mechanical Tests), samples of tensile test including FSW sample W6 (DH36) failed outside the welded region which means that weld tensile strength is still acceptable despite the presence of microcracks coming from precipitation. The tensile strength is also increased to 580MPa for sample W9 (DH36) compared to the strength of parent metal (475 MPa) as a result of microstructure refinement as discussed in section 5.6 (SEM FSW DH36). However, samples of DH36 W6 were fatigue tested and showed a decrease in fatigue resistance compared to DH36 W9 as a result of defects within the SZ of the welded joints. Microcracks coming from unsuitable welding parameters and also from the elemental precipitation especially TiN have certainly played the main role in this reduction in fatigue resistance. It is recommended to reduce the peak temperature of welding this type of steel by reducing the tool rotational speed below 500 RPM in order to avoid elemental precipitation/segregation.

-a-

-b-
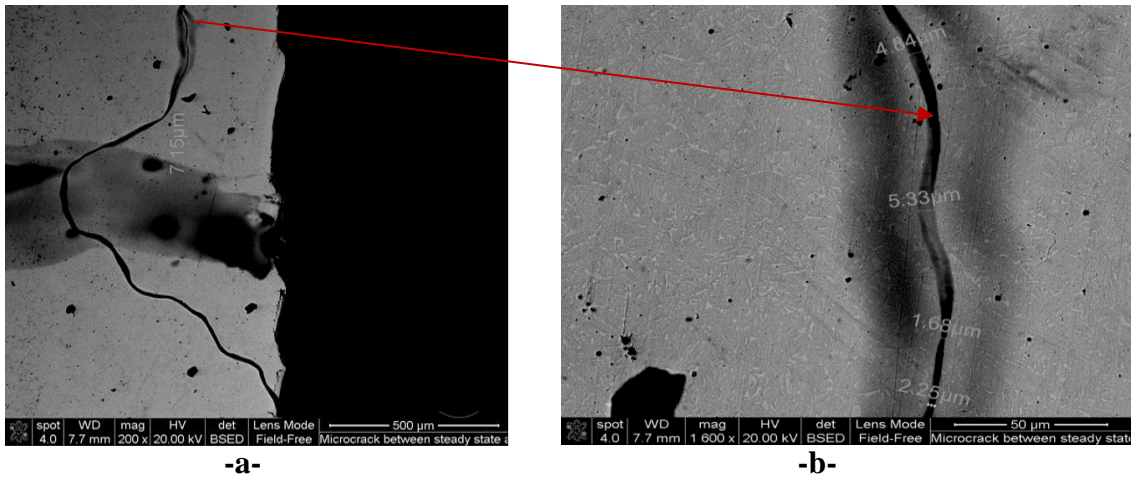
Figure 4.191: SEM image of a micro crack initiated from the top surface of FSW sample W1 (DH36) between the steady state and the plunge regions of the weld. -a- low magnification, -b- high magnification. The sample was sectioned in the direction of the weld line.
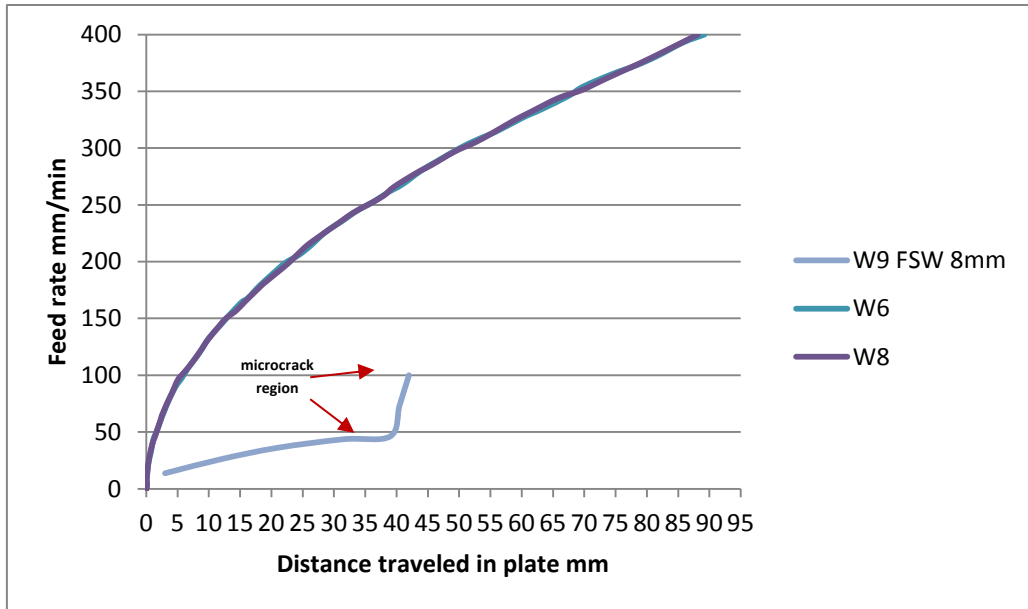
Figure 4.192: Feed rate and the distance travelled by the tool in the plate just before the steady state region.

-a-   -b-
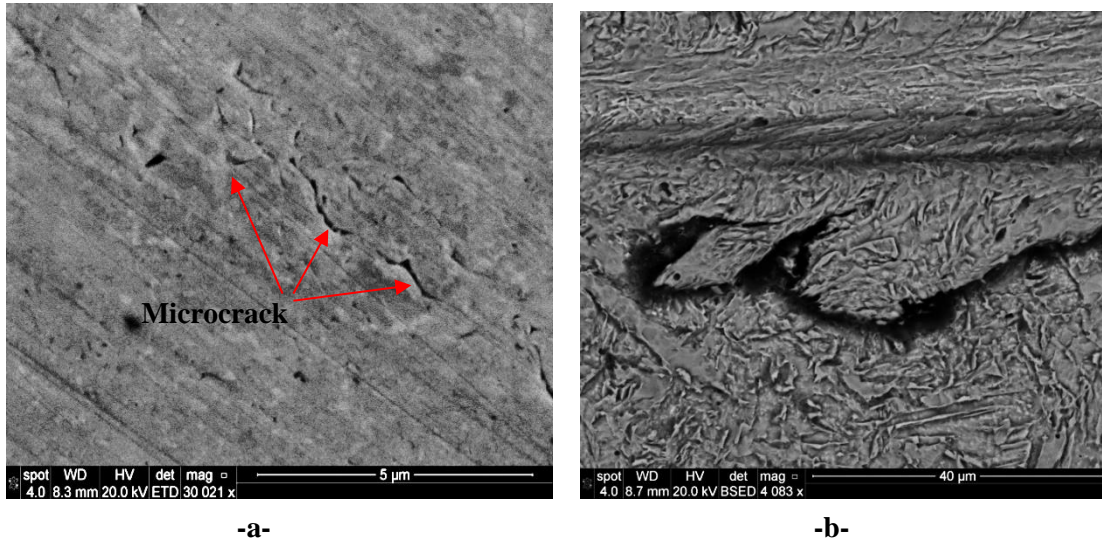
Figure 4.193: SEM images of microcracks inside the SZ. -a- between the plunge-steady state regions of FSW sample W6 (DH36), -b- between plunge-steady state regions of FSW sample W8 (DH36). The sample was sectioned in the direction of the welding line.
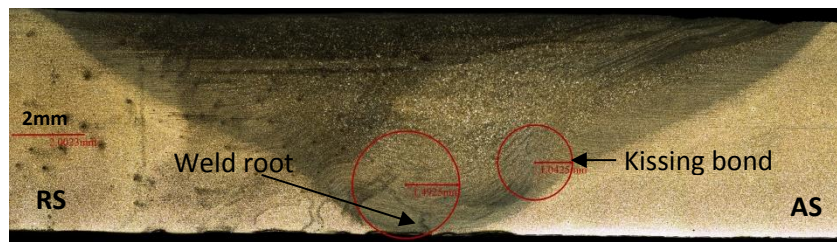
Figure 4.194: Weld root and kissing bond defects in 6mm FSW sample W8 (DH36).

-a-   -b-
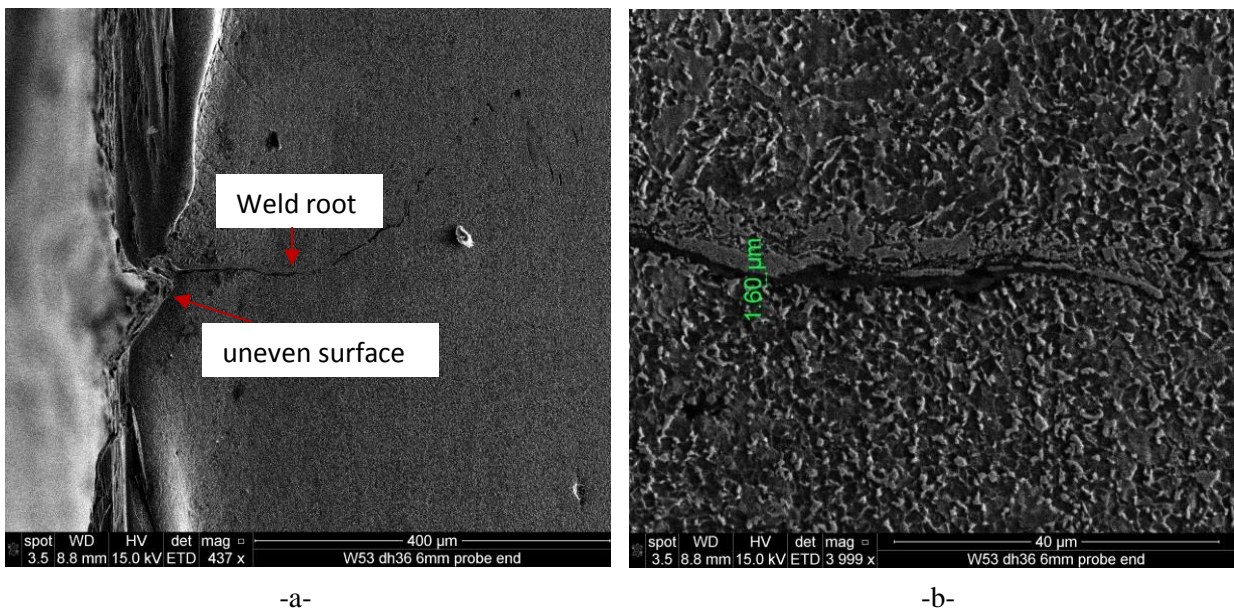
Figure 4.195: SEM images of the first and second types of new defects found in sample W8 (DH36) 6mm shown in Fig. 4 -a- Weld root, -b- kissing bond.

266
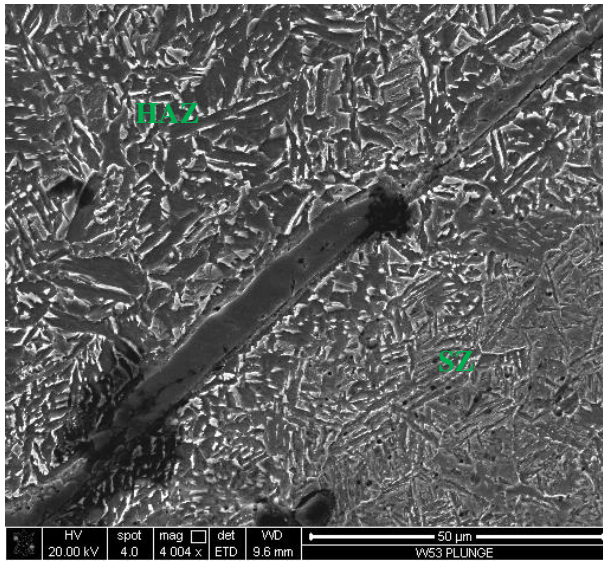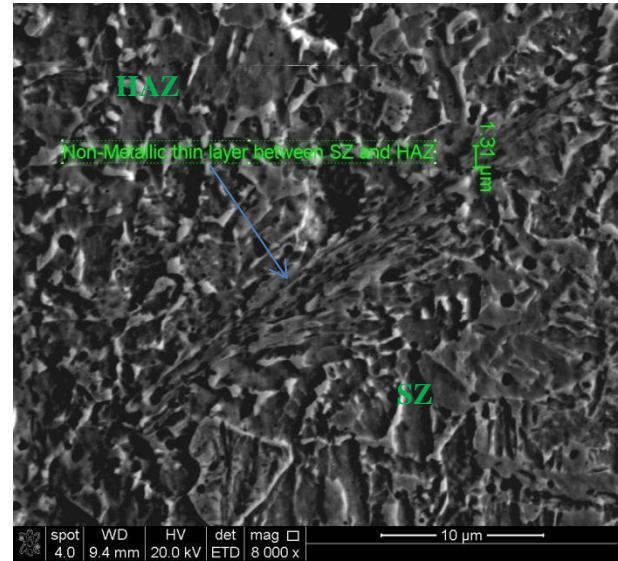
-a-   -b-

Figure 4.196: SEM image of a non-metallic layer of (Fe, Mn, Si, Al and O) between the SZ and HAZ found in sample W6 (DH36), -a- 10µm at the plunge period, -b- 1.3µm in steady state period.
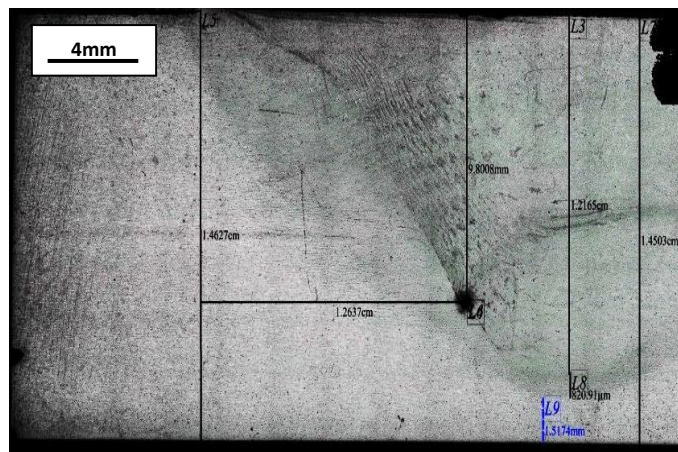
Figure 4.197: An IFM image of a void found in sample W10 (EH46) (steady state) on the AS.
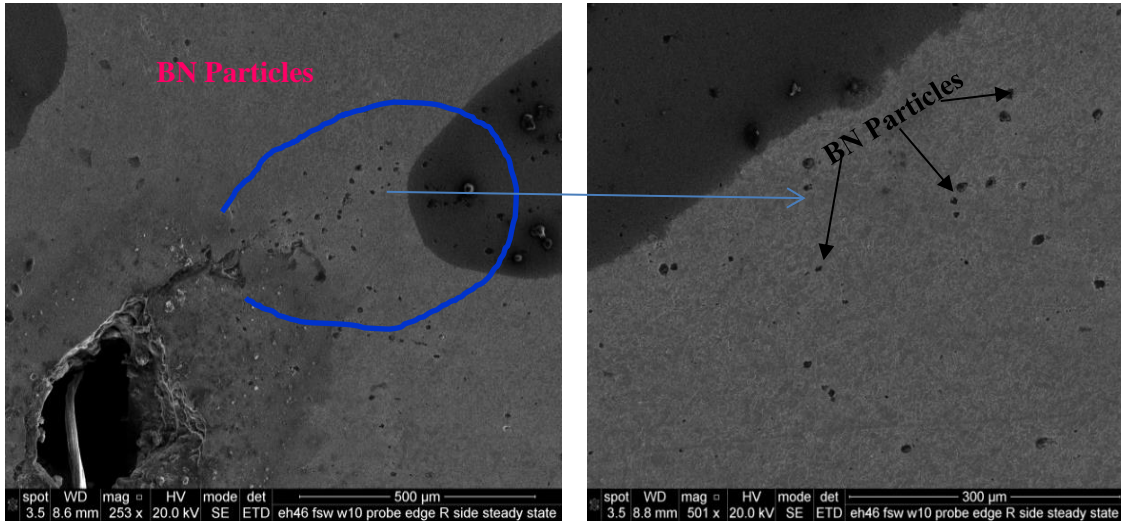
Figure 4.198: SEM images showing a large number of BN particles found near the void at AS, sample W10 (EH46) steel (steady state).
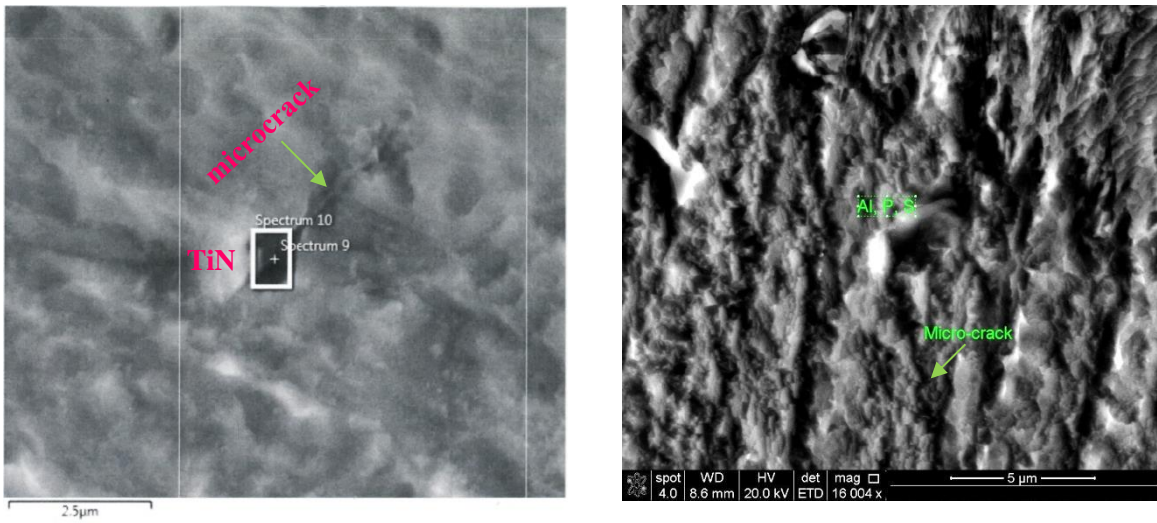
Figure 4.199: SEM image of the SZ of sample W6 (DH36) showing: -a- microcrack caused by TiN particle, -b-Microcrack caused by Al, P, S, rich precipitates.
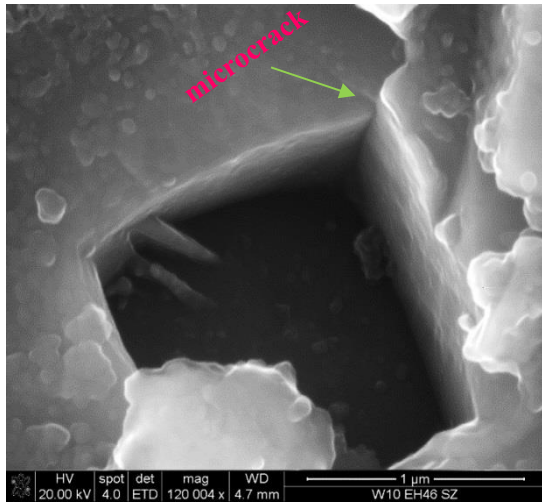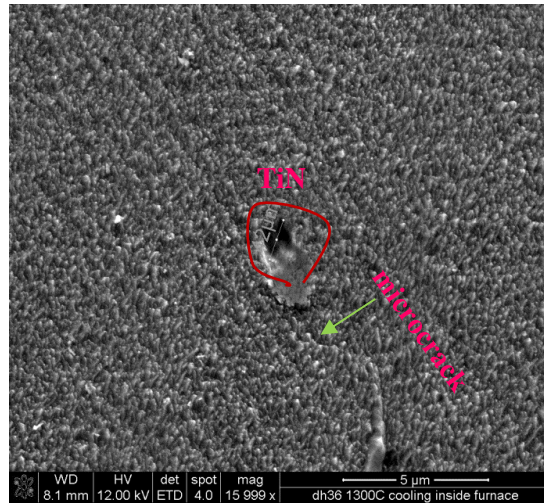
-a-   -b-

Figure 4.200: SEM images show microcracks caused by TiN precipitates (exceeding 1μm) -a- FSW sample W10 (EH46) SZ in the steady state region, -b- Unwelded DH36 steel sample heat treated to 1300°C with slow cooling (cooling inside furnace).
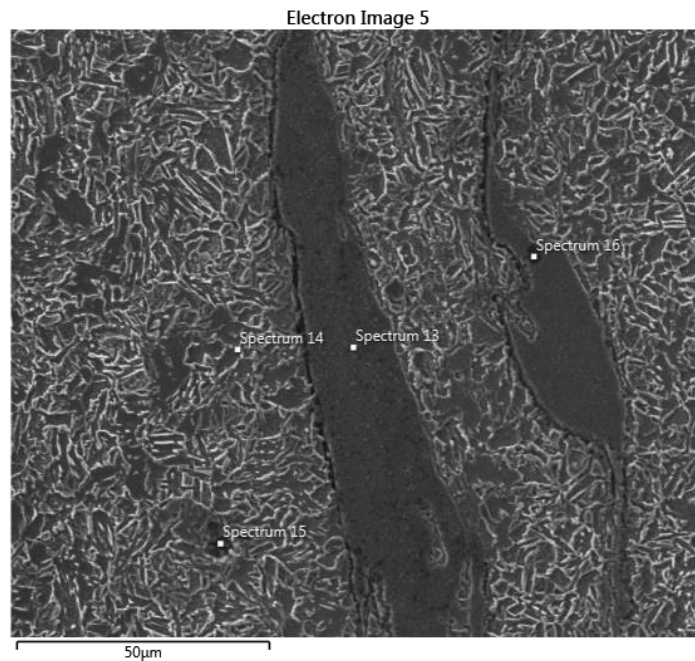
Figure 4.201: SEM image of non-metallic inclusion of Mn, Si, Al and O found in high FSW tool speeds of the SZ of sample W6 (DH36).

4.14 CFD Modelling Discussion.

4.14.1 Mesh refinement.

Figure 4.202 and Figure 4.203 show the peak temperature variations with reference to mesh refinement (fully sticking conditions) for sample W2 (DH36), and sample W2 (EH46), respectively. 1,300,460 tetra elements were adequate to provide temperature stability of DH36 W2, while 3,487,632 tetra elements was the limit of element refinement for EH46 W2, which resulted in a temperature difference of less than 10°C between the two iterations. The mesh refinement study in modelling the FSW is very important in order to show the independence of analysis on the mesh.

4.14.2 Material Properties of the Grade DH36 and EH46 Steels as a Function of Temperature.

As mentioned in section 3.4.9, the material thermal properties of steel including thermal conductivity and specific heat have been represented as a function of temperature. Figure 4.204 shows the variation of thermal conductivity of the workpiece in the contact region with the FSW tool at low speeds DH36 W2 (200 RPM, 100 mm/min) and DH36 W6 high speeds (550 RPM, 400 mm/min). Thermal conductivity decreases sharply in the contact region with the tool and especially on the AS. In sample DH36 W2 the affected area of the workpiece by the thermo-mechanical action of the tool is wider than in DH36 W6 due to the lower traverse speed. The specific heat of the workpiece in the contact region with the tool also changes especially at high tool speeds as shown in figure 4.205. As seen with the thermal conductivity, a wider region is affected by the tool thermo-mechanical action when the tool traverse speed is slow as in DH36 W2.

The tool thermal conductivity and specific heat of the hybrid FSW tool was constant with temperature during the CFD analysis.

4.14.3 FSW Model Results for 6mm thick Grade DH36 Steel.

The results of modelling the FSW process including torque model, sticking/slipping model and fully sticking model are presented in this section. The Fully sticking model has shown better results in terms of predicting the peak temperature and asymmetry especially at high tool speeds, thus it will be investigated extensively. Peak temperatures for samples DH36 W2 and W6 using the process parameters from the actual welding process but two different models have been compared with the fully sticking model. These others models are sticking/slipping model and torque model and will be discussed.

4.14.3.1 Torque Model

Contours of temperature distribution between the tool and workpiece for samples W2 and W6 are shown in figure 4.206 -a- and -b- respectively. Peaks temperatures of 1034°C (W2) and 1202°C (W6) were obtained under the tool shoulder. The HAZ in DH36 W2 is wider than in DH36 W6 due to the lower traverse speed in W2 and the asymmetry is high in the case of high tool speed as more material is affected by the thermo-mechanical action of FSW tool [61] [152]. Calculated temperatures of this model are highly dependent on the value of average torque recorded by the PowerStir FSW machine. The error arises with increasing fluctuations in the recorded torque as mentioned in section 4.1 (FSW graphs) and shown in the FSW graphs of figure 4.1 to figure 4.12. The causes of the fluctuation have also been outlined in section 2.10 (Modelling the FSW process).

4.14.3.2 Sticking/Slipping Model

Contours of temperature distribution between the tool and workpiece of DH36 W2 and W6 are shown in figure 4.207 -a- and -b- respectively. Peaks temperatures of 1010°C (W2) and 1250°C (W6) were obtained at the tool surface. Temperatures in the workpiece of W6 were lower than the tool surface due to the effect of relaxation in plastic flow and the decrease in the coefficient of friction value [178]. As in the torque model, the HAZ in W2 is wider than in W6 due to lower traverse speed and the asymmetry is high in the case of high tool speed as more material is affected by the thermo-mechanical action of FSW tool [61] [152].

4.14.3.3 CFD Model- Fully Sticking Discussion

1. Torque result: In this model the torque is calculated under the shoulder of the tool as it is found by Long et al. [67] that the torque from the shoulder represents the major part of the total torque which, in turn, comes mainly from the viscous and local pressure forces. Table 4.20 gives the values for the maximum temperature and torque obtained through the proposed numerical model for the 8 weld cases. Table 4.20 shows that the values for numerically-calculated torque are within the range of the torque experimentally measured by the FSW machine. Given that very limited numbers of 8 samples were welded using just six rotational and traverse speed variations; a clear relationship cannot be established between the tool speeds and the torque. However, comparing two sets of data presented in Table 4.20 (W1and W2 and W4 through W8) show that the torque decreases with an increase in tool rotational speed at a constant traverse speed. This result is in accordance with the results found in [67] for welding aluminium alloys. They have found, through simulation validated by experimental data, that an increase in tool rotating speed decreases the torque until reaching a relatively constant limit that is subject to only slight change with increasing tool rotational speed. They argued that the torque depends on the contact shear stress between the tool and workpiece and thus by increasing the tool rotational speed, the temperature of the welded region increases, causing a decrease in the contact shear stress and thus the torque. The relationship between torque and flow shear stress is described in equation 3.2 [67]. Atharifar et. al. [147] also reported a decrease in torque with increasing tool rotational speed and decreasing traverse speed as a result of a low viscosity field resulting from an accumulation in thermal energy. From this discussion, it is expected that torque increases with increasing traverse speed at a constant tool rotational speed. However, the welds provided for the current study did not include constant tool rotational speeds with different traverse speeds but a previous study on FSW of stainless steel has reported such a torque increase [177]. The axial and lateral forces in this work will not be discussed here because of the complexity and also due to the fact that the FSW machine was "position" controlled which means the tool was fixed at a constant vertical distance from the workpiece irrespective of the forces acting on the tool [16]. Table 4.20 includes three experimental welding cases with the same rotational/traverse speeds (W6, W7 and W8) but shows different axial/lateral forces. The CFD model can only give constant axial/lateral forces for fixed rotational and traverse speeds.

2 Temperatures of the workpiece: Figure 4.208 gives the CFD modelled temperature contours for the welding conditions studied for samples DH36 W1 through W8. W6 through W8 are presented in one image; they are repeated welds with the same welding rotational and traverse speeds but with different axial and lateral forces. For all cases shown in Figure 4.208 the predicted temperature is very high around the tool but the contour expands just after the contact region. This suggests that heat is moving slowly through the material because of the low thermal conductivity. They also reveal that the contours of temperature tend to be more compressed with high welding speed as shown for W4, W5 and W6-W8. This can lead to a faster cooling rate than those with a slow traverse speed.

Figure 4.209 shows the CFD graphs of temperature distribution between the leading and trailing sides of W1 to W6 of DH36 grade along the top plate surface. The difference in peak temperatures between leading and trailing sides increase as the tool speeds increase (as in W5 and W6) whereas in low tool speeds the difference is slight (as in W1 and W2). The cooling rates of DH36 W1 to W6 are shown in Figure 4.210; the time in this chart has been calculated by dividing the distance travelled along the workpiece distance by the tool traverse speed. Temperature-time curves of DH36 W2 and W6 are examples of low and high welding speeds which were recorded by TCs fixed at the bottom of the plate during steady state welding and have been compared with the CFD results and showed a good agreement as shown in Figure 4.211 and 4.212 respectively. The CFD predicted peak temperatures at the bottom of the plates show slightly higher values than those recorded by the TCs. This difference in peak temperature at the bottom of the plate may come from the assumption for the heat convection coefficient value in the CFD model which needs more experimental work to estimate the exact value of this coefficient. The curves of temperature vs time show that, despite the high tool rotational tool speed of samples DH36 W6 and W5 which were expected to generate a higher temperature in the tool/workpiece interface, the cooling rate was higher because of the higher traverse speed compared to samples W1 and W2.

It is also shown in Figure 4.208 (DH36 W1 and W2) which experienced low welding speeds; the temperature profile is almost distributed symmetrically around the tool radius. However, for welds with intermediate and high tool speeds (Figures 4.208 W3, W4 and W6) the maximum temperature was under the shoulder interface between the advancing side and the trailing edge but closer to the advancing side. This is the maximum temperature which can be expected in this location due to the material flow conditions around the tool which will be discussed later in the material flow section. Similar to this finding, Fehrenbacher et. al. [139]

273

developed a measurement system for FSW of aluminium alloys and measured the temperature of the interface between the tool and the plate experimentally using thermocouples and found that the maximum temperature was at the shoulder interface in the advancing-trailing side closer to the advancing side of the welds. Micallef et. al. [61] by using CFD modelling and experimental validation, found that the maximum temperature occurs on the advancing side and towards the rear of the shoulder's surface while the minimum temperature occurs in the pin region at the leading edge of the tool. Lower plastic deformation due to the lower viscosity at the front of the tool surface has been given as a reason for this minimum temperature. Darvazi et. al. [152], through numerical modelling, found that the maximum temperature in FSW of stainless steel 304L was in the back half of the shoulder region and towards the advancing side. They also found that there was more asymmetry in temperature under the shoulder compared to the regions away from it. Moreover, Atharifar et. al. [147] showed numerically and experimentally (using thermocouple readings) that the maximum temperature in FSW of aluminium was at the advancing side. This was attributed to the high relative velocity at the advancing side causing more viscoplastic material shearing and consequently the higher heat generation through plastic deformation and viscous heating.

As shown in Figure 4.208 the maximum temperature (under the shoulder) of 988°C and 1076°C with wide contours were observed for DH36 W1 and W2, respectively. Welds with higher tool speeds (DH36 W5 and W6-8) show a higher peak temperature of 1364°C and 1436°C respectively because of the high tool rotational speed but they have narrow contours and high temperatures towards the probe sides and probe end. Peaks temperatures of DH36 W1 to W6 have been recorded in Table 4.20 and it can be shown that maximum peak temperatures have exceeded 1100°C when the tool rotational speeds reached 500 RPM which can be shown in the case of high tool speeds weld (DH36 W5 and W6). The temperature of the FSW process has approached the melting point at the advancing-trailing side in W6 with a rotational speed of 550RPM. This result coincides with the metallographic examination of samples W6 and W8 (figure 4.153 to figure 4.179) which show elemental segregation of Mn, Si, Al and O which have been validated by heat treatment trials and showed that similar segregation only occurs when heating to a temperature of 1450 ^{o}C (figure 4.136 to figure 4.152).

The higher peak temperatures achieved at high tool rotational speeds (DH36 W6) which are close to the melting point of the parent material in a very small area localised on the

advancing-trailing side is mainly coming from applying fully sticking conditions which caused high deformation and material flow. Local melting may be expected at lower tool rotational speeds if the thermal conductivity of the workpiece is low as is the case when welding 304 stainless steel [176]. The predicted peak temperature modelled by CFD is expected to be lower in the case of applying the sticking/slipping conditions [178].

To present the temperature distribution at the shoulder/plate interface, Figure 4.213 illustrates the temperature contours for the 6 welding conditions undertaken in this work, the temperature colour bar are unified in one bar to enhance the contrast. It is shown that the asymmetry between advancing and retreating sides increases as the weld traverse speed increases; as shown in DH36 W4, W5 and W6. However, it is expected to observe a smaller Heat Affected Zones (HAZ) for these samples with higher tool traverse speeds. Low welding speeds (Figure 4.213 W1, W2 and W3.) showed a wider HAZ. Figure 4.214 shows the graphs of temperature distribution between AS and RS obtained from figure 4.213. The asymmetry is high between AS and RS for high tool speeds while the HAZ size of low traverse speeds as in W1 and W2 is bigger than the higher traverse speeds group. Micallef et al. [61] reported the same effects of welding speed on the size of HAZ for the same type and thickness of steel grade. Similarly, they found that the asymmetry between advancing and retreating sides of the welds was increased for the higher welding speeds (here in W4, W5 and W6-8). This was attributed to more material being pushed under the shoulder's periphery at the advancing side. From the CFD result, it is worth noting that samples produced with high welding speeds (W6-8) can reach temperatures close to the melting point in a small local region at the advancing-trailing side (Figure 4.208 W6-W8). The evidence of localized melting at the same advancing-trailing side has been reported previously [139] [178] for welding Aluminium alloys. Colegrove and Shercliff [56] found that maximum temperature calculated from CFD modelling of aluminium at 90mm/min and 500 RPM is exceeding the melting point. However, they suggested that in actual welds this temperature would be lower due to two reasons; firstly in the actual weld, slip between the tool and the workpiece can occur reducing the heat input and consequently avoiding melting. Secondly, the material softens considerably at high temperatures near the solidus which reduces the heat generation and hence, the temperature.

Comparing the maximum temperature for DH36 W3 and W5 (as shown in Figures 4.213) it is evident that although their ratio of rotational to the traverse speed is nearly the same (in Table 4.20: 1.2 and 1.25, respectively), the maximum temperature reached on the advancing-trailing side is quite different; 1130°C and 1364°C (1403K and 1737K), respectively. This suggests

that increasing tool rotational speed has a profound effect on heat production compared to the tool traverse speed.

Samples W3 and W4 (Figure 4.208 and Table 4.20) show that the maximum peak temperature of both welds is nearly equal [1130°C and 1143°C respectively] despite the slight increase in tool rotational speed and the high increase in tool traverse speed of W4. The stirred material at the probe-end of both welds has also shown the same peak temperatures, figure 4.215. This means that for these welds the increase in tool rotational speed from 300 to 325 RPM can give nearly the same maximum temperature despite the increase in traverse speed in W4 which led to a faster cooling rate and hence lower heat input. This consequently, resulted in a smaller HAZ as expected. Figure 4.215 shows that for higher rotational speeds welds the probe end has experienced higher temperatures as in DH36 W5 and W6, however increasing the tool traverse speed can cause a temperature drop towards the probe end as in the case of W4 compared to W2. Colegrove and Shercliff [56] also reported the same effect; that changing the tool rotational speed has a significant effect on the peak temperature and the increase in traverse speeds has decreased the size of HAZ.

Modelled temperature contours of the longitudinal cross section of the tool for all cases under study shown in Figure 4.213 are circular and tend to bend towards the tool shank. The tool collar acts as an insulator because of its low thermal conductivity, so most of the heat was partitioned between the PCBN-WRe and the shank from one side and the workpiece from another side. The Shank loses heat mainly by convection coming from the cooling system as previously described. From the contours of temperatures in Fig. 4.213, it can be confirmed that heat is mainly transferred by conduction through the tool parts unlike the workpiece in which heat can also be transferred by the material flow.

3. Comparison of Fully Sticking Model Results with Torque and Sticking/Slipping Models.

The results of the predicted peak temperatures for sample DH36 W2 and W6 using the fully sticking CFD model have been compared to the torque model and sticking/slipping model as shown in Table 5.1. Low tool rotational and traverse speeds of sample W2 (200RPM, 100mm/min) have shown similar peak temperatures (6% maximum difference), however, results of high tool speeds of W6 (550RPM, 400mm/min) showed more significant differences especially in the fully sticking case (16% maximum difference). The fully sticking model includes material rotation at speeds equal to FSW tool rotational speed, thus more heat is expected to be generated. This is in contrast to the sticking/slipping model as the value of heat generated and material relative velocity is controlled by the sticking/slipping parameter (eq. 3.35). The coefficient of friction has shown a significant decrease in the case of high tool rotational speed of 550 RPM as showed in figure 3.16 which in turn caused a relaxation in the heat generation at high rotational speeds of the FSW tool. In the torque model, it is proposed that the error comes from the fluctuation in the average value of input torque as discussed in torque model section. The result of peak temperature at high tool speeds (550RPM, 400mm/min) with fully sticking conditions has shown agreement with experimental results which have been represented by elemental segregation of Mn, Si, Al and O found in DH36 W6 and W8 samples (figure 4.153 to figure 4.179). Elemental segregation as a method of estimating peak temperature has been supported by experimental heat treatments which have shown that temperatures of 1450°C or more are required to produce the Mn, Si, Al and O elemental segregation, as shown in figure 4.136 to figure 4.152.

Table 5.1 Comparison of peaks temperatures of sample W2 and W6 DH36 using three different modelling assumptions.

Weld No. Temperature ^{o}C Model Assumption	W2 ^{o}C	W6 ^{o}C
Torque Model	1034	1202
Sticking/Slipping Model	1010	1250
Fully Sticking Model	1076	1436
Max % Difference	6%	16%

5. Correlation between Fully Sticking CFD Model and Experimental Results

Figure 4.216 and figure 4.217 compared the stirred zone and HAZ obtained from modelling with a sectioned, polished and etched macrograph of the actual welds that were used to produce the model, DH36 W2 and W6. It is shown that the width of the HAZ is located in temperatures range between (1273-1373 K) 1000-1100°C but not below (1173 K) 900°C (region located between contours 13 and 14 in W2 and contours 12 and 14 in W6 respectively). There is no specific rule to calculate the size of this zone as a function of tool speeds; hence the shape of SZ is not easy to determine from numerical CFD simulation. In previous work [61] the SZ geometry was studied using CFD to understand how it varies with the operating conditions of tool traverse and rotational speeds. The relative velocity was considered to represent the transition between stir and no stir. However, the exact value of velocity of stir is not given. In the current model the whole stirred and heat affected zones are compared with the temperature contour as shown in figure 4.216 and 4.217 for the steady state case of DH36 W2 and W6 respectively. It is evident that HAZ is located in the range of contour No.13 and No.14 in W2 and contour No.12 and No.14 in W6 where the minimum temperature reaches about 927°C which is above the A_1 transition zone of the Fe-C equilibrium phase diagram [179]. The difference between the computer generated V-shaped contour and the experimental macrograph can be attributed to the difference in plunge depth which was also reported by Micallef et al [61]. The suggested interpretation is that the difference due to the variation in plunge depth along the welding line can result in significant variation in temperature profile. The experimental recordings of the welding parameters included the plunge forces and plunge depth provided by the TWI for FSW of 6 and 8 mm plates of DH36 and also 14.8mm EH46 steel grades [TWI FSW graphs of DH36 and EH46 steel grade figure 4.1 to figure 4.27] showed many cases in which there was a drop in the plunge force (DH36 W9 figure 4.14 and the drop in temperature in EH46 W9 figure 4.26) when the plunge depth drops by parts of a millimetre. Micallef et. al. [61] suggested that the variation in the plunge depth is mainly caused by the change of plunge force due to uncontrolled factors such as alternating thicknesses of the workpiece. Wang et. al. [180] also observed similar variations in geometry of SZ due to the changes in the plunge depth during their welding experiments. The current model reveals an asymmetry in the temperature profile for all cases studied especially for high welding speeds (DH36 W4, W5 and W6). In CFD modelling of FSW of DH36 steel, Micallef et al. [61] reported a certain level of temperature asymmetry for high welding speed; however, they have not reported any

localised region in which the temperature can reach to near the solidus temperature under high tool speeds similar to DH36 W6 as their model was based on a sticking/slipping assumption. On the other hand, Long et al. [67] reported reaching a melting temperature in 2D-CFD modelling of aluminium alloys FS welded at very high tool rotational speeds exceeding 500 RPM. They argued, using the FSW experimental graphs; that the reduction in torque when increasing the tool rotational speed was due to a drop in the flow stress. One of the reasons behind this drop in the flow stress is thought to be an increase in the temperature and reaching the melting point in some localised regions. They have also argued that this local melting can lead to an intermittently lubricated contact condition between the tool and the workpiece.

The current fully sticking assumption in modelling the FSW process is in agreement with previous work which can be found in [56][177]. There is also previous work which was carried out on modelling the FSW process using different assumptions of heat generation but the authors argued that in experiments the temperature of FSW is higher than calculated when considering CFD FSW modelling in steel [60]. Also Colegrove et al. [57] suggested extending the hot compression tests to a high strain rate and a temperature near the solidus in order to incorporate the behaviour of material during the FSW process.

Comparison with other models, the current CFD result is in good agreement with the results obtained by Toumpis et al [16] for low tool speeds DH36 W1 (close to or above 1000°C) for the same steel grade, thickness and rotational/traverse speeds. However, the distribution of temperature in the SZ shows some difference. This might be due to the different geometry and viscosity ranges applied. The maximum temperature obtained from DH36 W5 1364°C is higher than their results 1250°C for the same welding condition. Moreover, the distribution of temperature between the advancing and retreating side was also different as here it shows more asymmetry than in their model. This difference in temperature value and distribution is certainly related to the assumptions of sticking/slipping.

6. CFD Modelled Surface Temperature of the Tool.

Figure 4.218 shows the temperature distribution around the PCBN tool surfaces for the different welding conditions of DH36 W1 to W6. It is shown from the CFD results that the PCBN-WRe part of the tool experiences a range of temperatures on the surface during welding; a lower temperature on the leading-retreating side of the tool and a higher temperature at the advancing-trailing side. The lowest temperature was on the probe end region at the front of the tool; this was also reported by Micallef et al. [61] where it was interpreted as an effect of a high viscosity value. The material at the front of the tool experiences lower plastic deformation because of the higher viscosity while the material at the trailing side experiences higher plastic deformation because of the effect of tool rotation which pushes the material to the back of the tool. Elbanhawy et al. [177] reported the same variation in temperature around the tool surface. As a comparison with the low rotational welding speed, the tool surfaces in the high welding speeds showed less temperature differences between leading and trailing edges due to the short period of time of each complete rotation and also the lowest difference in viscosity between leading and trailing sides as will be discussed in the viscosity section.

It is expected that the tool surfaces under the welding conditions for DH36 W3 and W4 will experience possible wear on the AS due to binder softening and thermo-mechanical action [19][23] [24]. The wear on the tool surface is highly likely to occur at the AS under the conditions of welding samples DH36 W5 and W6 as a result of the high temperature experienced.

Figure 4.219 shows that maximum temperature in sample DH36 W6 is located in the shear layer just outside the tool shoulder periphery. This is contrary to previous models which suggest that the maximum temperature is always under the tool shoulder. The interpretation for this finding is that as material is heated and pushed around the tool; it reaches a maximum value of strain rate that enables it to gain higher temperature as will be discussed in strain rate and velocity section.

7. Strain Tate and Velocity at the Tool/Workpiece Interface.

Figure 4.220 shows numerically calculated strain rate contours in the SZ for the 6 different DH36 FSW conditions studied (W1 through W6-8). It shows that strain rate increases with increasing tool speeds and that this is more dominant in the high welding speeds (W4, W5 and W6-8). Similarly, Fairchild et. al. [60] reported an increase in the strain rate with increasing welding speeds. The maximum value of strain for low welding speeds (W1 and W2) is in the periphery under the tool shoulder; this is because of the maximum relative velocity existing in this region as shown in Figure 4.221. However, with increasing tool rotational and traverse speed, the maximum value of strain rate was in the shear layer just outside the tool periphery. It should be added that there is a difference in strain rate values between the advancing and retreating sides especially for the high traverse speeds (W4, W5, W6-8). This difference in strain rate values may have resulted from an increased difference in the relative velocity between the advancing and retreating sides of the tool. It is shown that strain rate can reach to a value of $1000s^{-1}$ at the tool shoulder periphery especially for high tool speeds (W5 and W6) as a result of fully sticking conditions. The strain rate values for modelling the same steel grade and welding conditions were reported with lower values when the slipping conditions appear during the process [178]. Figure 4.221 shows the distribution of relative velocity in the contact surface of the tool/workpiece interface for the studied cases. For the low and medium tool rotational/traverse speeds the material velocity distribution is nearly symmetrical. The lowest value of relative velocity can be found at the probe end as a result of lower stirring from the tool probe end. The asymmetry in relative velocity which is mainly coming from the variation in the term "Usinθ" described in equation 3.57 is the main contributor to the asymmetry in the temperature, viscosity, and strain rate. This asymmetry consequently affects the mechanism of heat generation. Figures 4.220 and 4.221 also show that the difference between advancing and retreating sides in strain rate and velocity fields for all studied cases near the probe end is small and thus can almost produce a symmetrical SZ at that location. This is in agreement with Nandan et al. [55] where they argued that this is due to the rapid recirculation of plastic material which itself results in the local temperature distribution not varying significantly at the probe end. Comparing Figure 4.221 DH36 W1 through W6 shows that velocity is more sensitive to tool rotational speed where increasing tool rotational speed resulted in an increased relative velocity.

8. Local Pressure Distribution between AS and RS:

It is noticed from Figure 4.222 that there is a difference in local pressure values between the advancing and retreating sides which increases with increasing tool speeds. The retreating side showed a drop in pressure which can cause a consolidation defect [180]. This type of defect was reported in the retreating side as a result of insufficient internal pressure which in turn results in a drop in the forging forces which are required to keep material consolidation [180]. The current model suggests that more defects can be created in the weld where there is a greater difference in local pressure between advancing and retreating sides. The differences in local pressure increased with increasing traverse speed even when the tool rotational speed was increasing as shown in Figure 4.222, W4, W5 and W6. So it is expected that more defects can be found in the high traversing welds even with increasing the tool rotational speeds. For W4, W5 and W6 the local pressure contours also showed a significant change in the end of probe side at the AS, this inhomogeneity in pressure at that location can increase the possibility of void or crack initiation. The pressure change in this specific location can be the results of higher traversing speed which may cause a lack of material flow as will be discussed in the material flow section. Nandan et. al. [47] found that there is a significant difference in pressure at the lower portion of the workpiece due to the low temperature and strain rate which causes a higher flow stress and thus a higher pressure required to fulfil the material flow, this interesting result needs more investigation. W1 and W2 show a more homogeneous pressure distribution between the advancing and retreating sides, so defect formation is expected to be less likely. In all cases it is noticed that pressure is increasing with tool rotation and traverse speeds. The higher pressure shown in the advancing side rather than the retreating side is the results of formation of a stagnant zone which needs more pressure to achieve material flow.

Figure 4.223 shows the local pressure distribution in the tool/workpiece interface surface of W5 where the pressure in front of the tool is higher than in the trailing edge. The difference in pressure values between the leading and trailing edges is very high towards the tool periphery. Morisada et. al. [35] interpreted the high pressure value in front of the tool shoulder rather than the shoulder back as the results of tool traversing.

9. CFD Modelling of Material Flow around the Tool.

The material flow for two cases of welding is represented in this section. It is noted from Figure 4.224, W2 and W6 which are case studies of low and high welding speeds respectively, that material is flowing around the tool with an asymmetric shape especially for the high welding traverse speed. The flow is deflected at the retreating side in the direction of rotation. Previous experimental work by Schmidt et. al. [37] carried out on aluminium showed the same type of material flow, where marker foils of copper flowed around the tool, broken into pieces then reverted around the retreating side in the same direction of rotation. Morisada et. al. [34] used a W tracer with the aid of an X-Ray transmission system to monitor the material flow during FSW of aluminium (Al050) and low carbon steel. They found that in Al the W tracer can rotate many times around the probe, whereas, in steel the tracer moved along the rotating probe, passed through the retreating side and stopped at the back of the probe. They also found that the tracer velocity in steel was smaller than those of Al as steel is more resistance to material flow. They reported that the shape of the stirred zone in steel was changed because of the formation of a stagnant zone on the AS. Because of the relatively high deformation resistance behaviour of steel, they suggested a low tool rotational speed to achieve a uniform flow zone and optimal FSW conditions. In Figure 4.225, W2 and W6, the maximum flow was noted at the periphery of the tool shoulder of low and high welding speeds respectively and the flow decreases towards the probe end. Figures 4.224 and 4.225 show that the material adjacent to the tool periphery (shear layer) is highly affected by the tool rotation; so it gained velocity. The shear layer rotation means that this region experienced plastic deformation, a high strain rate, high temperature and thus low viscosity. This region forms, together with the main stirred zone, the final shape of the SZ. It is worth noting that the size of the shear layer increases with increasing tool rotational speed. Fig.4.225 W2 shows less thickness of shear layer compare to W6 due to the lower tool rotational speed. The shear layer size is larger around the shoulder but decreases towards the probe. As mentioned previously in the discussion of velocity and strain rate section that there is a stagnant zone that can cause defects. From Figure 4.225 it is shown that this region is located between the stream lines that show a rotation without flow reversal and the adjacent stream lines that show a reversal in flow on the AS. This region showed the minimum value of velocity around the tool ranged from 0.0024-0.1 m/s for W6. The stagnant region, as mapped in 3D shown in Figure 4.225 for sample W6, extends approximately from the mid thickness of the workpiece to the shoulder of the tool. The previous work [55] [181] has

reported the presence of wormhole defects in the same region of interest and they found that the occurrence of this defect increased as traverse speed increased due to inadequate material flow. Morisada et. al. [34] also suggested that the formation of a stagnant zone can lead to a defect in the SZ and that uniform material flow for steel is only achieved at low traverse speed. They interpreted the formation of a stagnant zone on the advancing side as being caused by a low heat input due to high traverse speed. For low traverse speed welds (Figure 4.225 W2) it is shown that the flow is nearly symmetrical and the stagnant zone is limited, this in turn caused nearly symmetrical velocity, strain rate and temperature fields and therefore created fewer defects. To demonstrate the importance of material flow as a main source of heating in FSW process, the heat transfer by convection to that by conduction represented by the Peclet number (P_e) is calculated as follows [55]:

$$Pe = \frac{\rho\, U_c\, C_p\, L_c}{k} \qquad (5.1)$$

U_c- is the characteristic velocity = 0.685 m/s for W6-8 (see Figure 10 W6), L_c-is the characteristic length which represent the shear layer thickness taken from the Infinite Focus Microscope (IFM) experiments and = 0.001m as average. So *Pe* is equal to 56.1 which indicates that material flow plays a major role in heat transfer during the FSW process of steel especially under the tool shoulder. The importance of material flow in heat transfer during the FSW process was also reported in [149] for modelling aluminium AA5083-H131 and they found that *Pe* number was still high even when the thermal conductivity is very high.

10. Estimating the SZ Dimensions from Viscosity Changes.

It is shown from Figure 4.226, W1 through W6 that viscosity decreases with increasing tool rotational speed, this decrease can encourage the layers of the material in contact with the tool to rotate with a specific velocity. The high values of viscosity just after this region will prevent material from moving due to the lack of plastic flow and thus defining the limits of the SZ. It is also worth noting that the calculated temperature around the tool was not enough to markedly decrease the viscosity and allow the material to flow. The strain rate is probably playing a significant role in decreasing the value of viscosity. Viscosity is inversely proportional to strain rate and temperature, so considering the CFD results of temperature and strain rate which show a decrease in temperature and strain rate towards the probe end, it is expected that viscosity will show an increase towards the probe end and this is the main reason for the V-shaped geometry around the contact region. Nandan et. al. 2007 [55] reported the same viscosity increase towards the probe end. It can also be shown that increasing the traverse speed in W4 caused an increase in viscosity modelled at the probe side bottom as compare to W3 which shows a lower value of viscosity although the tool rotational speed was lower. This can be attributed to less heat input towards the probe end in sample W4.

From the viscosity, strain rate, velocity and temperature contour, it can be inferred that the tool shoulder and probe side play the most important role in generating the heat required for welding, whereas, the probe end plays an insignificant role in stirring the material in contact. It is also shown from Figure 4.226 that the most affected zone by stirring is between the shoulder and probe side due to the combination of these two parts of the tool. Figure 4.227 and figure 4.228 show a comparison between the CFD viscosity profile results and the macrograph of the SZ (marked by the red line) of samples W2 and W6 respectively which shows an acceptable representation of the SZ with some slight differences which may be caused by variation in plunge depth as discussed previously. Figure 4.229 shows a top view of the local viscosity for the SZ of sample W2 and W6 low and high tool speeds respectively. From Figure 4.227 and figure 4.229 it can be confirmed that the value of viscosity in which material can flow for all cases under study ranges from 55000 - 9.8×10^6 Pa.s. The cut-off viscosity value is 9.8×10^6 Pa.s which is in good agreement with the previous work carried out on steel extrusion [55].

11. CFD Modelling of the Shear Stress on the Surface of the Tool.

The maximum shear stress predicted by the CFD model for low and medium welding speeds (W1, W2, W3 and W4) as shown in Figure 4.230 is associated with the leading edge of the tool towards the retreating side; which coincides with the prediction for the minimum temperature on the tool (see Figure 4.218). The reason for this is that the tool surface on the leading edge is in contact with higher degrees of viscosity than the trailing edge as shown in Figure 4.229, sample W2. High tool rotational speeds as in samples W5 and W6 show a nearly symmetrical shear stress distribution on the tool shoulder periphery. For constant traverse speeds (W4, W5, and W6) the model predicts that the shear stress will decrease with increasing tool rotational speed because of the associated increase in temperature. The model further predicts that the probe sides is subjected to a higher shear stress at lower tool rotational speed, as shown for W1 and W2 in Figure 4.230 because it experiences lower temperatures and higher viscosity (as shown in Figure 4.218 and Figure 4.226 respectively). The model for sample W4 predicts an increase in shear stress at the shoulder periphery and probe side leading edge compared to W3 because of the higher traverse speed. From the previous discussion, it is recommended to increase the tool rotational speed and decrease the traverse speed in order to reduce the tool wear especially at the probe side and shoulder periphery.

Experimentally, sectioned, polished and etched FSW samples of high tool rotational speeds W6 and W8 have shown a significant volume fraction of BN particles especially at the top surface of the SZ as shown in figure 4.169 and figure 4.170. Whereas sample W2 shows only very slight presence of BN in the SZ microstructure despite the higher shear stress (figure 4.230). This mean that the increase in temperature can be assumed the main reason for tool wear as it causes a softening of the W-Re binder [19][23] [24].

I. Mesh refinement and temperature output.
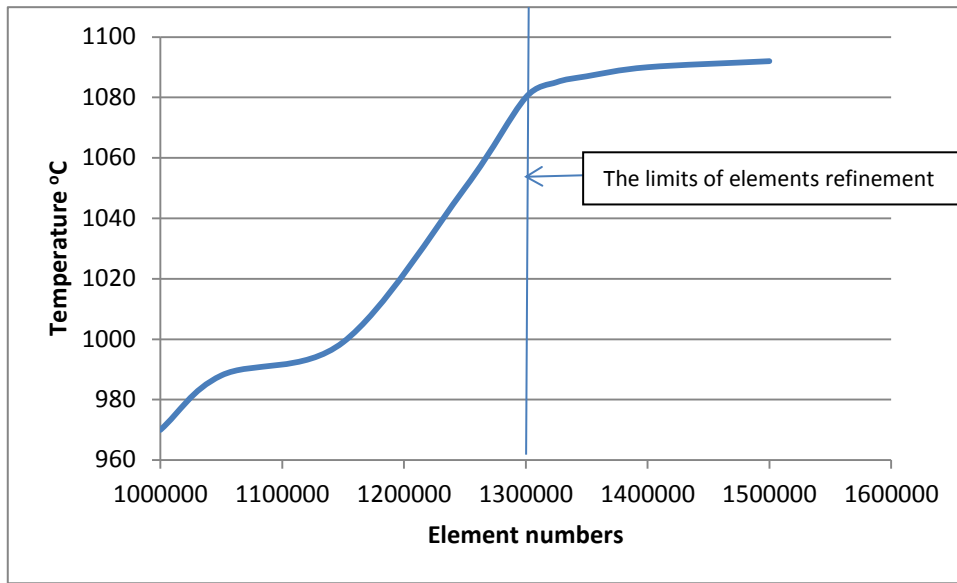
Figure 4.202: Variations in peak temperature results with reference to the number of elements (mesh refinement) of for sample W2, 6mm, DH36 steel.
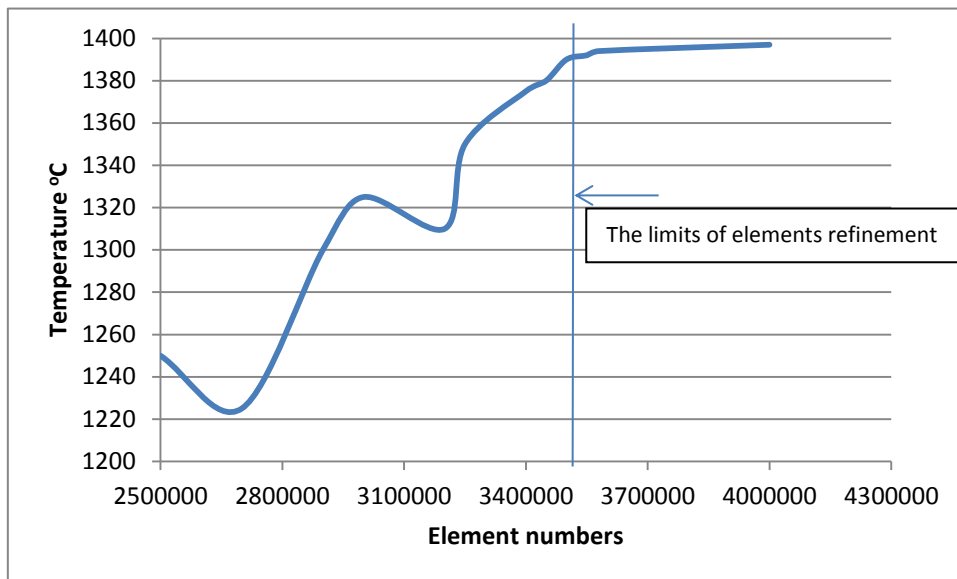
Figure 4.203: Variation in peak temperature results with reference to the number of elements (mesh refinement) of sample W2, 14.8mm, EH46.

II. CFD predictions for the variations in thermal conductivity and specific heat at the tool/workpiece contact region of 6mm DH36 steel.
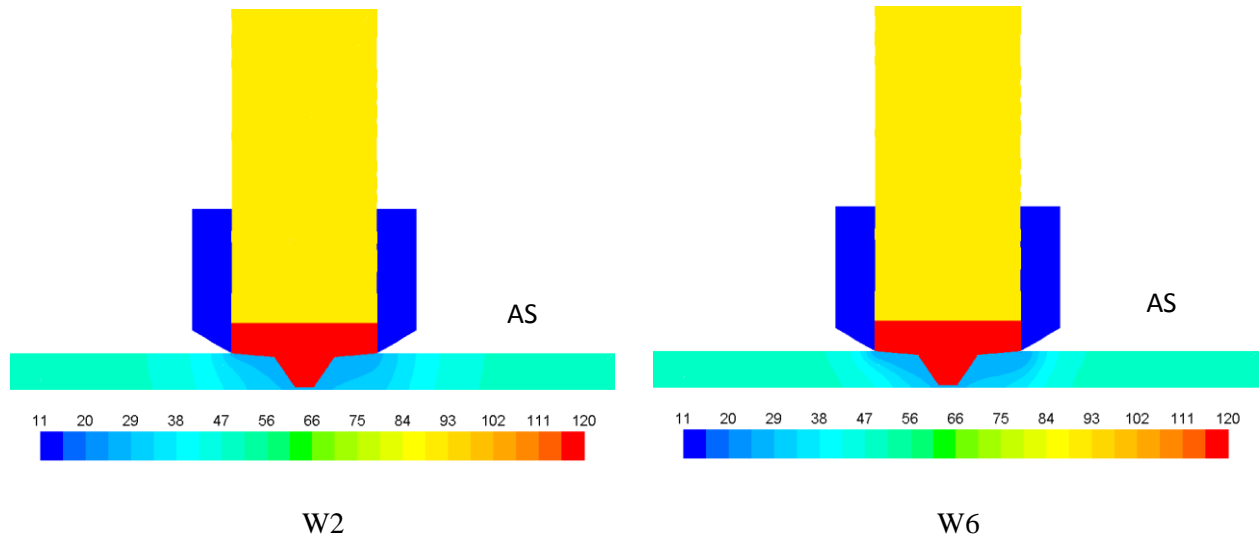
Figure 4.204: Thermal conductivity (W/m.^{o}C) contours of PCBN tool and DH36 plate (W2 at 200RPM, 100mm/min) and (W6 at 550RPM, 400mm/min), thermal conductivity of DH36 plate decreases during the FSW process according to equation 3.64.
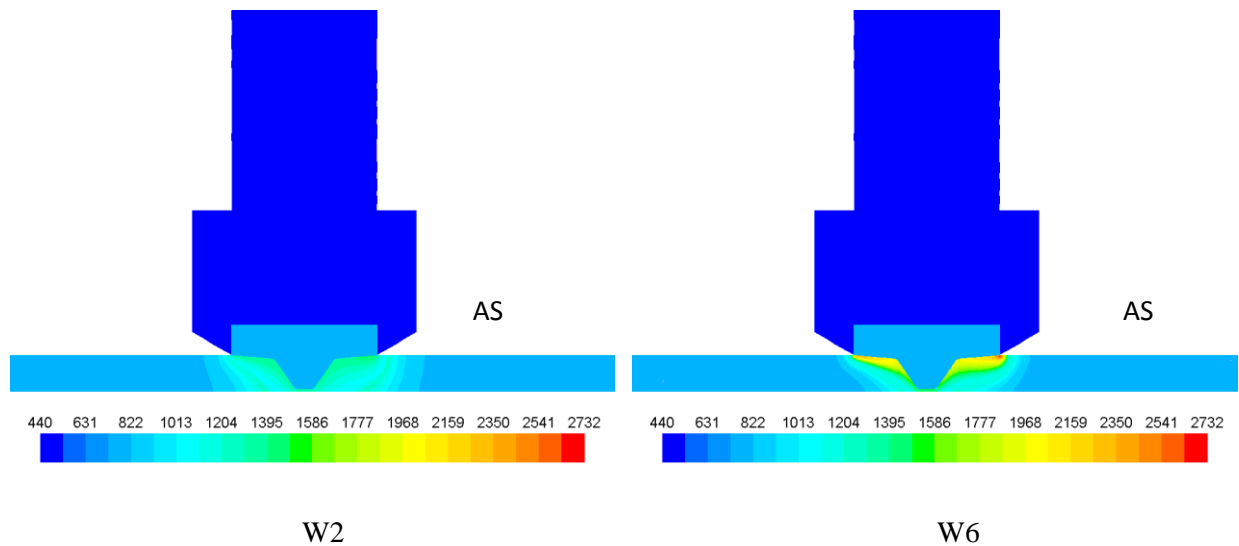
Figure 4.205: Specific heat (J/Kg.^{o}C) contours of PCBN tool and DH36 plate for sample W2 at 200RPM, 100mm/min and sample W6 at 550RPM, 400mm/min. The thermal conductivity of DH36 plate varies as a function of temperature during the FSW process according to equations 3.65 and 3.66.

288

III. FSW Model Result for DH36 Steel

A. Temperature Distribution using the Torque Model

-a- W2 200RPM, 100mm/min -b-W6 550RPM, 400mm/min
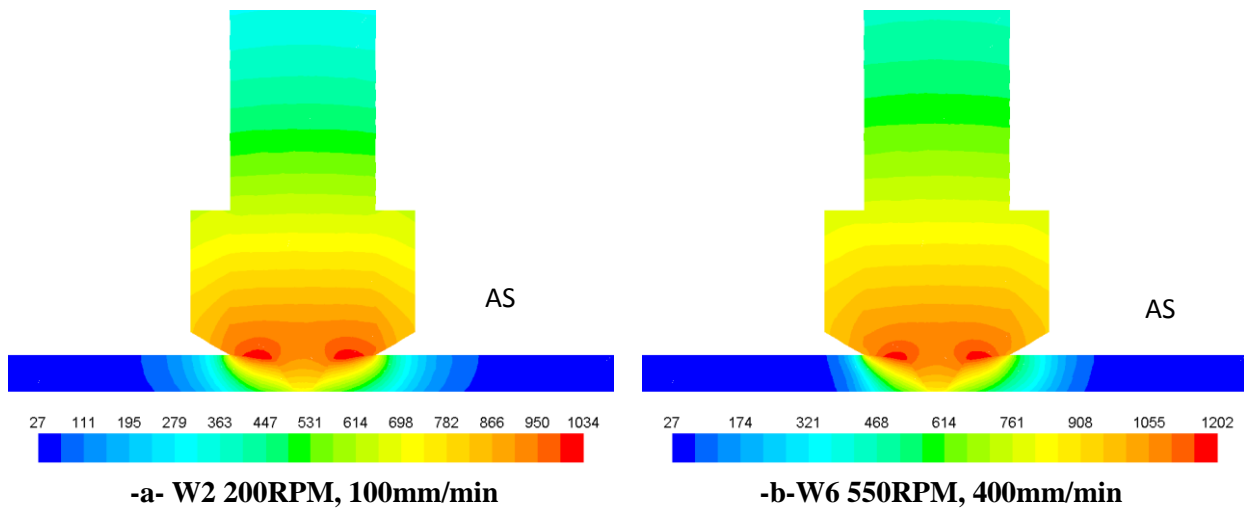
Figure 4.206: Temperature (^{o}C) contour distribution between the tool and workpiece (torque model). a- slow tool speed (DH36 W2), b- high tool speeds (DH36 W6).

B. Temperature Distribution using the Sticking/Slipping Model

-a- -b-
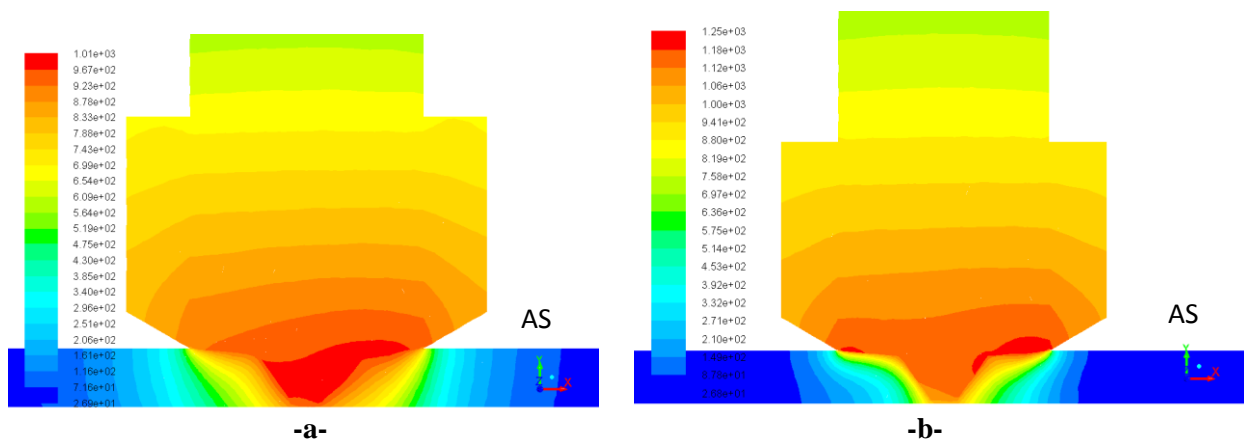
Figure 4.207: Temperature (^{o}C) contour distribution between the tool and workpiece (sticking/slipping model). a- slow tool speed (DH36 W2), b- high tool speeds (DH36 W6).

C. CFD Model Fully Sticking Assumption

1. Tool Torque

The calculated torque from the CFD model.

Table 4.20: Predicted values for the maximum temperature and torque obtained by the proposed numerical model for 8 welded samples with different rotational and traverse speeds.

Weld No.	Tool rotational speed (RPM)	Traverse speed (mm/min)	Rotational/ Traverse ratio	Maximum calculated temperature (^{o}C)	Calculated CFD Spindle Torque (N.m)	Calculated CFD tool Torque (N.m)	Average experimental tool torque (N.m)
W1	160	100	1.6	938	290	110	117
W2	200	100	2	1076	250	95	105
W3	300	250	1.2	1150	234	89	90
W4	325	400	0.81	1170	270	104	94
W4	500	400	1.25	1364	210	80	77
W6	550	400	1.38	1436	200	76	62
W7	550	400	1.38	1436	200	76	68
W8	550	400	1.38	1436	200	76	64

2. Temperature distribution in the tool workpiece interface.
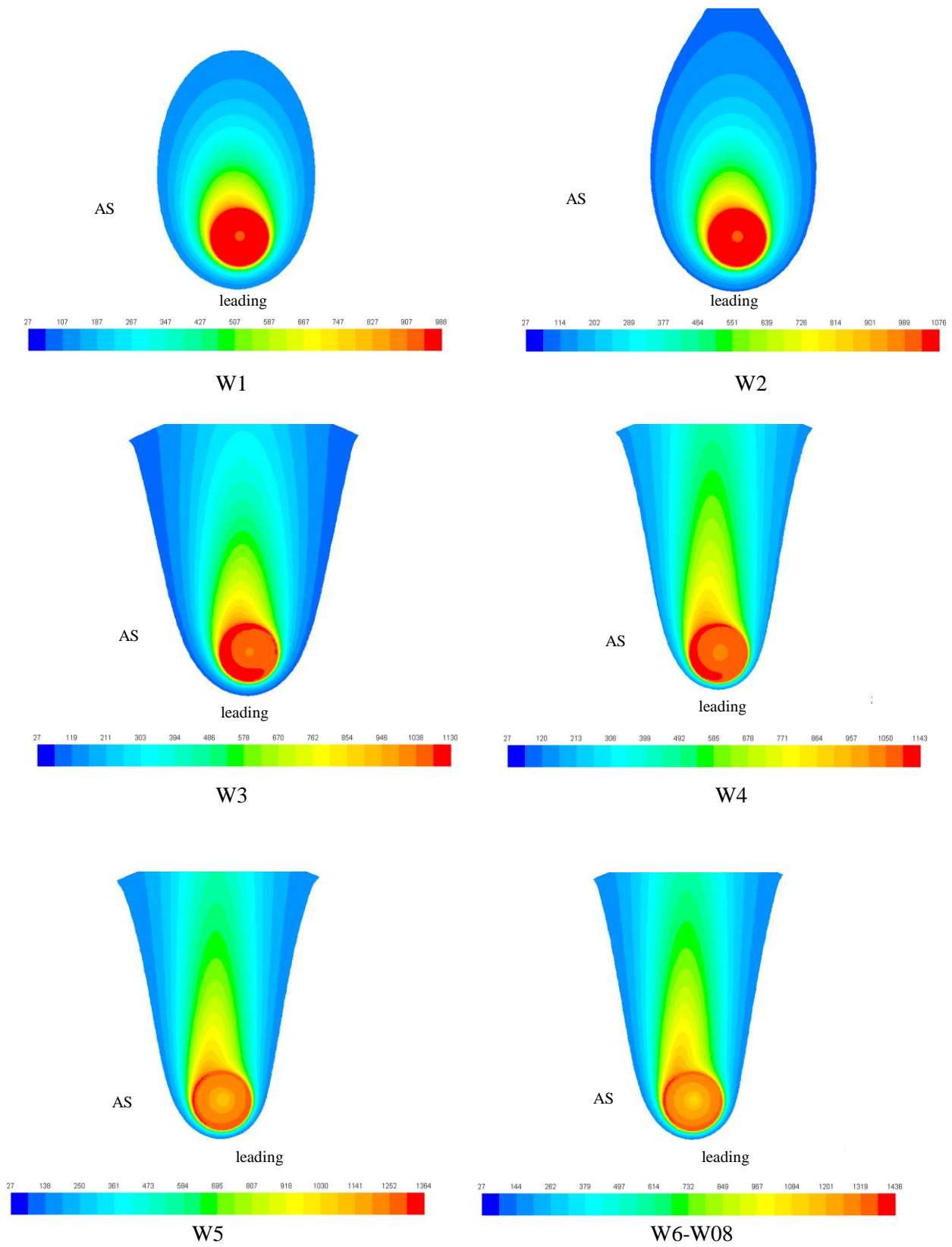
Figure 4.208: Top view of contours of temperature (°C) for 6 different welding conditions (samples DH36 W1 to W8) (CFD Fluent).
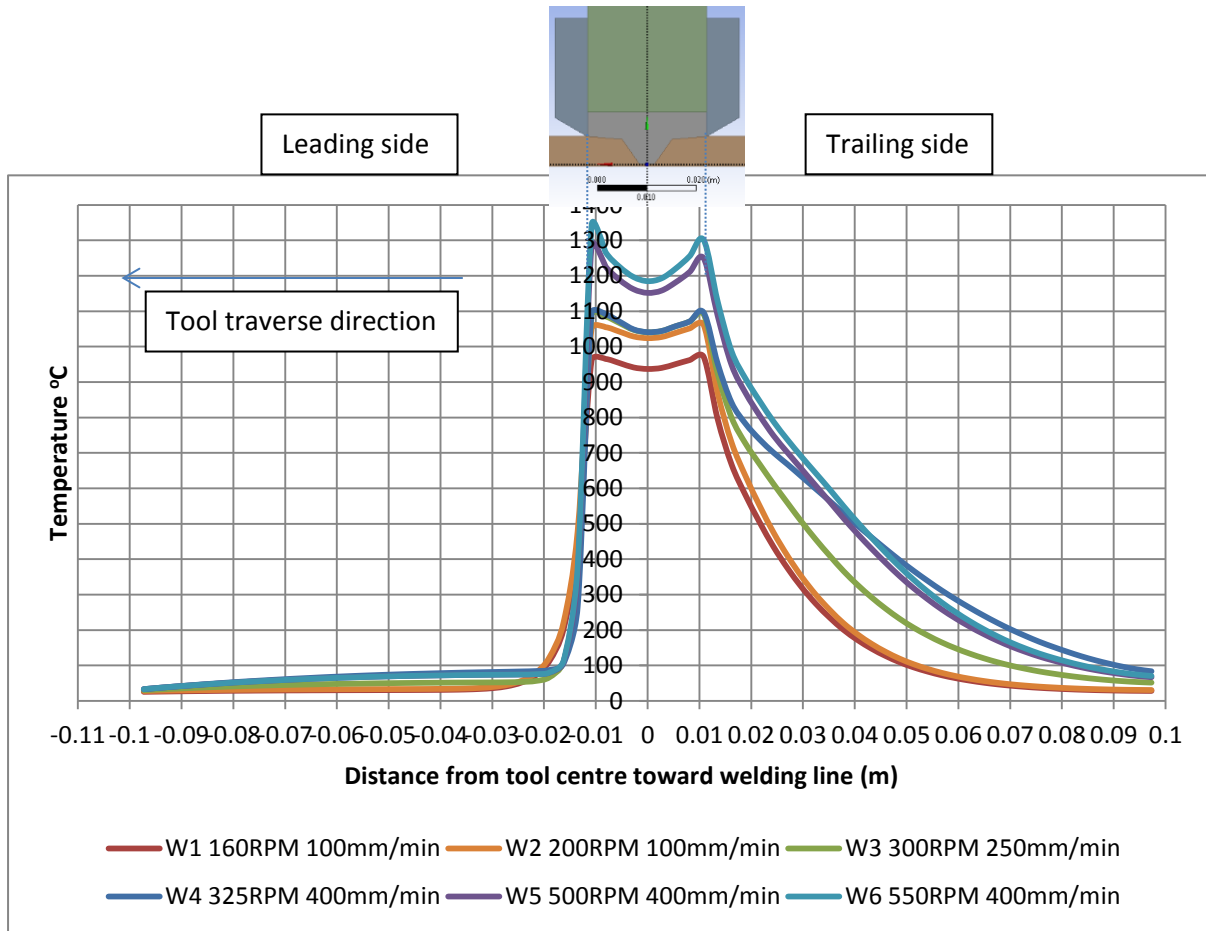
Figure 4.209: CFD results show the temperature distribution between the leading-trailing sides at the top of SZ of welded samples DH36 W1 to W6.
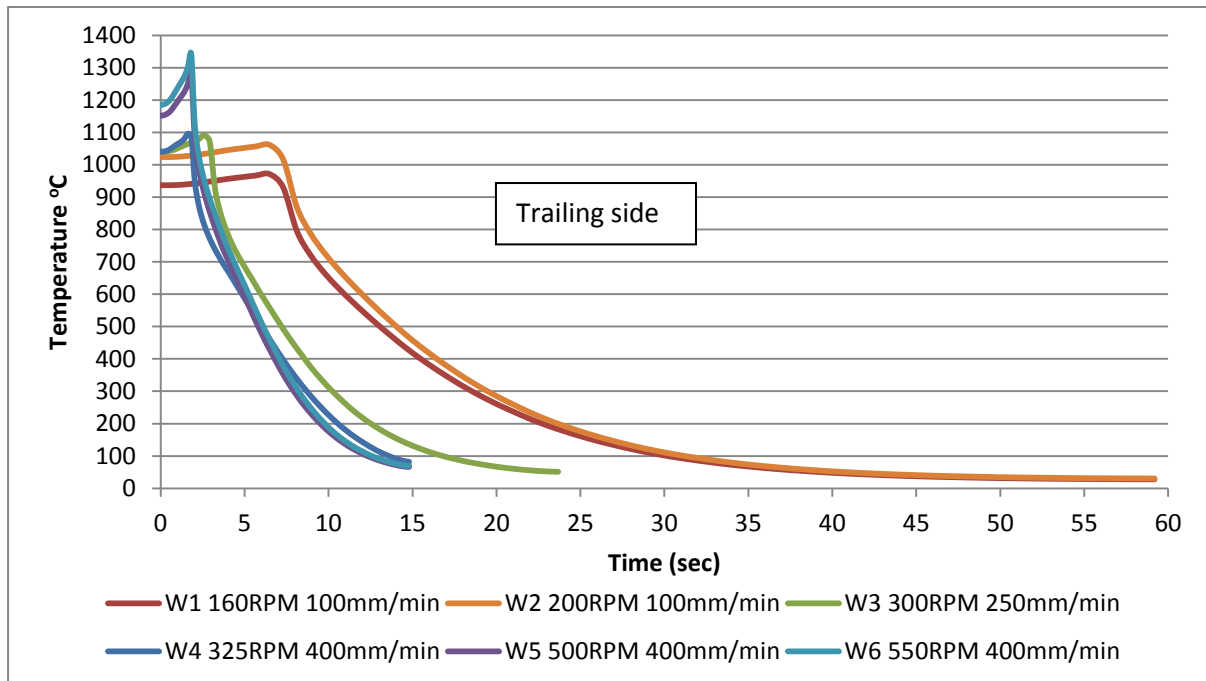
Figure 4.210: CFD results show the temperature-time curves toward the trailing side at the top of SZ of welded samples DH36 W1 to W6.

292
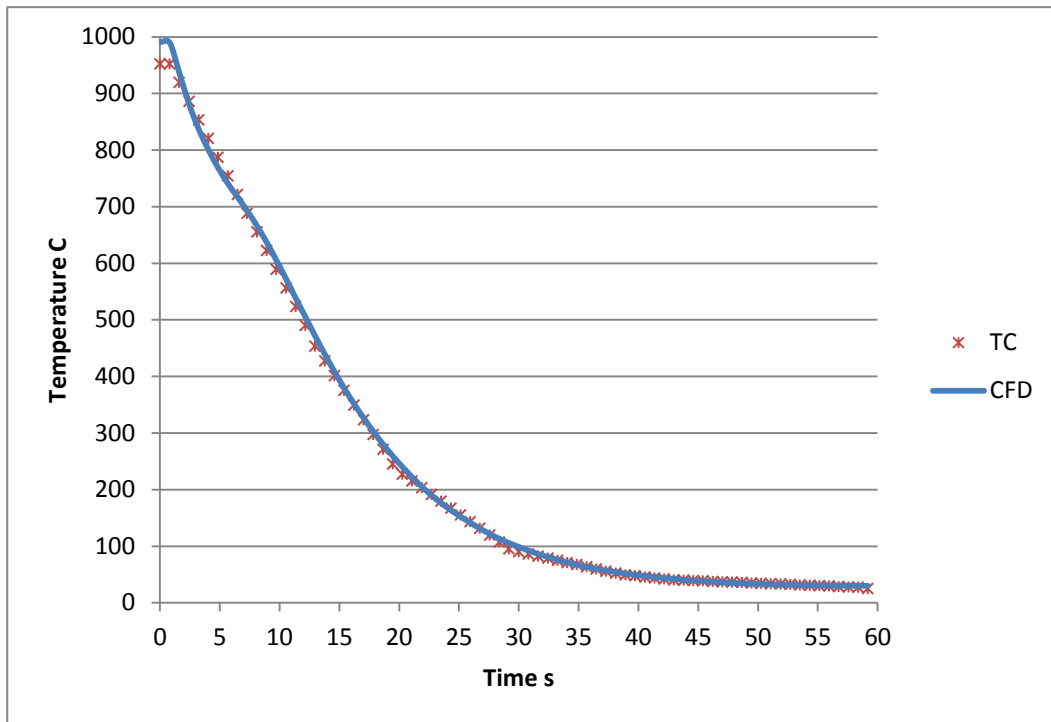
Figure 4.211: Temperature-time curve for sample DH36 W2, comparison of thermocouples data and CFD, model prediction. A distance of 100 mm staring from the plate bottom centre towards the welding line was divided by the welding velocity in order to represent the time (60 sec).
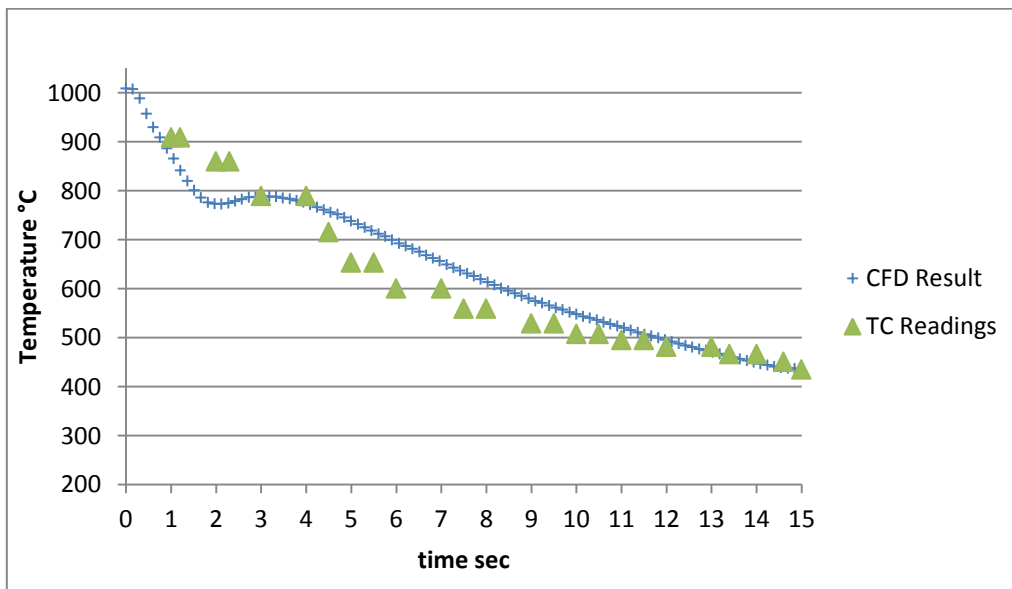
Figure 4.212: Temperature-time curve for sample DH36 W8, comparison of thermocouples data and CFD, model prediction. A distance of 100 mm staring from the plate bottom centre towards the welding line was divided by the welding velocity in order to represent the time (15 sec).
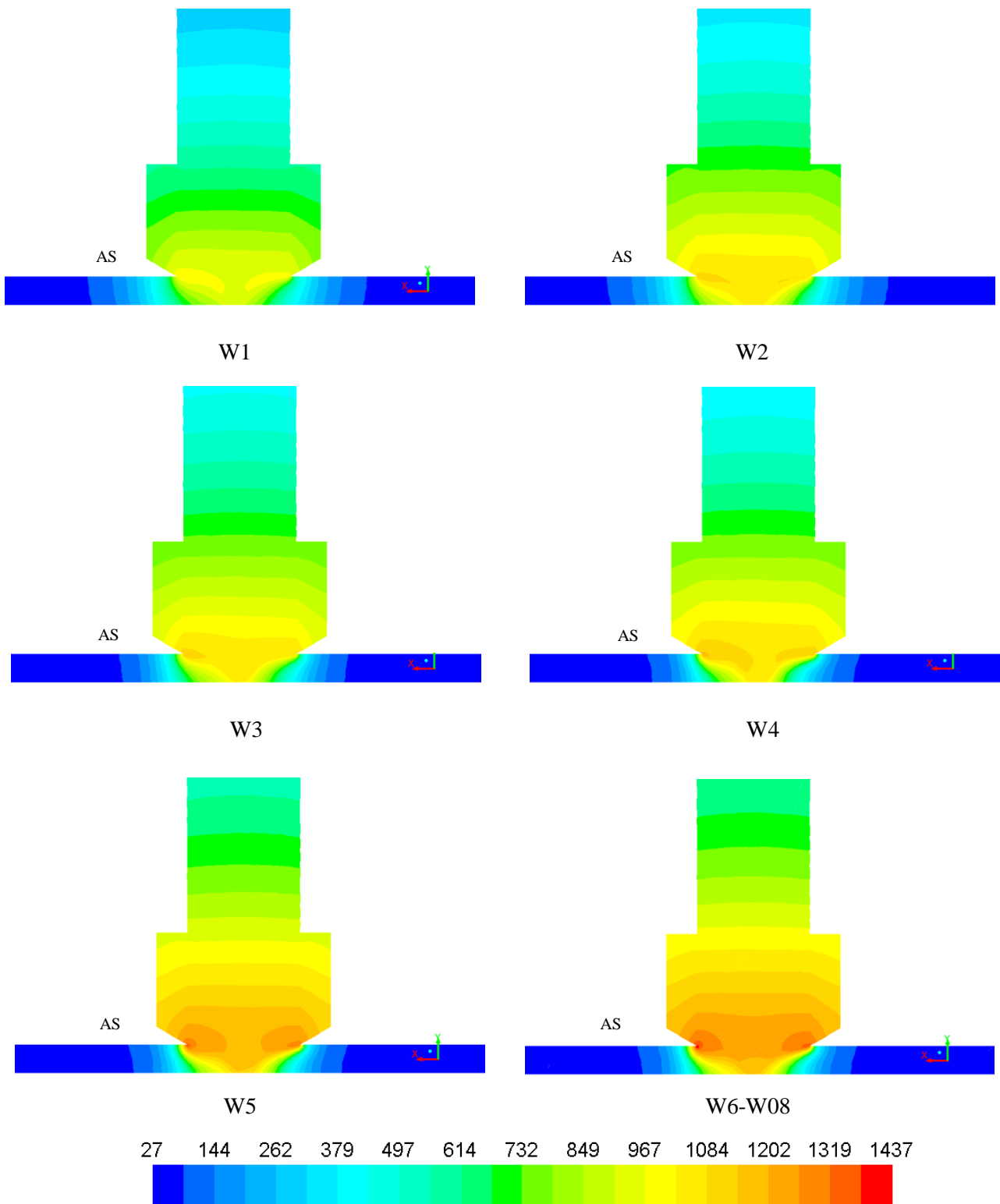
Figure 4.213: Side view, perpendicular to the welding direction, contours of temperature (°C) for 6 different welding conditions (samples DH36 W1 to W6) (CFD FLUENT). The cantor bar has been unified for better comparison.
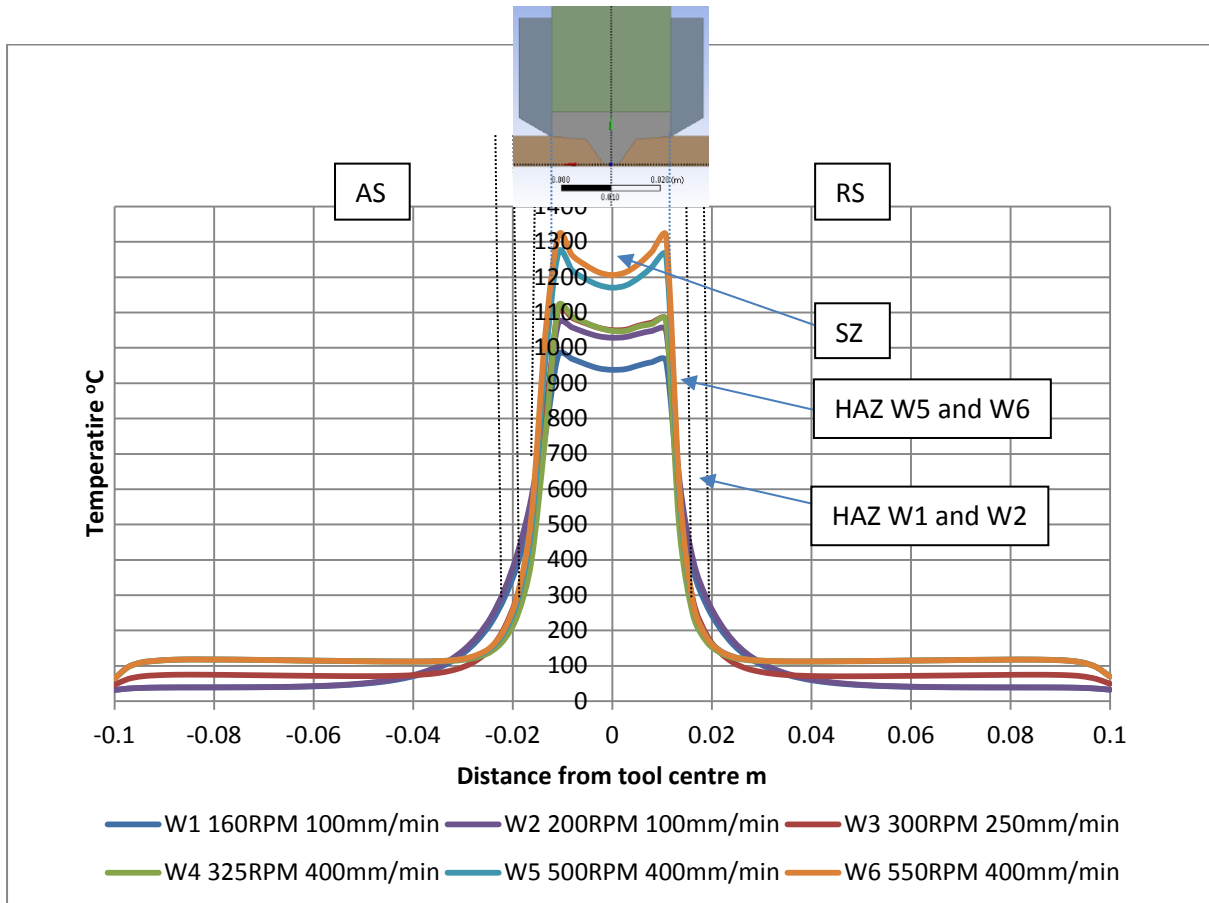
Figure 4.214: CFD results show the temperature distribution between the AS-RS at the top of SZ for samples DH36 W1-W6.
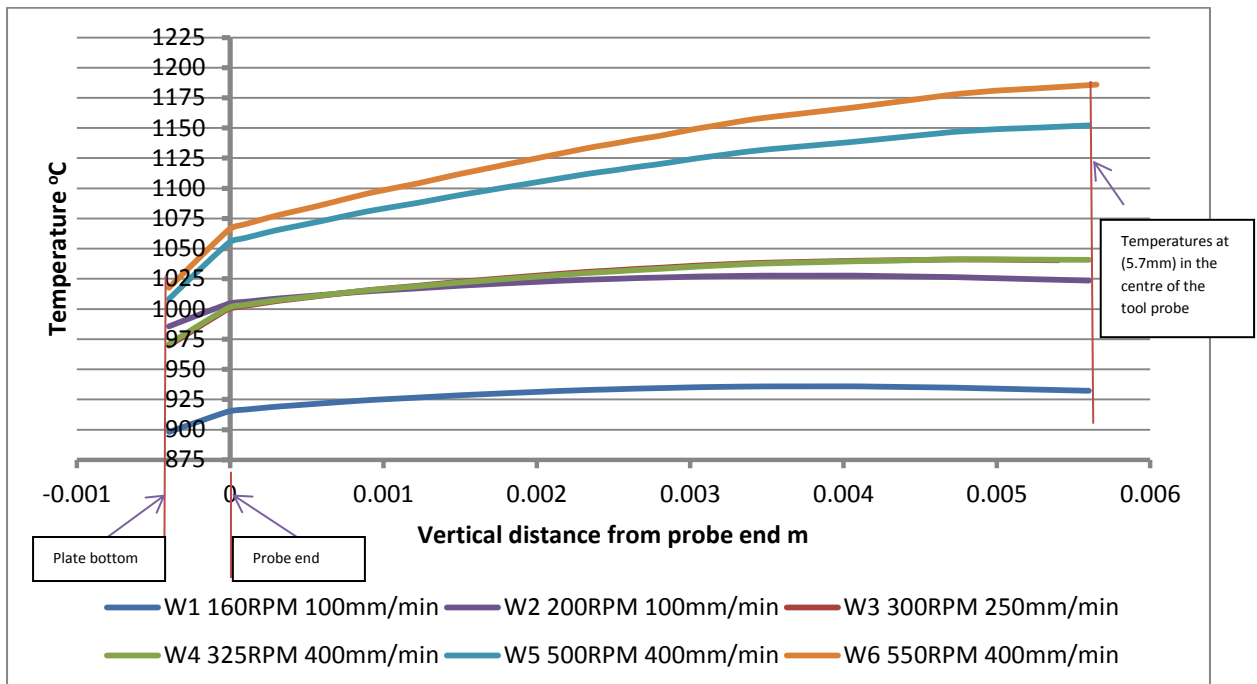
Figure 4.215: CFD results show the temperature distribution in the tool probe and plate bottom for samples DH36 W1-W6.
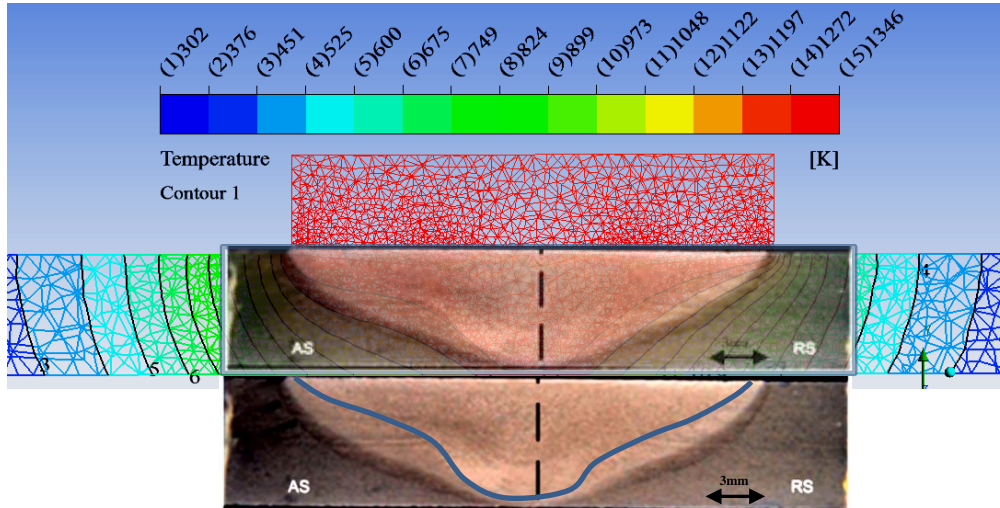
Figure 4.216: Comparing the numerical temperature contours (K) and the experimental steady state welding conditions for sample W1 (DH36) macrograph adapted from [61 p596]
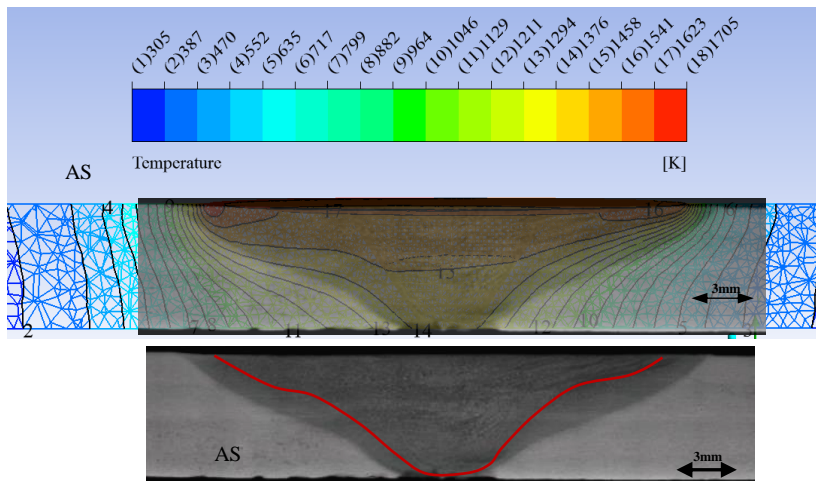
Figure 4.217: Comparing the numerical temperature contours (K) and the experimental steady state welding conditions macrograph (IFM) of sample DH36 W6.

6. CFD Model Result of the Surface Temperature of the Tool:
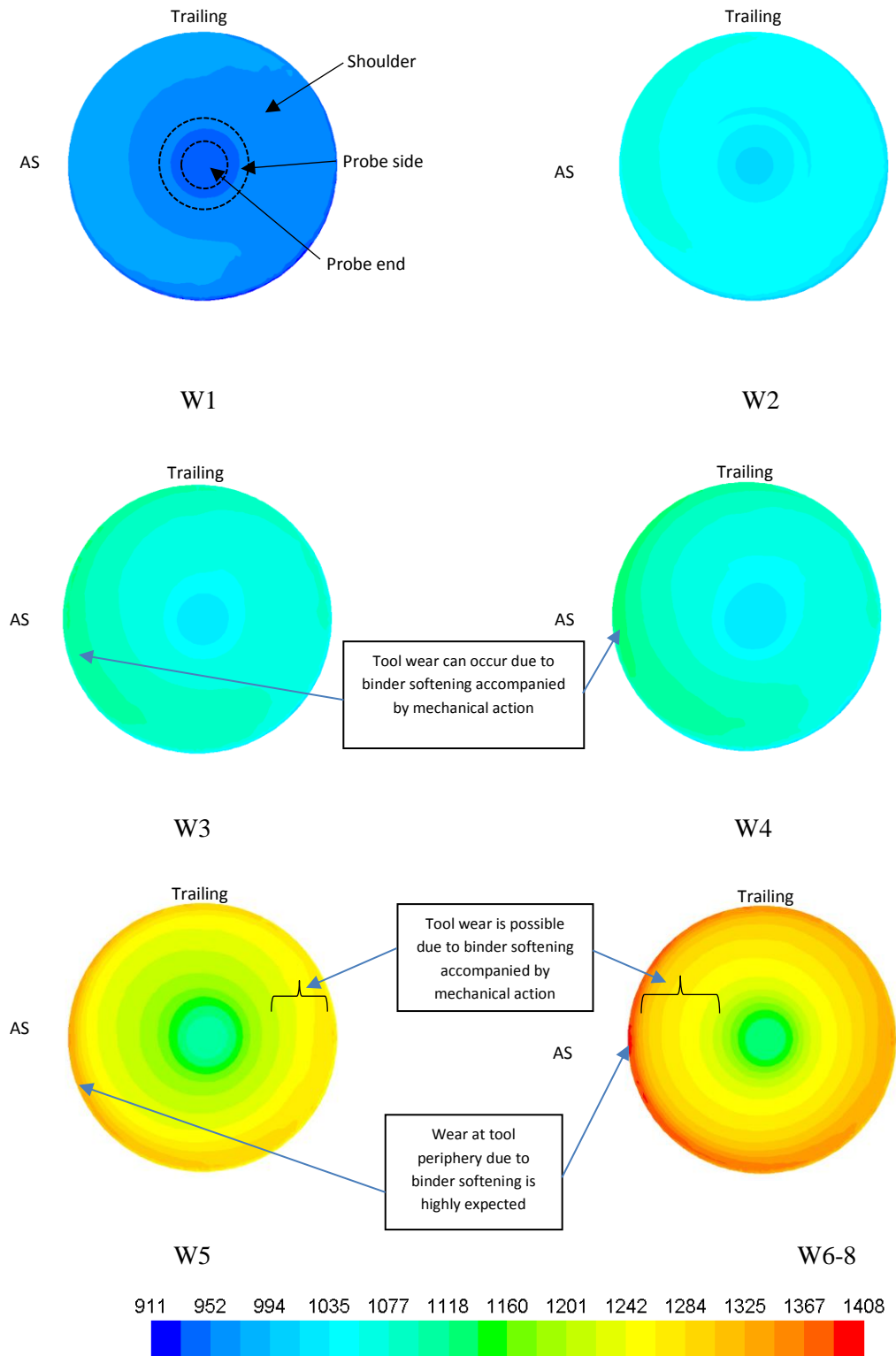
Figure 4.218: The temperature (^{o}C) contours around the PCBN tool surfaces for six different welding conditions; (samples DH36 W1 to W6-8)
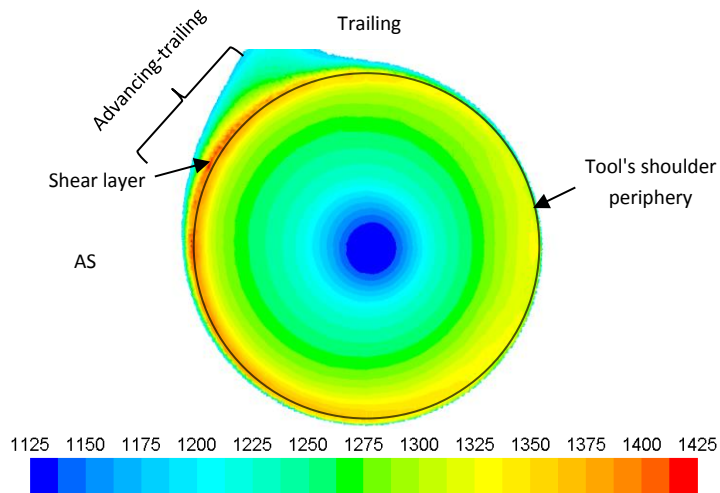
Figure 4.219: Temperature (°C) distribution on the tool surface and shear layer (TMAZ) for samples DH36 W6-8 showing the maximum temperature for high speed welds (550RPM).

7. Strain rate and velocity in the tool/workpiece interface:
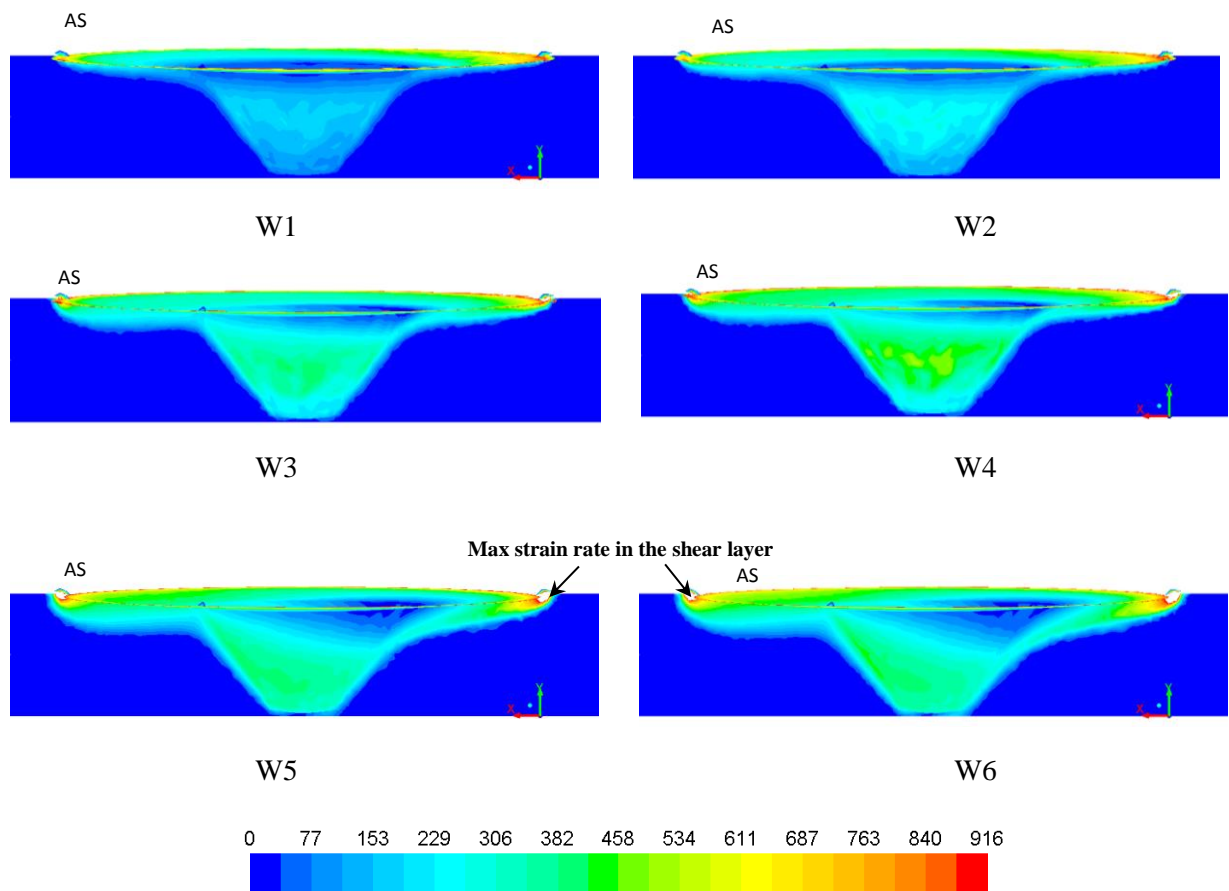
Figure 4.220: The distribution of strain rate (s⁻¹) in the contact surface of the tool/workpiece for the 6 different studied conditions samples DH36 W1 through to W6-8.
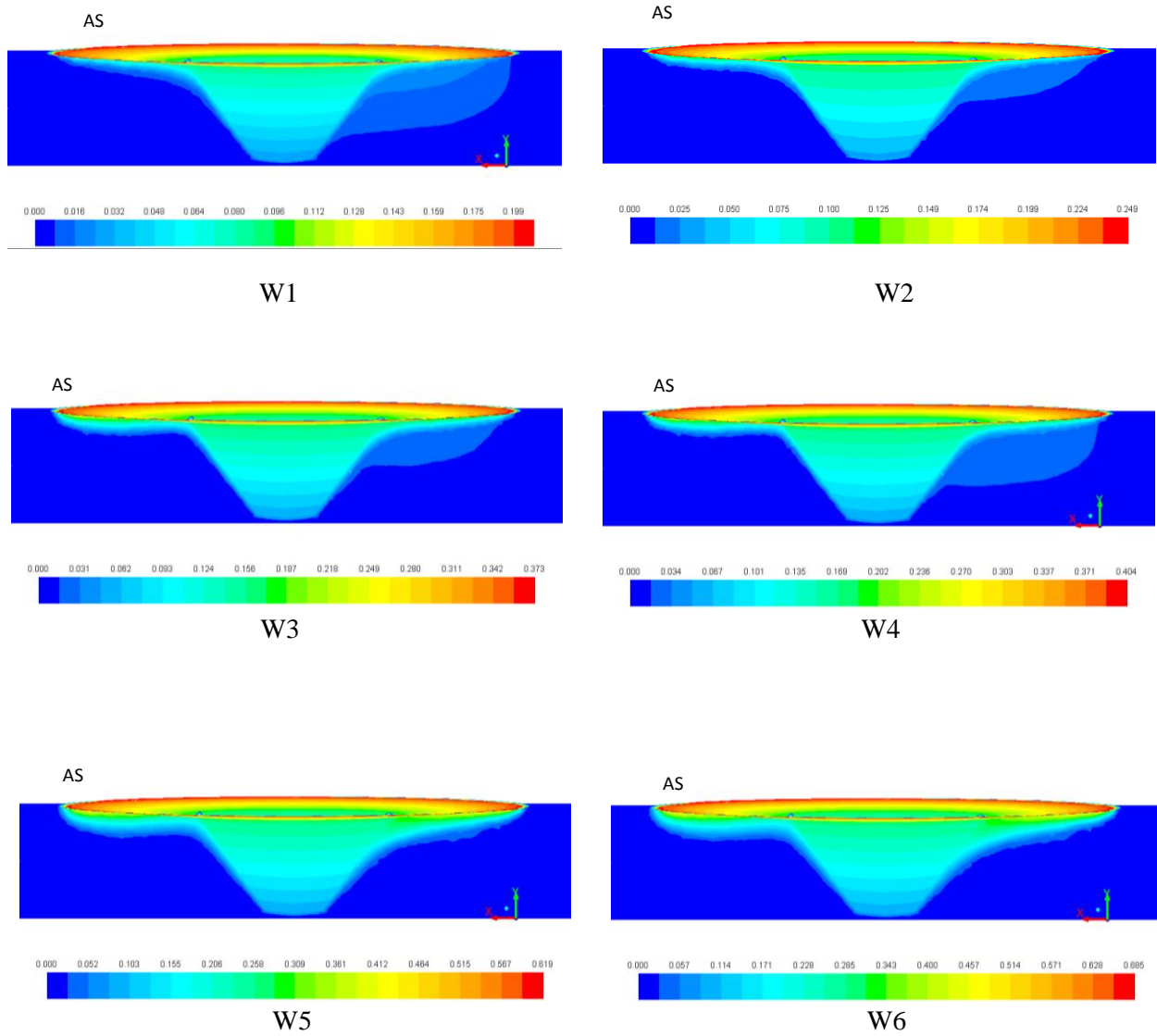
Figure 4.221: The distribution of relative velocity (m/s) between the tool/workpiece interfaces for the 6 different studied conditions samples DH36 W1 through W6.

8. Local Pressure distribution:
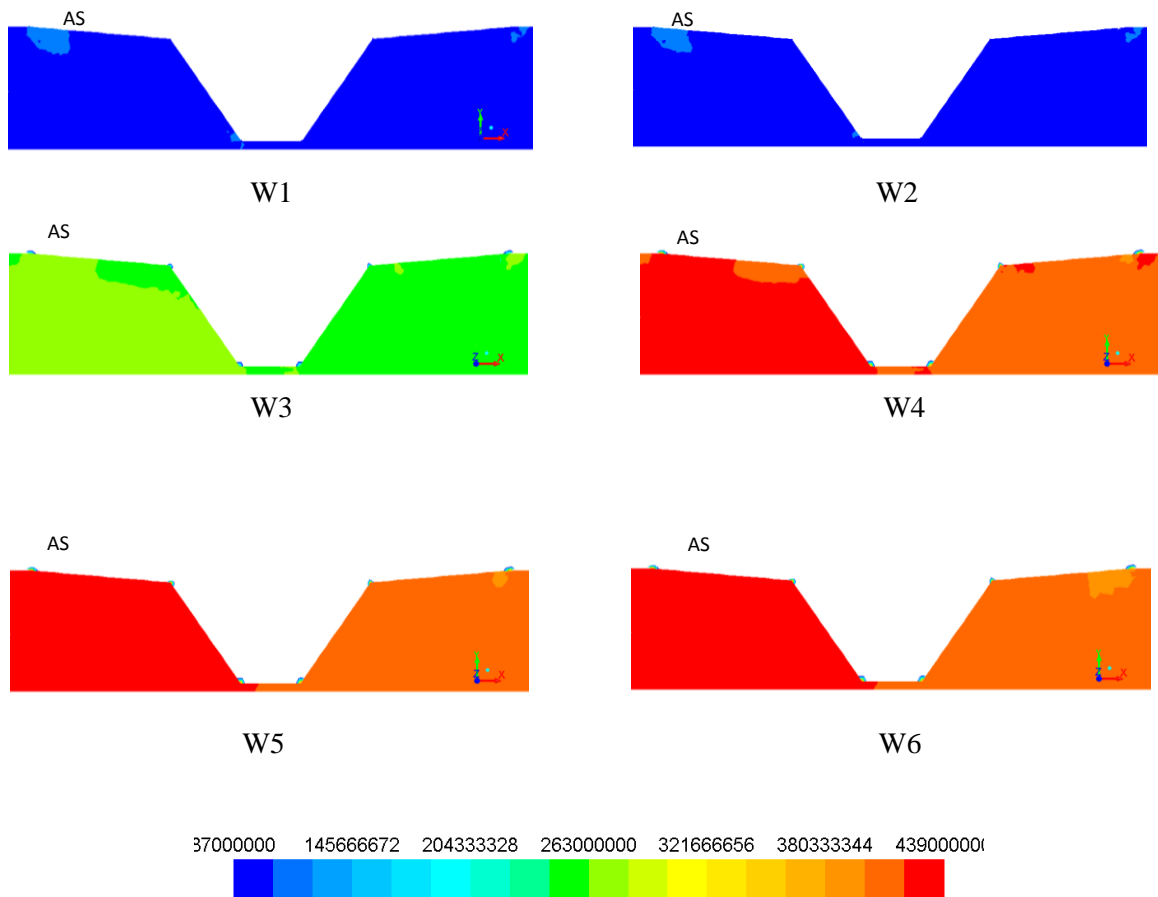
Figure 4.222: The distribution of local pressure (Pa) between the advancing and retreating sides.
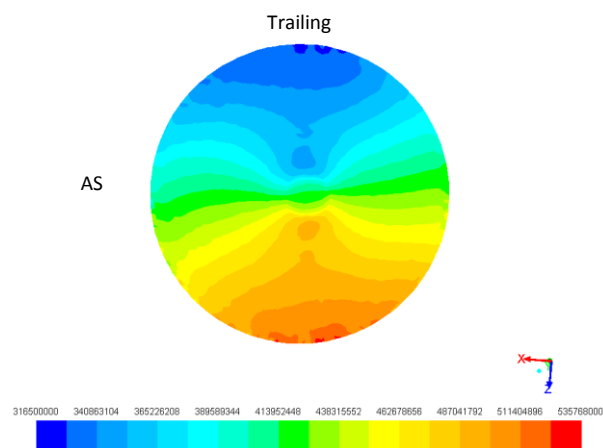
Figure 4.223: The CFD modelled local pressure (Pa) distribution between the leading and trailing side of the tool surface for sample W5.

9. CFD Model of the Material Flow around the FSW Tool.

a-W2 b-W6
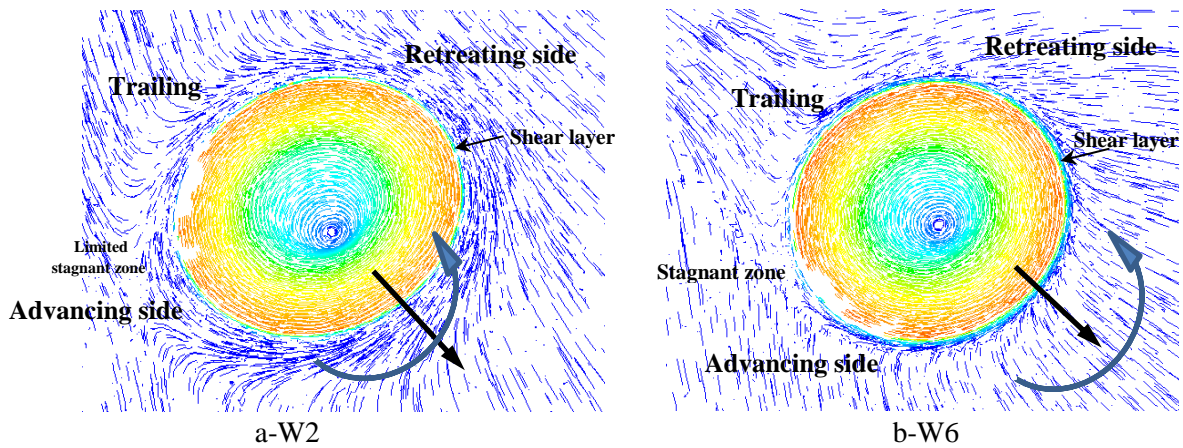
Figure 4.224: Material flow path lines in and around the tool/workpiece contact region -a- sample W2 and -b- sample W5 (3D top view).

-a- -b-

W2 W6
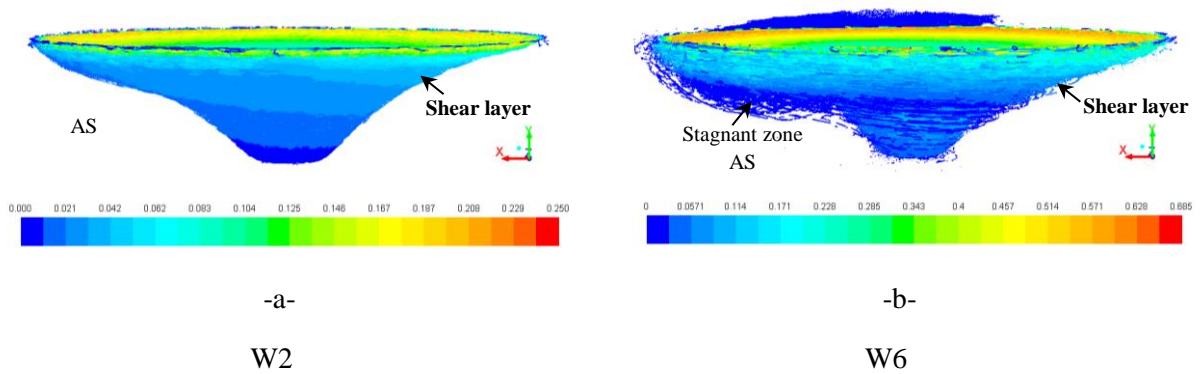
Figure 4.225: The material flow coloured by local velocity (m/s) (3D Advancing-Retreating sides) for -a-low tool speeds sample DH36 W2 and -b-high tool speeds for sample DH36 W6.

10. Estimating the size of the SZ based upon modelled changes in viscosity.

W1

W2

W3

W4

W5

W6-8
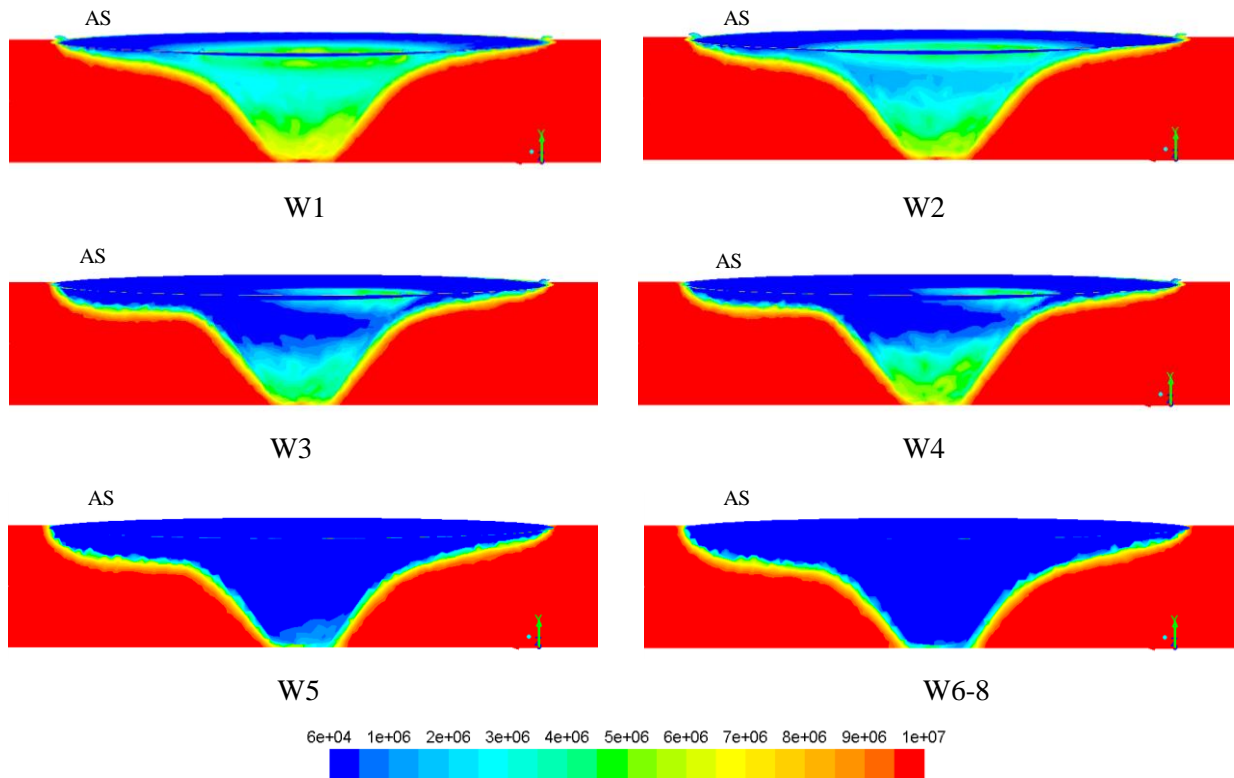
Figure 4.226: CFD model results showing the Viscosity (Pa.s) distribution around the tool/workpiece for welds DH36 W1 - W6 -W8.
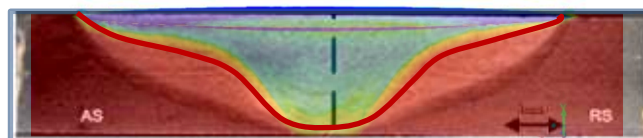
Figure 4.227: Comparison of CFD viscosity contours with IFM macrograph for sample DH36 W2, macrograph adapted from [61 p596].
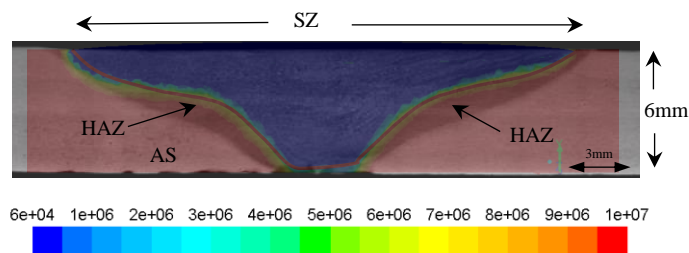
Figure 4.228: Comparison of CFD viscosity contours with IFM macrograph for sample DH36 W6.

Trailing

AS

-a-

W2

Trailing

AS

-b-

W6

55000   1273125 2491250 3709375 4927500 6145625 7363750 8581875 9800000
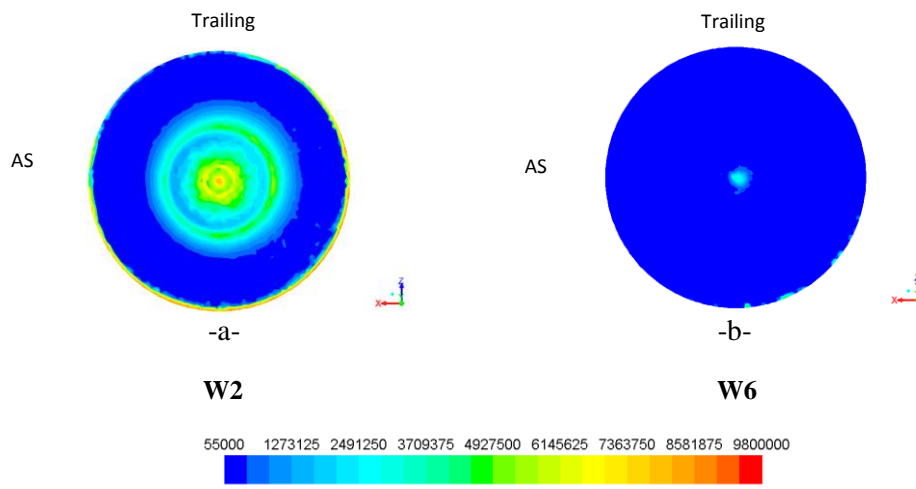
Fig. 4.229: Local values of viscosity (Pa.s) on the top surface of the SZ for -a- low tool speeds sample W2 and -b-high tool speeds sample W6.

11. Shear stress on the surface of the tool
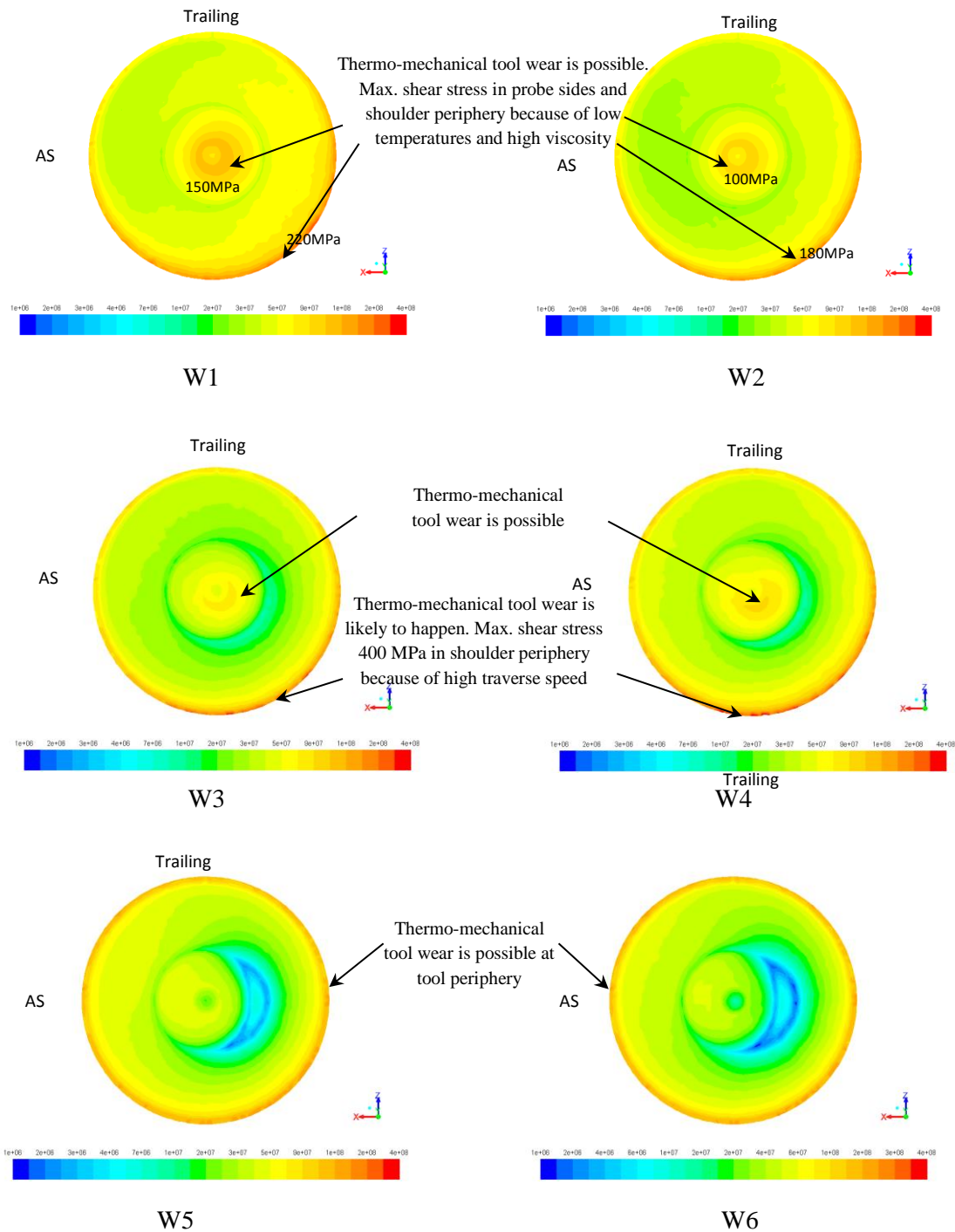
Figure 4.230: Predicted shear stress (Pa) contours on the tool surface (DH36 W1-W6)

4.14.4 FSW Tool Optimisation.

A suggested method for solving the issue of local melting and elemental segregation at high tool speeds has been presented in this work. Figure 4.231 shows the 6mm DH36 CFD modelling results of temperature, viscosity and strain rate when rotating only the probe (i.e. the shoulder is stationary) at 950 RPM with traverse speed of 400mm/min. The predicted peak temperature of 1148°C has been achieved; the stir zone size is also adequate. Even at such a high rotational speed, the predicted temperature did not reach melting point.

A suggestion for tool optimisation by changing the size of probe can achieve higher heat generation and a larger SZ without the need for using very high tool rotational speed. In a study carried out by the authors [176], a probe of 5.8mm length with 12mm diameter at the shoulder base has been adopted when modelling FSW of 304 stainless steel which has a low thermal conductivity (16 W/m.K) and thus issues of localised melting are present when welding with high rotational speeds. Figure 4.232 shows the results of CFD modelling for temperature, strain rate, velocity and viscosity contours of the SZ after using the optimised tool probe with a stationary shoulder. The CFD model predicts that a tool rotational speed of 550 RPM, and traverse speed of 400mm/min is enough to generate adequate temperature during FSW.

Temperature distribution ^{o}C

Viscosity Pa.s   Strain Rate 1/s
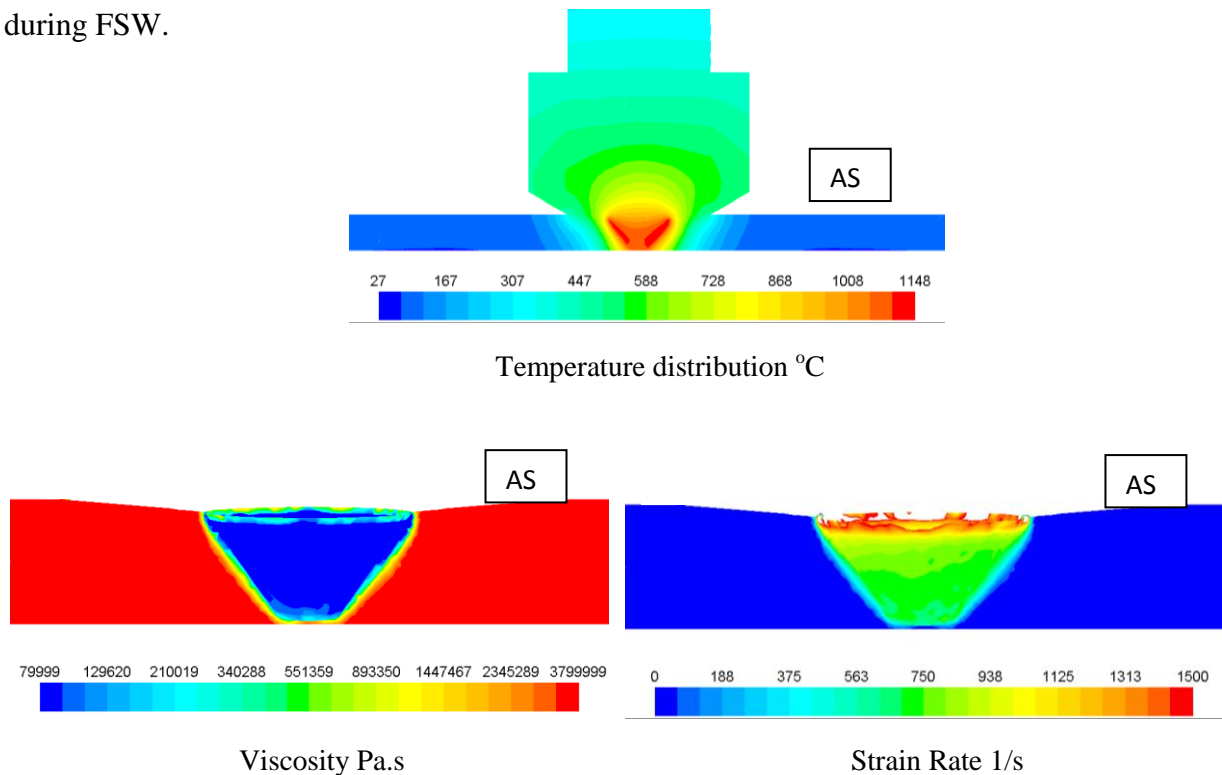
Figure 4.231: Stationary shoulder with probe speeds of 950RPM, 400mm/min

- **Tool Optimisation (stationary shoulder with increasing probe size)** [176]

a-Temperature distribution °C

b-Strain rate s⁻¹

c-Velocity m/s
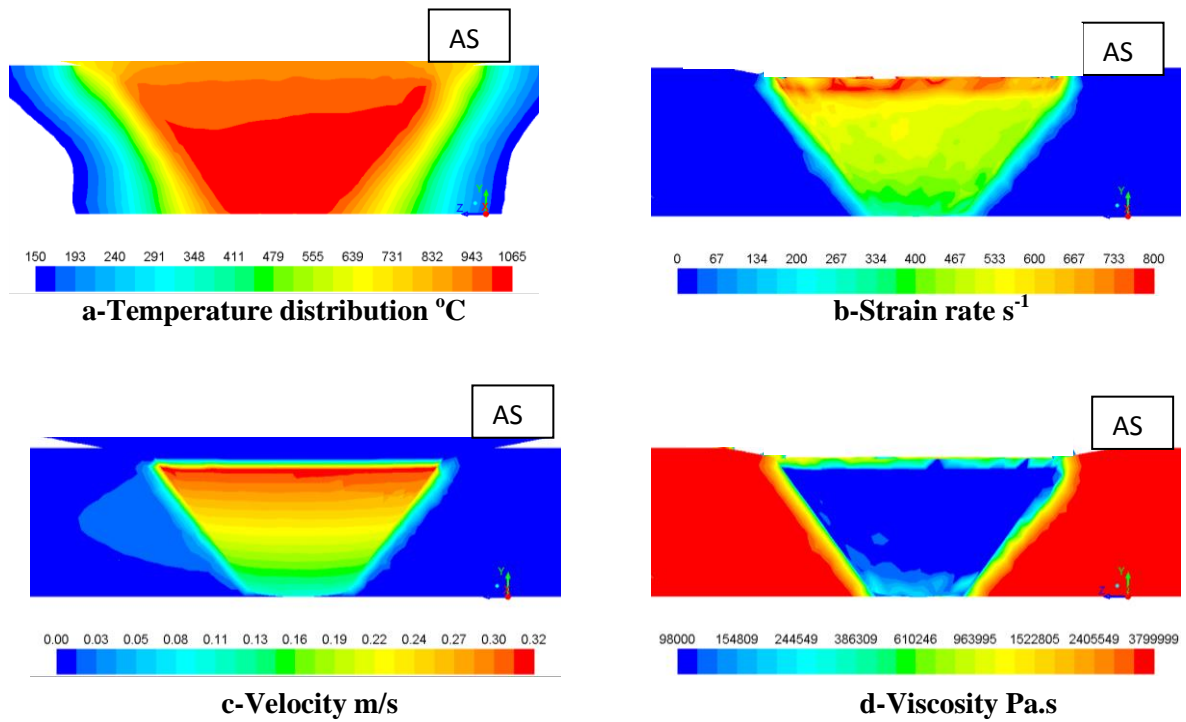
d-Viscosity Pa.s

Figure 4.232: The results of CFD modelling for temperature °C, strain rate s⁻¹, velocity m/s and viscosity Pa.s at the probe/workpiece interface after the optimisation study on the FSW tool, Tool speeds 550RPM/400mm/min. Material is 304 stainless steel. The shoulder of the tool is stationary [176].

4.14.5 Results' Discussion of CFD Modelling Grade EH46

4.14.5.1 Dwell Period: The EH46 steel plunge/dwell experiment has also been simulated with two sets of tool rotational speeds which are 120 RPM and 200 RPM with fully sticking conditions and a constant plunge depth of 12mm.

1. Temperature: The top view of the temperature contours of 120 RPM and 200 RPM dwell cases are shown in figure 4.233. As the plunge/dwell process does not include tool traverse speed, totally symmetrical temperature contours are found in the tool/workpiece contact region. Maximum peak temperatures were found under the tool shoulder, the HAZ size increases with increasing tool rotational speed due to the increase in thermo-mechanical action of the tool. Figure 4.234 shows the temperature contours of the tool and workpiece. Note that the temperature decreases towards the plate bottom. This decrease in temperature coincides with previous work which showed that the maximum temperature is mainly generated from the tool shoulder, whereas, the probe side contribution is less and the probe end contribution in heat generation is almost insignificant [50] [51]. Figure 4.235 shows the temperature distribution around the tool, CFD results are compared with the maximum peak temperatures measured from TC2 and TC5 of samples W1-W7 (see figure 3.11 and table 4.4). TCs reading from samples W1 and W2 show a difference between the CFD model results of approximately 80°C which can be attributed to the difference in plunge depth. The heat convection coefficient value which has been assigned at the plate bottom to compensate the backing plate and the anvil in the CFD analysis can introduce an error. TC readings from samples W3-W7 showed less difference (about 50°C) from the CFD results. The HAZ in Figure 4.235 has been determined between the SZ and a peak temperature of 900°C [179]. The width of HAZ estimated from the CFD model at the top surface for the 120 RPM group is determined equal to 3.5mm whereas for the 200 RPM group the length of HAZ was 4mm as shown in figure 4.235. This finding is in good agreement with IFM measurements for samples W1-W2 which are listed in table 4.6; the slight differences in HAZ width can be attributed to the difference in plunge depth [61].

2. Velocity and Strain Rate at the Tool/Workpiece Contact Region

Figure 4.236 shows the relative velocity distribution in the workpiece which comes from the material affected by the tool rotation. The velocity reaches its maximum value at the tool shoulder periphery and decreases towards the probe end and its value tends to vanish at the probe end. The material velocity in the contact region increases with the increasing tool rotational speed. 0.237 m/s was the maximum value of relative velocity at 120 RPM whereas the relative velocity has increased to 0.396 m/s when the tool rotational speed increased to 200 RPM.

Strain rate has shown similar behaviour to velocity with maximum values of 700 1/s at the tool periphery (figure 4.237). Strain rate contours also tend to be wider when tool rotational speed is increased from 120 RPM to 200 RPM due to the fact that more material has been affected by the tool thermo-mechanical action, this result is in agreement with the findings found in [34] [178]. The strain rate also shows a decrease towards the workpiece bottom and its values tends to vanish at the probe end centre as shown in figure 4.237.

3. Viscosity of the Workpiece at the Tool/Workpiece Contact Region

Viscosity contours for 120 RPM and 200 RPM plunge/dwell times are shown in figure 4.238. The shear layer size increases with the increase in tool rotational speed, due to the fact that more heat will be generated in the material in contact with the FSW tool; this in turn will encourage material layers to rotate with a specific velocity. Viscosity values show a significant decrease under the tool shoulder, the region between shoulder and probe shows the maximum TMAZ size as a result of the thermo-mechanical combination between the shoulder and the probe side. This finding coincides with the IFM measurements from sample W1-W7 as all the macrographs show that the TMAZ at the shoulder-probe is the most affected by the thermo-mechanical action of the tool. The probe end did not show a significant decrease in the value of viscosity that can enable the material in contact to rotate despite the high temperature which reached to 1000°C (figure 4.234). This can be attributed to the low values of strain rate at the probe end as the viscosity is inversely proportional to its value. The experiments using the IFM as shown in figure 4.40 for EH46 W1-W7 coincide with the CFD findings in figure 4.238; all the macrographs have shown that at the probe end the material is only experiencing heating without stirring. The cut-off value of viscosity after which no material flow occurs is equal to 9.6 x 10^6 Pa.s which is in agreement with previous work on steel extrusion [55].

4. Tool Surface Temperature and Shear Stress

Temperature distribution on the tool surface as shown in figure 4.239 for 120 RPM and 200 RPM are symmetrical with maximum temperatures located at the tool shoulder periphery. The temperature decreases towards the probe side and it reaches the minimum value at the probe end. Binder softening is highly expected in the high rotational tool speeds of 200 RPM especially at the tool shoulder periphery which in turn can cause, with the aid of mechanical action, significant tool wear [19][23] [24].

Shear stress on the tool surface as shown in figure 4.240 for 120 RPM and 200 RPM is symmetrical with the maximum shear stress located at the bottom of the probe side. Shear stress increases as rotational speed decrease as a result of the higher viscosity in contact with the FSW tool. The bottom of the probe side of 120 RPM (region-2 bottom assigned by the letter -c- as shown in figure 4.94) has shown the maximum shear stress value and thus tool wear at that location is expected. The microstructure as shown in the SEM image in figure 4.179 -b- of the probe side bottom of the sample welded from EH46 steel (120 RPM W6) is supporting the finding of the CFD regarding the tool wear as a result of increase in shear stress. Shear stress is also high at the tool shoulder periphery of the 120 RPM sample and also probe side bottom of 200 RPM welded samples as shown in figure 4.240.

The high temperature at the tool shoulder of the 200 RPM group and high shear stress at the tool shoulder periphery of 120 RPM sample can significantly cause wear on the tool surface. Experiments including SEM images of EH46 samples W1-W7 are supporting the findings of the CFD model as shown in Figure 4.171 to 4.178 where BN particles are present in the region of shoulder-probe as a result of the combination of binder softening and shear stress increasing at the FSW tool surface.

4.14.5.2 Modelling FSW of Grade EH46 at Steady State Welding Conditions.

The temperature distribution of EH46 steel in two welds which were produced as a case study for low and high traverse tool speeds of 50mm/min (W8) and 100mm/min (W10) with constant tool rotational speed of 150 RPM is shown in figure 4.241. A similar temperature distribution as in the DH36 steady state weld is found in the EH46 steady state CFD results where the maximum temperatures in both W8 and W10 are under the tool shoulder. Sample W10 has shown more asymmetry in temperature distribution as a result of increasing the traverse speed. More material is pushed towards the advancing-trailing side which showed the maximum peak temperature as discussed earlier in the section of temperature distribution of DH36 and also as demonstrated by previous work carried out on simulating the FSW process [61] [147] and [152]. This finding coincides with the experiments of SEM images (the microstructure evolution shown in figure 4.100 to 4.105) where sample W8 shows more asymmetry between AS and RS. Peak temperatures in both welds are nearly equal as the tool rotational speeds in both welds are equal. This suggests that tool rotational speed is the main source of heat generation in FSW whereas; the traverse speed is mainly controlling the cooling rate [56]. The temperature distribution between the leading and trailing sides as shown in figure 4.242 has also shown similar behaviour to DH36 CFD results shown in figure 4.209. The temperature profile contracts at the leading edge and expands at the trailing edge. Figure 4.243 shows the cooling rate of EH46 samples W8 and W10. There is a faster cooling rate in W10 due to higher tool traverse speed. The microstructural evolution of W8 and W10 in the SZ (figure 4.100 to figure 4.105) as discussed previously coincides with the CFD results where the W8 microstructure shows allotriomorphic ferrite (α_{all}) at the prior austenite grains with less bainite (B) present.

Figure 4.244 shows the temperature contours of transverse cross sections of the workpiece and the tool for samples W8 and W10. Both welds show asymmetry between the AS and RS. The HAZ in W10 is smaller than in W8 due to the higher tool traverse speed [56] [61]. Figure 4.245 shows the temperature distribution between the AS and RS of W8 and W10. TCs average reading on the AD at the steady state period have shown good agreement with only a slight difference in peak temperature from the CFD results.

The strain rate distribution showed a slight difference between samples W8 and W10 due to the same value of tool rotational speed being used. However greater asymmetry was found in sample W10 as a result of the increase in tool traverse speed. Viscosity contours as shown in

figure 4.247 shows a slight difference between W8 and W10, and a wider SZ in W8 than W10 as a result of a slower tool traverse speed. This was also shown in the IFM macrograph measurements (table 4.8) where the total SZ for W8 was bigger by 18mm^2 than W10. This was the result of more material stirring by the tool rotational speed at lower tool traverse speed.

Figure 4.248 shows the shear stress (Pa) distribution on the FSW tool surface for samples W8 and W10. The shear stress is high at the probe side and probe end for both welds. The SEM-EDS images taken from the probe end of W8 and W10 shown in figure 4.183 and figure 4.185 respectively show the existence of BN particles inside the microstructure of the stirred material. An increase in the surface shear stress was found on the retreating-leading side of W10 as a result of higher traverse speed. This finding is in agreement with the SEM images of the top surface of the SZ of W10 shown in figure 4.188 where many BN particles are present inside the microstructure as a result of the higher thermo-mechanical effect between the tool and the workpiece.

A. CFD model results for EH46 steel during the dwell stage.
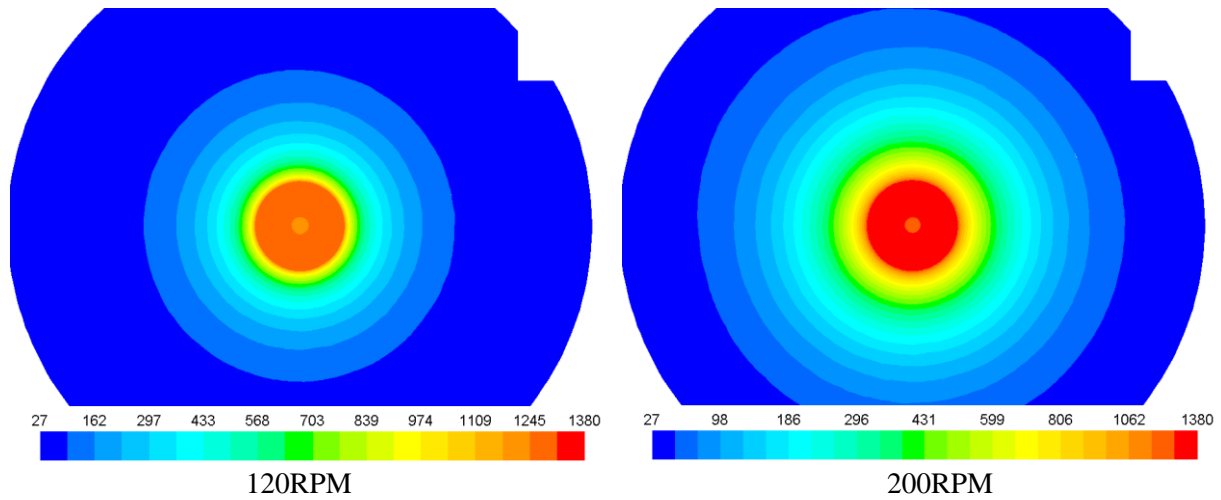
Figure 4.233: Temperature (^{o}C) contours at the top surface of EH46 plates during the dwell stage 120RPM and 200RPM.
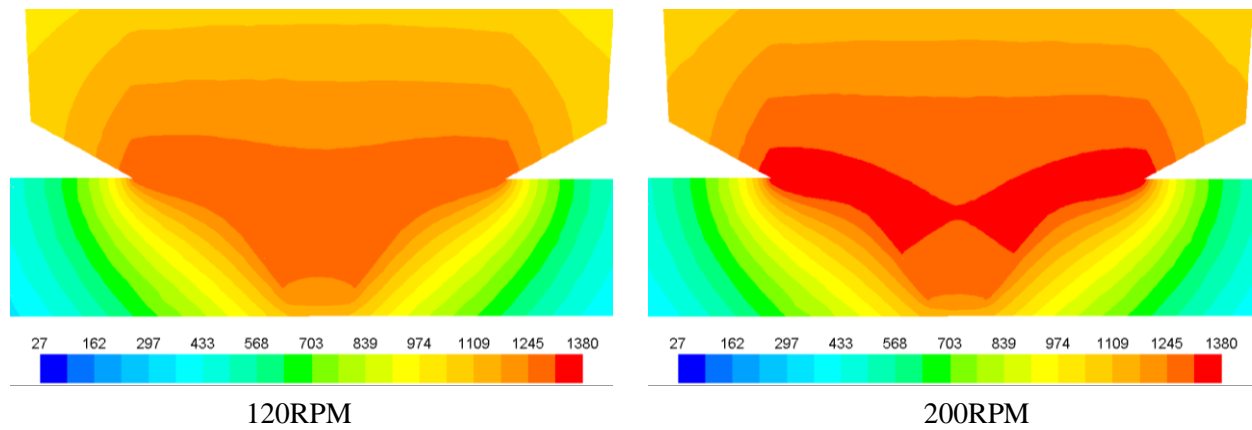
Figure 4.234: Transverse section shows the temperature (^{o}C) contour of the PCBN tool and the plate during the dwell stage for two tool rotational speeds, 120RPM and 200RPM.
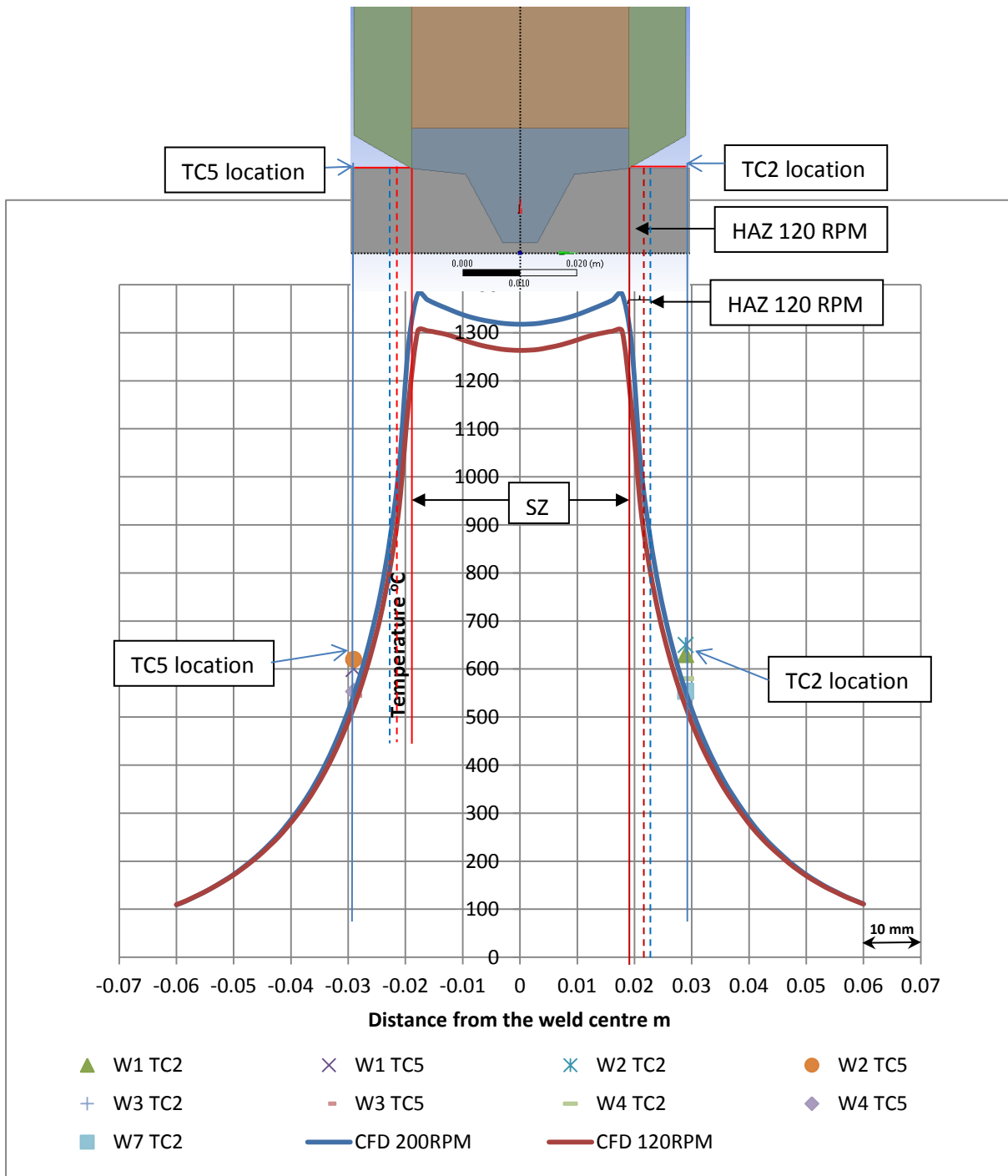
Figure 4.235: CFD results show the temperature distribution along the top centre of the FSW for grade EH46 steel during the dwell stage, 120RPM and 200RPM.
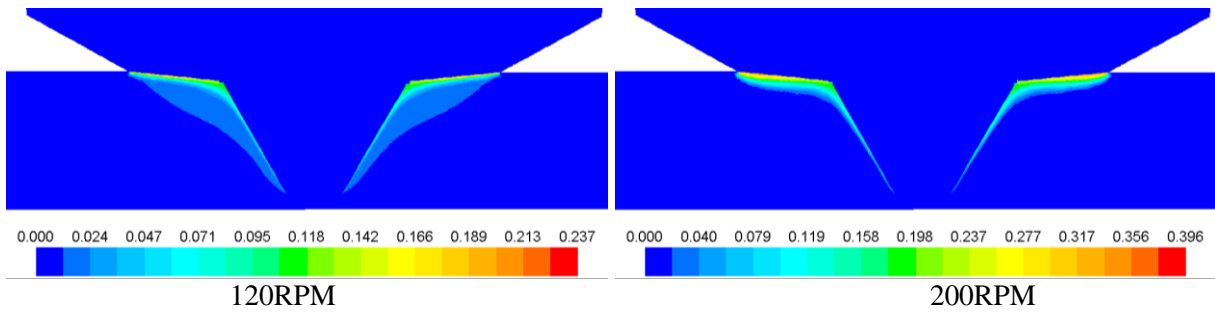
Figure 4.236: Transverse section shows the velocity contours (m/s) in the tool/workpiece contact region at the dwell stage for a tool rotational speed of 120 RPM and 200 RPM.
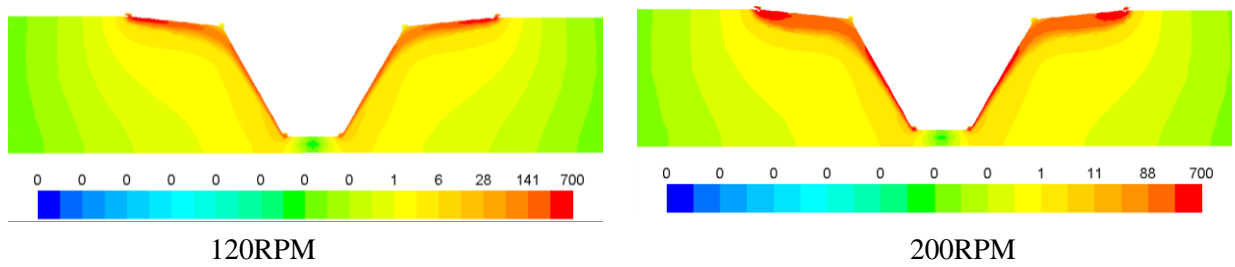
Figure 4.237: Transverse section shows the strain rate contours (1/s) in the tool/workpiece contact region at the dwell stage for a tool rotational speed of 120RPM and 200RPM.
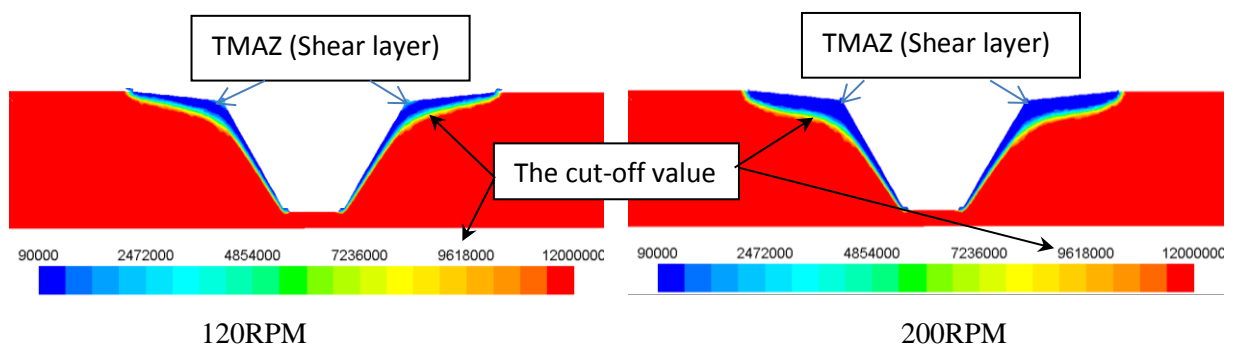
Figure 4.238: Transverse section shows the viscosity contours (Pa.s) in the tool/workpiece contact region at the dwell stage for a tool rotational speed of 120RPM and 200RPM.
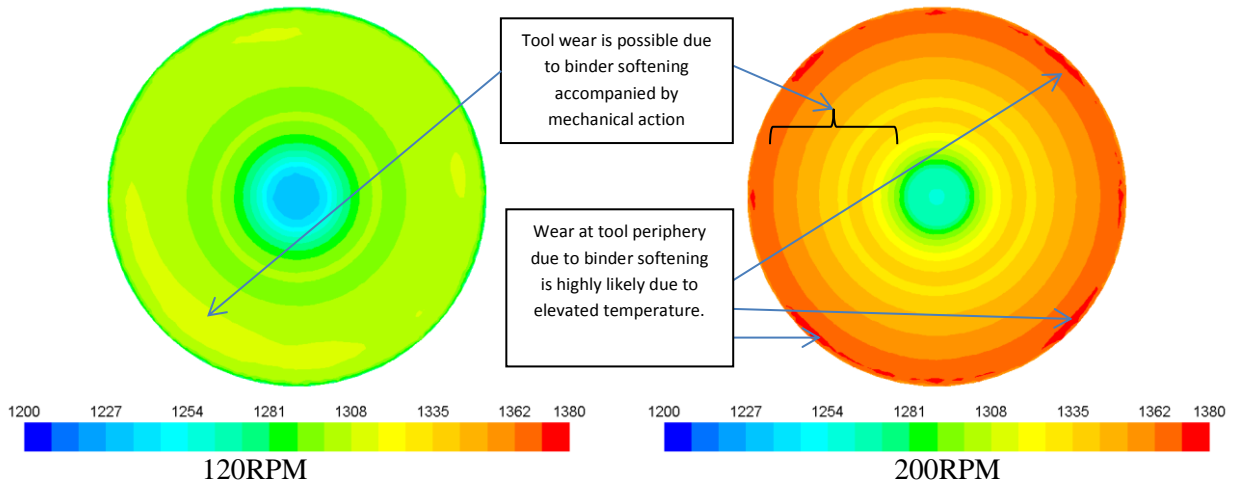
Figure 4.239: FSW tool surface temperature at 120 RPM and 200 RPM (dwell stage).
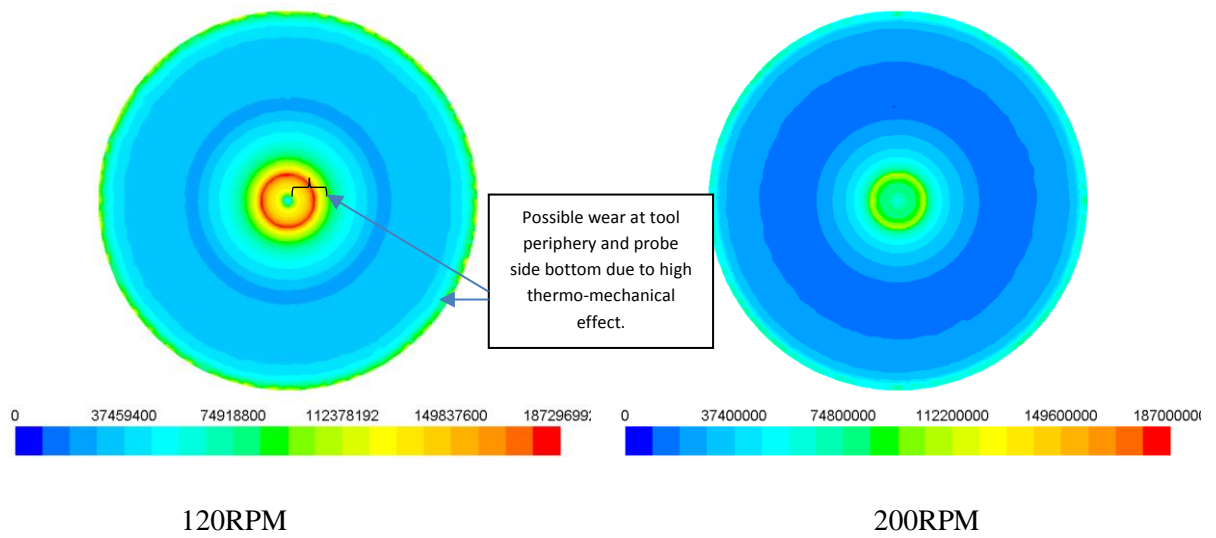
Figure 4.240: Tool surface shear stress (Pa) for tool rotational speeds of 120 RPM and 200 RPM (during dwell stage)

B. CFD Model Results for EH46 steel (steady state) samples W8 and W10.
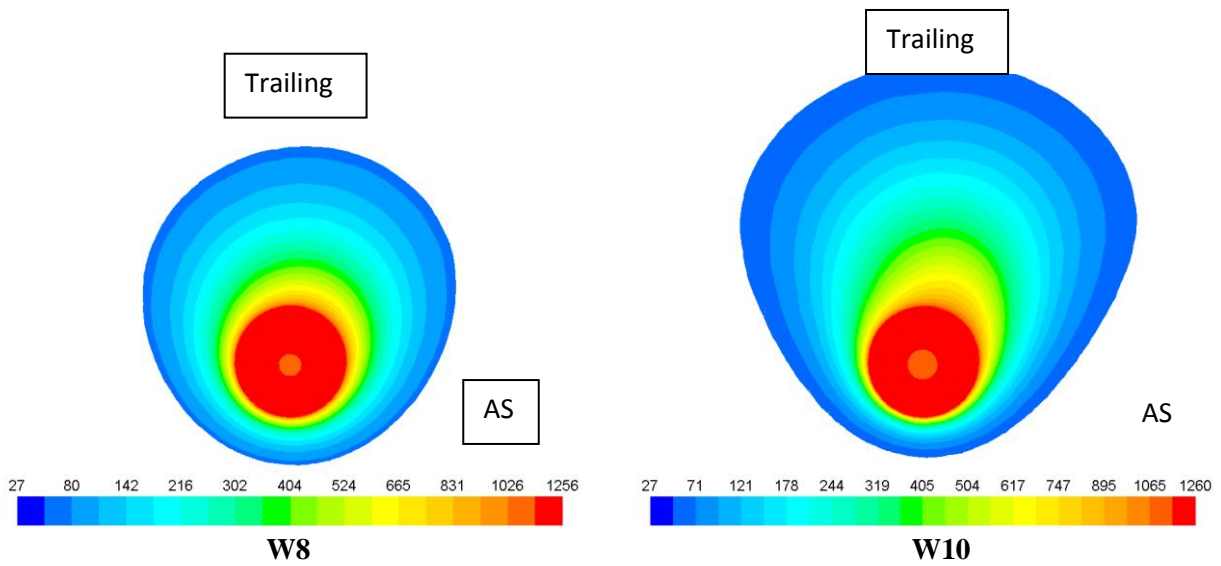
Figure 4.241: CFD modelled temperature (^{o}C) contours at the top surface of EH46 plates for samples W8 and W10 under steady state welding conditions.
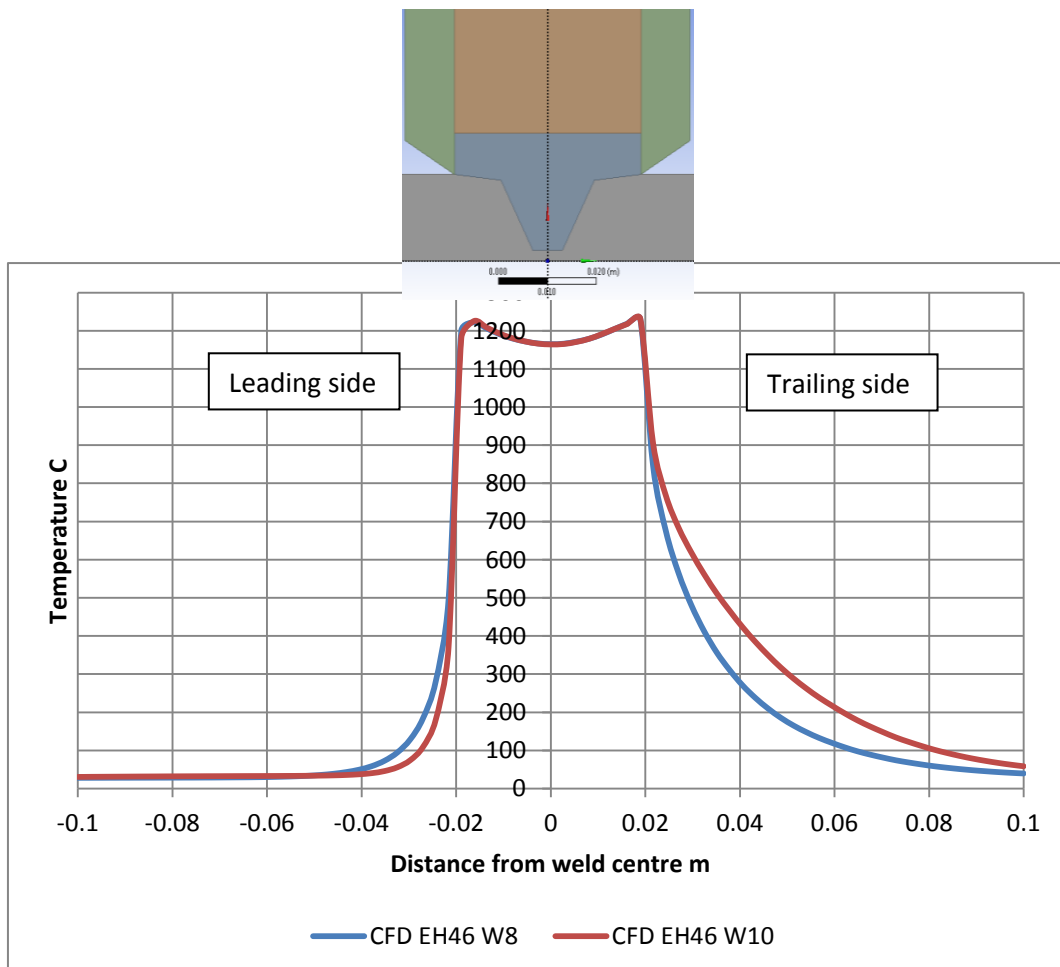
Figure 4.242: The CFD modelled temperature distribution between the leading and trailing sides for samples W8 and W10 FSW of 14.8mm EH46 steel.
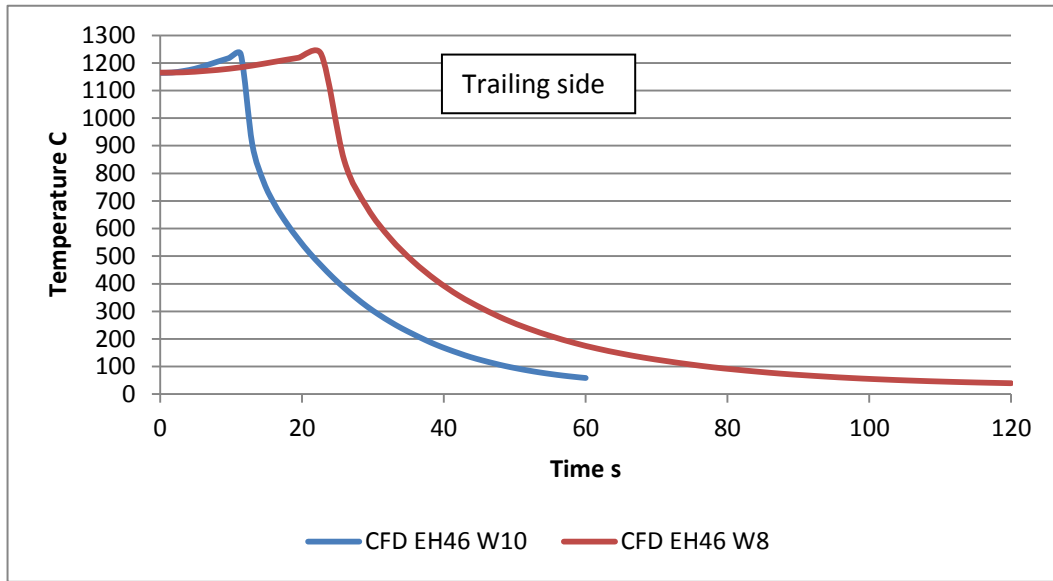
Figure 4.243: The CFD modelled cooling rate for samples W8 and W10 FSW of 14.8mm EH46 steel at the weld centre.
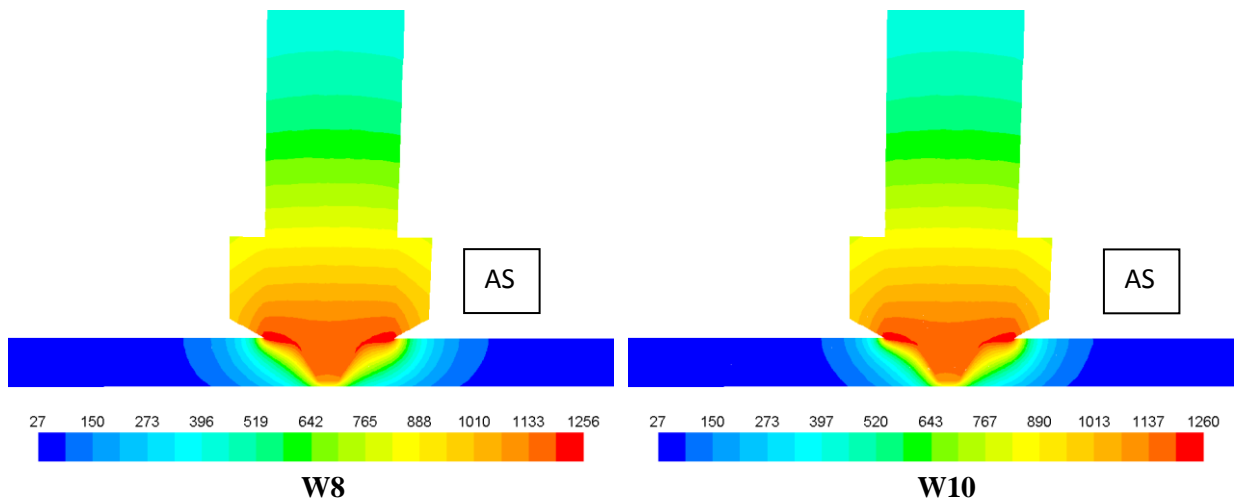
Figure 4.244: Transverse view shows the CFD modelled temperature (^{o}C) contour of the PCBN tool and the EH46 steel plate for samples W8 and W10.

317
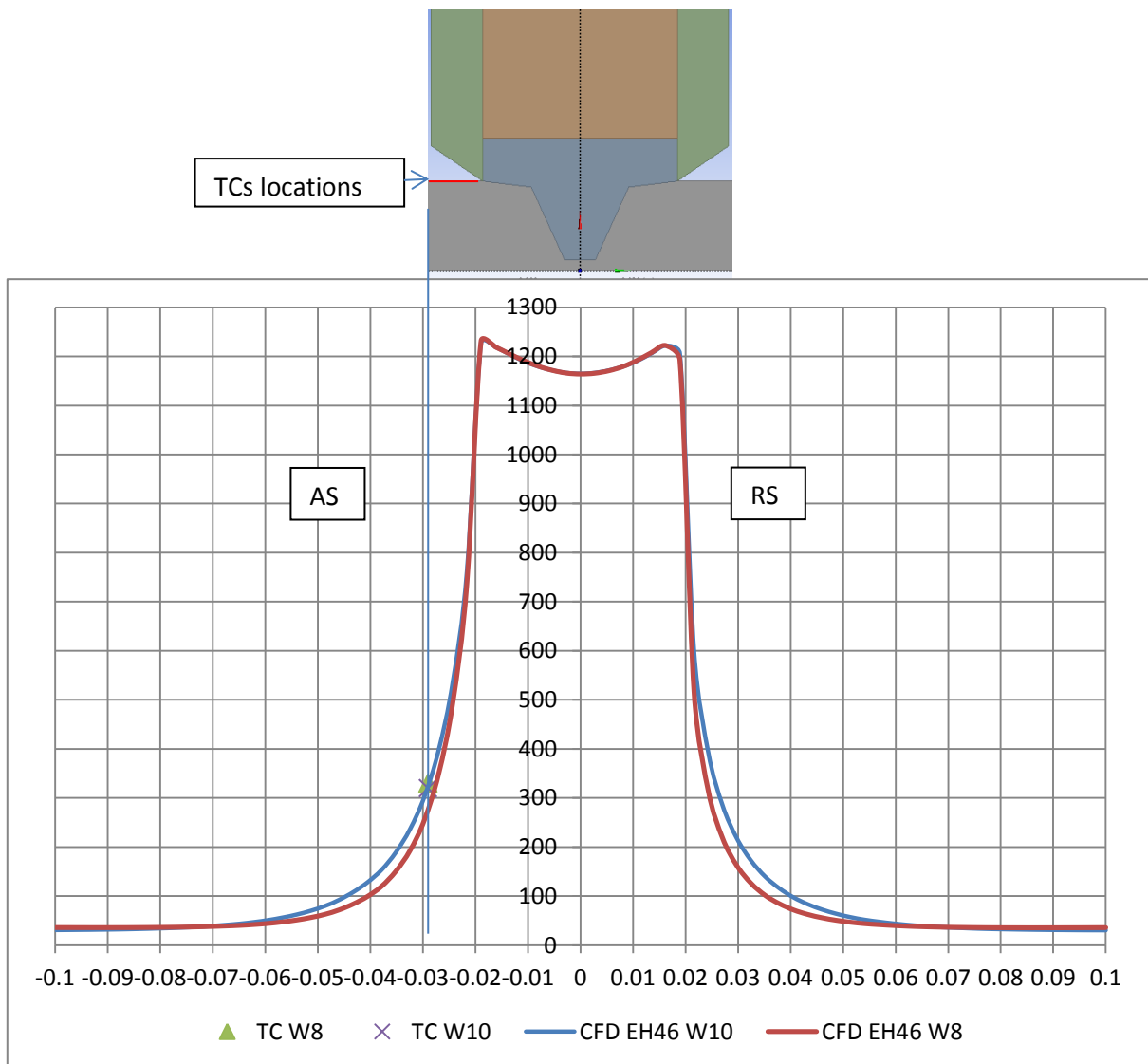
Figure 4.245: The thermo-coupled measured temperature distribution between AS and RS of samples W8 and W10 FSW of 14.8mm EH46 steel.
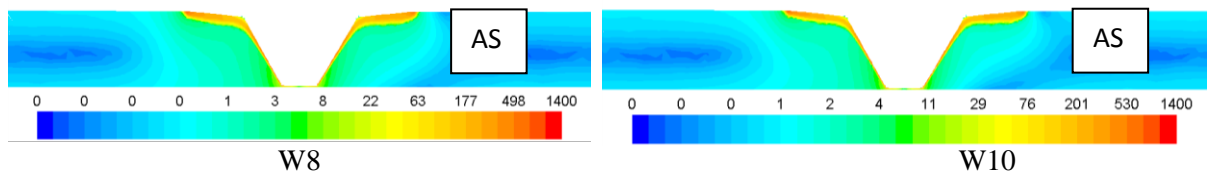
Figure 4.246: CFD modelled transverse views show the strain rate contour (1/s) of the plate for EH46 samples W8 and W10 at the contact region with the tool.
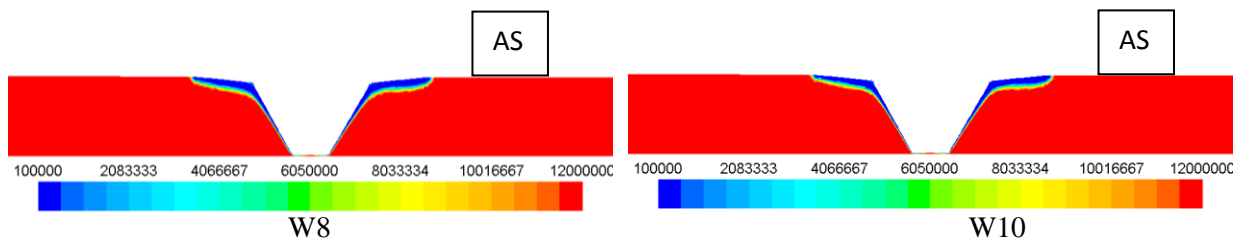
Figure 4.247: Transverse view shows the CFD modelled viscosity contour (Pa.s) of the plate for EH46 samples W8 and W10 at the contact region with the tool.
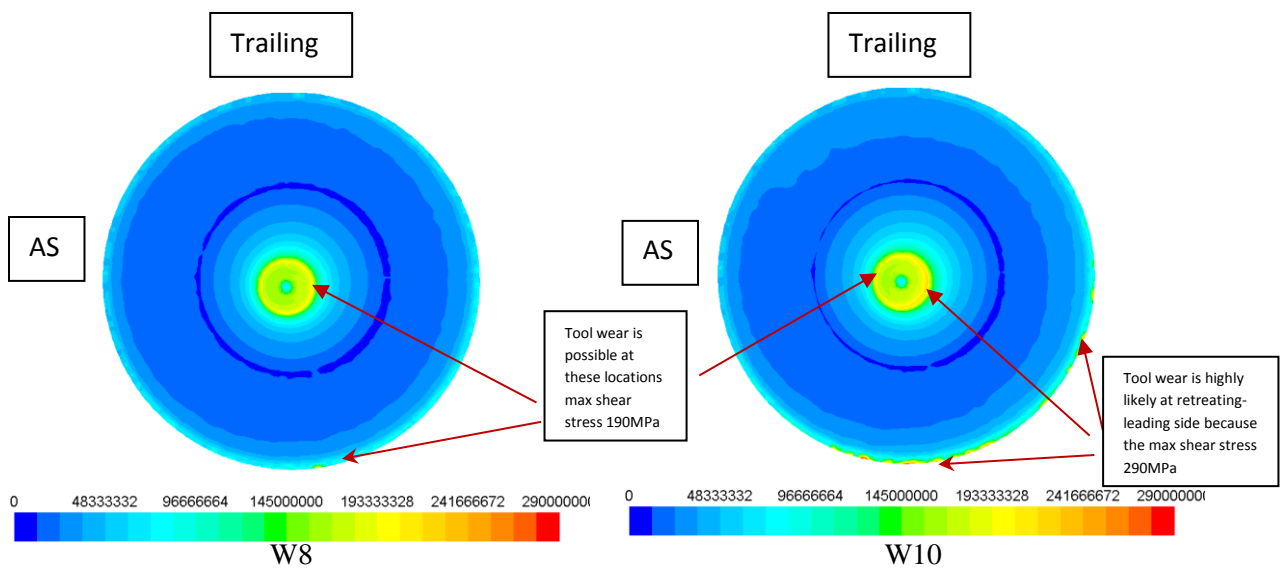
Figure 4.248: CFD modelled predicted shear stress (Pa) contours on the tool surface (EH46 samples W8 and W10)

5. Summary of Discussion

The following section summarises the discussion based on the results of this research which can be used to assess whether the objective at the beginning of the research were met.

➢ The tensile mechanical properties of the FSW joints when compared to the parent material have been improved. Sample W6 and W9 DH36 have recorded an increase in tensile strength from 570MPa to 590 MPa. All samples have failed outside the SZ under tensile testing.

➢ The microstructure in all welded samples for the two steel grades (DH36 and EH46) showed a phase transformation from ferrite and bands of pearlite to different phases including a mix of bainite+α_a in the top and middle of SZ to fine grains of ferrite and plates of cementite at the weld root.

➢ Alloying elements found in the parent metal such as Ti, Nb, Si and compounds such as MnS and alumina have undergone segregation /precipitation/ during the FSW process. As temperatures exceed 1250°C, TiN cubic precipitates were found, whereas, at temperatures equal or exceeding 1450°C a Mn, Si, Al and O spinel was observed. The evidence of precipitation of TiN and the segregation of a spinel of Mn, Si, Al and O has been employed for the first time to seek to identify the peak temperatures occurring during the FSW process.

➢ PCBN tool wear has been found to increase as tool rotational speed increases which generates greater heat and leads to W-Re binder softening. Tool wear was found to be very high at the tool shoulder periphery and at the probe end as a result of higher shear stress than in the rest of the FSW PCBN tool. Welding with medium tool rotational speeds at which the temperature does not exceed 1250°C is recommended.

➢ Defects in FSW were found to be associated with unsuitable welding parameters. Sudden increase in tool traverse speed from plunge to steady state welding has resulted in micro-crack initiation in DH36 sample W9. High tool traverse speed was also found to create a void at the AS of the weld joint as a result of poor material flow.

➢ The most appropriate surface contact assumption to model the FSW process was found to be the "fully sticking" contact conditions.

➢ The temperature at the advancing-trailing side of the weld was found to approach the melting point when using high tool rotational speeds which exceed 500 RPM. The assumption of a fully sticking surface condition predicted the temperatures which coincided with the formation of Mn, Si, Al and O spinel which only occurred when the peak temperatures exceeded 1400 ^{o}C. The CFD model result was also in agreement with the experimental tool wear findings. The PCBN tool wear was high when welding the steel grade DH36 samples (W6 and W8) a result of high thermo-mechanical action of the tool on the workpiece. The suggestion of tool optimisation by using a stationary shoulder and a larger diameter probe can address the issues of local melting of low thermal conductivity alloys (such as steel) especially when the tool speeds increase.

6. Conclusion

The research detailed in this thesis has investigated the friction stir welding process for two grades of steel, DH36 and EH46. The research has included assessment of the FSW joints microstructure and mechanical properties, precipitation/segregation of alloying elements, PCBN tool wear and welding defects. CFD modelling of the process in terms of peak temperature, torque, strain rate, viscosity and tool shear stress has been investigated extensively. The following conclusions have been drawn after assessment of the literature, completion of CFD based numerical analysis and laboratory based experimental work. The conclusions include as-welded mechanical properties, elemental precipitation/segregation, effects of welding parameters such as tool rotational/traverse speeds and plunge depth on weld joint quality, peak temperature, tool wear and welding defects. The result from laboratory based experimental work is compared with the predictions created from the results of CFD mathematical modelling.

Mechanical Properties.

1. There has been an improvement in the tensile strength of as-welded FSW joints when compared to the un-welded parent material. Tensile strength of FSW DH36 has increased to 580MPa compared to 560MPa of the PM. The hardness in the stir zone of the as-welded joint has also increased compared with the parent material as a result of microstructural refinement.

2. The tensile strength and fatigue resistance of as-welded FSW joints were consistently higher in the joints made at low tool speeds (200RPM, 100mm/min) compared to joints made at high tool speeds (550RPM, 400mm/min). This is because joints made at low tool speeds produced defect free joints.

Microstructural Analysis

3. Microstructural examination of the welded joints following FSW revealed that the ferrite and bands of pearlite in the parent material of DH36 and EH46 steel grades had undergone phase transformation which resulted in a microstructure consisting of a mix of bainite and acicular ferrite in the top and middle of SZ as a result of the high temperatures experienced which exceed the A_3 temperature on the Fe-C equilibrium phase diagram.

4. For both DH36 and EH46 FSW fine grains of ferrite and plates of cementite were found at the weld root as a result of dynamic recrystallization.

5. The microstructural elemental segregation in the 6mm thick DH36 samples W6 and W8 was found to have a detrimental impact on the mechanical properties (especially the fatigue resistance) of the welded joints. The average cycles to failure of welded joints produced at low tool speeds (200RPM, 100mm/min) were 642,935.5 whereas for the high tool speeds samples it was 115.078.

6. It has been shown that the peak temperature experienced by the parent material during the FSW process can be estimated by microstructural examination of TiN precipitation. Estimation of the peak temperature experienced by the parent material during the FSW process from microstructural examination of TiN precipitates represents an alternative to using TC's or thermal imaging camera techniques which may give errors during recording temperatures.

7. The heat treatment trials have shown that at temperatures exceeding $1450^{o}C$, elemental segregation of Mn, Si, Al and O spinel occurs.

Effects of Changes of FSW Process Parameters.

8. FSW was found to be very sensitive to plunge depth variations; small changes, parts of a millimetre, of plunge depth has a significant impact on the heat generation during the FSW process and thus can have an effect on the weld quality.

9. It was found that increasing the FSW tool plunge depth has a positive impact on the weld joints quality including fewer defects such as voids.

10. High tool rotational speed (exceeding 500 RPM) during the FSW process of 6mm DH36 grade can result in local melting on the advancing-trailing side. The existence of Mn, Al, Si and O elemental segregation which also include Zn in the microstructure of DH36 samples W6 and W8 gives an indication that the material in the tool/workpiece interface has experienced the solidus temperature.

11. PCBN FSW tool wear has been found to increase with increasing tool rotational speed as a result of W-Re binder softening due to the generation of excessive heat. The SZ top and weld root of the FSW joints are the regions which have the

highest volume fraction of BN particles when examined microstructurally. This indicates that the shoulder periphery and probe end of the tool are the regions that are most prone to wear.

12. Increasing the plunge depth increases tool wear as a result of increasing the surface contact area and thus the temperature in the tool/workpiece contact region.

13. Increasing tool traverse speed increases tool wear especially at the tool periphery due to the increase in the value of shear stress on the tool surface.

14. High tool traverse speeds as in DH36 samples W6 and W8 and in EH46 sample W10 were found to result in weld defects such as voids, weld root defect and kissing bonds. The lack in material flow during the FSW process was the main cause of these defects.

15. The micro-crack defect in the plunge-steady state region was found to initiate as a result of the lack of material flow when using unsuitably rapid tool traverse speeds.

16. Defects caused by TiN elemental precipitation have also been found in the FSW joints microstructure. These types of defects were the result of high welding temperature caused by the use of excessively high tool rotational speed. The resulting high temperature has caused in the precipitation of TiN cuboid particles which in turn can lead to stress concentrations and the subsequent initiation of microcracks.

Conclusion from CFD Modelling.

17. The CFD mathematical model has revealed a stagnant zone formed at high tool traverse speeds. It is concluded that the lack of material flow as a result of the stagnant zone formation is the main reason for voids, weld root defect and kissing bonds defects. The CFD results agree with the experimental work results in terms of weld defect formation.

18. The Fully sticking model was found to be more suitable for modelling the FSW process of steel than the sticking/slipping and/or torque models as it gives acceptable results for the calculation of the peak temperature, the SZ size, the HAZ size, the tool torque and the material flow characteristics.

19. The calculated temperature on the advancing-trailing side using the fully sticking assumption was found to approach the melting point of the parent material when

using high tool rotational speeds exceeding 500 RPM which showed good agreement with experimental work in terms of elemental precipitation/segregation.

20. CFD Model result were also in agreement with the tool wear findings where DH36 samples W6 and W8 showed significant wear as a result of the high thermo-mechanical action (high values of shear stress) of the tool surface on the workpiece.

21. The suggestion of tool optimisation by using a welding tool stationary shoulder and a bigger size probe end (as carried out in the CFD model) can solve the issues of local melting of low thermal conductivity alloys especially when the speed of the tool increases.

22. The current project findings may bring the commercialisation of FSW of steel a step closer because they introduced new techniques for measuring the peak temperature and estimating the maximum tool rotational speed that does not cause the segregation of a Mn, Si, Al and O spinel. The debate which can be found in previous work about the assumption of heat generation during FSW process including sticking/slipping has been discussed extensively in this project and the fully sticking assumption has been found to be more suitable in modelling the FSW process of steel.

7. Further Work

After assessment of the results of the work carried out during this research project, the following suggestions for further work can be made:

- Heat treatments in this work have been carried out without including the effect of strain rate on the time of phase transformation and elemental precipitation/segregation. On the Gleeble simulator the maximum peak temperatures that can be achieved are below 1100°C and the current heat treatments were in a temperature range that can reach to $1500\,^{\circ}\text{C}$. A suggested technique, in appendix B, has been proposed on how to simulate the FSW process which includes high peak temperatures and high strain rates.

- Modelling the FSW was based on a Eulerian steady state simulation which cannot be used to simulate the residual stresses that can be found in the weld joint as a result of local heating and cooling associated with the FSW process. A future project would ebe to develop the model to include the transient temperatures as a function of time and location in order to calculate the resulting residual stresses.

- To carry out FSW using an optimised tool which includes a stationary shoulder. The provided samples have been welded by using a PCBN tool as described in this project. It has been reported to TWI Company about the issues of elemental segregation which may happen when tool rotational speed increases to a specific limit. Carrying out welding with an optimised FSW tool including a stationary shoulder and bigger probe is advisable. It is anticipated that this can produce sound welds at higher tool rotational/traverse speed using a cheaper PCBN FSW tool.

8 References

_____

1. WeldGuru.com, 2016, USA, accessed June 2017, <http://weldguru.com/welding-history/>.

2. Cater S., 2013, Forge welding turns full circle: friction stir welding of steel, Ironmaking & Steelmaking, 40:7, 490-495, DOI: 10.1179/0301923313Z.000000000224.

3. Besharati-Givi M. K., Asadi P., 2014, Advances in Friction-Stir Welding and Processing, Woodhead Publishing.

4. Mishra RS, Ma ZY., 2005, Friction stir welding and processing. Mater Sci Eng R; Vol. 50 (1–2), pp.1–78.

5. Toumpis A. Gallawi A., Cater S., Molter L., 2014, A techno-economic evolution of friction stir welding of DH36 steel, 10th Friction Stir Welding Symposium ,10th FSWS, 20-22/05/2014, Beijing pp.1-11.

6. Sorensen C. D. and Nelson T. W., 2007, Friction Stir Welding of Ferrous and Nickel Alloys, ASM International, p113.

7. Packer S.M., Nelson T.W., Sorensen C.D., Steel R., and Matsunaga M., 2003, Tool and Equipment Requirements for Friction Stir Welding of Ferrous and Other High Melting Temperature Alloys, Proceedings of the Fourth International Symposium on Friction Stir Welding, May 14–16, 2003 (Park City, UT), TWI, paper on CD.

8. Cater S., Martin J., Galloway A., McPherson, 2013, Comparison between friction stir and submerged arc welding applied to joining DH36 and E36 shipbuilding steel, Friction stir welding proceeding VII, pp.49-58.

9. Toumpis A., Gallawi A., Polezhayeva H., Molter L., 2015, Fatigue assessment of friction stir welded DH36 steel, Friction Stir Welding & processing VIII, pp 11-19.

10. Kasai H., Morisada Y., Fujii H., 2015, Dissimilar FSW of immiscible materials: Steel/magnesium, Material Science and Engineering A, Vol. 624, pp. 250–25

11. Nilesh K., Rajiv S. M. and John A. B., 2013, Residual Stresses in Friction Stir Welding, ScienceDirect.

12. Boldsaikhan E., Corwin E., and Arbegast W., 2009, Detecting Wormholes in Friction Stir Welds from Welding Feedback Data, Midwest instruction and computing symposium, South Dakota, USA.

13. Roman R., and Martin K., 2014, Friction stir welded structures: Kissing bond defects, International Journal of Terra-space Science and Engineering, Vol. 6 (2), pp. 77-83.

14. Stevenson R., Toumpis A. , and Alexander G., 2015, Defect tolerance of friction stir welds in DH36 steel, Materials & Design, Vol. 87, pp.701–711.

15. TWI company, UK, 2016, accessed June 2017, International Symposium on Friction Stir Welding 17-19 May 2016 <http://www.twi-global.com/news-events/news/2016-04-fsw-symposium-programme/>.

16. Toumpis A. I., Gallawi A., Arbaoui L., Poletz N., 2014 , Thermo-mechanical deformation behaviour of DH36 steel during friction stir welding by experimental validation and modelling, Science and Technology of Welding and Joining, Vol 19, 8, pp. 653-663.

17. Pradeep A., 2012, A Review on Friction Stir Welding of Steel, International Journal of Engineering Research and Development e-ISSN: 2278-067X, p-ISSN: 2278-800X, www.ijerd.com Vol. 3, Issue 11, pp. 75-91.

18. Thomas W. M., Nicholas E D and Smith S D, 2001, Friction stir welding - tool developments TWI Ltd, Paper presented at the Aluminum Joining Symposium during the TMS Annual Meeting, New Orleans, Louisiana, USA.

19. Rai R., De A., Bhadeshia H K & DebRoy T., 2011, Review: friction stir welding tools, Science and Technology of Welding and Joining, Vol. 16 (4), pp. 325-342.

20. Perrett M. J., Peterson J., Steel R. and Packer S., 2011, Friction stir welding of industrial steels, Paper presented at TMS Annual Meeting. San Diego, CA., USA.

21. Megastir, 2013, Friction Stir Welding of high melting temperature materials, http://megastir.com/products/tools/fsw_tool.aspxpdf.

22. Seaman J. M., Thompson B., 2011, Challenges of Friction Stir Welding of Thick-Section Steel, Proceedings of the Twenty-first International Offshore and Polar Engineering Conference, Maui, Hawaii, USA, June 19-24.

23. Konkol P. J., and Mruczek M. F., 2007, Comparison of Friction Stir Weldments and Submerged Arc Weldments in HSLA-65 Steel Supplement to the Welding Journal, Vol 86, pp 187-195.

24. Ramalingam M. L. and Jacobson D. L., 1986, Elwvated Temperature Softening of Progressively Annealed and Sintered W-Re Alloys, Journal of Less Common Metals, 123, pp. 153-167.

25. R. M. Hooper, J. I. Shakib and C. A. Brookes: 'Microstructure and wear of TiC cubic BN tools', Mater. Sci. Eng. A, 1988, A106, 429–433.

26. Jasthi B. K., Arbegast W. J. and. Howard S. M, 2009, Thermal expansion coefficient and mechanical properties of friction stir welded invar (Fe–36%Ni)', J. Mater. Eng. Perform., Vol. 18, (7), pp. 925–934.

27. Zhang Y., Sato Y. S., Kokawa H., Park S. H. and Hirano S., 2008, Stir zone microstructure of commercial purity titanium friction stir welded using pcBN tool, Mater. Sci. Eng. A, Vol. 488, (1–2), pp. 25–30.

28. Schmidt H., & Hattel J., 2005. A local model for the thermomechanical conditions in friction stir welding. Modelling and Simulation in Materials Science and Engineering, Vol. 13(1), pp.77–93.

29. Kumar R., Singh K., Pandey S., 2012, Process forces and heat input as function of process parameters in AA5083 friction stir welds, Trans. Nonferrous Met. Soc., Vol. 22, pp. 288−298.

30. Longhurst W. R., Alvin M. S., George E. C. & Paul A. F., 2010, Torque control of friction stir welding for manufacturing and automation, Int J Adv Manuf Technol , Vol. 51, 9, pp 905–913.

31. Mehta M., Chatterjee K. & De A., 2013, Monitoring torque and traverse force in friction stir welding. from input electrical signatures of driving motors, Science and Technology of Welding and Joining Vol. 18, 3, pp. 191-197.

32. Pew J. W., Nelson T. W. and Sorensen C. D., 2007, Torque based weld power model for friction stir welding, Science and Technology of Welding and Joining Vol. 12, 4, pp 341-347.

33. Morisada Y., Imaizumi T. and Fujii H., 2015, Clarification of material flow and defect formation during friction stir welding, Science and Technology of Welding and Joining, Vol. 20, 2, pp. 130-137.

34. Morisada Y., 2014, "Three-Dimensional Visualization of Material Flow During Friction Stir Welding of Steel and Aluminium, Journal of Materials Engineering and Performance, Vol. 23, (11), pp.4143-4147.

35. Morisada Y., Fujii H., Kawahito Y., Nakata K. and Tanaka M., 2011, Three-dimensional visualization of material flow during friction stir welding by two pairs of X-ray transmission systems, Scripta Materialia, Vol. 65, pp. 1085–1088.

36. Sarker R., Pal T. K. and Shome M, 2014, Microstructure and properties of friction stir spot welding DP590 dual phase steel sheets, Science and Technology of Welding and Joining, V. 19, pp. 436-442.

37. Schmidt H.N., Dickerson T.L., Hattel J.H., 2006, Material flow in butt friction stir welds in AA2024-T3. Acta Mater. Vol. 54, pp. 1199–1209.

38. Guerra M., McClure J.C., Murr L.E., Nunes A.C., Jata K.V., Mahoney M.W., Mishra R.S., Semiatin S.L. and Filed D.P., 2001, Friction Stir Welding and Processing, TMS, Warrendale, PA, USA, pp. 25-31.

39. Colligan K., 1999, Material Flow Behaviour during Friction Stir Welding of Aluminium, Weld. J. Suppl., Vol. 78, 7, pp. 229s–237s.

40. Reynolds A.P., 2000, Visualization of Material Flow in Autogenous Friction Stir Welds Sci. Technol. Weld. Joining, Vol. 5 , pp. 120-124.

41. Reynolds A.P., Seidel T.U., Simonsen M., 1999, Proceedings of the First International Symposium on Friction Stir Welding, Thousand Oaks, CA, USA.

42. London B., Mahoney M., Bingel W., Calabrese M., Bossi R.H., Waldron D., Jata K.V., Mahoney M.W., Mishra R.S., Semiatin S.L., Lienert T. , 2003, Friction Stir Welding and Processing II, TMS, p. 3.

43. Smith C.B., Bendzsak G.B., North T.H., Hinrichs J.F., Noruk J.S., Heideman R.J., 1999, Ninth International Conference on Computer Technology in Welding, Detroit, Michigan, USA, p. 475.

44. Stewart M.B., Adamas G.P., Nunes A.C., Romine P., 1998, Developments in Theoretical and Applied Mechanics, Florida Atlantic University, USA, pp. 472–484.

45. Arbegast W.J., Jin Z., Beaudoin A., Bieler T.A., Radhakrishnan B., 2003, Hot Deformation of Aluminum Alloys III, TMS, Warrendale, PA, USA, p. 313.

46 Goetz R.L., Jata K.V., Jata K.V., Mahoney M.W., Mishra R.S., Semiatin S.L., Filed D.P. 2001, Friction Stir Welding and Processing, TMS, Warrendale, PA, USA, p. 35.

47. Nandan R., Lienert ,T. J, Debroy T., 2008, Toward reliable calculations of heat and plastic flow during friction stir welding of Ti-6Al-4V alloy, Int. J. Mat. Res., Vol. 99 (4), pp.434-444.

48. Jefferson P. W., 2006, A Torque-based weld power model for friction stir welding, PhD theses, Brigham Young University.

49. He X., Fengshou G., Andrew B., 2014, A review of numerical analysis of friction stir welding, Progress in Materials Science, Vol. 65, pp. 1–66.

50. Schmidt H. B., Hattel .J, 2004, Heat Source Models in Simulation of Heat Flow in Friction Stir Welding, International J of Offshore and Polar Engineering, Vol. 14,No.4, pp 41-48.

51. Schmidt H. B. & Hattel J.H., 2005. Modelling heat flow around tool probe in friction stir welding. Science and Technology of Welding and Joining, 10(2), pp.176–186.

52. Schmidt H.B. & Hattel J.H., 2008. Thermal modelling of friction stir welding. Scripta Materialia, Vol. 58(5), pp.332–337.

53. Hattel J., Sonne M. R , Tutum C., 2015, Modelling residual stresses in friction stir welding of Al alloys—a review of possibilities and future trends, Int J Adv Manuf Technol , Vol. 76, pp.1793–1805.

54. Nandan R., Roy G.G. , Debroy T., 2006, Numerical Simulation of Three-Dimensional Heat Transfer and Plastic Flow During Friction Stir Welding. Metallurgical and materials transaction A, Vol. 37A, pp1247-1259.

55. Nandan R. , Roy G.G., Lienert T.J., Debroy T., 2007, Three-dimensional heat and material flow during friction stir welding of mild steel. Acta Materialia, Vol. 55 (3), pp.883–895.

56. Colegrove P. A., Shercliff H. R., 2005, 3-Dimensional CFD modelling of flow round a threaded friction stir welding tool profile, Journal of Materials Processing Technology, Vol. 169, pp. 320–327.

57. Colegrove P. A., Shercliff H. R., Zettler R., 2007, A model for predicting the heat generation and temperature in friction stir welding from the material properties, Science and Technology of Welding and Joining, Vol. 12(4), pp.284-297.

58. Hasan A. F., Bennett C. J., & Shipway P. H., 2015, A numerical comparison of the flow behaviour in Friction Stir Welding (FSW) using unworn and worn tool geometries. Materials & Design, Vol. 87, pp. 1037–1046.

59. Cox C., Lammlein D., Strauss A. and Cook G, 2010, Modelling the Control of an Elevated Tool Temperature and the Effects on Axial Force During Friction Stir Welding, Materials and Manufacturing Processes, Vol. 25, 1278–1282.

60. Fairchild D., Kumar A., Ford S., Nissley N., 2009, Research concerning the friction stir welding of line-pipe steels, Trends in welding research, Proceedings of the 8th International Conference, pp 371-380.

61. Micallef, D., Camilleri, D., Toumpis, A., Galloway, A., & Arbaoui, L., 2016, Local heat generation and material flow in friction stir welding of mild steel assemblies. J Materials Design and Applications, Vol. 230 (2), pp. 586-602.

62. Cho H. H. , Sung-Tae H. , Jae-Hun R. , Hyun-Sik C. , Suk H. K., Russell J. S., Heung N. H., 2013, Three-dimensional numerical and experimental investigation on friction stir welding processes of ferritic stainless steel, Acta Materialia, Vol. 61, pp. 2649–2661.

63. Khandkar, M.Z.; Khan, J.A.; Reynolds, A.P., 2003, Prediction of temperature distribution and thermal history during friction stir welding: input torque based model Science and Technology of Welding and Joining, Vol. 8 (3), pp. 165-174.

64. Cui, S.; Chen, Z.W.; Robson, J.D., 2010, A model relating tool torque and its associated power and specific energy to rotation and forward speeds during friction stir welding/processing) International Journal of Machine Tools and Manufacture, Vol. 50, pp. 1023-1030.

65. Pew J.W.; Nelson T.W.; and Sorensen C.D., 2007, Torque based weld power model for friction stir welding, Science and Technology of Welding and Joining, Vol. 12, 4, pp. 341-347.

66. Roth A., Hake T., and Zaeh M.F., 2014, An Analytical Approach of Modelling Friction Stir Welding, Vol. 18, pp. 197–202.

67. Long T., Tang W., and Reynolds A. P., 2007, Process Response Parameter Relationships in Aluminium Alloy Friction Stir Welds, Science and Technology of Welding and Joining, Vol. 12 (4): pp. 311-317.

68. Nemat-Nasser S., Wei-Guo G., 2003, Thermomechanical response of DH-36 structural steel over a wide range of strain rates and temperatures, Mechanics of Materials, Vol. 35, pp. 1023–1047.

69. Klepaczko J.R., Rusinek A., Rodríguez J.A., Pecherski R.B., Arias A., 2009, Modelling of thermo-viscoplastic behaviour of DH-36 and Weldox 460-E structural steels at wide ranges of strain rates and temperatures, comparison of constitutive relations for impact problems , Mechanics of Materials, Vol. 41, pp. 599–621.

70. American Petroleum Institute, "Specification for line pipe," American Petroleum Institute, 2009.

71. Zheng L., Gao S., 2005, Production and application of high strength and high toughness pipeline steel with acicular ferrite,http://www.metal. citic.com /iwcm/UserFiles/img/cd/2005-HSLA-NB/HSLA-006.pdf.

72. Nandan, R., Debroy, T. & Bhadeshia, H., 2008, Recent advances in friction-stir welding – process, weldment structure and properties. Progress in Materials Science, Vol. 53(6), pp.980–1023.

73. Honeycomb R. W. and Bhadeshia H. K., 1995, Steels Microstructure and properties, 2nd edn, 133; London.

74. Pawłowski, B., 2011. Critical points of hypoeutectoid steel - prediction of the pearlite dissolution finish temperature Ac1 , JAMME , Vol. 49(2), pp.331–337.

75. Gautam J., Miroux A., Moerman J., Barbattic C, Van P. and Kestens L., 2012, Determination of the non-recrystallisation temperature (Tnr) of austenite in high strength C-Mn steels, Material Sci. Forum, Vol. 706, pp 2722-2727.

76. Failla D. M., 2009, Friction Stir Welding and Microstructure Simulation of HSLA-65 and Austenitic Stainless Steels, Ph.D Thesis, The Ohio State University.

77. Martino Di and Thewlis S.F, 2013, Transformation Characteristics of Ferrite/Carbide Aggregate in Continuously Cooled, Low Carbon-Manganese Steels. Metallurgical and Materials Transactions A, Vol. 45(2), pp.579–594.

78. Toumpis A., Gallawi A., Cater S., McPherson N., 2014, Development of a process envelope for friction stir welding of DH36 steel – A step change. Materials & Design, Vol. 62, pp.64–75.

79. Reynolds A. P., Tang W., Posada M. and DeLoach, J., 2003, Friction stir welding of DH36 steel, Science and Technology of Welding and Joining, Vol. 8, No. 6, pp.455-460.

80. Denise L., Susanne K. M. & Christian B., 2017, Acicular Ferrite Formation and Its Influencing Factors - A Review, Journal of Materials Science Research; Vol. 6, 1, pp. 24-43.

81. Bhadeshia H K and Honeycombe R W, 2006, Steels microstructure and properties,3rd edition. Cabmridge university, UK.

82. Bhadeshia H. K., 2001, Bainite in Steels - 2nd Edition , Cabmridge university, UK.

83. Hong S.G., Jun H.J., Kang K.B., Park C.G., 2003, Evolution of precipitates in the Nb–Ti–V micro-alloyed HSLA steels during reheating, Scripta Materialia, Vol. 48, pp. 1201–1206.

84. Cuddy L. J., 1985, Encyclopaedia of materials science and engineering, Oxford, Pregamom.

85. Fernández J., Illescas S., Guilemany J.M., 2007, Effect of microalloying elements on the austenitic grain growth in a low carbon HSLA steel, Materials Letters, Vol. 61, pp. 2389–2392.

86. Cuddy L. J., 1982, The Effect of Micro-alloy Concentration on the Recrystallization of Austenite During Hot Deformation, Thermomechanical Processing of Micro-alloyed Austenite, pp. 129-140.

87. Stock J., Enloe, C.M., Malley O., and Findle R.J., 2014, Cooling Rate Effects on the As-Cast Titanium Nitride Precipitation Size Distribution in a Low-Carbon Steel AIST Transactions, Vol. 11, No.4, pp. 180-186.

88. Nagata M. T., John G. S., and David K. M. , 2002, Titanium nitride precipitation behavior in thin-slab cast high-strength low-alloy steels, Metallurgical and Materials Transactions A, Vol. 33A, pp.3099-3110.

89. EL-fawakhry K. A., Mohammed F., Michael L. M. and Mamdouh M. E., 1991, Characterization of Precipitates in Vanadium and Titanium Micro-alloyed Steels, ISIJ International, Vol. 31. No. 9, pp. 1020-1025.

90. Wang M., Guo-guang C., Sheng-tao Qiu, Pei Z., and Yong G., 2010, International Journal of Minerals, Metallurgy and Materials, Volume 17, Number 3, P 276-281.

91. Hong, S.G., Jun H. J., Kang K. B., C.G Park, 2003, Scripta Materialia, Vol. 48 (8), pp.1201–1206.

92. McPherson NA, Galloway AM, Cater S., and Hambling S.J., 2013, Friction stir welding of thin DH36 steel plate. Sci Technol Weld Join; Vol. 18(5), pp.441–450.

93. Lienert T. J., 2004, Friction Stir Welding of DH-36 Steel, Proceedings from Joining of Advanced and Specialty Materials, Pittsburgh, Pennsylvania, ASM International.

94. Fowler S., Toumpis A., Galloway A., 2016, Fatigue and bending behavior of friction stir welded DH36 steel, The International Journal of Advanced Manufacturing Technology, Vol. 84, 9, pp 2659–2669.

95. Barnes S.J. , Bhatti A.R., Steuwer A., Johnson R., ALtenkirch J. and Withers P.J., 2012, Friction Stir Welding in HSLA-65 Steel: Part I. Influence of Weld Speed and Tool Material on Microstructural Development, Metallurgical and Materials Transactions A, Vol. 43A, pp. 2342-2355.

96. Lienert T. J., Stellwag W. L.,. Grimmett B. B and Warke R. W., 2003, Friction Stir Welding Studies on Mild Steel., Welding Journal, pp.1–9.

97. Lakshminarayanan A. K., Balasubramanian V., Salahuddin M, 2010, Microstructure, Tensile and Impact Toughness Properties of Friction Stir Welded Mild Steel, Journal of Iron and Steel Research International, Vol. 17, 10, pp.68-74.

98. Ozekcin, A., 2004, A Microstructural Study of Friction Stir Welded Joints of Carbon Steels. , International Journal of Offshore and Polar Engineering, Vol. 14, 4, pp. 284-288.

99. Cho H-H, Kang SH, Kim S-H, Oh KH, Kim HJ, Chang W-S, and Han H. N., 2012, Microstructural evolution in friction stir welding of high-strength line-pipe steel. Mater Des; Vol. 34, pp. 258–267.

100. Cui, L., Hidetoshi F., Nobuhiro T., Kazuhiro N., Kiyoshi N., Rinsei I and Muneo M., 2007, Transformation in Stir Zone of Friction Stir Welded Carbon Steels with different carbon content, ISIJ International , Vol. 47, 2, pp.299–306.

101. Fujii H. , Cui L., Tsuji N., Maedac M., Nakata K., Nogi K., 2006, Friction stir welding of carbon steels, Materials Science and Engineering A, Vol. 429, pp. 50–57.

102. Chung Y.D., Fujii H., Uejib R. and Tsujic N., (2010), Friction stir welding of high carbon steel with excellent toughness and ductility, Scripta Materialia, Vol. 63, pp. 223–226.

103. Chung Y. D., Fujii H., Ueji R. & Nogi K., 2009, Friction stir welding of hypereutectoid steel (SK5) below eutectoid temperature Science and Technology of Welding and Joining, Vol. 14, 3, pp. 233-238.

104. Sato Y.S, Yamanoi H., Kokawaa H. , Furuhara T., 2007, Microstructural evolution of ultrahigh carbon steel during friction stir welding, Scriptia Materialia , Vol. 57, 6, pp.557–560.

105. Choi D.H., Lee C. Y., Ahn B. W., Choi J., Yeon Y. M., SongK., Hong S., Lee W., Bang K., Jung S. B. , 2011, Hybrid Friction Stir Welding of High-carbon Steel, J. Mater. Sci. Technol., 2011, Vol. 27(2), pp. 127-130.

106. Elangovan K., Balasubramanian V., 2007, Influences of pin profile and rotational speed of the tool on the formation of friction stir processing zone in AA2219 aluminium alloy, Materials Science and Engineering A, Vol. 459, pp 7–18.

107. Lakshminarayanan A. K., and Balasubramanian V., 2011, Understanding the Parameters Controlling Friction Stir Welding of AISI 409M Ferritic Stainless Steel, Met. Mater. Int., Vol. 17, No. 6, pp. 969-981.

108. Roman R., Martin K., 2014, Friction stir welded structures: Kissing bond defects, International Journal of Terra-space Science and Engineering, Vol. 6(2), pp. 77-83.

109. Kima Y.G., Fujii H., Tsumura T., Komazaki T., and Nakata K., 2006, Three defect types in friction stir welding of aluminium die casting alloy, Materials Science and Engineering A, Vol. 415, pp. 250–254.

110. Tingey C., Galloway A., Toumpis A. , Cater S., 2015, Effect of tool centreline deviation on the mechanical properties of friction stir welded DH36 steel, Materials & Design , Vol. 65, pp. 896–906.

111. Han J., Li H., Zhu Z., Barbaro F., Jiang L., Xu H., 2014, Microstructure and mechanical properties of friction stir welded 18Cr–2Mo ferritic stainless steel thick plate, Mater. Des., Vol. 63, pp. 238–246.

112. Gibson B.T., Lammlein D.H., Prater T.J.,. Longhurst W.R, Cox C.D., Ballun M.C., 2014, Friction stir welding: process, automation, and control, J. Manuf. Process, Vol. 16, pp. 56–73.

113. Kim Z. Y.G., Fujii H., Tsumura T. , Komazaki T., Nakata K., 2006, Three defect types in friction stir welding of aluminium die casting alloy, Materials Science and Engineering A, Vol. 415, pp. 250–254.

114. Threadgill P.L., 2007, Terminology in friction stir welding, Sci. Technol. Weld. Join., Vol. 12, pp. 357–360.

115. British Standards Institution, 2013, Guide to methods for assessing the acceptability of flaws in metallic structures. BS 7910. London.

116. Hattel J., Sonne M. R , Tutum C.,2015, Modelling residual stresses in friction stir welding of Al alloys—a review of possibilities and future trends, Int J Adv Manuf Technol, Vol. 76, pp.1793–1805.

117. TWI company, 2015, UK, accessed June 2017, Residual Stresses, <http://www.twi-global.com/capabilities/integrity-management/engineering-critical-assessment/residual-stresses/>.

118. Fratini L., Pasta S., Reynolds A.P., 2009, Fatigue crack growth in 2024-T351 friction stir welded joints: longitudinal residual stress and microstructural effects, Int. J. Fatigue, Vol. 31, pp. 495-500.

119. Wang L., Davies C.M., Wimpory R.C., Xie L.Y., Nikbin K.M., 2010, Measurement and simulation of temperature and residual stress distributions from friction stir welding AA2024 Al alloy, Mater. High Temperatures, Vol. 27, pp. 167-178.

120. Altenkirch J., Steuwer A., Withers P.J., 2010, Process microstructure property correlations in Al_Li AA2199 friction stir welds, Sci. Technol. Weld. Joining, Vol. 15, pp. 522-527.

121. Gachi S., Belahcene F., Boubenider F., 2009, Residual stresses in AA7108 aluminium alloy sheets joined by friction stir welding, Nondestr. Test. Eval., Vol. 24, pp. 301-309.

122. Camilleri D., Micallef D. & Pierluigi M., 2015, Thermal Stresses and Distortion Developed in Mild Steel DH36 Friction Stir-Welded Plates: An Experimental and Numerical Assessment, Journal of Thermal Stresses, Vol. 38, 5, pp. 485-508.

123. Colegrove P., Chukwugozie I., Thistlethwaite A., Williams S., Nagy T., Wojciech S., Axel S. and Thilo P., 2009, The welding process impact on residual stress and distortion Sci. and Tech. of Weld and Join, Vol. 14 (8), pp 717-725.

124. Chen C.M. and Kovacevic R., 2006, Parametric Finite Element Analysis of Stress Evolution during Friction Stir Welding, the Proceedings of the Institution of Mechanical Engineers, Part B, Journal of Engineering Manufacture, Vol. 220, pp. 1359-1371.

125. Feng Z., Wang X. L., David S. A., Sklad S. P, 2007, Modelling of residual stresses and property distributions in friction stir welds of aluminium alloy 6061-T6 , Science and Technology of Welding and Joining, Vol. 12, 4, pp. 348-356.

126. Buffa G., Fratini L., Pasta S., 2009, Residual stresses in friction stir welding: numerical simulation and experimental verification, JCPDS-International Centre for Diffraction Data ISSN 1097-0002., pp. 444-453.

127. Nourani M., Milani A., Yannacopoulos S. and Yan C., 2014, Predicting residual stresses in friction stir welding of aluminium alloy 6061 using an integrated multi-physics model, Material Science Forum, Vols 768-769, pp. 682-689.

128. Luo Q., and Jones A. H., 2010, High-precision determination of residual stress of polycrystalline coatings using optimised XRD-sin2ψ technique. Surface & Coatings Technology, Vol. 205, pp. 1403-1408.

129. Withers, P.J. , Preuss M., Steuwer A., Pang J. W., 2007, Methods for obtaining the strain-free lattice parameter when using diffraction to determine residual stress. Journal of Applied Crystallography, vol. 40 (5), pp. 891–904.

130. Genzela Ch., Klausa M., Denksa I., Wulz H.G., 2005, Residual stress fields in surface-treated silicon carbide for space industry comparison of biaxial and tri-axial analysis sing different X-ray methods Materials Science and Engineering A, Vol. 390, pp. 376–384.

131. Klaus M. and Genzel Ch., 2017, Non-destructive separation of residual stress and composition gradients in thin films by angle and energy dispersive X-ray diffraction. Int. Theoretical concepts, J. Appl. Cryst., Vol. 50, pp. 252-264.

132. Fitzpatrick M.E., Fry A.T., Holdway P., Kandil F.A., Shackleton J.and Suominen L., 2005, Determination of Residual Stresses by X-ray Diffraction, Measurement Good Practice Guide No. 52, – Issue 2.

133. Steuwer A., Barnes S.J., Altenkirch J., Johnson R., and Withers P.J., 2012, Friction Stir Welding of HSLA-65 Steel: Part II. The Influence of Weld Speed and Tool Material on the Residual Stress Distribution and Tool Wear, Metallurgical and Materials Transactions A, Vol.43A, pp. 2356-2365.

134. Lombard H., Hattingh D.G., Steuwer A., James M.N., 2009, Effect of process parameters on the residual stresses in AA5083-H321 friction stir welds, Materials Science and Engineering A, Vol. 501, pp. 119–124.

135. Kumar A., Welzel U., and Mittemeijer E. J., 2006, Depth dependence of elastic grain interaction and mechanical stress: Analysis by x-ray diffraction measurements at fixed penetration/information depths, J of App Phy, Vol. 100, 114904.

136. Kumar N., Mishra R.S., Baumann J.A., 2014, Residual Stresses in Friction Stir Welding, Elsevier Inc.,Oxford, UK.

137. Altenkirch J., Steuwer A., Peel M., Richards D.G., Withers P.J., 2008, The effect of tensioning and sectioning on residual stresses in aluminium AA7749 friction stir welds, Mater. Sci. Eng. A Struct. Mater., Vol. 488, pp16-24.

138. Altenkirch J., Steuwer A., Peel M.J., Withers P.J., 2009, The extent of relaxation of weld residual stresses on cutting out cross-weld test-pieces, Powder Diffr., Vol. 24 (2), pp S31-S36.

139. Fehrenbacher A., Schmale, J. R., Zinn, M. R., & Pfefferkorn F. E., 2014, Measurement of Tool-Workpiece Interface Temperature Distribution in Friction Stir Welding. Journal of Manufacturing Science and Engineering, Vol. 136 (2), pp. 21009-1-21009-8.

140. Medina S. F., Quispe A. , Manuel G., 2014, Model for Strain-Induced Precipitation Kinetics in Micro-alloyed Steels, Metallurgical and Materials Transactions A, Vol. 45, Issue 3, pp 1524–1539.

141. Madina S. F.and Mancilla J. E., 1994, Static recrystallization of austenite and strain induced precipitation kinetics in titanium microalloyed steels, Acta metall. mater. Vol. 42, 12, pp. 3945-3951.

142. Zhu Z. H., Qiu S. T., 2012, Effect of Strain Rate on Nb(C,N) Precipitation in Micro Alloy Steel Slab, Advanced Materials Research, Vols. 535-537, pp. 633-638.

143. Takashi T., Takeshi F., Kazuya H. and Kazuhiko H., 2006, Austenite Grain Stability of Titanium-Modified Carburizing Steel, Solid State Phenomena Vol. 118 pp 3-8.

144. Gong P., Palmiere E.J., Rainforth W.M., 2015, Dissolution and precipitation behaviour in steels microalloyed with niobium during thermomechanical processing, Acta Materialia, Vol. 97, pp. 392–403.

145. Pickering F. B., The Basis of Quantitative Metallography, Institute of Metallurgical Technicians, London, 1976.

146. Arora A., Nandan R., Reynolds A.P. and DebRoy T., 2009, Torque, power requirement and stir zone geometry in friction stir welding through modelling and experiments, Scripta Materialia, Vol. 60, pp. 13–16.

147. Atharifar H., Lin D., and Kovacevic R ,2009, Numerical and Experimental Investigations on the Loads Carried by the Tool During Friction Stir Welding, Journal of Materials Engineering and Performance, Vol. 18 (4), pp. 339-350.

148. Jacquin, D., Meester B., Simar A., Deloison D., Montheillet F., Desrayaud C. , 2011. A simple Eulerian thermomechanical modeling of friction stir welding, Journal of Materials Processing Technology, Vol. 211(1), pp.57–65.

149. Grujicic, M., Arakere G., Yalavarth H.V, Yen C-F and Cheeseman B.A, 2010, Modelling of AA5083 Material-Microstructure Evolution During Butt Friction-Stir Welding. Journal of Materials Engineering and Performance, Vol. 19(5), pp.672–684.

150. ANSYS Company, 1978, accessed Aug 2016, <http://perso.crans.org/epalle/M2/MFNA/ SNECMA_14.5_L08_Mesh_Quality.pdf>.

151. ANSYS company, 1978, USA, accesses Aug 2016, Workbench help viewer manual 2016.

152. Darvazi, A.R. & Iranmanesh, M., 2014, Thermal modelling of friction stir welding of stainless steel 304L. The International Journal of Advanced Manufacturing Technology, Vol. 75 (9-12), pp.1299–1307.

153. Subrata P., Phaniraj M.P., 2015, Determination of heat partition between tool and workpiece during FSW of SS304 using 3D CFD modelling, Journal of Materials Processing Technology, Vol. 222, pp. 280–286.

154. Theodore B. L., Incropera F. P., David P., and Adrienne L. S., 2011, Fundamentals of Heat and Mass Transfer, 7th E,John Wiley and sons, USA.

155. Khandkar M. Z., Khan, J. A. & Reynolds, A. P., 2003. Prediction of temperature distribution and thermal history during friction stir welding: input torque based model, Science and Technology of Welding and Joining, Vol. 8(3), pp.165–174.

156. Lenard, J., Pietrzyk, M., and Cser, L., 1999, Mathematical and Physical Simulation of the Properties of Hot Rolled Products, Elsevier, Amsterdam pp.1-10.

157. Rie E., Masaya S., Masahiro S., 2010, Thermal-Conductivity Measurements and Predictions for Ni–Cr Solid Solution Alloys, Int. J. Thermophys , Vol. 31, pp. 1991–2003.

158. Nagasaka and Nishihara, 2003, Measurement of tool temperature during friction stir welding, Proceeding of forth international symposium on FSW, Park city, Utah.

159. Upadhyay P. and Reynolds A., 2011, Effects of Forge Axis Force and Backing plate Boundary Condition on FSW of AA6056, Friction Stir Welding and Processing, Vol. VI, pp. 147-158.

160. Mishra R. S.; Murray W. M., 2007, Friction Stir Welding and Processing, (ASM International, pp 163-167.

161. Al-Moussawi M., Smith A. J., Young A., Cater S. and Faraji M., 2016, An advanced numerical model of friction stir welding of DH36 steel, 11th Int. Symp. FSW, TWI Granta Park Cambridge, UK.

162. Madariaga I., Gutie´rrez I., Garcı´a-de C. A. and Capdevila C., 1999, Acicular ferrite formation in a medium carbon steel with a two stage continuous cooling, Scripta Materialia, Vol. 41, Issue 3, pp. 229–235.

163. Karmakar A., Kundu S., Roy S., Neogy S., Srivastava D.& Chakrabarti D., 2014, Effect of micro-alloying elements on austenite grain growth in Nb–Ti and Nb–V steels, Materials Science and Technology, Vol. 30 (6), pp 653-664.

164. Yamini Sima, 2008, Effect of titanium additions to low carbon, low manganese steel on sulphide precipitation, PhD Theses, University of Wollongong.

165. Zhang Y., Xu G., Zhou M. X., Yang H. L., Wang M., 2014, The Effect of Reheating Temperature on Precipitation of a High Strength Micro-alloyed Steel, Applied Mechanics and Materials, Vol. 508, pp. 8-11,

166. Jinlong Du, 2012, Examination of the effect of tin particles and grain size on the Charpy impact transition temperature in steels, M.Res. Ph.D thesis, University of Birmingham.

167. Dehghan-Manshadi A. and Dippenaar R. J., 2010, The behaviour of precipitates during hot deformation of low-manganese, titanium-added pipeline steels, Metallurgical and Materials Transactions A, Vol. 41A, pp. 3291-3296.

168. DeArdo A. J., 2003, Niobium in modern steels, International Materials Reviews, Vol. 48, pp. 371–402.

169. Stein G., Kirschner W. and Lueng J., 1997, pp104-115.Editors: Edward G Nisbett , Albert S Melilli , Steel Forgings: Second volume, Astm Special Technical Publication.

170. Shiraiwa T. , N. Fujino, 1969, Vth International Congress on X-Ray Optics and Microanalysis, Tübingen, September 9th–14th, pp 531-534.

171. Stock J., Enloe, C.M., Malley O, Findle R.J., 2014, AIST Transactions, Vol. 11, No.4, pp. 180-186.

172. Minna L., Mechanism and Kinetics of Transformation of Alumina Inclusions in Steel by Calcium Treatment, Doctoral Thesis, Helsinki University of Technology, 2006.

173. Al-Moussawi M., Smith A. J., Young A., Cater S. & Faraji M., 2017, Modelling of friction stir welding of DH36 steel, Int J Adv Manuf Technol, Published online 24 Feb 2017 on 10.1007/s00170-017-0147-y.

174. Orlando León-García, Roumen Petrov, Leo A.I. Kestens, 2010, Void initiation at TiN precipitates in IF steels during tensile deformation, Materials Science and Engineering A 527, 4202–4209.

175. J. H. Chen and R. Cao, 2015, Micro-mechanism of Cleavage Fracture of Metals, Chapter 3, p81-140, Elsevier Inc.

176. Smith A. J., AL-Moussawi M., Young, A. E., Cater S. and Faraji, M., 2016, Modelling of friction stir welding of 304 stainless steel. In: European Simulation and Modelling Conference, Univ. of Las Palmas.

177. Elbanhawy A., Chevallier E., Domin K., 2013, Numerical investigation of friction stir welding of high temperature materials, NAFEMS world congress, Salzburg, Austria.

178. Yang K. Y., Dong H., Kou S., 2008, Liquation tendency and Liquid-Film Formation in Friction Stir Spot Welding, Welding Journal, Vol. 87, pp. 202-211.

179. Leonard E. S., 1999, Light microscopy of carbon steel, ASM International, USA.

180. Wang H., Colegrove P.A., Santos J., 2013, Hybrid modelling of 7449-T7 aluminium alloy friction stir welded joints. Sci Technol Weld Join; Vol. 18, pp. 147–153.

181. Enkhsaikhan B., and Edward C., 2009, Detecting Wormholes in Friction Stir Welds from Welding Feedback Data, Midwest instruction and computing symposium, South Dakota, USA.

182. British standard EN-BS 895:1995, destructive tests on welds in metallic materials.

183. BS EN 15305:2008, Non-destructive testing-Test method for residual stress analysis by X-ray Diffraction.

8. Appendix A
User Defined Function (UDF)

```c
#include "udf.h"
```
1-Calculating the viscosity

```c
DEFINE_PROPERTY(viscosity, c, t)
{

    real Tref = 1473;
    real Q = 450000;
    real R=8.31;

    real visco;
    real temp = fabs(C_T(c, t));
    real strainrate = fabs(C_STRAIN_RATE_MAG(c, t));
    //Strain rate
real strainrate = sqrt(1/3*((C_DUDX(c, t)*(C_DUDX(c, t) + C_DUDX(c, t)) + C_DUDY(c, t)*
(C_DUDY(c, t) + C_DVDX(c, t)) + C_DUDZ(c, t)*(C_DUDZ(c, t) + C_DWDX(c, t))) + (C_DVDX(c,
t)* (C_DVDX(c, t) + C_DUDY(c, t)) + C_DVDY(c, t)* (C_DVDY(c, t) + C_DVDY(c, t)) +
C_DVDZ(c, t)*(C_DVDZ(c, t) + C_DWDY(c, t))) + (C_DWDX(c, t)*(C_DWDX(c, t) + C_DUDZ(c, t))
+ C_DWDY(c, t)* (C_DWDY(c, t) + C_DVDZ(c, t))
    + C_DWDZ(c, t)*(C_DWDZ(c, t) + C_DWDZ(c, t)))));

    real arreniuos = exp(((1 / temp) - (1 / Tref))*Q / R);
    real n = (0.2+3.966e-4*temp);

    real consistency = 500000000 - 327000 * temp;

    if (strainrate <= 0)

            visco = 3e9;
    else
            visco = (consistency*pow(strainrate, n - 1)*arreniuos);

    // , 1 / (0.2 + 3.966e-4*temp))))) / (3 * (strainrate));
    //printf("consistency:%g/n", consistency);
    //printf("viscoosity:%d\n", visco);
    //printf("strainrate:%g\n", strainrate);
    //printf("Arrenious:%g\n", arreniuos);
    //printf("temperature:%g\n", temp);
    //printf("viscoosity:%g\n", visco);
    //visco = strainrate;
    //printf("zener:%g\n", zener);
    //printf("n:%g\n", n);
    return visco;
    //printf("viscoosity:%g\n", visco);

}
```

2. Thermal Coductivity

```
DEFINE_PROPERTY(kimproved,c,t)
{
   real ktc;
    real temp = C_T(c,t);
     ktc = 23.16+51.96*exp(-2.03*temp*0.001);
   return ktc;
}
```

3.Sticking/Slipping heat flux at tool shoulder

```
DEFINE_PROFILE(Frictional_heat_flux,thread,index)
{
real x[ND_ND];
#define omega0 21
#define Rmax 0.012
#define deltao 0.37
#define muef 0.4
real mue;
real omegaV;
real temp;
real sticking;
real theta;
real R;
real pressure;
real yielstress;
real area = 0.001499;
real axialforce = 57500;
face_t f;
begin_f_loop(f,thread)
{
F_CENTROID(x,f,thread);
temp=F_T(f,thread);
if (temp <= 1000)
yielstress = (162.45-0.0159*temp)*1000000;
else
{
      yielstress = (483.67 - 0.3526*temp) * 1000000;
}
theta = -atan2(x[0], x[2]);
R = sqrt((x[2] * x[2]) + (x[0] * x[0]));
omegaV = omega0*R / Rmax;
sticking = 1 - exp(-1 * omegaV*R / (deltao*omega0*Rmax));
mue = muef*exp(-1 * sticking*omegaV*R);
pressure = axialforce / area;
F_PROFILE(f, thread, index) = ((sticking)*R*omega0*(yielstress)+(1-
sticking)*mue*omega0*R*(pressure))*1000;
//printf("heat flux shoulder:%g/n", F_PROFILE(f, thread, index));
//printf("sticking:%g/n", sticking);
}
end_f_loop(f,thread)
//printf("sticking:%g\n", sticking);
//printf("R:%g\n", R);
//printf("friction coeffecient:%g\n", mue);
//printf("Temperature:%g\n", temp);
//printf("omega:%g\n", omegaV);
```

```c
//printf("yielstress shoulder:%g/n", yielstress);
}




4.Sticking/Slipping heat flux at tool probe

DEFINE_PROFILE(Frictional_heat_flux_probe, thread, index)
{
        real x[ND_ND];
#define omega0 21

#define deltao 0.37
#define muef 0.4
        real mue;
        real omegaV;
        real temp;
        real sticking;
        real theta;
        real R;
        real Rma= 0.005;
        real area = 0.0003732;
        real axialforce = 57500;
        real pressure;
        real yielstress;
        face_t f;
        begin_f_loop(f, thread)
        {
                F_CENTROID(x, f, thread);
                temp = F_T(f, thread);
                if (temp <= 1000)
                        yielstress = (162.45 - 0.0159*temp) * 1000000;
                else
                {
                        yielstress = (483.67 - 0.3526*temp) * 1000000;
                }
                theta = -atan2(x[0], x[2]);
                R = sqrt((x[2] * x[2]) + (x[0] * x[0]));
                omegaV = omega0*R / Rma;
                sticking = 1 - exp(-1 * omegaV*R / (deltao*omega0*Rmax));
                mue = muef*exp(-1 * sticking*omegaV*R);
                pressure = axialforce / area;
                F_PROFILE(f, thread, index) = ((sticking)*R*omega0*(yielstress) +
sticking*mue*omega0*R*(pressure))*1000;

                //printf("heat flux probe:%g/n", F_PROFILE(f, thread, index));
                //printf("pressure:%g/n", pressure);
                //printf("yielstress:%g/n", yielstress);
        }
        end_f_loop(f, thread)
                //printf("sticking:%g\n", sticking);
        //printf("R:%g\n", R);
        //printf("friction coeffecient:%g\n", mue);
        //printf("Temperature:%g\n", temp);
        //printf("omega:%g\n", omegaV);
}
```

5. Representing Shoulder velocities in (X, y and z directions)

```
DEFINE_PROFILE(horizontal_velocity_sh, thread, index)
{
        real x[ND_ND];
#define omega 21
#define Rmax 0.012
#define deltao 0.37
        real omegaV;
        //real temp;
        real sticking;
        real theta;
        real R;
        face_t f;
        begin_f_loop(f, thread)
        {
                F_CENTROID(x, f, thread);
                        theta = -atan2(x[0] , x[2]);
                        R = sqrt((x[2] * x[2]) +(x[0] * x[0]));
                        omegaV = omega*R / Rmax;
                        sticking =1- exp(-1*omegaV*R/(deltao*omega*Rmax));
                F_PROFILE(f, thread, index) =(1-sticking)*omega*R*sin(theta);
                        //F_PROFILE(f, thread, index) = omega*R*sin(theta);
        }
        end_f_loop(f, thread)
                //printf("sticking:%g\n", sticking);
        //printf("R:%g\n", R);
}

DEFINE_PROFILE(lateral_velocity_sh, thread, index)
{
        real x[ND_ND];
#define omega 21
#define Rmax 0.012
#define deltao 0.37
        real omegaV;
        //real temp;
        real sticking;
        real theta;
        real R;
        face_t f;
        begin_f_loop(f, thread)
        {
                F_CENTROID(x, f, thread);
                theta = -atan2(x[0], x[2]);
                R = sqrt((x[2] * x[2]) + (x[0] * x[0]));
                omegaV = omega*R / Rmax;
                sticking = 1-exp(-1 * omegaV*R / (deltao*omega*Rmax));
                F_PROFILE(f, thread, index) = (1-sticking)*omega*R*cos(theta);
                //F_PROFILE(f, thread, index) = omega*R*cos(theta);
        }
        end_f_loop(f, thread)
                }

DEFINE_PROFILE(normal_velocity_sh, thread, index)
{
        real x[ND_ND];
#define omega 21
```

```
#define Rmax 0.012
#define deltao 0.37
#define pitch 2
        real omegaV;
        real R;
        face_t f;
        begin_f_loop(f, thread)
        {
                F_CENTROID(x, f, thread);
                R = sqrt((x[2] * x[2]) + (x[0] * x[0]));
                omegaV = omega*R / Rmax;
                //F_PROFILE(f, thread, index) = pitch*omegaV*R/(2*3.14);
                F_PROFILE(f, thread, index) =-1* pitch*omega*R / (2 * 3.14);
                //printf("normal-velocity-shoulder:%g\n", F_PROFILE(f, thread, index));
        }
        end_f_loop(f, thread)
}

6. Representing Probe-side velocities in (X, y and z directions)


DEFINE_PROFILE(horizontal_velocity_probside, thread, index)
{
        real x[ND_ND];
#define omega 21
#define Rp 0.005
#define deltao 0.37
        real omegaV;
        //real temp;
        real sticking;
        real theta;
        real R;
        face_t f;
        begin_f_loop(f, thread)
        {
                F_CENTROID(x, f, thread);
                theta = -atan2(x[0], x[2]);
                R = sqrt((x[2] * x[2]) + (x[0] * x[0]));
                omegaV = omega*R / Rp;
                sticking = 1 - exp(-1 * omegaV*R / (deltao*omega*Rmax));
                F_PROFILE(f, thread, index) = (1 - sticking)*omega*R*sin(theta);
                //F_PROFILE(f, thread, index) = omega*R*sin(theta);
                //printf("horizontal-velocity:%g\n", F_PROFILE(f, thread, index));
        }
        end_f_loop(f, thread)

                }

DEFINE_PROFILE(lateral_velocity_probeside, thread, index)
{
        real x[ND_ND];
#define omega 21
#define Rp 0.005
#define deltao 0.37
        real omegaV;
        //real temp;
        real sticking;
        real theta;
```

```
        real R;
        face_t f;
        begin_f_loop(f, thread)
        {
                F_CENTROID(x, f, thread);
                theta = -atan2(x[0], x[2]);
                R = sqrt((x[2] * x[2]) + (x[0] * x[0]));
                omegaV = omega*R / Rp;
                sticking = 1 - exp(-1 * omegaV*R / (deltao*omega*Rmax));
                F_PROFILE(f, thread, index) = (1 - sticking)*omega*R*cos(theta);
            //F_PROFILE(f, thread, index) = omega*R*cos(theta);
                //printf("lateral-velocity:%g\n", F_PROFILE(f, thread, index));
        }
        end_f_loop(f, thread)


                }

DEFINE_PROFILE(normal_velocity_probeside, thread, index)
{
        real x[ND_ND];
#define omega 21
#define Rp 0.005
#define deltao 0.37
#define pitch 2
        real omegaV;
        real R;
        face_t f;
        begin_f_loop(f, thread)
        {
                F_CENTROID(x, f, thread);
                R = sqrt((x[2] * x[2]) + (x[0] * x[0]));
                omegaV = omega*R / Rp;
                //F_PROFILE(f, thread, index) = pitch*omegaV*R / (2 * 3.14);
                F_PROFILE(f, thread, index) = -1*pitch*omega*R / (2 * 3.14);
                //printf("normal-velocity-probe:%g\n", F_PROFILE(f, thread, index));
        }
        end_f_loop(f, thread)

}
```